REPORT DOCUMENTATION PAGE

Form Approved OMB No. 0704-0188

1. AGENCY USE ONLY (Leave blank)	2. REPORT DATE	3. REPORT TYPE AND DATES COVERED
	1999	Conference Proceeding

4. TITLE AND SUBTITLE

Gaseous and Heterogeneous Detonations: Science to Applications

5. FUNDING NUMBERS

N00014-98-1-1055

6. AUTHOR(S)

Gabriel D. Roy, Sergei M. Frolov, Kazhikathra Kailasanath, Nicolay N. Smirnov (Editors)

7. PERFORMING ORGANIZATION NAME(S) AND ADDRESS(ES)

ENAS Publishers Ltd
Kashirskoe Shosse, 22-3
Moscow 115201/Russia

8. PERFORMING ORGANIZATION REPORT NUMBER

ISBN 5-89055-016-0

9. SPONSORING/MONITORING AGENCY NAME(S) AND ADDRESS(ES)

Office of Naval Research International Field Office
PSC 802 Box 39
FPO AE 09499-0039

10. SPONSORING/MONITORING AGENCY REPORT NUMBER

11. SUPPLEMENTARY NOTES

Papers presented at the International Colloquium on Advanced Experimentation & Computation of Detonations, September 14-17 1998, St. Petersburg, Russia.
This work relates to Department of Navy Grant N00014-98-1-1055 issued by the Office of Naval Research-Europe.
The United States has a royalty free license to exercise all rights under the Copyright claimed herein for Government Purposes.

12a. DISTRIBUTION/AVAILABILITY STATEMENT

Approved for Public Release; Distribution Unlimited.
Government Purpose Rights License. All other rights reserved by the copyright holder ENAS Publishers Ltd.

12b. DISTRIBUTION CODE

A

12. ABSTRACT (Maximum 200 words)

This document contains twenty-four selected papers presented at the International Colloquium on Advanced Experimentation & Computation of Detonations, September 14-17 1998, St. Petersburg, Russia. The papers discuss recent advances made in understanding detonation wave initiation, propagation, mitigation and control through experimental and computational studies. The book contains five Parts: Detonation Initiation, Detonation Wave Structure and Propagation, Detonation Mitigation and Congrol, Applications of Detonation Phenomena, and Detonability of Advanced Fuels. The volume is intended to be a tool to explore the international state of the art and an avenue for further follow-up for the researchers and practicing engineers.

14. SUBJECT TERMS

Conference proceeding, Detonations, Fuels, Engines

15. NUMBER OF PAGES

366

16. PRICE CODE

17. SECURITY CLASSIFICATION OF REPORT	18. SECURITY CLASSIFICATION OF THIS PAGE	19. SECURITY CLASSIFICATION OF ABSTRACT	20. LIMITATION OF ABSTRACT
UNCLASSIFIED	UNCLASSIFIED	UNCLASSIFIED	UL

GASEOUS AND HETEROGENEOUS
DETONATIONS:
SCIENCE TO APPLICATIONS

Edited by

Gabriel D. Roy
Office of Naval Research
Arlington, VA, USA

Sergei M. Frolov
N. N. Semenov Institute of Chemical Physics
Moscow, Russia

Kazhikathra Kailasanath
Naval Research Laboratory
Washington, DC, USA

Nickolay N. Smirnov
M. V. Lomonosov Moscow State University
Moscow, Russia

AQ F01-07-1422

Twenty-four selected papers on various aspects of detonation physics and chemistry presented at the International Colloquium on Advanced Experimentation & Computation of Detonations held in St.-Petersburg, September 14-17, 1998, are assembled together in this volume. Presented in the book are the recent advances made in understanding detonation wave initiation, propagation, mitigation, and control through experimental and computational studies. The book contains five Parts: Detonation Initiation, Detonation Wave Structure and Propagation, Detonation Mitigation and Control, Applications of Detonation Phenomena, and Detonability of Advanced Fuels. The volume is intended to be a tool to explore the international state of the art and an avenue for further follow-up for the researchers and practicing engineers.

PREFACE

$\mathcal{D}$emands on engines used for propulsion and stationary power are increasing, since current applications involve extreme operating conditions and wide variations in load. While performance is the key focus on propulsion engines, particularly for military applications, fuel cost and hence lower specific fuel consumption is the driving factor for stationary engines. Increased speed and range are also desired in addition to reliability and affordability. Though piston engines are extensively used today, gas turbines have taken the lead as primary engines for air, sea, and land power plant operations. Considerable research has been devoted to improve the performance and economy of gas turbine engines. Any further improvements will only be marginal, limited by the thermodynamic efficiency of the constant pressure Brayton cycle. An alternative is to operate an engine using a more efficient thermodynamic cycle. In this context, engines based on pulsed detonation waves, with rapid energy release rates, flexibility, simplicity and easy scalability, operating on a nearly constant volume Humphrey cycle offer a significant potential. Further, multi-tube, multi-cycle detonation engines, with tailored detonations can provide thrust vectoring without external mechanisms, and less moving parts.

Though detonation phenomenon has been studied extensively over the past several decades, and utilized in limited devices, application of detonation to propulsion or stationary engines is not yet realized. The coupling of the various mechanisms and the physical geometry of detonation chambers, and the thermal management are not fully understood. With the recent advances in supercomputing and non-intrusive combustion diagnostics, there has been a global resurgence on applied detonation research focussing on propulsion application. Agencies such as the Russian Foundation for Basic Research and the US Office of Naval Research have sponsored several research projects in detonation, and research and development have been pursued by industry in the US, Europe, and elsewhere. However, funds for research and development have been frugal globally, and have been decreasing in some cases. It was considered timely and appropriate to bring the world's leading researchers in detonation together, and to provide a forum for dissemination of recent research accomplishments, to review the state-of-the-art, and to plan for future efforts.

Consequently an International Colloquium was conducted on "Advances in Experimentation and Computation of Detonations" in St. Petersburg, Russia from September 14 to 17, 1998. The colloquium was jointly supported by the

US Office of Naval Research (ONR)*, ONR International Field Office Europe*, European Research Office of the US Army*, Combustion Council of the Russian Academy of Sciences, Russian Foundation for Basic Research, and ENAS Research & Education Company. Seventy five papers were included as oral and poster presentations. The papers covered the entire spectrum of detonation initiation, detonation wave structure and propagation, detonation mitigation and control, applications of detonation phenomena, and detonability of advanced fuels. Twenty four papers are revised and edited, and included in this volume.

We have attempted to select a proper spectrum of articles to present, as complete a picture as possible, on the advances in experimentation and computation of detonations from basic detonation initiation to practical applications. We have tried to organize the papers in a uniform and easily readable manner, and hope this volume provides adequate insight to the readers with information that will suit their needs. The addresses of the contributors, and a number of references given at the end of each article will enable the reader to further follow up or obtain more information, if needed. This book is intended as a reference for practicing engineers, and as a reference or text for advanced course in detonations.

This book is the result of a number of people who have rendered their time and talent. The editors acknowledge the excellent contribution made by Ms. Olga Frolova, Ms. Marina Sedakova, Ms. Lyudmila Kokushkina, and Mr. Peter Sedakov from ENAS Publishers in producing this volume. We also thank Academician A. G. Merzhanov, the Chair of the Combustion Council of the Russian Academy of Sciences, Prof. S. A. Tsyganov of the Russian Foundation for Basic Research, Prof. Yu. A. Gordopolov of the Institute for Structural Macrokinetics, and Ms. Irina Serova, Ms. Julia Vinyarskaya, and Mr. Alexander Melamed from ENAS Research & Education Company, who helped in organizing and conducting the colloquium, which made the publication of this book possible.

Gabriel Roy
Sergei Frolov
Kazhikathra Kailasanath
Nickolay Smirnov

---

*The content of the information does not necessarily reflect the position of the United States Government and no official endorsement should be inferred.

CONTENTS

Concluding Remarks

CONTRIBUTORS

R. G. AIVAZYAN
Institute for Structural Macrokinetics
Russian Academy of Sciences
Chernogolovka, Moscow Region 142432
Russia

V. V. AZATYAN
Institute for Structural Macrokinetics
Russian Academy of Sciences
Chernogolovka, Moscow Region 142432
Russia

V. S. BABKIN
Institute for Chemical Kinetics and
Combustion, Siberian Branch of the
Russian Academy of Sciences
Novosibirsk 630090, Russia

D. I. BAKLANOV
Gas Dynamics Department
High Energy Density Research Center
United Institute of High Temperature
Russian Academy of Sciences
Izhorskaya Str., 13/19
Moscow 127412, Russia

A. M. BARTENEV
N. N. Semenov Institute of Chemical
Physics, Russian Academy of Sciences
Kosigin Str., 4, Moscow 117977, Russia

V. YA. BASEVICH
N. N. Semenov Institute of Chemical
Physics, Russian Academy of Sciences
Kosigin Str., 4, Moscow 117977, Russia

V. V. BASKAKOV
M. V. Lomonosov Moscow State
University, Moscow 119899, Russia

L. BAUWENS
University of Calgary
University Drive N.W., 2500
Calgary, Alberta T2N 1N4, Canada

A. A. BELYAEV
N. N. Semenov Institute of Chemical
Physics, Russian Academy of Sciences
Kosigin Str., 4, Moscow 117977, Russia

L. BEZGIN
P. I. Baranov Central Institute of
Aviation Motors (CIAM)
Aviamotornaya Str., 2
Moscow 111250, Russia

A. P. BOICHENKO
M. V. Lomonosov Moscow State
University, Moscow 119899, Russia

A. A. BORISOV
N. N. Semenov Institute of Chemical
Physics, Russian Academy of Sciences
Kosigin Str., 4, Moscow 117977, Russia

D. BRADLEY
Department of Mechanical
Engineering, University of Leeds
Leeds LS2 9JT, United Kingdom

W. BREITUNG
FZK–INR, Postfach 3640
Karlsruhe D-76021, Germany

V. A. BUNEV
Institute for Chemical Kinetics and
Combustion, Siberian Branch of the
Russian Academy of Sciences
Novosibirsk 630090, Russia

V. K. CHERNYSHEV
Russian Federal Nuclear Center VNIIEF
Prospect Mira, 37, Sarov
Nizhegorodskaya Region 607190
Russia

B. S. ERMOLAEV
N. N. Semenov Institute of Chemical
Physics, Russian Academy of Sciences
Kosigin Str., 4, Moscow 117977, Russia

M. FISCHER
Institut für Technische Thermodynamik
Deutsches Zentrum für Luft- and
Raumfahrt (DLR), Postfach 800320
Stuttgart D-70503, Germany

S. M. FROLOV
N. N. Semenov Institute of Chemical
Physics, Russian Academy of Sciences
Kosigin Str., 4, Moscow 117977, Russia

A. GANZHELO
P. I. Baranov Central Institute of
Aviation Motors (CIAM)
Aviamotornaya Str., 2
Moscow 111250, Russia

B. E. GEL'FAND
N. N. Semenov Institute of Chemical
Physics, Russian Academy of Sciences
Kosigin Str., 4, Moscow 117977, Russia

O. GOUSKOV
P. I. Baranov Central Institute of
Aviation Motors (CIAM)
Aviamotornaya Str., 2
Moscow 111250, Russia

L. G. GVOZDEVA
Gas Dynamics Department
High Energy Density Research Center
United Institute of High Temperature
Russian Academy of Sciences
Izhorskaya Str., 13/19
Moscow 127412, Russia

M. HANANA
Institut de Méchanique
Université de Blida
Blida, Algeria

W. INGIGNOLI
Laboratoire de Combustion et de
Détonique, CNRS, ENSMA, BP 109
Futuroscope Cedex 86960, France

V. A. IVANOV
Russian Federal Nuclear Center VNIIEF
Prospect Mira, 37, Sarov
Nizhegorodskaya Region 607190
Russia

K. KAILASANATH
Laboratory for Computational Physics
and Fluid Dynamics
U.S. Naval Research Laboratory
Washington, DC, 20375, USA

B. A. KHASAINOV
N. N. Semenov Institute of Chemical
Physics, Russian Academy of Sciences
Kosigin Str., 4, Moscow 117977, Russia

S. V. KHOMIK
N. N. Semenov Institute of Chemical
Physics, Russian Academy of Sciences
Kosigin Str., 4, Moscow 117977, Russia

V. I. KOPCHENOV
P. I. Baranov Central Institute of
Aviation Motors (CIAM)
Aviamotornaya Str., 2
Moscow 111250, Russia

A. A. KORZHAVIN
Institute for Chemical Kinetics and
Combustion, Siberian Branch of the
Russian Academy of Sciences
Novosibirsk 630090, Russia

T. KRATZEL
Institut für Technische Thermodynamik
Deutsches Zentrum für Luft- and
Raumfahrt (DLR), Postfach 800320
Stuttgart D-70503, Germany

M. LAWES
Department of Mechanical Engineering
University of Leeds
Leeds LS2 9JT, United Kingdom

M. H. LEFEBVRE
Department of Chemistry
Royal Military Academy
Avenue Renaissance, 30
Brussels 1000, Belgium

C. LI
Laboratory for Computational Physics
and Fluid Dynamics
U.S. Naval Research Laboratory
Washington, DC, 20375, USA

S. P. MEDVEDEV
N. N. Semenov Institute of Chemical
Physics, Russian Academy of Sciences
Kosigin Str., 4, Moscow 117977, Russia

V. V. MITROFANOV
M. A. Lavrent'ev Institute of
Hydrodynamics, Siberian Branch of
the Russian Academy of Sciences
Novosibirsk 630090, Russia

M. G. NEUHAUS
N. N. Semenov Institute of Chemical
Physics, Russian Academy of Sciences
Kosigin Str., 4, Moscow 117977, Russia

V. F. NIKITIN
M. V. Lomonosov Moscow State
University, Moscow 119899, Russia

M. NIKOLIC
University of Calgary
University Drive N.W., 2500
Calgary, Alberta T2N 1N4, Canada

E. S. ORAN
Laboratory for Computational Physics
and Fluid Dynamics
U.S. Naval Research Laboratory
Washington, DC, 20375-5344, USA

E. PANTOW
Institut für Technische Thermodynamik
Deutsches Zentrum für Luft- and
Raumfahrt (DLR), Postfach 800320
Stuttgart D-70503, Germany

A. N. POLENOV
N. N. Semenov Institute of Chemical
Physics, Russian Academy of Sciences
Kosigin Str., 4, Moscow 117977, Russia

E. S. PROKHOROV
Lavrent'ev Institute of Hydrodynamics
Russian Academy of Sciences
Novosibirsk 630090, Russia

M. B. ROSE
Institut für Verbrennung und
Gasdynamik
Gerhard-Mercator-Universität
Duisburg, Duisburg 47048, Germany

P. ROTH
Institut für Verbrennung und
Gasdynamik
Gerhard-Mercator-Universität
Duisburg, Duisburg 47048, Germany

G. D. ROY
Office of Naval Research
Arlington, VA 22217, USA

N. B. SCHERBAK
Gas Dynamics Department
High Energy Density Research Center
United Institute of High Temperature
Russian Academy of Sciences
Izhorskaya Str., 13/19
Moscow 127412, Russia

N. N. SMIRNOV
M. V. Lomonosov Moscow State
University, Moscow 119899, Russia

A. M. STARIK
P. I. Baranov Central Institute of
Aviation Motors (CIAM)
Aviamotornaya Str., 2
Moscow 111250, Russia

A. A. SULIMOV
N. N. Semenov Institute of Chemical
Physics, Russian Academy of Sciences
Kosigin Str., 4, Moscow 117977, Russia

N. S. TITOVA
P. I. Baranov Central Institute of
Aviation Motors (CIAM)
Aviamotornaya Str., 2
Moscow 111250, Russia

A. V. TROTSYUK
M. A. Lavrent'ev Institute of
Hydrodynamics, Siberian Branch of
the Russian Academy of Sciences
Novosibirsk 630090, Russia

M. V. TYURNIKOV
M. V. Lomonosov Moscow State
University, Moscow 119899, Russia

U. UPHOFF
Institut für Verbrennung und
Gasdynamik
Gerhard-Mercator-Universität
Duisburg, Duisburg 47048, Germany

V. V. VAKHRUSHEV
Russian Federal Nuclear Center VNIIEF
Prospect Mira, 37, Sarov
Nizhegorodskaya Region 607190
Russia

P. J. VAN TIGGELEN
Laboratoire de Physico-Chimie de la
Combustion
Université Catholique de Louvain
Place Louis Pasteur, 1
Louvain La Neuve B-1348, Belgium

A. A. VASIL'EV
M. A. Lavrent'ev Institute of
Hydrodynamics, Siberian Branch of
the Russian Academy of Sciences
Novosibirsk 630090, Russia

G. K. VEDESHKIN
P. I. Baranov Central Institute of
Aviation Motors (CIAM)
Aviamotornaya Str., 2
Moscow 111250, Russia

A. VESER
FZK–INR, Postfach 3640
Karlsruhe D-76021, Germany

B. VEYSSIERE
Laboratoire de Combustion et de
Détonique, CNRS, ENSMA, BP 109
Futuroscope Cedex 86960, France

P. VIDAL
Laboratoire de Combustion et de
Détonique, CNRS, ENSMA, BP 109
Futuroscope Cedex 86960, France

G. I. VOLKOV
Russian Federal Nuclear Center VNIIEF
Prospect Mira, 37, Sarov
Nizhegorodskaya Region 607190
Russia

H.-Gg. WAGNER
George August University
Tammannstraße 6
Göttingen D-37077, Germany

D. N. WILLIAMS
University of Calgary
University Drive N.W., 2500
Calgary, Alberta T2N 1N4, Canada

F. A. WILLIAMS
Center for Energy and Combustion
Research, Deparment of Applied
Mechanics and Engineering Sciences
University of California at San Diego
La Jolla, CA 92013, USA

Yu. G. YARUNOV
P. I. Baranov Central Institute of
Aviation Motors (CIAM)
Aviamotornaya Str., 2
Moscow 111250, Russia

S. A. ZHDAN
M. A. Lavrent'ev Institute of
Hydrodynamics, Siberian Branch of
the Russian Academy of Sciences
Novosibirsk 630090, Russia

INTRODUCTION

$\mathcal{A}$lmost a century ago, in 1899, Chapman provided a theoretical estimate for the detonation velocity based on one-dimensional flow considerations and compared it with experimental data. Since then, significant progress has been made both in the experimentation and computation of detonations. The International Colloquium on Experimentation and Computation of Detonations was organized to provide a forum to assess the state-of-the-art and a means to disseminate this information to the international scientific community.

Although the study of detonation phenomena has been active during the past century, the application of detonations for non-destructive purposes, such as propulsion, drilling, pressing, protective coating, etc., has been studied only in the past few decades. It is hoped that recent advances, captured in this volume, will provide an additional impetus for the application of detonations for propulsion. With this point of view, though the topics covered in the Colloquium emphasized basic understanding of detonation initiation, structure, propagation, mitigation, and control, the discussions were focused towards making use of this basic understanding of detonations for applications to propulsion.

This book includes 24 selected contributions addressing various aspects of detonation physics and chemistry, presented by researchers from Belgium, Canada, France, Germany, Russia, United Kingdom, and the United States of America. From the response of researchers, there seems to be a balance in the experimental and computational studies carried out.

Part One, **Detonation Initiation** includes contributions on the most challenging problem in detonation physics. Experimental and theoretical studies on initiation of gaseous and heterogeneous detonations are presented. The issues addressed are the critical energy of detonation initiation, deflagration-to-detonation transition (DDT), enhancement of DDT, transition of confined detonations into unconfined ambience, and the use of advanced algorithms for computing transient flows with non-reactive and reactive shock waves. The applicability of various concepts of detonation initiation to Pulsed Detonation Engines (PDE) and Pulse Detonation Generators is also discussed.

Part Two, **Detonation Wave Structure and Propagation** includes experimental and theoretical contributions on detonation structure in gaseous media. The issues addressed are the multi-dimensional structure of self-sustaining gaseous detonation fronts, mechanisms of detonation propagation, transition from regular to irregular cellular patterns, detonation cell structure and size,

and gaseous detonation propagation and structure in tubes of variable cross section. Also addressed are the fundamental issues dealing with stability of a planar detonation wave.

Presented in Part Three, **Detonation Mitigation and Control** are the contributions on the aspects of gaseous and heterogeneous detonation control by various means, namely, by changing composition and density of the reactive mixture, by obstructions and wall inflections, external forcing, and by preliminary vibrational excitation of reactants. It is shown that the continuous spectrum of detonation propagation velocities, from the sonic level to the level of overdriven detonations, can be obtained by applying various controlling means. A particular emphasis is given to detonation suppression and re-ignition in technical structures.

Part Four, **Applications of Detonation Phenomena** deals with detonation applications in propulsion and power engineering. Propulsion applications are focussed towards ram accelerators and scramjets. Numerical simulations of transient flows is proved to be the efficient tool for designing the optimum shapes of the projectiles in ram accelerators and of the flameholders in a scramjet duct. The efficiency of cutting electric current contours by detonating a high explosive (HE) charge depends on electrophysical properties of detonation products. It is shown that a proper arrangement of the HE charge in the electric contour allows to produce current pulses with the amplitude of about 10^8 A and with a microsecond rising time in a load.

Part Five, **Detonability of Advanced Fuels** presents the studies of detonation properties of various gaseous, liquid, and solid fuels. Distributed injection of several fuels into the detonation chamber of a PDE is shown to be a promising approach for controlling fuel detonability and sensitivity to premature ignition under variable operating conditions of a PDE-driven vehicle. Premature ignition in a PDE, a topic of significant concern for the PDE performance, can also be controlled by various inhibitors. It is shown that small amounts of efficient inhibitors can narrow detonability limits of even hydrogen-air mixtures. Contributions on detonability of Aluminum and RDX particles in air are also of interest for possible applications of high energetic materials as fuels for a PDE.

It is evident that a great deal of research is going on around the world focussing on this interesting phenomenon — detonation. It is our sincere hope that this book will promote further investigations in this research area and help in formulating a dialogue among the members of the research community.

Editors

PART ONE

DETONATION
INITIATION

INITIATION OF DETONATION IN GASEOUS AND TWO-PHASE MIXTURES

A. A. Borisov

Diverse aspects of initiation of detonation in gaseous mixtures, liquid fuel sprays, and suspensions of solid particles primarily in air are discussed. The emphasis is made on the following problems.

(1) Direct initiation of gaseous detonation in ducts, including the following measurements: the minimum initiation energy, its dependence on the rate of energy deposition, density of the initiator, effect of chemical promoters and inhibitors, dependence of the detonation limits on the initiation energy, and shock wave-to-detonation transition.

(2) Direct initiation of detonation in unconfined clouds of various geometry, including a derived correlation between the initiation energies of plane and spherical detonation.

(3) Transition of detonation from ducts into unconfined mixture volumes.

(4) Experimental and theoretical approaches to estimating the initiation energies (the use of detonation cell size and direct kinetic data in calculations is discussed).

(5) Direct initiation of detonation in liquid sprays (experimental and hydrodynamic codes used to predict the minimum energy of initiation are considered, with particular attention paid to the kinetics of heat evolution behind shock fronts in these two-phase mixtures).

(6) Direct initiation of dust suspensions of both low- and high-density, with and without solid oxidizers added.

(7) The effect of premature burning of liquid and solid fuels on the initiation of detonation or deflagration-to-detonation transition (DDT).

(8) The mechanism of DDT and the methods for shortening pre-detonation distances in all systems.

(9) Detonation initiation with injection either of hot reactive gases or self-igniting additives.

A conclusion is drawn that initiation of detonation can be facilitated by the following: addition of some chemical promoters, injection of hot gases or chemicals that produce temperature and concentration gradients, and by enhancing turbulence. In heterogeneous mixtures, the powerful factor affecting detonation onset is ignition or preheating of the condensed particles before sending the initiating gasdynamic pulse.

INTRODUCTION

One of the most important problems arising in practical applications of detonation of gas and two-phase systems, including safe handling of gaseous, liquid, and powdered fuels, is determining how detonation waves are initiated and what the critical conditions are for detonation to start spreading. This is particularly true for large-scale fuel–air clouds.

There are two major approaches to solve the problem, namely, direct initiation, i.e. fast localized energy deposition to generate a strong shock wave capable of inducing detonation wave propagation, and various means of forcing DDT. In both approaches, the kinetics of heat release in shocked explosive media is the major factor governing the critical conditions for detonation initiation.

Processes involved in heat release in gaseous and two-phase mixtures include different physical steps. Therefore, even similar chemical reactions occur under dissimilar conditions in homogeneous and heterogeneous media. Hence initiation of detonation in gaseous and two-phase mixures should be considered separately.

Direct experimental determination of the critical conditions for initiation of detonation would answer all questions put forward by designers of detonation devices or by safety engineers, but unfortunately it is a prohibitively expensive way of solving the problem. For this reason, researchers of detonation processes concentrate mainly on numerical modeling and semi-empirical methods when attempting to predict the behavior of combustible mixtures under particular conditions of interest.

Certainly, these predictive methods should be based on understanding the nature of nonsteady shock wave propagation in reactive media, and on proper physical models of the process.

This paper briefly reviews the available models, practical techniques for efficient detonation initiation, and peculiarities inherent in this essentially nonsteady process, which is still poorly understood. The subject is too vast to cover all details within a paper. Therefore, along with a brief analysis of general

4

achievements in this field, special emphasis will be made on the results obtained by the author and his research group.

DIRECT INITIATION OF DETONATION

1. Gaseous Mixtures

Not going far back to the history of investigations, it is worth mentioning early studies have postulated the following:

(i) the critical initiation energy is proportional to t_r^n (where t_r is the reaction time behind the detonation front and n is the geometry index equal to 1, 2, and 3 for plane, cylindrical, and spherical initiators, respectively),

(ii) there exists a critical radius of the blast wave produced by the initiator at which its amplitude drops to the value corresponding to the Chapman–Jouguet (CJ) detonation, and

(iii) this critical radius depends on the reaction rate and defines both the critical energy of the initiation source and the minimum size of a cloud which can support detonation [1–4].

All these conclusions were essentially based on the Zel'dovich–von Neumann–Döring (ZND) model of detonation waves. Although the ZND model is physically grounded and a very helpful idealization of a real detonation wave, later on it was clearly demonstrated both experimentally and theoretically that a detonation is essentially three-dimensional and steady-state only on average (see, e.g., [5] and references therein). Instability of detonation waves and their three-dimensional structure raise serious questions concerning the validity of the Arrhenius kinetics with an average temperature in one-dimensional modeling of realistic detonation initiation. Direct photographs (see, e.g., [6] and Struck's comments therein) show unequivocally the cellular structure not only of CJ detonations but of the incipient detonation kernel, which means that the mixture is actually ignited behind the shock front in hot spots where temperature is significantly higher than the average temperature.

Before analyzing the quantitative results of experiments on determination of the critical energy of detonation initiation, the initiation sources needed to obtain physically meaningful and reproducible results should first be characterized. The first and basic condition is that the source must generate a blast wave with an amplitude high enough (at least exceeding the CJ value) to start and complete the chemical reaction within a time interval approximately equal to the characteristic decay time of the blast wave. Otherwise, the critical energy
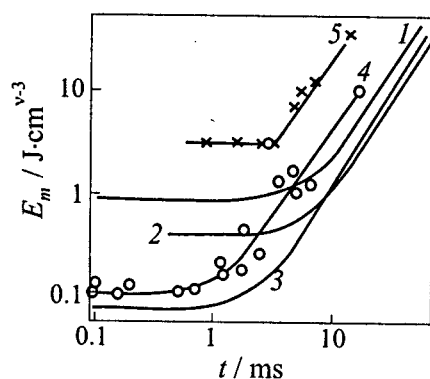
Figure 1 The critical energy for direct detonation initiation as a function of the energy deposition time [7]. Calculations for stoichiometric chlorine–hydrogen mixture: 1 — cylindrical initiation, radius of the energy deposition zone $r_0 = 2$ mm; spherical initiation: 2 — $r_0 = 2.5$ mm, 3 — $r_0 = 1$ mm. Experiments: cylindrical initiation of stoichiometric mixtures: 4 — acetylene–oxygen, 5 — hydrogen–oxygen
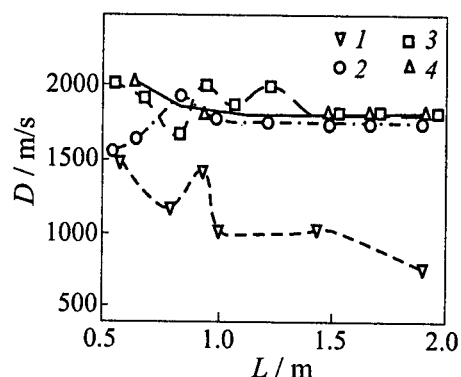
Figure 2 Blast wave velocity vs. distance at different energies of condensed explosive charges: 1 — 2.3 MJ/m^2, 2 — 3.1, 3 — 4.0, 4 — 6.6. Stoichiometric propane–air mixture

will be a function of the source power or the time of energy deposition. This is clearly seen from Fig. 1 taken from [7]. The critical energy ceases to depend on the energy deposition time after it becomes less than a certain value determined by the initial blast wave amplitude.

Thus the sources most convenient for direct detonation initiation are the detonating charges of either condensed or gaseous explosives, which immediately produce blast waves of a controlled amplitude. Sensitive mixtures, such as fuel–oxygen or acetylene–air, can be initiated by exploding wires and lasers or electric discharges. For these sources, the deposited energy should be the only parameter governing blast wave propagation in a reactive medium, provided its amplitude exceeds that of the shock wave leading the CJ detonation in the initiated mixture. The latter condition is always met when condensed explosives or exploding wires are used as the initiators. Gas-phase initiators may generate blast waves that are quite weak but of a long duration, which are also capable of initiating detonation with a longer delay and over long predetonation distances.

Consider the peculiarities of detonation initiation by sources of different density. Figure 2 illustrates the blast wave velocity as a function of distance from detonating condensed explosive charges of various energy. The charges imitated plane blast sources (detonating cord spiral, layer of liquid nitromethane, and plastic explosive sheet were used) in a tube. As seen, the blast velocity ei-
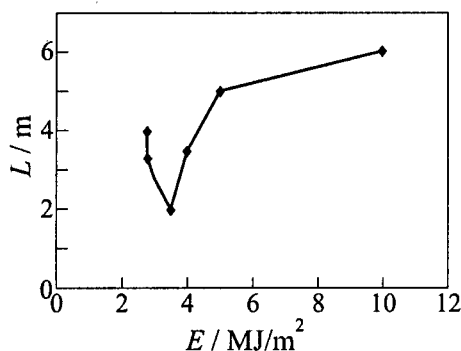
Figure 3 Predicted distance to the steady-state CJ detonation against the initiation energy. The curve is calculated by 1D code with an effective reaction kinetics for a propane–air mixture
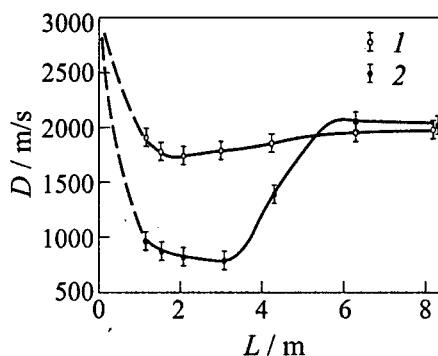
Figure 4 Variation of the wave velocity along the tube length in a propane–air mixture initiated by detonation of a propane–oxygen mixture with a total energy: $1 - 3.0$ MJ/m^2 and $2 - 2.6$ MJ/m^2

ther decays monotonically to the CJ level or passes (at lower initiator energies) through a shallow minimum, or series of minima to attain the same level. The distance needed for the detonation velocity to reach the steady-state level is much greater than the average reaction zone length in the CJ wave (see Fig. 3). At subcritical energies the shock wave velocity never rises to the CJ level.

Detonation of gaseous initiation charges produces similar flow patterns whenever the initial blast wave velocity exceeds the CJ velocity in the test mixture. However, if the initial blast wave has an amplitude slightly below that of the shock wave leading the CJ detonation, but the total energy of the initiator is higher than the critical energy for initiation by condensed explosives, quite a peculiar phenomenon is observed. The wave velocity drops very deep (below 1000 m/s) and then recovers to the CJ level (Fig. 4). This process could be referred to as shock-to-detonation transition, rather than direct detonation initiation. The phenomenon has some common features with galloping detonations. In both cases, a low-amplitude shock wave with a long compression zone induces mixture self-ignition in the shocked gas and leads to DDT.

The explosion mode under discussion belongs to the parametric region in Fig. 5, where the critical energy of detonation initiation depends on the initial pressure of the initiating mixture. Detonation is initiated via shock-to-detonation transition when charges of condensed energetic materials are placed in a casing. Because of its inertia and generation of intense transverse shock waves by fragments, the casing drastically reduces the initial blast wave amplitude but makes the wave compression phase much longer. Experiments show that with a properly chosen ratio between the masses of the casing and explosive

7
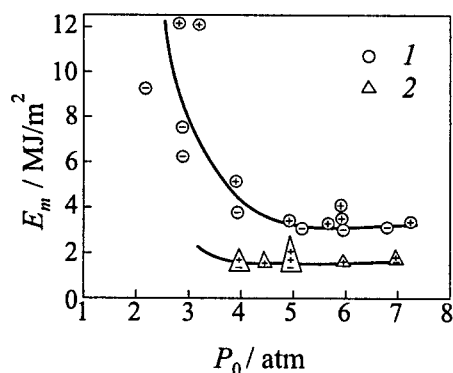
Figure 5 Minimum energy of direct detonation initiation vs. the initial pressure in the initiator section: 1 — stoichiometric propane–air mixture, 2 — stoichiometric hydrogen–air mixture. Initiator is a detonating acetylene–oxygen mixture. $+$ and $-$ pertain to "go" and "no go" runs
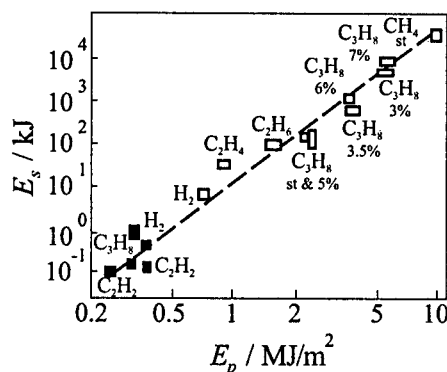
Figure 6 Critical energy of direct initiation of spherical detonation (E_s, J) vs. the critical energy of plane detonation initiation (E_p, MJ/m^2) for various fuel oxygen (filled symbols) and fuel–air (open symbols) mixtures

material, the effective critical energy can be reduced as compared to initiation by unconfined charges.

The horizontal portions of the curves in Fig. 5 are consistent with the critical initiation energy measured in experiments with condensed explosive initiators. Calculations show that the curves level off approximately at initial pressures at which the blast wave generated in the test mixture has an amplitude equal to the shock pressure in the CJ detonation relevant to this mixture. Hence, as soon as the initial blast wave is stronger than the lead shock of the CJ detonation, the critical energy of direct detonation initiation is no longer dependent on the density of the initiator charge.

Thus, under realistic conditions, the minimum energy of an explosive source is not the only key factor governing the initiation process. The profile of the blast wave and blast duration are also important factors.

Wave instability and deviations from the ZND model necessitate, first, experimental verification of the above fundamental postulates and, second, modification of the kinetic equations for modeling initiation processes. It is instructive to start with the relation between the reaction time and the critical energy of direct detonation initiation. Determination of the critical initiation energy for spherical detonations is one of the most expensive experimental procedures, in particular for low-reactivity fuel–air mixtures. The difficulties associated with using large initiating charges and huge mixture clouds can easily be circumvented by performing measurements of the critical energy for initiating plane detonations in tubes. Then, the critical energy for unconfined clouds can be found from the

theoretical relationship between the energies for different initiation geometries. Clearly, this latter relationship must be reliably established before being used for this purpose.

Figure 6 presents the results of measurements of critical energies of detonation initiation in fuel–oxygen (filled symbols) and fuel–air (open symbols) mixtures. The measured energies in the graph are grouped near a straight line with a slope equal to 3.0, which is in line with the first of the above-mentioned postulates. According to this postulate, the critical energy for spherical detonation initiation, E_s, is proportional to the reaction time to the third power and the critical energy for plane detonation initiation, E_p, is proportional to the reaction time to the first power. Hence, in logarithmic coordinates the slope of the $E_s(E_p)$ dependence should be 3.0. Although this relationship follows from the dimensional analysis, this consistency is somewhat surprising, because the conditions for reaction progress behind the lead shock front (e.g., the temperature gradient in the reaction zone) in both geometries are different. Anyway, this empirical correlation supporting the general theoretical model is very helpful in assessing the detonability of low-reactivity combustible mixtures. For example, the available data on the critical energy of detonation initiation in unconfined methane–air mixtures lack consensus, ranging from 1 kg TNT to more than 100 kg TNT. Based on our theoretical model, a value of about 10 kg TNT is most reasonable.

Additional information about the relation between the energy of direct detonation initiation and reaction time can be deduced by conducting experiments on initiation of a mixture with chemical additives to change the reaction time (promoters and inhibitors). The experiments performed in shock tubes indicate that the most efficient promoters of self-ignition of hydrocarbons in air (nitrates) shorten the ignition delays (by a factor of about two at most) at temperatures existing behind the lead shock fronts of the CJ detonations. Addition of *iso*-propylnitrate to a mixture of piperylene with air in the amount of about 0.15 of the fuel concentration nearly halves the energy of initiation of plane detonation. This is consistent with the general dependence.

The situation with inhibitor additives is more intricate. Both the shock tube and detonation experiments show that such a popular combustion inhibitor as tetrafluorodibromoethane (TFDBE) does not significantly affect the ignition delays and detonation wave properties. However, at some TFDBE concentrations, incombustible hydrocarbon–inhibitor–air mixtures detonate, disproving the commonly adopted point of view that the detonability range is much narrower than the flammability limits. The kinetic measurements suggest that the energy of direct detonation initiation in tubes should be nearly independent of the inhibitor concentration within some reasonable interval, as illustrated by Table 1.

The slight rise of the critical initiation energy with the TFDBE concentration can be attributed to a purely physical factor — the decrease in the temperature behind the shock front due to the high specific heat of the additive.

Table 1 Parameters of detonation initiation in heptane–TFDBE–air mixtures (TFDBE — tetrafluorodibromoethane, is used as inhibitor)

% TFDBE in fuel	Critical initiation energy E_p, MJ/m^2	Detonation velocity D, m/s	Propagation mode
50	2.5	1720	go
75	2.5	—	no go
75	5.0	1700	go
75	3.5	1675	go
0	1.3	—	no go
0	2.5	1770	go

Experimental determination of the critical energy of detonation initiation, even in tubes, is quite costly. Therefore, its numerical prediction based on the known reaction kinetics would be helpful in solving practical problems. The question arises: What kind of kinetic data should be used in these calculations?

A numerical analysis of the ignition kinetics with the use of detailed reaction mechanisms shows that under the conditions typical of detonation waves, the induction period constitutes the major fraction of the reaction time for all detonable mixtures. However, self-ignition of hydrocarbon–air mixtures behind reflected shock waves in a shock tube exhibits a very pronounced stage of energy release, which in many cases is commensurate with (or exceeds) the induction period. This is because actual mixture ignition behind shock waves takes place in hot spots. Non-synchronous mixture ignition in various hot spots makes an impression of a greatly extended energy release stage. The ratio between the times characterizing the two main self-ignition stages is illustrated in Fig. 7, where the induction periods and explosion times are plotted in Arrhenius coordinates. For comparison, Fig. 8 shows the temperature history during explosion of a methane–air mixture under conditions close to those existing in a detonation wave. It is the type of ignition shown in Fig. 7 that occurs in realistic detonation waves. Therefore, in numerical models of detonation initiation within the one-dimensional ZND model, it is necessary to use empirical relations for the induction periods and explosion times. This is more accurate for the 1-D ZND model than the detailed chemical mechanism, because the effect of inhomogeneous temperature distribution in the mixture due to collisions of transverse shock waves is included in the ignition characteristics measured in shock tubes. The latter mechanisms should be used when the numerical modeling of the initiation process is performed in three dimensions and with a size of computational cells small enough to resolve hot spots that arise in the shocked gas.

This inference is based on a comparison of the critical energies for plane and spherical detonation initiation calculated using global kinetic equations approx-
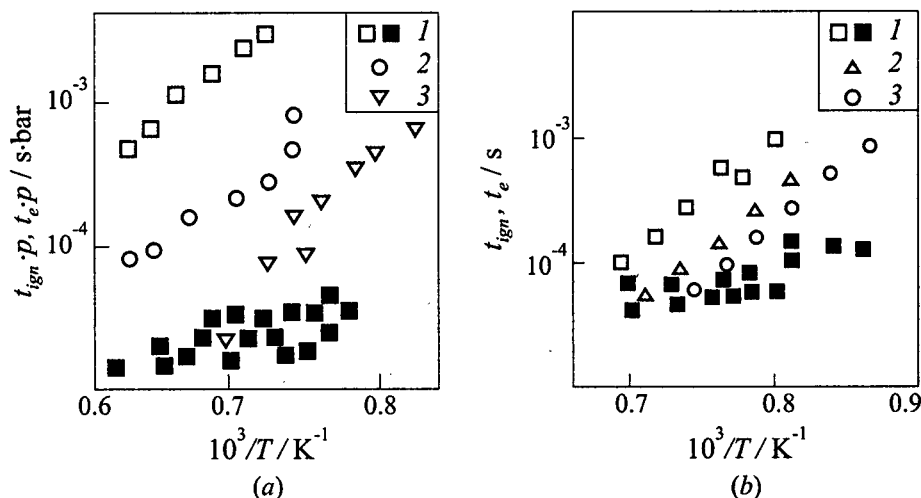
Figure 7 Arrhenius plots of the ignition delays (open symbols) and explosion times (filled symbols): (a) 1 — $6CH_4 + 12O_2 + 82Ar$; 2 — $3.3C_3H_8 + 16.6O_2 + 80.1Ar$; 3 — $1.5n\text{-}C_7H_{16} + 16.5O_2 + 82Ar$; (b) $4.3C_3H_8 + 21.3O_2 + 74.4N_2$: 1 — 1 atm; 2 — 2 atm; 3 — 5 atm
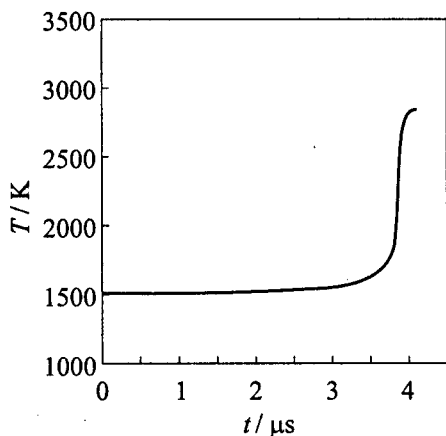
Figure 8 Predicted temperature history in a $CH_4 + 2(O_2 + 3.76N_2)$ mixture at 28.3 atm

imating the experimental data on ignition delays and reaction times for propane–air and hydrogen–air mixtures. The result of this comparison is shown in Figs. 9 and 10. When using detailed kinetics, we failed to fit calculations to the experiment so well. Combination of the effective heat release kinetics determined from shock tube experiments with one-dimensional gasdynamic computations is one of the most convenient methods for predicting the critical conditions of detonation initiation. These calculations do not require powerful computers and the computation time is very short even on a PC. One-dimensional computer codes can easily incorporate various types of initiation sources. However, as calculations show, for rough estimates one can disregard the specific features of particular source types, provided the initial amplitude of the blast wave produced in the test mixture is much higher than the CJ detonation pressure in this mixture.
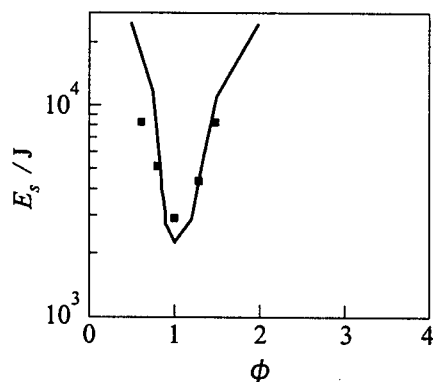
Figure 9 Measured (symbols) and predicted (curve) critical energies of direct initiation of spherical detonation in a hydrogen–air mixture at various equivalence ratios ϕ
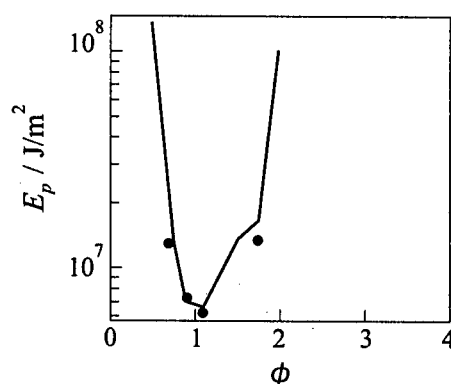
Figure 10 Measured symbols and predicted (curve) critical energies of direct initiation of plane detonation in a propane–air mixture at different equivalence ratios ϕ

Under certain conditions (e.g., for low-reactivity mixtures complemented by a large difference in the equivalence ratio between the detonation products of initiator and the gaseous mixture), mixing at the interface may contribute to the initiation process adding some energy, released by burning within the mixing layer. Mixing due to hydrodynamic instabilities at the interface is several orders of magnitude more intense than the conventional molecular diffusion. Figure 11 illustrates the instability development at the interface between the detonation products of a TNT charge and ambient air. This effect should also be taken into account when refining the results of rough estimates.

Measuring the effective parameters of heat release kinetics at high temperatures is not an easy task and there is still some doubt concerning the applicability of these measurements to describe the hot spot ignition in real detonation waves. For this reason, many researchers prefer to use a kinetics-related parameter readily measured in steady detonation waves, that is, the detonation cell size. A comprehensive review of the models and analytical expressions suggested for predicting the critical energy of direct detonation initiation can be found in [8]. These models (ranging from very simple and straightforward to quite sophisticated ones) are essentially based on an assumption that the detonation cell size (longitudinal or transverse), measured from soot prints, is proportional to the reaction time with a proportionality coefficient depending on mixture properties and detonation wave characteristics. Without going into an analysis of the models, which are actually various applications of the same idea, it is worth emphasizing that, in spite of the physical clearness of the idea, the relation between the cell size and reaction time is not unique. Therefore all the analytical
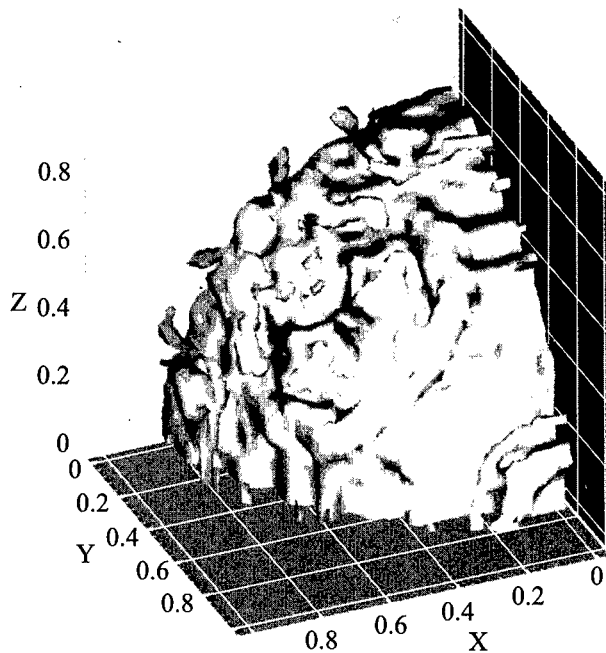
Figure 11 Three-dimensional calculations of instability of the interface between the detonation products of a spherical TNT charge and air

expressions for assessing the critical initiation energy should be considered as approximate. This is demonstrated by a plot of experimental values of E_s (J) vs. the longitudinal cell size b (mm) reported in [9] ($E_s(b) = 17b$), in which the scatter of the data exceeds one order.

All of the available models use experimental values of the critical energy of detonation initiation. This naturally raises a question concerning the correctness of energy measurements in view of the efficiency of energy deposition. Since detonation is initiated by the blast wave, which is produced by the deposited energy, the most popular method for evaluating this energy is the use of point (or strong) explosion relations. Experimental dependencies of the blast velocity on the distance traveled by the wave are approximated by the appropriate relations for point explosion, with energy chosen as the fitting parameter. Taking into account the scatter in experimental data on the initiation energy, this approach seems to be quite reasonable.

Transition of detonation from a duct into an unconfined mixture cloud can also, in some cases, be considered a direct initiation of detonation because it includes the stages of detonation decay and re-initiation under conditions close
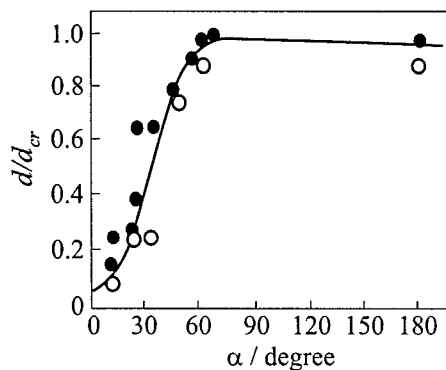
Figure 12 The critical diameter for detonation transition from a tube into a large volume as a function of the cone angle α. Open and filled circles pertain to 'no go' and 'go' runs, respectively. Mixtures: hydrogen–oxygen and methane–oxygen
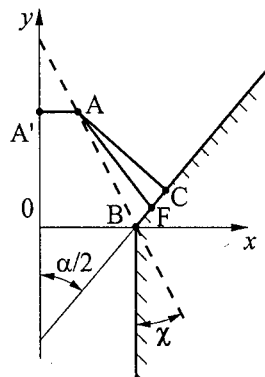
Figure 13 Schematic of detonation transition from a tube into a cone

to critical. It is commonly recognized that detonation is easy to initiate in ducts, either directly or via DDT. This is often used to initiate detonation in either a larger diameter duct or unconfined clouds. The critical tube diameter for this transition was measured in many studies, and an approximate rule was suggested which defines this critical diameter as 13 transverse detonation cell sizes. Although not always met, this rule proved to be very helpful in assessing the hazard of detonation initiation in large mixture volumes arising in accidents. This rule can be grounded by considering a simplified schematic of the process, but this analysis is beyond the scope of this paper. Discussed here is only how these measurements can be used to assess the critical energy of direct detonation initiation.

Experiments with different mixtures show that the critical diameter of a duct, at which detonation keeps going in the unconfined cloud, is a function of the angle of the cone through which detonation waves travel from the duct to the cloud. This dependence is shown in Fig. 12. As seen from the figure, the critical diameter ceases to depend on the cone angle when its value exceeds $60°$. This means that at greater cone angles a part of the mixture at the periphery does not contribute to detonation reinitiation, because the amplitude of the diffracting wave is too low for the mixture to self-ignite within a reasonable time interval.

Schematic of the flow pattern in the cone is shown in Fig. 13. The rarefaction wave emanating from point B, with the head spreading along trajectory BA, attenuates the wave and produces a zone AFC which contains unburnt gas mixture. Under the critical or subcritical conditions, the rarefaction wave head

14

reaches the duct axis either at the instant when detonation is re-initiated in the AFC zone or well before this re-initiation. Hence, we can suppose that under critical conditions the total energy contained in the AFC zone suffices to directly initiate unconfined detonation (hemispherical for a cylindrical duct and hemi-cylindrical for a slot). The critical volume (and energy) of the AFC zone should be calculated at the angle of 60°, after which the critical diameter no longer depends on the angle. Thus the critical energy of direct detonation initiation is a sum of the internal and kinetic energies of the gas mixture within the AFC zone, $E_{cr} = K(E_{int} + E_{kin})$, where K is a constant coefficient. Assuming that (a) the line AC is straight and normal to the cone surface, (b) line AF is straight, (c) the reaction zone behind the initial plane detonation front is much shorter than the critical diameter, and (d) no reaction takes place in the AFC zone before its self-ignition, the oblique shock wave velocity can be written as:

$$D = D_0 \frac{\cos(\chi + \alpha/2)}{\cos \chi}$$

The shocked gas volume is

$$V = \frac{\pi d_{cr}^3}{24} \left\{ \left(\frac{D_0}{U} + \cot \frac{\alpha}{2} \right) \sin \frac{\alpha}{2} \left(\frac{D_\alpha}{U} - \frac{u_\alpha}{U} \right) \left[2 + \sin \frac{\alpha}{2} \left(\frac{D_\alpha}{U} + \frac{u_\alpha}{U} \right) \right] \right\}$$

and its specific energy is

$$E_{int} + E_{kin} = P \frac{1 - (P_0/P)(\gamma + 1)/(\gamma_0 - 1)}{\gamma - 1} + \frac{\rho u_\alpha^2}{2}$$

Here U is the velocity component of the lateral rarefaction wave perpendicular to the detonation propagation direction; P, ρ, u_α, and γ are the pressure, density, gas velocity, and the ratio of the specific heats behind the shock front. The zero subscript labels quantities in the initial gas mixture. The parameters of detonation and shock waves were calculated by using a standard code. The calculated critical energies fit experimental data if K is assumed equal to 1.03. The greatest error in calculated critical energies comes from the uncertainty in the critical diameter. The estimated values are listed in Table 2. The critical energy of initiation of plane detonation is found by dividing the total energy of the shocked gas by the area of the surface described by line AC.

When estimating the energy of direct initiation, one should keep in mind that detonations can propagate only under certain conditions. However, a simple physical analysis suggests that in unconfined clouds the only limiting condition is the cloud size. It should be greater than the distance needed to reach the steady CJ state, which is not necessarily equal to the critical radius introduced in early papers on detonation initiation. Thus, there is no fundamental detonation limit for spherical detonation because as the cloud size and initiator energy tend to infinity, the fuel or oxidizer concentration in detonable mixtures can be

Table 2 The critical energy for detonation initiation in various fuel–air mixtures

Mixture	d_{cr} cm	Spherical detonation		Plane detonation	
		E_s^{cal} kJ	E_s^{exp} kJ	E_p^{cal} MJ/m^2	E_p^{exp} MJ/m^2
H$_2$ + air	13^a	2.6	3.4	0.3	0.7
	20	9.6	4.7	0.5	—
C$_2$H$_2$ + air	11.5^a	3.2	6.3	0.3	—
	12	3.6	5.8	—	—
C$_2$H$_4$ + air	31	64	43	1.2	1.0
	38	116	64	1.5	—
C$_2$H$_6$ + air	59^a	427	130	2.2	1.8
	67	642	170	2.5	—
C$_3$H$_8$ + air	60^a	483	210	2.5	2.7
	70	760	340	3.0	—

^{a}Estimated by formula $d_{cr} = 13\lambda$.

arbitrarily small. Fundamental detonation limits can exist only when energy and momentum losses come into play. Although this sounds somewhat paradoxical, it is meaningless to compare detonation limits in tubes and unconfined clouds because they arise due to different reasons.

2. Heterogeneous Mixtures

Heterogeneous mixtures differ from gases in the kinetics of heat evolution behind shock waves which necessarily includes in this case the stages of mixing and inhomogeneous temperature evolution in the shocked gas. This results in an extension of the heat release profile. Both experiment and simple physical considerations show that normal liquid fuel sprays are more reactive than suspensions of solid particles of the same characteristic size because liquid drops are mechanically shattered by the gaseous flow. Therefore, direct detonation initiation in heterogeneous mixtures can be modeled only if both physical and chemical processes are taken into account.

The commonly adopted model of heat release kinetics in sprays neglects inhomogeneous distribution of the fuel and temperature in the shocked medium and assumes that the heat release rate is controlled by droplet break-up. Suggested here is a modified model allowing for this inhomogeneity and aimed at predicting the energy of direct detonation initiation in sprays. Not going into mathematical details of the model, we outline its basic features. The approach reduces to the following description.

(1) A droplet is deformed and stripped by the flow and produces an annular conical micromist cloud around the droplet periphery; the rate of mass transfer to the cloud is calculated by the well-known hydrodynamic relations. As estimates show, this stage is terminated over a time interval which is much shorter than the average heat release times observed experimentally in detonation waves, and therefore can be assumed instantaneous.

(2) The micromist cloud nearly instantaneously mixes with the hot gaseous oxidizer and self-ignites. Unfortunately, the temperature in the cloud is very hard to estimate. On the one hand, the oxidizer gas has a higher temperature than the average value because of the bow shock in front of the droplet and deceleration of the gas by the entrained liquid mist. On the other hand, heating and evaporation of the liquid in the wake cools the gas. According to estimates, the fuel mass stripped up to the instant of mixture self-ignition is normally less than 20% of the droplet mass. Therefore, one can assume, without significant loss of generality and accuracy of calculations, that the temperature in the wake equals the average gas temperature calculated with allowance for particle acceleration. Self-ignition of the cloud is computed by the law of homogeneous chemical kinetics.

(3) Then the volume of the cloud V_{dr}, and the fuel mass m in it are estimated assuming that the wake is a turbulent mixing layer emanating from the deformed droplet rim with a cone angle α:

$$V_{dr} = 75 d_0^3 \left(\frac{\rho_1}{\rho_g}\right) [B^{-1} \ln(1 + B)]^2 \tan \alpha$$

$$m = 24 m_0 \left(\frac{\rho_1}{\rho_g}\right)^{1/6} \nu_1^{1/3} \nu_g^{1/6} 2[(1 + B)^{-1/2} - 1] B^{-1} (d_0 U_g)^{-1/2}$$

where $B = (15/4) C(\rho_1/\rho_g)$, C is the drag coefficient, ρ_1 and ρ_g are the densities of the liquid and gas, ν_1 and ν_g are the viscosities of the liquid and gas, d_0 is the initial droplet size, U_g is the gas velocity, and m_0 is the initial droplet mass.

The temperature in the wake varies according to the following law:

$$c_g \rho_g \frac{dT}{dt} = n V_{dr} Q W$$

where n is the number of droplets per unit volume, c_g and ρ_g are the specific heat and density of the gas mixture, Q is the heat of reaction, and W is the chemical reaction rate.

(4) After the wake self-ignites and the main droplet disintegrates due to Lamb–Taylor instability into n' fragments, the cloud of these fragments starts

burning in the diffusion mode by the droplet burning law, and the temperature of the mixture can be obtained from:

$$c_g \rho_g \frac{dT}{dt} = \frac{\pi}{4} n n' Q_l \rho_l K (d_1^2 - Kt)^{1/2}$$

or

$$c_g \frac{dT}{dt} = n_0 Q_l \rho_l \pi K \left[d_1^3 - \frac{(T - T_1)\rho_0 2 C_g}{3 n_0 \rho_l Q_l \pi} \right]^{1/3}$$

where T_1 is the temperature corresponding to the beginning of integration of the equation, K is the evaporation constant, and n' is the number of fragments formed after break-up of the main droplet body.

Calculations for a fuel simulating gasoline show that inhomogeneity of the mixture increases the critical energy of detonation initiation by a factor of about 3 to 5. The predicted values are consistent with experimental findings.

The situation with solid particles is less complicated on the one hand, because normally the shape of particles does not change behind the shock front even at the gasification stage, and more complicated, on the other, because the shape of particles is rarely regular and the heat transfer parameters and drag force acting on them are known only roughly. Both experimental and theoretical estimates demonstrate that only mixtures of particles whose minimum size does not exceed 5 μm are detonable. This makes numerical modeling of detonation initiation in suspensions of solid particles easier because they acquire the gas velocity much faster than they ignite.

The most popular model of solid particle ignition and burning is based on the concept of ignition temperature. According to this concept, a particle is ignited when its average temperature reaches a prescribed value. After that the particle burns. The main problem is how to prescribe the ignition temperature, T_{ign}. This parameter is often used to fit calculations to experimental data, but can also be predicted from an analysis of the physical processes. For example, for aluminum particles T_{ign} turned out nearly equal to aluminum melting point, which is explained by the fact that melted Al particles in an oxidizer flow are shattered and expose an active metal surface to the oxidizer. The measured and predicted critical energy of detonation initiation in Al suspensions with particle size close to 1 μm are quite consistent. Detonability of such suspensions is similar to that of propane–air mixtures. Interestingly, coating of Al particles with volatile oxidizers or active fuels (BaO_2, polyvanadate, carborane, fluorinated hydrocarbons) reduces markedly (by a factor of 0.6–0.7 for plane wave initiation) the critical initiation energy. This can be also predicted by the suggested models. The model was successfully tested in calculations of the minimum energy of direct initiation of explosive powders (HMX, RDX, TNT) suspended in air.

Thus, the available models are capable of predicting the critical energies of direct detonation initiation in all types of detonable mixtures, at least with an accuracy commensurate with the experimental accuracy.

INITIATION BY WEAK SOURCES

Initiation by weak sources implies that detonation onset includes a stage of burning. The DDT problem has repeatedly been tackled theoretically but so far with not very much of success. The classical pattern of this transition is perfectly understood but only qualitatively. It includes the stages of

(i) acceleration of the laminar flame due to the growth of its surface area,

(ii) turbulent flame wrinkling and generation of intense transverse and longitudinal quasi-acoustic waves,

(iii) formation of a shock wave with an inhomogeneous temperature distribution behind its front,

(iv) mixture self-ignition in hot spots arising due to collisions of transverse compression waves behind the main shock front; acceleration of the flames originating at these hot spots and spreading along the temperature gradients around the hot spots up to local onset of detonation; the average temperature of the shock-compressed gas is still lower than that required to ignite the mixture with reasonably short induction periods, and

(v) coalescence of the locally born detonation waves with each other and with the leading shock front to produce an overdriven detonation throughout the duct section area which decays to the CJ state.

Stages (ii)–(iv) are least amenable to computer simulation because they require adequate models of turbulence to calculate flame acceleration and generation of compression waves and very fine computational grids to resolve hot spot ignition and flame acceleration. A modified k–ε model of turbulence and effective ignition kinetics (taken from shock tube measurements), as well as some simplifying assumptions, yield, despite relatively rough modeling, the results which are approximately consistent, even quantitatively, with the measured predetonation distances.

However, the classical DDT scheme provides very long predetonation distances unsuitable for practical applications. It is efficient only in the presence of surfaces inducing turbulence. As to spherical geometry, so far no experimental evidence of pure DDT from a point-like weak source has been reported.

The key objective of the present work is to discuss the methods of shortening these distances, rather than to analyze the whole DDT process. There are a few experimental methods for reducing predetonation distances. The most popular approach is to introduce the so-called Shchelkin spiral which turbulizes the flow near the duct walls. Another approach is to use small-diameter tubes (predetonation distances are known to diminish with decreasing tube diameters) and a cone to let the detonation wave enter ducts of a larger size without decaying. But even with these approaches, one is incapable of reducing predetonation

distances to lengths reasonably short for practical devices. Our experiments have proved that the most efficient approach is installation of perforated discs in a duct with a blockage area decreasing and the disc spacing increasing with distance from the ignition source. The main idea behind this method is to use jet ignition of the mixture in the compartments between the discs. It is hot jets that pass through perforations in the discs rather than flame fronts. They increase the burning rate drastically. With this method we were able to produce a detonation in a hydrogen–air mixture at the distance of about 1 m in a tube 120 mm in diameter, and at the distance of 1.5 m in a propane–air mixture in a tube of the same diameter. In a smooth tube of the same diameter, the expected predetonation distance would exceed 100 m.

Jet ignition is very efficient in transforming mixture burning into detonation or detonation-like modes of reaction propagation, no matter what kind of a jet is used: hot reaction products, burning mixture, or reactive oxidizer, e.g. fluorine [10]. The authors of [10] suggested an interesting hypothetical scheme of the detonation initiation process which includes formation of shock waves in the vortex arising at the leading jet edge. Interaction of these waves produces a Mach disc which in the final run serves as a detonation precursor. Whatever the particular gasdynamic pattern of the transition process, jet ignition has a common basis — blast wave acceleration in the media with temperature and concentration gradients which ends up in close coupling between the shock wave and the heat release front [11]. The physical nature of detonation development in inhomogeneous mixtures is quite obvious. Shock waves can be augmented by heat release in the gas behind its front when the gas temperature (or radical concentration) and chemical reaction rate is high enough for any changes in the wave amplitude to significantly affect the heat release, and when reaction time gradient in the medium is small enough that a small perturbation arising due to a local reaction is capable of inducing reaction in neighboring layers. The criterion for coupling suggested in [12] reflects this idea: the reaction front should propagate at a velocity approximately equal to the representative velocity of perturbations

$$\frac{dt_{ign}}{dl} \sim (\gamma RT)^{1/2}$$

where t_{ign} is the ignition delay time, l is the distance, γ is the ratio of specific heats, and R is the gas constant.

The best method of detonation initiation by weak sources most suitable for practical purposes is mixture preheating to a preignition state or sending a weak shock wave through a burning heterogeneous mixture. Three experimental observations vividly illustrate the efficiency of this approach. The first is ignition of mixtures behind reflected shock waves, where reactions originating in hot spots are transformed into detonation within a few centimeters. In practice, this phenomenon results in extremely high pressure overshoots at the ends of long ducts. The second experimental evidence is fast transition of a weak shock

20
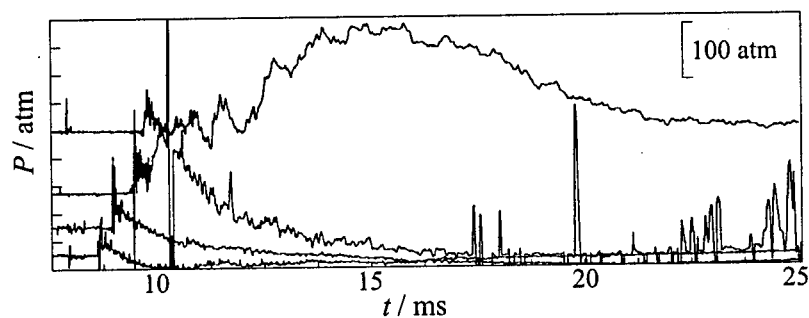
Pressure gauge	1	2	3	4
max. pressure, atm	50	35	110	190
V, m/s	2450		2180	2300

Figure 14 Pressure records for a detonation wave initiated by explosion of an ethylene–oxygen mixture (5 MJ/m^2) in an Al + NH$_4$NO$_3$ mixture suspended in the detonation products of ethylene–oxygen mixture. The average heterogeneous mixture density is about 3 kg/m^3. Al and NH$_4$NO$_3$ were initially spread throughout the floor of a tube 120 mm in diameter filled with an ethylene–oxygen mixture at atmospheric pressure, detonation of this mixture lofted the solid particles and fired the same mixture at 5.5 atm in a small initiator volume. As seen, detonation with full heat release sets in at the third pressure gauge. Curve numbers increase upward

wave spreading through a burning suspension of large kerosene drops in oxygen. This observation has a direct relevance to excitation of high-amplitude pressure pulses in liquid-propellant combustion chambers. And finally, Figs. 14, 15, and 16 illustrate how easily a detonation can be initiated in a burning dust suspension (Al + NH$_4$NO$_3$) either by weak shock wave sources (explosion of a gaseous mixture) (Figs. 15 and 16) or by the DDT process (Fig. 16). All our attempts to initiate detonation in these suspensions in cold air failed.

ACKNOWLEDGMENTS
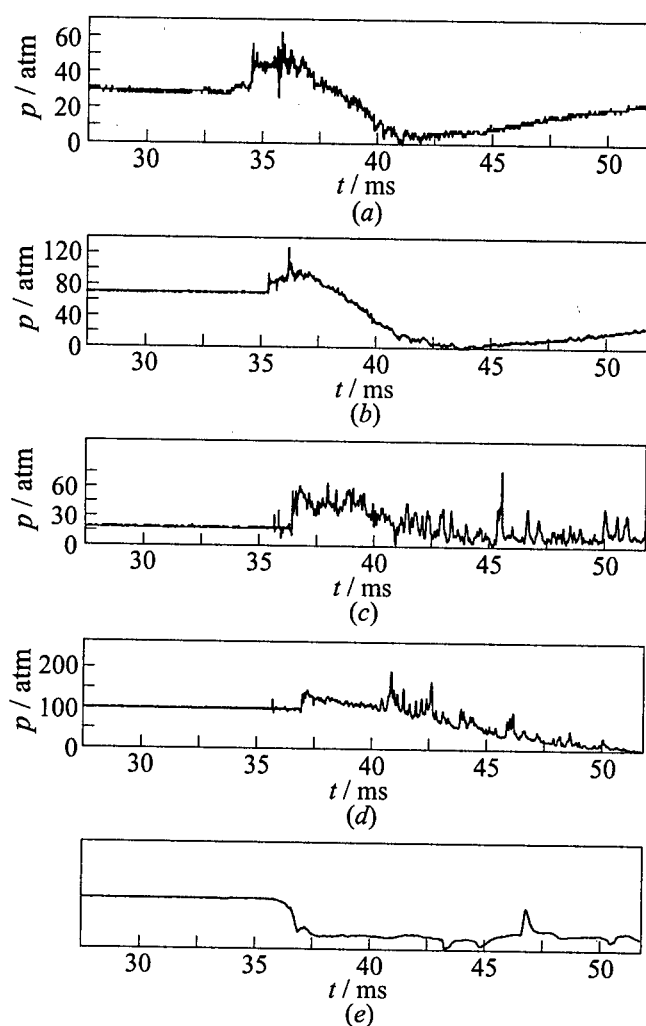
Figure 15 Detonation initiation in Al+NH$_4$NO$_3$ suspension in air by explosion of the same gas charge as in Fig. 14. Burning Al + NH$_4$NO$_3$ mixture is injected from a small cylindrical combustion chamber mounted at the end of the same tube as in Fig. 14. The average suspension density in the tube is about 3 kg/m^3. Pressure gauges: 1 (*a*), 2 (*b*), 3 (*c*), and 4 (*d*); (*e*) — luminosity record
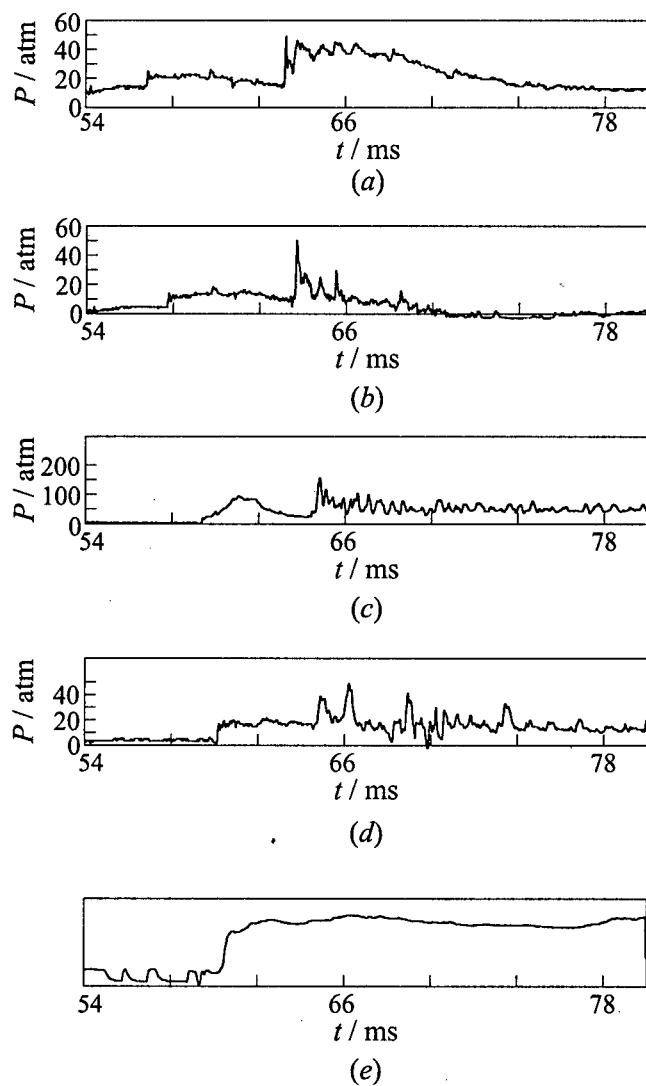
Figure 16 Same as in Fig. 15, but without gaseous initiator

REFERENCES

1. Zel'dovich, Ya. B., "To the Theory of Detonation Propagation in Gaseous Systems," *Sov. J. Experimental Theoretical Physics*, **10**, 5, 1940.

2. Von Neumann, J., Progress Report on Theory of Detonation Waves, Office of Scientific Research and Development, Rep. No.5, 49, 1942.

3. Sedov, L. I., *Similarity and Dimension Methods in Mechanics*. Nauka, Moscow, 1970.

4. Zel'dovich, Ya. B., Kogarko, S. M., and Simonov, N. N., "Experimental Investigation into Spherical Gas Detonation," *Sov. J. Technical Physics*, **26**, 8, 1744, 1956.

5. Shchelkin, K. I., and Troshin, Ya. K., *Gasdynamics of Combustion*. USSR Akademy Sci. Publ., Moscow, 1963.

6. Bach, G. G., Knystautas, R., and Lee, J. H., "Direct Initiation of Spherical Detonations in Gaseous Explosives," *Proc. 12th Symposium (International) on Combustion*, The Combustion Institute, Pittsburgh, PA, 1968.

7. Levin, V. A., Markov, V. V., and Osinkin, S. F., "Modeling of Detonation Initiation in a Gaseous Combustible Mixture by Electric Discharge," *Sov. J. Chemical Physics*, **3**, 4, 611, 1984.

8. Vasil'ev, A. A., Marginal Modes of Gas Detonations, Doctor-of-Science Thesis, M. A. Lavrent'ev Institute of Hydrodynamics, Novosibirsk, 1995.

9. Bokhon, Yu. A., and Shulenin, Yu. V., "Minimum Energy of Initiation of Spherical Gas Detonation in Some Hydrogen Mixtures," *Sov. J. Doklady USSR Academy Sci.*, **245**, 3, 623, 1979.

10. Murray, S. B., Moen, I. O., Thibault, P. A., Knysautas, R., Lee, J. H. S., and Sulmistras, A., "Initiation of Hydrogen–Air Detonations by Turbulent Fluorine–Air Jets," In: *Dynamics of Detonations and Explosions, Progress in Astronautics and Aeronautics Ser.* AIAA Inc., Washington, DC, **133**, 91, 1991.

11. Zel'dovich, Ya. B., Librovich, V. B., Makhviladze, G. M., and Sivashinsky, G. I., "On the Development of Detonation in Non-Uniformly Preheated Gas," *Acta Astronautica*, **15**, 313, 1970.

12. Frolov, S. M., Gel'fand, B. E., and Tsyganov, S. A., "Initiation of a Detonation Wave Due to Multistage Self-Ignition," In: *Dynamics of Detonations and Explosions, Progress in Astronautics and Aeronautics Ser.* AIAA Inc., Washington, DC, **133**, 133, 1991.

DETONATION INITIATION IN GASEOUS AND HETEROGENEOUS SYSTEMS

A. A. Vasil'ev, S. A. Zhdan, and V. V. Mitrofanov

Preferable models for determination of critical initiation energies for detonation wave formation in gaseous and heterogeneous systems (fuel droplets – gaseous oxidizer) are discussed. For gas–droplets systems, a new simple method for estimating the critical initiation energies and analytical formulas are proposed on the basis of numerical investigations of spray detonation initiation. For gaseous mixtures, the priority is given to "multi-point" initiation model based on considering the collisions of transverse waves as the micro-initiators of a multi-front detonation ("hot points"). For various fuel–oxygen and fuel–air mixtures, the dependencies of the critical initiation energy on mixture composition, droplets size, etc. are defined, that allow comparison of detonation hazards of various reactive systems under plane, cylindrical and spherical initiation. The calculated results correlate reasonably with available experimental data.

INTRODUCTION

The analyses of experimental and theoretical results on spray and gaseous detonations are presented elsewhere (e.g. [1–6] and [7–9], respectively). One of the basic problems in the detonation theory for gaseous and heterogeneous media is detonation initiation by intense shock wave (SW), formed as a result of a local energy deposition. This important problem was successfully solved by using physico-mathematical models for non-steady gaseous and spray detonation together with experimental investigations.

The mathematical models of spray detonation initiation [11–18] are based on the conservation equations of mechanics of heterogeneous medium [10] (disperse mixtures). The detonation wave (DW) in gas–droplets reacting mixture consists of a lead SW and a relaxation zone behind SW, where the following processes take place: acceleration of droplets, their deformation and possible break-up, phase transition, convection and diffusion of mixture components, chemical reactions, etc.

A set of simplifying assumptions is usually adopted, including the following:

(i) characteristic distances of considerable change in average flow properties are much greater than the distance between individual droplets;

(ii) viscosity manifests itself only in the interaction between gas and condensed phases;

(iii) compressibility of droplets and collisions between droplets can be neglected;

(iv) for polydispersed fuel sprays, the size distribution of droplets is discretized by the finite number of groups, k, containing droplets of equal sizes.

Such mathematical models of non-steady spray detonations were implemented into computer codes. The codes were used to investigate and numerically analyse the specific features of detonation evolution in heterogeneous (gas–droplets) systems and also used to calculate the critical energies of detonation initiation, E_*.

However, to obtain the value of E_* for a given gas–droplets mixture at any specific condition it is necessary to numerically solve the whole set of complex non-stationary differential equations of heterogeneous mechanics. It should be mentioned, that such a procedure is also typical for homogeneous gaseous systems, in which non-stationary equations of gas-dynamics and chemical kinetics are usually solved. Therefore, it is important to formulate simple models and obtain analytical formulas for estimating the detonation initiation energies for both gas–droplets and gaseous mixtures, by applying some important dependencies between governing parameters inherent to the problem. The aim of this paper is to obtain such dependencies on the basis of numerical simulation of DW in heterogeneous media.

CALCULATED RESULTS FOR GAS–DROPLETS MIXTURES

The evolution of DW in gas-droplets systems, as well as the initiation energy of spherical, cylindrical and plane gas–droplets detonations of hydrocarbon fuels with initiators of different energy density (point explosion, high explosive charge, detonation of reacting gas mixture) were studied numerically [15–18].

It is found from the analysis of the numerical solutions, that there exists the critical energy E_*, such that the explosion dynamics differs considerably for the explosion energy $E_0 > E_*$ and $E_0 < E_*$ (Fig. 1). Solid curves in Fig. 1 show the evolution of DW in the case with $E_0 > E_*$. In this case, after initiation the DW attains a minimum propagation velocity $D_{\min} < D_0$, where D_0 is the steady
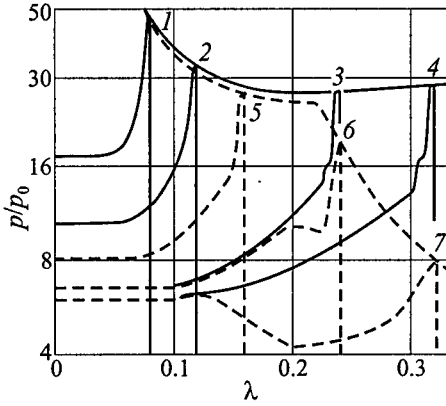
Figure 1 Predicted explosion dynamics under supercritical (solid curve) and subcritical (dashed curve) initiation of detonation in gas–droplets mixture. $\lambda = r/r^0$ is the dimensionless distance, $\tau = tu_1/d_0(\rho_2^0/\rho_{10})^{0.5}$ is the dimensionless time

detonation velocity. Then, after passing the minimum, the DW velocity starts to increace towards D_0 "from below." Dashed curves in Fig. 1 show the case with $E_0 < E_*$. Clearly, there exists a distance, corresponding to a certain shock radius, r_f^*, such that at $r_f > r_f^*$ the detonation wave decays. The value of r_f^* decreases with decreasing E_0. The magnitude of E_* depends on the ignition delay and fuel droplet size.

Non-monotonic behavior of unsteady DW velocity is typical for all calculations. DW attains minimum velocity $D_{\min}$ at distance $\lambda_f = r_f/r^0 \approx \nu/8$, where $r^0 = (E_0/\alpha_\nu p_0)^{1/\nu}$ is the dynamic radius, p_0 is the initial pressure, $\nu = 1, 2, 3$ for planar, cylindrical and spherical symmetry, respectively, α_ν is the parameter of the blast model. The values of $D_{\min}$ decrease monotonically, with decreasing point explosion energy and with increasing droplet size in a fuel spray.

Explosion of a monodispersed fuel spray in gaseous oxidizer contains two independent parameters with the dimension of length: $r_0 = (E_0/p_0)^{1/\nu}$, and droplet diameter d_0. The characteristic time for a droplet is $t_0 = d_0(\rho_2^0/\rho_1)^{0.5}/u_1$. For the ideal DW, the propagating velocity D_0 correlates with the characteristic length $\lambda_0 = t_0 D_0 = d_0(\rho_2^0/\rho_{10})^{0.5}/(\sigma_0^{0.5} - 1/\sigma_0^{0.5})$, where $\sigma_0 = \rho_1/\rho_{10}$, and $u_1 = D_0(1 - 1/\sigma_0)$ are the density ratio and gas velocity behind SW. To obtain the quantitative dependencies of the minimum velocity $D_{\min}$ of non-steady DW on the governing parameters r_0, d_0, and ν in a heterogeneous medium, particular calculations were performed for spherical, cylindrical and plane geometries.

The analysis of the minimum velocity, based on calculated data, shows that the ratio $D_{\min}/D_0$ depends only on the dimensionless combination $x = \lambda_0/r_0$ and is independent of ν. The values of $D_{\min}$ for monodispersed sprays of hydrocarbon fuels can be presented as a universal function of x:

$$\frac{D_{\min}}{D_0} = 1 - 69x \qquad (1)$$

For polydispersed fuel sprays consisting of k groups of droplets, $k + 1$ independent parameters: d_{i0} $(i = 2, \ldots, k + 1)$ and r_0, exist with the dimension of length. It is not clear *a priori*, whether Eq. (1) is correct in this case. By comparing the results of calculations of $D_{\min}$ for mono- and polydispersed sprays,

it is possible to show, that a polydispersed spray with the Nukiyama–Tanasawa size distribution function [19] can be represented by the monodispersed spray with an average droplet diameter d_{av} and with the minimum velocity of non-steady DW to be the same as for the original polydispersed spray. Tests show that $d_{av} = d_{3,2}$ with

$$d_{3,2} = \frac{\sum_{i=2}^{k+1} n_{i0} d_{i0}^3}{\sum_{i=2}^{k+1} n_{i0} d_{i0}^2} = \frac{\alpha_d}{\sum_{i=2}^{k+1} \alpha_{i0}/d_{i0}}$$

where α_d is the volume fraction of droplets in the mixture, and α_i is the volume fraction of droplets of size d_i.

The analysis of numerical solutions for detonation initiation of monodispersed and polydispersed sprays of liquid fuels in air or oxygen with droplet diameter $d_0 = 50$–700 μm showed, that the critical dynamic radius of direct detonation initiation (by intense SW) is independent of the problem geometry:

$$r^0(\nu) = \left(\frac{E_{*\nu}}{p_0}\right)^{1/\nu} \cong const = r_c \qquad (2)$$

where $E_{*\nu}$ is the critical initiation energy relevant to symmetry index ν. Experimental data on initiating liquid hydrocarbon sprays in air by ball and cord charges of condensed explosive correlate well with Eq. (2).

The constancy of r_c for different ν is not a strictly proved theoretical conclusion, but it is very useful for estimations. At a known initiation energy for some spatial symmetry, it is possible to determine r_c and then the initiation energies for the other symmetry as

$$E_{*\nu} \cong p_0 r_c^\nu \qquad (3)$$

Another useful correlation obtained on the basis of numerical solutions is the ratio of r_c to the critical radius, $r_{c\nu}$, where DW attains minimum velocity:

$$r_{c\nu} \cong \frac{\nu r_c}{8} \qquad (4)$$

With the help of Eqs. (3) and (4), it is possible to express the initiation energies per unit area of the wave front at critical radius for different ν, as:

$$\frac{E_{*1}}{2} = 0.5 p_0 r_c , \qquad \frac{E_{*2}}{2\pi r_{c2}} = 0.64 p_0 r_c , \qquad \frac{E_{*3}}{4\pi r_{c3}^2} = 0.57 p_0 r_c$$

These values turn out to be close to each other in all the three cases of symmetry.

APPROXIMATE INITIATION MODEL FOR HETEROGENEOUS GAS–DROPLETS SYSTEMS

Equation (1) yields critical detonation parameters if it is modified in such a way that the chemical ignition delay of evaporated fuel, $t_{ig} = K(\rho_{10}/\rho)^m (T_{10}/T)^n \exp(E_{act}/RT)$, is taken into account, where E_{act} is the activation energy, R is the gas constant, m and n are the exponents, K is the pre-exponential factor, T_{10} is the temperature of shock-compressed gas at $D = D_0$. The decrease in DW velocity to a value below D_0 during initiation by an explosion source is determined mainly by the amount of energy required for creating the zone of shock-compressed unreacted substance (the "chemical peak zone"). For instantaneous vaporization and consumption of fuel shed from droplets, this zone is of the order of $2\lambda_0$ thickness, and weakly depends on the DW velocity in an interval $(0.7-1.0)D_0$. Ignition delays increase the thickness of the zone by the value $x_{ig} = x_0 y^M \exp[\beta(y^\alpha - 1)]$, where $y = D_0/D_{min}$, $\beta = E_{act}/RT_{10}$, $M = \alpha m - 1 + \delta(n + 1)$, $\alpha = d \ln T/d \ln D$, $\delta = d \ln \sigma/d \ln D$ [20]. Considering this adjustment, the following equation for y can be obtained from Eq. (1):

$$1 - \frac{1}{y} = 34.5 \frac{2\lambda_0 + x_0 y^M \exp[\beta(y^\alpha - 1)]}{r_0} \tag{5}$$

This equation has a solution if the parameter r_0 exceeds a definite critical value r_c, which is derived from the joint solution of Eq. (5) and the equation obtained by differentiating Eq. (5) with respect to y. The correlation for the critical velocity y_c takes the form

$$A = 0.5[(y - 1)(M + \alpha\beta y^\alpha) - 1]y^M \exp[\beta(y^\alpha - 1)], \qquad A = \frac{\lambda_0}{x_0} \tag{6}$$

After solving Eq. (6) one can obtain the critical value r_c from the equation

$$r_c = 34.5 x_0 \frac{2A + y_c^M exp[\beta(y_c^\alpha - 1)]}{1 - 1/y_c} \tag{7}$$

At $A = 0$, Eqs. (6), (7) determine the critical parameters y_g, r_g for a given fuel. If the fuel is already in the gaseous phase, then the formulas correspond to initiation of gaseous detonation. In this case, it is convenient to rewrite Eq. (7) in the form:

$$\frac{r_c}{r_g} = \frac{1 - 1/y_g}{1 - 1/y_c} \cdot \frac{2A + y_c^M \exp[\beta(y_c^\alpha - 1)]}{y_g^M \exp[\beta(y_g^\alpha - 1)]} \tag{8}$$

In the general case, Eq. (6) is solved iteratively together with Eq. (7). Therefore, knowing the equations for chemical ignition delays from Eqs. (6)–(8), it is
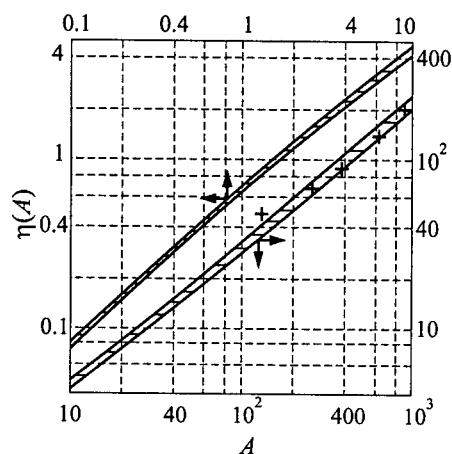
Figure 2 A plot of $\eta = r_c/r_g - 1$ vs. $A = \lambda_0/x_0$ based on Eqs. (6)–(8). Dashed area reflects the dependence of η on α, β, and M. The plus (+) sign corresponds to detailed numerical simulations

possible to determine detonation initiation parameters in heterogeneous (gas–droplets) or gaseous mixtures.

Let us analize the behavior of solution of Eq. (8). Denote $\eta = r_c/r_g - 1$. According to Eqs. (6) and (8), η is the function of four parameters, $\eta = F(\alpha, \beta, M, A)$. For most realistic detonating mixtures, α, β, and M vary within the following ranges: $\alpha \in [1.4, 1.6]$, $\beta \in [5, 10]$, $M \in [-0.5, 0.5]$. The numerical results for Eq. (8) with α, β, and M varied within these ranges, are presented in Fig. 2 as dependencies $\eta(A)$. The width of a dashed strip demonstrates the dependence on α, β, and M. Shown in the same figure, using the sign +, are the results of detailed numerical solution of the initiation problem [17] for suspensions in oxygen. It is seen, that function η increases monotonically with A and weakly depends (within $\pm 15\%$) on α, β, and M. Moreover, for fuel–air mixtures ($A \in [0\text{--}10]$), the range of change of η is less than 6% at a fixed A. So, the parameter $A = \lambda_0/x_0$ is the basic dimensionless parameter depending on the critical radius. This fact is principally important for a constructive approach to determine the critical initiation energies of heterogeneous detonations. It allows, for any gas–droplets mixture, the use of graphic dependence $\eta(A)$ in Fig. 2 to obtain the values of initiation energy of heterogeneous detonation instead of solving the set of Eqs. (6)–(8).

APPROXIMATE INITIATION MODELS FOR GASEOUS SYSTEMS

The numerical calculations for gaseous mixtures within the framework of a one-dimensional detonation model (e.g., [21–22]) describe in detail a qualitative picture of one-dimensional initiation: attenuation of an initiating wave at initiator energy $E < E_*$ and formation of DW at $E \geq E_*$ (as for gas–droplets systems). In [23], a quantitative approach of calculating E_* with a parameter taken from experiments is suggested and implemented for the stoichiometric hydrogen–air mixture within the framework of "detailed" kinetics model. Other mixtures

needed new calculations. A realistic DW in a gaseous mixture differs essentially from the classical plane model. As a matter of fact, the DW is a multi-front pulsating system consisting of shock waves, rarefaction waves, contact discontinuities, local zones of chemical reactions, etc. (e.g, [24–25]). Despite non-uniformity and non-stationarity, a certain regular structure with a characteristic linear scale, called transverse size of an elementary cell a, is typical for the DW.

About twenty approximate models for a one-dimensional detonation initiation in gaseous mixtures are known so far. All were analyzed previously in [26, 8]. Such models allow the estimation of a value of E_* with some accuracy.

In a multi-front DW, at any time instant, the induction zone differs significantly (up to two orders of magnitude) for various elements of the DW front. At these conditions, using a uniform ignition delay for a whole front (as is the case in one-dimensional models) can strongly misrepresent the initiation conditions. The reason for this is that ignition event is governed by a local temperature in the 'hot spots' rather than by the average temperature. Such spots in a real DW are the sites of collisions of transverse waves. The account of non-one-dimensional collisions of shock-wave configurations in a realistic detonation front allows to essentially lower the level of the critical initiation energy (in comparison with one-dimensional models). Such a model of multi-point initiation (MPI) was suggested for the first time in [27] and then modified in [28–29]. The most detailed description of the MPI-model is presented in [26].

According to the latest version of the model, the energy of individual "hot spots," E_{00} and the critical initiation energies (for $\nu = 1, 2, 3$), are defined by the following formulas:

$$
\begin{aligned}
E_{00} &= 4\varepsilon^2 \alpha \rho_0 D_0^2 b^2 \\
E_1 &= \frac{\pi(d_{**}/a)}{4b} E_{00} = A_1 \rho_0 D_0^2 b \\
E_2 &= \frac{\pi(d_{**}/a)}{2} E_{00} = A_2 \rho_0 D_0^2 b^2 \\
E_3 &= 2\pi \tan \varphi (d_{**}/a)^2 b E_{00} = A_3 \rho_0 D_0^2 b^3
\end{aligned}
\tag{9}
$$

where $\tan \varphi = a/b$, b is the longitudinal cell size, ε is one of the solutions in the detonation cell model [30], α is the parameter of the strong explosion model, d_{**} is the critical diameter for reinitiation of spherical detonations under diffraction, ρ_0 is the initial gas density, and D_0 is the ideal detonation velocity.

Other approximate models for estimating E_* are worth noting. In [20, 31], the following relationships are suggested:

$$
\begin{aligned}
R_{cr} &\cong 8\nu k^2 \left(\sigma_{10} + \frac{1}{\sigma_{10}} - 2 \right) \frac{\lambda_{10}}{3 E_{act}/RT_{10}} \\
E_{*\nu} &= \alpha_\nu p_0 \left(\frac{8 R_{cr}}{\nu} \right)^\nu
\end{aligned}
\tag{10}
$$

31

where E_{act} is the effective activation energy of the induction period (within the framework of the average description by the help of the Arrhenius equation), $k = I/U$ is the ratio of enthalpy I to internal energy U, $\lambda_{10} = (D_0 - u_0)\tau_{10}$ is the induction zone width behind a shock wave propagating at velocity D_0, and σ is the density ratio across such a wave.

According to Eqs. (6), (7), one should set $A = 0$ when considering gaseous mixtures. Expanding the resultant expressions into a series in terms of $(y - 1)$ and considering only quadratic terms, approximate expressions for y_g, r_g, and $E_{*\nu}$ are obtained:

$$y_g = \frac{1 + 2\xi^{-1}}{1 + (1 + 4\alpha^2\beta/\xi^2)^{0.5}}$$

$$r_g = \frac{92x_0}{y_g - 1} \approx \frac{105\alpha}{C\sigma_0}b \tag{11}$$

$$E_{*\nu} = p_0 r_g^{\nu}$$

where $\xi = \alpha\beta + M$. At $\beta \geq 7$, one can obtain the approximate solution for y_g and r_g with a required accuracy, e.g., $y_g - 1 \approx 0.1$, etc. According to data in [28, 32–34], coefficient $C = 1.4 \pm 0.6$. Moreover, for fuel–air mixtures C is lower than for fuel–oxygen mixtures.

Let us take $C = 1.1$ and 1.7 for fuel–air and fuel–oxygen mixtures, respectively. The resulting dependence (11) of the critical initiation parameters on the width of the induction zone correlates with data in [35], and the general form of relations is similar to that obtained in [36, 37]. The only differences are the multipliers before b^{ν} or x_0^{ν}. When compared with experimental data, the accuracy of predictions based on Eqs. (10), (11) is approximately the same as that attained by using the models of [38, 39].

In [7], the critical energy of spherical detonation initiation is defined as

$$E_c = \frac{2197\pi\gamma_0 p_0 J \mathrm{M_{CJ}}^2 a^3}{16} \tag{12}$$

where $\mathrm{M_{CJ}}$ is the Mach number of the ideal DW, $J \cong Q/(\nu D_0)$, Q is the chemical energy release in the DW.

In [40], the critical energy of spherical detonation initiation is considered to be proportional to the induction zone length, l_{10}, which is calculated on the basis of a detailed kinetic mechanism:

$$E_{*3} = B\lambda_{10}^3 \tag{13}$$

where the coefficient B is determined from a measured value of E_{3*} for a fixed mixture composition and then considered constant for other mixtures of the given fuel.

The formulas of other available models show a much greater discrepancy when compared with experimental data and therefore are not discussed here.

COMPARISON OF CALCULATED AND EXPERIMENTAL RESULTS

Unfortunately, only a small portion of experimental data on detonations is related to initiation of fuel–droplets systems. Therefore, the comparison of calculated results with experimental data can be performed only in a few cases. For example, in [41], when initiating detonation of a cylindrical monodispersed spray of kerosene in oxygen (fuel droplet size $d_0 = 400\ \mu$m) by an explosive charge, the value $E_c \approx 0.34$ MJ/m was obtained. The experiments were performed in a sector shock tube at controlled fuel concentrations with the mixture equivalence ratio $\phi = 0.33$. The calculated values for this case are 0.57 MJ/m $< E_c <$ 0.75 MJ/m. The correlation of calculated and experimental data for gas–droplets systems with the accuracy of a factor of 2 should be considered good, since the kinetic data for heterogeneous ignition exhibit considerable discrepancy.

The proposed method for estimating the detonation initiation energy for gas–droplets systems allows sorting of heterogeneous mixtures by their detonation sensitivity and explosion hazards. Referring to Fig. 2, within the range $A \in$ (0–10) (which corresponds to fuel–air mixtures with droplet sizes $d_0 \le 1$ mm) the dependence $\eta(A) = r_c/r_g - 1$ can be approximated (with an accuracy $\pm 5\%$) by the formula

$$\eta(A) = \frac{1.6A}{\ln(1 + 1.6A)} - 1 \tag{14}$$

According to Eq. (14), function $\eta(A)$ increases with parameter $A = \lambda_0/x_0$ slower than linearly. The sensitivity index for heterogeneous (gas–droplets) media is constructed for equal values of droplet diameters d_0 (or, more precisely, equal values of λ_0) and coincides with the sensitivity index of the corresponding gaseous (vapour) reacting mixtures. That is, the following statement is put forward:
> "If the sensitivity indices for gas (vapour) mixtures are arranged in the line:

$$r_{g,1} \to r_{g,2} \to r_{g,3} \to \cdots$$

> then for any λ_0 the sensitivity indices of gas–droplets mixtures with respect to detonation in air can be arranged in the same line:

$$r_{c,1} \to r_{c,2} \to r_{c,3} \to \cdots\ ^"$$

Example: Knowing the critical radius of gaseous detonation, r_g and the activation energy β, it is possible to determine the critical initiation radii of heterogeneous detonation. Consider the stoichiometric benzene–air mixture, $\phi = 1$. According to the experimental data of [42, 43], a vaporized benzene–air mixture with $\phi = 1$ is initiated by 0.3 kg of TNT. Converting to critical radius, one obtains $r_g = (E_0/p_0)^{1/3} = 2.3$ m.

33

The activation energy of benzene is $E_{act} \approx 35$ kcal/mol [44], therefore for $D_0 = 1800$ m/s, $\beta = E_{act}/RT_* = 11.4$; $\alpha = 1.446$, $\sigma_0 = 6.6$. Parameter $A = \lambda_0/x_0$ can be expressed in terms of r_g and β using the second formula in Eq. (11): $A = 150\beta\lambda_0/r_g$. For benzene of density $\rho_2^0 = 700$ kg/m^3, from the correlation for λ_0 one obtains $\lambda_0 = 11.85d_0$ (m). Then the critical initiation radii of heterogeneous detonations, r_c, can be obtained from Eq. (14) depending on initial diameter of benzene droplets, d_0, in a fuel spray. Table 1 shows the values of r_c and critical initiation energies for a set of droplet diameters d_0 in a stoichiometric benzene–air mixture.

Table 1 Predicted critical dynamic parameters of heterogeneous detonations of stoichiometric benzene–air mixture

d_0 μm	A	r_c m	E_{*1} MJ/m^2	E_{*2} MJ/m	E_{*3} MJ
0	0.00	2.3	0.24	0.54	1.23
50	0.44	3.04	0.31	0.94	2.85
100	0.88	3.69	0.37	1.38	5.1
200	1.76	4.84	0.49	2.37	11.5
400	3.52	6.85	0.69	4.75	32.6
800	7.04	10.33	1.05	10.8	111.7
1000	8.80	11.94	1.21	14.4	172.4

In a short paper it is impossible to present all calculated and experimental results. For gaseous mixtures, only the data on critical initiation energies are presented here.

It should be mentioned that for individual mixtures the experimental data for all types of symmetry of detonation initiation is very limited, so it is difficult to check the accuracy of Eqs. (9) or Eqs. (10), (11) for different ν. However, one complete set of data is shown in Figs. 3 to 5. Figures 3, 4, and 5 show, depending on the critical initiation energy for plane, E_1 (Fig. 3) and cylindrical, E_2 (Fig. 4) symmetry, as well as the critical explosive charge weight m_{3*} for initiation of a spherical detonation (Fig. 5) of the stoichiometric methane–oxygen mixture depending on nitrogen dilution [26]. Calculated data were obtained in [45] with Eqs. (9) being used.

The experimental spherical initiation data was the only collection that can be used to compare the different formulas for estimating critical initiation energies. Such a comparison was presented in [8, 26]. Figures 6 to 8 show the critical explosive charge weights m_{3*}, required for initiation of spherical detonations in typical fuel–air mixtures, depending on fuel concentration.

The comparison shows good agreement between predicted and measured data.
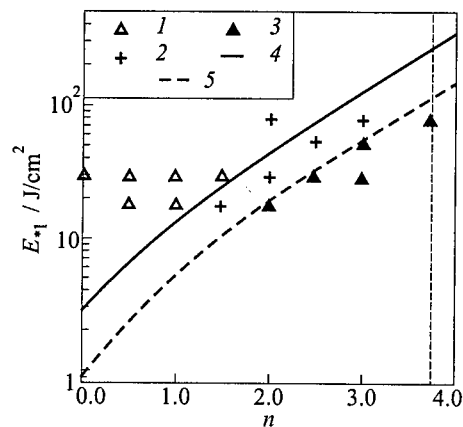
Figure 3 Critical initiation energy for plane detonation vs. nitrogen dilution for $0.5CH_4 + O_2 + nN_2$ mixture. Symbols — experiments (see [26]): *1* — detonation, *2* — unstable mode, *3* — flame, *4, 5* — models [26]. Vertical dashed line corresponds to air
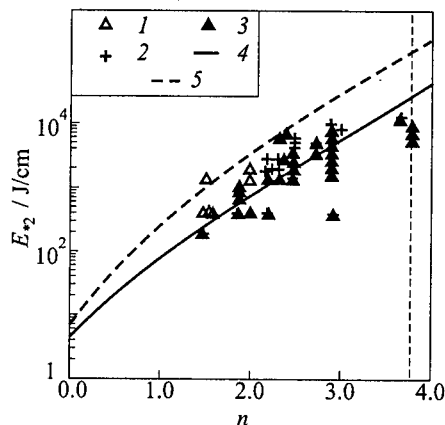
Figure 4 Critical initiation energy for cylindrical detonation vs. nitrogen dilution for $0.5CH_4 + O_2 + nN_2$ mixture. Symbols — experiments (see [26]): *1* — detonation, *2* — unstable mode, *3* — flame, *4, 5* — models [26]. Vertical dashed line corresponds to air
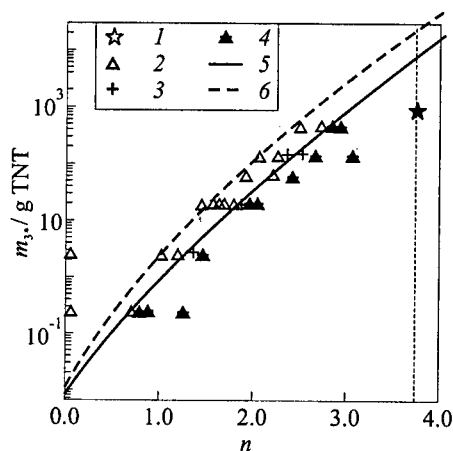
Figure 5 Critical explosive charge weight for initiating spherical detonation vs. nitrogen dilution for $0.5CH_4 + O_2 + nN_2$ mixture. Symbols — experiments (see [26]): *1* — quasi-detonations, *2* — detonation, *3* — unstable mode, *4* — flame, *5, 6* — models [26]. Vertical dashed line corresponds to air
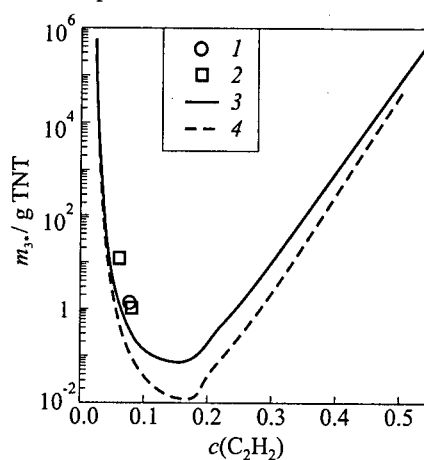
Figure 6 Critical explosive charge weight for initiation of spherical detonations in C_2H_2–air mixture vs. molar fuel concentration. Symbols — experiments (see [26]): *1, 2* — detonation. Curve *3* — models [8, 26], curve *4* — models [20, 32]

35
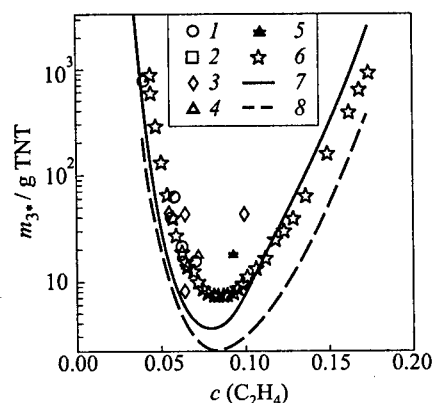
Figure 7 Critical explosive charge weight for initiation spherical detonations in C_2H_4–air mixture vs. molar fuel concentration. Symbols — experiments (see [26]): 1–5 — detonations, 6 — flame. Curve 7 — models [8, 26], curve 8 — models [20, 32]
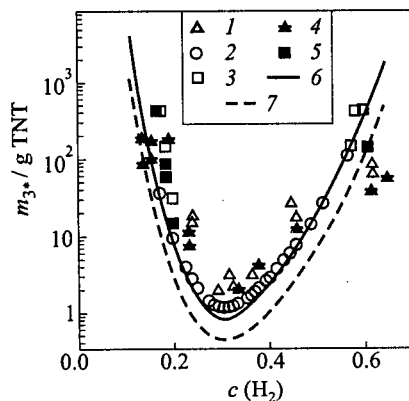
Figure 8 Critical explosive charge weight for initiation spherical detonations in H_2–air mixture vs. molar fuel concentration. Symbols — experiments (see [26]): 1–3 — detonations. Curves 6 — models [8, 26], curve 7 — models [20, 32]

CONCLUDING REMARKS

The approximate model for gas–droplets (and gaseous as a limiting case) systems, presented in this paper, and the "multi-point" detonation initiation model for gaseous mixtures correspond adequately to experimental data and can be recommended for estimating detonation hazards of different fuels.

REFERENCES

1. Webber, W. T., "Spray Combustion in the Presence of a Travelling Wave," *Proc. 8th Symposium (International) on Combustion*, The Combustion Institute, Baltimore, MD, 1962, 1129–1140.

2. Cramer, F. B., "The Onset of Detonation in a Droplet Combustion Field," *Proc. 9th Symposium (International) on Combustion*, New York – London, Academic Press, 1963, 482–487.

3. Dabora, E. K., and Weinberger, L. P., "Present Status of Detonations in Two-Phase Systems," *Acta Astronautica*, 1, 3/4, 361–372, 1974.

4. Borisov, A. A., and Gelfand, B. E., "Survey on Detonation in Two-Phase Systems," *Archivum Thermod. Spalan.*, 7, 2, 273–287, 1976.

5. Gelfand, B. E., "Contemporary State and Investigation Problems of Detonation in the System of Liquid Droplet–Gas," *Chemical Physics of Combustion Processes and Explosion. Detonation*, Chernogolovka, 1977, 28–39.

6. Nettleton, M. A., "Shock-Wave Chemistry in Dusty Gases and Fogs: A Review," *Combustion Flame*, 28, 1, 3–16, 1977.

7. Benedick, W. B., Guirao, C. M., Knystautas, R., and Lee, J. H., "Critical Charge for Direct Initiation of Detonation in Gaseous Fuel–Air Mixtures," In: *Dynamics of Explosion, Progress in Astronautics and Aeronautics Ser.* (Eds. J. R. Bowen, J.-C. Leyer, and R. I. Soloukhin), NY, **106**, 1986, 181–202.

8. Vasil'ev, A. A., "Gaseous Fuels and Detonation Hazards," *Proc. 28th Fraunhofer ICT-Conference* (Ed. N. Eisenreih), Germany, 1997, 50/1–50/14.

9. Vasil'ev, A. A., "The Experimental Methods and Calculating Models for Definition of the Critical Initiation Energy of Multi-Front Detonation Wave," *Proc. 16th ICDERS*, University of Mining and Metallurgy, AGH, Cracow, Poland, 1997, 152–155.

10. Nigmatulin, R. I., *Multi-Phase Dynamics.* Moscow, Nauka, 1987.

11. Zhdan, S. A., "Calculation of Spherical Heterogeneous Detonation," *Sov. J. Physics Combustion Explosion*, **4**, 586–593, 1976.

12. Zhdan, S. A., "Calculation of Heterogeneous Detonation Considering Fuel Droplet Deformation and Breakup," *Sov. J. Physics Combustion Explosion*, **2**, 258–263, 1977.

13. Zhdan, S. A., "Spot Explosion in Combustible Two-Phase Medium," *Continuum Dynamics*, **32**, Novosibirsk, 36–46, 1977.

14. Zhdan, S. A., and Mitrofanov, V. V., "Calculation of Critical Initiation Energy of Heterogeneous Detonation," In: *Detonation. Critical Phenomena. Physical and Chemical Transformations in Shock Waves.* Chernogolovka, 50–54, 1978.

15. Mitrofanov, V. V., Pinaev, A. V., and Zhdan, S. A., "Calculations of Detonation Waves in Gas–Droplet Systems," *Acta Astronautica*, **6**, 3/4, 281–296, 1979.

16. Zhdan, S. A., "Calculation of Heterogeneous Detonation Initiation by Condensed Explosion Charge," *Sov. J. Physics Combustion Explosion*, **17**, 6, 105–111, 1981.

17. Zhdan, S. A., "Detonation Waves in Gas–Droplet Systems upon Explosion of a Cylindrical Charge," *Abstracts of 8th ICDERS*, Minsk, 50, 1981.

18. Voronin, D. V., and Zhdan, S. A., "Calculation of Heterogeneous Detonation Initiation in a Tube by Explosion of Hydrogen–Oxyden Mixture," *Sov. J. Physics Combustion Explosion*, **20**, 4, 112–116, 1984.

19. Williams, F. A., *Combustion Theory.* Palo Alto – London, 1964.

20. Mitrofanov, V. V., "Some Critical Phenomena in Detonation, Associated with Momentum Loss," *Sov. J. Physics Combustion Explosion*, **19**, 4, 169–174, 1983.

21. Korobejnikov, V. P., *Tasks of the Theory of Point Explosion in Gases.* Nauka, Moscow, 1973.

22. Levin, V. A., and Markov, V. V., "Occurrence of a Detonation at Concentrated Energy Deposition," *Sov. J. Physics Combustion Explosion*, **11**, 4, 623–633, 1975.

23. Levin, V. A., Markov, V. V., and Osinkin, S.F., "Initiation of Detonation in Hydrogen–Air Mixture by a Spherical TNT Charge," *Sov. J. Physics Combustion Explosion*, **31**, 2, 91–95, 1995.

24. Shchelkin, K. I., and Troshin, Ja. K., *Gasdynamics of Combustion.* USSR Academy Sci. Publ., Moscow, 1963.

25. Voitzehovsky, B. V., Mitrofanov, V. V., and Topchian, M. E., *Structure of Detonation Front in Gases.* Siberian Branch of the USSR Academy Sci. Publ., Novosibirsk, 1963.

26. Vasil'ev, A. A., *Near-Critical Modes of a Gas Detonation.* Novosibirsk, 1995.

27. Vasil'ev, A. A., "An Estimation of Initiation Energy for Cylindrical Detonations," *Sov. J. Physics Combustion Explosion*, **14**, 3, 154–155, 1978.

28. Vasil'ev, A. A., Nikolaev, Ju. A., and Uljanitsky, V. Ju., "Critical Energy of Initiation of Multi-Front Detonation," *Sov. J. Physics Combustion Explosion*, **15**, 6, 94–104, 1979.

29. Vasil'ev, A. A., and Grigorjev, V. V., "Critical Conditions for Propagation of Gas Detonations in Abruptly Divergent Channels," *Sov. J. Physics Combustion Explosion*, **16**, 5, 117–125, 1980.

30. Vasil'ev, A. A., and Nikolaev, Yu. A., "Closed Theoretical Model of a Detonation Cell," *Acta Astronautica*, **5**, 983–996, 1978.

31. Zhdan, S. A., and Mitrofanov, V. V., "Simple Model for Calculating the Initiation Energy of Heterogeneous and Gas Detonations," *Sov. J. Physics Combustion Explosion*, **21**, 6, 98–103, 1977.

32. Vasil'ev, A. A., Nikolaev, Yu. A., and Ulyanitsky, V. Yu., "Calculation of Cell Parameters of Multi-Front Gas Detonations," *Sov. J. Physics Combustion Explosion*, **13**, 3, 404–408, 1977.

33. Manzhaley, V. I., Subbotin, V. A., and Scherbakov, V. A., "Stability Thresholds and Relation of Cell Size of Gas Detonations with Kinetic Constants of Explosive Gas Mixtures," In: *Chemical Physics of Combustion and Explosion. Detonation.* Chernogolovka, 45–48, 1977.

34. Gel'fand, B. E., Frolov, S. M., and Nettleton, M. A., "Gaseous Detonation — a Selective Review," In: *Progress Energy Combustion Sci.* **17**, 327–371, 1991.

35. Zel'dovich, Ya. B., Kogarko, S. M., and Simonov, N. N., "Experimental Study of Spherical Gaseous Detonation," *J. Technical Physics*, **26**, 8, 1744–1768, 1956.

36. Lee, J. H., "Initiation of Gaseous Detonation," *Annual Review Physical Chemistry*, **28**, 75–104, 1977.

37. Ulyanitskiy, V.Yu, "On the Role of "Flash" and Collision of Transversal Waves in Forming Multi-Front Structure of Detonation Waves in Gases," *Sov. J. Physics Combustion Explosion*, **17**, 2, 127–133, 1981.

38. Bull, D. C., Elworth, J. B., and Hooper, G, "Initiation of Spherical Detonations in Hydrocarbon/Air Mixtures," *Acta Astronautica*, **5**, 11–12, 997–1008, 1978.

39. Vasil'ev, A. A., "Research of Critical Initiation of Gas Detonations," *Sov. J. Physics Combustion Explosion*, **19**, 1, 121–131, 1983.

40. Westbrook, C. K., and Urtiew, P. A., "Chemical Kinetic Prediction of Critical Parameters in Gaseous Detonations," *Proc. 19th Symposium (International) on Combustion*, The Combustion Institute, Pittsburgh, PA, 615–623, 1982.

41. Nicholls, J. A., Bar-Or, R., Gabrijel, Z. *et al.*, "Recent Experiments on Heterogeneous Detonation Waves," *AIAA J.*, **288**, 4, 1979.

42. Alekseev, V. I., Dorofeev, S. B. *et al.*, Experimental Study of Detonation Initiation in Motor Fuel Sprayed in Air, Preprint IAE-4872/13, Moscow, Atominform, USSR, 1989.

43. Alekseev, V. I., Dorofeev, S. B. *et al.*, "Experimental Study of Large-Scale Unconfined Fuel Spray Detonations," In: *Dynamic Aspects of Explosion Phenomena.* (Eds. A. L. Kuhl, *et al.*), Progress in Astronautics and Aeronautics Ser., AIAA Inc., Washington, **154**, 1993, 95–104.

44. Scherbakov, V. A., Experimental Study of Cell Size Relation to Kinetic Parameters of Gas Explosive Mixtures, Diploma work, NSU, Novosibirsk, 1977.

45. Vasil'ev, A. A., Valishev, A. I., Vasil'ev, V. A., Panfilova, L. V., and Topchian, M. E., "Parameters of Detonation Waves at Higher Pressure and Temperature," *Rus. J. Chemical Physics*, **16**, 11, 114–118, 1997.

INITIATION OF ADIABATIC EXPLOSION BY ACCELERATED CURVED SHOCKS: A THEORETICAL AND NUMERICAL STUDY

P. Vidal and B. Khasainov

A theoretical and numerical study on the initiation of adiabatic explosions by accelerated curved shocks in homogeneous explosives is presented, with special attention paid to the critical conditions for initiation. The characterization of the response of a reactive substance to a compression by a shock is important to the understanding of problematic events, such as shock amplification by the chemical heat release and the transition to detonation. Most homogeneous substances decompose according to a two-stage mechanism, induction and explosion. Induction is the period of time when the reaction progress variable remains small. This stage is described here by the one-step forward irreversible Arrhenius reaction rate. The induction time corresponds to the rapid growth of the dependent variables or, mathematically, to a logarithmic singularity in the material distributions of the dependent variables. In the induction zone, these distributions are expressed as first-order expansions in the reaction progress variable about the shock. Then, the framework of the procedure is the formal Cauchy problem (initial-values problem) for quasi-linear hyperbolic sets of first-order differential equations, such as the balance laws for adiabatic flows of inviscid fluids considered in this study. When a shock front is used as the data surface, the solution to the Cauchy problem yields the flow derivatives at the shock, thus the induction time, as functions of the normal velocity and acceleration, D_n and $\delta D_n/\delta t$, and the shock total curvature C. Next, a necessary condition for explosion is derived as a constraint among D_n, $\delta D_n/\delta t$ and C that ensures bounded values of the induction time. This criterion is an illustration of Semenov's hypothesis, namely, the critical condition for explosion to occur is that the heat production term just exceeds the loss term. Here, the production term is the chemical heat release rate and the (adiabatic) loss term is governed by a combination of D_n, $\delta D_n/\delta t$ and C. The violation of the criterion defines a critical shock dynamics as a relationship among D_n, $\delta D_n/\delta t$ and C that generates infinite induction times. Depending on the rear boundary conditions, which determine the shock dynamics, this event can be interpreted as either a non-initiation or the decoupling of the shock and the flame front induced by the shock. The approach is illustrated by a simple analytic solution to the problem

39

of the initiation by impact of a non-compressible piston. From the continuity constraint in the material speed and acceleration at the contact surface of the piston and the explosive, the dynamics of the shock induced in the explosive an derived. Then, the induction time and the initiation condition are rewritten in terms of the piston speed, acceleration and curvature. These theoretical results are finally compared with those of our direct numerical simulations in the case of impacts on a gaseous explosive by planar or curved, constant-speed or accelerated pistons.

NOMENCLATURE

p, T, y, v, e, $h = e + pv$: pressure, temperature, reaction extent, specific volume, internal energy and enthalpy, respectively.

$\bar{e}(p, v, y)$: "incomplete" equation of state; defines the Gruneisen coefficient $g = v/(\partial \bar{e}/\partial p)$, the frozen sound speed, $c = \sqrt{v^2(p + \partial \bar{e}/\partial v)/(\partial \bar{e}/\partial p)}$, the thermicity coefficient $\sigma = -c^2/v(\partial \bar{e}/\partial y)/(\partial \bar{e}/\partial p)$ and the specific heat $Q_{pv} = -\partial \bar{e}/\partial y$ released at constant v and p.

$\hat{e}(T, v, y)$ and $\hat{h}(T, p, y)$: defined as $d\hat{e} = C_v\, dT + (T\partial p/\partial T_{vy} - p)\, dv - Q_{vT}\, dy$ and $d\hat{h} = C_p\, dT + (v - T\partial v/\partial T_{py})\, dv - Q_{pT}\, dy$.

C_v, C_p: heat capacities, at constant v and at constant p, respectively.

Q_{vT}, Q_{pT}: specific heats at constant v and T and at constant p and T, respectively. With the nondimensional coefficients $\gamma = C_p/C_v$, $\omega = Q_{pT}/Q_{vT}$ and $\theta = \gamma/\omega$, one establishes the identities $Q_{pT}/C_pT = g\sigma/(\theta - 1)$ and $Q_{vT}/C_vT = g\sigma\theta/(\theta - 1)$.

t, u: time and material speed.

Indices ∞, 0, n, cr: designate the states before and after the shock, the normal to the shock, and the critical conditions, respectively.

Indices p, v, st, π: designate isobaric, isochoric, planar steady-state or impact-generated transformations, respectively.

D_n, $\delta D_n/\delta t$, C: normal velocity, normal acceleration and total curvature of the shock, respectively.

$M_\infty = D_n/c_\infty$, $M = (D_n - u_{n0})/c_0$, Ω: Mach numbers of the shock and of the flow at the shock, ratio of the slope of the Rayleigh–Mikhelson line to that of the Hugoniot curve. We recall the identity $\Omega = (1 - g/2(v_\infty/v_0 - 1))/(M^{-2} - g/2(v_\infty/v_0 - 1))$.

Ideal gas with constant molar mass: $pv = r_\infty T$, $Q_{pv} = Q_{vT}$, $\omega = 1$, $\theta = \gamma = const$, $g = \gamma - 1$, $\Omega = M_\infty^{-2}$ (r is the ratio of the universal gas constant R to the molar mass m_{mol} of the fluid). The strong-shock limit in gases corresponds to $\Omega = 0$.

$w = dy/dt$, $\theta(\theta - 1)^{-1}\sigma w$, $v^{-1}dv/dt = div\ \mathbf{u}$: reaction rate, e.g., the Arrhenius law (1), heat-production rate, volumetric expansion rate (i.e., adiabatic heat-loss rate), respectively.

t_c, ν, T_a, F: intrinsic chemical time, effective reaction order ($O(1)$) and activation temperature (usually T_a/T_0 is $O(10)$), arbitrary state function (less temperature-sensitive than the exponential in (1), often a power law $\sim T^m$ where m is $O(1)$).

τ, ℓ: induction time and length for arbitrary transformations, respectively.

1   INTRODUCTION

Shock-wave dynamics in homogeneous relaxing media is an important topic in compressible fluid mechanics that plays a role in a broad variety of problems such as, the structuring evidenced in Type Ia supernovae (e.g., [1]), terrestrial chemical explosives (e.g., [2, 3]), shock amplification and the shock-to-detonation transition processes caused by chemical heat release (e.g., [4]). The central problem is to relate the characteristic time of heat release, better known as the induction time, to the shock dynamics. The subject of this paper is the initiation of the adiabatic heat release in an explosive substance by a shock of arbitrary dynamics.

Adiabatic heat release implies that heat transfer phenomena exhibit much shorter characteristic times than the characteristic time of the initiation process, both at the reaction-zone scale and at the explosive micro-structure scales. This assumption holds for most homogeneous explosives, as well as for heterogeneous explosives at sufficiently high solicitations pressures (e.g., [5–7]). Arbitrary shock dynamics implies that the shock dynamics are neither restricted nor specified. We specifically investigate, theoretically and numerically, the effect of the shock dynamics on the initiation stage to better understand the necessary conditions that lead to a shock induced heat release. The central objective is to describe the coupling between the shock dynamics and the chemical kinetics of heat release.

For simplicity, we restrict our study by considering homogeneous explosives. Most of them exhibit a two-stage decomposition, the induction and the recombination. The induction stage is treated here as an initial value-problem, with the shock taken as the data surface. The attention is focused on the dependence of the characteristic time of induction on the shock dynamics. The induction

properties are shown to be determined by the shock state and by the material derivatives of the flow at the shock. The former depends only on the shock normal velocity, and the latter are related to the shock normal velocity, normal acceleration and total curvature. The fact that the flow derivatives at the shock are closely related to the shock dynamics is a well-known feature of gasdynamics. There exist quite a few works on the topic, mostly restricted to two-dimensional steady-state flows (e.g., [8–14]). Jouguet [15] was apparently among the first who used this feature for studying detonation acceleration. This feature is actually a property of any system of equations endowed with a hyperbolic structure, and is referred to by mathematicians as the Cauchy problem (e.g., [16]). Here this formalism is used to study the induction of adiabatic explosions behind shocks, and to derive a necessary condition for shock-initiation as a constraint on the shock dynamics (*cf*. Section 2), and is illustrated in Section 3.

2 METHOD

Most homogeneous substances exhibit a two-stage decomposition: the induction and the recombination stages. This process, at least the induction stage, is well represented by the Arrhenius formula

$$\frac{dy}{dt} = t_c^{-1} F \left(1 - y\right)^{\nu} \exp\left(\frac{-T_a}{T}\right) \tag{1}$$

The magnitude of the ratio T_a/T_0 in the initial induction-state (index 0, $t_0 = 0$, $y_0 = 0$, e.g., the shock state) results in rate-state sensitivity and, usually, is a large number, typically $O(10)$. As a consequence, the recombination is often the fastest stage, and therefore is commonly referred to as the explosion. Heterogeneous condensed explosives can also react as homogeneous ones if the solicitation pressure is sufficiently large [6, 7]. During induction stage, the reaction extent y remains small. To the leading order, the rate given by Eq. (1) behaves as the 0th-order rate, with the state function F kept constant (i.e., $\nu = 0$, $F = const$).

First consider the expansion of a variable f in the Taylor Series $f(t) = f_0 + t\left(df/dt\right)_0 + \ldots$ about the initial induction-state. Then apply it to y and exchange the parts of t and y:

$$f(t) = f_0 + y(t) \left(\frac{df}{dt} \bigg/ \frac{dy}{dt}\right)_0 + \ldots \tag{2}$$

Then apply the new expansion given by Eq. (2) to the ratio T_a/T. Substituting it in Eq. (1), with $\nu = 0$ and $F = F_0$, one obtains a first-order ordinary differential

equation. The solution of this equation, $y(t)$, inserted in Eq. (2), leads to the material distributions:

$$f(t) = f_0 + \tau \left(\frac{df}{dt}\right)_0 \ln \left(1 - \frac{t}{\tau}\right)^{-1} \tag{3a}$$

valid for any f, including y. The induction time is defined as the time τ:

$$\tau = 1 \left/ \left(\frac{d}{dt} \frac{-T_a}{T}\right)_0 \right. \equiv \left(\frac{T_0}{T_a}\right) \left/ \left(\frac{1}{T} \frac{dT}{dt}\right)_0 \right. \tag{3b}$$

of reaction runaway Eq. (3b): which is modeled by the logarithmic singularity in Eq. (3a).

Any rate that behaves like $\exp(A)$ for small $y's$ actually yields an induction time equal to $1/(dA/dt)_0$ when A increases with time. The effects of ν and of the variations in F can thus be studied by noticing that the regression term $F(1 - y)^{\nu}$ is better approximated by $F_0 \exp[y((d\ln F/dt)/(dy/dt) - \nu)_0]$ than by F_0, insofar as T_a/T_0 is large (cf. Nomenclature). The above procedure then leads to material distributions that are inferred from Eq. (3a) by replacing τ of Eq. (3b) by the corrected induction time $\tau_+ = \tau[1 - \tau(\nu dy/dt - d\ln F/dt)_0]^{-1}$. Thus, the problem essentially exists in determining the initial value of the material derivative of temperature T.

It is convenient to recall that the combination of the First Law of Thermodynamics for adiabatic evolution of perfect fluids and of the restrictions for material trajectories of the differentials of the equations of state $e = \hat{e}(T, v, y)$ or $h = \hat{h}(T, p, y)$ leads to (cf. Nomenclature)

$$\frac{1}{T} \frac{dT}{dt} = \frac{Q_{pT}}{C_p T} w + \frac{gv}{c^2} \frac{dp}{dt} = \frac{Q_{vT}}{C_v T} w - \frac{g}{v} \frac{dv}{dt} \tag{4a-b}$$

Consequently, it is sufficient to determine the initial values of dp/dt or dv/dt.

The framework of the formal Cauchy problem is adopted to address the case where the data surface is a shock-type discontinuity. Then variables immediately behind the shock form a one-parameter family, specifically the normal shock velocity D_n. Given the state before the shock, they are obtained by solving the set of equations consistent of the Rankine–Hugoniot relations and the material equation of state. Thus, $f_0 = f_0(D_n)$, (e.g., [17]).

The classical expressions for isobaric or isochoric induction times, τ_p or τ_v, have the forms:(e.g., [18, 19]),

$$\tau_p = \frac{T_0}{T_a} \left(\frac{C_p T}{Q_{pT}}\right)_0 \frac{t_c}{F_0} \exp \left(\frac{T_a}{T_0}\right) \equiv \frac{T_0}{T_a} \left(\frac{\theta - 1}{g\sigma w}\right)_0 \tag{5a}$$

$$\tau_v = \frac{T_0}{T_a} \left(\frac{C_v T}{Q_{vT}}\right)_0 \frac{t_c}{F_0} \exp \left(\frac{T_a}{T_0}\right) \equiv \frac{\tau_p}{\theta_0} \tag{5b}$$

These are readily obtained from Eq. (3b) by setting $dp/dt = 0$ in Eq. (4a) or $dv/dt = 0$ in Eq. (4b).

Consider now the quasi-linear, first-order, hyperbolic set of partial differential equations for adiabatic flows of perfect fluids, restricted for simplicity to one-dimensional evolution,

$$\frac{dv}{dt} - v\frac{\partial u_n}{\partial n} = \frac{\alpha v u_n}{n}, \quad \frac{du_n}{dt} + v\frac{\partial p}{\partial n} = 0 \qquad (6a\text{-}b)$$

$$\frac{dp}{dt} + \left(\frac{c}{v}\right)^2\frac{dv}{dt} = \frac{c^2}{v}\sigma w, \quad w(p, v, y) = \frac{dy}{dt} \qquad (6c\text{-}d)$$

Equation (6c) follows from the First Law of Thermodynamics and α is equal to 0, 1 or 2 for planar, cylindrical or spherical geometry, respectively. Apply next the derivative operator along the shock trajectory

$$\frac{\delta.}{\delta t} = \frac{\partial.}{\partial t} + D_n\frac{\partial.}{\partial n} \equiv \frac{d.}{dt} + (D_n - u_n)\frac{\partial.}{\partial n} \qquad (7a\text{-}b)$$

to three variables p, u_n and v of the three conservation laws (6a, b, c). As a result, three additional equations are obtained which, together with the previous ones, form a nonhomogeneous linear system of six equations for the shock expressions of the six derivatives $(d./dt, \partial./\partial n) \circ (p, u_n, v)$. After resolution, we differentiate the Rankine-Hugoniot relations and the material equation of state so as to express the terms $\delta f_0/\delta t$ as functions of the velocity D_n and the acceleration $\delta D_n/\delta t$ of the shock. Indeed, assuming a constant and quiescent state before the shock, we formally have $\delta f_0/\delta t = (df_0/dD_n)(\delta D_n/\delta t)$. Omitting index 0 from now on, we eventually arrive at

$$\frac{v_\infty}{D_n^2}\frac{dp}{dt} = \frac{-v}{v_\infty}\frac{\sigma w - S_1}{1 - M^2}, \quad \frac{1}{v}\frac{dv}{dt} = \frac{\sigma w - M^2 S_1}{1 - M^2} \qquad (8ab)$$

$$\frac{1}{D_n}\frac{du_n}{dt} = \frac{-v}{v_\infty}\frac{\sigma w - S_2}{1 - M^2} \qquad (8c)$$

$$\frac{1}{T}\frac{dT}{dt} = g\frac{1 - \theta M^2}{\theta - 1}\frac{\sigma w + \left((\theta - 1)M^2/(1 - \theta M^2)\right)S_1}{1 - M^2} \qquad (8d)$$

$$\frac{\tau}{\tau_{st}} = \left(1 + \frac{T_a}{T}\frac{3 + \Omega}{1 - \Omega}\frac{gM^2}{1 - M^2}\left(\frac{v_\infty}{v} - 1\right)\Delta_{sh}\right)^{-1} \qquad (8e)$$

$$\frac{\tau_{st}}{\tau_p} = \frac{1 - M^2}{1 - \theta M^2}, \quad \ell_{st} = (D_n - u_n)\tau_{st} \qquad (8fg)$$

where

$$S_1 = \left(\frac{v_\infty}{v} - 1\right)\left(\frac{v}{v_\infty}D_n C + \frac{3+\Omega}{1-\Omega}\frac{1}{D_n}\frac{\delta D_n}{\delta t}\right) \tag{8h}$$

$$S_2 = \left(\frac{v_\infty}{v} - 1\right)\left(\frac{v}{v_\infty}D_n C + \frac{1+2M^2+\Omega}{1-\Omega}\frac{1}{D_n}\frac{\delta D_n}{\delta t}\right) \tag{8i}$$

$$\Delta_{sh} = \frac{\tau_{st}}{D_n}\frac{\delta D_n}{\delta t} + \frac{1-\Omega}{3+\Omega}\ell_{st}C \tag{8j}$$

The quantity C denotes the ratio α/N, where N is the shock position, and τ_{st} and ℓ_{st} are the induction time and length behind a planar constant-velocity shock, for example, that of the planar steady-state detonation (e.g., [17]). The expression (8d) of dT/dt is obtained by replacing dp/dt in Eq. (4a) by Eq. (8a) or dv/dt in Eq. (4b) by Eq. (8b), that of the induction time Eq. (8e) is then inferred from Eq. (3b). The other derivatives, $(\partial./\partial t, \partial./\partial n)$, can be obtained from Eq. (8a–c) and of the definition of the material derivative.

It is not difficult to demonstrate that formulas (8a–d) also apply to multi-dimensional flows, with detailed chemical kinetics. The quantity C then designates the shock total curvature (i.e., $C = div\, n_0$, n_0 is the outward unit vector normal to the shock surface), and the scalars y, w and σ must be interpreted as the vectors $y(y_k)$, $w(w_k = dy_k/dt)$ and $\sigma(\sigma_k)$, $k = 1, \ldots, K$, respectively, where y_k is the mass fraction of the kth species and K is the number of considered species in the mixture.

The solution to the Cauchy problem (the derivatives) is unique if the data surface (the shock) is not characteristic. Expressions (8a–c) show that this condition is met if the flow Mach number M is different from 1.0 at the shock. For most materials, M is always smaller than 1.0, so that the above-used developments are admissible. The cases M = 1 (characteristic data surface) are beyond the scope of the present work (e.g., [20–22]). Thus, the expressions of the shock derivatives and the induction time are only functions of D_n, $\delta D_n/\delta t$ and C.

Now, we formulate a necessary condition for adiabatic explosion in temperature-sensitive reactive media, which states that, at the beginning of the decomposition process, the heat-production rate must exceed the adiabatic heat-loss rate (i.e., the volumetric expansion rate, cf. Eq. (4b) and Nomenclature). This ensures that the initial rate of change of temperature is positive, so that the induction time is bounded (cf. Eq. (3b)). The analysis of Eqs. (8d–e) thus yields

$$1 + \frac{T_a}{T}\frac{3+\Omega}{1-\Omega}\frac{gM^2}{1-M^2}(\frac{v_\infty}{v} - 1)\Delta_{sh} > 0 \tag{9}$$

Our criterion closely resembles that of Semenov and Frank-Kamenetskii for non-adiabatic explosion (e.g., conductive heat-loss through the wall of a well-stirred reactor, (e.g., [18, 19])). The cancellation of the left-hand side of Eq. (9)

defines a velocity acceleration—curvature critical relationship that generates infinite induction times. Depending on the rear and lateral boundary conditions that determine the shock dynamics, the violation of Eq. (9) can describe a decoupling of the reaction front and the shock, as for example in the cellular structure of gas-phase detonations, or the impossibility for the shock to generate ignition. The latter case is illustrated below.

3 APPLICATION

Consider the impact of a noncompressible piston on an explosive. By continuity, the specifications of the piston normal speed, u_n, normal acceleration, du_n/dt and total curvature, C, define the rear-boundary conditions for the shock at the time of impact. From the Rankine-Hugoniot relations and Eq. (8c), we infer the velocity and the acceleration (Eq. (10a)) of the shock, respectively, then the impact-generated delay τ_π (Eq. (10b) with Eq. (8e)), so that we can finally turn the initiation condition at Eq. (9) into the constraint of Eq. (10e) on the piston speed, acceleration and total curvature. Thus, we have

$$\frac{\delta D_n}{\delta t} = \frac{(1-\Omega)\,D_n}{1+2\mathrm{M}^2+\Omega}\left(\frac{\sigma w - u_n C}{v_\infty/v - 1} + \frac{1-\mathrm{M}^2}{u_n}\frac{du_n}{dt}\right) \tag{10a}$$

$$\frac{\tau_\pi}{\tau_{\pi o}} = \left(1 + \frac{T_a}{T}\frac{g\mathrm{M}^2(v_\infty/v - 1)\,(3+\Omega)}{1+2\mathrm{M}^2+\Omega}\Delta_\pi\right)^{-1} \tag{10b}$$

$$\frac{\tau_{\pi o}}{\tau_v} = \theta\frac{1+2\mathrm{M}^2+\Omega}{1+2\theta\mathrm{M}^2+\Omega}, \quad \ell_{\pi o} = (D_n - u_n)\tau_{\pi o} \tag{10cd}$$

$$\Delta_\pi \equiv \frac{\tau_{\pi o}}{u_n}\frac{du_n}{dt} - \frac{2\ell_{\pi o}C}{3+\Omega} > \Delta_{\pi\mathrm{cr}} \tag{10e}$$

$$\Delta_{\pi\mathrm{cr}} = -\frac{T}{T_a}\frac{1+2\mathrm{M}^2+\Omega}{g\mathrm{M}^2(v_\infty/v - 1)(3+\Omega)} \tag{10f}$$

where $\tau_{\pi o}$ and $\ell_{\pi o}$ are the induction time and length associated with the impact of a planar constant-velocity piston $(C = 0,\ du_n/dt = 0)$.

The analysis of Eq. (10c) reveals that the induction time $\tau_{\pi o}$ lies in between τ_p and τ_v (Eq. (5a, b)) because $\theta > 1$ necessarily. Also, for perfect gases (i.e., $\theta = \gamma$), by noticing that γ is then close to 1, we observe that $\tau_{\pi o}$ is about the arithmetic mean of τ_p and τ_v. We thus analytically generalize the result numerically obtained in [23] for the case of the ideal gas with a constant molar mass.

The ratio $\tau_{\pi o}/\tau_v$ for this ideal gas is represented in Fig. 1 as a function of the Mach number of the induced shock, M_∞ for the two values 1.4 and 1.2 of
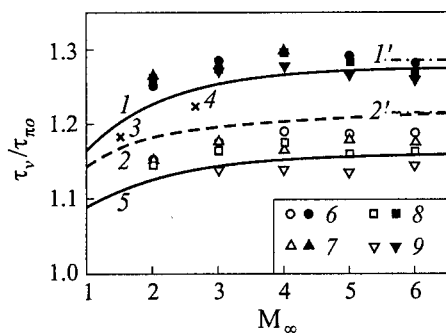
Figure 1 Normalized induction time under constant-speed planar impact (Eq. (10c)) for $\gamma = 1.4$ (*1, 2, 3, 4*) and $\gamma = 1.2$ (*5*). *1* and *5* — present model, *2* — [13], *3* — [23], *4* — [24], *1'* and *2'*: strong-shocks asymptotes for *1* and *2*, open and solid symbols: our numerical simulations for $\gamma = 1.2$ and 1.4, respectively, *6* — $N_{\text{cell}} = 1000$, *7* — 2000, *8* — 4000, *9* — 8000.
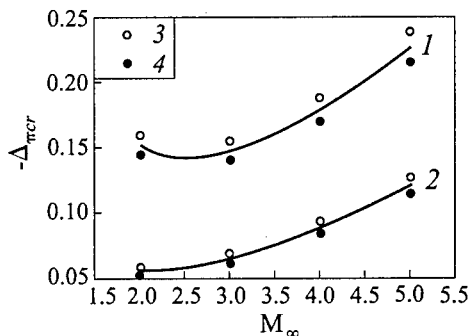
Figure 2 Normalized critical piston dynamics (Eq. (10f)) for initiation by impact. The initiation domains are below the curves. The numerical simulations correspond to planar impacts. (*1*: $\gamma = 1.2$, $Q_{pv}/r_\infty T_\infty = 50$, $T_a/T_\infty = 40$, *2*: $\gamma = 1.4$, $Q_{pv}/r_\infty T_\infty = 30$, $T_a/T_\infty = 80$), simbols *2* and *3* correspond to 'no initiation' and 'initiation'

the ratio of specific heats, γ. Our results for $\gamma = 1.4$ agree well with those of the numerical works [23–25].

We then have numerically determined isochoric induction times τ_v^{num}, by integration of Eqs. (1) and (6c) with $dv/dt = 0$, and induction times under constant-velocity planar impacts $\tau_{\pi o}^{\text{num}}$, by direct numerical simulation using a Lagrangian code. These induction times were defined as the instants of time when y equals 1. The calculations were carried out for $\nu = 0$ and $F = 1$. Two sets of control parameters for typical gaseous explosives have been used, specifically (i) $\gamma = 1.2$, $T_a/T_\infty = 40$, $Q_{pv}/r_\infty T_\infty = 50$, $t_c = 10^{-10}$ s, $m_{\text{mol}} = 0.03$ kg/mol, $T_\infty = 298$ K, $p_\infty = 10^5$ Pa, (i.e., $T_a = 11919$ K and $Q_{pv} = 4.13$ MJ/kg), and (ii) $\gamma = 1.4$, $T_a/T_\infty = 80$, $Q_{pv}/r_\infty T_\infty = 30$, $t_c = 10^{-10}$ s, $m_{\text{mol}} = 0.02$ kg/mol, $T_\infty = 298$ K, $p_\infty = 10^5$ Pa, (i.e., $T_a = 23838$ K and $Q_{pv} = 3.72$ MJ/kg). The accuracy of the simulation depends on the number of cells, N_{cell} in the computational domain. The length of this domain was adjusted for each impact velocity with $N_{\text{cell}} = 500$ so that explosion occurs when the shock reaches the end of the domain, and was kept the same for the same impact speed when increasing N_{cell}. When this accuracy is sufficient, the ratios $\tau_{\pi o}^{\text{num}}/\tau_v^{\text{num}}$, shown in Fig. 1, agree well with those of our model.

Still for the ideal gas, Fig. 2 presents the variation of the theoretical normalized critical piston dynamics $\Delta_{\pi \text{cr}}$ of Eq. (10f) as a function of M_∞. For

47
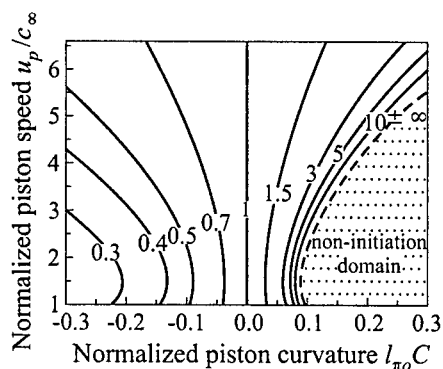
Figure 3 Level lines of the normalized induction time under impact by a curved non-accelerated piston (*cf*. Eq. (10*b*)). The dashed line represents the critical piston curvature (*cf*. Eq. (10*f*)) that produces infinite induction times, and separates the domains of non-initiation and initiation (negative and positive induction times, respectively). $\gamma = 1.4$, $T_a/T_\infty = 80$, $Q_{pv}/r_\infty T_\infty = 30$
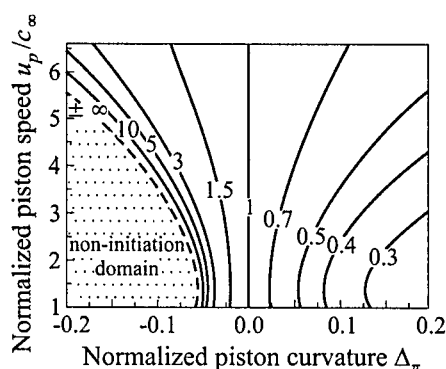
Figure 4 Level lines of the normalized induction time under impact in Eq. (10*b*). The dashed line represents the critical piston dynamics Δ_π of Eq. (10*f*) that produces infinite induction times, and separates the domains of non-initiation and initiation (negative and positive induction times, respectively). $\gamma = 1.4$, $T_a/T_\infty = 80$, $Q_{pv}/r_\infty T_\infty = 30$

example, for a given curvature, we observe that the smaller the piston speed, the smaller the critical deceleration.

Figure 2 also displays the results of direct numerical simulations of impacts by a uniformly decelerated planar piston ($C = 0$, $\Delta_\pi < 0$) for normalized acceleration ($\tau_{\pi o}^{num}/u_n$)(du_n/dt) chosen 5 % smaller or larger than the theoretical normalized critical values. The lengths of the calculation domains were taken 4 times longer than for the nonaccelerated planar impact associated with the same u_n/c_∞ and, so as to retain the corresponding accuracy $N_{cell} = 2000$ (*cf.* Fig. 1), divided into 8000 cells. The numerical criterion of noninitiation is that, for too large decelerations, the reaction extent y eventually freezes at a constant value much smaller than 1 before the shock reaches the end of the calculation domain. A good agreement between the results of our model and of our simulations is again obtained.

Depending on the specified piston kinematics, the criterion (10*e*) can also be used to determine the minimal piston curvature that prevents explosion. For instance, Fig. 3 presents the variations, after Eq. (10*b*), of the induction time behind the shock generated by the impact of a constant-velocity curved piston (i.e., $du_n/dt = 0$, $C \neq 0$) as a function of the piston speed and total curvature. The piston speed is normalized by the sound speed c_∞ in the medium in front of the shock. The piston (or shock) curvature is normalized by the induction

length $\ell_{\pi o}$ behind the shock generated by the impact of a planar constant-speed piston, with the same speed as that of the curved piston (*cf.* Eq. (10*e*)). For the chosen set of control parameters (*cf.* Fig. 3), a normalized piston speed u_n/c_∞ equal to 4 corresponds to a shock Mach number D_n/c_∞ equal to 5. For this value of piston speed, the critical total curvature of the piston is approximately $0.15/\ell_{\pi o}$. In the case of a spherical piston, this corresponds to a critical radius equal to about 13.3 $\ell_{\pi o}$. This is a rather large number, which suggests that small defects on the surface of a planar piston can induce large variations in the induction properties. Thus, a very careful machine tooling of the piston surface is recommended for performing valuable induction-time measurements in planar-impact experiments. The same conclusion likely applies to the reflection surface of a shock-tube, though formulas (10) do not describe this situation.

Similarly, Fig. 4 presents the variations, after Eq. (10*b*), of the induction time behind the shock generated by the impact of a curved accelerated piston as a function of the piston speed and piston dynamics Δ_π (10*e*). For a planar piston, Δ_π is equal to the piston acceleration, normalized with the induction time $\tau_{\pi o}$ behind the shock generated by a planar constant-speed piston, with the same speed as that of the accelerated piston (*cf.* Eq. (10*e*)). The control parameters are the same as for the case described in Fig. 3. For a normalized piston speed equal to 4, the critical deceleration for initiation by a planar-piston impact is approximately $0.12 u_n/\tau_{\pi o}$. This value represents the largest rate of decrease of piston speed for initiation.

4   DISCUSSION

In conclusion, we have carried out (i) an analytical study of the induction stage of the adiabatic explosion behind a shock of arbitrary dynamics and (ii) obtained a necessary condition for explosion that defines a critical shock dynamics. Our approach, applied to two classical problems of gasdynamics of reactive systems, shows its reasonable predictive ability, and also represents in this context a simple alternative to perturbation methods (e.g., [25]). These results are useful to better interpret phenomena of compressible reactive hydrodynamics and to validate numerical simulations.

Other problems can be solved, such as initiations in shock tubes or by compressible, finite-length projectiles. Their solutions cannot be valuably summarized here. The main difficulty lies in the definition of the rear boundary conditions for the shock. We emphasize that the fulfillment of the necessary condition (9) does not ensure explosion: the initial-values problem considered here cannot describe nonlocal events such as the back-up of a release wave towards the shock. The bounded-delay criterion (9) must then be modified so that the delay is smaller than the time necessary for the release wave to reach the induction locus.

ACKNOWLEDGMENTS

REFERENCES

1. Grun, J. et al., Physical Review Letters, 66, 2738, 1991, and the sample works referenced in it.
2. Presles, H. N., C. R. Acad. Sci. Paris, 314, II, 575, 1991.
3. Presles, H. N. et al., Int. J. Shock Waves, 6, 111, 1996.
4. Campbell, A. W. et al., Physics Fluids, 4, 498, 1961.
5. Vidal, P., and Khasainov, B., Acad. Sci. Paris, to appear, 1998.
6. Bowden, F. P., and Yoffe, A. D., Initiation and Growth of Explosions in Liquids and Solids. Cambridge University Press, Cambridge, 1952.
7. Dremin, A. et al., Detonation Waves in Condensed Media. Nauka, Moscow, 1970.
8. Lighthill, M. J., Phil. Mag., 40, 214, 1949.
9. Hayes, W. D., and Probstein, R. F., Hypersonic Flow Theory. Academic Press, New York, 1966.
10. Hornung, H. G., J. Fluid Mechanics, 74, 143, 1976.
11. Hornung, H. G., Int. J. Shock Waves, 8, 11, 1998.
12. Cheret, R., C. R. Acad. Sci. Paris, 301, 961, 1988.
13. Vidal, P., et al., C. R. Acad. Sci. Paris, 315, 791, 1992.
14. Vidal, P., et al., C. R. Acad. Sci. Paris, 316, 177, 1993.
15. Jouguet, E., Mécanique des Explosifs. Doin et fils, 1917.
16. Hadamard, J., Le Problème de Cauchy et les Equations aux Dérivées Partielles Linéaires Hyperboliques. Hermann, Paris, 1932.
17. Fickett, W., and Davis, W. C., Detonation. ISBN 0-520-03587-9, University of California Press, 1979.
18. Zel'dovich, Ya. B. et al., The Mathematical Theory of Combustion and Explosions. ISBN 0-306-10974-3, Plenum Publishing Corporation, 1985.
19. Merzhanov, A. G. et al., Chemical Physics Reports, 15, 793, 1996.
20. D'yakov, S. P., Sov. J. Experimental Theoretical Physics, 27, 288, 1954.
21. Kantorovitch, V. M., Sov. J. Experimental Theoretical Physics, 6, 1179, 1958.
22. Joulin, G., and Vidal, P., Hydrodynamics and Nonlinear Instabilities. Chapter 5, ISBN 0-521-45503-0, Cambridge University Press, Cambridge, 1998.
23. Clarke, J. F., and Cant, R. S., Dynamics of Flames and Reactive Systems. Progress in Astronautics and Aeronautics Ser., 95, 142, 1985.
24. Jackson, T. L., and Kapila, A. K., SIAM J. Applied Mathematics, 45, 130, 1985.
25. Blythe, P. A., and Crighton, D. G., Proc. Royal Society London, A426, 189, 1989.

AMR CALCULATION OF IGNITION AND DETONATION FORMATION IN REACTIVE GAS BY SHOCK WAVE FOCUSING

M. Rose, U. Uphoff, and P. Roth

Adaptive mesh refinement (AMR) is used to calculate the focusing process of a shock wave propagating into a reactive mixture, which is enclosed in a cylindrical volume. A one-step reaction mechanism is used to model the chemistry of a stoichiometric H_2/O_2-mixture. The fluid flow is described by the two-dimensional reactive Euler equations, which are integrated in time using an operator splitting technique. The convective part is treated by the Harten-Yee TVD-scheme, and the chemical source terms can be integrated exactly. Calculations are performed for incident shock Mach numbers ranging from 1.7 to 2.2. At lower shock strength, $M \leq 2.1$, the complex interaction of reflected shock and expansion waves during the focusing process dominate the wave field, therefore chemistry is not significant. The computed results show the same wave patterns as experimental results for a similar setup. In case of the higher Mach number of 2.2, the calculations lead to the ignition of a detonation wave in the focal region. The detonation wave becomes spherical and interacts with the diffracted shock wave, resulting in an even more complex wave field.

INTRODUCTION

Shock and pressure waves can propagate in reactive mixtures without inducing ignition and subsequent reaction activity. It is possible that such waves are reflected from and focused by curved surfaces, thus generating a region of high energy density near the gasdynamic focus, where explosion reactions can start. Therefore, shock wave focusing has been applied in a variety of scientific and engineering applications [1]. Shock wave focusing in non-reacting fluids has found a major application in the form of extracorporeal shock wave lithotripsy, which is used in the medical field to treat kidney stones disease as described by Sturtevant [2].

The first fundamental theoretical investigations of converging cylindrical and spherical shock waves were done by Guderly [3]. By using linear acoustic theory, he came to the conclusion that the pressure at the center of convergence becomes infinite.

Detailed experimental and numerical investigations, i.e. by Milton [4], Sturtevant and Kulkarny [5], Choi and Baek [6], and Sun and Takayama [7] revealed the importance of nonlinear effects dominating the final stage of the focusing process, especially for the case of strong shock waves. These investigations show that only a limited pressure increase by the curved shock wave is possible. Nevertheless, the high local energy density can cause a reactive mixture to ignite. The interaction of a fast combustion wave with the diffracted and reflected shock waves leads to a multifacetted wave field, as numerically investigated by Rose *et al.* [8]. The numerical problems known from shock wave focusing computations are even amplified when dealing with chemical reactions. Like in detonation formation, a high spatial resolution of strong gradients in combination with the extremely widened time scales involved is necessary. The use of a very fine grid size is therefore crucial for a reliable calculation of the reactive parts of the fluid flow.

In the present work, the focusing process leading to the ignition of a stoichiometric H_2/O_2-mixture is investigated by numerical simulations based on the 2D reactive Euler equations. The computational setup is similar to a circular reflector, which is connected to a rectangular shock tube, as used for the holographic interferometric studies of shock wave focusing by Sun and Takayama [7]. An operator splitting technique is applied to handle fluid flow and chemistry separately. The convective part is integrated using the Harten-Yee TVD-Method [9] and the integration of chemical source terms is performed by an explicit Euler method.

A one-step reaction mechanism is used to model the chemistry of the premixed gases and an adaptive mesh refinement technique (AMR) is applied to get an adequate resolution of steep gradients, especially in the ignition and reaction zones.

MODELING

Governing Equations

The Euler equations are commonly used to describe the dynamics of a compressible, inviscid fluid. In 2D space, these equations take the following form:

$$\frac{\partial \mathbf{U}}{\partial t} + \frac{\partial \mathbf{F}}{\partial x} + \frac{\partial \mathbf{G}}{\partial y} = \mathbf{S} \tag{1}$$

In this equation $\mathbf{U}$, $\mathbf{F}$, $\mathbf{G}$, and $\mathbf{S}$ denote the vectors of the conserved properties, fluxes, and source terms, respectively. For a gas mixture containing N species of densities ρ_1 to ρ_N, these vectors have the form:

$$\mathbf{U} = (\rho_i, \ldots, \rho_N, \rho u, \rho v, \rho E)^t$$

$$\mathbf{F} = (\rho_1, \ldots, \rho_N u, \rho u^2 + p, \rho u v, u(\rho E + p))^t$$

$$\mathbf{G} = (\rho_1 \nu, \ldots, \rho_N \nu, \rho u v, \rho v^2 + p, v(\rho E + p))^t$$

$$\mathbf{S} = (\dot{\omega}_1 \ldots, \dot{\omega}_N, 0, 0, 0)^t$$

The density of the mixture is $\rho = \sum_{i=1}^{N} \rho_i$, its velocity in cartesian co-ordinates is $\mathbf{v} = (u, v)^t$, and its temperature and pressure are denoted with T and p, respectively. The total energy E of the gas phase is calculated as the sum of the internal and kinetic energies:

$$E = \int_{T_{ref}}^{T} c_\nu \, dT + \frac{1}{\rho} \sum_{i=1}^{N} \rho_i \Delta h_{fi} + \frac{1}{2}(u^2 + v^2) \tag{2}$$

where Δh_{fi} is the enthalpy of formation of species i at a reference temperature. It is assumed that the gas obeys the ideal gas law:

$$p = \rho R T \tag{3}$$

The formation and consumption of species 1 to N due to homogeneous reactions are included into the source terms $\dot{\omega}_1, \ldots, \dot{\omega}_N$. The chemistry is modeled by a simple one-step reaction mechanism ($N = 2$):

$$\mathbf{A} \xrightarrow{k} \mathbf{B} \tag{4}$$

It describes the irreversible conversion of gas species $\mathbf{A}$ into gas product $\mathbf{B}$. The rate coefficient k is described by a one-step Arrhenius law:

$$k = k_0 \exp\left(-\frac{E_a}{RT}\right) \tag{5}$$

The chemical source terms $\dot{\omega}_A$ and $\dot{\omega}_B$ are taken under these simplified assumptions as follows:

$$\dot{\omega}_A = -k\rho_A, \qquad \dot{\omega}_B = k\rho_B$$

Numerical Method

The integration of the Euler equations (1) is performed by an operator splitting technique, which handles fluid flow and chemistry separately:

$$\mathbf{U}_{t+\Delta t} = \mathcal{L}_{flow}^{\Delta t/2} \mathcal{L}_{chem}^{\Delta t} \mathcal{L}_{flow}^{\Delta t/2} \mathbf{U}_t \tag{6}$$

The convective part is integrated using the Harten-Yee TVD-Method [9] represented by

$$\mathcal{L}_{flow}^{\Delta t/2} = \mathcal{L}_y^{\Delta t/2} \mathcal{L}_x^{\Delta t/2}$$

The integration operators in the x- and y-direction on a discretized cartesian grid are of the form:

$$\mathcal{L}_x^{\Delta t/2} \mathbf{U}_t^{i,j} = \mathbf{U}_t^{i,j} - \frac{\Delta t/2}{\Delta x} \mathbf{J}_\mathbf{F}(\widetilde{\mathbf{F}}_t^{i+1/2} - \widetilde{\mathbf{F}}_t^{i-1/2})$$

$$\mathcal{L}_y^{\Delta t/2} \mathbf{U}_t^{i,j} = \mathbf{U}_t^{i,j} - \frac{\Delta t/2}{\Delta y} \mathbf{J}_\mathbf{G}(\widetilde{\mathbf{G}}_t^{j+1/2} - \widetilde{\mathbf{G}}_t^{j-1/2})$$

where $\mathbf{J}_\mathbf{F}$ and $\mathbf{J}_\mathbf{G}$ are the Jacobians of the flux vectors $\mathbf{J}_\mathbf{F} = \partial \mathbf{F}/\partial \mathbf{U}$ and $\mathbf{J}_\mathbf{G} = \partial \mathbf{G}/\partial \mathbf{U}$, evaluated somewhere between the states $\mathbf{U}_t^{i,j}$ and $\mathbf{U}_t^{i+1,j+1}$. The numerical fluxes $\widetilde{\mathbf{F}}_t^{i+1/2}$ and $\widetilde{\mathbf{G}}_t^{j+1/2}$ at the center of computational cell (i, j) are calculated from the physical flux terms $\mathbf{F}$ and $\mathbf{G}$ in Eq. (1) by:

$$\widetilde{\mathbf{F}}_t^{i+1/2} = \frac{1}{2}[\mathbf{F}(\mathbf{U}_t^{i,j}) + \mathbf{F}(\mathbf{U}_t^{i+1,j}) + \mathbf{R}_\mathbf{F}^{i+1/2} \Phi_\mathbf{F}^{i+1/2}]$$

$$\widetilde{\mathbf{G}}_t^{j+1/2} = \frac{1}{2}[\mathbf{G}(\mathbf{U}_t^{i,j}) + \mathbf{G}(\mathbf{U}_t^{i,j+1}) + \mathbf{R}_\mathbf{G}^{j+1/2} \Phi_\mathbf{G}^{j+1/2}]$$

The matrices $\mathbf{R}_\mathbf{F}^{i+1/2}$ and $\mathbf{R}_\mathbf{G}^{i+1/2}$ consist of the right eigen vectors of the flux Jacobians $\mathbf{J}_\mathbf{F}$ and $\mathbf{J}_\mathbf{G}$, respectively, and the vectors $\Phi_\mathbf{F}^{i+1/2}$ and $\Phi_\mathbf{G}^{j+1/2}$ depend on the eigen values of the corresponding Jacobians.

The large dissipation of first order numerical schemes is corrected in a nonlinear way by the antidiffusive flux terms $\mathbf{R}_\mathbf{F}^{i+1/2} \Phi_\mathbf{F}^{i+1/2}$ and $\mathbf{R}_\mathbf{G}^{j+1/2} \Phi_\mathbf{G}^{j+1/2}$, making the method of higher order. In Eq. (6), $\mathcal{L}_{chem}$ is the operator used for representing the chemical source terms. For the single-step reaction mechanism of Eq. (4), the new composition of the gas mixture containing species $\mathbf{A}$ and $\mathbf{B}$ is calculated from:

$$\mathcal{L}_{chem}^{\Delta t} \rho_{\mathbf{A},t+\Delta t/2}^{i,j} = \rho_{\mathbf{A},t+\Delta t/2}^{i,j} e^{-k_0 \Delta t e^{-E_a/RT_{t+\Delta t/2}^{i,j}}} \tag{7}$$

$$\mathcal{L}_{chem}^{\Delta t} \rho_{\mathbf{B},t+\Delta t/2}^{i,j} = \rho_{\mathbf{B},t+\Delta t/2}^{i,j} e^{k_0 \Delta t e^{-E_a/RT_{t+\Delta t/2}^{i,j}}} \tag{8}$$
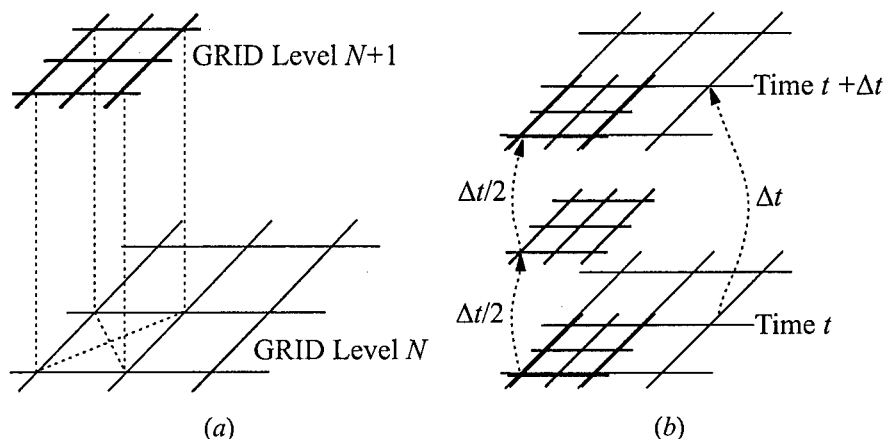
Figure 1 Illustration of the mesh refinement algorithm: (*a*) Cell of grid level N flagged for refinement by a factor of two in both coordinate directions, (*b*) Cell refined by a factor of two is integrated two times in time by half the timestep used for the course mesh

The new total energy of the mixture according to the new composition is calculated by using Eq. (2).

To get the desired resolution of regions with strong gradients and intense chemical activity, the computational mesh is locally refined by superimposing grids with finer meshes. The mesh refinement algorithm is illustrated in Fig. 1. One cell of grid level N has been flagged for refinement according to some criterion, e.g. dealing with gradients in pressure or density, and is then divided into four smaller cells on the next higher grid level shown in Fig. 1a. After interpolating the appropriate boundary conditions from the grids of level N to the new grids of level $N + 1$, the integration with respect to time can be performed as illustrated in Fig. 1b. To guarantee the Courant-Fredrichs-Levy (CFL)-condition, the finer grid is integrated two times in time by using half a timestep applied for the coarse mesh. The mesh refinement technique is described in detail by Quirk [10].

RESULTS AND DISCUSSION

Initial and Boundary Conditions

The numerical method described was applied to study the development of the wave field when a shock wave propagates into a quiescent stoichiometric H_2/O_2-
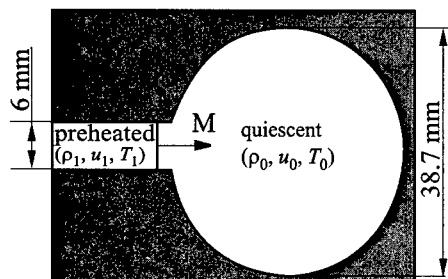
Figure 2 Schematic of a shock wave propagating into a combustible gas mixture

mixture with initial conditions $p_0 = 0.1$ bar and $T_0 = 300$ K. The properties used in the Arrhenius expression (5) are $k_0 = 1.5 \cdot 10^9$ s^{-1} and $E_a = 12000$ J·mol^{-1}, respectively. A schematic drawing of the setup is given in Fig. 2. It is identical with the experimental setup used by Sun and Takayama [7], but scaled by a factor of 0.1 to guarantee a sufficient spatial resolution in combination with reasonable computational costs.

Three levels of refinement are used on a curvilinear cartesian grid. Because of the symmetrical character of the problem, only the upper half plane in Fig. 2 is considered, with mirroring boundary conditions on the plane of symmetry. The criterion according to which cells are flagged for refinement is based on the combination of local variations in density and mass fraction of the reaction product. The refinement factor 2 was used from the basic grid to level one, whereas a refinement factor of 4 was used from level one to level two and from level two to level three. The spatial resolution on the finest grid is $8 \cdot 10^{-6}$ m. Calculations were performed for Mach numbers of the incident wave ranging from 1.7 to 2.2.

Case 1: Chemistry is insignificant

At Mach numbers ranging from 1.7 to 2.1, our calculations reveal the same wave patterns as observed by the experiments and the numerical computations of Sun and Takayama [7, 11]. Figure 3 shows the evolution of the pressure field in the upper half plane of the circular reflector after the shock wave is discharged from the shock tube. The initially planar shock wave is diffracted around the sharp corner at the exit of the shock tube. This results in a curved shock wave with a foot, which is perpendicular to the circular wall as illustrated in Fig. 3a. The diffracted shock wave is followed by a secondary shock, which is created by a locally supersonic jet emanating from the shock tube. The mechanisms leading to the formation of the secondary shock wave are described in detail in the work of Sun and Takayama [11].

While the curved shock wave further propagates, its interaction with the wall becomes an inverse Mach reflection as shown in Fig. 3b, before it transits to a direct Mach reflection, consisting of a regular reflection and a triple point, leaving the circular wall (Fig. 3c). After the total reflection (Fig. 3d), the central part
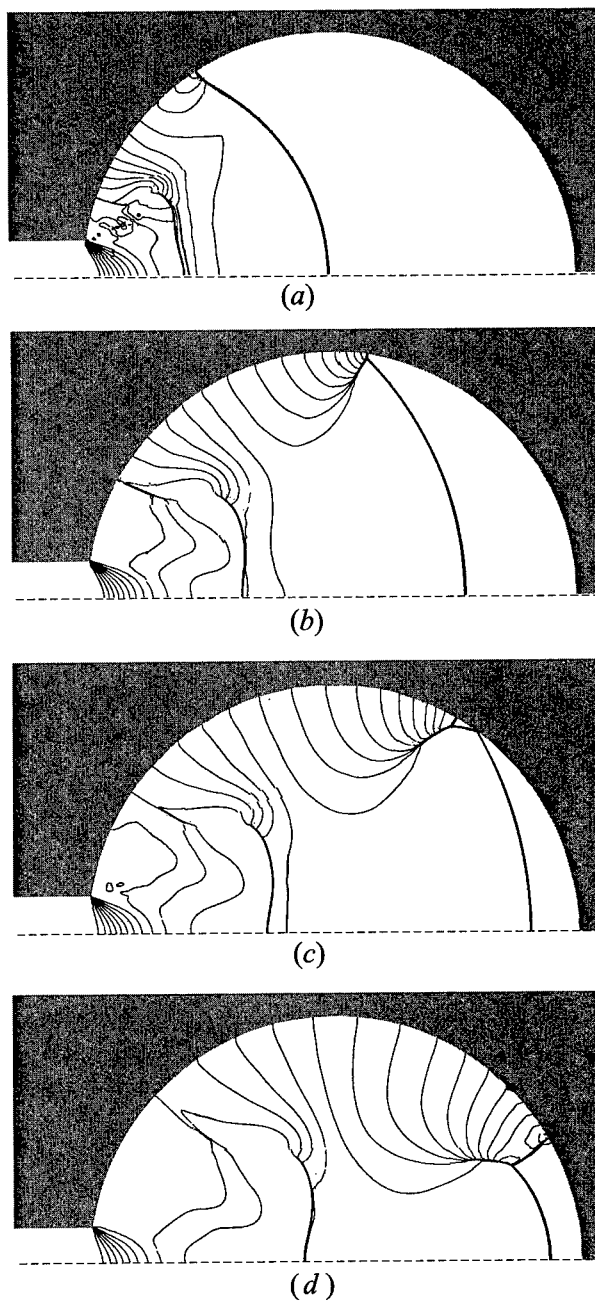
Figure 3 M = 1.9: Lines of constant pressure for different time instants relative to the focusing time: (a) −404 μs, (b) −264 μs, (c) −195 μs, (d) −92 μs
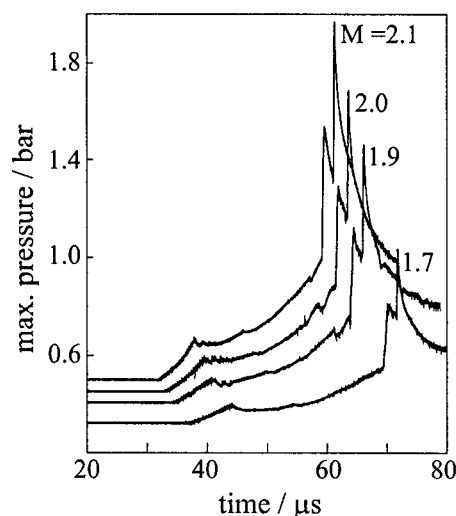
Figure 4 Evolution of maximum pressure for initial Mach numbers of 1.7, 1.9, 2.0, and 2.1

of the concave shaped reflected shock wave is bounded by two triple points (the lower one not shown here due to symmetry reasons). These triple points propagate towards the focal region and merge at the same time when the convex shaped shock wave coalesces at the centerline. Figure 4 shows the evolution of the maximum pressure in the circular section during the focusing process for four Mach numbers ranging from 1.7 to 2.1. The maximum pressure develops qualitatively similar for all four shock strengths. When the shock wave enters the circular reflector, the maximum pressure becomes irregular, but the mean values continuously increase. There is a jump in maximum pressure when those parts of the shock wave, which connect the triple points with the surface of the reflector, are first reflected on the plane of symmetry. The second stepwise increase in the maximum pressure is obtained at the focal point, when the two triple points collide. This leads to a maximum pressure of about 1 bar for an initial shock strength of M = 1.7 and of about 2 bar for M = 2.1. After focusing is finished, the maximum pressure decreases rapidly. The calculations show that chemistry plays an insignificant role during the focusing process under these conditions.

Case II: Chemistry is significant

For a higher initial Mach number of 2.2, the local pressure and temperature peaks in the focus are sufficient to ignite the mixture as indicated in Fig. 5. The upper and lower parts of each figure show lines of constant pressure and density, respectively. The initial stages of the wave reflection and focusing process (Figs. 5a and 5b) are similar to the earlier discussed low Mach number case, see Fig. 3. But now Fig. 5c shows reaction ignition and the formation of a detonation wave in the focal point some delay time after the focusing process is finished. The ignition of the detonation wave is also indicated by the first steep increase of maximum pressure up to about 14 bar shown in Fig. 6. The combustion wave then propagates into the preheated unburned gas and the right
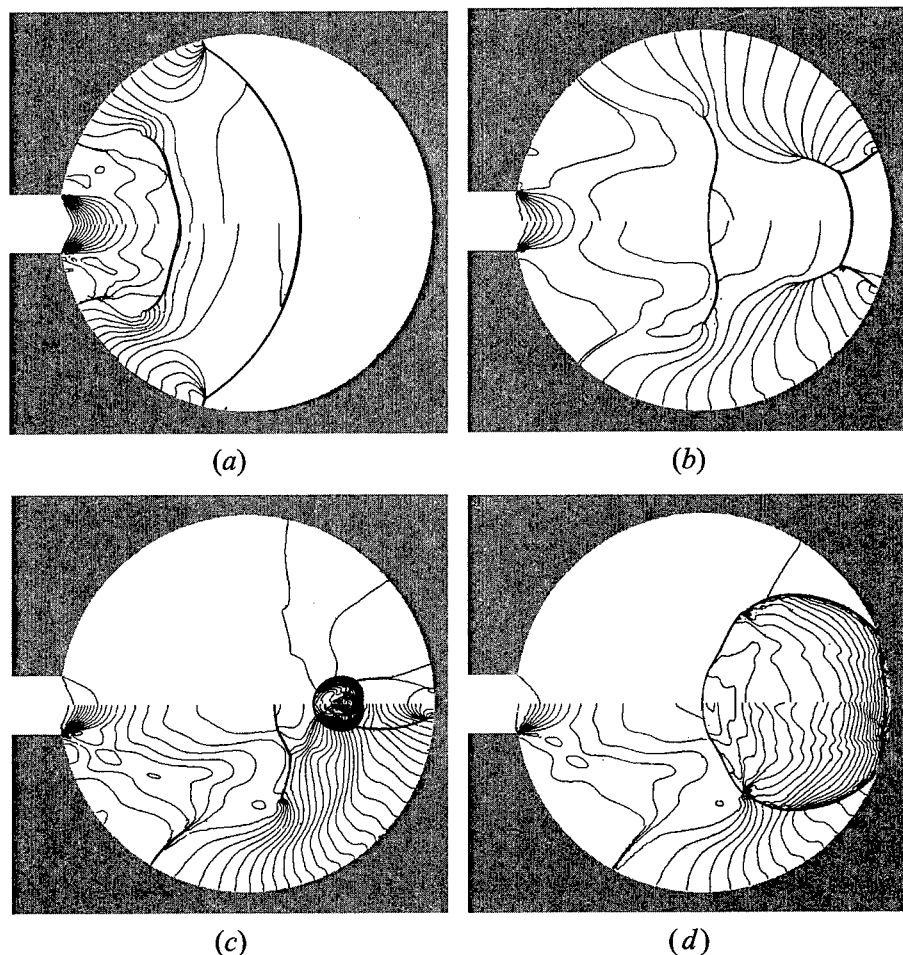
Figure 5 M = 2.2: isobars (upper half) and isochors (lower half) for different time instants relative to the ignition time: (a) -33 μs, (b) -8 μs, (c) $+11$ μs, (d) $+39$ μs

part is reflected by the circular wall about 36 μs after ignition. The reflected detonation wave becomes evident in Fig. 5d. Since this shock is not driven by chemical heat release, it does not further contribute to the propagation of the combustion wave.

The graph of maximum pressure in Fig. 6 shows two additional pressure peaks at about 5 and 7 μs after ignition. The physical reason for these can be explained by an enlarged view of the focal region as shown in Fig. 7. The upper and lower parts of Fig. 7a–d show lines of constant pressure and density, respectively. The
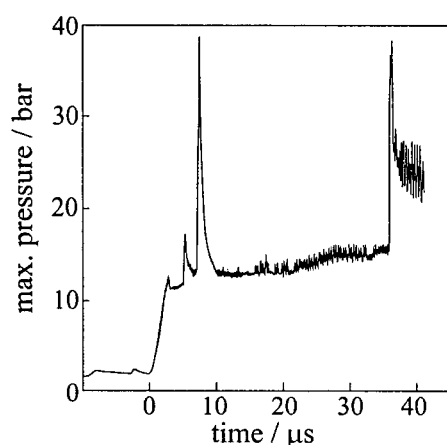
Figure 6 Evolution of maximum pressure for an initial Mach number of 2.2

ignition of a combustion wave is indicated in Fig. 7a. The calculations show that shortly after ignition this combustion wave is separated by a slip line into two different regions. The slip line, connecting the triple points with the focus, is not as sharply resolved in these plots as the fronts of the shock and combustion waves, but it nevertheless becomes obvious. The frontal part of the combustion wave, which is closer to the leading Mach stem, connecting the two triple points, corresponds to a developing detonation wave. It is indicated in the upper half of Fig. 7a by the high concentration of isochors close to the focus. The rear part of the combustion wave, which is on the outer side of the dividing slip line, corresponds to a deflagration wave, exhibiting no discontinuity in pressure. While growing, the detonation wave becomes C-shaped and interacts with the shock configuration in front of it (Fig. 7b). This leads to the local peak in maximum pressure about 5 μs after ignition. The third pressure peak, shown in Fig. 6 at about 7 μs after ignition, is caused by the colliding of the upper and lower parts of the detonation wave, forming a nearly spherical detonation wave as shown in Fig. 7d.

The good and efficient adaption of the AMR is illustrated in Fig. 8 for a time instant shortly after the reflection of the detonation wave. Both the density field (the upper part) and the corresponding computational mesh with all levels of refinement (the lower part), are shown in the upper figure. The clustering of very fine meshes close to the sharp corner at the exit of the shock tube, at the secondary shock front close to the wall, and at the positions of the detonation and reflected detonation wave is clearly seen. The inhomogeneities in the flow field in front of the detonation wave cause local disturbances in the detonation front structure. Due to its unstable character, these disturbances accumulate in the detonation front and small detonation cells are formed. An area of about 1.2×0.8 mm^2 from the upper part of the detonation front is enlarged in the lower illustration of Fig. 8. For this transient configuration, the size of the detonation cells is approximately 0.2 mm.

CONCLUDING REMARKS

The 2D reactive Euler equations were solved by an adaptive mesh refinement technique to investigate the focusing behavior of a diffracted shock wave in a

(a) (b)

(c) (d)
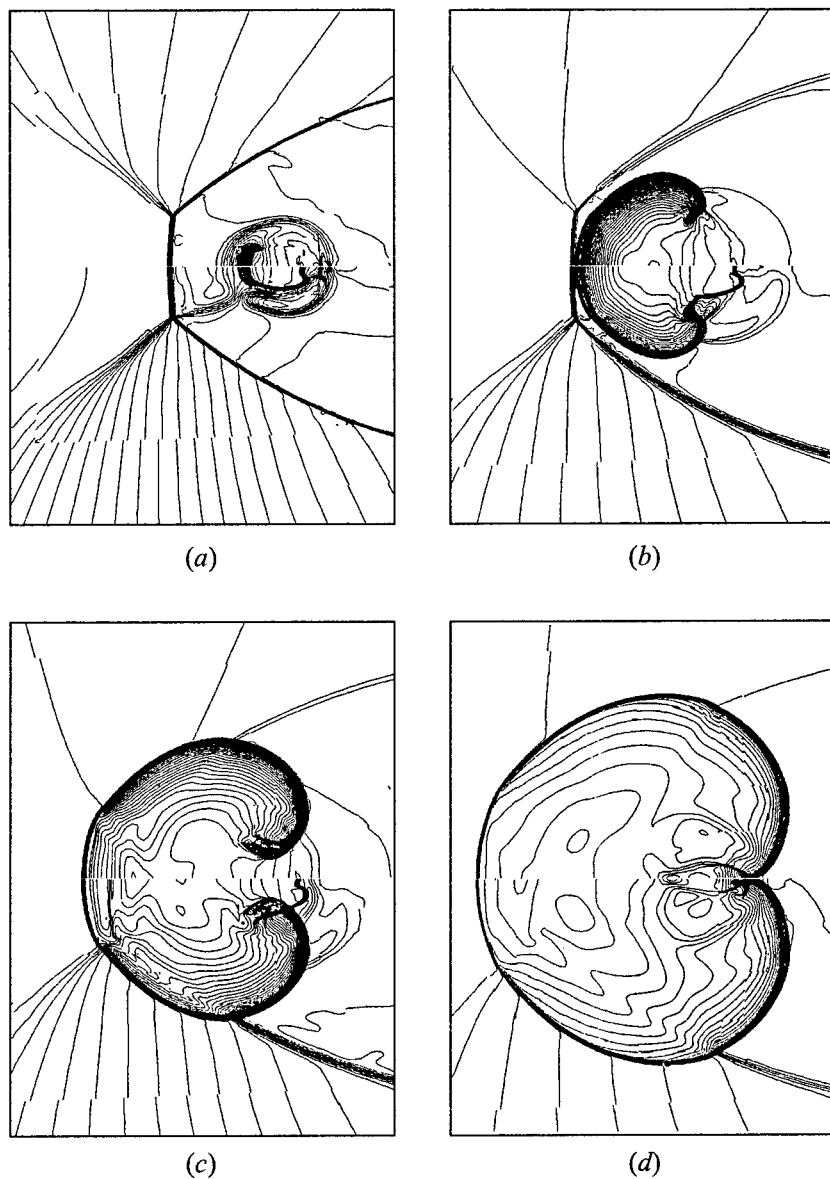
Figure 7 $M = 2.2$: isobars (upper half) and isochors (lower half) in the focal region for different time instants relative to start of ignition: (a) +0.9 μs, (b) +4.0 μs, (c) +5.7 μs, (d) +7.4 μs

61
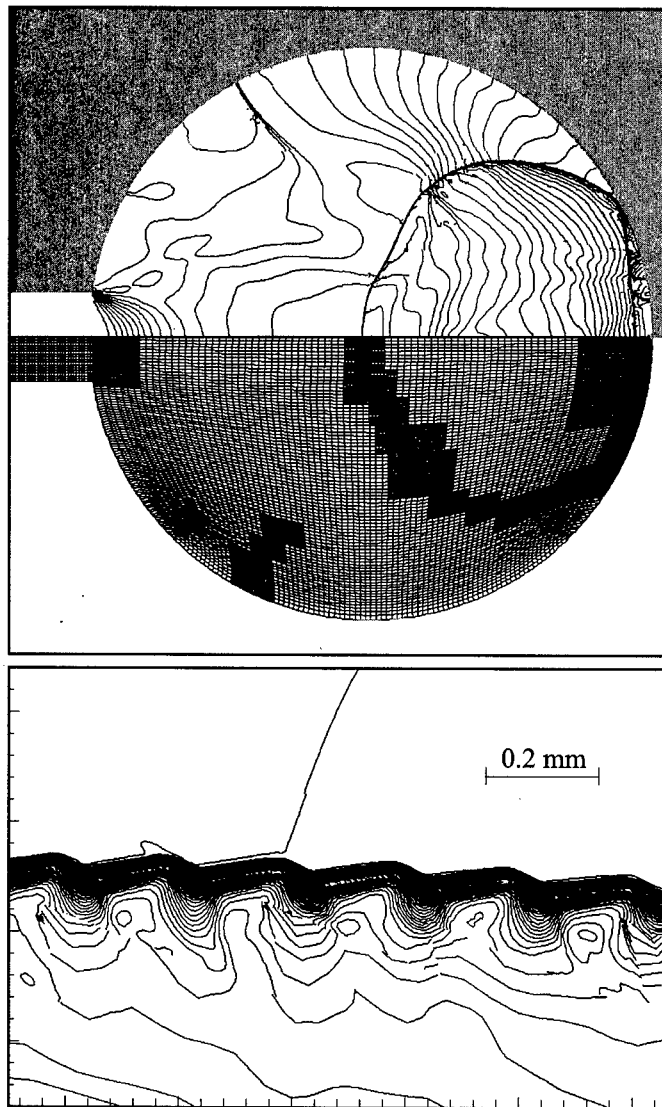
Figure 8 Top: Density fields at one time instant illustrating the wave pattern developed after reflection of the detonation wave and the corresponding computational grid distribution. Bottom: Enlarged portion of the detonation front

combustible mixture. For shock waves of low Mach numbers ranging from 1.7 to 2.1, the wave field in the focal region shows nearly the same characteristics as observed by experiments.

For a higher shock Mach number of about 2.2, the local peaks in pressure and temperature in the focal volume are sufficient to ignite the mixture. This gives rise to a detonation wave, which partly interacts with the diffracted shock wave. This interaction of a hydrodynamic shock with a combustion wave results in multifacetted wave patterns.

The combination of an adaptive method with high resolution shock capturing techniques yields a good representation of the diffracted and reflected shocks, as well as the detonation wave. Due to the use of a locally refined grid close to the reaction zone of the combustion wave, this region of high chemical activity is resolved with reasonable computational costs.

REFERENCES

1. K. Takayama, Ed. *Proc. Workshop (International) on Shock Wave Focusing*, Tohoku University, Sendai, 1989.

2. Sturtevant, B., "The Physics of Shock Focusing in the Context of Extracorporeal Shock Wave Lithotripsy," *Proc. Workshop (International) on Shock Wave Focusing* (Ed. K. Takayama), Tohoku University, Sendai, 1989, 39–89.

3. Guderly, G., "Starke kugelige und zylindrische Verdichtungsstosse in der Nahe des Kugelmittelpunktes bzw. der Zylmderachse," *Luftfahrtforschung*, **19**, 302–312, 1942.

4. Milton, B. E., "The Focusing of Shock Waves in Two-Dimensional and Axisymmetrical Ducts," *Proc. Workshop (International) on Shock Wave Focusing* (Ed. K. Takayama), Sendai, Tohoku University, 1989, 155–192.

5. Sturtevant, B., and Kulkarny, V. A., "The Focussing of Weak Shock Waves," *J. Fluid Mechanics*, **73**, 4, 651–671, 1994.

6. Choi, H. S., and Baek, J. H., "Computations of Nonlinear Wave Interaction in Shock Wave Focussing," *J. Comp. Fluids*, **25**, 5, 509–525, 1996.

7. Sun, M., and Takayama, K., "A Holographic Interferometric Study of Shock Wave Focussing in a Circular Reflector," *Int. J. Shock Waves*, **6**, 323–336, 1996.

8. Rose, M., Uphoff, U., and Roth, P., "Ignition of a Reactive Gas by Focussing of a Shock Wave," *Proc. 16th ICDERS*, Cracow, Poland, 1997, 554–556.

9. Yee, H. J., "Upwind and Symmetric Shock Capturing Schemes," NASA TM 89464, 1987.

10. Quirk, J. J., An Adaptive Grid Algorithm for Computational Shock Hydrodynamics, Technical Report, College of Aeronautics, Cranfield Institute of Technology, 1991.
11. Sun, M., and Takayama, K., "The Formation of a Secondary Shock Wave Behind a Shock Wave Diffracting at a Convex Corner," *Int. J. Shock Waves*, **7**, 287–295, 1997.

DEFLAGRATION TO DETONATION TRANSITION IN GASES AND ITS APPLICATION TO PULSED DETONATION DEVICES

N. N. Smirnov, V. F. Nikitin, A. P. Boichenko,
M. V. Tyurnikov, and V. V. Baskakov

The paper presents the results of theoretical and experimental investigations of deflagration to detonation transition (DDT) in gaseous hydrocarbon–air mixtures. The DDT process is shown to be the key factor ensuring the reliable operation of pulse detonation generators. A multiplicity of DDT scenarios in methylene cyclopropane (C_4H_6)–air mixtures is observed. Visualization of the flow was performed by the Schlieren method with a laser light source. It is shown that two major scenarios of DDT discovered by Salamandra, Oppenheim, Soloukhin and their co-workers for hydrogen–oxygen mixtures were also typical for hydrocarbon–air mixtures. In addition, several other mechanisms of the detonation onset in the flow precompressed by the accelerating flame were discovered. Thus, five different scenarios were distinguished in total. Theoretical investigations of a multi-dimensional process of the detonation onset showed that the core features of the process were the thermal explosions occuring in hot spots in the precompressed gas ahead of the non-uniform turbulent flame. The thermal explosions could develop rather rapidly into the detonation modes or into the slower combustion modes, thus providing enough time for other hot spots to reach auto-ignition. Thus, the detected multiplicity of DDT scenarios is caused by the different state of the precompressed gas ahead of the flame. Theoretical and experimental investigations of the DDT characteristics in hydrocarbon–air mixtures allowed the authors to create a pulsed detonation generator producing periodical stable detonation waves with the frequency of 10 Hz.

INTRODUCTION

The detonation phenomenon was first discovered in 1881 by Mallard and Le Chatelier [1] and Bertelot and Vieille [2, 3] who were the first to investigate flame

propagation in homogeneous gaseous mixtures and detect the supersonic mode of combustion wave travelling at velocities of thousands of meters per second. This combustion mode got the name "out of tone" combustion, or "detonation."

The earlier theoretical explanations of this phenomenon were given by Mikhelson [4], Chapman [5] and Jouguet [6] and that gave birth to intense studies of detonations.

One of the major differences between the two known combustion modes — deflagration and detonation — is in the energy conversion scenario. In a deflagration wave, the chemical energy of a metastable mixture is transformed into the thermal and kinetic energy of expanding reaction products, while in a detonation wave a part of the chemical energy is converted into the energy of compression of the reaction products.

For a long time, high pressures arising in detonation waves inhibited the applications of the phenomenon for non-destructive purposes. Nevertheless, the application of the detonation mode of burning fuel–air mixtures can be advantageous for some propulsion issues, for example, drilling and protective coating, that have been studied in the past decades. It has been shown that all the above applications need efficient devices for generating pulse detonations.

The main problems to be solved, when creating the efficient pulse detonation devices, are:

(1) providing the conditions for self-sustaining propagation of detonation waves (homogeneous or heterogeneous mixtures, detonability limits),

(2) detonation initiation, and

(3) arranging periodic regimes with high frequencies.

Among different types of detonation initiation, the simplest and most reliable is periodic spark ignition and detonation onset in the DDT process. The most widely used fuels are hydrocarbons.

The present paper is aimed at the experimental and theoretical investigation of DDT in gaseous mixtures and the sensitivity of the process to variations in the governing parameters.

BACKGROUND

There were many experimental studies [7–16] of deflagration in a combustible gas mixture, where acceleration of deflagration to detonation was detected in tubes. It was shown, that detonation waves can originate in the vicinity of the flame zone [9, 11], very close to the primary shock wave [12], and in any place in between [10, 13–16]. Authors [17–24] numerically modeled the detonation onset in such systems. Most researchers considered one-dimensional models

and simplified single-stage reactions. Molecular transport properties were neglected [18–21, 32], and the studies were primarily focused on understanding the reasons for the onset of detonation on the initial non-uniformities of temperature and species concentrations. The presence of such non-uniformities (temperature and concentration gradients) could spontaneously lead to detonation initiation after ignition of initially quiescent gas.

One-dimensional calculations, in which sinusoidal disturbances were superimposed on a linear gradient, were used in [25] to examine the effect of disturbance amplitude and frequency on the size of mixed region required for DDT.

Theoretical investigations [21] showed that even in the absence of the initial non-uniformities, exothermic chemical reactions in an inviscid gas, accelerated by a shock wave, support the convergence of characteristics leading to the detonation formation behind the shock wave.

Other studies [17, 22–24] were focused on modeling detonation initiation in a viscous thermoconductive gas. Various stages of combustion from initiation to onset of detonation, when a heat flux was applied to a semi-infinite region filled with an active mixture, were analyzed in detail. The research [22, 23] used a two-step kinetic model which accounted for the induction period and made it possible to investigate the instabilities arising in detonation propagation. The mathematical models [22, 23] made it possible to give a qualitative explanation of the multiplicity of DDT scenarios found in experiments [15]. The numerical results [22] showed that, in the absence of disturbances in the zone of compressed gas between the leading shock wave and the flame zone, the detonation wave is likely to originate just in front of the flame zone following the "gradient" mechanism [18–20]. When a number of shock waves, overtaking each other, precede the deflagration wave, the birth of two detonation waves, that propagate in opposite directions, takes place on the contact surface that is formed as a result of shock collision [22, 23]. Thus, flow disturbances created the conditions for hot spots originating in the compressed gas in front of the flame zone, giving rise to "explosion in the explosion" [12].

By now, there exist different points of view on the DDT mechanism: the onset of detonation in a number of hot spots [9, 12] ("explosion in the explosion") and the gradient mechanism [18–20] ("spontaneous flame"). Flow non-uniformities in turbulent accelerating flames seem to play a decisive role in determining the DDT scenario [15, 16]. Nevertheless, upon the ignition in a hot spot, the gradients of temperature and concentration, established due to molecular transfer processes, are likely to be responsible for the detonation onset. Numerical results show that those microscale gradients could be sufficient to initiate detonation, but the onset of detonation is strongly influenced by the kinetics of the induction period and of the exothermic steps of chemical reaction [22, 23, 32]. Thus, self-ignition in a hot spot could result either in the formation of a detonation wave or in flame propagation, that was as well detected in the experiments [15]. Recent experimental and theoretical investigations of the onset of detonation behind

67

the reflected shock waves [16, 33] showed that double shock–flame interaction also led to formation of similar hot spots.

In the macroscale, DDT is strongly influenced by turbulence causing flame acceleration and thus, providing the conditions for the detonation onset [14] in the compressed gas, ahead of the flame front. To shorten the predetonation length, thus providing "mild" detonation initiation in tubes within reasonable length scales, it is necessary to introduce additional turbulization into the flow. This could be done in the following ways:

(1) introducing the Shchelkin spiral in the beginning of the tube near walls [14];

(2) using the wider turbulizing chambers incorporated in the first sections of the tube where the ignition takes place [15, 26];

(3) filling the entire tube with circular orifice plates thus essentially blocking the flow [27].

Installing the turbulizing elements near the walls of the tube proved to be very effective and probably substantiates theoretical implications that detonation is likely to appear near the walls [28]. Experimental results [15] also indicated that "explosion in the explosion" in the DDT process took place close to the walls rather than in the center of the flow.

The wider turbulizing chambers incorporated in the ignition sections of the detonation tubes [15, 26] proved to be very effective in shortening the predetonation length in gaseous hydrocarbon–air mixtures. In smooth-walled tubes under normal conditions, the predetonation length for hydrocarbon–air mixtures was equal to 80–120 tube diameters [31]. The use of turbulizing elements of this type allowed the overdriven detonation to be obtained in gasoline–air mixtures within the distance 1.5–2 m from the initiating section, which then decayed to a Chapman–Jouguet (CJ) mode [26]. Blocking the tube with circular orifice plates could hardly guarantee the onset of the CJ detonation within the length of 3.3 m. The use of turbulizing chambers for promoting the detonation onset made the predetonation length much less sensitive to tube diameter in the range of 30–100 mm [29].

The experimental data on the influence of initial gas pressure and temperature on the predetonation length is limited [30]. As reported in [30], the experimental results in tubes showed the decrease in the predetonation length with pressure, while the results on the predetonation length sensitivity on gas temperature were contradictory. Some results showed the increase of the predetonation length with temperature and the others showed a slight decrease of the predetonation length and time with temperature [26]. Thus, the sensitivity of the DDT to variation of the governing parameters needs further investigations.

Conducting numerous experimental investigations of DDT in hydrocarbon–air mixtures [15, 23, 26] drove the authors of the present paper to the conclusion

that it was hardly possible to maintain the same initial and boundary conditions in all the experiments. The multiplicity of the transition mechanisms observed in experiments [15] under nearly the same initial conditions showed that even minor uncontrolled fluctuations of initial and boundary conditions could cause major changes in the transition mechanism.

Thus, in our opinion, it is possible to maintain exactly the same initial conditions only in numerical experiments. The aim of our study is using the results of experiments to create a numerical model that could provide a method, by varying some of parameters and keeping the rest of them unchanged, to determine the influence of governing parameters on the development of DDT. Numerical models for DDT in gaseous and multiphase mixtures will serve as a powerful tool in studying optimal characteristics of pulsed detonation devices.

The results presented in this paper are related to "mild" detonation initiation in homogeneous fuel–air mixtures.

1   EXPERIMENTAL INVESTIGATIONS

Experimental investigations of DDT mechanisms were carried out in a confined channel of square 25×25 mm cross section filled with a hydrocarbon–air mixture.

Visualization of the flow was performed by the Schlieren method with the help of a laser source. A chamber 50 mm in diameter was installed near the ignition source to accelerate the flame in the tube. An optical section was installed for the photoregistration of different stages in the development of the transition process.

1.1   Experimental Technique

The schematic of the test tube is shown in Fig. 1. The tube consists of 10 separate sections. The optical section *3* is aimed for the photoregistration of the transition processes and could be installed in any place along the tube, with the total tube length kept unchanged. The location of the optical section was characterized by the distance, L, to the closed end where ignition was facilitated.

The wider ignition chamber *1* and forechamber *2*, both 50 mm in diameter, were installed in the beginning of the tube to serve as flow turbulizing elements producing no blockage of the tube cross section. Those elements proved to be very effective in flame acceleration after the mixture was ignited by a spark plug *4*.

The pressure detector *6* (with own oscillation frequency 40 kHz), having the external cylindrical surface 18 mm in diameter, was screwed into the orifice in the center of the lower part of the optical section. The detector was used to
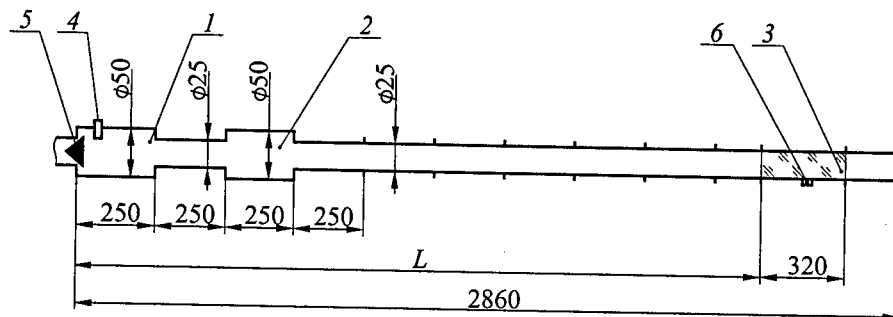
Figure 1 The schematic of the experimental detonation tube: *1* — ignition chamber, *2* — forechamber, *3* — optical section of square cross section 25 × 25 mm, *4* — ignition device, *5* — reverse valve, *6* — piezoelectric pressure detector

check the instant when the leading shock wave passed the optical section and to synchronize photoregistrations. A detailed description of the synchronization scheme can be found in [34]. The detector *6* could also serve as a source of an additional disturbance (1 mm high) in the optical section.

Combustible mixture entered the channel through the reverse valve *5* and escaped from the tube into the atmosphere through the open end. The mixture was ignited by the electric spark (the energy of discharge was 50 mJ ± 5%). The reverse valve *5* could close due to the pressure differential in the ignition chamber *1*, arising from combustion. The tube was filled with a stoichiometric mixture of methylene cyclopropane (C_4H_6) and air at temperature $T_0 = 300$ K.

The optical scheme of the Schlieren registrator (photochronograph) is shown in Fig. 2. Lenses *4* and *5* formed the horizontal light sheet with an extension (0.5 mm thick) along the axis of channel symmetry. Lenses *7* and *9* formed the picture of light sheet thickness on the photographic film. Mirrors *10* and *11* formed the complete set of high-speed camera ensured the ray division to form two pictures equal in intensity. Lens *12* compensated the difference of the ray motion. Wedge *13* removed the partial superposition of pictures. Rotating four-sided mirrors *14* and *15* sweep the beams in time, thus (x, t) diagrams of the process were obtained. Synchronization of the photography with the instant of wave passing the optical section was performed as described in [34].

1.2 Results of Experiments

The following wave picture was observed in the predetonation section ($L = 1530$ mm). Several primary shock waves were propagating in front of the turbu-
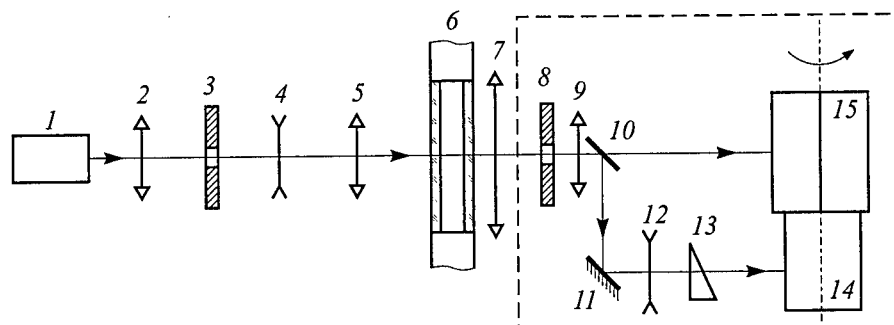
Figure 2 The optical scheme: *1* — Argon laser generating continuous radiation with the wave length 0.46–0.52 μm; *2, 5, 7,* and *9* — positive lenses, *3* — slot electromagnetic gate; *4* and *12* — negative lenses, *6* — optical section, *8* — electro-magnetic gate of the high-speed camera, *10* — semi-transparent mirror, *11* — mirror, *13* — optical wedge, *14* and *15* — four-sided mirrors sweeping the light beams. Lenses *2, 4, 7, 9,* and *12* are spherical. Lense *5* is cylindrical

lent flame. Some of those waves resulted from the piston effect of the combustion products flowing through the ignition chamber and forechamber. The others were formed due to coalescing the compression waves, caused by the accelerated turbulent flame. The last shock waves overtook the primary ones, until a strong shock wave supported by the flame-induced compression waves was formed ahead of the flame.

In the transition section, different cases of DDT took place. Figures 3 to 7 illustrate the types of flow patterns in the transition zone registered in the optical section. The flame was propagating from the left to the right, time increasing from bottom to top. Thus, the photochronograms give the x–t diagrams of the process.

Figure 3 shows the case when the detonation wave occurs just ahead of the flame zone. Figure 4 illustrates the detonation originating in the compressed unburned gas between the leading shock wave and the flame zone. It is seen that the onset of detonation was preceded by the wave interactions. The primary shock moving at the velocity of 500 m/s was overtaken by the strong shock formed ahead of the turbulent flame. As a consequence of this interaction, the leading shock propagating at the velocity of 1190 m/s and the contact surface moving behind it were formed. The center of mixture ignition occurred on the contact surface giving birth to detonation waves propagating in both directions. The retonation wave (moving backward) propagated as a detonation wave in the zone of compressed unburned gas in motion (the absolute velocity 960 m/s), and after colliding with the flame zone decayed to a shock wave. The absolute

71
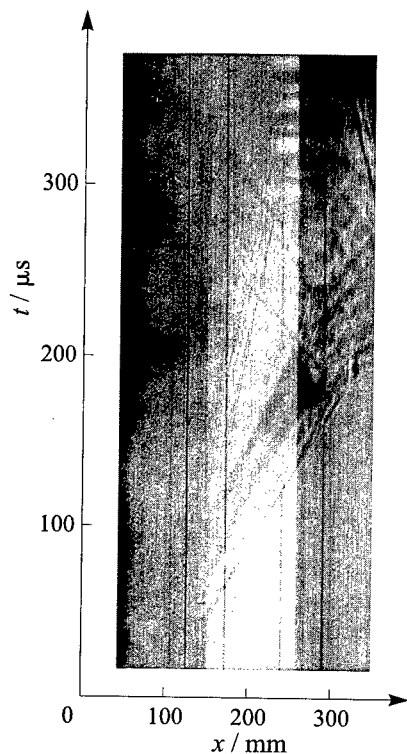
Figure 3 Schlieren photochronogram of DDT. Detonation occurs in the flame zone
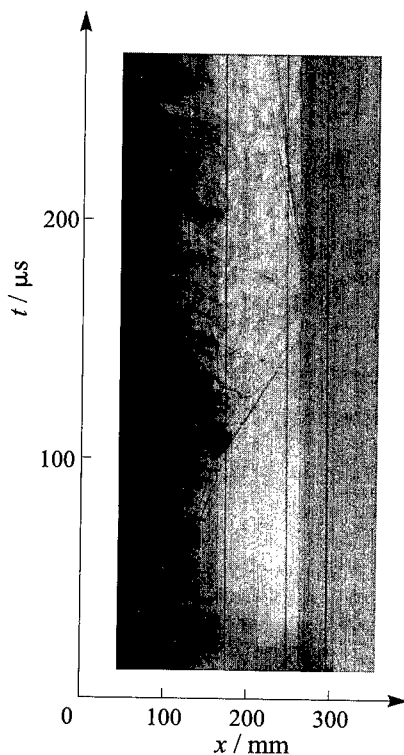
Figure 4 Schlieren photochronogram of DDT. Detonation occurs ahead of the flame zone in the compressed unburned gas between the leading shock wave and the flame. The center of mixture ignition lies on the contact surface formed due to interactions of primary shocks and gives birth to detonation waves propagating in both directions

velocity of the retonation wave increased to 1190 m/s after entering the quiescent reaction products. The detonation wave moving forward (absolute velocity 2980 m/s) overtook the leading shock and entered the undisturbed mixture as an overdriven detonation wave, which gradually slowed down to a self-sustained wave. Compression waves generated by the flame, overtook the overdriven detonation, thus influencing the attenuation character of the latter. Thus, the two major scenarios of DDT detected for hydrocarbon–air mixtures were similar to those detected in [9–12] for hydrogen mixtures. However, hydrocarbon–air mixtures exhibit a wider variety of scenarios.
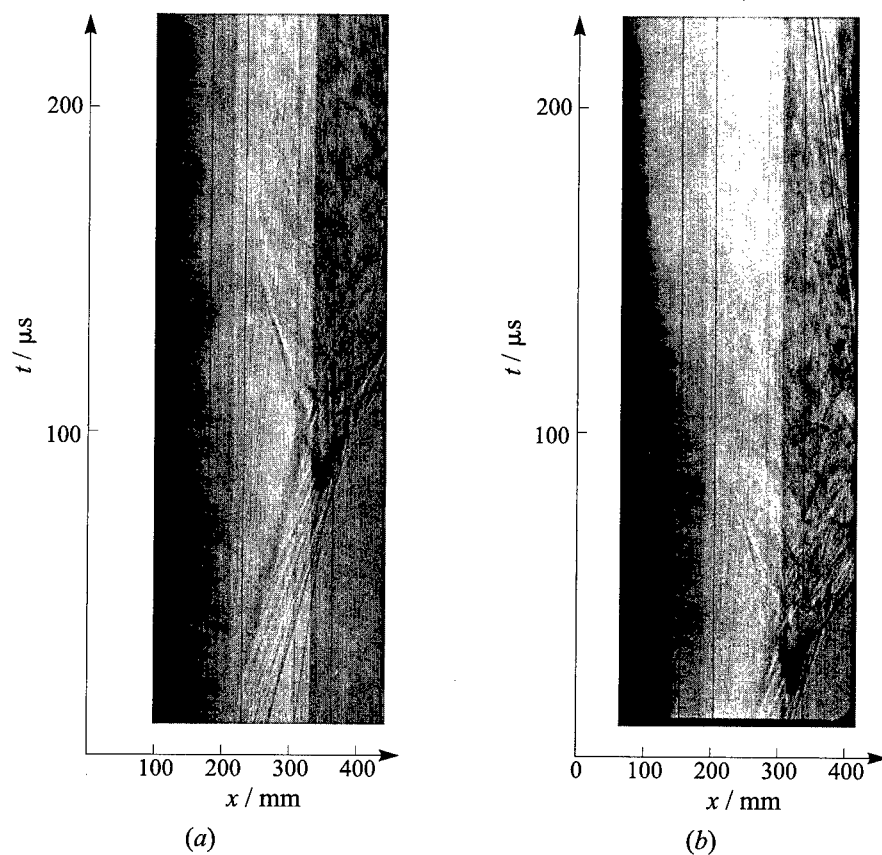
Figure 5 Schlieren photochronograms (*a*, *b*) of DDT. Origination of spontaneous flame in a hot spot between the leading shock and the flame zone. Detonation develops a bit later in the same zone

Figures 5*a* and 5*b* show ignition and spontaneous flame development in a hot spot on a contact discontinuity ahead of the turbulent flame in the gas compressed by the leading shock. The detonation waves, developed a bit later, propagated from the hot spot in both directions and, then, repeated the scenario of Fig. 4.

In the region between the detonation and retonation waves, the waves spreading from the detonation origin in different directions at high velocities were observed. The waves spreading ahead overtook and reinforced the detonation wave, and the waves spreading backwards overtook and reinforced the retonation wave. These waves, resulting from reflection of the detonation wave from the tube

73
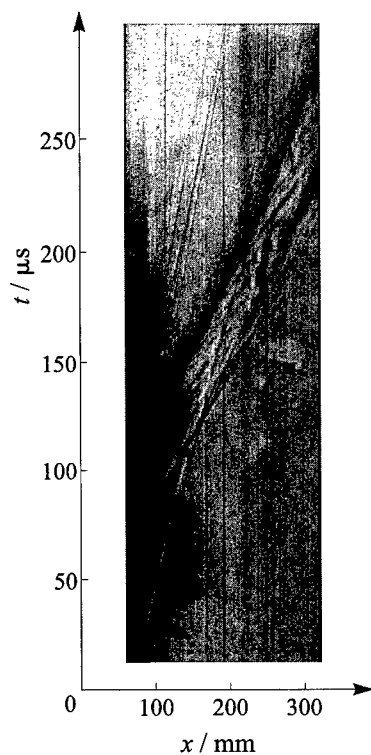
Figure 6 Schlieren photochronogram of DDT. Auto-ignition ahead of the flame zone on a flow non-uniformity (at contact discontinuity) in the precompressed gas leading to normal deflagration propagating in both directions from the hot spot
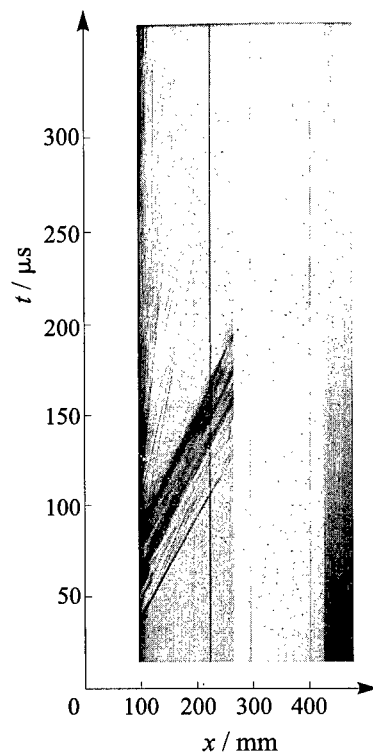
Figure 7 Schlieren photochronogram of DDT. Successive autoignitions occurring in a number of hot spots in the compressed unburned gas ahead of the flame front. Those auto-ignition events bring to formation of detonation and retonation waves (the latter is seen in the upper part of the figure moving to the left)

walls, were initially transverse. Therefore, the trajectories of motion of these waves formed the parabolas at the photochronograms that were convex towards the location of detonation origin. This testified the fact that "explosion in the explosion" was likely to take place near the wall [28]. The parabolas vertices were displaced ahead in time, testifying that the cross waves were carried by the flow of combustion products. The location of DDT was characterized qualitatively by the formation of a retonation wave, by the change in the character of radiation from the combustion front, and by the severe oscillations in combustion products.

Ignition in the hot spot in the compressed gas ahead of the turbulent flame should not necessarily result in formation of detonation waves in the same spot. Figure 6 illustrates the case when the strong shock and the primary shocks, supported by the turbulent flame, collided and formed a contact surface as a result of the interaction. After some induction time, the ignition of gas adjacent to the contact surface occurred between the leading shock and the flame zone. The combustion zone was expanding in both directions at a normal burning velocity. "Explosion in the explosion" occurred out off the frames of the optical section.

Figure 7 illustrates the case when successive mixture ignitions occurred in a number of hot spots in the precompressed unburned gas ahead of the flame. The arising combustion centers were enlarged in both directions, which lead to formation of bulk combustion between the flame and the leading shock. The detonation wave arose in the zone of bulk mixture combustion closer to the leading shock and beyond the photographic zone. The retonation wave moving backward at the velocity of 1350 m/s in the upper part of Fig. 7 testifies to that fact.

Comparison of Figs. 3 to 7 clearly shows the stochasticity of the detonation origin locations and the transition scenarios. The detonation onset in the experimental setup took place at distance $L = 1800$–2000 mm from the ignition point.

1.3 Analysis of Experimental Results

The experimental investigations proved that the two major DDT scenarios discovered by Salamandra, Oppenheim, Soloukhin, and their co-workers for hydrogen–oxygen mixtures [7–12] were also typical for hydrocarbon–air mixtures. Also, several other mechanisms of the detonation onset in the flow precompressed by the accelerating flame were discovered. Thus, five different scenarios could be distinguished.

I Detonation waves can be traced from the flame zone, accelerating rapidly in the precompressed gas, and after interacting with the overtaken leading shock, next forming the overdriven detonation wave in the undisturbed mixture and then gradually decaying to the CJ mode.

II The onset of detonation takes place on one of the flow non-uniformities (contact discontinuities) ahead of the flame, in the precompressed gas between the leading shock and the flame zone (the classical "explosion in the explosion"). This local explosion gives birth to both detonation and retonation waves.

75

III Spontaneous flame propagating in all directions at a high apparent velocity, appears in the non-uniformly precompressed gas between the flame zone and the leading shock that finally brings to formation both detonation and retonation waves.

IV The secondary combustion zone originates in the precompressed gas ahead of the main flame zone, due to auto-ignition at a contact surface, with flame propagating in both directions at a normal burning velocity similar to that in the main flame. That finally leads to the formation of detonation and retonation waves in the long run.

V Ignition takes place, locally, and practically simultaneously, on flow non-uniformities in a number of spots, in the precompressed gas ahead of the main flame zone. Those ignitions give birth to flame zones expanding in time. The increase in the flame surface and in the energy release per unit volume leads to a rapid pressure rise and formation of detonation and retonation waves. Macroscopically, the flow pattern looks like a bulk explosion or a fast spontaneous flame. But on refining the resolution, one can see a stochastic ignition time shift from one hot spot to another. The sequence of ignitions is also stochastic testifying to the fact that auto-ignitions in different hot spots take place independently and do not form in succession or belong to one chain process.

2 NUMERICAL INVESTIGATIONS OF THE DDT PROCESS

The numerical modeling of the DDT was aimed at investigating the sensitivity of the process to variations of the governing parameters. Following the methods developed in [22, 23], we investigated the influence of initiation conditions and the characteristic times of the induction and exothermic stages. However, for developing a model capable of describing all the stages of the process, namely, ignition, flame acceleration, and transition to detonation, we incorporated a turbulence model into the set of governing equations following [35].

2.1 Mathematical Model

Consider the unsteady motion of an initially quiescent, combustible, viscous, and heat-conductive gas, bounded by rigid non-catalytic walls. The modified k–ε model accounting for the near-wall damping effect (by making use of the Lam–Bremhorst low Reynolds model) is used to describe the gas flow. Among

the chemical components involved in the process, four groups are distinguished: fuel, oxidizer, inert components, and reaction products. Assume that only these components play a decisive role, and that there is no need to distinguish all the intermediate and final products of thermal decomposition of fuel and oxidizer. We deal with the mass concentration of the kth component, with $k = 0$ related to oxidizer, $k = i$ related to inert components, and $k = p$ related to reaction products. The chemical kinetics is modeled by a two-step mechanism [36, 37]: (i) the induction period, when parameter δ changes from 1 to 0, with the rate $\dot{w}_\delta = K_\delta^0 \delta\rho \exp(-E_\delta/RT)$ and unchanged mixture properties and (ii) the exothermic reaction stage with the rate $\dot{w} = KY_k\rho^2\chi(-\delta)\exp(-E_a/RT)$, when the mixture composition and properties undergo changes. Here E_a and E_δ are the activation energies; $k = 0$ or f, depending on the initial mixture composition,

$$\chi(z) = \begin{cases} 0, & \text{if } z < 0 \\ 1, & \text{if } z \geq 0 \end{cases}$$

Assume that the gas is a mixture of perfect gases, i.e.

$$e_k = c_{\nu k}T + h_{0k}, \qquad p_k = \rho_k \frac{R}{W_k}T$$

where e_k is the specific internal energy of the kth component, $c_{\nu k}$ is the specific heat, W_k is the molar mass, h_{0k} is the chemical energy, T is the temperature of the mixture, R is the universal gas constant.

The set of governing equations for the averaged values of flow parameters (averaging bars are omitted) has the following form:

$$\frac{\partial \rho}{\partial t} + \nabla \cdot (\rho \vec{u}) = 0 \tag{1}$$

$$\frac{\partial \rho\delta}{\partial t} + \nabla \cdot (\rho\vec{u}\delta) = -\dot{w}_\delta - \nabla \cdot \left(\vec{I}_\delta + \vec{I}_\delta^t\right) \tag{2}$$

$$\frac{\partial \rho Y_k}{\partial t} + \nabla \cdot (\rho\vec{u}Y_k) = \nu_k W_k \dot{w} - \nabla \cdot \left(\vec{I}_k + \vec{I}_k^t\right) \tag{3}$$

$$\frac{\partial \rho\vec{u}}{\partial t} + \nabla \cdot (\rho\vec{u} \otimes \vec{u}) = -\nabla p + \nabla \cdot \left(\tau + \tau^t\right) \tag{4}$$

$$\frac{\partial \rho E}{\partial t} + \nabla \cdot (\rho\vec{u}E) = -\nabla \cdot p\vec{u} - \nabla \cdot \left(\vec{I}_q + \vec{I}_q^t\right) + \nabla \cdot \left((\tau + \tau^t) \cdot \vec{u}\right) \tag{5}$$

where ρ, $\vec{u}$, and p are the averaged mixture density, velocity, and pressure, respectively; $E = \sum_k Y_k e_k + u^2/2 + k_T$ is the total specific energy; k_T is the average kinetic energy of turbulent pulsations; ν_k is the stoichiometric coefficient. To

close the set of Eqs. (1) to (5), the k–ε model for compressible flows is used. The turbulent fluxes are modeled in the following way:

$$\tau + \tau^t = \rho\left(\nu + \nu^t\right)\left(\nabla\vec{u} + \nabla\vec{u}^T - \frac{2}{3}\nabla\vec{u}I\right) - \frac{2}{3}\rho k_T I$$

$$\vec{I}_k + \vec{I}_k^t = \rho\left(D + \frac{\nu^t}{\sigma_i}\right)\nabla \cdot Y_k$$

$$\vec{I}_q + \vec{I}_q^t = \vec{J}_q + \vec{J}_q^t + \sum_k\left(c_{pk}T + h_{0k}\right)\left(\vec{I}_k + \vec{I}_k^t\right)$$

$$\vec{J}_q + \vec{J}_q^t = -\left(\lambda + \rho c_{pk}\frac{\nu^t}{\sigma_t}\right)\nabla \cdot T$$

where I is the unit tensor of the second order; $\nabla\vec{u}^T$ is the transposed matrix $\nabla\vec{u}$; ν is the molecular kinematic viscosity; ν^t is the turbulent kinematic viscosity; D is the mean molecular diffusion coefficient; λ is the mean thermal conductivity coefficient for the mixture.

The turbulent kinematic viscosity is modeled according to the k–ε model:

$$\nu^t = C_\mu^0 f_\mu \frac{k_T^2}{\varepsilon}$$

where ε is the dissipation of turbulent pulsations.

The model is closed by the two equations for the kinetic energy of turbulent pulsations k_T and its decay due to dissipation ε:

$$\frac{\partial\rho k_T}{\partial t} + \nabla \cdot (\rho\vec{u}k_T) = \nabla \cdot \left(\rho\left(\nu + \frac{\nu^t}{\sigma_k}\right)\nabla k_T\right) + \tau^t : \nabla u - \rho\varepsilon \tag{6}$$

$$\frac{\partial\rho\varepsilon}{\partial t} + \nabla \cdot (\rho\vec{u}\varepsilon) = \nabla \cdot \left(\rho\left(\nu + \frac{\nu^t}{\sigma_\varepsilon}\right)\nabla\varepsilon\right) + \frac{\varepsilon}{k_T}\left(C_{1\varepsilon}\tau^t : \nabla u - C_{2\varepsilon}\rho\varepsilon\right) \tag{7}$$

To take into account the near-wall damping effect, the coefficients C_μ, $C_{1\varepsilon}$ and $C_{2\varepsilon}$ of the stanard k–ε model are modified [35] in accordance with the so-called "low Reynolds" models:

$$C_\mu = C_\mu^0 f_\mu, \qquad C_{1\varepsilon} = C_{1\varepsilon}^0\frac{f_1}{f_\mu}, \qquad C_{2\varepsilon} = C_{2\varepsilon}^0 f_2$$

where f_μ, f_1 and f_2 are the positive functions: $0 < f_\mu \leq 1$, $f_1 \geq 1$, $0 < f_2 \leq 1$.

The values of the constants of the k–ε model obtained by comparing the results of numerical and physical experiments are the following:

$$C_\mu^0 = 0.09, \qquad \sigma_k = 1, \qquad \sigma_\varepsilon = 1.3,$$

$$C_{1\varepsilon}^0 = 1.45, \qquad C_{2\varepsilon}^0 = 1.92, \qquad \sigma_i = \sigma_t = 1$$

The boundary conditions for the volume G are:

$$\partial G: \quad \vec{u} = 0, \quad k_T = 0, \quad \frac{\partial \varepsilon}{\partial \vec{n}} = \frac{\partial \sigma}{\partial \vec{n}} = \frac{\partial Y_k}{\partial \vec{n}} = \frac{\partial T}{\partial \vec{n}} = 0 \qquad (8)$$

where $\vec{n}$ is a vector normal to the boundary ∂G.

Combustion initiation is performed by the chemical energy release in a certain relatively small volume G_r within the computational domain G. Thus, the initial conditions for the set of Eqs. (1) to (7) take the form:

$$t = 0, \quad G \setminus G_r: \quad \vec{u} = 0, \quad \rho = \rho_0, \quad T = T_0, \quad \delta = 1, \qquad (9)$$

$$Y_k = Y_{k0}, \quad k_T = k_{T0}, \quad \varepsilon = \varepsilon_0$$

$$t = 0, \quad G_r: \quad \vec{u} = 0, \quad \rho = \rho_r, \quad T = T_r, \quad \delta = 0, \quad (10)$$

$$Y_k = Y_{kr}, \quad k_T = k_{T0}, \quad \varepsilon = \varepsilon_0$$

To solve the set of Eqs. (1) to (7), the splitting by coordinates method is used according to MacCormack [39], which simplifies the solution and increases the allowable time step. Each operator is also split into two parts: the parabolic and the hyperbolic–parabolic, including the source terms. The parabolic operator is solved using the implicit Laasonen scheme [39], while the hyperbolic-parabolic part is solved using the MacCormack explicit scheme. The computational technique is described in detail in [35].

2.2 Results of Numerical Modeling

The numerical investigations of DDT were performed for both one-dimensional (1D), and multi-dimensional cases. 1D modeling, following the one-dimensional scheme of photoregistration in experiments (see Section 1), was aimed at investigating the experimentally detected peculiarities of the transition mechanism. On the one hand, 1D models are usually very fruitful for understanding the nature of physical phenomena at a macroscale, and on the other hand, the most important characteristic features of complicated multi-dimensional flows can also be observed in 1D flows. The influence of a multi-dimensional flow pattern on the detonation onset was also investigated.

The results were obtained for the model values of the governing parameters. Thus, only qualitative comparison with the experiments was possible.

2.2.1 One-Dimensional Modeling

The methods for numerical modeling of 1D problems of the detonation onset in a viscous thermo-conductive gas, based on the Navier–Stokes equations and de-

Curve	$t \times 10^4$	$\overline{U}_{s.w}$	$\overline{U}_{def}$
1	985	3.317	2.980
2	1.529	3.423	3.240
3	1.961	3.622	4.096
4	2.191	3.857	5.101
5	2.245	3.965	6.167
6	2.277	4.062	9.021
7	2.291	4.129	11.193
8	2.314	11.376	11.299
9	2.414	9.849	9.974
10	2.612	8.763	8.646
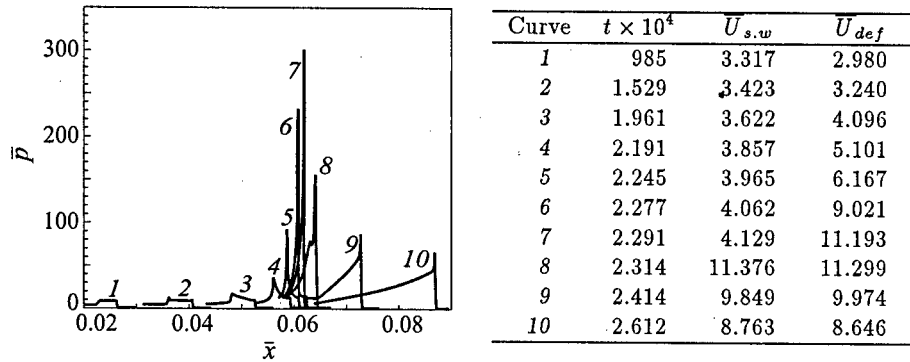
Figure 8 Calculated successive pressure profiles in a gas mixture for the case of DDT. Numbered curves correspond to different times. Corresponding times, as well as the shock wave ($\overline{U}_{s.w}$) and flame ($\overline{U}_{def}$) velocities for the curves are given in the table

scribed in [22, 23], shed some light on the problem of multiplicity of DDT scenarios. Calculations showed, in the absence of strong flow non-uniformities ahead of the flame, the detonation wave develops from the flame zone following the spontaneous mechanism. The results are displayed in Fig. 8 in non-dimensional variables:

$$\overline{x} = \frac{x}{L}, \qquad \overline{t} = \frac{ta_0}{L}, \qquad \overline{p} = \frac{p}{p_*}, \qquad \overline{u} = \frac{u}{a_0}, \qquad \overline{T} = \frac{T}{T_*}$$

where a_0 is the speed of sound in the initially quiescent gas. The values of the governing parameters are:

$$\gamma_0 = 1.4, \qquad \frac{c_p}{c_{p0}} = 1.2, \qquad \frac{W_0}{W} = 0.8, \qquad \text{Re} = \frac{\rho_0 a_0 L}{\mu_0} = 10^6$$

$$\text{Pr} = \frac{\mu_0 c_{p0}}{\lambda_0} = 0.72, \qquad \text{Sc} = \frac{\mu_0}{\rho_0 D_0} = 0.72$$

$$\frac{\sum_k W_k \nu_k h_{0k}}{W_f \nu_f c_{pk} T_0} Y_f^0 = 10, \qquad \frac{L}{a_0} K_\delta^0 = 10^9, \qquad \frac{K_\delta^0}{K \rho W} = 1$$

$$\frac{E_a}{RT_0} = 8.4, \qquad \frac{E_\delta}{RT_0} = 24, \qquad p_* = \rho_0 a_0^2, \qquad T_* = T_0$$

It is seen in Fig. 8 that the initially formed combustion wave lags behind the shock formed after the forced ignitions (curves *1* and *2*). The combustion wave can be detected in pressure profiles as the rarefaction wave. The pressure in the zone between the shock and the combustion front increases with time, with the maximal increase rate found immediately ahead of the flame front (curves *3* and *4*). As the reaction zone accelerates rapidly, its length decreases. The dimensionless flame velocity ($\overline{U}_{def}$), the leading shock velocity ($\overline{U}_{s.w}$), and the times

corresponding to pressure curves *1* to *10* are given in the table to the right of Fig. 8. It is seen that with pressure rise, both the flame and the leading shock accelerate, but the flame acceleration is much faster (curves *3*, *4*, and *5*). The detonation wave forms in the compressed gas in the vicinity of the flame front (curve *6*). The detonation then moves ahead of the leading shock wave (curve *7*). After the detonation interacts with the leading shock, an overdriven detonation wave that spreads through the fresh mixture (curve *8*) is formed. Its velocity on entering the undisturbed gas is $\overline{U}_D \approx 10$, which exceeds the CJ detonation velocity $\overline{U}_{CJ} = 7.2$. Gradually, its intensity falls down (curves *9* and *10*), and the detonation approaches the CJ regime.

A different scenario can occur in the presence of strong flow non-uniformities, between the leading shock and the flame zone. Those non-uniformities can arise due to collisions of multiple shock waves preceding the flame front. A typical example is the case, when the ignited zone of gas is located at some distance from the closed end of the tube. Under these conditions, weak shock waves propagate in both directions and the shock reflected from the closed end overtakes the leading shock. Figure 9 shows pressure (solid curves) and temperature (dashed curves) profiles in this case for a number of times. A sharp rise of temperature up to $\overline{T} \approx 10$ takes place in the flame zone. Two weak shock waves precede the deflagration wave (solid curves *1* and *2*). The interaction of the two shock waves gives birth to a rarefaction wave (solid curve *3*), moving backward to the flame front, and the contact discontinuity (dashed curves *3*, *4*, and *5*), that exists between the leading shock and the flame zone at $t \geq t_3$. The zone between the leading shock and the contact surface has a higher temperature. Thus, the induction period in this zone is less than that between the flame front and the contact surface. The first thermal explosion takes place in the gas layer that has been at the higher temperature for the longer time, i.e. in the gas layer located very close to the contact surface (curves *6*).

Following the gradient mechanism, two detonation waves propagating in opposite directions are formed in this zone (curves *7* and *8* in Fig. 9*b*). The intensity of the retonation (reverse detonation) wave falls down upon entering the reaction products (curve *9*). The principal forward detonation wave propagates towards the leading shock (curve *9*). After it interacts with the leading shock, an overdriven detonation is transmitted into the uncompressed mixture (curve *10*) and gradually slows down to the CJ speed. Thus, the numerical investigations show that contact discontinuities present in the flow can serve as the sources for mixture self-ignition, or the "hot spots." However, the self-ignition in the "hot spot" does not always result in detonation formation. Deflagration waves can also propagate in both directions from a "hot spot."

Figure 10 shows the successive pressure and temperature profiles for the case when the secondary ignition in the compressed gas ahead of the flame front gives birth to deflagration waves. The results shown in Fig. 10 were obtained using the k-ε model for the following modified reaction kinetics:

(a)

(b)
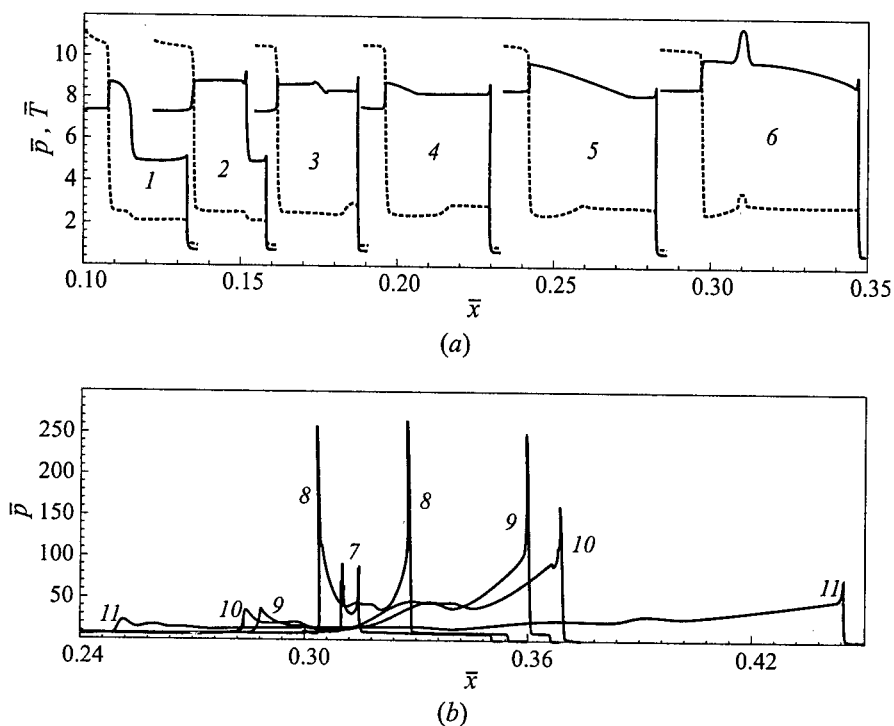
Figure 9 Calculated pressure (solid lines) and temperature (dashed lines) profiles at different times for the case of DDT. Two weak shock waves precede the deflagration wave (1, 2) and a contact surface forms as a result of shocks collision (3, 4, and 5). Auto-ignition occurs at the contact surface (6), that gives birth to two detonation waves propagating in opposite directions (7 and 8). One of those waves becomes a shock wave on entering the combustion gas (9, 10, and 11), the other enters the undisturbed unburned mixture as an overdriven detonation wave (10) and then slows down to a Chapman–Jouguet mode (11). Curves 1 to 11 correspond to $t = 0.000622$ (1), 0.000755 (2), 0.000891 (3), 0.001064 (4), 0.001283 (5), 0.001536 (6), 0.001550 (7), 0.001568 (8), 0.001607 (9), 0.001618 (10), 0.001717 (11)

1st stage: $\dot{w}_\delta = K_\delta \rho^2 \dfrac{W}{W_f} Y_f \exp\left(\dfrac{E_\delta}{RT}\right)$

(11)

2nd stage: $\dot{w} = K \dfrac{\rho^2 W^2}{W_a W_o} Y_a Y_o \exp\left(\dfrac{E}{RT}\right)$

where $W = \left(\sum_k Y_k/W_k\right)^{-1}$ is the mean molar mass of the mixture. At the first stage, the fuel component is converted into the activated state $(F \rightarrow A)$, at the second stage the activated fuel enters into the exothermic reaction with oxidizer $(A + O \rightarrow 2P)$. The values of the governing parameters are
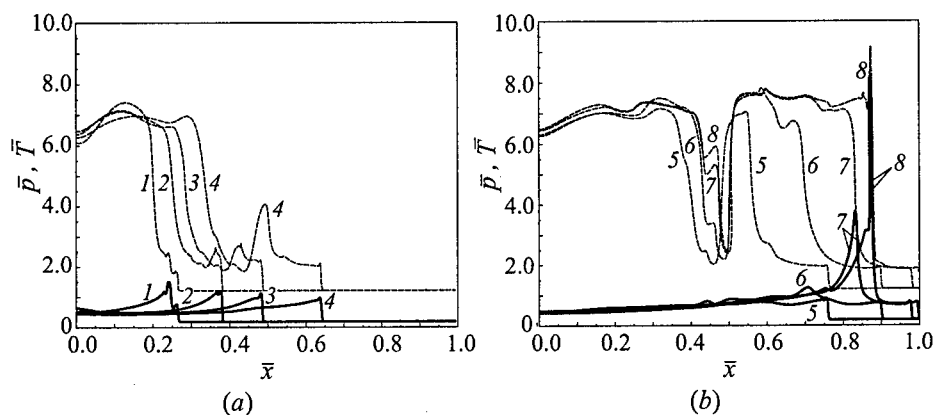
Figure 10 Calculated pressure (dashed lines) and temperature (solid lines) profiles for the case of DDT, when secondary ignition in the compressed gas ahead of the flame gives birth to normal deflagration waves one of which finally leads to detonation. Curves correspond to the following times: 1 — 750 μs, 2 — 1177, 3 — 1555, 4 — 2145, 5 — 2617, 6 — 3184, 7 — 3514, 8 — 3592

$$\frac{E_\delta}{RT_0} = 17.3 \,, \qquad \frac{E_a}{RT_0} = 10.7 \,, \qquad \frac{K_\delta}{K} = 10^{-1}$$

$$\frac{\sum_k W_k \nu_k h_{0k}}{W_f \nu_f} \, \frac{Y_f^0}{c_{p0} T_0} = 10 \,, \qquad \frac{L}{a_0} K_\delta \rho W = 0.3 \cdot 10^4$$

$$k_0 = 20 \text{ m}^2/\text{s}^2 \,, \qquad \varepsilon_0 = 100 \text{ m}^2/\text{s}^3 \,, \qquad \frac{W^0}{W} = 1$$

The successive pressure profiles (solid curves in Figs. 10a, 10b) and temperature profiles (dashed curves in Figs. 10a, 10b) are displayed in dimensionless variables ($p_* = 0.5$ MPa and $T_* = 250$ K). It is seen that the flame is preceded by two shock waves (curves 1) overtaking one another. After their collision, a contact surface is formed (curves 2), which diffuses in time. Auto-ignition occurs at the contact surface (curves 3 and 4) which gives birth to two deflagration waves propagating in both directions (curves 5). The deflagration wave propagating up the flow towards the primary flame zone is displaced down, by the gas flow, (curves 5 and 6) because its velocity is much less than that of the gas flow. The deflagration wave propagating downstream gives birth to a detonation wave (curves 6, 7, and 8). The detonation is formed due to the gradient mechanism in

83

the gas between the leading shock and the contact surface. Thus, self-ignition in a hot spot on the contact surface could give birth to two secondary deflagration waves leading to the detonation onset.

The numerical modeling explained the mechanism of "explosion in the explosion" taking place on a contact discontinuity, formed as a result of interaction between shock waves ahead of the accelerating flame. The zone of compressed gas ahead of the contact surface has a higher temperature and smaller induction delay than that between the flame and the contact surface. The reason is that the gas behind the contact surface was compressed sequentially in a series of shock waves and expanded in a rarefaction wave, while the gas ahead of it was compressed up to the same pressure in a single shock, thus attaining higher entropy and temperature. The first thermal explosion takes place in the gas layer that has been at the higher temperature for the longer time, i.e. the gas layer compressed in the earliest stages by a single strong shock wave. That is the layer located just near the contact surface.

Depending on the flow history and the induction delay gradients in the vicinity of the contact surface, the thermal explosion can lead to formation of two detonation or normal deflagration waves propagating in opposite directions. The normal deflagration waves caused by one or several successive auto-ignitions (thermal explosions) at contact discontinuities in the precompressed gas, propagating in both directions from the place of the origin, cause further compression and heating of the gas thus decreasing the induction period and leading to detonation formation.

The multiplicity of the "hot spots" present in the flow ahead of the accelerating flame can lead to multiplicity of DDT scenarios.

2.2.2 Two-Dimensional Modeling

To investigate the influence of the multi-dimensional character of the flow on the detonation onset, the two-dimensional axisymmetrical problem was considered. The mixture was ignited at the axis in the lower part of the chamber (see Fig. 11). The governing parameters are:

$$\frac{E_\delta}{RT_0} = \frac{E_a}{RT_0} = 8.0 \, , \qquad\qquad \frac{K_\delta}{K} = 10^{-2}$$

$$\frac{\sum_k W_k \nu_k h_{0k}}{W_f \nu_f} \, \frac{Y_f^0}{c_{p0} T_0} \approx 10 \, , \qquad\qquad \frac{L}{a_0} K_\delta \rho W = 0.2$$

$$k_0 = 1 \text{ m}^2/\text{s}^2 \, , \qquad\qquad \varepsilon_0 = 10 \text{ m}^2/\text{s}^3$$

Figures 11 a to f show the successive stages of the process development after ignition in the form of plots of reaction intensity functions $\dot{\omega}_\delta$ for the first reaction stage.
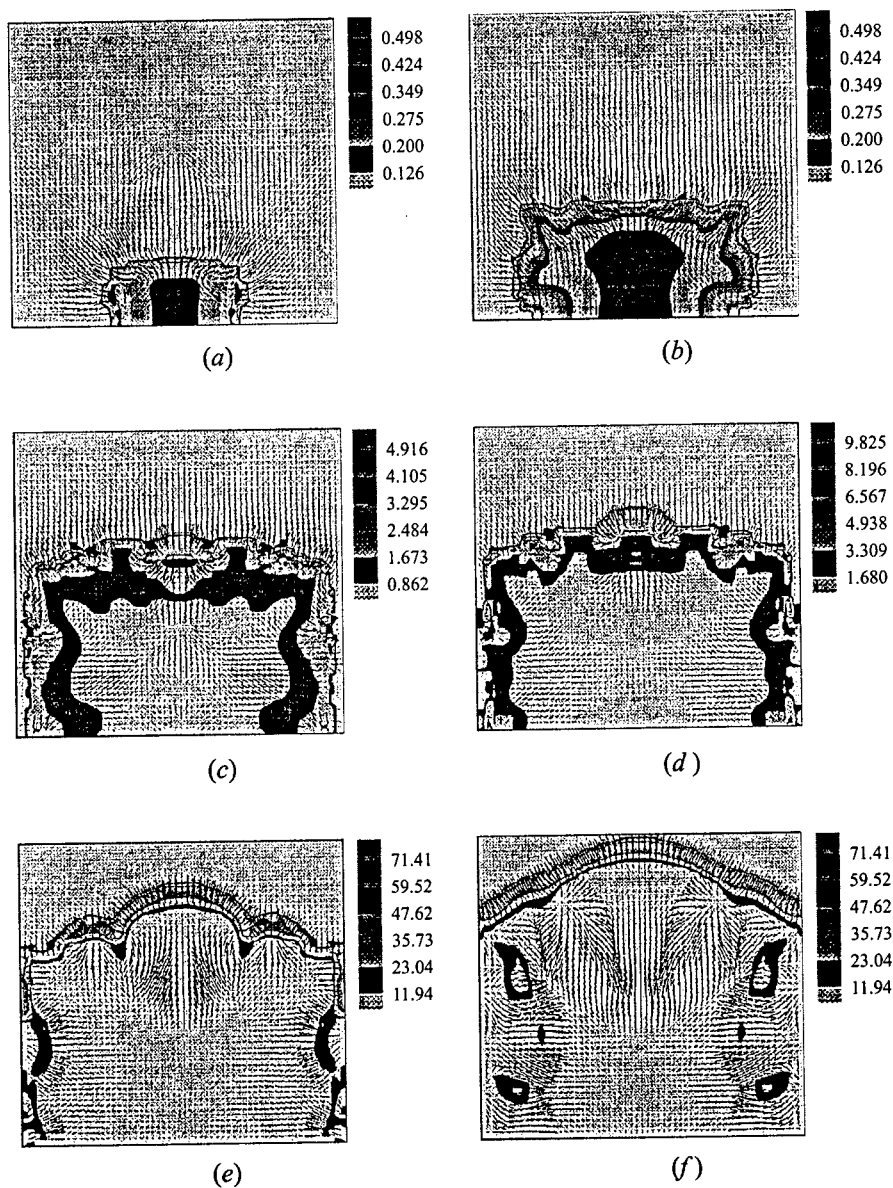
Figure 11 Calculated maps of the activation reaction intensity (in 10^{-2} 1/s) for successive stages of flame propagation in a cylindrical volume with a vertical axis of symmetry: (a) $t = 9.7$ ms, (b) $t = 14.2$ ms, (c) $t = 16.25$ ms, (d) $t = 16.35$ ms, (e) $t = 16.46$ ms, (f) $t = 16.54$ ms

It is seen that after ignition, the fast turbulent flame propagates in all the directions (Fig. 11a). The rate of its propagation near the walls is smaller due to turbulence damping. The flame becomes curved due to its instability and has an irregular reaction intensity (Fig. 11b). As a result, a number of "hot spots" occur in the flame zone, wherein the reaction intensity is much higher. Those "hot spots" give birth to local thermal explosions of different intensity (Fig. 11d). This is testified by the gas velocity vectors pointing in all the directions outside the zones of thermal explosions (Figs. 11d, 11e). Finally, the leading shock with the cellular structure is formed, with reaction intensity attaining maximum just in the zones adjacent to the wave front near the triple points (Figs. 11e, 11f).

Figures 12a to f illustrate pressure maps for the successive times. The scales are given to the right of the figures (in 10^{-5} Pa). It is seen that the ignition causes a weak compression wave that, after reflecting from the walls, converges in the center, intensifying combustion (Figs. 12a, 12b). The reaction intensification in the "hot spots" produces local pressure peaks (Figs. 12c, 12d). Finally, a strong shock wave of irregular structure occurs (Figs. 12e, 12f).

The successive stages of detonation wave propagation along the tube and its reflection from the closed end are shown in Fig. 13. The model of turbulence used in these computations essentially smoothes the disturbances. Nevertheless, the cellular structure of the detonation wave can clearly be seen, though its detailed description is hardly possible using the $k-\varepsilon$ model.

The results show that multi-dimensional character of the flow provides more opportunities for the "hot spots" origination, even in the case of simplified modeling. That brings one to the conclusion that the presence of turbulizing chambers of a wider cross section mounted into the tube should promote the "hot spots" formation due to multiple reflections of disturbances from the walls, thus shortening the predetonation lengths.

3 APPLICATION OF THE DDT PHENOMENON IN PULSED DETONATION GENERATORS

When thinking of using the detonative combustion for the creation of pulse detonation generators one is faced with the problem of a reliable periodic initiation of detonation waves. The results of experimental and theoretical investigations described above suggest a scheme for a device fed by a gaseous hydrocarbon-air mixture. The periodic spark ignition by an automobile spark plug should guarantee the detonation onset at tube lengths within the range of 2 m. The schematic of the device is shown in Fig. 14.

The device is fed by the gasoline–air mixture from a V-shaped automobile engine 1 while a part of it works as a compressor preparing the mixture. This type of feeding was chosen to meet the requirements of applying the generator
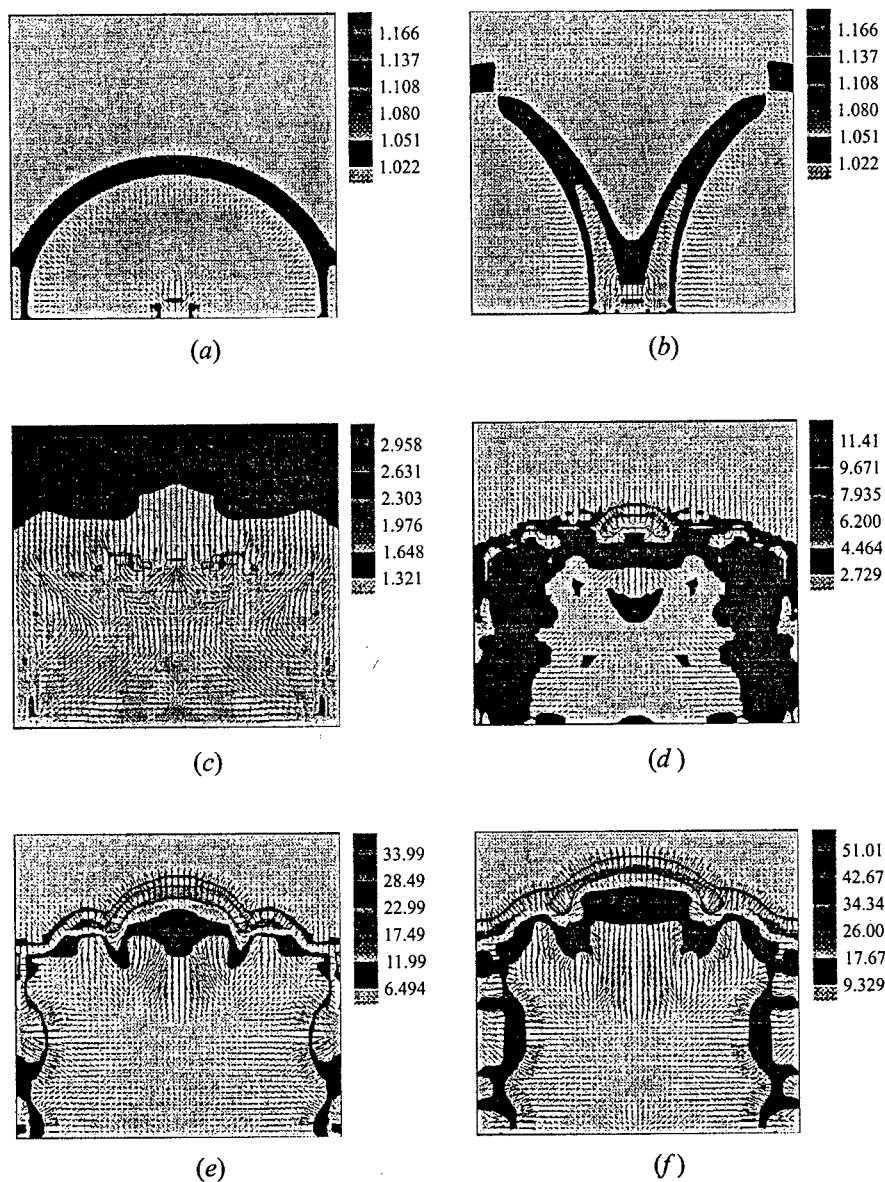
Figure 12 Calculated maps of pressure (in 10^{-5} Pa) for successive stages of flame propagation and onset of detonation in a cylindrical vessel with a vertical axis of symmetry: (a) $t = 1.76$ ms, (b) $t = 3.39$ ms, (c) $t = 16.0$ ms, (d) $t = 16.35$ ms, (e) $t = 16.46$ ms, (f) $t = 16.50$ ms
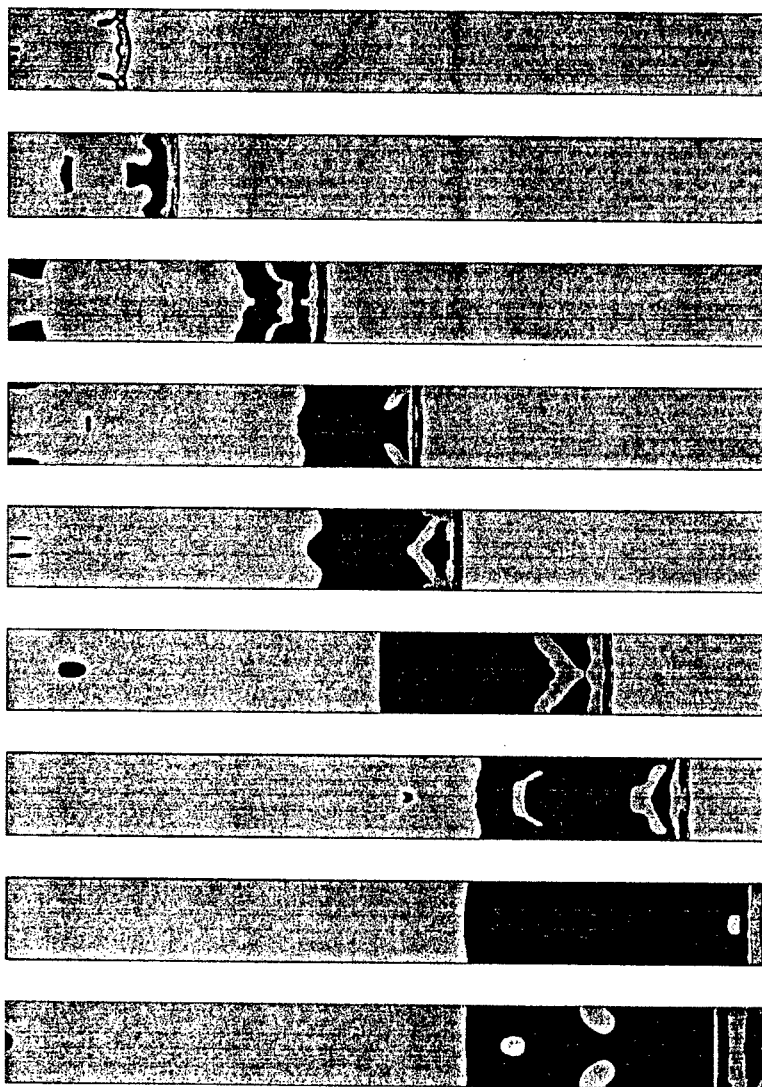
Figure 13 Pressure maps for successive stages of two-dimensional detonation wave propagation along the tube and its reflection from the closed end. Mapping colors are the same as shown in Fig. 12f
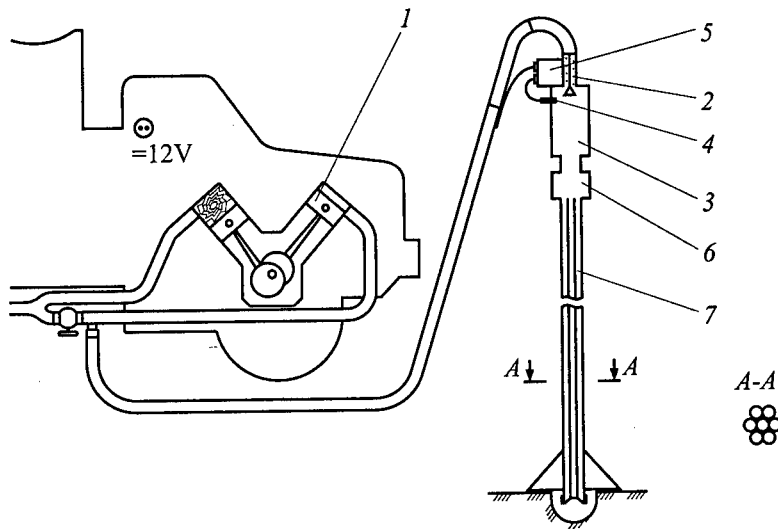
Figure 14 Schematic of the pulsed detonation generator fed by gasoline–air mixtures from an automobile engine. The cross section A–A shows a pack of seven detonation tubes

for drilling purposes. Other applications (propulsion, etc.) will certainly need different principles of mixture formation. The combustible mixture is delivered into the ignition chamber (*3*), 100 mm in diameter, through the reverse valve *2*. The mixture is ignited by the automobile spark plug *4*, and the igniting device *5* which needs a power supply of 12 V.

The pressure rise caused by combustion closes the reverse valve *2* and pushes the mixture into the forechamber *6* that serves as an additional turbulizing element. Further flame acceleration and transition to detonation takes place in the pack of seven tubes *7* (each 25 mm in diameter) connected with the forechamber. The use of seven tubes, arranged as shown in Fig. 14 (cross section A–A), instead of a single tube of a wider cross section is due to the fact the DDT process is more stable in tubes of smaller diameter. An overdriven detonation wave in the tubes is formed at a distance of 2–3 m depending on the mixture composition and initial conditions. Then the detonation wave gradually slows down to the CJ regime.

Using the device for drilling purposes required the maximal intensity for the reflected wave. Investigations of wave reflections at different stages of DDT [38] showed that the maximal rates of loading were obtained under reflection of over-

driven detonation waves. Thus, the length of the device had usually the limit of 3 m to operate in the mode of overdriven detonation waves. Nevertheless, the device proved to be reliable in operating with much longer tubes (up to 7 m).

The frequencies of detonation wave generation varied from 5 to 10 Hz depending on the length of the device and the power of the feeding compressor. The slowest stage of the cycle — refilling the device with a fresh mixture — was the limiting process that determined the frequency of the pulses.

The onset of detonation took place in all seven tubes nearly at one and the same distance from the forechamber. To minimize the divergence in the predetonation lengths, orifices were made in the adjacent walls of the tubes to provide free access of heated combustion products from one tube to another.

Experiments with gasoline of different octane numbers (92 and 76) showed that the predetonation length was shorter for gasoline 76 – air mixtures. The increase of the mixture temperature from 20 °C to 70 °C also shortened the predetonation lengths and the predetonation time. Thus, the maximum frequency of 10 Hz of stable detonation wave generation in a pack of tubes 3 m long was achieved.

CONCLUDING REMARKS

Theoretical and experimental investigations of DDT in hydrocarbon–air mixtures have led to an explanation of the multiplicity of scenarios of the process and the mechanism of "explosion in the explosion" taking place at a contact discontinuity formed as a result of interactions between shock waves ahead of the accelerating flame.

The results show that the core of the process is actually a thermal explosion taking place in a hot spot formed due to flow non-uniformities ahead of the flame at contact discontinuities. Depending on the flow history and induction delay gradients in the vicinity of the hot spot, the thermal explosion can develop rather rapidly to a detonation mode, or it can develop into a slower combustion mode, providing enough time for other hot spots to reach autoignition.

The additional energy release due to multiple ignition causes further compression and heating of the gas, thus decreasing the induction period and creating more favorable conditions for detonation formation. Sequential thermal explosions in the hot spots give birth to spherical detonation waves overtaking the leading shock. Thus, a structure with relatively large, irregular cells could be formed during the first stages of the onset of detonations.

Theoretical and experimental investigations of the DDT characteristics in hydrocarbon–air mixtures showed that flow non-uniformities in the precompressed gas and multiple shock interactions provide the conditions for hot spot formation, thus promoting the detonation onset.

The use of turbulizing chambers of a wider cross section provides both turbulizing the flame zone and the piston effect for expanding reaction, causing multiple compression waves to interact with each other ahead of the flame. Experimental investigations proved the turbulizing forechambers mounted into the ignition section to be most effective for shortening the predetonation lengths in tubes and ensuring stability of the DDT process.

Thus, the results of investigations led to the creation of the pulsed detonation generator, which emits periodic stable detonation waves with a frequency of 10 Hz. The generator has a very simple initiator and because it does not have movable parts, it is very reliable.

ACKNOWLEDGMENTS

REFERENCES

1. Mallard, E., and Le Chatelier, H., *Compt. Rend Acad. Sci.*, Paris, **93**, 145, 1881; *Ann des Mines*, Ser. 8, **4**, 296.

2. Bertelot, M., and Vielle, P., *Compt. Rend Acad. Sci.*, Paris, **93**, 18, 1881.

3. Bertelot, M., *Sur la force des materières explosives d'apres la Thermochimie*, Paris, **1**, 135, 1883.

4. Mikhelson, V. A., "On Normal Combustion Velocity of Explosive Gaseous Mixtures," In: *Scientific Bulletin of Imperial Moscow University, Ser. Physics & Mathematics*. Moscow, 10, 1–92, 1893.

5. Chapman, D. L., "On the Role of Explosion in Gases," *Phil. Mag.*, **47**, 90, 1899.

6. Jouget, E., *J. Mathematics*, 347, 1905.

7. Salamandra, G. D., and Tsoukhanova, O. A., "On Formation of a Shock Wave Ahead of Accelerating Flame," In: *Physical Gasdynamics*. USSR Academy Sci. Publ., 151–162, 1959.

8. Salamandra, G. D., "On Interaction of a Flame with a Shock Wave," In: *Physical Gasdynamics*. USSR Academy Sci. Publ., 163–167, 1959.

9. Oppenheim, A. K., and Soloukhin, R. I., *Annual Review Fluid Mechanics*, **5**, 31, 1973.

10. Salamandra, G. D., Bazhenova, T. V., and Zaitsev, S. G., *Some Methods of Exploration of Quick Going Processes and Their Application to Investigation of Detonation Formation*. USSR Academy Sci. Publ., Moscow, 1960.

11. Soloukhin, R. I., *Methods of Measurements and Main Results of Experiments in Shock Tubes*. Novosibirsk State University Publ., Novosibirsk, 1969.

12. Urtiew, P. A., and Oppenheim, A. K., "Experimental Observations of the Transition to Detonation in an Explosive Gas," *Proc. Royal Society London*, **A295**, 13, 1966.

13. Urtiew, P. A., and Oppenheim, A. K., "Transverse Flame-Shock Interactions in an Explosive Gas," *Proc. Royal Society London*, **A304**, 379, 1968.

14. Shchelkin, K. I., and Troshin, Ya. K., *Gasdynamics of Combustion*. USSR Academy Sci. Publ., Moscow, 1963.

15. Smirnov, N. N., and Tyurnikov, M. V., "Experimental Investigation of Deflagration to Detonation Transition in Gaseous Hydrocarbon–Air Mixtures," *Combustion Flame*, **100**, 661–668, 1995.

16. Thomas, G. O., and Brown, C. J., "Experimental Observation of Shock–Flame Interaction Leading to DDT," *Proc. 7th Conference (International) on Numerical Combustion, York*, 1998, 22.

17. Clarke, J. F., and Riley, N., "Combustion Theory: a Report on Euromech 203," *J. Fluid Mechanics*, **167**, 409–414, 1986.

18. Zel'dovich, Ya. B., Librovich, V. B., Makhviladze, G. M., and Sivashinsky, G. I., "On the Onset of Detonation in a Nonuniformly Preheated Gas," *Sov. J. Applied Mechanics Technical Physics*, **2**, 76, 1970.

19. Zel'dovich, Ya. B., Gelfand, B. E., Tsyganov, S. A., Frolov, S. M., and Polenov, A. N., "Concentration and Temperature Nonuniformities of Combustible Mixtures as a Reason of Pressure Waves Generation," In: *Dynamics of Explosions*. (Eds. A. Kuhl *et al.*), Progress in Astronautics and Aeronautics Ser., AIAA Inc., New York, **114**, 99, 1988.

20. Frolov, S. M., "The Effects of Non-Ideality on the Explosion Origin and Propagation," Dr. Sci. Thesis. Moscow: N. N. Semenov Institute of Chemical Physics, 1992.

21. Demyanov, Yu. A., Sekrieru, G. V., Igoshin, A. I., Kireev, V. T., and Pinsky, V. L., *One-Dimensional Flows of Real Gas*. Shtinitsa, Kishinev, 1980.

22. Smirnov, N. N., and Panfilov, I. I., "Deflagration to Detonation Transition in Combustible Gas Mixtures," *Combustion Flame*, **101**, 91–100, 1995.

23. Smirnov, N. N., Panfilov, I. I., Tyurnikov, M. V., and Berdyuguin, A. G., "Theoretical and Experimental Study of Deflagration to Detonation Transition and Instability of Detonation Structure in Gases," *Archivum Combustionis*, **15**, 1–2, 81–103, 1995.

24. Clarke, J. F., Kassoy, D. R., and Riley, N., "On a Direct Initiation of a Plane Detonation Wave," *Proc. Royal Society London*, **A408**, 129–148, 1986.

25. Montgomery, C. J., Khokhlov, A. M., and Oran, E. S., "The Effect of Mixing Irregularities on Mixed Region Critical Length for Deflagration to Detonation Transition," *Combustion Flame*, **115**, 1/2, 38–50, 1998.

26. Smirnov, N. N., and Boichenko, A. P., "Deflagration to Detonation Transition in Gasoline–Air Mixtures," *Sov. J. Physics Combustion Explosion*, **22**, 2, 65–68, 1986.

27. Knystautas, R., Lee, J. H. S., Sheperd, J. E., and Teodorczyk, A., "Flame Acceleration and Transition to Detonation in Benzene–Air Mixtures," *Combustion Flame*, **115**, 424–436, 1998.

28. Noskov, M. A., Frolov S. M., Wolanski, P., and Tatschl, R., "The Effect of Shock Induced Turbulent Boundary Layer on Deflagration to Detonation Transition in Ducts," *Archivum Combustionis*, **15**, 1–2, 49–58, 1995.

29. Smirnov, N. N., and Zverev, I. N., *Heterogeneous Combustion*. Moscow Univ. Publ., Moscow, 446, 1992.

30. Nettleton, M. A., *Gaseous Detonations: Their Nature, Effects and Control*. Chapman and Hall Publ., London – New York, 1987.

31. Lindstedt, R. P., and Michels, H. J., "Deflagration to Detonation Transition in Mixtures of Alkane LNG/LPG Constituents with O_2/N_2," *Combustion Flame*, **72**, 1, 63–72, 1988.

32. Kailasanath, K., and Oran, E. S., "Ignition of Flamelets Behind Incident Shock Waves and the Transition to Detonation," *Combustion Science Technology*, **34**, 345–362, 1983.

33. Khokhlov, A. M., Oran, E. S., and Thomas, G. O., "Numerical Simulation of Deflagration-to-Detonation Transition: the Role of Shock–Flame Interactions in Turbulent Flames," *Combustion Flame*, **117**, 323–339, 1999.

34. Smirnov, N. N., and Tyurnikov, M. V., "Schlieren Method of Optical Registration of Combustion to Detonation Transition in Gaseous Mixtures," In: *Non-Intrusive Combustion Diagnostics*. (Eds. K. K. Kuo and T. P. Parr), Begell House Inc., New York – Wellingford (UK), 465–475, 1994.

35. Smirnov, N. N., and Nikitin, V. F., "Unsteady-State Turbulent Diffusive Combustion in Confined Volumes," *Combustion Flame*, **111**, 222–256, 1997.

36. Levin, V. A., and Markov, V. V., *Izvestiya USSR Akademy Sci., Ser. Fluid Mechanics*, **5**, 89–93, 1974.

37. Korobeinikov, V. P., *Problems of Point-Blast Theory*. American Institute of Physics, New York, 1991 (Translation).

38. Smirnov, N. N., Panfilov, I. I., Tyurnikov, M. V., Berdyuguin, A. G., Dushin, V. R., and Presnyakov, Yu. P., "Theoretical and Experimental Investigation of Combustion to Detonation Transition in Chemically Active Gas Mixtures in Closed Vessels," *J. Hazardous Materials*, **53**, 195–211, 1997.

39. Anderson, D. A., Tannehill, J. C., and Pletcher, R. H., *Computational Fluid Mechanics and Heat Transfer*. Hemisphere Publ. Corp., 1984.

PART TWO

DETONATION WAVE STRUCTURE AND PROPAGATION

THE STRUCTURE OF PROPAGATING DETONATIONS

E. S. Oran

Recent information, derived primarily from multi-dimensional numerical calculations, is compiled and used to explain some current understanding of the structure of propagating detonations. The occurrence and importance of cellular structure and transverse shock waves, the creation of unburned detonation pockets behind the wave front, irregularity of detonation cells, and oblique detonation structure are discussed. It is shown that detonation cells are likely to occur in many types of detonations, including those in thermonuclear supernovae. Finally, information on detonation decay, reignition, and propagation is combined to describe the behavior of a transmitted detonation wave.

1 INTRODUCTION AND BACKGROUND

The general understanding of the structure of detonations has developed from the simplest theories that account for global features to more complex theories that require a considerable amount of background knowledge to grasp. Sometimes there were erroneous diversions or "red herrings" in this process; sometimes there were even simplifications. More insight has lead to a realization that previous simpler pictures were somewhat idealized and only addressed part of the problem.

The original thermodynamic analysis of Chapman [1] and Jouguet [2], the CJ hypothesis, deals only with steady-state energetics of detonation waves, not taking into account chemical reaction kinetics. The premise is that all of the energy release occurs as compression occurs at the front of the shock wave. This theory is successful because it predicts steady detonation velocities so well. However, its basic conceptual flaw is that it assumes that the width of the shock front is only a few mean-free-paths of the molecules. Chemical reactants really need many thousands of collisions to reach the final product. Without taking into account the finite width of a reaction zone, the theory cannot be used to interpret nonsteady phenomena associated with detonation extinction or failure, which depend on more details of the structure.

Independently, Zel'dovich [3], von Neumann [4], and Döring [5] realized that the chemical reaction zone has a finite size, and that this concept could be developed to explain observed phenomena. In the ZND theory, the wave front is more complicated: the leading shock wave compresses and heats the material which subsequently undergoes chemical reactions. Thus, there is a reaction wave effectively attached to, but lagging behind, the leading shock front. Extensive work was done to use elements of this theory to explain observed features of detonations, such as the detonation critical diameters and spinning detonations, neither of which could be described by the CJ theory. The critical diameter, for a gas, may be defined as the smallest diameter tube in which a detonation can propagate, and for an explosive charge, the smallest size charge that can detonate without any outside support. Spinning detonations appeared as a bright spot at the front of a detonation, spinning around the axis of the tube containing an energetic gas. Reviews of the history of the discovery, analysis, and gradual understanding of these phenomena have been given by, for example, Oppenheim *et al.* [6], Edwards [7], Fickett and Davis [8], Strehlow [9], Lee [10], and Dremin [11], and these will not be covered here.

A full review of detonation structure would describe initiation, stability, structure, and extinction. In this paper, we concentrate on structure with some comments on reinitiation and extinction. Detonation initiation has been discussed elsewhere in this book in the paper by Borisov [12], and there is a recent excellent review of stability by Stewart [13]. The complexities of detonation structure were first brought to light by high-resolution instrumentation, then explained to some extent by theoretical analysis (see [8, 9]) and numerical simulations [14–16]. In this paper, we use the results of multi-dimensional simulations to present selected aspects of what we have learned about detonation structure.

2   THE MULTI-DIMENSIONAL STRUCTURE OF A DETONATION CELL

It is now well known that the front of a self-sustained detonation, propagating in an energetic gas, is not uniform and planar. Its structure is complex and multi-dimensional, involving interactions between incident shocks, Mach stems, transverse waves, and boundaries of the regions through which the detonation is moving [17, 9]. This complexity of the structure at the front of the detonation is illustrated by Fig. 1, which was chosen as a starting point for the discussion that follows. This figure, taken from a series of numerical simulations of detonation propagating through a low-pressure, argon-diluted mixture of hydrogen and oxygen [18], shows instantaneous maps of pressure, streamwise velocity, and specific (local) energy release for the entire computational grid after a reasonable time into the computation. At the front of the detonation, the figure shows Mach

98

Pressure

Streamwise Velocity

Specific Energy Release
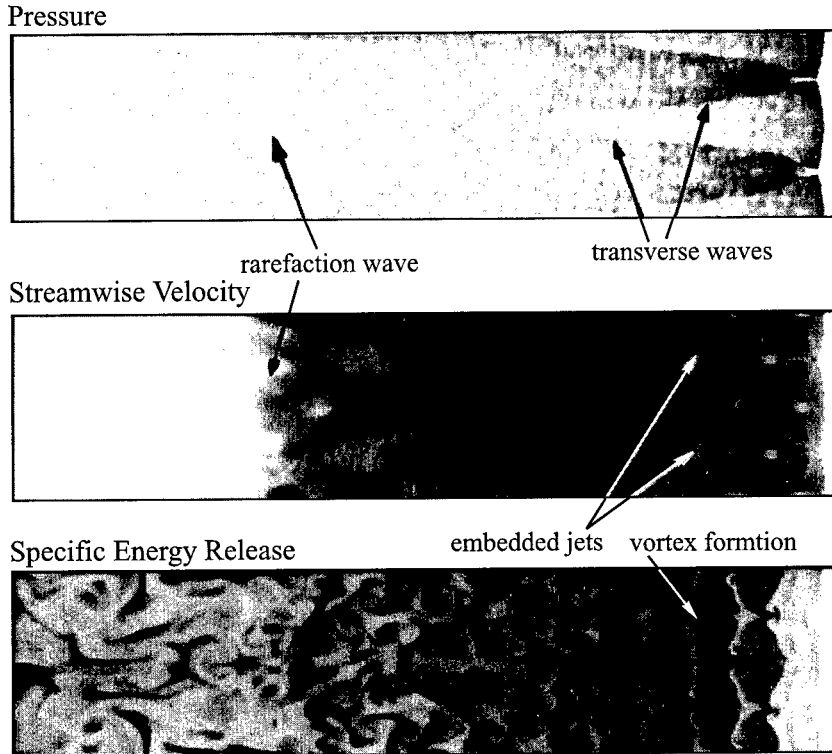
Figure 1 Computed instantaneous contours of pressure, streamwise velocity, and specific energy release for a two-dimensional detonation propagating from left to right in a 0.06 m channel in a $H_2:O_2:Ar/2:1:7$ mixture, at 6.7 kPa and 298 K at timestep 24,000, time 415.9 μs [18]

stems, incident shocks, transverse shocks, large vortices, and other features of a dynamic supersonic flow.

A major feature of the propagation not shown in Fig. 1, is the dynamic motion of the shocks in the system. This motion is better illustrated in Fig. 2, which uses a series of pressure maps at evenly spaced intervals to show the evolution of a "detonation cell" [16, 19, 20]. Here, the connection of the paths of the triple points produces the cellular structure that has become known as a characteristic feature of gaseous detonations. The structure was first observed in experiments (Denisov and Troshin [17] and Voitsekhovskii *et al.* [21]) through the smoke-foil technique. This was followed by experiments that also used open-shutter and schlieren photography (for example, Oppenheim *et al.* [6], Shchelkin [23], Edwards [24, 7], Soloukhin [25], Strehlow (see [9, 26, 27]), and Schott [28]). Experiments and analyses done during the 1960's and 1970's have made funda-

99
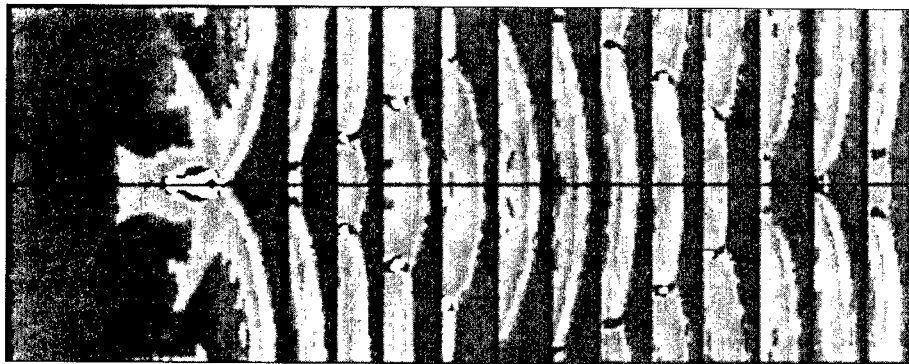
Figure 2 Computed sequence of pressure contours from a computation of a detonation cell for a mixture of $H_2:O_2:Ar/2:1:7$. The cell length is about 77 mm and the ratio of the width to the length of the cell 0.61. The computed detonation velocity is 1623 m/s (Chapman-Jouget velocity is 1619 m/s) [19, 20]. The black lines superimposed on the contours trace the paths of the triple points

mental contributions to our understanding, which in turn, posed some of the basic questions we are addressing today.

Thus the triple points formed at the intersection of the transverse wave, Mach stem, and the incident shock trace out the patterns that are called detonation cells. The size of the cellular structure of a gaseous detonation is related to properties of the material and the chemical reaction mechanism. Long chemical reaction times or induction times correlate with large detonation cells. The general rule is that the detonation cell length is about 20–50 times the one-dimensional detonation wave thickness. The structure is sometimes obscured for certain material conditions or if the detonation is heavily overdriven, but it appears to occur consistently in self-sustained gas phase detonations. We also have indications that such structures occur in liquid and perhaps even in solid explosives. Extensive experimental data show that the size and regularity of this cell structure is characteristic of the particular combination of initial material conditions, such as composition, density, and pressure (see, for example, [8, 9]).

A striking feature that can be extracted from the details of the calculation shown in results, such as Figs. 1 and 2, is the complex Mach structure and how it evolves in time [9, 16, 18, 28–30]. Close to the origin of the detonation cell, the triple point structure is characteristic of a single Mach reflection. The Mach stem is strong and the incident shock is sustained by the chemical reactions behind it. The size of the induction zone between the leading shock and the reaction wave is very small. As the triple points move further, the chemical reactions become more decoupled from the incident shock. Mach configuration develops into a double Mach reflection, and then more complex Mach structures. As this
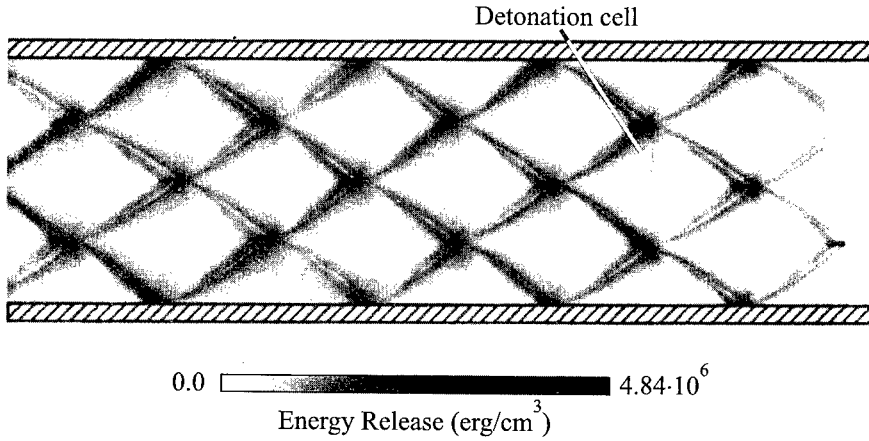
Figure 3 Time history of the local specific energy release $\epsilon_{i,j}$, from the same computation that produced Fig. 1, showing that detonation propagation is extremely regular and produces a repeating, cellular pattern [18]

happens, the size of the induction zone increases substantially and the transverse waves close to the triple point diverge in a region corresponding to the induction zone behind the incident shock. Beyond this induction zone, the curvature of the transverse waves reverses.

Experiments [32] have shown that large amounts of energy are released behind the transverse waves. The distribution of energy within the detonation cell, and particularly behind the transverse waves, can be measured in terms of the density of energy released $\epsilon_{i,j} = \sum_{\Delta t} \Delta e^{i,j}_{\text{chem}}$, where (i,j) is a location in space and $\Delta e^{i,j}_{\text{chem}}$ is the chemical energy change during each interval of time that goes into the summation. The distribution of ϵ, Fig. 3, is strikingly similar to the open shutter experiment described by Oppenheim [32]. It confirms that the evolution of a detonation cell is associated with a large amount of energy released behind the transverse waves, in the neighborhood of the triple point. In general, the energy release behind the triple points greatly exceeds the amount of energy released behind the major extent of the leading shock.

Now consider Fig. 4, which shows more details in the vicinity of the transverse shock, where the secondary energy-release contours appear. The points A, B, and C along the transverse shock in the temperature contours are triple points. There is a shock refraction at point BB, which can be seen by examining the temperature and specific energy-release contours together. In the vicinity of the transverse shocks, there is a region with slightly higher temperature behind the incident shock. This region begins at BB and continues downstream to point C. The existence of this region suggests that the refraction of the transverse

Temperature   Slip line

298   2800 K

Pressure   Shock BC   Shock AB

$6.67 \cdot 10^3$ $3.0 \cdot 10^5$ Pa

Energy Release

0.0 $1.0 \cdot 10^5$ J/m^3
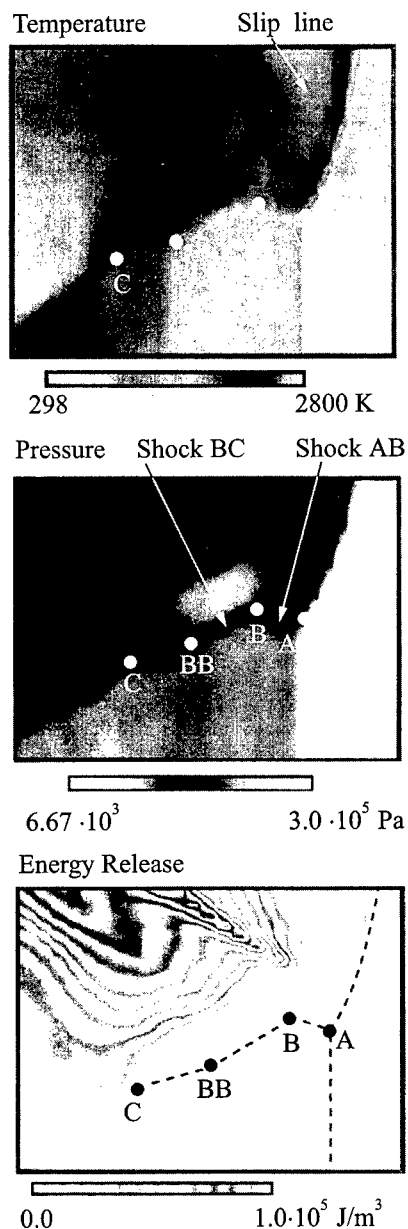
Figure 4 Temperature, pressure, and energy-release contours in the vicinity of the transverse shock, taken from the computation shown in Fig. 1 [18]

shock at BB is due to the interaction between the initial reaction plane, behind the incident shock, and the transverse wave. The specific-energy contours also support this possibility by showing that point BB is located just behind the energy-release front downstream of the incident shock. As the energy release increases downstream of BB, the interaction of the reaction zone and the transverse waves generates another refraction at point C. The complex structure observed is characteristic of a marginal detonation.

The $\epsilon_{i,j}$ map in Fig. 5 is consistent with previous observations. The reaction front and the Mach stem are closely coupled. However, behind the incident shock, there is a significant distance between the shock and reaction fronts. In fact, it appears that the reaction front may already be decoupled from the incident shock at this stage. The energy release is greatest in a small region just behind the Mach stem that is above the initial triple point, A. The next greatest energy release is in a wide region that extends behind the transverse shock BC. Figure 5 shows contours of the accumulated energy release along the top half of the detonation cell, behind the shock BC and behind the Mach stem just above point A. This figure shows the effect of the transverse shock structure on the cellular energy release. The contours show that there is little energy release behind shock AB. This observation is consistent with other observations, [17, 33, 34], in which shock segments AB and BC appear abruptly at a location two-thirds into the cell and the lengths of the shock segments grow
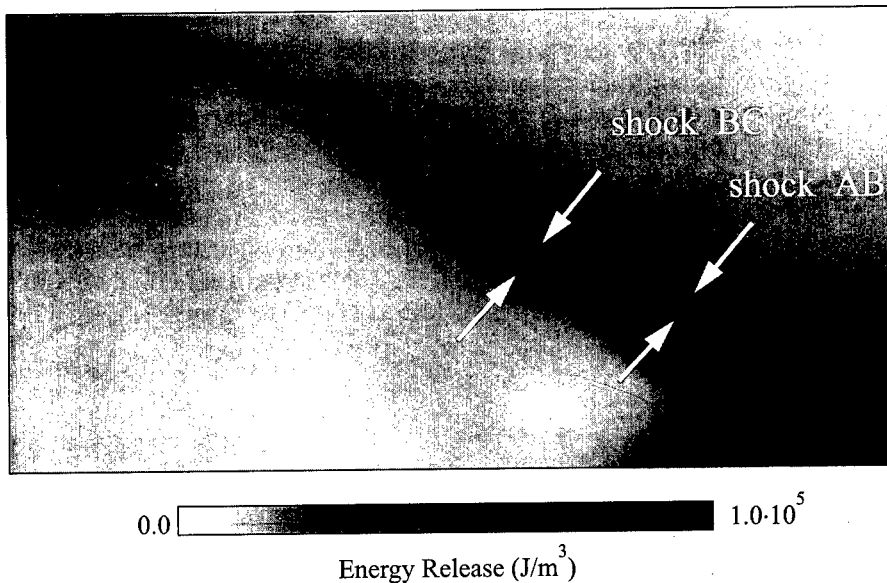
Figure 5 Enlargement of the energy-release contours in the region before triple-point collisions, resulting from complex multiple shock structure [18]

as the triple points approach the collision at the center of the cell. The energy-release contours in Fig. 6 show that, near the end of the detonation cell, the size of the area of energy release behind shock BC increases. However, the length of shock segment AB appears to be fairly constant after its initial development. A conclusion of this discussion is that the general configuration of the shock-detonation structure along the transverse wave is similar to that which occurs for spinning detonations [9].

The development of the cellular structure from the beginning of a simulation is illustrated in Fig. 7 in the form of a gray-scale map of the maximum pressure reached at each location in space [35]. This figure may be compared to smoke-foil records, as they are similar to experimental patterns produced by a detonation wave on the coated surfaces. The light tracks give the trajectories of the triple points that form the cellular structure. The pressure peaks when the triple points collide with each other, or with the walls. In these calculations, no explicit perturbation is put on the initial one-dimensional wave, and yet the system still evolves into the observed structure because of the the noise from numerical roundoff. As the detonation wave propagates, the interaction between triple points becomes less regular. Sometimes, one triple point catches up to another, moving in the same direction, and coalesces with it. At other times, a triple

103
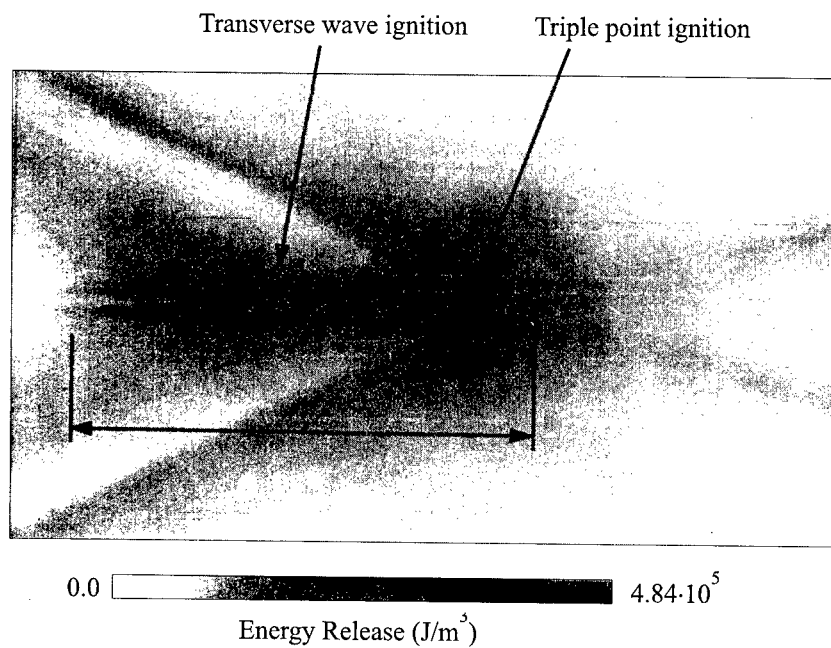
Figure 6 Enlargement of the energy-release contours in the vicinity of a triple-point collision [18]
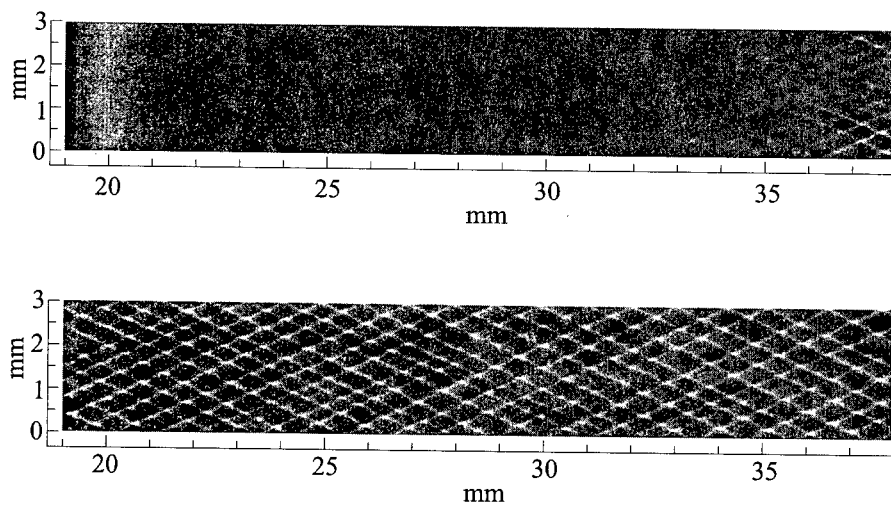
Figure 7 Detonation history presented by contours of maximum pressure for a computation modeling the propagation of a detonation in a hydrogen–oxygen mixture at atmospheric pressure [35]

point decays and disappears. The number of triple points gradually decreases, and those remaining become stronger. Finally, there is a quasi-steady-state regime where the triple points can appear or disappear, but the average number is not changed.

The detonation propagates in a regular, cellular pattern that is qualitatively similar to the ones observed in experiments and simulations for highly diluted gaseous mixtures of H_2–O_2–Ar [16]. In addition to the primary energy release that occurs behind the Mach stem near the triple point, there is a secondary energy release inside the detonation cell, and this first appears about two-thirds of the way through the cell. This secondary energy release is due to the transverse wave detonations observed in the experiments of marginal detonations [17, 33, 34].

3   UNREACTED DETONATION POCKETS

One initially unexpected but potentially important phenomenon, found in the experiments and simulations, is the formation of unreacted pockets of material behind the detonation front [36, 16]. Experiments first showed such pockets, but their implications were unexplored until they were seen in numerical simulations. Figure 8 is a series of frames from a calculation similar to that shown above, but in a very narrow channel. The high aspect ratio of the figure highlights the effect and helps to show the mechanism by which it occurs. The figures on the left show the extent of reaction. The detonation propagates to the right into the unreacted gas mixture and fully reacted gas is on the left side. The various shades in between represent different degrees of reactedness and together comprise the detonation front. The third frame shows a detached pocket of unburnt gas behind the detonation front. The figures on the right show the temperature of the gases in the various regions. The figures show a cold, unreacted pocket cut off by interacting shock waves.

The formation of the unburned pockets can be traced directly to the curvature of the transverse shock waves. When two transverse waves collide or one hits a wall, the interaction can cut off a portion of unreacted, cold material. If the material in the pockets burns slowly enough, the process effectively draws energy out of the detonation and can provide a mechanism for detonation extinction. If the pockets burn rapidly, they can generate new pressure pulses that perturb the system and cause new cellular structures to form at the detonation front. These findings are interesting because they show how an initially homogeneous material can develop an extremely inhomogeneous structure as shocks move through it. These findings are important because the existence of unreacted pockets and their properties can determine whether a detonation lives or dies. The existence of unburned pockets provides a multi-dimensional fluid-dynamic mechanism by

EXTENT OF REACTION   TEMPERATURE
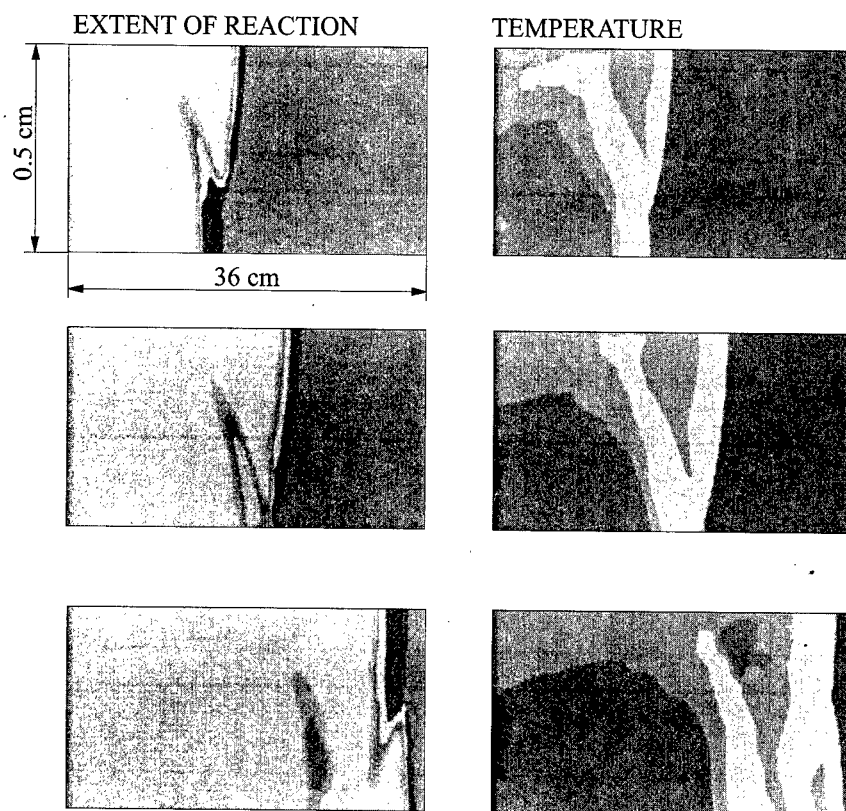
Figure 8 Extent of reaction and temperature contours for a detonation propagating in a small tube. The detonation is propagating from left to right. Cold, unreacted pockets form and are left behind the detonation front [36]

which a detonation can die in a situation where, in one dimension, it might be expected to propagate.

Since the initial discussions of unreacted pockets in mixtures of hydrogen and oxygen in narrow channels, the existence of pockets has been shown to occur in many materials and even in mixtures in wide channels, depending on properties of the the reaction mechanism. Gamezo [35, 37] has undertaken a more systematic study in which he observed that stronger triple points are associated with larger pockets and more irregular structures, while the form of the pockets varies as the effective activation energy of the material increases. For self-sustained detonations, the pockets burn quickly enough for the effects of the energy release to be felt by the detonation front, and the delayed burning supports the detonation. When the burning occurs behind the front by a length of

106

approximately one or two detonation cells, the pockets extract energy from the detonation front. In the discussions below, we refer to the pockets as they affect properties of astrophysical supernovae and reignition in layered detonations.

4 COMPLEX AND IRREGULAR CELL STRUCTURES

We now believe that the picture of the structure of a propagating detonation, described above, is basically correct. However, for most energetic materials, it is still too simple. The structure of most propagating detonations is usually much more complex: sometimes there are substructures within a detonation cell, and sometimes the structures are very irregular. These effects can be traced to complexities in different chemical reaction mechanisms and in the differences in thermophysical properties of the material. For example, detonation cells created in some materials contain substructures that resemble either a full or a partial cell. This is the case, for example, for gaseous nitromethane, as shown by Presles and coworkers [38]. This kind of structure and substructure appears to be the result of sequential chemical reactions, in which there are multiple induction and energy-release stages. It is also the case, as summarized below, for the cellular structure in thermonuclear detonations in Type Ia supernovae [39].

Another feature of detonations is irregular cellular structure. Most of the experimental results showing detonation cells do not show the consistent sizes and spacings of transverse waves that we have seen in the highly diluted, low-pressure, hydrogen–oxygen detonations described above. Instead, the structure is very irregular, sometimes to the point where the size of a cell may not be clearly determined. In the experiments, regular cellular patterns appear in low-pressure mixtures of hydrogen and oxygen, that are highly diluted with argon, as we have predicted in the calculations. If the pressure is higher, the mixture is less dilute or argon is replaced by molecular nitrogen, the structure becomes irregular.

The question now is what can be said about irregularity in the gas phase. To begin to answer this, Lefebvre *et al.* [29] performed calculations of detonations in hydrogen–oxygen diluted with argon, as above, and compared these to calculations of hydrogen–oxygen diluted with nitrogen, which is known to produce irregular structures. Figure 9, a summary of the position of the shock triple points in these two calculations, shows the less-regular structure of the nitrogen-diluted mixture. This indicates that the multi-dimensional structure of a detonation depends on the differences of the thermodynamic properties in the induction zones behind the Mach stem and the incident shock. Whereas the chemical induction times for equivalent nitrogen and argon dilutions are essentially the same, the rate and amount of energy release is different. Thus, the relative sizes of the energy-release zones and final temperature behind the Mach

107

Time (μs)

(a)

Time (μs)

(b)
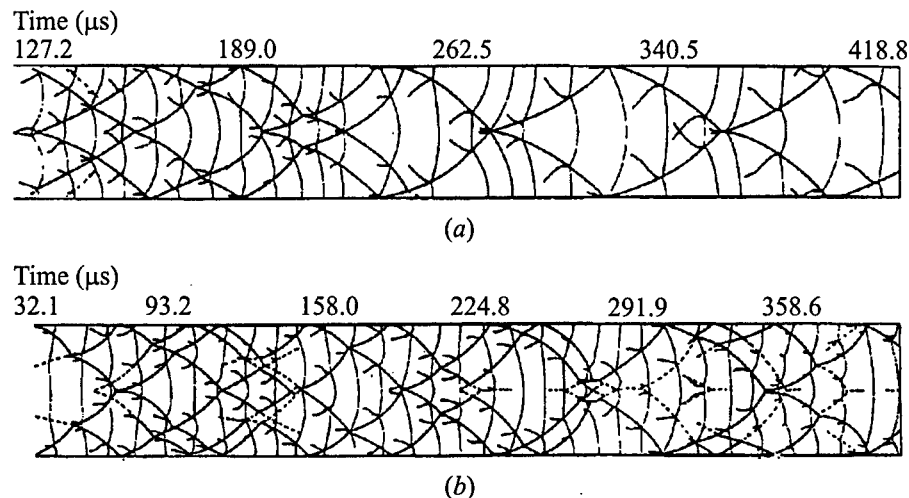
Figure 9 Computations of the locations of triple points in detonations of hydrogen–oxygen mixtures at 50 Torr and 298 K in 6.0 cm channels. (a) Mixture of $H_2:O_2:Ar/2:1:7$ that, after a few microseconds, forms a regular structure. (b) Mixture of $H_2:O_2:N_2/2:1:7$ that shows more irregular structure [29]

stem and incident shock are different for argon and nitrogen dilution. As shown in the figure, a more irregular structure is characterized by a higher frequency of the appearance and disappearance of triple points, larger variation of the shock velocity inside the detonation cell and deeper penetration of unreacted pockets into the reaction zone.

Some insight into the mechanism causing the irregularity of the structures was provided by studies of detonation cell structure in liquid nitromethane [40, 41]. These simulations incorporated a detailed equation of state for liquid nitromethane and a parametric model for the chemical reactions that was based on the rather limited available experimental data. Two quantities were defined: the induction parameter in the form, $\tau_i = A_i \exp(E_i/RT)$, and an energy release time, which also had an Arrhenius form, $\tau_r = A_r \exp(E_r/RT)$. The initial calculations were performed with the experimentally derived values of the τ_i and τ_r. The outstanding feature of these results is that the detonation structure appeared very irregular, consisting of a series of strong triple points that persist and weak triple points that appear and disappear.

The next question is the origin of this irregular structure and what controls its behavior. When E_i was increased, the difference of the size of the induction zones behind the Mach stems and reflected shocks increased. The resulting structure was then quite regular and qualitatively similar to the dilute hydrogen–oxygen calculations described above. An interesting feature of this calculation is the

formation of large unreacted pockets behind the propagating detonation front. Similar studies were carried out which varied the energy release parameters. From these, it was found that detonation structure is also affected by the energy release parameters, A_r and τ_r. Instantaneous energy release leads to a one-dimensional structure. Very fast energy release results in less regular structures, and very slow energy release results in large pockets and highly curved fronts. In this last case, the detonation may die out.

The recent parametric studies by Gamezo [35] use a considerably simpler chemical model and assume the equation of state of an ideal gas. These studies correlated irregular structure with strong triple points and large unreacted pockets, both of which occurred at high activation energies. The work described earlier [18] used a detailed and somewhat complex chemical reaction mechanism and performed a series of resolution tests. This showed that as the resolution was increased, the detonation structure reached a point in which an irregular structure became quite regular. The cellular structures computed for the conditions in Type Ia supernova all appear somewhat regular, but quite complex due to the complex reaction mechanism [39]. This is, in effect, a high-activation energy system. Unreacted pockets are observed for all of these structures. To date, these various results for quite different reaction models seem to have contradictory elements. The unreacted pockets seem universal, and may be present for most systems, either regular or irregular. Unifying all of these results into a set of concepts consistent with each other and experiments is a topic for future research.

5 UNIVERSALITY OF CELLULAR STRUCTURE

Type Ia supernovae are the brightest known stellar objects and most frequent type of supernovae observed. They are believed to be explosions of white dwarf stars that have accreted enough mass to be unstable and explode. A single explosion releases approximately 10^{51} ergs of energy into the interstellar medium, and these explosions are the major source of all iron-group elements formed in the universe. Because of the constancy of the energy release and the uniformity of their spectra, Type Ia's are used as "standard candles" to estimate the age, size, and curvature of the universe by comparing their intrinsic luminosity to their apparent brightness.

Typical densities and temperatures in the supernova are $\rho \simeq 10^5$–10^{10} g/cm^3 and $T \simeq 10^9$–10^{10} K, respectively. Under these conditions, matter is fully ionized and composed of ideal Fermi–Dirac gases of electrons and positrons, equilibrium Planck radiation, and a practically ideal Boltzmann gases of ions. Thermonuclear burning in supernovae involves many reactions of nuclei from hydrogen to zinc. The main reaction in the explosion is $^{12}C + ^{12}C$, which produces oxygen and

releases $\simeq 50\%$ of the available nuclear energy. The remaining energy is released by a subsequent complicated reaction chain that produces nuclei from carbon to nickel with protons, neutrons and α-particles.

Even though the absolute values of physical quantities and the nature of the reactions are so different between explosions in terrestrial gases and supernovae, many common or analogous physical mechanisms control the processes. Burning starts near the dense center of the star at zero gravity. As a thermonuclear flame burns and the star expands, it is distorted by hydrodynamic instabilities, and then propagates outward into a regime with higher gravity and lower densities and temperatures. At the radius where the Rayleigh–Taylor instability begins to dominate, the flame becomes a turbulent deflagration [42].

The subsequent behavior is the subject of active study because there are several possibilities after the deflagration forms. First, the turbulent deflagration could be strong enough to burn through and release enough energy to unbind the star. Another possibility is the transition of the deflagration to a detonation, which continues the energy release process in the material. However, it now appears most likely that the deflagration is quenched as it moves into less reactive, expanding outer material. In this case, the star will eventually implode in a recompression phase. During this phase, the unreacted material will detonate [43].

The chemical and physical parameters that are required for a numerical simulation of a supernova blast are less uncertain than those in any but the most idealized terrestrial combustion systems. At the energies of supernovae, many of the nuclear reactions have been directly measured in accelerator experiments, and reasonably good theories calibrated by experiments exist for those reactions that have not been measured directly. The key reactions determining the energy release and production of major nuclear species during the explosion are known to within a factor of two or better. The typical dependence of nuclear reaction rates on temperature is $\simeq \exp(-Q/T)$ or $\simeq \exp(-Q/T^{1/3})$. This exponential temperature dependence of nuclear reactions makes them qualitatively similar to terrestrial chemical reactions, though the typical nuclear burning time scales, $\simeq 10^{-5}$–10^{-11} s, are much shorter. The equation of state has a simple form, $P = (\gamma - 1)E$ with $\gamma \simeq 1.3$–1.6, and is known with accuracy better than 1%. There is thermal conduction which is well known, but there are no molecular diffusion effects (Le $= \infty$).

The difficulty is that the disparities in scales are even larger than in terrestrial problems. The radius of an unexploded white dwarf, is $\simeq 2 \times 10^8$ cm, which is much larger than any terrestrial combustion apparatus. (This expands during the burning phase to $\simeq 10^9$ cm.) Depending on the density, the thickness of a laminar nuclear flame in a carbon–oxygen white dwarf is $\simeq 10^{-3}$–10 cm, and the thickness of the carbon detonation front is about one hundred times larger, $\simeq 10^{-1}$–10^3 cm. These are comparable to the thickness of gas-phase terrestrial combustion processes. Ratios of temperature, density, and pressure across these

110

fronts are comparable to those in terrestrial combustion systems. Any theory of supernovae explosions must be consistent with the observed spectra and their variations with time. Recent numerical simulations have examined some of the fundamental properties of the propagation of flames and detonations in Type Ia supernovae, and other simulations have attempted to model the complete explosion process.

Recent numerical simulations [39] have begun to examine a possible structure of a detonation propagating in this thermonuclear material. It has been shown that there are three somewhat distinct stages in the thermonuclear reaction mechanism. The first stage is carbon burning, the second is oxygen burning, and the third is silicon burning. Because of the disparity in the timescales of the three reaction processes, the cellular structure appears to have extremely disparate scales, ranging millimeters to kilometers in scale. Figure 10 shows the computed cell structure for the three stages in a background density of 5×10^6 g/cm^3. Summaries of computed cell size as a function of density are given in Fig. 11.

One of the important effects of the cellular structure is tied to the creation of unreacted pockets on the largest, silicon scale. In these cases, the existence of such large pockets could mean that a detonation is extinguished sooner than would be predicted from a one-dimensional calculation. The next step would be to use the estimates of the cell sizes, and sizes of pockets formed, to determine the conditions under which a detonation would be extinguished, the amount of material remain unburned, and how this would change computed abundances. This may be compared to those abundances derived from observed spectra.

6   OBLIQUE DETONATIONS

An oblique detonation may be considered either as a deviation from the idealized planar structure or as an inherent part of the structure of a detonation. For example, oblique detonations occur when the geometry changes so that detonations encounter obstacles or wedges. Also, as seen above, there are oblique detonations that comprise part of the cellular structure. Recently, there has been extensive interest in oblique detonation because they are fundamental to the detonation structure in the detonative mode of ram accelerators.

A fundamental question that had to be resolved was whether an oblique detonation could be a steady, stable structure and if so, what is its structure. To address this, Li *et al.* [44, 45] performed a series of simulations to determine whether a detonation can sit stably on a wedge and, if so, to determine the resulting wave structure. In these calculations, the detonation was generated as a shock impinged on a wedge in an energetic stoichiometric mixture of hydrogen and oxygen diluted with nitrogen. Each computation was for a specific Mach
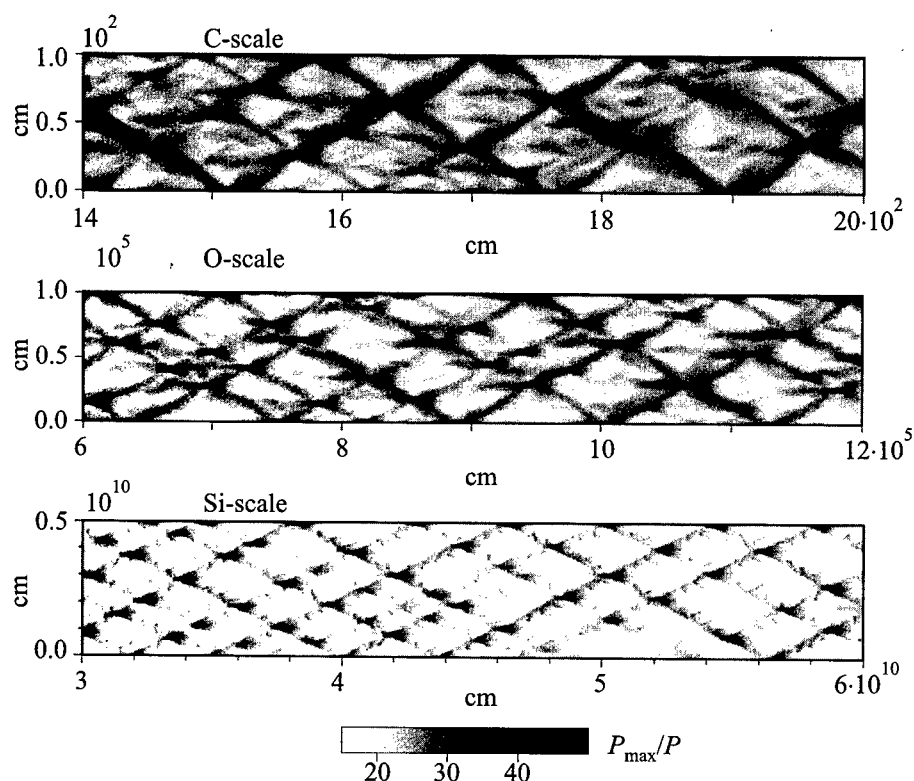
Figure 10 Computed detonation histories presented by the maximum pressure fields for a detonation propagating in a material typical of a Type Ia supernovae in the region with density 5×10^6 g/cm^3 and pressure 3.15×10^{23} erg/cm^3 [39]. The thermonuclear reactions have three distinct scales representing the burning of carbon, oxygen, and silicon

number of the incident shock, angle of the wedge, and amount of nitrogen diluent. All of these conditions contribute to the strength of the resulting detonation.

Typical contours for the case of a stable, oblique detonation structure in a hydrogen–oxygen mixture are shown in Fig. 12. The structure, looking from left to right above the wedge, has the following features:

– There is an oblique shock that starts at the tip of the wedge and extends upwards at an angle from the wedge surface. Behind this shock is the induction region (dark area in the induction parameter contours), in which hydrogen and oxygen are beginning to react and produce various reaction intermediates. This is generally a thermoneutral stage for hydrogen–oxygen reactions.
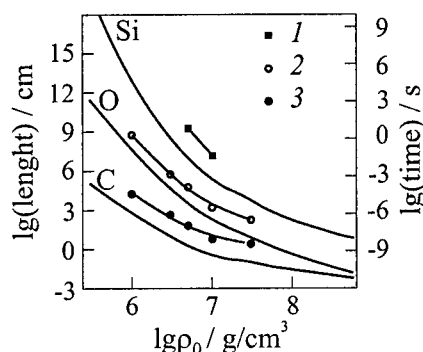
Figure 11 Key length scales and time scales as a function of initial density of self-sustained detonations in material typical of Type Ia supernovae [39]. The solid lines are the half-reaction lengths and times for steady-state one-dimensional detonations. The points are the detonation cell sizes, computed for two-dimensional detonations: *1* — Si-cells, *2* — O-cells, *3* — C-cells

– When the radical concentration becomes high enough in the induction region, product is formed, and energy is released. Thus moving to the right of the induction zone, there is a set of compression waves. These represent gradual changes in pressure and temperature generated by the energy released.

– These compression waves converge above the wall, at a point on the leading shock, steepen it, and reduce the induction time. The result is that at some height above the wall, the coupling between the leading shock and the reaction zone becomes very close and the leading shock becomes a detonation.

– The regions behind the leading shock and the leading detonation are at different densities, temperatures, and characterized by different fluid velocities. These regions are separated by a slip line originating at the point where the leading shock transitions to a detonation. This structure is summarized in the schematic at the bottom of Fig. 12.

The detonation structure sits stably on the wedge for a wide range of material composition, initial conditions in the flow, and wedge angles [44, 45]. Large perturbations on a stable system cause temporary changes in the flow, but it returns to the stable configuration. However, if too much energy is released, as might occur if the conditions are changed, the flow behind the leading shock becomes shocked, which drives the detonation angle to the point where it no longer sits stably, but moves downstream and out of the computational domain.

This work has defined the basic structure of a shock attached to a detonation. The existence of this structure has been verified in experiments by Dabora [46] and Tonello *et al.* [47], as well as by a number of more recent theoretical analyses and simulations.

7 LAYERED DETONATIONS AND TRANSMISSION

We end this paper by describing simulations performed by Jones *et al.* [47–50], based on experiments by Lui *et al.* [52, 53], to examine the diffraction,

113
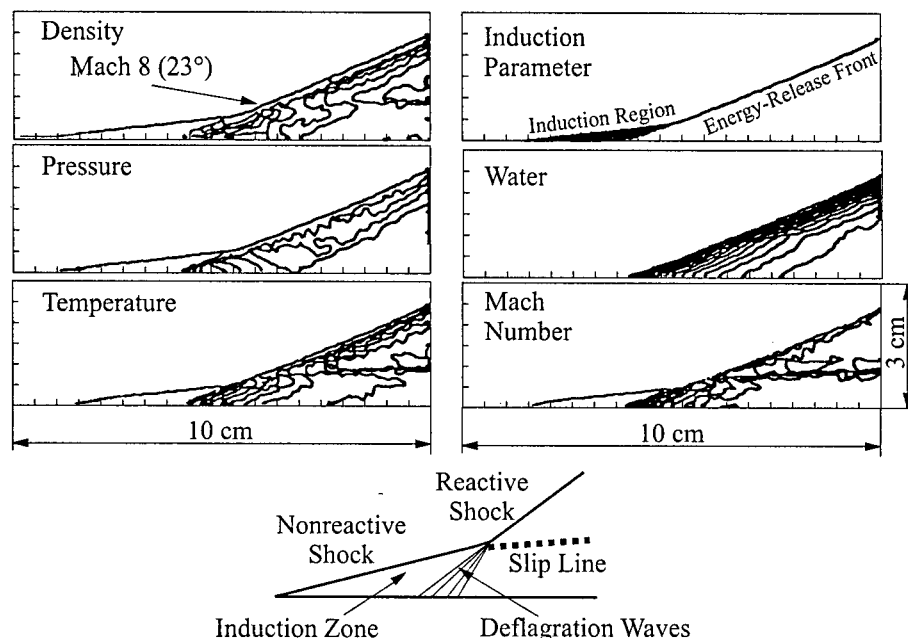
Figure 12 The top six contours are computed for the steady detonation structure on a 23° wedge in a Mach 8, stoichiometric hydrogen–air mixture. The bottom is a schematic which shows the basic structure of the oblique detonation. This consists of nonreactive, oblique shock, an induction region, a set of deflagration waves, and a "reactive shock" in which the shock is closely coupled with the energy release [44, 45]

decay, and reignition that occurs when a detonation propagates into a region of increased cross-sectional area. These computations show many of the structures and behaviors described above, but now in a somewhat different geometry and therefore a more complex flow. A detonation, propagating in hydrogen–oxygen mixture at 1 atm, 300 K, moves through a tube. At some point, the bottom wall ends abruptly, and the detonation expands laterally (is transmitted) into either the same mixture or one of another dilution or stoichiometry. Because of the expansion, the reaction front decouples from the leading shock and forms a decaying blast wave ("bubble") followed by a reaction front (a turbulent flame). Then, depending on the initial conditions, the shock and reaction front either continue to decouple or detonation re-occurs. It might reignite "spontaneously" before the leading shock reaches the bottom wall, or it might reignite as a result of the leading shock reflecting from the wall and forming a hot region. In some cases, the detonation may appear to "gallop" as it reignites, only to decay again, reignite, and so forth.

114

In one of the most recent studies [54], the detonation reignited just after it was transmitted. In this case, the mechanism for reignition is repeated shock heating of unreacted material, as successive **decaying** transverse waves (shocks) continually recompress and reheat the same unreacted material. Simulations of this situation were in close qualitative (and to some extent quantitative) agreement with experiments. In this case, the mechanism of reignition is most likely the formation of a hot spot that has the right conditions for transition.

In other cases, either for weaker detonations or less initial overdrive, the transverse waves are weaker and do not lead to immediate reignition. The detonation first appears to be quenched by the expansion process, but then is reignited and quenched again several times in a series of shock reflections from the bounding walls. Finally, the detonation is reignited and propagates as a multi-dimensional detonation with the expected pattern of detonation cells.

As an example, we show the late-time results of a simulation in which the initiating detonation was at 1.2% overdrive. Figure 13 shows the pressure and reaction-progress variable from 126 μs to 198 μs. (The original detonation was propagating from left to right. Consider first, the pressure contours starting at 126 μs. A strong exothermic center or reignition center occurred just before a shock reflected from the top wall. Here it is propagating downwards and downstream. The overall structure at the front at 126 μs consists of a detonation (heavy, dark lines at the front) connected to a shock front at a triple point. From the triple point, another shock extends upstream. At 138 μs, the newly ignited, cylindrical detonation begins to break into detonation cells and by 150 μs, the detonation appears to have essentially died out again.

The corresponding reaction-variable contours at 126 μs show a series of regions of burned material (hatched area) from failed reignition centers. The fronts of these peninsular shaped regions are generally flames, not detonations, as can be seen by the virtually constant pressure across them. By 144 μs, the transverse waves in the cylindrically expanding detonation cells have carved out unburned pockets of material which help this detonation to decay. By 156 μs, the remnants of these pockets are scattered throughout the region behind the leading shock structure. The last reignition shown is at the bottom reflection by 156 μs. This center is strong and propagates downstream and upwards, and finally becomes a self-sustained, propagating cellular detonation.

The nature of the detonation front in the final regime shows a number of features that we expect of a highly resolved, self-propagating detonation structure. First, there are the triple points and shock-reaction zone structure and interactions typical of the cellular structure of the detonation front. Experimental data [9] indicate that the detonation cells have a width somewhere between 0.1 and 0.3 cm which, because of the extreme extrapolations involved, is probably only good to within a factor of two or three. The calculations presented here show a mean size of approximately 0.40 cm, which is within the estimated range.

115
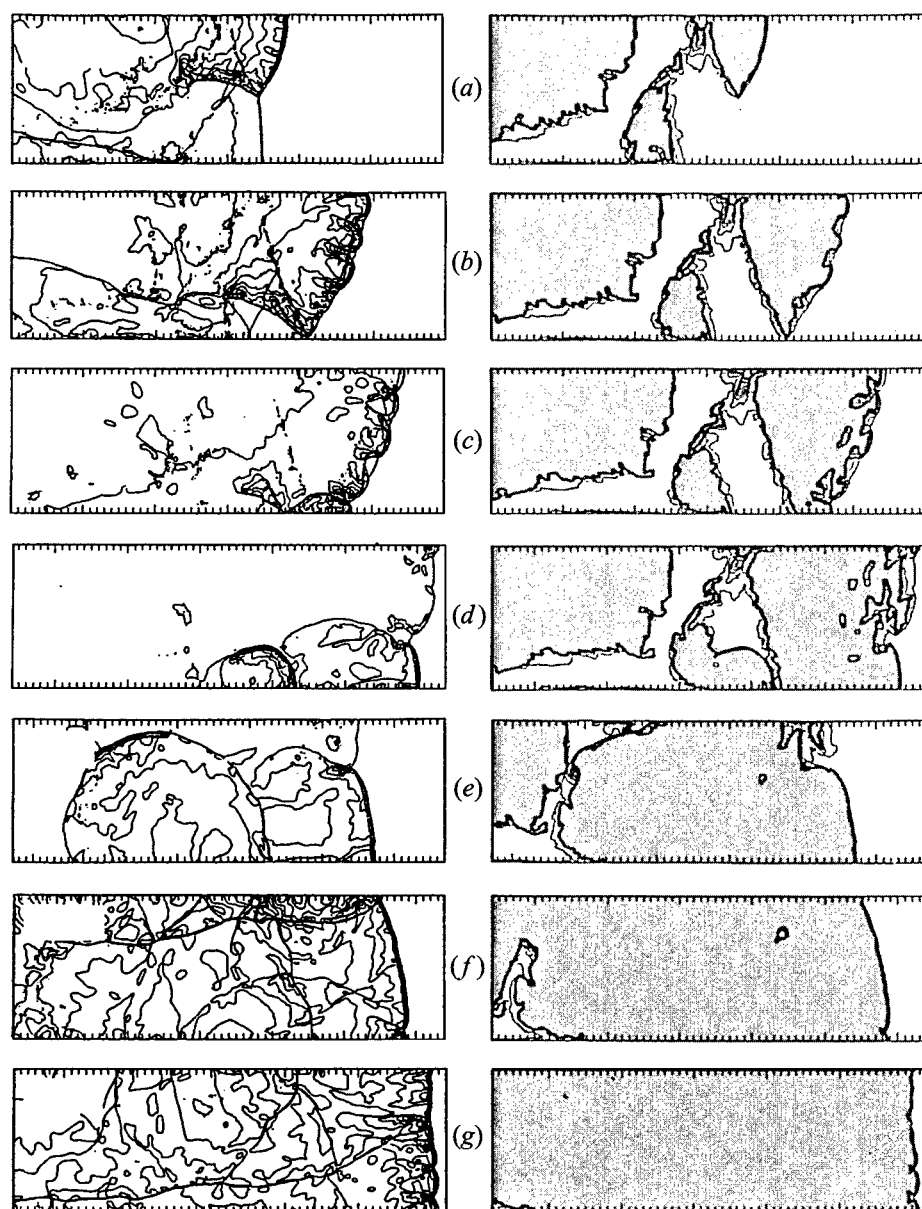
Figure 13 Pressure (left) and reaction-variable (right) contours for the weakly over-driven detonation simulation. The hatched regions of the reaction-variable contours, the chemical reactions have gone to completion [54]. (a) $t = 126$ μs, (b) 138, (c) 144, (d) 156, (e) 168, (f) 180, (g) 198

Second, the calculations demonstrate several different mechanisms by which the initial decaying detonation can be reignited. Specific mechanisms, that occur in any given situation, depend in part on the energetics of the explosive studied, the strength of the initiating shock or detonation, and the geometry of the tube. When a more energetic mixture is used, the detonation may be reignited behind the first Mach stem formed on reflection of the blast wave off the bottom of the tube. These reignition centers occur either at the intersection of a shock with a flame front (a contact surface), or in the region behind a Mach stem created by the shock reflection from the wall [55].

8 DISCUSSION

Initially, information about the structure of detonations was obtained experimentally from smoke-foil measurements, and then later from other methods such as schlieren and open shutter photography. These measurements were accompanied by extensive theoretical analysis. All of this gave us the underpinnings of what we now know.

More recently, it has been possible to add numerical simulation to the arsenal of tools used to study detonation structure. There are two major contributing physical processes in gas-phase detonations, chemical reactions with local energy release and compressible fluid dynamics, that need to be coupled to represent a detonation. To first approximation, the various physical diffusion processes may be neglected in regions of the detonation far from bounding walls. Because of the apparent simplicity of the contributing physical processes, there have been extensive efforts in recent years to simulate detonation structure. However, the apparent simplicity disappears and the subject becomes infinitely more complex and dramatic when multi-dimensional fluid interactions, multi-species, multi-step chemical kinetics, or nonideal equations of state must be considered.

In the early 1970's, computing the properties of a one-dimensional unsteady detonation with a reasonable chemical model was a chore. Now we can do this for two-dimensional simulations and, to some extent, for three-dimensional detonations. This new capability has arisen from both the development of robust numerical algorithms and an enormous increase in our computational resources. The numerical algorithms are robust monotone methods that can solve the time-dependent compressible reactive Euler and Navier-Stokes equations and reliably capture shocks. Computational resources, both in terms of computational speed and memory available, have advanced to the point where the work done on a 1970's supercomputer can now be done on a desktop workstation. These advances, specifically detonation computations, have been discussed elsewhere [55–57] and so were not covered here.

117

This paper has discussed only a small selection of what is known about detonation structure. In particular, it presents some of what is known based on what we have learned or confirmed from numerical simulation. As this is an area of continuing research, both for reasons of basic understanding and for its practical importance, this exposition is not conclusive or evenhanded. More detailed discussions, including information about the three-dimensional structure and structure in more complex configurations, will be presented in many of the papers in this meeting. In fact, there is a need now for a more thorough review, in which details of the theory, experiments, and simulations are all brought to bear on the problem.

ACKNOWLEDGMENTS

REFERENCES

1. Chapman, D. L., *Phil. Mag.*, **47**, 90–104, 1899.
2. Jouguet, E., *J. Mathem. Pures Appl.*, **1**, 347–425, 1905; and **2**, 5–85, 1906.
3. Zel'dovich, Ya. B., *Sov. J. Experimental Theoretical Physics*, **10**, 542–568, 1940; English translation: *NACA TM 1261*, 1960.
4. Von Neumann, J., "Theory of Detonation Waves," In: *John von Neumann, Collected Works.* (Ed. A. J. Taub), **6**, McMillan, NY, 1942.
5. Döring, W., *Ann. Phys.*, **43**, 421–436, 1943.
6. Oppenheim, A. K., Manson, N., and Wagner, H. Gg., *AIAA J.*, **1**, 2243, 1963.
7. Edwards, D. H., *Proc. 12th Symposium (International) on Combustion*, The Combustion Institute, Pittsburgh, PA, 819–828, 1969.
8. Fickett, W., and Davis, W.C., *Detonation.* University of California Press, Berkeley, CA, 1979.
9. Strehlow, R. A., *Combustion Fundamentals.* McGraw-Hill, New York, 1979.
10. Lee, J. H. S., *Ann. Rev. Chem.*, **28**, 75, 1977.
11. Dremin A. N., "Towards Detonation Theory," *J. Physique IV*, **C4**, 259–276, 1994.
12. Borisov, A. A., "Initiation of Detonation in Gaseous and Two-Phase Mixtures," In: *Gaseous and Heterogeneous Detonations: Science to Applications.* (Eds. G. D. Roy, S. M. Frolov, K. Kailasanath, and N. N. Smirnov), ENAS Publ., Moscow, 1999, 3–24.

13. Stewart, D. S., *Proc. 27th Symposium (International) on Combustion*, The Combustion Institute, Pittsburgh, PA, 1998 (to appear).

14. Taki, S., and Fujiwara, T., *AIAA J.*, **16**, 73–77, 1978.

15. Taki, S., and Fujiwara, T., *Proc. 18th Symposium (International) on Combustion*, The Combustion Institute, Pittsburgh, PA, 1981, 1671–1681.

16. Kailasanath, K., Oran, E. S., Boris, J. P., and Young, T. R., *Combustion Flame*, **61**, 199–209, 1985.

17. Denisov, Yu. N., and Troshin, Ya. K., *Proc. 8th Symposium (International) on Detonations*, 1962, 419–431.

18. Oran, E. S., Weber, J. W., Jr., Stefaniw, E. I., Lefebvre, M. H., and Anderson, J. D., *Combustion Flame*, **113**, 147–163, 1998.

19. Lefebvre, M. H., Oran, E. S., Kailasanath, K., and Van Tiggelen, P. J., *Progress in Astronautics and Aeronautics Ser.*, **153**, 64–67, 1993.

20. Lefebvre, M. H., and Oran, E. S., *Int. J. Shock Waves*, **4**, 277–283, 1995.

21. Voitsekhovskii, B. V., Mitrofanov, V. V., and Topchian, M. E., *The Structure of a Detonation Front in Gases*. Siberian Branch of the USSR Academy of Sci., Novosibirsk, 1963. English translation: Report WP-AFB FTC/MT/64/527, Wright-Patterson Air Force Base, Ohio, 1966.

22. Shchelkin, K. K., *Uspekhi USSR Academy Sci.*, **87**, 273; Translation in *Sov. Phys. — Usp.*, **9**, 780, 1965.

23. Edwards, D. H., and Parry, D. J., *Proc. 1st Symposium on Gasdynamics of Explosions*, Brussels, 1967.

24. Soloukhin, R. I., *Uspekhi Phys. Nauk*, **80**, 525, 1963; Translation in *Sov. Phys. — Usp.*, **6**, 523, 1964.

25. Strehlow, R. A., *Physics Fluids*, **7**, 908, 1965.

26. Strehlow, R. A., Liaugminas, R., Watson, R. H., and Eyman, J. R., *Proc. 11th Symposium (International) on Combustion*, The Combustion Institute, Pittsburgh, PA, 1967, 683–691.

27. Schott, G. L., *Proc. 4th Symposium (International) on High Explosive Detonation*, White Oak, Maryland, 1964.

28. Lefebvre, M. H., Oran, E. S., Kailasanath, K., and Van Tiggelen, P. J., *Combustion Flame*, **95**, 206–218, 1993.

29. Edwards, D. H., Hooper, G., Job, E. M., and Parry, D. J., *Acta Astronautica*, **15**, 323–333, 1970.

30. Soloukhin, R. I., *Combustion Flame*, **10**, 51–58, 1966.

31. Oppenheim, A. K., *Introduction to Gasdynamics of Explosions*. Springer-Verlag, New York, 34, 1970.

32. Strehlow, R. A., *Combustion Flame*, **12**, 81–101, 1968.

33. Crooker, A. J., Phenomenological Investigation of Low Mode Marginal Planar Detonations, Ph. D. Dissertation, University of Illinois, 1969.

34. Gamezo, V. N., Desbordes, D., and Oran, E. S., "Reactive Flow Dynamics in Cellular Detonation Waves," *Int. J. Shock Waves*, 1998 (to appear).

35. Oran, E. S., Young, T. R., Boris, J. P., Picone, J. M., and Edwards, D. H., *Proc. 9th Symposium (International) on Combustion*, The Combustion Institute, Pittsburgh, PA, 1982, 573–582.

119

36. Gamezo, V. N., Desbordes, D., and Oran, E. S., *Combustion Flame*, **116**, 154–165, 1998.

37. Gamezo, V. N., private communication.

38. Gamezo, V. N., Wheeler, J. C., Khokhlov, A. M., and Oran, E. S., "Multi-Level Structure of Cellular Detonations in Type Ia Supernovae," *Astrophys. J.*, 1998 (to appear).

39. Guirguis, R., Oran, E. S., and Kailasanath, K., *Combustion and Flame*, **65**, 339–366, 1986.

40. Guirguis, R., Oran, E. S., and Kailasanath, K., *Proc. 21st Symposium (International) on Combustion*, The Combustion Institute, Pittsburgh, PA, 1987, 1659–1668.

41. Khokhlov, A. M., *Astrophys. J.*, **449**, 695–713, 1995.

42. Khokhlov, A. M., Oran, E. S., and Wheeler, J. C., *Astrophys. J.*, **478**, 678–688, 1997.

43. Li, C., Kailasanath, K., and Oran, E. S., *Progress in Astronautics and Aeronautics Ser.*, **153**, 231–240, 1993.

44. Li, C., Kailasanath, K., and Oran, E. S., *Physics Fluids*, **6**, 1600–1611, 1994.

45. Broda, J. C., and Dabora E. K., In: J. R. Bowen Ed. *Dynamics of Exothermicity*. Gordon and Breach, 1994.

46. Tonello, N., Sichel, M., and Kauffman, C. W., *Int. J. Shock Waves*, **5**, 225–238, 1995.

47. Jones, D. A., Sichel, M., Oran, E. S., and Guirguis, R., *Proc. 23rd Symposium (International) on Combustion*, The Combustion Institute, Pittsburgh, PA, 1990, 1805–1811

48. Jones, D. A., Sichel, M., Guirguis, R., and Oran, E. S., *Dynamics of Detonations and Explosions*, Progress in Astronautics and Aeronautics Ser., AIAA Inc., Washington, DC, **133**, 200–219, 1991.

49. Oran, E. S., Jones, D. A., and Sichel, M., *Proc. Royal Society London*, **A436**, 1992, 267–297.

50. Jones, D. A., Sichel, M., Oran, E. S., *Int. J. Shock Waves*, **5**, 47–57, 1995.

51. Liu, J. C., Liou, J. J., Sichel, M., Kauffman, C. W., and Nicholls, J. A., *Proc. 21st Symposium (International) on Combustion*, The Combustion Institute, Pittsburgh, PA, 1987, 1659–1668.

52. Liu, J. C., Sichel, M., and Kauffman, C. W., *Progress in Astronautics and Aeronautics Ser.*, **114**, 264–283, 1988.

53. Jones, D. A., Kemister, G., Tonello, N. A., Oran, E. S., and Sichel, M., "Numerical Simulation of Detonation Reignition in H_2–O_2 Mixtures in Area Expansion," *Int. J. Shock Waves*, 1998 (to appear).

54. Oran, E. S., Boris, J. P., Jones, D. A., and Sichel, M., *Progress in Astronautics and Aeronautics Ser.*, **153**, 241–252, 1993.

55. Oran, E. S., In: J. R. Bowen Ed. *Dynamics of Exothermicity*. Gordon and Breach, New York, 253–290, 1996.

56. Oran, E. S., In: R. Sarma Ed. *Aerothermochemistry for Hypersonic Technology*. Lecture Series 1995-04, von Karman Institute for Fluid Dynamics, Brussels, 1996.

57. Oran, E. S., *Proc. 4th Symposium (International) on Special Topics in Chemical Propulsion: Challenges in Propellants and Combustion 100 Years after Nobel*, Begell House Inc., New York, 1997, 985–997.

ON RECTANGULAR AND DIAGONAL THREE-DIMENSIONAL STRUCTURES OF DETONATION WAVES

M. Hanana, M. H. Lefebvre, and P. J. Van Tiggelen

Experimental results, presented in this work, enable us to classify the three-dimensional (3D) structure of detonations into two fundamental types: a rectangular structure and a diagonal structure. The rectangular structure is well documented in the literature and consists of 2 two-dimensional (2D) waves. These 2D waves are orthogonal and travel independently from each other. The soot record in such a case shows classical diamond detonation cell exhibiting "slapping waves." Those structures are not fundamentally 3D but may be described as $2 \times 2D$. The diagonal structure has not yet been reported as such and is characterised by soot records without slapping waves. These structures have been occasionally mentioned in the literature, and incorrectly called "planar mode." However, the recent experiments performed by the authors indicate that such a structure is actually 3D, with triple points moving along the diagonal line of the tube cross section. The axes of the transverse waves are canted at 45° to the wall, accounting for the lack of slapping waves. Those diagonal structures are the only ones fundamentally 3D. The diagonal structure exhibits a better sustaining mechanism than the rectangular mode. It is possible to reproduce these diagonal structures, at will, by appropriate control of the experimental ignition procedure. The characteristics of the diagonal structure show some similarities with detonation structure in round tubes. Such diagonal structures have not yet been reported in 3D numerical modeling.

INTRODUCTION

The interaction of Mach configurations has been used to describe the structure of detonation cells. A well-documented description is given in the review article of Strehlow [1], summarising the work of the pioneering Russian groups: Shchelkin and Troshin [2], as well as Voitsekhovskii, Mitrofanov and Topchian [3]. Strehlow's paper also describes, very thoroughly, the experimental data obtained by

121

White *et al.* [4] and by Oppenheim's group [5], indicating the way the writing pattern is achieved on the soot plate.

Strelhow [1] has classified the regularity of the writing pattern on the soot plate. Libouton *et al.* [16] demonstrated also that the structure regularity is related to the way the heat is released during the chemical process. For extremely regular patterns, Strehlow [1] noticed two different modes for the wave propagation: the rectangular mode and the planar mode. He relates those different modes to the tube geometries. According to Strehlow [7, 8], the rectangular mode is usually observed and the "planar mode" is typical of the tubes with a very narrow rectangular cross-section. Moreover, Strehlow wrote [1], "the planar mode occurs when the preferred transverse spacing of the detonation is at least five times the width of a narrow channel. It is the simplest self-sustaining detonation mode which may be studied since it is two-dimensional non-steady." Such a statement is misleading because the so-called planar mode has been recorded in tube with an aspect ratio of about 2, that is $3\,^1/_4$ in to $1\,^1/_2$ in. Biller [9] has given a better approach when he wrote: "At first glance it appears that it is a planar mode detonation. However, this is not the case ... In this case the axes are canted at some angle to the tube walls, thus, accounting for the apparent absence of the slapping wave ... At the present time, it is not understood why, under these particular test conditions, the detonation chooses this type of orientation."

Recently, Williams *et al.* [10, 11] have achieved a numeric model of a 3D structure of self-sustaining detonations. Starting from a 2D periodic solution, they added a 3D perturbation perpendicular to the motion of the initial 2D transverse waves. The solution reached a periodic regime corresponding to the rectangular mode of Strehlow [7, 8], where two sets of transverse waves propagate perpendicular to one another, out of phase by approximately 90°. From the vortex sheets generated along the triple point lines, they have been able to distinguish between the different zones of the leading front shock (Mach stem and incident shock).

EXPERIMENTAL SET-UP

All experiments have been conducted in an aluminum square tube about 9 m long with a cross section 9.2×9.2 cm^2. The detonation in the studied mixture is ignited by a detonation in a 2-m long booster section. Ionization gauges, located before and after the test section, record the average detonation velocity. The test section is 1-m long and consists of soot plates for recording the shock structure. Some experiments have been performed using four plates in the test section (one on each wall of the tube). The latter configuration enables us to observe accurately the symmetry of the cellular structure and the respective

Figure 1 Experimental set-up. Labels *1*, *4* and *2*, and *3* represent velocity and pressure gauges, respectively, *5* — high pressure chamber, *6* — low pressure chamber, *7* — diaphragm, *8* — pump, *9* — measurement chain, *10* — amplifier, *11* — scope

position of the structure in space. Moreover, experiments have been conducted using an "end plate" in order to record the front view of the shock structure. This end plate had to be perforated to allow the flow of fresh and burnt gases through the tube. Figure 1 gives a description of the experimental set-up.

EXPERIMENTAL DATA

The composition of the studied mixture is stoichiometric hydrogen/oxygen diluted with 70% argon at room temperature. The initial pressure is 50 Torr (6.7 kPa). In those experimental conditions, the number of transverse waves travelling in opposite directions is two. Figure 2 shows typical soot prints.

Two types of structures are observed: structures with slapping waves, as indicated in Figs. 2*a* and 2*b*, and a structure without slapping wave, called the "diagonal mode" (Fig. 2*c*). In the case exhibiting slapping waves, the position of the latter is more often located at mid-cell of the printed cellular structure (Fig. 2*a*). Sometimes, the slapping wave is located at the apex of the printed cell (Fig. 2*b*) and in a few cases the slapping wave occurs randomly between these two extreme positions. Figure 2 shows also soot records from the front view of the detonation: Figs. 2*a* and 2*b* show the rectangular shape of the imprints of the travelling waves, and Fig. 2*c* shows that in the case with no-slapping wave the aspect of the soot imprint of the travelling waves in the tube is diagonal.

(a)

(b)

(c)

Figure 2 Three types of multidimentional structures recorded on soot plates. The mixture composition is $H_2/O_2/7Ar$ at an initial pressure of 6.7 kPa. The square plate on the right displays the front view of the shock structure. (a) Structure with slapping waves, both orthogonal structures being in phase. (b) Srtructure with slapping waves, both orthogonal structures being out of phase. (c) Structure without slapping wave

Table 1 Detonation velocity and cell sizes taken from the soot imprints for three types of cellular structure

	Average velocity m/s	Cell spacing mm	Cell length mm
Rectangular structure (in phase)	1420	92	163
Rectangular structure (out of phase)	1420	92	165
Diagonal structure	1500	92*	120

*Corresponding to the apparent cell width (see discussion in the text).

124

The overall structures with slapping waves are longer than the structures without slapping waves although the spacing (width of the printed cell) is identical (Table 1). The average detonation velocities are also reported in Table 1. The experimental ratios between the cell width and the cell length are equal to 0.56 and 0.77, for rectangular and diagonal structures respectively.

All structures are quite reproducible (in terms of shape, size, detonation velocity, etc.). It is important to note that we were able to reproduce the structures without slapping waves, at will, by appropriately controlling the ignition procedure. So, the diagonal structures are quite reproducible and do not occur haphazardly as mentioned in [7].

DISCUSSION

The experimental results allow classification of the detonation structures into two fundamental types: (1) a rectangular structure and (2) a diagonal structure.

The rectangular structure consists actually of 2 two-dimensional waves. The 2D waves are orthogonal and travel independently from one another. Usually both structures are "in phase," which means that the apices of both orthogonal structures are located in the same tube cross section. The soot record in such a case shows the classical diamond detonation cell exhibiting "slapping waves" in the middle of the cell. A schematic of this type of detonation cell is represented in Fig. 3 a. However, because each of them may independently be adjusted to the tube geometry, it is possible to observe the structures that are "out of phase." The extreme case of phase shift occurs when the apex of the first wave and the middle of the second one are located in the same tube cross section. In that case, the soot record shows the presence of slapping waves at the apex of the detonation cell (Fig. 3 b). As a consequence, those structures are not fundamentally three-dimensional but have to be described as 2 × 2D. The transverse motion of the front shocks is parallel to the wall of the detonation tube and consequently, their soot records form a rectangular structure (Figs. 2 a and 2 b). As a result, it is reasonable to call such a structure "rectangular." A schematic diagram of this motion is depicted in Fig. 4. One can observe that four lines of triple points shape the shock structure. Consequently, a piling up of octahedrons and tetrahedrons forms one cycle of the overall detonation structure, filling up the entire cross section of the tube. Table 2 gives the number of elementary volumes per detonation cycle for the three observed structures. The spacing (width) of the detonation cell on the soot record (Fig. 2) is the actual size of the octahedron edge.

The diagonal structure has not yet been reported as such and is characterised by a soot record without slapping waves. These structures have been occasionally mentioned in the literature, but incorrectly called "planar mode," i.e. purely 2D,

and inappropriately considered as "marginal detonation." However, the recent experiments we performed indicate that such structures are actual 3D with the triple point lines moving parallel to the diagonals of the tube cross section. Consequently, their soot records form a diagonal pattern (Fig. 2c). As a result, it is reasonable to call such a structure "diagonal." Figure 3c represents a drawing of the whole cycle of the detonation structure. A schematic diagram of the motion of the front shock is represented in Fig. 5.

The axes of the transverse waves are canted at 45° to the wall, accounting for the lack of slapping waves. We conclude that those diagonal structures are the only ones fundamentally three-dimensional. The elementary volumes filling up the entire cross section of the tube during one complete cycle of the detonation wave are made of full and partial octahedrons as reported in Table 2. The spacing (width) that is observed on the soot record (Fig. 2c) is not the actual size of the central octahedron edge. The real size of the edge of the octahedron is equal to $w/\sqrt{2}$, where w is the apparent spacing of the detonation cell as recorded on the soot plate. Eight lines of triple points form the overall structure of the front shock (Fig. 5). The time evolution of those triple point lines provides intertwined surfaces that form the central octahedron volume.

It should be pointed out, that a number of triple point lines in the diagonal structure is two times larger

(a)

(b)

(c)

Figure 3 Drawing of the soot imprints of the three types of multidimensional structures as they have been recorded on the four sides of the tube. The cross sections of each type of the structures at three different times of the detonation cycle are resresented: (a) Structure with slapping waves, both orthogonal structures being in phase. (b) Structure with slapping waves, both orthogonal structures being out of phase. (c) Structure without slapping waves

Figure 4 Schematic diagram of the front shocks at different locations of the cycle of the detonation cell. The case represented here is "in phase" (rectangular type). The arrows show the motion of the four triple point lines generating the central octanhedron faces. *I* — development of Mach stem inside the central octahedron, *II* — development of incident wave inside the central octahedron

Table 2 Shape of the elementary three-dimensional volumes filling one cycle of the detonation wave over the whole tube cross section

	Octahedron			Tetrahedron		
Rectangular structure (out of phase)	1 full	—	4quarter	—	8 half	—
Rectangular structure (in phase)	—	4 half	—	2 full	—	8 quarter
Diagonal structure	1 full	4 half	4 quarter	—	—	—
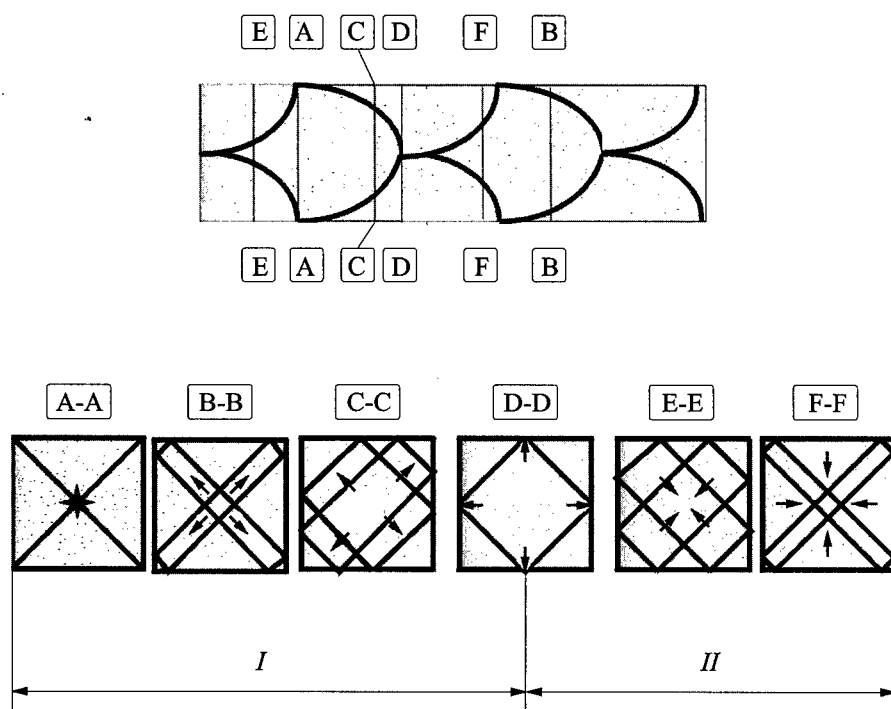
Figure 5 Schematic diagram of the front shocks at different locations of the cycle of the detonation cell. The detonation represented here does not exhibit slapping waves (diagonal type) and the shocks are canted at an angle of 45° to the wall. The arrows show the motion of four out ot eight triple point lines generating the central octahedron faces. For clarity, the motion of the other four triple point lines is not shown. *I* — development of Mach stem inside the central octahedron, *II* — development of incident wave inside the central octahedron

than in the rectangular structure, and therefore there are two times as many transverse waves.

Thus, the diagonal structure exhibits a better sustaining mechanism than the rectangular mode: the average wave velocity of the diagonal structure is larger than the velocity of the rectangular structure, and the actual cell sizes of the diagonal structure are smaller than those relevant to the rectangular structure (see Table 1). Pressure profiles of the leading and reflected shocks (not presented in this paper) also confirm the better sustaining mechanism of the diagonal structure.

The spacing (width) should not be considered as a general appropriate parameter for correlation purposes since the spacing of the diagonal structure recorded

128

on the soot print does not represent the actual cell width. The cell length of both rectangular and diagonal structures recorded on soot plates represents the actual size of the octahedron, and the cell length is therefore the fundamental geometric characteristics of the detonation structure.

Moreover, the properties of the diagonal structure show some similarities with those of detonation structures in round tubes (multiple heads spinning detonation). Note that the diagonal structure has not yet been reported in 3D numerical modeling.

CONCLUDING REMARKS

The most common detonation structure, the one exhibiting slapping waves, is actually a superposition of 2 two-dimensional orthogonal structures. We called such a structure a "rectangular structure," because the triple point lines are running parallel to the tube walls. The structure exhibiting no slapping wave at all is basically a 3D structure that we called "diagonal structure," because the triple point lines propagate diagonally in the tube. All features of the diagonal structure (average velocity, type and size of elementary volumes, shock pressure, number of triple point lines) are consistent with a structure better sustained than the rectangular one. Contrary to previous thoughts, the diagonal structure is neither marginal, nor rarely or randomly observed; the way detonation ignition occurs is the key parameter to induce one or the other type of the structure.

ACKNOWLEDGMENTS

REFERENCES

1. Strehlow, R. A., "Gas Phase Detonations: Recent Developments," *Combustion Flame*, **12**, 81–101, 1968.
2. Shchelkin, K. I., and Troshin, Y. K., *Gasdynamics of Combustion*. Monobook Corporation, Baltimore, 1965.
3. Voitsekhovskii, B. V., Mitrofanov, V. V., and Topchian, M. E., *Structure of a Detonation Front in Gases*. Siberian Branch of the USSR Academy Sci. Publ., Novosibirsk, 1963, Translation: Wright-Patterson Air Force Base.

4. White, D. R., and Cary, K. H., *Physics Fluids*, **6**, 749–758, 1963.

5. Oppenheim, A. K., *Introduction to Gasdynamics of Explosions*. International Centre of Mech. Sci., Course of Lectures No.48, Springer-Verlag, 1970.

6. Libouton, J. C., Jacques, A., and Van Tiggelen, P. J., "Cinétique, Structure et Entretien des Ondes de Détonations," *Proc. Colloquium (International) Berthelot–Vieille–Mallard–LeChatelier, 1st Specialists Meeting (International) of the Combustion Institute*, 1981, Bordeaux, France.

7. Strelhow, R. A., "Multi-Dimensional Detonation Wave Structure," *Acta Astronautica*, **15**, 345–357, 1970.

8. Strehlow, R. A., "Nature of Transverse Waves in Detonations," *Acta Astronautica*, **14**, 539–548, 1969.

9. Biller, J. R., An Investigation of Hydrogen–Oxygen–Argon Detonations, Technical Report AAE 73-5-UILU-ENG-73/0505, University of Illinois, 1973.

10. Williams, D. N., Bauwens, L., and Oran, E. S., "Detailed Structure and Propagation of Three-Dimensional Detonations," *Proc. 26th Symposium (International) on Combustion*, The Combustion Institute, Pittsburgh, PA, 1996, 2991–2998.

11. Williams, D. N., Bauwens, L., and Oran, E. S., "The Effects of Aspect Ratio on Detonation Structure in Rectangular Ducts," *Proc. 16th ICDERS*, 1997, 374–376.

THEORY OF MULTI-DIMENSIONAL DETONATION INSTABILITY

Forman A. Williams

Multi-dimensional instabilities of planar detonations that lead to cellular structures are discussed on the basis of recent research. The research makes use of a distinguished limit in which the propagation Mach number is large and the difference between the specific heats at constant pressure and at constant volume is small. In this limit, the Neumann-state Mach number is small and the fractional variations of the pressure change after the Neumann state are also small for moderately overdriven conditions. Under these conditions, the heat release is comparable in magnitude with the thermal enthalpy at the Neumann state, resulting in post-shock flow that is quasi-isobaric in the first approximation. The dispersion relation shows that, except under extremely highly overdriven conditions, there always exists a transverse wavelength range over which the planar detonation is unstable, independent of the strength of the temperature dependence of the heat release rate. The physical basis of this result is indicated and proper descriptions of the chemistry are ❁ addressed, including appropriate reduced chemistry.

INTRODUCTION

Gaseous detonations are cellular because the planar detonation is unstable to nonplanar disturbances. The causes of this type of instability have been studied extensively in the past, but complete understanding is not yet available. Recently, some advances have been made to help clarify relationships between the chemistry and the instability. Explanations of these results are offered here, as are reduced chemical-kinetic descriptions that can be used in theoretical studies.

131

FAILURE OF ONE-STEP ACTIVATION-ENERGY ASYMPTOTICS

The stability of planar detonations to planar disturbances has been addressed [1] on the basis of a one-step Arrhenius approximation for the chemical rate of heat release in the limit of large activation energy E. An appropriate nondimensional activation energy is

$$\beta = \frac{E}{R^\circ T_N^\circ} \tag{1}$$

where R° is the universal gas constant and T_N° the temperature at the Neumann state (just behind the shock) for the steady, planar, unperturbed detonation. A formal expansion is considered for the limit $\beta \to \infty$. In this limit, to leading order, for the unperturbed detonation, the so-called square-wave model is recovered, in which there is an induction length L such that no heat release occurs for a distance L behind the shock. Then all of the heat release occurs instantaneously. Although this model can be a useful zeroth approximation for the undisturbed detonation, its stability is pathological. The pathology sometimes has been termed the Zaidel paradox, because, the same type of behavior was found in 1961 by Zaidel for a square-wave model not based on activation-energy asymptotics. A simplified model can readily illustrate the essence of the Zaidel paradox.

If U_N° is the velocity at the Neumann state of the unperturbed planar wave, then in the unperturbed state the induction length L is $U_N^\circ \tau$, where τ denotes the induction time. The entropy-wave delay causes the burnt-gas plane to respond to Newmann-state perturbations a time τ later. Hence, the chemical-kinetic condition obtained from activation-energy asymptotics for large β is, apart from a possible constant factor of order unity,

$$\frac{1}{L(t)} \frac{dL(t)}{dt} = -\frac{\beta}{T_N(t-\tau)} \frac{dT_N(t-\tau)}{dt} \tag{2}$$

In a time-dependent situation, it follows from simple kinematics that

$$\frac{dL(t)}{dt} = D(t) - B(t) \approx -B(t) \tag{3}$$

where $D(t)$ is the detonation propagation velocity (the shock velocity) and $B(t)$ is the velocity of the heat-release (burning) plane. The approximate equality at the end of Eq. (3) applies for changes occurring at large β, because then the heat-release plane varies in velocity much more strongly than the shock. The effect of $B(t)$ is like that of a piston driving pressure waves upstream towards the shock. Since these pressure waves typically travel appreciably faster than the

132

flow velocity U_N°, the acoustic effect at the Neumann state is instantaneous in a first approximation, compared to the induction time lag τ. Thus, the Neumann pressure $P_N(t)$ varies in proportion to $B(t)$. Since, in these changes, $T_N(t)$ is approximately proportional to $(\gamma - 1)P_N(t)$, where γ, near unity, is the ratio of specific heats, Eq. (2) can be written approximately as

$$\frac{1}{L(t)}\frac{dL(t)}{dt} = -\frac{\beta(\gamma - 1)}{B(t - \tau)}\frac{dB(t - \tau)}{dt} \tag{4}$$

For small changes about average unperturbed values $L(t) = L^{\circ}$ and $B(t) = B^{\circ}$ use of Eq. (3) in Eq. (4) gives

$$B(t) = \beta(\gamma - 1)\frac{L^{\circ}}{B^{\circ}}\frac{dB(t - \tau)}{dt} \tag{5}$$

where $L^{\circ}/B^{\circ} = \tau$ by definition. With a characteristic reciprocal time defined as (apart from a constant factor of order unity), replacement of $t - \tau$ by t in Eq. (5) yields

$$\frac{dB(t)}{dt} = \alpha B(t + \tau) \tag{6}$$

Equation (6) is an equation that effectively exhibits a negative time lag. The derivative depends on the value at a later, rather than earlier, time. Since τ is positive, Eq. (6) is an equation of the advance (rather than delay) type. Solutions to such equations are absolutely unstable, irrespective of the sign of α. If, for example, solutions of the type $B \sim e^{(\sigma + i\omega)t/\tau}$ are sought, where ω is a nondimensional frequency and σ a nondimensional growth rate, then it is found from Eq. (6) that

$$(\sigma + i\omega)e^{-(\sigma + i\omega)} = b \tag{7}$$

where $b \equiv \alpha\tau$ is a constant. It is well known [2] that the pair of real equations obtained from the real and imaginary parts of Eq. (7) possess an infinite number of solutions, having increasingly positive values of σ and ω. In particular, for large positive values of ω, these solutions have $\omega \to (2n+1/2)\pi$ and $\sigma \to \ln[(2n+1/2)\pi/b]$, where n is a large positive integer. It may be concluded, that in the limit $\beta \to \infty$, one-step activation-energy asymptotics produces a denumerably infinite number of increasingly unstable modes of increasing frequency.

It is, of course, true that for finite values of β there are only a finite number of unstable modes. However, use of the methods of activation-energy asymptotics is mathematically incorrect for such a problem, unless there are a large number of unstable modes. Such methods, which currently are employed quite extensively with a small number of unstable modes (sometimes none), may provide qualitative simulations of unstable detonations and are not mathematically rigorous. A

133

revision of the chemical-kinetic description in addressing detonation stability is needed. One-step activation-energy asymptotics is fine for deflagration structure, deflagration stability and detonation structure, but not for detonation stability. As was correctly recognized in the early work of Erpenbeck and others, the Zaidel paradox effectively invalidates results from models of this general class.

Moreover, it is found, by looking numerically [2] at one-dimensional stability with chemistry such as that of hydrogen–oxygen detonations, that one-step activation-energy asymptotics is inappropriate for describing the stability of real detonations. Although there is an induction period that is strongly dependent on T_N, the heat release after this period occurs slowly, at rates largely dependent on three-body reactions, with very little dependence on T_N. Instead of the heat release occurring instantaneously, it occurs over an extended region in a manner that is insensitive to T_N. The stability for such chemistry will, of course, be very different from that predicted by one-step activation-energy asymptotics. More general classes of chemical-kinetic models have been identified that encompass the real-chemistry type of behavior in describing detonation stability [2, 3].

MULTI-DIMENSIONAL INSTABILITY AT ZERO ACTIVATION ENERGY

The same type of simplified reasoning, given above, demonstrating planar instability for one-step chemistry of high activation energy, also indicates instability for nonplanar disturbances even at zero activation energy. The presence of such multi-dimensional instabilities under all practical conditions has recently been demonstrated analytically [3]. This type of instability has not been commonly recognized and is well hidden from perturbation analyses. If one begins with a chemical description that is stable to planar perturbations, there, still, is always a neutrally stable mode for nonplanar disturbances of long wavelength, as first obtained by D'yakov and Kontorovich. Perturbation methods applied to calculate the influences of the inner detonation structure on the stability of this DK mode for large, but finite, wavelengths show that the effects are stabilizing for large but finite wavelengths. All modes are stable if the planar detonation is stable to planar disturbances. Similarly, perturbations for the limit of small wavelengths show that acoustic effects stabilize the neutrally stable mode of zero wavelength. Perturbations carried out from either end thus suggest stability. Calculations have shown, however, that there always is an intermediate range of transverse wavelengths, of order $L^\circ/M_N \sim L^\circ/\sqrt{\gamma - 1}$, where M_N is the Mach number at the Neumann state, over which instability occurs.

To understand this instability, it is helpful to focus attention on the transverse divergence of the transverse velocity component at the Neumann state, $\nabla \cdot V_N$. For the nearly constant-density flow in the vicinity of the Neumann state behind a

strong shock, mass conservation shows this to be the negative of the longitudinal derivative of the longitudinal component of velocity, that is, the flow convergence in the longitudinal direction. Since flow convergence increases velocities and correspondingly increases L, the reaction-zone length, for a given fixed reaction time τ, roughly speaking, varies as

$$\frac{1}{L(t)}\frac{dL(t)}{dt} \sim \tau\frac{d\nabla \cdot V_N(t-\tau)}{dt} \tag{8}$$

since L responds after the transit time of order τ on the average. Equation (8) clearly bears a resemblance to Eq. (2), and Eq. (3) again can be applied. Again, considering the piston effect of $B(t)$ to be transmitted acoustically nearly instantaneously to the shock, it is seen that locally

$$\frac{dB}{dt} \sim \frac{dP_N}{dt} \sim \frac{d\nabla \cdot V_N}{dt} \tag{9}$$

which, when used along with Eq. (3) in Eq. (8), gives

$$B(t) \sim -\tau\frac{dB(t-\tau)}{dt} \tag{10}$$

Replacing $t - \tau$ by t in Eq. (10) yields Eq. (6) with α a constant times $-\tau$. An effectively negative time delay thus again arises, producing instability. This is not so sharp an effect as that for high activation energy because the heat release occurs gradually over the time τ, but in a rough qualitative sense, the effect nevertheless exists. Since available criteria for detonation stability all refer, in some way, to overall effective activation energies, this instability does not conform to the usual criteria.

BIFURCATION

The classical approach to descriptions of nonlinear phenomena, such as cellular detonations, is to find a condition of neutral stability and introduce a suitable nonlinear expansion about that point to calculate the characteristics of the weakly unstable modes. The preceding discussion indicates that, for multi-dimensional detonation instability, there is no suitable bifurcation point. There always exists a finite range of finite growth rate in the dispersion relations. It is, however, possible to address physically uninteresting limiting values of parameters where bifurcation may occur. The preceding arguments presume that the heat release is comparable with the thermal enthalpy at the Neumann state, a realistic selection. If the heat release is sufficiently small compared with that enthalpy, then in the first approximation the detonation is just a shock wave,

135

Table 1 A short mechanism for acetylene detonation; specific reaction-rate constants k are $k = BT^n e^{-E/R^\circ T}$

No.	Reaction	B^a	n^a	E^a
	Hydrogen–Oxygen Chain			
1	$H + O_2 \rightarrow OH + O$	3.52×10^{16}	-0.7	17070
2	$OH + O \rightarrow H + O_2$	1.15×10^{14}	-0.324	-175
3	$H_2 + O \rightarrow OH + H$	5.06×10^4	2.67	6290
4	$OH + H \rightarrow H_2 + O$	2.22×10^4	2.67	4398
5	$H_2 + OH \rightarrow H_2O + H$	1.17×10^9	1.30	3626
6	$H_2O + H \rightarrow H_2 + OH$	6.72×10^9	1.30	20210
7	$OH + OH \rightarrow H_2O + O$	$k = 5.46 \times 10^{11} \exp(0.00149T)$		
8	$H_2O + O \rightarrow OH + OH$	7.60×10^0	3.84	12780
	Direct Recombination			
9^b	$H + H + M \rightarrow H_2 + M$	7.20×10^{17}	-1.0	0
10^c	$H + OH + M \rightarrow H_2O + M$	2.20×10^{22}	-2.0	0
11^b	$O + O + M \rightarrow O_2 + M$	1.14×10^{17}	-1.0	0
	Hydroperoxyl Formation and Consumption			
12^c	$H + O_2 + M \rightarrow HO_2 + M$	6.76×10^{19}	-1.4	0
13	$HO_2 + H \rightarrow OH + OH$	1.70×10^{14}	0.0	874
14	$HO_2 + H \rightarrow H_2 + O_2$	4.28×10^{13}	0.0	1411
15	$HO_2 + H \rightarrow H_2O + O$	3.10×10^{13}	0.0	1720
16	$HO_2 + O \rightarrow OH + O_2$	2.00×10^{13}	0.0	0
17	$HO_2 + OH \rightarrow H_2O + O_2$	2.89×10^{13}	0.0	-497
	Water-Gas Shift			
18	$CO + OH \rightarrow CO_2 + H$	4.40×10^6	1.5	-741
19	$CO_2 + H \rightarrow CO + OH$	4.97×10^8	1.5	21446
	Initiation and Fuel Consumption			
20	$C_2H_2 + O_2 \rightarrow HC_2O + OH$	2.00×10^8	1.5	30086
21	$C_2H_2 + O \rightarrow HC_2O + H$	6.51×10^6	2.09	1560
22	$HC_2O + O \rightarrow 2CO + H$	9.64×10^{13}	0.0	0
23	$HC_2O + O_2 \rightarrow 2CO + OH$	2.00×10^{13}	0.0	0

^{a}Units: mole/cm^3, s^{-1}, K, cal/mole.

^{b}Chaperon efficiencies: N_2, O_2, 1.0; CO, 1.9; CO_2, 3.8; H_2, 2.5; H_2O, 16.3.

^{c}Chaperon efficiencies: same as b except H_2O, 12.0.

which is known to be stable (for the gaseous mixtures of practical interest here). Therefore, bifurcation may be expected in a particular range of low heat release. Even some early numerical work, for example by Erpenbeck, focused on such small heat release in studying detonation instability. By completing bifurcation analyses under various conditions for small heat release, better understanding of multi-dimensional detonation instability may be obtained. The

cellular structures of real detonations, however, probably seem to be nonlinear phenomena beyond the range of such classical bifurcation studies, at least quantitatively.

REDUCED CHEMISTRY

Computations of detonation dynamics with full chemistry, employing reactive Euler equations with shock jump conditions, challenge computer capabilities for all but the simplest chemical systems. There is special interest in both hydrogen and acetylene as fuels because of their relative ease of detonation. The hydrogen chemistry has few enough steps that essentially full-chemistry detonation calculations can be done [2], but the acetylene chemistry does not. One detailed description of acetylene flame chemistry has 613 reversible elementary steps [4]. Practical calculations for acetylene need a shorter chemical description.

Table 1 suggests a short mechanism for acetylene detonations involving only 23 irreversible steps. Preliminary study indicates that this short mechanism should be sufficient for most acetylene detonation problems. The first 19 steps in this table are taken from earlier work [5]. The last 4, specific to acetylene, appear to be the most important ones from a recent study [4] and use the rate parameters given there, with the rate of the last step doubled to account for the addition path to $CO_2 + CO + H$. It would be interesting to see if the 23-step mechanism can be tested computationally. It may be remarked that the first 17 steps in Table 1 also could be employed for hydrogen detonations if some of the last 8 of these were allowed to be reversible. As it stands, Table 1 really contains only 18 steps, 5 of which are reversible.

From the viewpoint of systematically reduced chemistry, by use of steady states and partial equilibria [5], a two-step approximation can be good for hydrogen–oxygen, with a radical-consumption step, the reverse of which is initiation, and a chain-carrying oxygen-consumption step which is branching. It would be desirable if a corresponding two-step approximation could be developed for acetylene, but that does not appear to be possible. A three-step approximation for acetylene, however, seems attractive. Because of the 3 atom conservation relations among the 11 species, from a reduced-chemistry viewpoint the short mechanism in Table 1 is an 8-step mechanism. The production rates w_i of the 11 species, in terms of the elementary reaction rates ω_k of Table 1, are

$$w_{C_2H_2} = -\omega_{20} - \omega_{21}$$

$$w_{HC_2O} = \omega_{20} + \omega_{21} - \omega_{22} - \omega_{23}$$

$$w_{O_2} = -\omega_1 + \omega_2 + \omega_{11} - \omega_{12} + \omega_{14} + \omega_{16} + \omega_{17} - \omega_{20} - \omega_{23}$$

137

$$w_{CO_2} = \omega_{18} - \omega_{19}$$

$$w_{H_2O} = \omega_5 - \omega_6 + \omega_7 - \omega_8 + \omega_{10} + \omega_{15} + \omega_{17}$$

$$w_{CO} = -\omega_{18} + \omega_{19} + 2\omega_{22} + 2\omega_{23} \tag{11}$$

$$w_{HO_2} = \omega_{12} - \omega_{14} - \omega_{15} - \omega_{16} - \omega_{17}$$

$$w_{H_2} = -\omega_3 + \omega_4 - \omega_5 - \omega_6 + \omega_9 + \omega_{14}$$

$$w_{OH} = \omega_1 - \omega_2 + \omega_3 - \omega_4 - \omega_5 + \omega_6 - 2\omega_7 + 2\omega_8 - \omega_{10}$$
$$+ 2\omega_{13} + \omega_{16} - \omega_{17} = -\omega_{18} + \omega_{19} + \omega_{20} + \omega_{23}$$

$$w_H = -\omega_1 + \omega_2 + \omega_3 - \omega_4 + \omega_5 - \omega_6 - 2\omega_9 - \omega_{10} - \omega_{12}$$
$$- \omega_{13} - \omega_{14} + \omega_{18} = -\omega_{19} + \omega_{21} + \omega_{22}$$

$$w_O = \omega_1 - \omega_2 - \omega_3 + \omega_4 + \omega_7 - \omega_8 - 2\omega_{11} + \omega_{15}$$
$$- \omega_{16} - \omega_{21} - \omega_{22}$$

By introducing steady states for HC_2O, H, OH, HO_2 and H_2, as appropriate here, and making suitable truncations, the three-step mechanism

$$C_2H_2 + 2O_2 \rightarrow 2CO + H_2O + O \qquad\qquad I$$

$$2O \rightarrow O_2 \qquad\qquad II \qquad (12)$$

$$CO + \frac{1}{2}O_2 \rightarrow CO_2 \qquad\qquad III$$
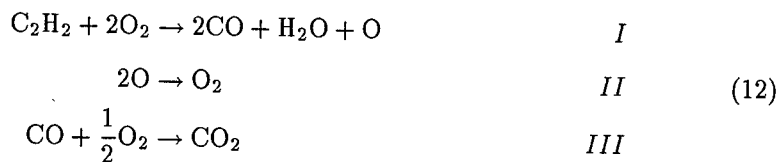
can be derived, having the respective rates

$$w_I = \omega_{20} + \omega_{21}$$

$$w_{II} = \omega_9 + \omega_{10} + \omega_{11} + \omega_{12} \tag{13}$$

$$w_{III} = \omega_{18} - \omega_{19}$$

In terms of the rate parameters listed in Table 1 and the concentrations $[i]$ of various species i, these rates can be written explicitly as

$$\omega_I = [C_2H_2]\left(k_{20}[O_2] + k_{21}[O]\right) \tag{14}$$

$$\omega_{II} = [M]\left(k_9[H]^2 + k_{10}[H][OH] + k_{11}[O]^2 + k_{12}[H][O_2]\right) \tag{15}$$

and

$$\omega_{III} = \left(\frac{K_1 K_2 k_{18}^3}{2K_3 k_{12}}\right)^{1/2} \frac{[H_2O]^{1/2}[CO]^{1/2}}{[M]^{1/2}}\left\{1 - \frac{k_{19}[CO_2]}{2k_{12}[M][O_2]}\right\} \tag{16}$$

Equilibrium constants appearing in these expressions are

$$K_1 = \frac{k_1}{k_2}, \qquad K_2 = \frac{k_3}{k_4}, \qquad K_3 = \frac{k_5}{k_6} \tag{17}$$

For ω_{II}, the concentrations [H] and [OH] are to be obtained from the shuffle partial equilibria

$$[H] = \left(\frac{K_2}{K_1^2 K_3}\right)^{1/2} \frac{[H_2O]^{1/2}[O]^{1/2}}{[O_2]}$$

$$[OH] = \left(\frac{K_2}{K_3}\right)^{1/2} [H_2O]^{1/2}[O]^{1/2} \tag{18}$$

It may be seen from step I of Eq. (12) that, unlike hydrocarbons, there is radical production rather than radical consumption associated with fuel consumption. This accounts for the much easier detonability of acetylene. The radical recombination step, step II, involves 3-body processes and is slower. The slow CO oxidation, step III, is obtained from our earlier work. It is because the CO oxidation is so slow and because it releases so much heat that the three-step description seems needed instead of only two steps. This 3-step description should readily be useable in computational studies of acelylene detonation dynamics. It may also fit into the earlier [3] general rate framework for investigating detonation stability.

CONCLUDING REMARKS

In general, it may be concluded from this work, that chemistry more complicated than the one-step Arrhenius approximation is needed to describe the stability and dynamics of real detonations. Suitable reduced chemistry for this purpose is becoming available.

ACKNOWLEDGMENTS

REFERENCES

1. Buckmaster, J., and Neves, J., *Physics Fluids*, **31**, 3571–3576, 1988.
2. Clavin, P., and He, L., *J. Fluid Mechanics*, **306**, 353–378, 1996.
3. Clavin, P., He, L., and Williams, F. A., *Physics Fluids*, **9**, 3764–3785, 1997.
4. Lindstedt, R. P., and Skevis, G., *Combustion Science Technology*, **125**, 73–137, 1997.
5. Williams, F. A., "Reduced Kinetic Schemes in Combustion," In: *Propulsion Combustion: Fuels to Emissions*. (Ed. G. D. Roy), Taylor and Francis, Washington, DC, 1997, 93–128.

FORMATION OF HIGH-SPEED GAS FLOW AT COMBUSTION IN THE REGIME OF MULTI-STEP DETONATION

D. I. Baklanov, L. G. Gvozdeva, and N. B. Scherbak

The conditions for formation of non-stationary complexes, consisting of shock waves and flame fronts, have been experimentally investigated in channels of variable cross-section. The mechanism of detonation formation after reflection of the non-stationary complex from a rigid wall is described. The arising detonation mode is called the Regime of Multi-Step Detonation (MSD). Experiments were made in a straight closed tube filled with hydrogen–oxygen–nitrogen mixture, and in an open duct, which narrows towards the outlet, filled with methane–oxygen mixture. In the latter case, the repeated mode of detonative combustion was obtained. The influence of the frequency of MSD origin on the concentration limits was investigated. A possibility of stabilizing MSD formation was considered by providing additional ignition of the combustible mixture. The influence of ignition location and timing between ignition and shock arrival at the ignition site, was investigated. For the setup used, the greatest effect was achieved in the case where the site of additional ignition was located 20 mm away from a converging part of the tube and ignition triggered 50 μs prior shock arrival. The investigations have been able to achieve MSD with a probability of 0.995 at a pulse repetition rate ranging from 0.5 to 10 Hz. The possibility of applying MSD mode in practice, e.g. in propulsion devices, is also discussed.

INTRODUCTION

Non-stationary explosion regimes can be generated by preliminary compression of a combustible mixture by a shock wave and subsequent ignition of the mixture to obtain detonation. The state diagram of this regime is shown in Fig. 1.

Initial state (pressure P_1) corresponds to point A_1. Shock compression results in transition from point A_1 to intermediate state A_2 (pressure P_2) along the shock Hugoniot H_1. The parameters of the detonation products relevant to point A_2 are defined by point C_2 on the detonation Hugoniot J_2. Pressure P_4

at point C_2 is higher than pressure P_3 at state C_1 lying on the detonation Hugoniot J_1. Point C_1 corresponds to the Chapman–Jouguet (CJ) parameters of the detonation wave propagating through the gas at initial pressure P_1, point A_1.

To initiate detonation, a non-stationary complex (consisting of a primary shock wave and a flame) for compression of a combustible mixture, and an additional (secondary) shock wave, which is to explode or detonate the combustible mixture precompressed by the primary shock wave, is necessary. This latter complex will be referred to as the Multi-Step Detonation (MSD).

MSD mode can arise during deflagration-to-detonation transition (DDT) in short tubes [1–3], or when a detonation wave propagates in channels of variable cross-section [4, 5]. As a result, very high abnormal pressure (P_4) can be attained, which is 2 to 6 times higher than the CJ pressure (P_3) of the initial combustible mixture. In the case of detonation in short tubes, the appearance of MSD mode has a stochastic character. For practical purposes, we study the MSD mode in channels of variable cross-section [6–8]. In this case, for obtaining MSD mode, the unsteady processes of detonation decay under diffraction and detonation reinitiation under shock reflection are used.

Figure 1 Hugoniots for different initial states of combustible gas. $A_1(P_1,\ V_1)$ — initial state, $A_2(P_2,\ V_2)$ — precompressed state, H_1 — initial shock Hugoniot, J_1 — initial detonation Hugoniot, H_2 — shock Hugoniot for precompressed state, J_2 — detonation Hugoniot for precompressed state, C_1 and C_2 — CJ points, A_1B_1, A_2B_2 — Rayleigh lines

SINGLE-PULSE MODE

Experimental Setup for Studying MSD Mode Formation

Experiments in a single-pulse mode were made in a detonation tube that consisted of cylindrical sections of different diameters (Fig. 2).

The pieces of tubes with diameters 8, 16, 64, and 83 mm were linked by conic transition elements with the expansion angle 16°. Average propagation velocities of detonation waves, shock waves and flame fronts were obtained by using the records of photo-diodes and pressure gauges, installed along the detonation tube. Ignition was triggered by a weak spark located at the closed end
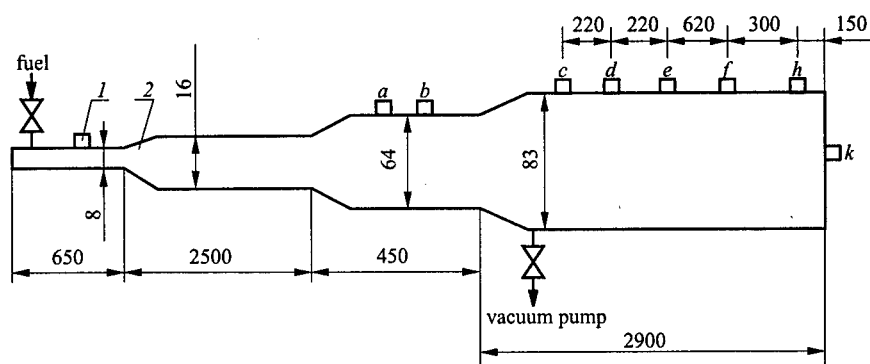
Figure 2 Detonation tube of variable cross-section (sizes in mm). *1* — ignition block, *2* — detonation chamber, *a–k* — pressure gauges and photo-diodes

of the 8-mm section. Hydrogen–oxygen–nitrogen mixtures, $2H_2 + \alpha(O_2 + \beta N_2)$, at initial pressures ranging from 50 to 100 kPa and temperature from 283 K to 293 K were used. Nitrogen-to-oxygen ratio β was varied from 0 to 3.64, and coefficient α was varied from 0.5 to 1. Hydrogen–air mixtures were also used. Hydrogen content in the hydrogen–air mixture was 29.6% or 37.2% (vol.); initial pressure was 80–110 kPa in this case. The gases were premixed in a special mixing device. The overall time given for the mixing has never been less than 24 hours. Before filling the detonation tube with a combustible mixture, it was evacuated to 100 Pa.

The waves arising in the detonation tube were identified by analyzing the records provided by photo-diodes and pressure gauges, which were mounted at the same cross-sections of the detonation tube (*a–k* cross-sections, Fig. 2) and operated simultaneously. Pressure gauges detected detonation and shock waves and did not respond to flame fronts. While photo-diodes responded to detonations and flame fronts, they were practically insensitive to shock waves due to the system of diaphragms placed in front of photo-diodes [6]. Thus, when a detonation wave passed the sensors, the data acquisition system simultaneously recorded the signals from a pressure gauge and a photo-diode (Fig. 3). When a shock wave passed the sensors, only a signal of a pressure gauge was recorded (Fig. 4). If the flame front passed the sensors, the signal was delivered only by a photo-diode. To find average velocities of the waves, identical sensors were mounted in different sections of the detonation tube. From the measured time intervals between the signals detected by sensors and known distances between the sensors, it was possible to determine average velocities of detonation waves, shock waves, and flame fronts. Besides, in the case of the MSD mode, the width

143
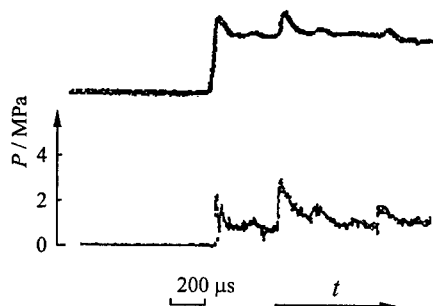
Figure 3 Calibration oscillogram of detonation wave propagation in $2H_2 + O_2$. Upper curve — luminosity record gauge, lower curve — pressure record. $P_0 = 70$ kPa
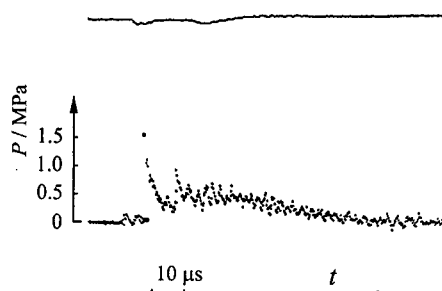
Figure 4 Calibration oscillogram of shock wave propagation in $2H_2+0.58(O_2+2.65N_2)$ mixture. Lower curve — pressure record, upper curve — luminosity record. $P_0 = 70$ kPa

of the MSD can be determined based on a measured time interval τ and a known shock wave velocity (Fig. 5).

Formation of MSD Mode in a Duct of Variable Cross-Section

The construction of the detonation tube allowed us to obtain (in the 83-mm tube) both the steady detonation wave, and the non-stationary complex consisting of shock waves and a flame front. Investigated in detail were $2H_2 + O_2 + 2.57N_2$, $2H_2 + 0.58(O_2 + 2.65N_2)$, 29.6% H_2 + air and 37.2% H_2 + air mixtures.

For hydrogen–oxygen–nitrogen mixtures, the non-stationary complex consisted of three shock waves and a flame front (Fig. 5). For hydrogen–air mixtures, the non-stationary complex consisted of two shock waves and a flame front (Fig. 6). In the latter case, the whole 8-mm tube and a part of the 16-mm tube were filled with the stoichiometric hydrogen–oxygen mixture, and the decoupling of the detonation wave did not happen during its transition from the 8-mm tube into the 16-mm tube.

The appearance of a non-stationary complex was due to decoupling of detonations during diffraction and due to reflection of retonation waves from the closed end of the 8-mm section. It was established, that during DDT in the 8-mm section, filled with $2H_2 + 0.58(O_2 + 2.65N_2)$ mixture at $P_0 = 70$ kPa, detonation was formed. A retonation wave, arising in the tube, propagated into combustion products towards the ignition site. After reflection of the retonation wave from the end wall of the 8-mm section, a secondary wave formed and propagated be-

144
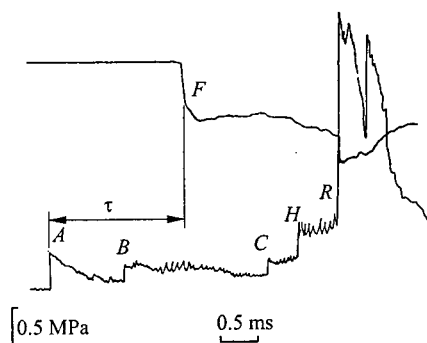
Figure 5 Luminosity (upper curve) and pressure (lower curve) records of propagating MSD regime in the 83-mm tube (cross-section d in Fig. 2). $P_0 = 70$ kPa. $2H_2 + 0.58(O_2 + 2.65N_2)$ mixture is ignited in 8-mm tube
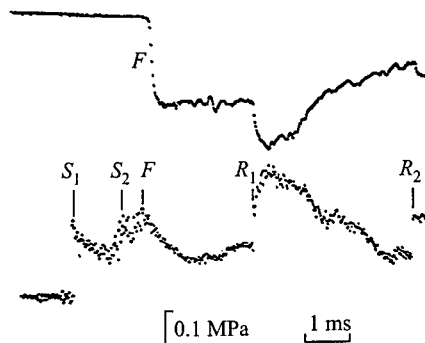
Figure 6 Typical luminosity (upper curve) and pressure (lower curve) oscillograms in the cross-section d (Fig. 2) of the 83-mm section at appearance of detonation during propagation of MSD regime. $P_0 = 100$ kPa, 29.6% H_2 + air mixture

hind the detonation wave. It is the shock wave B in Fig. 5. During transition from the 8-mm section to the 16-mm section, the detonation wave decoupled to a shock wave and a combustion front, and then, after some time, reinitiation of detonation occurred. As a result, new detonation and retonation waves were formed in the 16-mm section. This new retonation wave was a reason for the second shock wave C (Fig. 5) arising due to reflection of the retonation wave from the closed end of the 8-mm section. During transition into the next section of diameter 64 mm, the detonation wave decoupled again to a shock wave A and a combustion front F, and such a configuration moved into the 83-mm section. As a result, the primary shock A, the secondary shock B, the flame front F, and the secondary shock C (Fig. 5) propagated through the 83-mm section. In the case when ignition of combustible mixture occurred in the 16-mm section, or in the case of H_2 + air mixture, the pressure transducers in cross-sections c, d, e and f (Fig. 2) detected a system of two shock waves S_1 and S_2, and the flame front F (Fig. 6).

Formation of High Pressure Flows in the Case of MSD in a Single-Pulse Mode

During transition to detonation and reflection of the unsteady complex, the flows with high dynamic parameters can form. Characteristic conditions for the deton-

145
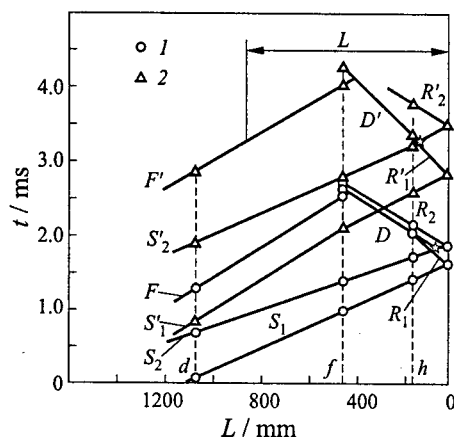
Figure 7 X–t diagram of shock waves and flame front propagation in the second half of the 83-mm section. $P_0 = 100$ kPa, 29.6% H_2+air mixture, ★ — place of detonation formation. 1 — $M_s = 1.67$; 2 — $M_s = 1.42$

ation onset behind the reflected shock wave have been established for all the mixtures considered. It was found, that the location of the detonation origin is determined by the position of a point where reflected shock waves R_1 and R_1' collide with the secondary shocks S_2 and S_2' (Fig. 7). At the moment of collision of the waves, flame fronts F and F' should be at a distance L from the end-wall, which does not exceed a certain limiting value. This distance should not exceed 1.3 m for the case when three shock waves propagate in the 83-mm tube filled with $2H_2 + O_2 + 2.57N_2$ mixture, and when the velocity of the first shock varies within the range $M_s = 1.52$–1.7. For $2H_2 + 0.58(O_2 + 2.65N_2)$ mixture, this distance should not exceed 1.1 m (with $M_s = 1.1$–1.6). For 29.6% H_2+air mixture, $L \leq 1.4$ m (with $M_s = 1.43$–1.54). For 37.2% H_2 + air mixture, $L \leq 1.2$ m (with $M_s = 1.4$–1.67). If the distance from the flame front to the collision site of the waves exceeds the limiting value, the transition to detonation does not occur. This fact indicates the significant role of the turbulent flame front in generating compression waves, which influence the detonation onset. The intensity of the colliding shocks is not sufficient for igniting the combustible mixture.

The pressure measured in the case of MSD mode was compared with the CJ detonation pressure. CJ detonation was obtained during the transition of detonation from the 64-mm tube to the 83-mm tube. To produce CJ detonation in the 83-mm tube, the main part of the 64-mm tube was filled with a stoichiometric hydrogen–oxygen mixture. At initial pressure of 70 kPa, the pressure attained at the detonation front in $2H_2 + 0.58(O_2 + 2.65N_2)$ mixture was 1.3 ± 0.1 MPa. For comparison, in the case of MSD mode, pressure amplitudes behind the developed detonation wave (at a distance 150 mm from the end-wall of the 83-mm tube) were 4.0 ± 0.2 MPa.

For the case of MSD mode in 29.6% H_2 + air mixture at initial pressure of 100 kPa, pressure amplitudes behind the developed detonation wave (at a distance of 150 mm from the end-wall of the 83-mm tube) were 4.2 ± 0.2 MPa. For the case of CJ detonation, these values were less than 1.4 MPa at similar initial conditions.

As a result of the experiments, it was found that the unsteady complex, consisting of shock waves and a flame front, can be generated under subcriti-

146

Figure 8 Detonation chamber of variable cross-section: *1* — supply manifold for fuel and oxidizer; *2* — ignition unit; *3* — precombustion chamber; *4* — adapter; *5* — main chamber; *6* — amplification unit; *7* — overdriven detonation channel; *8* — bypass channel; *9* — flow controller; *a–l* — measurement stations

cal conditions of detonation propagation in a channel of variable cross-section (during transition from a tube of smaller diameter to a tube of larger diameter). The formation of detonation behind reflected shocks is possible in the presence of a turbulent flame, in spite of the fact that the temperature of the combustible mixture is lower than the ignition temperature. Parameters of the developed detonations were significantly higher than those of the CJ detonation.

REPEATED MODE

To use the MSD concept in practical applications, it is necessary to arrange a repeated mode of generating the MSD regime. Such experimental studies were performed in a detonation chamber (DC) of variable cross-section (Fig. 8) for $CH_4 + 2O_2$ mixture with pulse frequency 0.5–10 Hz. The range of the oxygen access coefficient, $\alpha = Q_{O_2}/(2Q_{CH_4})$ was varied from 1 to 1.8. The aim of the experiments was to determine the parametric region of the MSD mode. The bypass channel (*8*) and controller (*9*) were absent at this stage of experimentation.

Depending on mixture composition, the detonation in the main chamber occurred either in the CJ or in MSD mode. For methane–oxygen mixtures with $\alpha < 1.2$, detonation occurred in the main chamber with the average prop-

agation velocity in the last section $D = 2300 \pm 20$ m/s (for $\alpha = 1$), and $D = 2280 \pm 30$ m/s (for $\alpha = 1.2$). The range of α from 1.2 to 1.4 appeared to be relevant to transient processes. At $\alpha = 1.2$, in most cases, the detonation wave emerged into the main chamber. However, sometimes this did not occur, and the MSD mode was observed along the entire length of the main chamber. At $\alpha \geq 1.4$, MSD mode was characteristic along the entire length of the main chamber, and this fact was a requisite condition for the emergence of the MSD mode. At $\alpha \geq 1.8$, the non-stationary complex occurred in the main chamber, while the MSD mode was not realized. In this case, the pressure in the shock wave was less than 1.0 MPa, while the average propagation velocity at the inlet up to the amplification unit was $W_S' < 800$ m/s. Therefore, the concentration limit of the MSD mode existence in the DC of variable cross-section was in the range of $1.4 \leq \alpha \leq 1.8$, when using methane–oxygen mixtures.
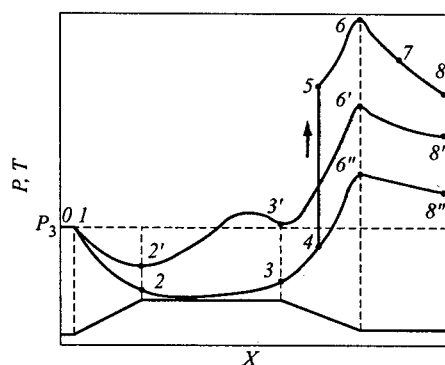
Figure 9 Gas pressure P and temperature T at the shock wave front averaged over the channel cross-section

These processes can be described in a one-dimensional approximation. Consider the process of MSD mode formation (Fig. 9). The detonation wave gets out of the prechamber (curve section 0–1) and, when propagating through the divergent part, transforms into the MSD mode consisting of a shock wave and combustion front (1–2). This process first occurs near the channel walls and then propagates to the channel axis. The parameters of a combustible mixture behind the shock front decrease continuously along the entire length of the divergent part. When the MSD mode enters the main chamber, its intensity (propagation velocity) rises initially due to reflection of the shock wave from the channel wall, and then due to acceleration of the flame front (2–3). The width of the MSD mode increases during the motion in the main chamber, because the shock velocity exceeds that of the flame front. The parameters of the combustible gas behind the shock wave start to increase.

Further increase in the thermodynamic parameters of the gas in the shock front is due to the Mach reflection of the shock wave in the amplification unit (3–4). The shock-compressed gas heats up to the self-ignition temperature and explodes, so that a detonation wave is generated (4–5). At first, the detonation wave propagates in the precompressed combustible mixture (5–6–7), then overtakes the shock wave (point 7) and further propagates through the undisturbed gas as an overdriven detonation (7–8). The distance travelled by the detonation wave, before it overtakes the shock wave, depends on the propagation velocities

148

Table 1 Gas flow parameters for the MSD and detonation processes in the detonation chamber initially filled with the methane–oxygen mixture

α	P_2 MPa	P_5 MPa	P_2 MPa	W'_S m/s	W_S m/s	D m/s	Remark
1.8	1.2 ± 0.1	3.9 ± 0.5	3.9 ± 0.3	1010 ± 100	2550 ± 200	2130 ± 30	MSD
1.6	1.3 ± 0.5	3.8 ± 0.5	4.7 ± 0.5	1120 ± 70	2800 ± 300	2170 ± 30	MSD
1.4	1.5 ± 0.1	4.0 ± 0.4	5.0 ± 0.5	1200 ± 80	2750 ± 200	2250 ± 30	MSD
1.4	3.0 ± 0.2	1.3 ± 0.07	3.2 ± 0.1	2240 ± 30	2470 ± 40	2250 ± 30	Det.
Point	f	f	h	L_{g-f} 151 mm	L_{h-l} 62 mm	L_{a-b} 240 mm	

of these waves relative to each other and on the initial distance between them. The detonation wave is subject to Mach reflection in the convergent channel (5–6), and thus the gas parameters behind it increase continuously. When the detonation wave reaches the channel of constant cross-section, it weakens, and the parameters of the detonation products decrease (6–8).

In the MSD regime described above, the gas parameters averaged over the cross-section of the DC channel are represented in Fig. 9 by curve 0–1–2–3–4–5–6–7–8. The parameters of the detonation products, when a detonation wave is produced in the main chamber and amplified in the convergent channel, are given by the curve 0–1–2'–3'–6'–8'. Curve 0–1–2–3–4–5–6''–8'' characterizes the gas parameters in the absence of explosion or detonation in the amplification unit behind the incident shock wave. This pattern is observed when the incident shock wave is relatively weak.

Table 1 presents the gas flow parameters for the MSD and detonation processes in the DC, when methane–oxygen mixtures are used. Here, P_2 is the pressure at the front of the incident shock in the respective cross-section, P_5 is the pressure at the front of the reflected shock that comes to the given section from a convergent channel, W_S is the shock velocity, and D is the detonation velocity. The significant increase of pressure P_5 in all MSD regimes, in comparison with the detonation regime is evident.

Stability of MSD in the Repeated Mode

When the MSD is accomplished in the DC, operating in the repeated mode, the concentration limits of MSD existence become narrower.

The major factor affecting the stability of MSD initiation is the variation of the detonation intensity. During operation in the repeated mode, the tempera-

ture of the combustible mixture at the wall increases and, consequently, a drop in mixture density occurs. This process is similar to the addition of an inert gas to the combustible mixture, therefore, the detonation intensity decreases. For example, in the case of detonation in a stoichiometric methane–oxygen mixture under natural cooling of the DC walls, the wall temperature increased from 298 K to 600 K. This caused a reduction in the detonation velocity from 2290 to 2238 m/s and in the pressure drop from 3.0 to 2.4 MPa in the precombustion chamber at $\alpha = 1.2$. It was found, that no MSD was initiated during the first pulses. In this case, the detonation wave always reinitiated in the main chamber, after diffraction in the adapter with the angle of 16°. The detonation velocity about the reinitiation site exceeded that of stationary detonation. Thereupon, the detonation wave slowed down and reached the stationary mode. In subsequent pulses, after diffraction, the detonation wave sometimes failed to be reinitiated in the main chamber, and the MSD emerged.

The simplest engineering solution for stabilizing the MSD mode generation involves the scheme with splitting the detonation wave. In this case, the DC is additionally fitted with a bypass channel (Fig. 8, point 8) and a flow controller (Fig. 8, point 9). One end of the bypass channel was joined to the precombustion chamber, and the other was joined to the main chamber or the amplification unit. A detonation wave was transferred via the bypass channel to the detonation chamber. It was timed with the passage of the shock wave through the given section by selecting the length of the bypass channel, according to the formula

$$H = D(t + \delta t)$$

where H is the length of the bypass channel, D is the detonation velocity, t is the time interval between the entry of detonation into the bypass channel and the arrival of the shock wave to the point where detonation leaves the bypass channel, and δt is the time of mismatch. This modification is equivalent to arranging an additional ignition source in the system.

The effects of location of this ignition on the emergence of the MSD mode, as well as the time shift between the moment of ignition and the arrival of shock to the given section, were studied.

As was shown by the investigations, the ignition at a distance of 5 to 30 mm before the amplification unit was most effective. In this case, the shock wave generated by detonation was enhanced during its propagation in the convergent channel, and effectively precompressed the combustible mixture. Ignition of the mixture at a distance larger than 30 mm from the beginning of the amplification unit resulted in burning a considerable amount of mixture prior to the initiation of explosion. In this case, the combustible mixture was strongly diluted by combustion products and impaired the detonability of the mixture. As a result, weak detonation waves formed or no detonation developed.

The effect of an additional ignition source on stabilizing the MSD mode was studied in two cases: ignition in front and behind the shock wave. In case the gas was ignited behind the shock wave, the flame front was convected downstream. The parameters of shock-compressed combustible gas decreased with time; therefore, the longer the time interval between the passage of the shock wave and ignition, the more additional energy needs to be delivered into the gas in order to attain the required explosion parameters. When ignition was delayed above 300 μs, additional ignition did not result in higher probability of generating the MSD mode. According to the experimental data, the greatest effect was attained when the additional ignition was triggered 50 μs prior to the arrival of the shock wave.

CONCLUDING REMARKS

1. As a result of experimental investigations, the peculiarities of formation and propagation of detonation in channels of variable cross-section were determined for hydrogen–oxygen–nitrogen and hydrogen–air mixtures. The mechanism and conditions of formation of the MSD, consisting of shocks and the flame front, were revealed.

2. The probability of the MSD onset under propagation of detonation in channels of variable cross-section is much higher, than under propagation of detonation in channels of constant diameter. It was shown, that the MSD mode results in a significant pressure rise in comparison with the detonations.

3. Experimental studies were performed in a DC of variable cross-section for $CH_4 + 2\alpha O_2$ mixture with pulse frequency of 0.5–10 Hz. It was found, that the pressure in the MSD was higher than in the detonation regime. The concentration limit of the MSD mode existence in a DC of variable cross-section was within the range of $1.4 \leq \alpha \leq 1.8$, when using methane–oxygen mixtures.

4. At the repeated mode of generating detonation waves, the concentration limits of the MSD origin are narrower in comparison with a single-mode generation of detonation waves. The compensation of this negative effect may be achieved by providing additional ignition of the combustible mixture, for example, by splitting the main detonation wave.

5. Current investigations show a possibility to apply the MSD mode for practical purposes, in particular, the aircraft engine, to realize an effective conversion of fuel energy into the kinetic energy of aircraft flight.

REFERENCES

1. Kogarko, S. M., "Investigation of Pressure at the Tube End During Unsteady Rapid Combustion," *Physics — Technical Physics*, **38**, 9, 1875, 1958.

2. Chan, C. K., and Dewit, W. A., "Deflagration to Detonation Transition in End Gases," *Proc. 20th ISWW*, GALCIT, Pasadena, 1995, 403.

3. Dorofeev, S. V., Kochurko, A. S., Sidorov, V. P., Bezmelnitsin A. V., and Breitung, W. M., "Experimental and Numerical Studies of the Pressure Field Generated by DDT Events," *Int. J. Shock Waves*, **5**, 375, 1996.

4. Baklanov, D. I., Gvozdeva, L. G., Davydov, A. N., Lagutov, Y. P., Sharov, Y. L., and Scherbak, N.B., "Anomalous High Pressure Regions in Propagation of Detonation Waves in a Channel with Variable Cross-Section," *Proc. Symposium (International) on Hazards, Prevention and Mitigation of Industrial Explosions, Second Specialist Meeting (International) on Fuel–Air Explosions*, Christian Michelsen Research Institute, Fantoft, Norway, 1996.

5. Teodorczyk, A., and Thomas, G. O., "Experimental Study of Flame Acceleration in Tubes and Implication for Testing Explosion Arrestors," *Proc. Symposium (International) on Hazards, Prevention and Mitigation of Industrial Explosions, Second Specialist Meeting (International) on Fuel–Air Explosions*, Christian Michelsen Research Institute, Fantoft, Norway, 1996.

6. Baklanov, D. I., and Gvozdeva, L. G., "Non-Stationary Processes of Burning in Detonation Waves Propagating Inside the Channels of Variable Cross-Section ," *Rus. J. High Temperature*, **33**, 6, 958–961, 1995.

7. Baklanov, D. I., and Gvozdeva, L. G., "An Influence of a Supplementary Ignition on the Stability of the Appearance of a Double Non-Stationary Discontinuity Mode in Combustion Chambers," *Rus. J. High Temperature*, **34**, 2, 1–4, 1996.

8. Baklanov, D. I., Gvozdeva, L. G., and Scherbak, N.B., The Formation of High Pressure Gas Flow in Frequency Mode During Non-Stationary Propagation of Detonation, AIAA Paper No.98-2562, 1998.

SIMULATION OF DETONATION CELLS IN WIDE CHANNELS

M. Nikolic, D. N. Williams, and L. Bauwens

Experiments indicate that relevant aspects of the propagation of detonations are related to the "natural" cell size. However, from the standpoint of analysis and computational studies, the well-posedness of the cell-size concept is not so clear. Until recently, even two-dimensional computations could only be performed in narrow domains. Thus, resulting in a cell width that adapts to the domain, with half a cell across as a minimum. Wider computations show that cells which appeared regular and periodic in narrow computations become irregular, given a sufficiently wide domain. Since the cell size varies, whether the concept of cell size is indeed well-posed or not, is unclear, except for mixtures exhibiting a very regular structure. Additionally, the number of cells obtained in given domain widths, hence their size, retains a strong dependency upon the initial conditions for a very long time. On the other hand, the average size obtained in wide channels has a very consistent value. The value is independent of the width of the channel and of the initial conditions, making it quite predictable. Finally, a convergence analysis shows that the grid resolution used is adequate, since the conclusions remain unchanged as the grid is refined.

INTRODUCTION

In contrast with inert shocks, which can be described by a Riemann problem, dimensionally, for detonations in open space, i.e., in a domain much larger than other length scales, the chemistry provides a time scale which, combined with the speed of sound, results in a characteristic length. But because the activation energy is typically high, the chemical time- and length scales will be very different, depending upon the value of temperature that is used when calculating the reaction rate. Global measures can be obtained from a ZND solution. But when a simple chemical model is used, such as a single-step Arrhenius model with complete chemistry, the time and length to completion become infinite. Instead, the half reaction length and time, based on the point where one half of the critical

reactant has been consumed, are often used. However, there is no easy way to measure the half reaction length. Furthermore, its value is typically an order of magnitude smaller than the size of the cells observed on smoke foils, which is a very obvious scale that is easy to measure experimentally. Thus, it was natural to present experimentally obtained "dynamic detonation parameters" correlated to the cell size measured on smoke foils [1, 2], taken as the obvious characteristic length. In particular, the critical tube diameter and its relation to cell size have been extensively studied experimentally, and predictive empirical relationships have been proposed [3, 4].

As long as experiments yield regular cells, the concept of cell size may appear to be a reasonable measure of the overall characteristic length. But this is of little help for mixtures yielding irregular structures. Assuming that regular cell sizes provide a meaningful length scale larger than the chemical time, some equivalent would be needed for irregular cases.

Computations provide a convenient tool for studying the relationship between cell topology, chemistry and other parameters. But, most computations so far have been limited to domain widths that yield a single cell. In this case, the computation effectively adds an extra length scale and the cell size becomes the width of the domain [5–12]. Still based upon narrow channels, one could envision alternate definitions of the cell size resulting from the following procedure: Starting from a computational domain which yields half a cell across the channel, the width is gradually increased until one full cell appears. Then the width is further increased until one and a half cells appear, and so forth. Or, an alternative approach would be to decrease the channel width until the half cell disappears completely. But the results below show that switching is too unpredictable for an alternate definition based upon switching to make sense. On the other hand, recognizing that the cells will be irregular for most mixtures, one can always introduce an average size which, in computations, equals the width of the domain divided by the number of cells across, which remains constant. The results show that the average size is very predictable.

Finally, the effect of resolution has been assessed, using up to forty meshes per half reaction length. This is because in the regions where temperature is high, the chemical scales become small [8] and a resolution that appears satisfactory elsewhere becomes locally very coarse.

PHYSICAL AND NUMERICAL MODEL

The flow is simulated using the reactive Euler equations. The fluid is an ideal gas with constant specific heats, molecular weight and heat of reaction. Diffusion of heat, mass and momentum is neglected. Chemistry is modelled by the one-step

154

Arrhenius law. The initial condition is a one-dimensional ZND detonation to which a perturbation is added. The unburned mixture enters the computational domain at steady, overdriven ZND detonation velocity with no reflection at the outflow. Free slip boundary conditions are imposed on the sides of the domain. Dimensionally, this problem is characterized by the ratio of specific heats γ, the dimensionless heat release Q, the dimensionless activation energy E^0 and the overdrive parameter f.

A fractional step, direction-split numerical method was used based upon the flux corrected transport algorithm [13–14]. This method is second order accurate in space and time and it has proven to be quite successful for detonations [8–12, 15–18]. The time steps are based upon a maximum Courant number of 0.4.

RESULTS

The case corresponding to the dimensionless parameters $f = 1.2$, $Q = 50$, $E = 10$ and $\gamma = 1.2$ was considered. This case has been widely studied in one, two and three dimensions [6–8, 10, 12], but only in narrower channels in which the cells appeared regular. This dimensionless case corresponds approximately to low pressure mixtures of hydrogen–oxygen, diluted with 60% to 80% of Argon or Helium. It yields a fairly complex cell structure corresponding to a longitudinally stable, yet transversally unstable ZND wave [6, 7, 19]. The numerical parameter varied was the width of the computational domain, i.e. the channel width L_y perpendicular to the flow direction. The channel width L_y has been made dimensionless with respect to the chemical half-reaction length for the ZND-wave, $L_{1/2}$. The initial conditions correspond to the one-dimensional ZND-solution, on which a density perturbation was superimposed. The perturbations which were used consisted of one half sine wave, referred to as perturbation mode one, and one full sine wave, referred to as perturbation mode two, in the transverse direction, at the shock. The half-wave is antisymmetric about the centerline, while the full wave is symmetric. Uniform resolutions of 20 and 40 grid points per $L_{1/2}$ were used, in both the longitudinal x- and the transverse y-direction simultaneously. Obviously, to maintain the same Courant number at the higher resolution, the time step is halved so that the number of time steps and the sizes of the two-dimensional computation double. Hence, the CPU time increases by a factor 8.

The initial perturbation develops into the characteristic fish scale pattern and the computation is continued until, after a stabilization phase, the cells reach a more or less periodic regime. The results shown correspond to that regime. Initially, all computations were performed with perturbation mode two at the lower resolution, with results shown as numerical smoke foils on Fig. 1. The
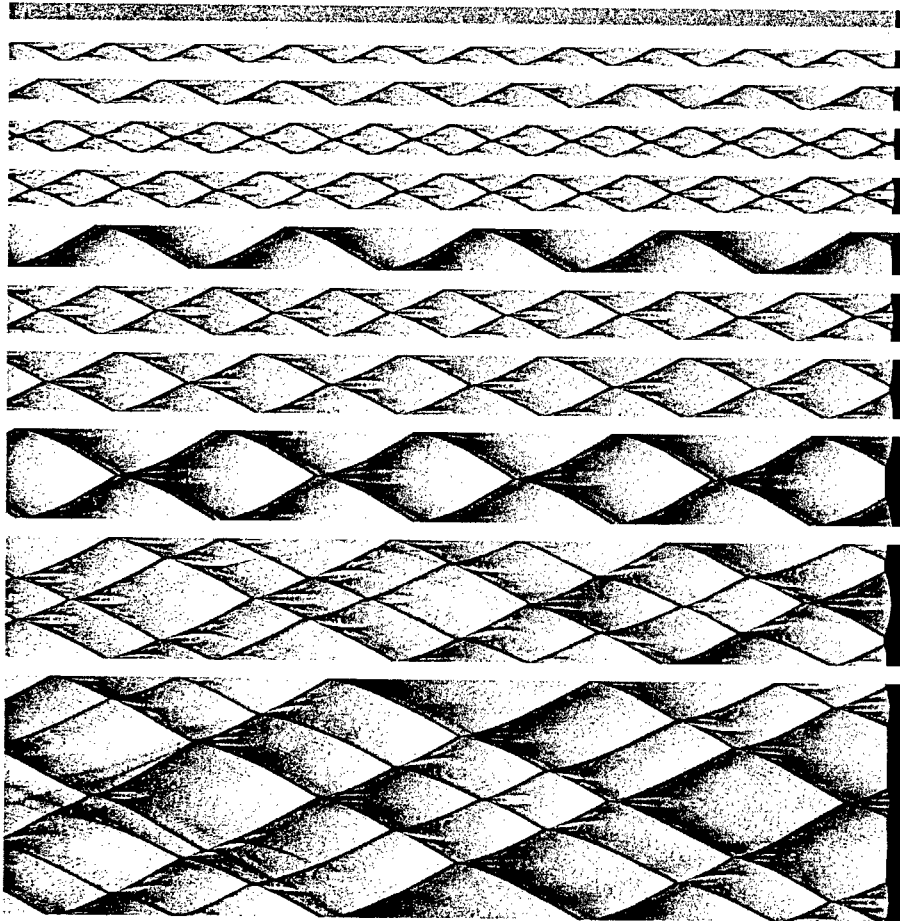
Figure 1 Numerical smoke foils for a increasing sequence of computational widths, equal to, from top, 2.95, 3, 4, 5, 6, 7, 8, 10, 15, 20 and 40 half reaction lengths. Results for perturbation mode two, lower resolution

channel width was varied, from one-half to 100 times $L_{1/2}$. As expected, no cell was observed for very narrow channels and fairly irregular cells appeared for larger domains. For perturbation mode two, the transition from no cells to half a cell occurs for a width between 2.95 and 3 times $L_{1/2}$ and the transition from half a cell to one full cell occurs between 4 and $5L_{1/2}$. For widths up to $15L_{1/2}$, one full cell appears and for $20L_{1/2}$, two full cells are observed. The channel width of 40 times $L_{1/2}$ produces 3 full cells across. For perturbation mode one, channel widths were varied between 1.4 and 100 times $L_{1/2}$
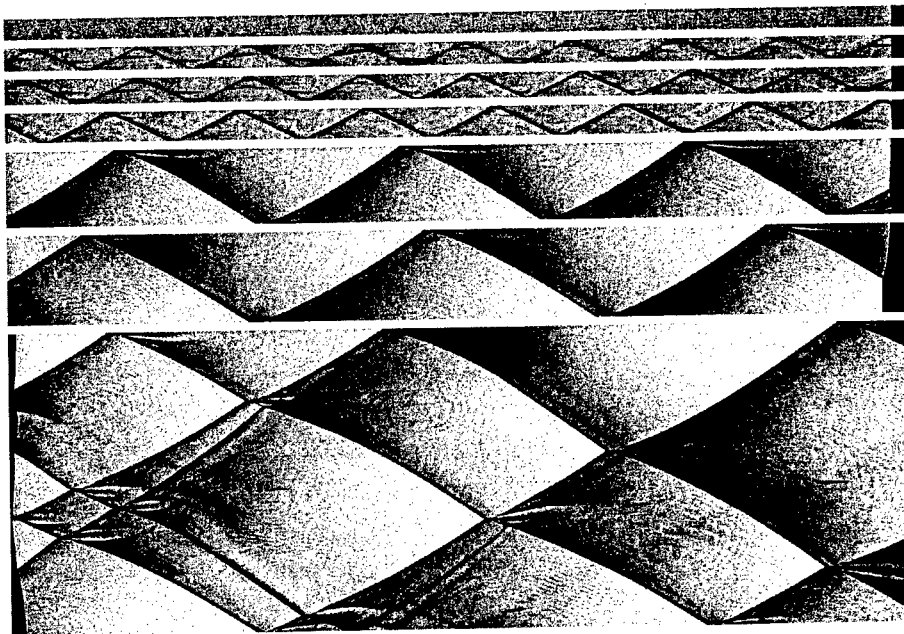
Figure 2 Numerical smoke foils for computational widths equal to 1.4, 1.5, 1.6, 2, 5, 6 and 20 half reaction lengths, perturbation mode one, higher resolution

at the lower resolution, but only up to 10 times $L_{1/2}$, and then for 20 times $L_{1/2}$. High resolution results are shown on Fig. 2 and low resolution results on Fig. 3, except for the $100L_{1/2}$ wide channel, which is shown separately on Fig. 4. At both resolutions, half cells started appearing between 1.4 and 1.5 times $L_{1/2}$ and the transition to a full cell in the channel width did not occur until the width was increased to 6 times $L_{1/2}$. Finally, to illustrate the overall procedure, Figs. 5 and 6 show complete smoke foils corresponding to the entire computation.

Overall, no significant differences were noted between the two resolutions. Qualitatively, at higher resolution, the small ripples observed on the numerical smoke foils are less noticeable, because they are more closely spaced and of smaller size. These ripples result from an interaction between the grid and the leading shock, which is close to parallel to the grid and in relation to which it only moves slowly. This results in a staircasing effect, with the shock aligned with the grid over some distance, and then, jumping to the next grid line, with which it remains aligned for a while etc. The ripples correspond to these points where the shock jumps from one grid line to the next. Otherwise, as expected,

157
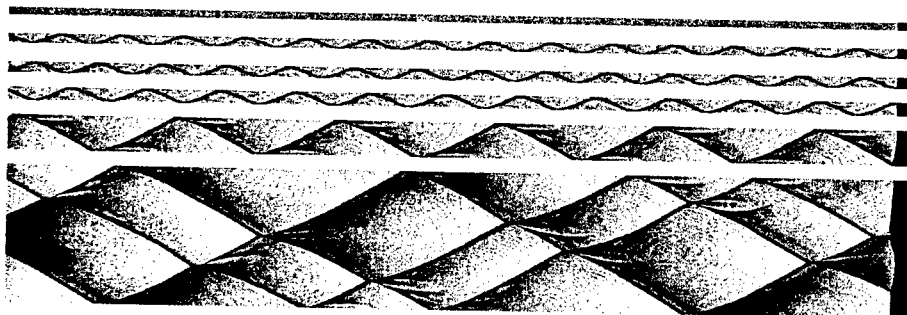
Figure 3 Numerical smoke foils for computational widths equal to 1.4, 1.5, 1.6, 2, 5, and 20 half reaction lengths, using perturbation mode one, lower resolution
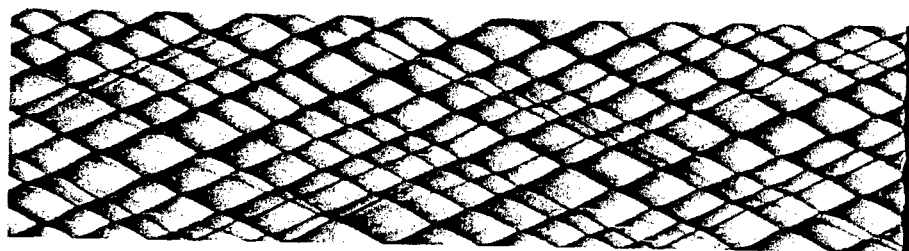
Figure 4 Numerical smoke foils for computational widths equal to 100 half reaction lengths, mode one, lower resolution

the cell boundaries are sharper and better defined at higher resolution. Some finer details become clearer, especially for the very narrow channels (e.g. 1.6 times $L_{1/2}$), which are made up of a smaller number of grid points across. In wide channels, merging and splitting of cells becomes very clear, although this did occur at low-resolution also.

DISCUSSION

For perturbation mode two, a minimum cell width of approximately 6 times $L_{1/2}$ is consistently observed in narrow channels. But as the width increases, the cells adopt a larger size of approximately 14 times $L_{1/2}$. As the result for the width of $7L_{1/2}$ shows, it appears there is a range of favored sizes and that
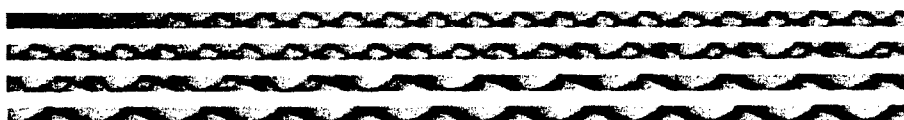
Figure 5 Entire computation, starting from perturbed ZND solution (on left); width of 7 half reaction lengths, perturbation mode two, lower resolution

Figure 6 Entire computation, starting from a perturbed ZND solution (on left); width of 40 half reaction lengths, perturbation mode two, lower resolution

the actual size eventually reached may well depend upon seemingly insignificant events, that occurred early in the process of development. However, once a given pattern becomes well-established, it appears to be stable, even though it is not necessarily the preferred one.

For perturbation mode one, the results show a smaller minimum cell size of approximately 3 times $L_{1/2}$ in narrow channels, increasing to around 13 times $L_{1/2}$ in wider channels. But in this case, as one increases the width, initially, the half-cell appears simply to grow larger. For a width of $20L_{1/2}$, one and a half cell is observed, which is close to the average value in wide channels.

The crucial difference between the two perturbation modes is that mode one allows for much smaller cells. Since perturbation mode one is made up of half a sine wave, its topology is much closer to the half-cell. Mean while mode two, a full sine wave, is symmetric about the centerline, just like full cells. Thus, it is not surprising that mode two exhibits a tendency toward preferentially exciting a full cell, as noted on Fig. 1, and widths of 5 and $6L_{1/2}$. From this perspective, perhaps it is these two results that should be seen as an anomaly, instead of the channel width of $7L_{1/2}$, which corresponds roughly to the equilibrium cell size of $14L_{1/2}$. In contrast, mode one has no difficulty in triggering a half-cell, even in very narrow channels, in which the cell barely survives and the mode two perturbation would be quickly damped. A similar effect is noted for a channel width of $20L_{1/2}$, for which mode one yields one cell and a half across, while mode two produces two cells across.

The results in wide channels are interesting in another respect. Indeed, for the first time, irregular cells are observed for the conditions under study. As shown in previous computations for $f = 1.2$, $Q = 50$, $E = 10$ and $\gamma = 1.2$ [6–8, 10, 12], computational domains that accommodate only half a cell, or one full cell, yield regular, fully periodic smoke foils. Then, the cell size is obviously determined by the width of the domain. But, the current results show that as soon as the domain width allows for one and a half cell across, the cells become irregular and periodicity is lost. In relatively narrow channels, that can only accommodate a cell and a half, the number of cells across the channel still remains constant as time is progressing, while their size fluctuates. But for larger widths, periodic appearance and disappearance occurs; this is clear on Fig. 4, and even in the much narrower computation for $20L_{1/2}$ on Fig. 2. Appearance and disappearance seem to be controlled by the dynamics of the triple point motion and reflection at the side boundaries of the computational domain. The process appears to have a long memory, with a behavior largely controlled by the initial conditions. The irreversibilities behind the leading shock do not appear to play a significant role. Thus, the behavior is consistent with the propagation modes predicted by shock dynamics models [20].

As for the issue of cell size, clearly, the minimum size that appears in narrow channels is much smaller than the typical sizes obtained in wide channels. On the other hand, some sort of a preferred average size is quite apparent in the results, with, in this case, a value of approximately 13 to 14 half reaction lengths. This size is reached consistently in sufficiently wide channels, regardless of the perturbation mode and of the resolution used. In most cases, as long as the perturbation mode exhibits an adequate symmetry to trigger the preferred mode, this also appears to be the size at which, in most cases, the switch from $N/2$ to $(N + 1)/2$ cells across the channel occurs. Unfortunately, this switch is not very consistent.

CONCLUDING REMARKS

The multi-dimensional detonation cell size has been investigated numerically in narrow and wide channels, including a resolution analysis that showed the following conclusions to be grid-independent.

The results show that, at least for moderately irregular cells, a predictable average size is obtained in wide channels. This vindicates the concept and provides a measure of the "natural" cell size. Furthermore, it appears that, normally, the transition from one half cell to a full cell, from a full cell to a cell and a half etc. occurs approximately when the channel width is increased to

the point where it allows for an additional half cell, with all cells of the natural size. However, this transition does not occur in a predictable manner, but clearly depends upon the initial perturbation, which has to contain a sufficiently strong component at the appropriate frequency. Unfortunately, this may well make an approach based upon finding transition widths too unpredictable to be useful.

REFERENCES

1. Lee, J. H. S., *Annual Review Fluid Mechanics*, 311–336, 1984.
2. Lee, J. H. S., In: *Gaseous and Dispersed Media*. (Ed. A. A. Borissov), Kluver, Amsterdam, 1991.
3. Moen, I. O., Sulmistras, A., Thomas, G. O., Bjerketvedt, D., and Thibault, P. A., *Proc. 10th ICDERS*, Berkeley, CA, 1985.
4. Moen, I. O., Funk, J. W., Ward, S. A., Rude, G. M, and Thibault, P. A, *Progress in Astronautics and Aeronautics Ser.*, **94**, 55–79, 1985.
5. Moen, I. O., Funk, J. W., Ward, S. A., and Rude, G. M., *Proc. 9th ICDERS*, Poitiers, France, 1983.
6. Bourlioux, A., and Majda, A. J., *Combustion Flame*, **90**, 211–229, 1992.
7. Bourlioux, A., and Majda, A. J., *Phil. Trans. Royal Society London. A*, **350**, 29–68, 1995.
8. Quirk, J. J., In: *Combustion in High-Speed Flows*. (Eds. J. Buckmaster *et al.*), 575–596, 1994.
9. Williams, D. N., Bauwens, L., and Oran, E. S., *Int. J. Shock Waves*, **6**, 93–110, 1996.
10. Bauwens, L., and Williams, D. N., *AIAA Paper No.96-0343*, 34th Aerospace Sciences Meeting, Reno, NV, 1996.
11. Williams, D. N., and Bauwens, L., *Proc. CFD96*, CFD Society of Canada, 1996.
12. Williams, D. N., Bauwens, L., and Oran, E. S., *Proc. 26th Symposium (International) on Combustion*, The Combustion Institute, Pittsburgh, PA, 1997.
13. Boris, J. P., and Book, D. L., *Meth. Comp. Phys.*, **16**, 85–129, 1976.
14. Oran, E. S., and Boris, J. P., *Numerical Simulation of Reactive Flow*. American Elsevier, New York, 1987.
15. Oran, E. S., Young, T. R, Boris, J. P., Picone, J. M., and Edwards, D. H., *Proc. 19th Symposium (International) on Combustion*, The Combustion Institute, Pittsburgh, PA, 573–582, 1982.
16. Kailasanath, K., Oran, E. S., Boris, J. P., and Young, T. R., *Combustion Flame*, **61**, 199–209, 1985.

17. Fujiwara, T., and Reddy, K. V., *Memoirs of the Faculty of Engineering*, Nagoya University, **41**, 1, 1989. Also: *Proc. 14th ICDERS*, Coimbra, Portugal, 1993.

18. Lefebvre, M. H., Oran, E. S., Kailasanath, K., and Van Tiggelen, P. J., *Combustion Flame*, **95**, 206–218, 1993.

19. Erpenbeck, J. J., *Physics Fluids*, **7**, 684–696, 1964.

20. Yao, J., and Stewart, D. S., *J. Fluid Mechanics*, **309**, 225–275, 1996.

NUMERICAL SIMULATION OF THE STRUCTURE OF TWO-DIMENSIONAL DETONATIONS IN H_2–O_2–Ar

A. V. Trotsyuk

Two-dimensional structure of detonation waves in $2H_2 + O_2 + X$Ar mixtures was studied numerically in a wide range of initial pressures and argon (Ar) concentrations. A good agreement between numerical results and experimental data was obtained. The influence of the method of detonation initiation (one or several sources, their symmetric or asymmetric location) on the steady structure was studied. Variation in the wave structure induced by varying the channel width was examined. A qualitative difference in the behavior of the 2D wave structure was found for the mixtures with regular detonation cells ($X > 0$) and those with irregular cells ($X = 0$) as observed in experiments.

INTRODUCTION

Extensive experimental and theoretical studies of detonation in gases [1, 2] showed that the real structure of the detonation front differs significantly from that predicted by the one-dimensional theory [3]. The flow behind a plane front of a detonation wave (DW) is unstable [4, 5]. Because of the growth of initial disturbances, the leading front is no longer smooth and exhibits a complex structure repeated in time. The main element of this structure is a triple configuration consisting of the Mach stem (overdriven DW), incident wave (decaying wave), and reflected (transverse) wave adjacent to them at the triple point.

Collisions of transverse waves moving over the DW front in opposing directions, lead to the reproduction of the front structure in time. The trajectories of triple points are the two intersecting families of lines that form a network of diamond cells. The transverse size of the cell, a, determined as the average distance between the trajectories of one family measured in the direction normal to DW propagation, is a characteristic size in the structure of the DW front.

The objective of the present work is the numerical simulation of the multifront detonation structure. Many papers have been devoted to solving this prob-

lem [6–20]. The following common and specific features can be identified in the approaches to describing the compressible chemically reacting flows.

The fluid dynamics was treated in terms of the Euler equations for a compressible medium, i.e., all diffusive effects (thermal conductivity, viscosity, molecular diffusion) were ignored. The paper [20] is of interest because in addition to the Euler equations, compressible Navier–Stokes equations were solved, and the results obtained were compared. The authors of [16] mentioned the studies wherein the Navier–Stokes equations were used in a truncated form (without molecular diffusion).

Another common feature is the use of the ideal gas approximation $p/\rho = RT/\mu$ as a thermal equation of state, where p is the pressure, ρ is the density, T is the temperature, μ is the mean molar mass of the mixture.

The main difference is observed in using the models of chemical kinetics and energy release. The authors of [18–20] used a simple, extremely idealized model of a single-step irreversible monomolecular reaction $A \rightarrow B$ with the Arrhenius dependence of the reaction rate on temperature. A similar model was used in [2] to describe detonation flows, and in [4, 5] to study analytically the stability of a plane detonation front. The authors of [6–9, 17] used a two-step induction parameter model, which was put forward in [26]. The second step (heat release) was described according to the kinetic equation taken from [3]. It was shown in [21], however, that both the form of this equation and the choice of constants applied are quite arbitrary. The use of this type of kinetics yields a wrong (too strong) dependence of the heat release on temperature. A model of chemical kinetics based on the analysis of a system of detailed kinetic equations with the use of physically clear approximations was also suggested in [21].

The induction parameter model was also used in [10–14]. Contrary to the aforementioned papers, the second step of the model in [11–13] was calibrated using the data obtained in 1D calculations of the DW with the help of the detailed kinetic mechanism. In more simplified approaches [10, 14] and [13], a heat release rate was assumed constant during a prescribed time period (5 μs and 20 μs) after completion of the induction period. A comparison of these two descriptions revealed [13] the influence of the amount and the rate of heat release on the structure of 1D detonations.

Numerical simulation [15, 16] was performed using a detailed kinetic mechanism of chemical reactions.

Another important issue is the use of the caloric equation of state $U = U(\rho, T)$, where U is the internal energy. The approximation $\gamma = const$ [6–9, 14, 17, 18], where $\gamma = c_p/c_v$ is the ratio of specific heats, leads to the relation for the thermodynamic part of internal energy: $U_T = p/(\gamma - 1)\rho$. One of the variants of this approach [11, 12] consists in using different constant values of γ before and after the shock front. The paper [13] was devoted to the study of the influence of various models for γ on the DW structure, including the model

164

taking into account the shape of the dependence of γ on temperature and species concentrations.

Chemical reactions in the DW change the chemical composition of the mixture and, hence, μ. Nevertheless, the studies [6–9, 17–20] were performed assuming $\mu = const$. The authors of [10–14] said nothing about their considerations on this issue. Only the detailed kinetics in [15, 16] gave a correct description of the changes in the chemical composition of the medium.

The problem of using the models with constant γ and μ was discussed in detail in [25].

As shown in [24], it is necessary to correlate the models of chemical kinetics and the caloric equation of state with each other, taking into account the Second Law of Thermodynamics. Only with this correlation, the maximum value of entropy and the minimum value of the corresponding thermodynamic potential are ensured (exactly) in the state of chemical equilibrium. None of the papers mentioned above show any understanding of the necessity of performing this procedure. Thus, the authors of [6–14, 17–20] arbitrarily combined various models of kinetics and thermodynamics, which were the best in their opinion, to obtain a proper description of chemically reacting flows. In case the detailed kinetics is used, there are no contradictions with the Second Law of Thermodynamics if the rates of forward and reverse reactions are correlated by means of the equilibrium constants for the reactions [27] (note that the available descriptions of detailed kinetic mechanisms usually contain only forward reaction rate constants).

Thus, the simulation of the processes of chemical transformation in the DW is far from being perfect. The situation could be significantly improved by using the model of kinetics of chemical reactions developed in [21–23] and the thermodynamic model of the caloric equation of state [24] correlated with the kinetic model, which are free of the above drawbacks. Its use (with a comparable accuracy of kinetic calculations [28]) does not require extreme performance and RAM capacity of computers, as in the case of simulations using the detailed kinetic mechanisms [15, 16]. These requirements significantly restrict both the range of the problems available for the study and the number of researchers.

In available literature, the simulation of detonation in realistic chemically reacting gaseous mixtures is limited to a stoichiometric hydrogen–oxygen mixture with two different degrees of dilution, namely $(H_2 : O_2 : Ar)/(2 : 1 : 7)$ [13–16], $(H_2 : O_2 : N_2)/(2 : 1 : 7)$ [13, 15], and $(H_2 : O_2 : Ar)/(2 : 1 : 4.5)$ [11, 12]. The initial pressure range is also very narrow and contains only two values: 65 Torr [11, 12] and 50 Torr [13–16]. In fact, the cellular structure of the front for a stoichiometric hydrogen–air mixture was not obtained in [10].

In the present work, the structure of detonation of a stoichiometric hydrogen–oxygen mixture was numerically studied within a wide range of argon concentrations from 0% to 70% and initial pressures from 0.0866 bar to 0.405 bar. The calculated cell size was compared with the experimental data. The influence of

165

the type of detonation initiation and the channel width on the final structure of the detonation front was studied.

PHYSICAL MODEL

Hereinafter, the following notations are used: ρ is the density; u and v are the fluid velocities in the x and y directions, respectively; E and U are the total energy and internal energy per unit mass; μ is the mean molar mass of the mixture; Y is the induction parameter with $Y = 1$ at the beginning and $Y = 0$ at the end of the induction zone; p is the pressure; T is the temperature; μ_a, μ_{min}, μ_{max} are the molar masses of the mixture in the atomic, extremely dissociated and extremely recombined states, respectively; E_D is the mean dissociation energy of the reaction products; R is the gas constant; a and b are the width and length of the detonation cell, respectively; the subscript 0 denotes the quantities in the initial state.

The dynamics of the compressible chemically reacting medium can be described by 2D Euler equations

$$\frac{\partial \mathbf{q}}{\partial t} + \frac{\partial \mathbf{F}(\mathbf{q})}{\partial x} + \frac{\partial \mathbf{G}(\mathbf{q})}{\partial y} = \mathbf{W} \tag{1}$$

where

$$\mathbf{q} = (\rho, \ \rho u, \ \rho v, \ \rho E, \ \rho \mu, \ \rho Y)^T$$

$$\mathbf{F}(\mathbf{q}) = (\rho u, \ \rho u^2 + p, \ \rho u v, \ u(\rho E + p), \ \rho \mu u, \ \rho Y u)^T$$

$$\mathbf{G}(\mathbf{q}) = (\rho v, \ \rho u v, \ \rho v^2 + p, \ v(\rho E + p), \ \rho \mu v, \ \rho Y v)^T$$

$$\mathbf{W} = (0, \ 0, \ 0, \ 0, \ \rho W_\mu, \ \rho W_Y)^T$$

$$E = U + \frac{1}{2}(u^2 + v^2)$$

The origin of coordinates coincides with the left bottom corner of a plane rectangular channel with width H, which is closed at one side. The x-axis is directed along the lower channel wall in the direction of DW propagation, the y-axis is directed upwards, normal to the x-axis.

To describe the chemical transformation in the substance, a two-step induction parameter model [26] is used in the following form

at $0 < Y \leq 1$:

$$W_Y = -\frac{1}{\tau_{ind}}$$

$$W_\mu = 0 \tag{2}$$

$$U = \frac{1}{\gamma_0 - 1} \frac{p}{\rho} + E_D \left(\frac{1}{\mu_0} - \frac{1}{\mu_{\min}} \right)$$

at $Y = 0$:

$$W_Y = 0$$

$$W_\mu = W_\mu(T, \mu, \rho) \tag{3}$$

$$U = U(T, \mu)$$

The first, induction, step $(0 < Y \leq 1)$ was modeled in this work in accordance with the kinetics [29]:

$$\tau_{ind} = 4.17 \cdot 10^{-14} \exp \left(\frac{18100}{RT} \right) [O_2]^{-1/2} [H_2]^{-1/2} \left(\frac{\text{mole·s}}{\text{cm}^3} \right)$$

After the completion of the induction period $Y = 0$, and the heat release step is described by the following model [21–23]:

$$W_\mu(T, \mu, \rho) = 4K_+ \rho^2 \frac{(1 - \mu/\mu_{\max})^2}{\mu}$$

$$-A_2 T^{3/4} \rho \left(1 - \exp \left(-\frac{\theta}{T} \right) \right)^{3/2} \exp \left(-\frac{E_D}{RT} \right) \left(\frac{\mu}{\mu_{\min}} - 1 \right)$$

together with the caloric equation of state [24]:

$$U(T, \mu) = \left(\frac{3}{4} \left(\frac{\mu}{\mu_a} + 1 \right) + \frac{3}{2} \left(\frac{\mu}{\mu_a} - 1 \right) \frac{\theta/T}{\exp(\theta/T) - 1} \right) \frac{RT}{\mu}$$

$$+ E_D \left(\frac{1}{\mu} - \frac{1}{\mu_{\min}} \right) \tag{4}$$

All of the constants entering the last two equations and referring to the gaseous mixture under study were calculated according to [22–24] prior to numerical experiments with this mixture and were kept fixed in the course of DW simulation.

The system of governing equations is closed by the thermal equation of state for the ideal gas

$$\frac{p}{\rho} = \frac{RT}{\mu} \tag{5}$$

To ensure the absence of gas flow at the upper, lower and left walls of the channel, the "solid wall"-type boundary conditions were set using the technique [30].

At the right boundary, the conditions of undisturbed initial state of the gas were set:

$$\mathbf{q} = \mathbf{q}_0 = (\rho_0,\ \rho_0 \cdot \mathbf{0},\ \rho_0 \cdot \mathbf{0},\ \rho_0 E_0,\ \rho_0 \mu_0,\ \rho_0 \cdot \mathbf{1})^T$$

NUMERICAL METHOD

The hyperbolic system (1)–(5) was solved numerically. The following discretization in space and time was performed. A uniform fixed grid with the total number of cells N_y and cell size $h_y = H/N_y$ was used in the y-direction. A moving grid with the total number of cells N_x was used in the x-direction, N_{x1} of these cells formed a uniform grid with the cell size h_x. In almost all calculations, h_x was set equal to h_y. The uniform grid moved together with the leading shock front of the DW in such a way that it covered the flow regions with large gradients of parameters and/or shock waves, and thus the fine DW structure was captured. A typical value of N_{x1} was 80. The remaining $N_{x2} = N_x - N_{x1}$ cells formed a non-uniform grid that occupied the region between the closed left end of the channel and the beginning of the uniform grid. The use of adaptive moving grids with local refinement allowed us to have a fine resolution where necessary, using a significantly smaller number of cells, as compared with the case of uniform splitting of the computational domain. The time step was determined at each time layer of the solution from the stability condition [30].

The numerical solution of system (1)–(5) on the 2D grid described above was found using the finite-volume MUSCL TVD schemes. A fourth order scheme [31, 32] was used in the region with the uniform grid, and the scheme [34] modified for such grids following [33] was used in the region with the non-uniform grid. The TVD approach allows an accurate and high-resolution calculation of shock waves without explicitly tracking the hydrodynamic discontinuities. This property of the TVD schemes is particularly valuable when it is necessary to simulate 2D flows with complex shock wave configurations, which are not always known *a priori*. A computational technique with explicit tracking of discontinuities and flowfield splitting into separate domains would significantly complicate the code structure. Thus, the use of the shock-capturing technique for simulating DW allowed for calculating the overall domain in a single manner.

Implementation of the MUSCL scheme requires the solution of the Riemann problem for finding the fluxes through the control volume faces. Since this operation is to be executed frequently, finding the exact solution of this problem, especially for the case of chemically reacting gas, would lead to a substantial increase in CPU time. Two approximate methods of solving the Riemann problem were used in the present study: the Roe solver [35, 36] and the van Leer

solver [37, 38]. These methods were generalized to the case of chemically reacting gas with the caloric equation of state (4) in accordance with [39, 40].

The van Leer flux-vector splitting has a larger scheme viscosity in comparison with the Roe solver which, in turn, in its pure form [35, 36] allows for the rarefaction shock waves to appear in computations. To avoid this phenomenon, the method was modified, following [41], by adding the entropy viscosity. Multiple test computations of 1D problems for both reacting and non-reacting flows showed that neither method has any particular advantage. Since the Roe solver requires a significantly larger number of computer operations to calculate a single time layer, the van Leer solver was used to simulate 2D flows.

The system of equations (1)–(5) is a hyperbolic system of conservation laws with stiff relaxation terms. The stiffness of this system during its integration in time is caused by the source term $\mathbf{W}$, which models thermochemical processes. Many papers are devoted to the development of integration methods of such systems. Detonation flows with rather low initial pressures $p_0 < 1$ bar were modeled in the present study, and the system stiffness was not clearly expressed. Thus, the integration in time was performed using the explicit Euler method. In this case, the values of the Courant number were CFL $= 0.2$–0.3. A code version using the ASIRK method [42] of the second order accuracy in time was developed and tested.

RESULTS OF COMPUTATIONS

It is known from the experiment that the DW structure is independent of the initiation method and energy as soon as the DW reaches a self-sustaining propagation regime. The initial conditions for the system (1)–(5), therefore, can be set in a quite arbitrary form. It is only necessary that the initiation energy exceeds the critical value. In the numerical experiment presented here, the initial distribution is a plane DW with the instantaneous chemical reaction ("square wave" model): a shock wave of finite width with the Chapman–Jouguet point, adjacent to it from behind, and the subsequent self-similar chemically equilibrium rarefaction wave. To generate initial transverse disturbances, a certain additional amount of energy was introduced in some regions at the shock front. The shock thickness, the size y of the regions with the additional energy, and the number of the regions were set so that a successful initiation of the DW was ensured. The determination of the critical initiation energy was out of the scope of the present study.

The procedure of determining the detonation cell size was a combination of procedures [6–8] and [12]. The number of initial transverse waves changed with varying the number and positions of the initiation sources. Variation of the
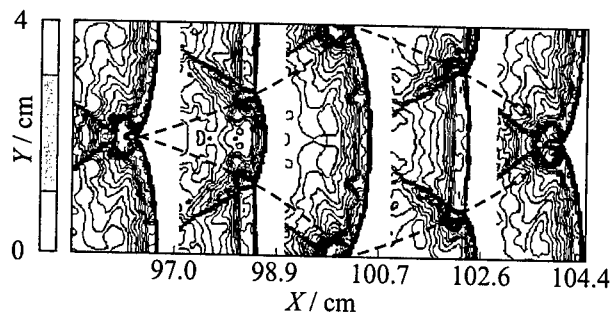
Figure 1 Density contours of a detonation wave propagating in $2H_2+O_2+60\%$ Ar mixture in a 4-cm wide channel at $p_0 = 0.0866$ bar. The initiation scheme is shown on the left side; $N_x = 100$, $N_y = 100$, $D_{CJ} = 1727$ m/s, $\overline{D} = 1656$ m/s, where $\overline{D}$ is the mean detonation velocity over the length of the detonation cell, $a/b = 0.556$

channel width affected the number of remaining transverse waves on the front of the self-sustained DW, and, thus, the cell size was determined.

An interesting feature was observed in the calculations: the response of the wave structure to the variation of H depends on the chemical composition of the mixture. Figures 1 to 3 show the front structures for the mixture $2H_2 + O_2 + 60\%$ Ar at $p_0 = 65$ Torr $= 0.0866$ bar and $H = a$, $2a$, $1.5a$. Figures 4 to 5 show the same for mixture $2H_2 + O_2$ at $p_0 = 0.2$ bar and $H = a$, $1.5a$. In all cases, the initiation was symmetric. When comparing Figs. 1 and 3 with Figs. 4 and 5, one notices that a 1.5-fold increase in H leads to the onset of a new pair of transverse waves in one case, whereas the DW structures remain topologically equivalent in the other case. It is known from experimental data that the mixtures diluted by Ar exhibit very regular cell structures, while the DW structure in the stoichiometric $2H_2 + O_2$ mixture is irregular. The irregularity of the structure is proven by the simultaneous presence of cells with different transverse sizes on soot imprints, whereas the regular structure consists of the identical cells. This is the exact cause for different responses of these two mixtures to the variation of H.

The influence of the initiation method on the final DW structure was also studied for $2H_2 + O_2$ mixture. Figures 6 and 7 show a system of transverse waves at $p_0 = 65$ Torr $= 0.0866$ bar and $H = a$ for the case of asymmetric and symmetric initiation by three sources. In complete agreement with the numerical studies [11, 12] and extensive experimental data, the cell structure does not depend on the initial conditions of detonation excitation.

A different situation arises when $H = 1.5a$. Figure 8 shows the results of DW simulation in $2H_2 + O_2 + 60\%$ Ar mixture for a single-source symmetric ini-

170

Figure 2 Density contours of a detonation wave propagating in $2H_2+O_2+60\%$ Ar mixture in a 8-cm wide channel at $p_0 = 0.0866$ bar. The initiation scheme is shown on the left side; $N_x = 100$, $N_y = 200$, $D_{CJ} = 1727$ m/s, $\overline{D} = 1727$ m/s
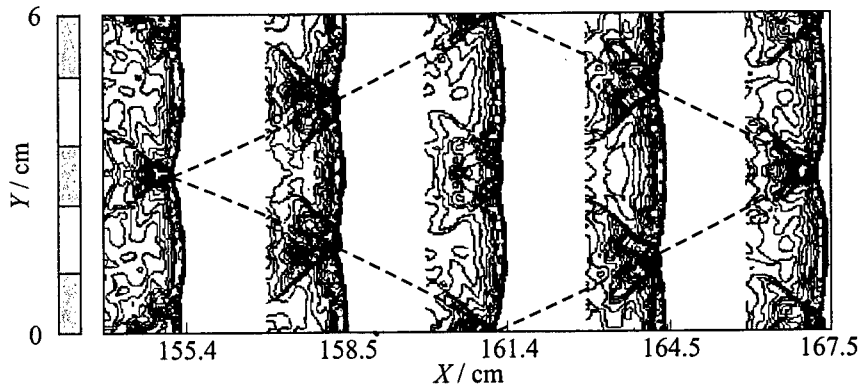
Figure 3 Density contours of a detonation wave propagating in $2H_2 + O_2 + 60\%$ Ar mixture in a 6-cm wide channel at $p_0 = 0.0866$ bar. The initiation scheme is shown on the left side; $N_x = 100$, $N_y = 150$, $D_{CJ} = 1727$ m/s, $\overline{D} = 1698$ m/s, $a/b = 0.5$

tiation. When comparing Figs. 3 and 8, one concludes that the cell structure is also independent of the number of initiation sources. The structures are equivalent, while the density isolines in Fig. 8 are plotted in smaller time intervals. The thick broken curves denote the trajectories of the main triple points and the thin broken curves indicate the trajectories of the secondary points. However,

171

Figure 4 Density contours of a detonation wave propagating in $2H_2 + O_2$ mixture in a 0.6-cm wide channel at $p_0 = 0.2$ bar. The initiation scheme is shown on the left side; $N_x = 100$, $N_y = 100$, $D_{CJ} = 2749$ m/s, $\overline{D} = 2731$ m/s, $a/b = 0.5$
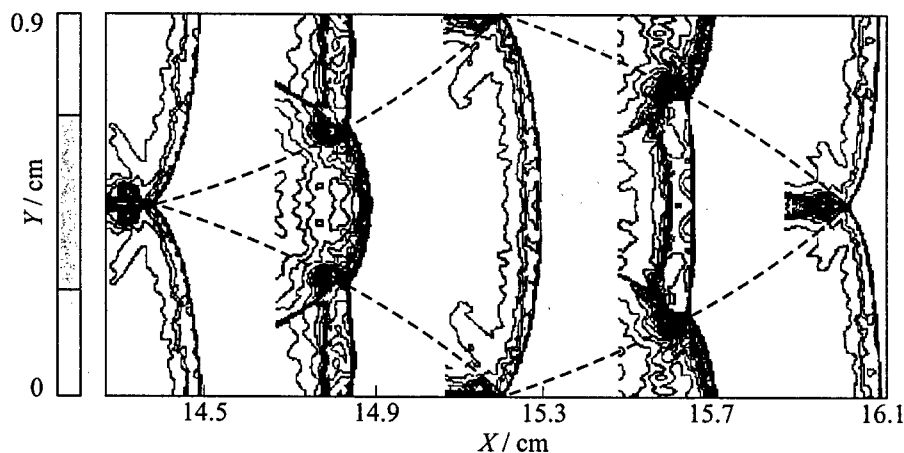
Figure 5 Density contours of a detonation wave propagating in $2H_2 + O_2$ mixture in a 0.9-cm wide channel at $p_0 = 0.2$ bar. The initiation scheme is shown on the left side; $N_x = 100$, $N_y = 180$, $D_{CJ} = 2749$ m/s, $\overline{D} = 2799$ m/s, $a/b = 0.554$

upon the asymmetric initiation by two sources, a qualitatively different structure is formed (Fig. 9). Instead of four transverse waves (two main and two secondary waves) now one has three identical transverse waves. Such a configuration corresponds to the propagation of a DW with the front consisting of 1.5 detonation cells. The upper two thirds of the structure in Fig. 9 are equivalent to one cell in Fig. 1. It seems of interest to verify experimentally the existence of two qualitatively different configurations of transverse waves in the channel
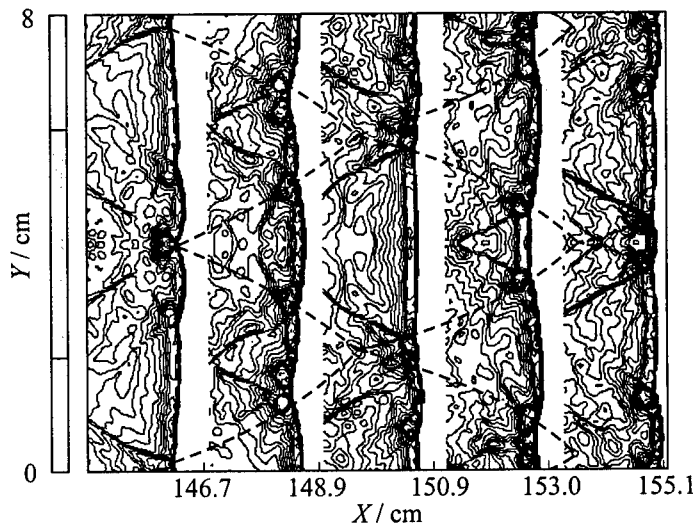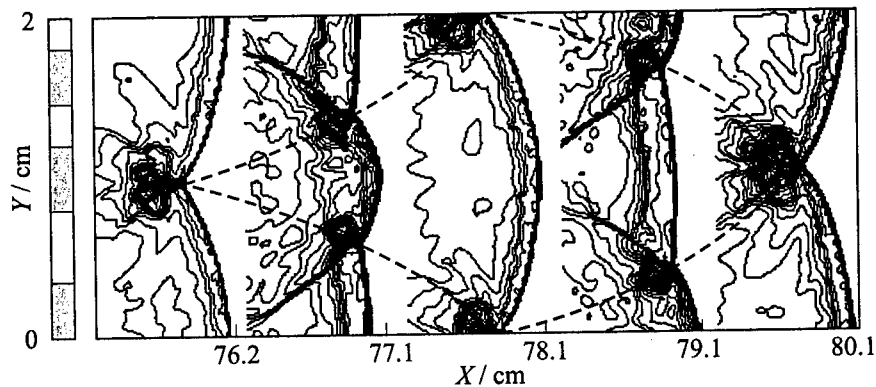
Figure 6 Density contours of a detonation wave propagating in $2H_2 + O_2$ mixture in a 2-cm wide channel at $p_0 = 0.0866$ bar. The initiation scheme is shown on the left side; $N_x = 100$, $N_y = 100$, $D_{CJ} = 2704$ m/s, $\overline{D} = 2685$ m/s, $a/b = 0.514$
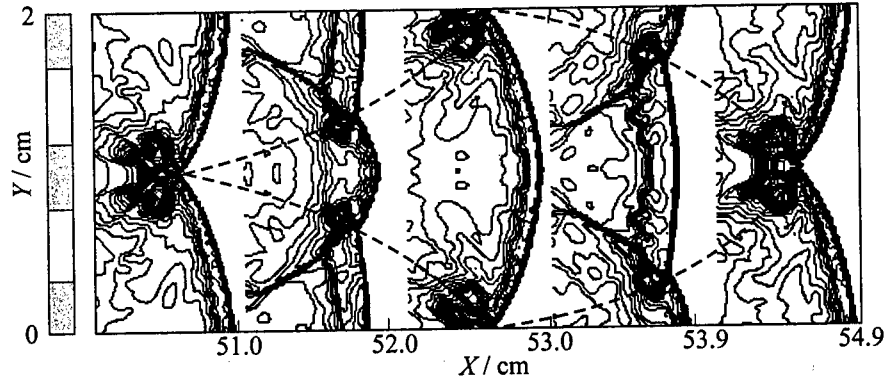
Figure 7 Density contours of a detonation wave propagating in $2H_2 + O_2$ mixture in a 2-cm wide channel at $p_0 = 0.0866$ bar. The initiation scheme is shown on the left side; $N_x = 100$, $N_y = 100$, $D_{CJ} = 2704$ m/s, $\overline{D} = 2674$ m/s, $a/b = 0.516$

with $H = 1.5a$ and to find the factors that determine the final state to which the DW structure relaxes.

Figure 10 shows the results of the numerical experiments on determining a as a function of the initial pressure for $2H_2 + O_2 + X$Ar mixtures, where $X = 0\%$, 50%, 60%, and 70%. The data obtained is compared with the experimental results [43, 44]. An extremely good agreement of the transverse size of detonation cells is clearly seen. This provides the grounds to believe that the model (1)–(5) can be successfully used for studying the non-stoichiometric H_2–O_2 system and the cases with other diluents.
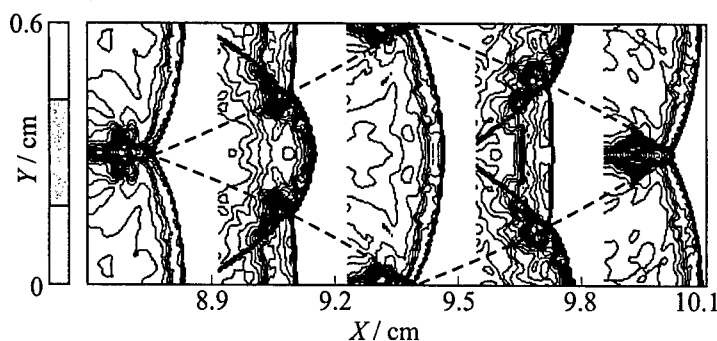
173
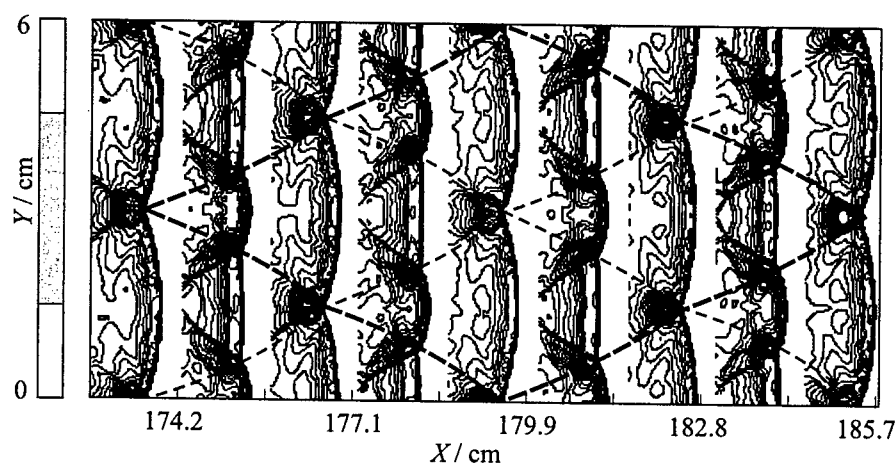
Figure 8 Density contours of a detonation wave propagating in $2H_2 + O_2 + 60\% Ar$ mixture in a 6-cm wide channel at $p_0 = 0.0866$ bar. The initiation scheme is shown on the left side; $N_x = 100$, $N_y = 150$, $D_{CJ} = 1727$ m/s, $\overline{D} = 1704$ m/s, $a/b = 0.517$
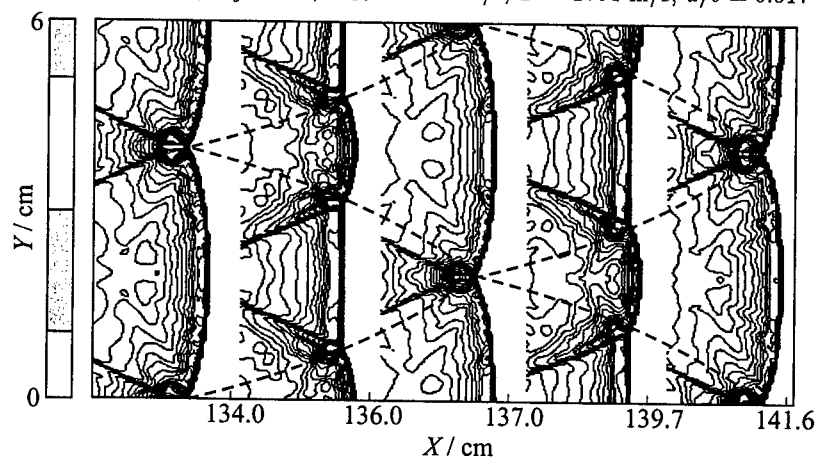
Figure 9 Density contours of a detonation wave propagating in $2H_2 + O_2 + 60\% Ar$ mixture in a 6-cm wide channel at $p_0 = 0.0866$ bar. The initiation scheme is shown on the left side; $N_x = 100$, $N_y = 150$, $D_{CJ} = 1727$ m/s, $\overline{D} = 1672$ m/s, $a/b = 0.532$

CONCLUDING REMARKS

Thus, in the present work the DW structure in $2H_2 + O_2 + X Ar$ mixture with $X = 0\%, 50\%, 60\%$, and 70% was studied numerically within a wide range of initial pressures from 0.0866 to 0.405 bar. The obtained data for the detonation cell size a demonstrates a good quantitative agreement with experimental findings. The influence of the initiation method on the final steady DW structure was

174

also studied. An interesting feature concerning the influence of the location of the initiation sources on the number and final configuration of transverse waves for the channel width $H = 1.5a$ was observed. The symmetric initiation by a single source or several sources leads to formation of a structure containing four transverse waves (two main and two secondary waves). Three identical transverse waves are formed upon the asymmetric initiation by two sources. The changes in the wave structure, caused by the channel width variation, were also studied. A qualitatively different behavior of the 2D wave structure was observed for the mixtures with regular $(X > 0)$ and irregular $(X = 0)$ detonation cells.

Figure 10 Comparison the calculated detonation cell width a with experimental data [43, 44] for $2H_2 + O_2 + X$Ar mixtures $(1,\ 3,\ 7)$. $1,\ 2 - X = 0\%$Ar, $3,\ 4 - X = 50\%$Ar, $5,\ 6 - X = 60\%$Ar, $7,\ 8,\ 9 - X = 70\%$Ar. $2,\ 4,\ 5,\ 8 -$ calculated in this paper, $6 - $ [11], $9 - $ [15, 16]

ACKNOWLEDGMENTS

REFERENCES

1. Voitsekhovskii, B. V., Mitrofanov, V. V., and Topchian, M. E., *The Structure of a Detonation Front in Gases.* Wright–Patterson AFB AD-633821, 1966.

2. Fickett, W., and Davis, W. C., *Detonation.* University of California Press, Berkeley, CA, 1979.

3. Zel'dovich, Ya. B., and Kompaneets, A. S., *The Theory of Detonation.* Moscow, Gostekhteorizdat, 1955.

4. Erpenbeck, J. J., "Stability of Idealized One-Reaction Detonations," *Physics Fluids,* **7**, 684–696, 1964.

5. Lee, H.I., and Stewart, D.S., "Calculation of Linear Detonation Instability: One-Dimensional Instability of Plane Detonation," *J. Fluid Mechanics*, **216**, 103–132, 1990.

6. Taki, S., and Fujiwara, T., "Numerical Analysis of Two-Dimensional Non-Steady Detonations," *AIAA J.*, **16**, 1, 73–77, 1978.

7. Taki, S., and Fujiwara, T., "Numerical Simulation of Triple Shock Behavior of Gaseous Detonation," *Proc. 18th Symposium (International) on Combustion*, The Combustion Institute, Pittsburgh, PA, 1981, 1671–1680.

8. Taki, S., and Fujiwara, T., "Numerical Simulations of the Establishment of Gaseous Detonation," In: *Dynamics of Shock Waves, Explosions and Detonations*. (Eds. J.R. Bowen, *et al.*), Progress in Astronautics and Aeronautics Ser., N.Y., AIAA Inc., **94**, 1983, 186–200.

9. Markov, V.V., "Numerical Simulation of Formation of a Multi-Front Detonation Wave Structure," *Sov. J. Doklady USSR Academy Sci.*, **258**, 2, 314–317, 1981.

10. Oran, E.S., Boris, J.P., Young, T., Flanigan, M., Burks, T., and Picone, M., "Numerical Simulations of Detonations in Hydrogen–Air and Methane–Air Mixtures," *Proc. 18th Symposium (International) on Combustion*, The Combustion Institute, Pittsburgh, PA, 1981, 1641–1649.

11. Kailasanath, K., Oran, E.S., Boris, J.P., and Young, T.R., "Determination of Detonation Cell Size and the Role of Transverse Waves in Two-Dimensional Detonations," *Combustion Flame*, **61**, 199–209, 1985.

12. Oran, E.S., Kailasanath, K., and Guirguis, R.H., "Numerical Simulations of the Development and Structure of Detonations," In: *Dynamics of Explosions*. (Eds. A.L. Kuhl *et al.*), Progress in Astronautics and Aeronautics Ser., N.Y., AIAA Inc., **114**, 1988, 155–169.

13. Lefebvre, M.H., Oran, E.S., Kailasanath, K., and Van Tiggelen, P.J., "The Influence of the Heat Capacity and Dilutent on Detonation Structure," *Combustion Flame*, **95**, 206–218, 1993.

14. Lefebvre, M.H., Oran, E.S., Kailasanath, K., and Van Tiggelen, P.J., "Simulation of Cellular Structure in a Detonation Wave," In: *Dynamic Aspects of Detonations*. (Eds. A.L. Kuhl *et al.*), Progress in Astronautics and Aeronautics Ser., N.Y., AIAA Inc., **153**, 1993, 64–77.

15. Oran, E.S., "Numerical Simulations of Unsteady Combustion," In: *Combustion, Detonation, Shock Waves. Proc. Zel'dovich Memorial*. (Eds. A.G. Merzhanov and S.M. Frolov), Moscow, ENAS Publ., **1**, 1995, 228–247.

16. Oran, E.S., Weber, J.W., Stefaniw, E.I., Lefebvre, M.H., and Anderson, J.D., "A Numerical Study of a Two-Dimensional H_2–O_2–Ar Detonation Using a Detailed Chemical Reaction Model," *Combustion Flame*, **113**, 147–163, 1998.

17. Schöffel, S.U., and Ebert, F., "Numerical Analyses Concerning the Spatial Dynamics of an Initially Plane Gaseous ZND Detonation," In: *Dynamics of Explosions*. (Eds. A.L. Kuhl *et al.*), Progress in Astronautics and Aeronautics Ser., N.Y., AIAA Inc., **114**, 1988, 3–31.

18. Cai, W., "High-Order Hybrid Numerical Simulations of Two-Dimensional Detonation Waves," *AIAA J.*, **33**, 7, 1248–1255, 1995.

19. Sjögreen, B., "Numerical Computation of Three-Dimensional Detonation Waves on Parallel Computers," Report 162/1994, Department of Scientific Computing, Uppsala University, Uppsala, Sweden, 1994.

20. Lindström, D., "Numerical Computation of Viscous Detonation Waves in Two Space Dimensions," Report 178/1996, Department of Scientific Computing, Uppsala University, Uppsala, Sweden, 1996.

21. Nikolaev, Yu. A., "Model of Chemical Reactions at High Temperatures," *Combustion, Explosion, and Shock Waves*, **14**, 4, 1978.

22. Nikolaev, Yu. A., and Fomin, P. A., "Analysis of Equilibrium Flows of Chemically Reactng Gases," *Combustion, Explosion, and Shock Waves*, **18**, 1, 53–58, 1982.

23. Nikolaev, Yu. A., and Fomin, P. A., "Approximate Equation of Kinetics in Heterogeneous Systems of the Gas – Condensed-Phase Type," *Combustion, Explosion, and Shock Waves*, **19**, 6, 737–745, 1983.

24. Nikolaev, Yu. A., and Zak, D. V., "The Agreement of Models of Chemical Reactions in Gases with the Second Principle of Thermodynamics," *Combustion, Explosion, and Shock Waves*, **24**, 4, 1988.

25. Fomin, P. A., and Trotsyuk, A. V., "An Approximate Calculation of the Isentrope of a Gas in Chemical Equilibrium," *Combustion, Explosion, and Shock Waves*, **31**, 4, 455–458, 1995.

26. Korobeinikov, V. P., Levin, V. A., Markov, V. V., and Chernyi, G. G., "Propagation of Blast Waves in a Combustible Gas," *Acta Astronautica*, **17**, 529–537, 1972.

27. Rumer, Yu. B., and Ryvkin, M. S., *Thermodynamics, Sstatistical Physics and Kinetics*. Moscow, Nauka, 1977.

28. Fomin, P. A., Private communication, June, 1996.

29. White, D. R., "Density Induction Times in Very Lean Mixtures of D_2, H_2, C_2H_2, and C_2H_4 with O_2," *Proc. 11th Symposium (International) on Combustion*, The Combustion Institute, Pittsburgh, PA, **147**, 1966.

30. S. K. Godunov Ed. *Numerical Solution of the Multi-Dimensional Problems of Gaseous Dynamics*. Moscow, Nauka, 1976.

31. Yamamoto, S., and Daiguji, H., "Higher-Order-Accurate Upwind Schemes for Solving the Compressible Euler and Navier–Stokes Equations," *J. Comp. Fluids*, **22**, 2/3, 259–270, 1993.

32. Daiguji, H., Yuan, X., and Yamamoto, S., "Stabilization of Higher-Order High Resolution Schemes for the Compressible Navier–Stokes Equation," *Int. J. Numerical Methods for Heat and Fluid Flow*, **7**, 2/3, 250–274, 1997.

33. Lin, S.-Y., and Chin, Y.-S., "Comparison of Higher Resolution Euler Schemes for Aeroacoustic Computations," *AIAA J.*, **33**, 2, 237–245, 1995.

34. Chakravarthy, S. R., and Osher, S., "A New Class of High Accuracy TVD Schemes for Hyperbolic Conservation Laws," AIAA Paper No.85-0363, AIAA 23rd Aerospace Sciences Meeting, Reno, Nevada, 1985.

35. Roe, P. L., "Approximate Riemann Solvers, Parameter Vectors, and Difference Schemes," *J. Comp. Phys.*, **43**, 357–372, 1981.

36. Roe, P. L., and Pike, J., "Efficient Construction and Utilization of Approximate Riemann Solutions," In: *Computing Methods in Applied Sciences and Engineering VI*. (Eds. R. Glowinski and J.-L. Lions), North-Holland, 1984, 499–513.

177

37. Van Leer B., "Flux-Vector Splitting for the Euler Equations," ICASE Report 82-30, 1982. In: *Lecture Notes in Physics*, New York – Berlin, Springer-Verlag, **170**, 507, 1982.

38. Anderson, W. K., Thomas, J. L., and van Leer, B., "A Comparison of Finite Volume Flux Vector Splitting for the Euler Equations," AIAA Paper No.85-0122, AIAA 23rd Aerospace Sciences Meeting, Reno, Nevada, 1985.

39. Vinokur, M., and Montagné, J.-L., "Generalized Flux-Vector Splitting and Roe Average for an Equilibrium Real Gas," *J. Comp. Phys.*, **89**, 276–300, 1990.

40. Vinokur, M., "An Analysis of Finite-Difference and Finite-Volume Formulations of Conservation Laws," *J. Comp. Phys.*, **81**, 1–52, 1989.

41. Harten, A., and Hyman, J. M., "Self-Adjusting Grid Methods for One-Dimensional Hyperbolic Conservation Laws," *J. Comp. Phys.*, **50**, 235–269, 1983.

42. Shen, J. W., and Zhong, X., "Semi-Implicit Runge-Kutta Schemes for Non-Autonomous Differential Equations in Reactive Flow Computations," AIAA Paper No.96-1969, 1996.

43. Strehlow, R. A., and Engel, C. D., "Transverse Waves in Detonations: II. Structure and Spacing in H_2–O_2, C_2H_2–O_2, C_2H_4–O_2, CH_4–O_2 Systems," *AIAA J.*, **7**, 3, 492–496, 1969.

44. Strehlow, R. A., "Gas Phase Detonations: Recent Developments," *Combustion Flame*, **12**, 2, 81–101, 1968.

PART THREE

DETONATION MITIGATION AND CONTROL

THE WAYS OF EXPLOSION CONTROL

V. V. Mitrofanov

The paper reviews modern achievements in the explosion control problem as it relates to the author's own scientific interests. The basic parameters of explosion are the detonation velocity D, total energy release, and pressure impulse. Explosion can be readily controled by varying the explosive charge composition, density and physical structure (for heterogeneous systems). As compared with trivial possibilities of changing the parameters of ideal detonation, non-ideal detonation shows essentially wider range of controlling measures. The increase in D by 1.5–2 times and even more, as compared with the Chapman–Jouguet velocity D_{CJ}, can be achieved in heterogeneous systems, if specific conditions for the fast transition of an initiating pulse are created. The widest range of changes in D at $D < D_{CJ}$ is attained in gas mixtures placed into inert porous media. Approximately the same range of reduced D is realized in bubbly media. In general, by varying composition and heterogeneous structure of explosive charges, it is possible to virtually continuously change the propagation velocity of a self-sustaining explosion wave from about 10 m/s to 10–14 km/s. A wide range of density change (50–200 kg/m^3) is possible for heterogeneous explosive mixtures based on superlight polystyrene foam. Other ways of controlling explosion are based on using transient and non-stationary explosion processes and on externally forcing the detonation wave by mass, momentum, and energy fluxes. There is less emphasis on these approaches than the first, but ultimately they allow us to change explosion parameters in a narrower range. One more way of explosion control deals with the geometrical influence on the detonation wave by designing channels of a special configuration. In particular, these are channels with obstructions of variable blockage ratio and annular channels for attaining continuous spin detonation.

INTRODUCTION

The paper deals with the control of a self-sustaining explosion wave accompanied by a fast exothermic reaction and propagating in a substance at a high speed (primarily supersonic), that is, the control of **detonation waves (DW)**. The

mechanism of DW propagation can be different, not always being the shock–governed mechanism. The objective is to show how one can control DW and what achievements are known in this field.

To control DW means changing its parameters, initiating or quenching DW when required. Of particular interest are the parameters of explosion, such as the detonation velocity, total energy release, pressure impulse, and sometimes the temperature of the products. All basic ways of explosion control have been found earlier. Below we classify the ways of explosion control as follows:

First way: variation of explosive charge composition, charge density, and charge structure (for heterogeneous systems);

Second way: use of transient and non-stationary explosion processes;

Third way: external forcing of DW by a force, power, and/or mass flux;

Fourth way: geometrical influence on DW in channels of special shape.

There are some possibilities of practical application of explosion control. These are: (1) transmitting a pressure, thermal or flame impulse at a required speed (non-electric means of initiation, special engineering); (2) controlling the explosion effect during technological procedures based on explosion; (3) reducing the destruction ability of accidental explosions; (4) applying the controlled detonation in combustion chambers of propulsion devices.

Given below is a review of some modern advances in the problem which are familiar to the author. Of course, they are concerned with the author's own scientific interests. The results obtained mainly in the Department of high-speed processes of the Lavrent'ev Institute of Hydrodynamics will be presented. The attention will be primarily concentrated on the controlled change of detonation parameters. The problem of detonation initiation is omitted, because it is considered in other papers presented in this book (see [1, 2]). The problem of the detonation suppression is discussed only in connection with the critical detonation conditions.

FIRST WAY OF DETONATION CONTROL: VELOCITY AND TEMPERATURE

The velocity (D_{CJ}) and temperature (T_{CJ}) in the "ideal" Chapman–Jouguet (CJ) detonation wave is primarily controlled by the explosive mixture composition and its initial thermodynamic parameters. Among **gaseous explosives**, the widest range of DW velocity can be achived in $H_2/O_2/N_2$ mixtures by changing the fuel concentration (Fig. 1a). Clearly, the highest calculated velocity is about
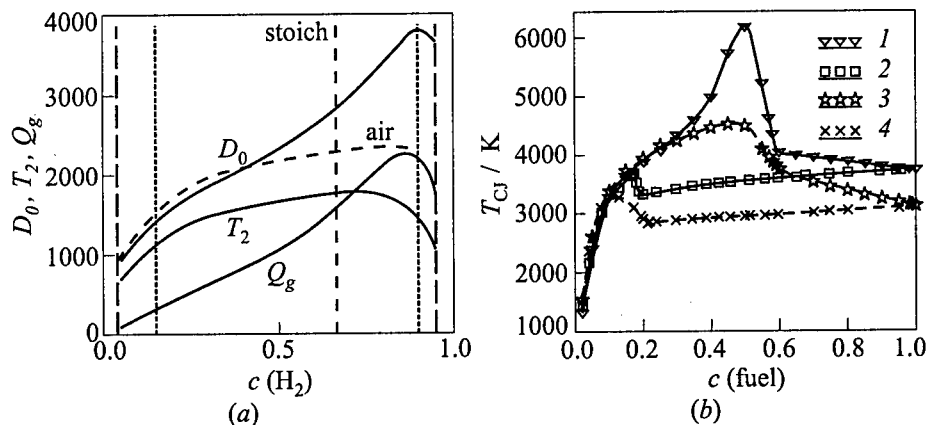
Figure 1 Calculated detonation parameters vs. fuel molar concentration in hydrogen/oxygen mixtures (a) [3] and cyanogen/oxygen mixtures (b) [4]. D_0 is the CJ detonation velocity, m/s; T_2 is the shock temperature, K; Q_g is the reaction heat, kcal/kg; 1 — C_2N_2-O_2, 2 — C_2N_2-air, 3 — C_2H_2-O_2, 4 — C_2H_2-air

3800 m/s while the lowest approaches 1300 m/s near the detonation limit [3]. In gaseous mixtures, the steady DW exhibits a cellular or spin structure in all cases except for detonations in very narrow tubes and in an obstacle-filled space [4, 5]. The propagation velocity deficit of such DW, caused by various "losses," is relatively small:

$$0.8 < \frac{D}{D_{CJ}} < 1 \tag{1}$$

The highest temperature and luminosity of DW are achieved in hydrogenless high-energy mixtures balanced for $2CO + N_2$ products, similar to analogous HE-compositions [6]: gas mixture $C_2N_2 + O_2$ has $T_{CJ} > 6000$ K at $p_0 = 10^5$ Pa and $T_0 = 298$ K (Fig. 1b). The lowest temperatures T_{CJ} are attaind near concentration detonability limits of mixtures containing high-active fuels. In gaseous mixtures $(T_{CJ})_{min} \approx 2500$ K, $(T_{SW})_{min} \approx 1400$ K, where T_{SW} is the shock temperature.

Very wide possibilities of explosion control exist for **heterogeneous systems** [7]. In this connection, the bubbly medium is of particular interest. If the interphase mass and heat transfer is absent, the pressure in bubbles and liquid is the same, and the liquid density $\rho_l = const$, it can be shown that the CJ velocity in the bubbly medium is defined by the expression:

$$D_b = D_g \frac{(c_0)_b}{(c_0)_g} \tag{2}$$

183
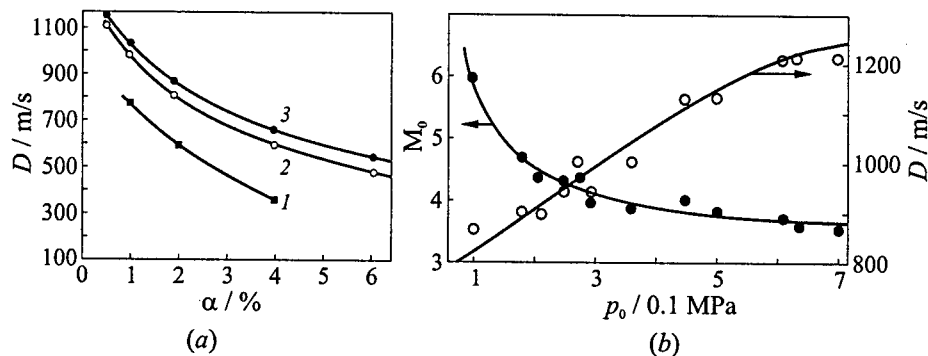
Figure 2 (*a*) Measured velocity of bubble detonations in water–glycerin liquids with C_2H_2/O_2 bubbles vs. volumetric concentration of bubbles α at various glycerin content β: *1* — 0, *2* — 0.25, *3* — 0.5. (*b*) Measured velocity of bubble detonations and detonation Mach number M_0 in oil "VM-3" with O_2 bubbles vs. initial pressure at $\alpha = 1\%$ [8–10]

where $(c_0)_b$ is the initial speed of the low-frequency sound in the bubbly medium, $(c_0)_g$ is the speed of sound in the gas. The ratio in Eq. (2) is defined as

$$\frac{(c_0)_b}{(c_0)_g} = \sqrt{\frac{(\rho_0)_g}{\alpha(1-\alpha)\rho_l}} \tag{3}$$

where α is the volumetric concentration of bubbles. This ratio has a minimum at $\alpha = 0.5$ and can be made less than 1/30 by changing α and decreasing gas density $(\rho_0)_g$ with the initial pressure. Therefore it appears possible to gain $D \cong 100$ m/s. However, for achieving D lower than 300 m/s, special measures for stabilizing the medium at $\alpha > 0.08$ are required. In the experiments performed by Sychev and Pinaev [8–10], the magnitude of D was changed from 1150 m/s to 350 m/s. Some of their experimental data is shown in Fig. 2. In fact, there are deviations of the measured detonation velocity from the calculated values (up to 30%) caused by bubble oscillations, heat and mass transfer, and liquid compressibility, but this does not effect a principal possibility of controlling the detonation velocity in bubbly media.

It should be emphasized that there exists a unique possibility of controlling D by changing the initial pressure p_0 at a fixed mass concentration of explosive gas in the bubbly medium. Due to the fact that $(\rho_0)_g \sim p_0$, and $\alpha \sim 1/p_0$ at $\alpha\rho_g = const$, it follows from Eqs. (2) and (3):

$$D \sim p_0$$

at $\alpha \ll 1$. This possibility has yet to be checked experimentally. The data in Fig. 2b are obtained for somewhat different conditions, when $\alpha = const$ in a two-phase reactive system.

FIRST WAY OF DETONATION CONTROL: INCREASING DETONATION VELOCITY ABOVE D_{CJ}

The essential increase in the velocity of self-sustaining detonation compared to the CJ velocity D_{CJ} can be achieved in heterogeneous systems [7, 11–15]. For this purpose, special conditions for the fast transmission of an initiating impulse should be provided. The increase in D over D_{CJ} by a factor of 2–2.5 was obtained in suspensions of lead azide with coarse particles in an evacuated tube [11]. But the most favorable conditions for the fast transmission of the initiating impulse appear in tubes with a layer of a primary explosive on the walls. The highest DW velocities, attaining 14 km/s, were detected in such systems with the layer of lead azide $\sim$ 0.2 mm thick in a steel channel, 8 mm in diameter, filled with helium at $p_0 \sim 0.1$ MPa [13]. Similar effects were observed when air was used as an oxidizer or when heterogeneous systems were evacuated: in polyethylene tubes, covered inside with a very thin layer of fine-dispersed lead azide, the DW velocity $D \cong 1800$ m/s (at $D_{CJ} \cong 1300$ m/s) was obtained recently [14]. The value of D_{CJ} is calculated as the velocity of the ideal CJ detonation for a charge of the same substances under conditions of uniform distribution over the tube cross-section. Moreover, in the latter experiments, the DW propagates in the spinning mode. The value of D exceeding D_{CJ} was also obtained by 2D numerical simulation of detonation in a tube with the annular RDX-suspension layer [15].

FIRST WAY OF DETONATION CONTROL: PRESSURE AND ENERGY

The explosion pressure is proportional to the specific energy per unit volume. Therefore, the pressure impulse and the total energy of explosions can be readily controlled by changing the initial density ρ_0 of a charge of a given composition. For gaseous mixtures kept in hermetically sealed chambers, the control parameter is the initial pressure p_0. In other cases, it is advantageous to use heterogeneous explosive mixtures with a variable ρ_0 applying **low-density foams**. Specifically, the foamy urea-formaldehyde resin and foamy polystyrene are successfully used for the preparation of such mixtures [16–20]. Usually, the dispersed oxidant (am-

185
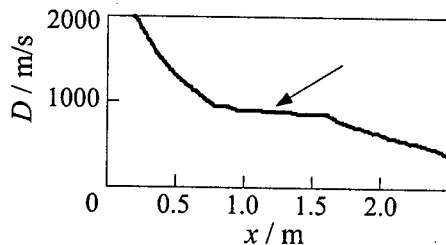
Figure 3 The slowly damping quasi-detonation (shown by the arrow) of super-low-density foamy polystyrene in a steel tube; $d = 35$ mm, $\rho_0 = 60$ kg/m^3 [18]

monium nitrate) or HE is added to the foam to get the low-density explosive. In such systems, due to the change in the composition and density of the mixture, it is possible to vary the total power of charge, detonation parameters, and the detonation wave profile within wide ranges, and thereby to increase the efficiency of explosion. The characteristic data of the mixtures can be changed from the lowest achieved values $\rho_0 \sim 50$ kg/m^3, $P_{det} \sim 100$ MPa up to the values relevant to solid HE.

It is likely that there is a possibility of reducing the lowest values even more. The foamy polystyrene has its own minimal density $\rho_0 \sim 6$ kg/m^3 and can be gasified in the regime of quasi-detonations under the action of relatively weak shock waves [19] (see Fig. 3). In this case, the calculated detonation parameters are very low:

$$D_{CJ} = 892 \text{ m/s}$$

$$T_{CJ} = 1010 \text{ K}$$

$$P_{CJ} = 3.6 \text{ MPa}$$

Under these conditions, chemical reactions are initiated by jets of hot products rather than by shocks. This explosion mode is not a self-sustaining one, however it appears suitable in the technology of rock destruction [18].

Detonations of mixtures based on super low-density foamy polystyrene exhibit a number of interesting peculiarities which are still unclear and should be studied further [19]. This is also true for a possibility of **controlling DW by relatively weak electric and magnetic fields**, as reported at the 4th International Conference "Lavrent'ev Readings" [20].

SECOND WAY OF DETONATION CONTROL: USE OF NONSTATIONARY EXPLOSION PROCESSES

Variations of explosion parameters are observed in any unsteady explosion process. One of the approaches to keep them controlled is based on directing the unsteady process into the desired way. The example of using unsteady processes for obtaining "soft" (sparing) explosion action has been already demonstrated in the previous section (Fig. 3), as the slowly damping quasi-detonation. In this
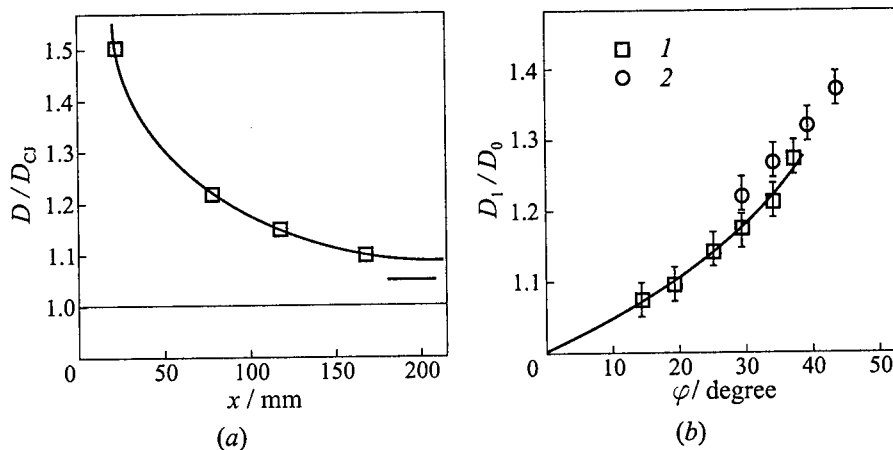
Figure 4 Velocities of overdriven DW obtained by controlled DDT (a, experiments by Gavrilenko *et al.*, 1983) and by contracting the channel cross-section (b); x is the axial coordinate, φ is the wedge (1) or cone (2) angle [36]

example, the charge composition (at given charge sizes) and the detonator mass are the control parameters.

The next two examples deal with the premeditated explosion sharpening due to the process of **deflagration-to-detonation transition (DDT)**. In the first example, a reinforced DW is obtained in a channel of constant cross-section. For this goal, a portion of inert gas is issued into a middle part of the channel, filled initially with an explosive mixture [21]. The inert gas interrupts the detonation that is initiated at the channel inlet. As a result, a shock wave (SW) forms and compresses the explosive mixture behind the inert gas. Subsequently the self-ignition followed by DDT occurs in the compressed mixture. The gas-dynamic parameters of generated DW, namely, density, pressure, particle velocity, and dynamic pressure are increased as compared to the steady detonation parameters of the initial mixture. After the DW catches up to the leading SW, an **overdriven DW** arises in the initial mixture for a while. Its velocity drops gradually as shown in Fig. 4a. The process can be used for fast acceleration of solid particles in devices for detonative coating of steel surfaces by powders [22].
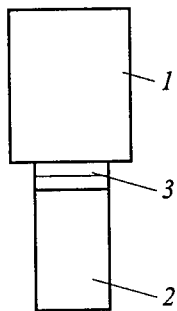
Figure 5 Two-chamber device for obtaining elevated explosion parameters. *1* — combustion chamber, *2* — detonation chamber, *3* — turbulizer for fast DDT

The controlled DDT can also be efficiently used for obtaining elevated explosion parameters in a device represented schematically in Fig. 5. The device

187

consists of two chambers: the bigger upper chamber (*1*), and the smaller lower chamber (*2*). The chambers are connected through a special turbulizer (*3*) and filled with an explosive gas mixture.

The flame is initiated in the top of chamber *1*. It propagates downward and compresses the initial gaseous mixture in the two chambers due to the expansion of burnt gases. During the flame propagation through the turbulizer, DDT occurs and the mixture in chamber *2* detonates at elevated pressure and density. The process can be controlled by changing the sizes of chambers and by choosing proper gas components of the explosive mixture.

The increase of DW parameters is defined by the following relations:

$$p_{2,\mathrm{CJ}} = \frac{p_2 + \rho_2 D_{2,\mathrm{CJ}}^2}{\gamma + 1} \approx p_{1,\mathrm{CJ}} \cdot \frac{\rho_2}{\rho_1}$$

$$\left(\frac{\rho_2}{\rho_1}\right)_{\max} = \left(\frac{T_{\mathrm{ign}}}{T_1}\right)^{1/(\gamma-1)} \approx 10 \tag{4}$$

where T_{ign} is the temperature of adiabatic auto-ignition in chamber *2*.

A substantial decrease in the average detonation velocity D in gas mixtures can be achieved, due to periodical or entire destruction of the cellular DW structure when DW propagates in a tube with special obstacles, such as Shchelkin spiral [23] or partitions with orifices [24]. In this case, the most important control parameter is the blockade ratio $BR = 1 - (d_2/d_1)^2$, where d_1 and d_2 are the inner diameters of the tube and the spiral or the orifice, respectively. The other essential parameter at $d_2 \gg a$ is a/d_2, where a is the cell size in the detonation front. Under condition $a/d_2 < 0.1$, parameter BR becomes insignificant and obstacles do not influence DW parameters. In these systems, local non-stationary effects are combined with the geometry and force actions on the DW.

A nonstationary explosion process can also be used for producing a high explosion impulse in open chambers [25, 26]. In [26], the reactive impulse from gaseous explosions in a cylindrical chamber was calculated and measured. The mixture was charged into the chamber through the closed end and occupied a part or the whole length of the chamber. In the former case, the remaining part of the chamber volume was filled with air. When the ratio of chamber-to-charge lengths was varied from 1 to 7–10, the specific impulse from detonation of acetylene–oxygen mixture was increased from 1600 to 5000–5400 m/s. In the case of fuel–air mixtures, the maximal theoretical specific impulse per unit mass of fuel exceeds 30,000 m/s for methane and acetylene. In this process, the impulse increases due to pushing an additional mass of the unheated air with the expanding explosion products.

188

THIRD WAY OF DETONATION CONTROL: EXTERNAL FORCING

Special force, power, and mass actions on DW may occur separately or in different combinations. Under any external forcing, the DW becomes a "non-ideal" wave with variable parameters. The external actions are frequently used for mitigating detonations, which ceases when a critical level of forcing is exceeded. This was first shown by Zel'dovich [27] and later by many others. According to [27] and more detailed studies [28], the relative deficit of detonation velocity is maximum at the critical level of any action:

$$\frac{D_{\mathrm{CJ}} - D_{cr}}{D_{\mathrm{CJ}}} \approx \frac{RT_S}{E_a} \tag{5}$$

where D_{cr} is the minimal velocity of steady DW under the critical action, T_s is the leading shock temperature in the DW front corresponding to the Zel'dovich–von Neumann–Döring (ZND) model, E_a is the activation energy of chemical reaction at the induction period, and R is the universal gas constant. Equation (5) is compatible with Eq. (1), i.e. it is valid for realistic gas detonations propagating in smooth tubes of sufficiently large diameter. Among different external actions, the power (energetic) forcing is the least effective, because any output (loss) or input of heat in the reaction zone is compensated in a considerable part by the shift in chemical equilibrium. For example, for DW in $2H_2 + O_2$ mixture the relative heat loss $\Delta Q/Q_{\mathrm{CJ}} = 0.23$ gives the velocity deficit $\Delta D/D_{\mathrm{CJ}} = 0.038$; for $C_2H_2 + 2.5O_2$ mixture $\Delta D/D_{\mathrm{CJ}} = 0.1$ is attained by the loss of about 60% of heat Q_{CJ} released in the ideal DW [29]. The other actions, including the combined actions, are more effective. Their effect is less compensated by the chemical equilibrium shift.

Equation (5) is correct when the chemical reaction in DW is initiated due to heating in the leading SW. However, if initiation is performed by the other mechanism, the velocity can essentially decrease. As shown in [30, 31], the DW velocity can be reduced by a factor of two, due to friction of the flow with tube walls or by other external momentum action, when initiation limits in D are absent. Heat loss results in additional D reduction.

The combination of several actions affect DW propagating in channels, e.g. when special periodically placed obstacles are used. This effect is very pronounced in a system containing the explosive gas mixture inside an inert porous medium [32–35]. In this case, there exist several actions on the reacting flow, namely, a momentum (force) action, heat loss, and local geometric and non-stationarity effects. Therefore, the widest range of explosion steady-state wave velocities $D < D_{\mathrm{CJ}}$ (5-fold reduction and more) is realized in these systems owing to the gradual increase in action intensities (Fig. 6). The governing parameters are the pore size, the initial pressure of the gaseous mixture, and the species con-
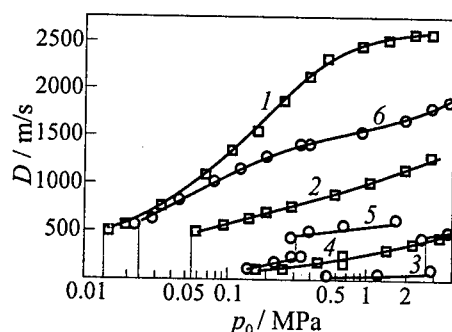
Figure 6 Detonation and fast combustion velocities of gas mixtures in inert porous media [33, 34], δ is the size of steel or stone granules filling the detonation tube. 1 — $C_2H_2 + 2.5O_2$, $\delta = 0.6$–1.2 mm, 2 — $8\%C_2H_2$ + air, $\delta = 12$ mm, 3 — $7\%C_2H_2$ + air, $\delta = 0.7$–1.2 mm; $\delta = 2.5$–3.5 mm: 4 — $18\%H_2 + O_2$, 5 — $17\%H_2 + O_2$, 6 — $H_2 + O_2$

centrations. The transition to low speeds is accompanied by changing the mechanism of mixture ignition from the incident SW-induced ignition to the reflected SW-induced ignition and then to the convective jet ignition mechanism [36]. Moreover, at low propagation velocities the boundary between detonation and deflagration vanishes. The gradual transition of D from a supersonic ($D > c_0$) to a subsonic value ($D < c_0$) is realized when changing a governing parameter of the system (here c_0 is the speed of sound in the initial gaseous mixture without porous medium). Simultaneously, a discontinuous shock front in the pressure profile transforms to a smooth hump [33–34].

Notice that the limiting conditions for the propagation of gas explosion in inert porous media are approximated by the Peclet criterion:

$$\text{Pe} = \frac{d\rho_{01}u_n}{\lambda_{01}} > \text{Pe}_{cr} \approx 60 \tag{6}$$

where d is the maximum pore diameter, u_n is the normal flame velocity, ρ_{01} and λ_{01} are the gas density and thermal conductivity in the initial state, respectively. In different cases, the critical Peclet number can deviate up and down from this mean value by a factor of 2 [33].

FOURTH WAY OF DETONATION CONTROL: SHAPING OF CHANNEL OR CHAMBER

The geometrical influence on DW is commonly combined with other control means. This has already been shown by some preceding examples. Here, two more specific examples of the fourth way of explosion control will be presented. The first example is concerned with the DW amplification when it propagates along the channel with contracting cross-section. Transmission of the DW from the channel of constant cross-section into the section contracting at a constant angle and then into the narrow channel of constant cross-section was studied experimentally by Gavrilenko and Prokhorov [36]. In this case, the DW becomes

(a)

(b)

(c)

(d)

(e)
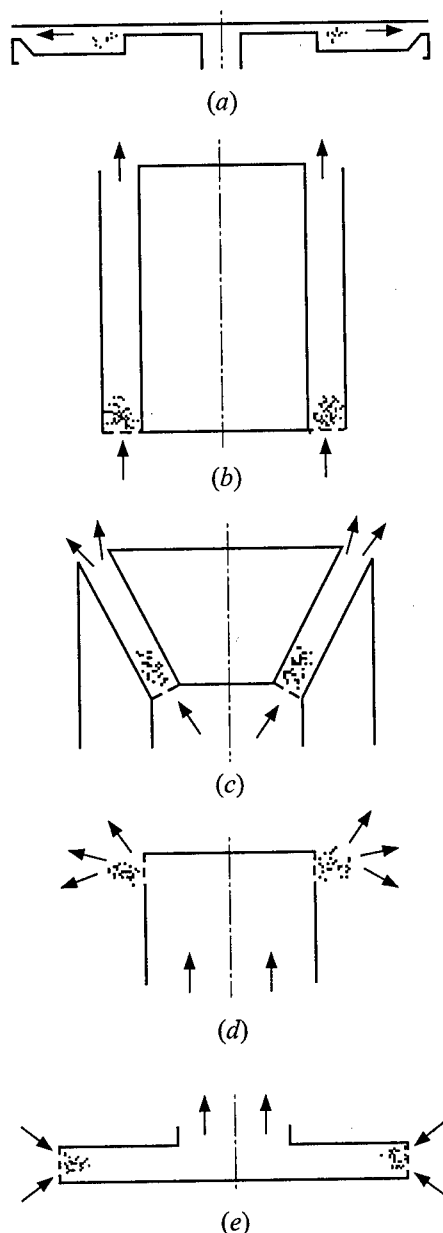
Figure 7 Schematics of experimental chambers for detonation burning of fuel/oxygen (a–d) and fuel/air (e) mixtures

overdriven but the spatial flow pattern is rather complicated. The obtained overdrive degree D_1/D_0 at the inlet to the narrow channel depends on the wall inclination angle and the relation between the initial and final cross-section areas. The dependencies of this quantity on the wedge and cone angles are shown in Fig. 4b. The maximal overdrive degree obtained in the experiments is close to 1.7. The 2D numerical simulation of the process exhibits significant axial and radial oscillations of wave parameters [37].

The next example of the geometrical effect on the DW is connected with realizing the continuous spin detonation in annular chambers. The idea and first implementation of the continuous detonation belong to Voitsekhovskii [4, 38]. In an annular chamber, the continuity of detonation is attained by multiple passages of a solitary DW, or several DWs, over a closed path with the reaction products behind the wave, periodically replaced by a fresh mixture that is capable of detonating (in the same wave at the next loop or in the next wave if there are several waves). This process is presently studied most thoroughly in the Lavrent'ev Institute of Hydrodynamics [39–44]. Here, the continuous detonation of a series of fuel–oxygen and fuel–air mixtures in annular chambers of various geometries were investigated by Bykovskii *et al.* The basic schemes of detonation chambers used in the experiments are shown in Fig. 7.

The summary of the study is presented below:

1. All tested gaseous and liquid fuels (acetylene, hydrogen, propane, methane, kerosene, gasoline, benzene, alcohol, acetone, diesel fuel) are capable of continuously detonating in the mixtures with oxygen in annular chambers.

2. There exist critical (minimum) dimensions of a chamber for the detonation process to be realised. A simple geometrical shape of a chamber, that is an annular cylinder without a nozzle contraction, proved to be appropriate for most cases. However, there exists a possibility of varying the chamber shape and using conical, flat radial, and more complicated-shape chambers. For a highly reactive fuel mixture, continuous detonation can be maintained even in a free-ring fuel charge above the nozzle of the cylindrical injector (see schematics in Fig. 7).

3. The quality of liquid–fuel spraying and mixture formation has a pronounced effect on the detonation stability and limits.

4. Dilution of oxygen with nitrogen results in a sharp reduction in the detonability range. The continuous detonations of fuel–air mixtures (with hydrogen, methane, sprayed kerosene and diesel fuel) is accomplished only in a disk-shaped chamber 0.2 m in diameter with a swirling flow directed from the periphery to the central outlet opening.

The flow of products escaping from the chamber of scheme b in Fig. 7 depends on the chamber relative length $\Lambda = l/\pi d$, where d is the DW track diameter. The flow is almost stationary at $\Lambda \gg 1$, and it is very unstable at $\Lambda \ll 1$. In the latter case, an air portion can replace the detonation products near the outlet opening, and the effect of the specific impulse increase can be obtained by the analogy with the non-stationary effects mentioned above.

CONCLUDING REMARKS

1. Variations of mixture composition, initial pressure, and a heterogeneous structure of charges of some explosive mixtures allow intentional changes in the detonation velocity from about 100 m/s to 10–14 km/s.

2. It is also possible to reduce, almost continuously, the velocity of a self-sustaining explosion wave from the CJ detonation velocity to rather low values of about 10 m/s by means of a force, energy, and non-stationary geometric forcing of the explosion wave.

3. The explosive heterogeneous mixtures based on super-low-density combustible foams are suitable for controlling explosion pressure and energy

within a wide range from gas–mixture-relevant to HE-relevant parameters.

4. A considerable change of explosion parameters can be achieved in controlled, non-stationary processes, such as DDT and wave reflections.

5. The continuous spinning detonative burning of gaseous and liquid fuels can be accomplished in annular chambers. Such a process can be used in propulsion devices in both stationary and pulsating combustion modes, depending on the design parameters of the engine.

REFERENCES

1. Borisov, A. A., "Initiation of Detonation in Gaseous and Two-Phase Mixtures," In: *Gaseous and Heterogeneous Detonations: Science to Applications.* (Eds. G. D. Roy, S. M. Frolov, K. Kailasanath, and N. N. Smirnov), ENAS Publ., Moscow, 1999, 3–24.

2. Vasil'ev, A. A., Zhdan, S. A., and Mitrofanov, V. V., "Detonation Initiation in Gaseous and Heterogeneous Systems," In: *Gaseous and Heterogeneous Detonations: Science to Applications.* (Eds. G. D. Roy, S. M. Frolov, K. Kailasanath, and N. N. Smirnov), ENAS Publ., Moscow, 1999, 25–39.

3. Vasil'ev, A. A., Valishev, A. I. *et al.*, "Detonation Hazards of Hydrogen Mixtures," *Proc. Symposium (International) On Hazards, Prevention, and Mitigation of Industrial Explosion. Colloquium on Gas, Vapor, Hybrid and Fuel–Air Explosion,* Schaumburg, USA, 1998, 391–413.

4. Voitsekhovskii, B. V., Mitrofanov, V. V., and Topchian, M. E., *Structure of Detonation Front in Gases.* Sibirian Branch of the USSR Academy Sci., Novosibirsk, 1963.

5. Mitrofanov, V. V., "Gas Detonation Mechanisms in View of Today," In: *Combustion, Detonation, Shock Waves. Proc. Zel'dovich Memorial.* (Eds. A. G. Merzhanov and S. M. Frolov), Moscow, ENAS Publ., 1, 1995, 328–345.

6. Vasil'ev, A. A., Valishev, A. I., and Vasil'ev, V. A., "The Detonation Safety of Gaseous Fuels. Acetylene and Cyanogen," *Proc. 16th ICDERS,* University of Mining and Metallurgy, Cracow, Poland, 1997, 594.

7. Mitrofanov, V. V., *Detonation Waves in Heterogeneous Media.* Novosibirsk State University Press, Novosibirsk, 1988.

8. Pinaev, A. V., and Sychev, A. I., *Sov. J. Physics Combustion Explosion,* **22**, 3, 109–118, 1986.

9. Pinaev, A. V., and Sychev, A. I., *Sov. J. Physics Combustion Explosion,* **23**, 6, 76–84, 1987.

10. Sychev, A. I., *Rus. J. Physics Combustion Explosion*, **31**, 5, 83–91, 1995.

11. Mitrofanov, V. V., and Bakirov, I. T., "Detonation of Sensitive Explosive Suspension in Vacuum," *Rus. J. Physics Combustion Explosion*, **30**, 2, 122–124, 1994.

12. Mitrofanov, V. V., "On Very High-Speed Detonation of Explosives with Longitudinal Cavities," *Sov. J. Physics Combustion Explosion*, **11**, 1, 73–81, 1975.

13. Bakirov, I. T., and Mitrofanov, V. V., *Sov. J. Doklady USSR Academy Sci.*, **231**, 6, 1315–1318, 1976.

14. Mitrofanov, V. V., and Subbotin, V. A., "Spin Detonation of Explosive Dust Layer in Vacuumed Tubes," In: *Advances in Experimentation & Computation of Detonations. Book of Abstracts.* (Eds. G. D. Roy, S. M. Frolov, K. Kailasanath, and N. N. Smirnov), Moscow, ENAS Publ., 1998, 111–112.

15. Zhdan, S. A., and Prokhorov, E. S., "Structure of a Detonation Wave in a Channel Partially Filled with a RDX Particle Suspension," In: *Gaseous and Heterogeneous Detonations: Science to Applications.* (Eds. G. D. Roy, S. M. Frolov, K. Kailasanath, and N. N. Smirnov), Moscow, ENAS Publ., 1999, 351–362.

16. Solov'ev, V. S., Andreev, S. G., *et al.*, "Combustion and Explosion," *Proc. 3rd USSR Symposium on Combustion and Explosion*, Moscow, Nauka, 1972, 451–454.

17. Bolkhovitinov, L. G., and Khvostov, Ju. B., *Nature*, **274**, 5674, 882–883, 1976.

18. Kalinina, N. M., Nifad'ev, V. I., and Savinkov, V. D., Explosive, Patent SU1811688 A3, 1989.

19. Nifad'ev, V. I., and Kalinina, N. M., *Sov. J. Physics Combustion Explosion*, **28**, 6, 63–70, 84–89, 1992.

20. Nifad'ev, V. I., and Kalinina, N. M., "Detonation of Low-Density Explosive Mixtures Based on Polystyrene Foam in External Electric and Magnetic Fields," *Proc. 4th Conference (International) "Lavrent'ev Readings" on Mathematics, Mechanics and Physics*, Lavrent'ev Institute of Hydrodynamics, Novosibirsk, 1995, 155.

21. Gavrilenko, T. P, Krasnov, A. N., and Nikolaev, Yu. A., "Gas Detonation Transfer Through an Inert Gas Plug," *Sov. J. Physics Combustion Explosion*, **18**, 2, 127–131, 1982.

22. Gavrilenko, T. P., Nikolaev, Yu. A., and Ul'yanitski, V. Yu., RF Patent No.1628558, 1989.

23. Shchelkin, K. I., *Fast Combustion and Spin Detonation of Gases.* Voenizdat, Moscow, 1949.

24. Lee, J. H., Knystautas, R., and Freiman, A., "High Speed Turbulent Deflagration and Transition to Detonation in H_2–Air Mixtures," *Combustion Flame*, **56**, 227–279, 1984.

25. Back, I. H., Dowler, W. L., and Varsi, G., "Detonation Propulsion Experiment and Theory," *AIAA J.*, **13**, 10, 1418, 1983.

194

26. Zhdan, S. A., Mitrofanov, V. V., and Sychev, A. I., "Reactive Impulse from the Explosion of a Gas Mixture in a Semi-Infinite Space," *Rus. J. Physics Combustion Explosion*, **30**, 5, 90–97, 1994.

27. Zel'dovich, Ya. B., "On the Theory of Propagation of Detonation in a Gaseous System," *Sov. J. Experimental Theoretical Physics*, **10**, 5, 542–568, 1940.

28. Frolov, S. M., The Effects of Non-Ideality on the Explosion Origin and Propagation, Dr. Sci. Thesis. N. N. Semenov Institute of Chemical Physics, Moscow, 1992.

29. Nikolaev, Yu. A., and Topchian, M. E., "Calculations of Non-Equilibrium Flows in Detonation Waves," *Sov. J. Physics Combustion Explosion*, **13**, 3, 393–404, 1977.

30. Rybanin, S. S., "On the Theory of Detonation in Rough Tubes," *Sov. J. Physics Combustion Explosion*, **5**, 3, 395, 1969.

31. Mitrofanov, V. V., "Some Critical Detonation Phenomena Connected with Momentum Losses," *Sov. J. Physics Combustion Explosion*, **19**, 4, 169–174, 1983.

32. Mamontov, G. M., Mitrofanov, V. V., and Subbotin, V. A., "Detonation Regimes of Gas Mixtures Within a Hard Porous Medium," In: *Detonation*. Institute of Chemical Physics, Chernogolovka, 106–110, 1980.

33. Pinaev, A. V., and Lyamin, G. A., "The Main Regularities of Subsonic and Detonation Combustion of Gases in Inert Porous Media," *Sov. J. Physics Combustion Explosion*, **25**, 4, 75–85, 1989.

34. Lyamin, G. A., Mitrofanov, V. V., Pinaev, A. V., and Subbotin, V. A., "Propagation of Gas Explosion in Channels with Uneven Walls and in Porous Media," In: *Dynamic Structure of Detonations in Gaseous and Dispersed Media*. (Ed. A. A. Borissov), Kluwer Acad. Publ, Netherlands, 1991, 51–76.

35. Babkin, V. S., "Filtrational Combustion of Gases. Present State of Affairs and Prospects," *Pure and Applied Chemistry*, **65**, 2, 335–344, 1993.

36. Gavrilenko, T. P., and Prokhorov, E. S., "The Overdriven Detonation Wave in Gas," *Sov. J. Physics Combustion Explosion*, **17**, 6, 121–125, 1981.

37. Zhdan, S. A., and Prokhorov, E. S., "Formation and Propagation of Overdriven Gas Detonation Waves in Conic Converging Channels," *Rus. J. Physics Combustion Explosion*, **31**, 5, 92–100, 1995.

38. Voitsekhovskii, B. V., "Stationary Detonation," *Sov. J. Doklady USSR Academy Sci.*, **129**, 6, 1254–1256, 1959.

39. Mikhailov, V. V., and Topchian, M. E., "To the Studies of Continuous Detonation in an Annular Channel," *Sov. J. Physics Combustion Explosion*, **1**, 4, 20–23, 1965.

40. Edwards, B. D., "Maintained Detonation Waves in an Annular Channel: a Hypothesis which Provides the Link Between Classical Acoustic Combustion Instability and Detonation Waves," *Proc. 16th Symposium (International) on Combustion*, The Combustion Institute, Pittsburgh, PA, 1976.

41. Bykovskii, F. A., and Mitrofanov, V. V., "Detonative Combustion of Gas Mixture in a Cylindrical Chamber," *Sov. J. Physics Combustion Explosion*, **31**, 5, 107–117, 1980.

195

42. Bykovskii, F. A., Vasil'ev, A. A., Vedernikov, E. F., and Mitrofanov, V. V., "Detonative Burning of Gas Mixtures in Radial Annular Chambers," *Sov. J. Physics Combustion Explosion*, **30**, 4, 111–119, 1994.

43. Bykovskii, F. A., and Vedernikov, E. F., "Continuous Detonative Combustion of the Annular Layer of Gas Mixture," *Rus. J. Physics Combustion Explosion*, **32**, 5, 17–20, 1996.

44. Bykovskii, F. A., Mitrofanov, V. V., and Vedernikov, E. F., "Continuous Detonative Combustion of Fuel–Air Mixtures," *Sov. J. Physics Combustion Explosion*, **33**, 3, 120–131, 1997.

PROPAGATION, DECAY AND RE-IGNITION OF DETONATIONS IN TECHNICAL STRUCTURES

M. Fischer, E. Pantow, and T. Kratzel

In the present work, an experimentally proven mathematical-physical model for detonation propagation, decay and re-ignition processes in technical structures is developed. The model allows for the analysis and assessment of complex technical structures, with respect to safety in case of detonative combustion.

1   INTRODUCTION

For the propagation, decay and re-ignition of detonation processes and for the design of protection systems against accompanying shock waves, the interaction of detonation front structures with confining structures is of primary importance. Therefore, experimental and theoretical investigations have been carried out to study detonations in complex geometries. Decoupling and recoupling mechanisms of shocks and flame fronts in technical geometries play a key role in detonation propagation behavior [1–4].

Current safety devices, like detonation arresters, are mostly designed on the basis of practical experience and engineering estimates. However, there is a lack of simple but powerful theoretically based models and numerical simulation tools, which are needed to further improve corresponding safety devices by taking into account the essential phenomena of shock–flame front decoupling and recoupling mechanisms.

The diffraction of detonation fronts is well studied by a number of researchers [5–20]. In particular, the significance of the critical tube diameter was emphasized. However, the conditions and limits for recoupling of shocks, and flame fronts after detonation decoupling have been investigated only in a few papers.

197

2 MODELING OF SHOCK-INDUCED COMBUSTION

The objective of the present paper is modeling of detonation propagation for analyzing and assessing technical structures in regard to their feedback effect on the detonation propagation process itself. The applicability for practical needs was an aspect of primary concern. On one hand, the essential effects of detonation propagation have to be adequately described, and on the other hand, the CPU costs for analyzing real technical systems should remain meaningful. For the fluid-dynamic modeling, the flow was assumed inviscid and compressible, thus governed by the Euler equations:

$$rcl\frac{\partial \rho}{\partial t} + \nabla \cdot (\rho \mathbf{v}) \quad = \quad 0 \tag{1}$$

$$\frac{\partial}{\partial t}(\rho \mathbf{v}) + \nabla(\rho \mathbf{v} \otimes \mathbf{v}) \quad = \quad 0 \tag{2}$$

$$\frac{\partial}{\partial t}(\rho e) + \nabla \cdot ((\rho e + p)\mathbf{v}) \quad = \quad 0 \tag{3}$$

where t is the time, ρ is the density, $\mathbf{v}$ is the velocity, p is the pressure and e is the total energy. The total energy is the sum of the internal energy u and the kinetic energy $v^2/2$. To decrease the CPU time required, only a two-dimensional case is considered. Two-dimensional Euler equations take the form:

$$\frac{\partial \rho}{\partial t} + \frac{\partial(\rho u)}{\partial x} + \frac{\partial(\rho v)}{\partial y} = 0 \tag{4}$$

$$\frac{\partial(\rho u)}{\partial t} + \frac{\partial(\rho u^2 + p)}{\partial x} + \frac{\partial(\rho u v)}{\partial y} = 0 \tag{5}$$

$$\frac{\partial(\rho v)}{\partial t} + \frac{\partial(\rho u v)}{\partial x} + \frac{\partial(\rho v^2 + p)}{\partial y} = 0 \tag{6}$$

$$\frac{\partial(\rho e)}{\partial t} + \frac{\partial(\rho u(e + p/\rho))}{\partial x} + \frac{\partial(\rho v(e + p/\rho))}{\partial y} = 0 \tag{7}$$

where x and y are the coordinates, and u and v are the corresponding velocity components. These equations were solved using the Mac Cormack scheme [21] on a structured computational mesh. To get a good resolution of discontinuities, a Flux Corrected Transport (FCT) algorithm [22, 23] was applied and adapted to varying grid size.

For modeling the chemical reactions, a two-stage induction–reaction model was used. The first step, the induction stage, was assumed to be thermally

neutral, while in the second step, the reaction stage, the chemical energy was released. Similar models have been presented elsewhere [24, 25]. In this study, the model was derived for mixtures with atmospheric initial conditions. For the induction stage, the Arrhenius formulation was used:

$$w_\alpha = \frac{d\alpha}{dt} = \frac{1}{\tau_i} = -Ap^n e^{-B/T} \tag{8}$$

where w_α is the reaction rate of the induction parameter α, τ_i is the induction time and T is the temperature. Parameters A, B, and n were obtained using a detailed H_2–O_2 kinetic mechanism [26]. The parameters found were remarkably independent of the mixture composition. For the mixture with 55% N_2 dilution, the following values were obtained:

$$n = 1; \qquad A = 6.29 \cdot 10^7 \ (\text{bar·s})^{-1}; \qquad B = 11042 \text{ K} \tag{9}$$

For describing the exothermic reaction stage, a reaction parameter β is introduced. Its rate of change, $w_\beta d\beta/dt$ can roughly be described by a global model. Because the reaction stage is short compared to the induction stage, the errors encountered in global modeling can be considered sufficiently small. Thus, for this stage an another Arrhenius formulation is used:

$$w_\beta = -Cp\beta e^{-D/T} \tag{10}$$

Parameters C and D were determined by calculating the time of 50% energy release at different constant temperatures and pressures based on detailed chemistry. For nitrogen dilutions these parameters take the values

$$C \quad = \quad 1.9 \ (\text{bar·s})^{-1} \cdot \varphi_{H_2} \tag{11}$$

$$D \quad = \quad 5000 \text{ K} \tag{12}$$

where φ_{H_2} is the mole fraction of hydrogen. The coupling is provided by the expression for the enthalpy of the mixture

$$h = \beta h_1 + (1 - \beta)h_2 \tag{13}$$

where h_1 is the enthalpy of the unburnt mixture, and h_2 is the enthalpy of the burnt mixture. These enthalpies were taken from JANAF tables [27]. Here, the different dilutions had their major influence.

3 EXPERIMENTAL SETUP

The experiments were carried out using a 4000 mm long tube of rectangular 100 mm × 25 mm cross-section. Detonation was initiated by transition from
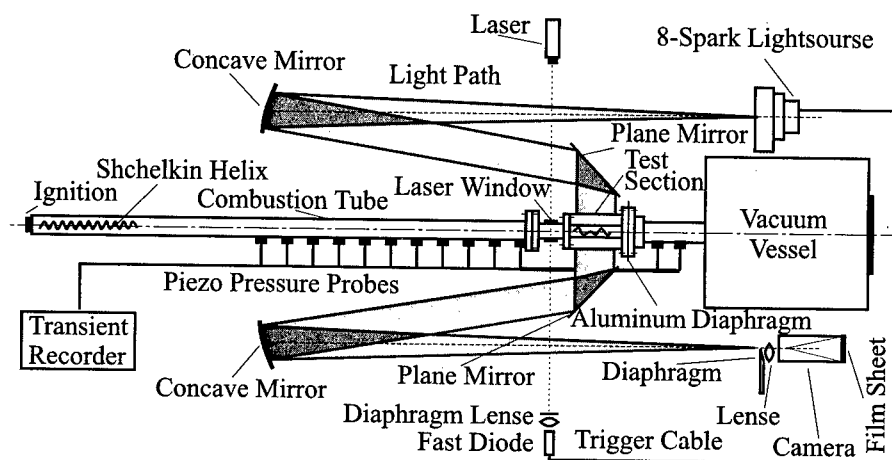
Figure 1 Experimental setup with the combustion tube and Schlieren optics

deflagration using a 1500 mm long Shchelkin helix. The schematic of the experimental setup is shown in Fig. 1. To observe the detonation propagation, Krantz–Schardin Schlieren optics with an 8-spark light source was used.

Hydrogen–oxygen mixtures diluted by varying amounts of nitrogen or argon were investigated in the experiments.

4 RESULTS OF EXPERIMENTS AND MODELING

4.1 Plane Detonations

Before analyzing detonations in complex geometries, the developed mathematical-physical model has to be experimentally checked to see if detonation propagation mechanisms are correctly described in planar channels with different H_2/air and H_2/O_2/Ar-mixtures.

To be able to better compare the results of experiments with simulations, Schlieren-optical graphs have been calculated based on the density field of the flow [28]. Figure 2 shows a detonation front in a H_2/O_2-mixture with a high Argon dilution.

Figure 3 shows the development of the cellular structure of a detonation front from an initially plane overdriven detonation.
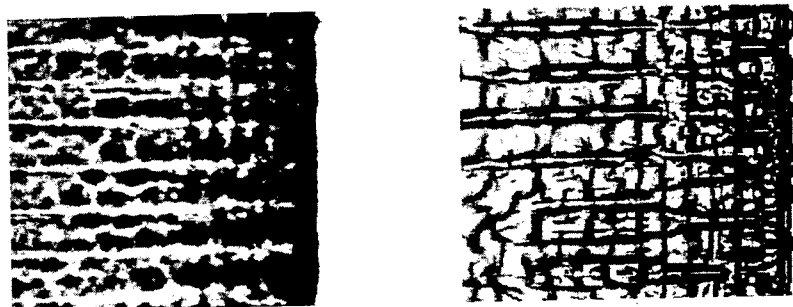
Figure 2 Detonation front in a mixture of 20% H_2, 10% O_2 and 70% Ar in a planar channel 27 mm height. Left: Experiment (Schlieren photograph). Right: Simulation (Schlieren-optical graph)
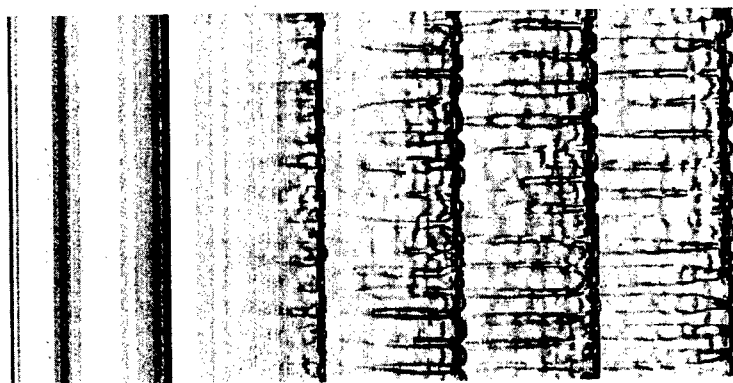
Figure 3 Simulated Schlieren-optical representation of the history of the cellular detonation front structure

Besides, one can expect that in mixtures with high specific heats a transition occurs from a rather regular front structure in the overdriven state, to a more irregular front structure in the Chapman-Jouguet (CJ) state. Figure 4 shows this transition. Clearly, the distances between transverse shocks are expanded, in the course of detonation evolution.

The comparison between experimental and predicted results shows a rather good agreement concerning the essential dynamic effects of plane detonations,

201

Figure 4 Simulated Schlieren-optical representation of the history of the transition of overdriven detonations to the CJ state

e.g. dealing with the detonation cell size and the degree of regularity of the detonation front structure. Note that no adoption of parameters to detonation-specific empirical data was done. Important were the improvements in the thermodynamic model, e.g. the consideration of variable specific heats of mixture components. Moreover, high resolution of shocks by means of the FCT-algorithms allows the precise representation of details. Therefore, the simulation based on mathematical-physical models opens new insights into the mechanisms of detonation propagation with great practical relevance.

4.2 Sudden Expansion of Flow Cross Section

In the case of sudden expansion of flow cross-section, the decoupling and recoupling of shock and flame fronts, i.e. the re-ignition of detonation processes, are investigated experimentally and by simulation.

Continuous Detonation Propagation

When the number of detonation cells in the entry cross-section exceeds the critical value, one can expect, in principle, the detonation processes will survive. Figure 5 shows Schlieren photographs of experiments for a d/λ-ratio of 11 and a cross-section expansion of 1:3. For the experiments and the model calculations, $H_2/O_2/Ar$ mixture was chosen to get small detonation cell widths and, as a result, smaller cross-sections. The cross-section before the expansion was 27 mm × 25 mm, and after the expansion, 80 mm × 25 mm. For the entrance cross-section, a critical detonation cell number of 10 was found.

202
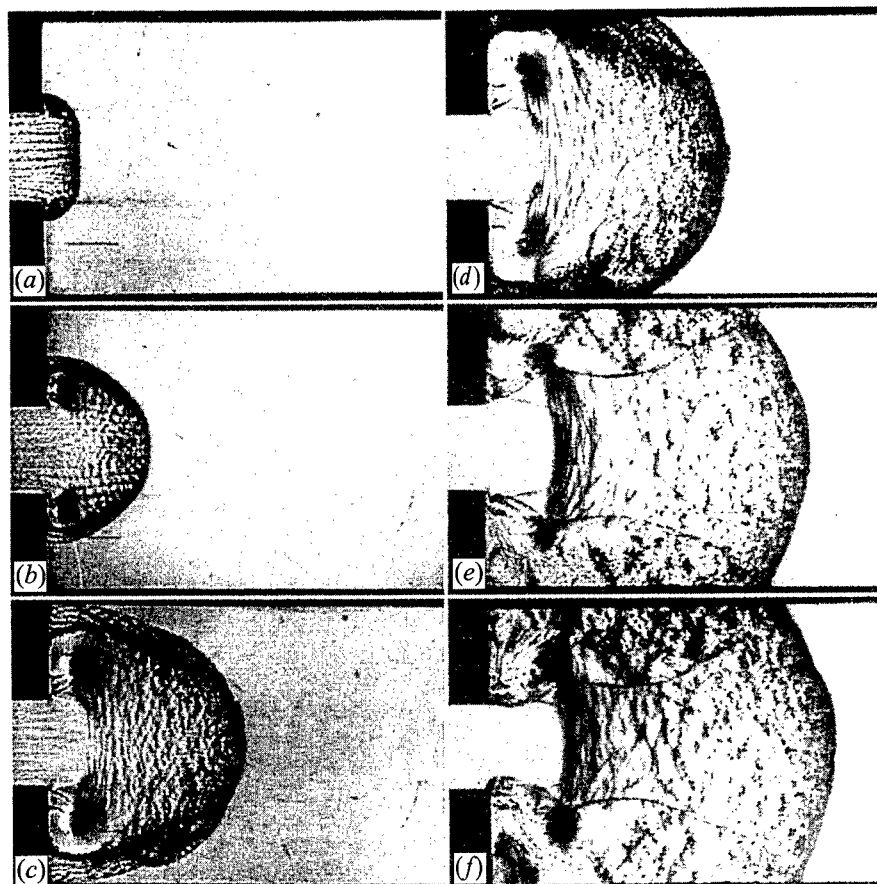
Figure 5 Schlieren photograph of the survival of a detonation process due to transverse shock waves. Expansion ratio 1:3. Unburnt gas mixture: $2H_2 + O_2 + 65\%$ Argon

In the simulation, the same effect could be observed. In Fig. 6, the detonation is maintained by transverse shock waves after an intermediate lateral decoupling of the shock and the flame. In the model calculation, the detonation front structure is also transformed from regular to irregular.

Complete Decoupling and Re-Ignition

By increasing the Argon dilution from 65 to 70% the detonation cell width was increased to reduce the number of cells in the entrance cross-section below

203
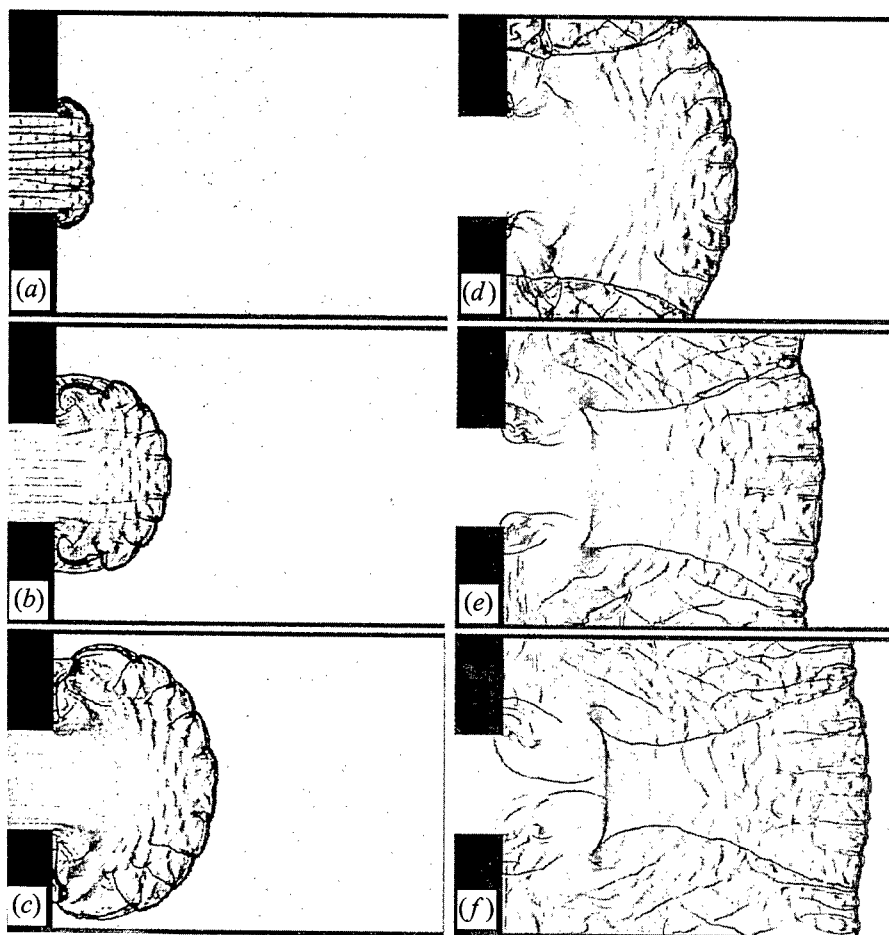
Figure 6 Model calculation of maintaining detonation processes due to transverse shock waves. Expansion ratio 1:3. Unburnt gas mixture: $2H_2 + O_2 + 60\%$ Argon

the critical number. One can observe in Fig. 7 how shock and flame fronts become shortly decoupled. The curved main shock wave is reflected at the wall. After a short time, the regular reflection is transformed into a Mach reflection, which is so strong that the mixture is again ignited to a detonation mode. In a very short time, transverse shocks appear. The small distance between the transverse shocks indicates that an overdriven detonation occurred.

Figure 8 shows the result of the corresponding model calculation. The same effects are observed when compared to the experiment of Fig. 7.
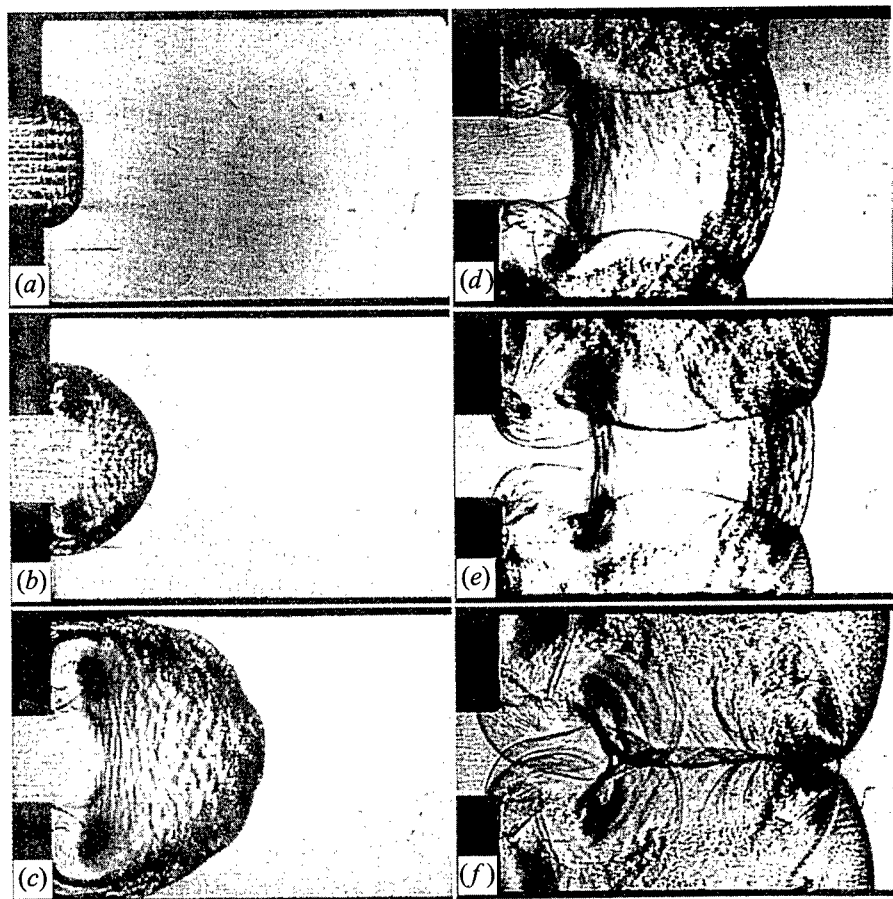
Figure 7 Schlieren photograph of detonation re-ignition due to Mach reflection behind an expanded cross-section. Expansion ratio 1:3. Unburnt gas mixture $2H_2 + O_2 + 70\%$ Argon

Irreversible Decay of Detonation

In the case of further dilution of the mixture, the shock reflection at the walls can finally create no re-ignition of detonation, i.e. the decoupling of shock and flame is irreversible. The Schlieren photograph in Fig. 9 shows such a decoupling process, and Fig. 10 shows Schlieren-optical representation obtained on the basis of the model calculation. A good agreement with the experiment is clearly seen.

205
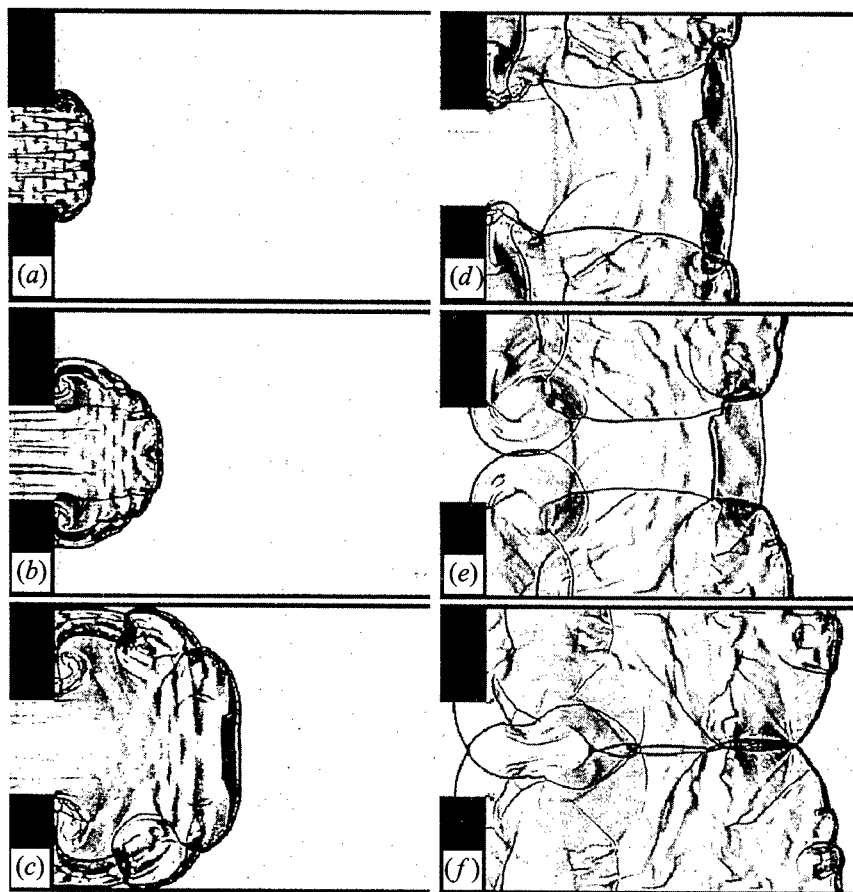
Figure 8 Model calculation of the experiment shown in Fig. 7: Detonative re-ignition due to Mach reflection after expansion of cross-section. Expansion ratio 1:3. Unburnt gas mixture $2H_2 + O_2 + 70\%$ Argon

4.3 Application to Detonation Arrestor Design

Figures 11 and 12 show the good agreement between the results of experiments and model calculations for the case of detonation arrestors of conventional design.

The problem with conventional detonation arrestors is that in full size technical structures detonative re-ignition behind the arrestor cannot be prevented.

Figure 13 shows the detonation propagation through an improved, innovative detonation arrestor design. The re-ignition of a detonation can be prevented with such a design.
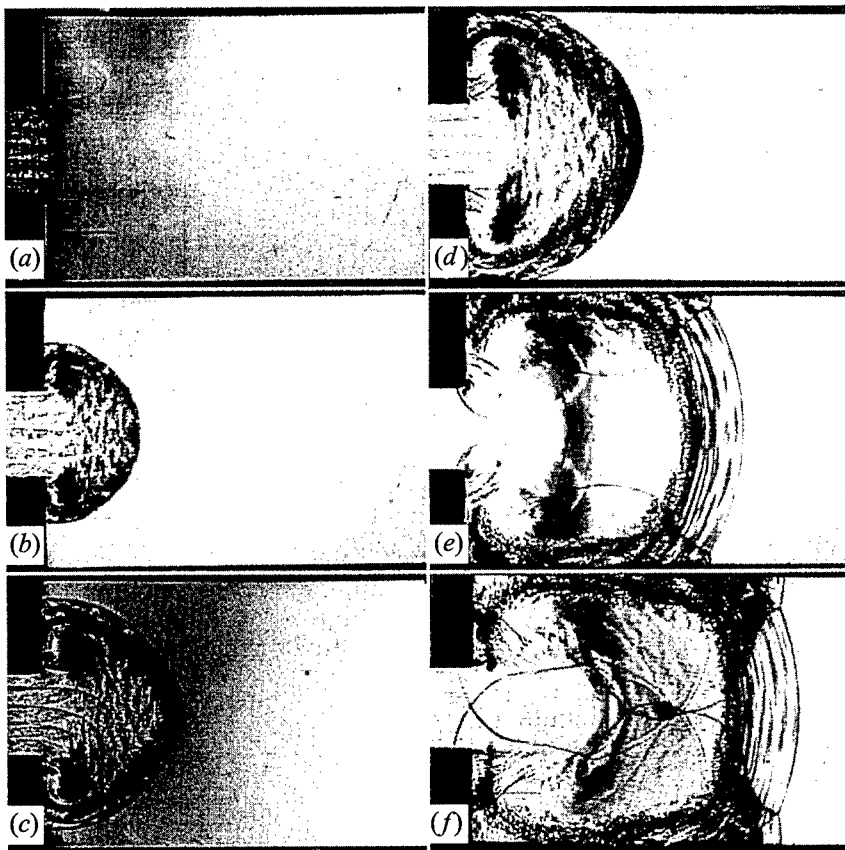
Figure 9 Schlieren photograph of irreversible detonation decay behind an expanded cross-section. Expansion ratio 1:3. Unburnt gas mixture $2H_2 + O_2 + 73\%$ Argon

5 CONCLUDING REMARKS

In the present work, an experimentally proven mathematical-physical model for detonation propagation, decay and re-ignition in technical structures is developed. The model allows up to perform the analysis and assessment of complex technical structures with respect to safety in the case of detonative combustion.

A two-step model for the chemical reaction was developed on the basis of Zel'dovich – Döring – von Neumann detonation model, considering all important thermal material properties and their influence on the structure of detonations. The relation between the degree of the irregularity of detonation structure and the mixture specific heat was analyzed and described in agreement with experi-
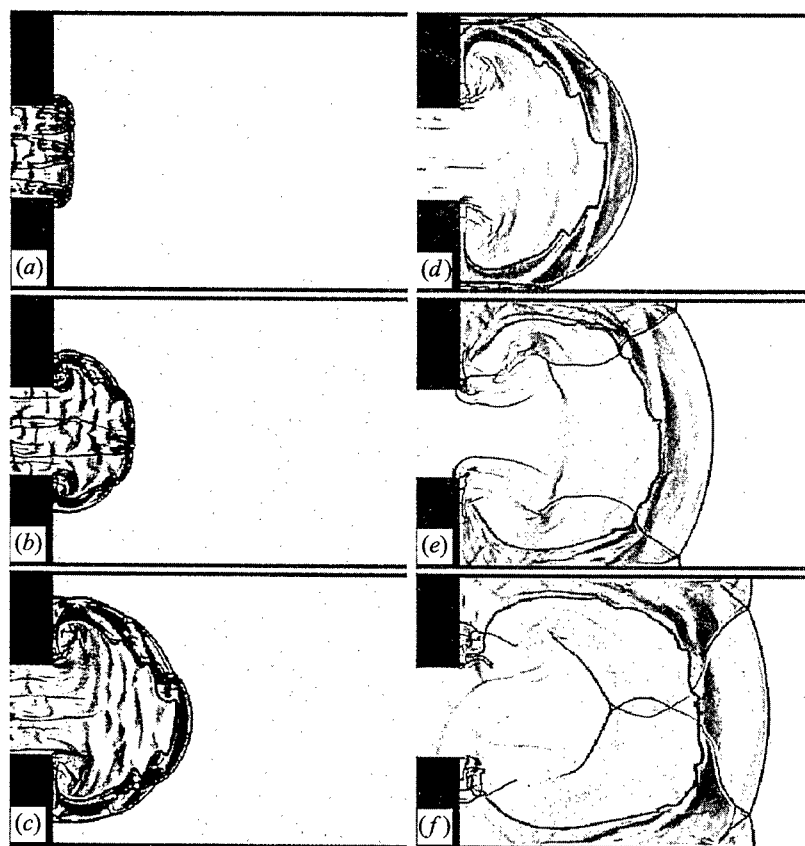
Figure 10 Model calculation of the experiment shown in Fig. 9: irreversible detonation decay behind an expanded cross-section. Expansion ratio 1:3. Unburnt gas mixture $2H_2 + O_2 + 80\%$ Argon

ments using a variety of hydrogen, oxygen and inert gas compositions. In mixtures with high specific heat and therefore low von Neumann-shock temperature, strong transverse shocks are necessary to maintain the detonation propagation process. The transverse shock waves also lead to sudden re-ignition of already decoupled portions of the detonation front, thus initiating irregular structure of the detonation front. This means, e.g. for DDT processes that the originating detonation can be only overdriven because no transverse shocks still exist at that time.

For further experimental verification of the developed model, the detonation propagation through abrupt changes of the tube cross-section was investigated. The mechanisms and phenomena of decoupling processes of shock and flame
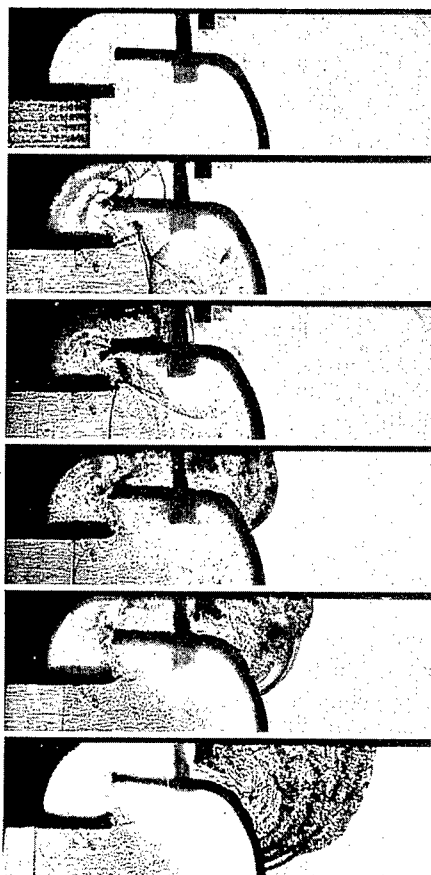
Figure 11 Schlieren photograph of detonation propagation and decay in a conventional detonation arrestor. Unburnt gas mixture: $2H_2 + O_2 + 75\%$ Argon
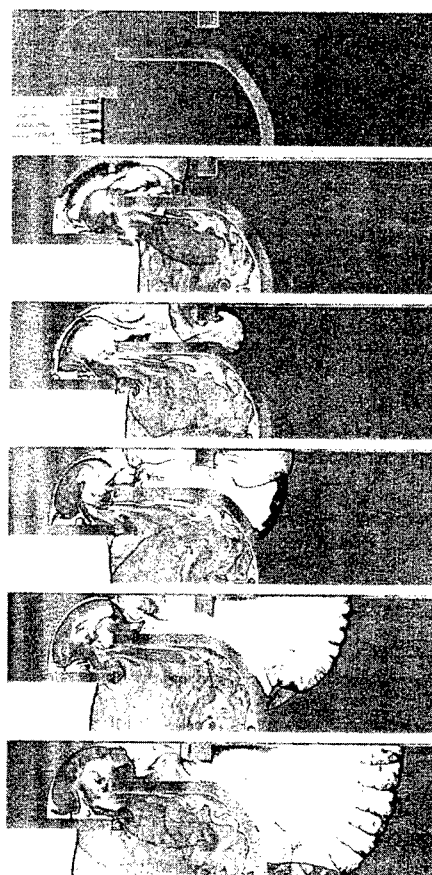
Figure 12 Model calculation of shown in Fig. 11

fronts and the detonative re-ignition due to shock reflections were systematically investigated in experiments for this case. As a result, the following mechanisms and phenomena could be analyzed and described.

At entry cross-sections larger than the critical tube width, the maintenance of detonations, if already decoupled, takes place due to transverse waves coming out of the middle of the detonation front. Below the critical tube width, shock and flame will decouple completely downstream of the expansion cross-section.

209
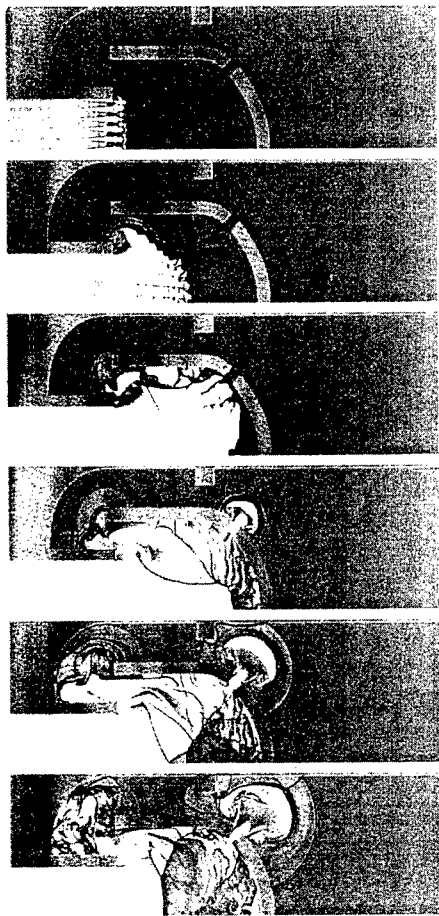
Figure 13. Model calculation of the ensured suppression of a detonation front by the arrestor of improved, innovative concept

Due to the Mach reflection of the bowed main shock at the confining walls, detonative re-ignition is possible. The number of detonation cells necessary for this re-ignition is often smaller than the value of the critical width. The condition for re-ignition is the achievement of an overdriven state at which the detonation can propagate without strong transverse shock waves. In the case of abrupt increase in cross-section, there exists an expansion ratio such that a detonative re-ignition is impossible after decoupling of the shock wave and the flame. Besides the critical width or diameter, the expansion ratio of tube cross-section is an important parameter for safety assessment of technical structures, in which detonative combustion occurs.

The similarity criterion for scaling the decoupling mechanisms from laboratory to technical dimensions is the ratio of detonation cell size to the entry cross-section. For detonative re-ignition processes, the propagation Mach numbers must also be considered. With that, the transferability of lab-scale experimental results to technical scale is possible using simulation calculations with the developed model.

As an example for the applicability of the experimentally validated model for full scale detonation arrestors, an improved design has been developed and tested in full size. In most of the present detonation arrestors, detonative re-ignition downstream of the arrestor device is a serious problem.

The developed innovative design of detonation arrestors is based both on the expansion of the detonation in an expansion volume inerted by pre-combustion, that is inherently initiated by the detonation itself and the corresponding design measures. By this, a high nonpenetrating reliability is assured.

210

REFERENCES

1. Pantow, E., "Ausbreitung und Zerfall von Detonationsfronten in Wechselwirkung mit technischen Strukturen," *VDI-Fortschrittsberichte Reihe 7*, Stromungsmechanik, **330**, ISBN 3-18-333007-5.

2. Pantow, E., Fischer, M., and Kratzel, T., "Decoupling and Recoupling of Detonations Associated with Sudden Expansion," *Proc. 15th ICDERS*, Boulder, 1995.

3. Pantow, E., Fischer, M., and Kratzel, T., "Nonstationary Detonation Propagation in Complex Geometries," *Proc. 26th Symposium (International) on Combustion*, The Combustion Institute, Pittsburgh, PA, 1996.

4. Pantow, E., Fischer, M., and Kratzel, T., "Detonation Front Structures in Hydrogen Combustibles," *Proc. 16th ICDERS*, Cracow, Poland, 1997.

5. Mitrofanov, V. V., and Soloukhin, R. I., "The Diffraction of Multifront Detonation Waves," *Soviet Physics — Doclady*, **9**, 12, 1055–1058, 1965.

6. Oppenheim, A. K., Manson, N., Wagner, H.-Gg., "Recent Progress in Detonation Research," *AIAA J.*, **1**, 10, 2243–2252, 1963.

7. Oppenheim, A. K., "Novel Insight into the Structure and Development of Detonation," *Acta Astronautica*, **11**, 391–400, 1965.

8. Strehlow, R. A., and Fernandes, F. D., "Transverse Waves in Detonations," *Combustion Flame*, **9**, 109–119, 1965.

9. Edwards, D. H., and Parry, D. J., "The Structure of Transverse Waves in Detonations," *Acta Astronautica*, **14**, 533–537, 1969.

10. Moen, I. O., Murray, S. B., Bjerketvedt, D., Rinnan, A., Knystantas, R., and Lee, J. H. S., "Diffraction of Detonation from Tubes into a Large Fuel–Air Explosive Cloud," *Proc. 19th Symposium (International) on Combustion*, The Combustion Institute, Pittsburgh, PA, 1982, 635–644.

11. Guirao, C. M., Knystantas, R., Lee, J. H. S., Benedick, W., and Berman, M., "Hydrogen–Air Detonations," *Proc. 19th Symposium (International) on Combustion*, The Combustion Institute, Pittsburgh, PA, 1982, 583–590.

12. Murray, S. B., and Lee, J. H. S., "On the Transformation of Planar Detonation to Cylindrical Detonation," *Combustion Flame*, **52**, 269–289, 1983.

13. Liu, Y. K., Lee, J. H. S., and Knystantas, R., "Effect of Geometry on the Transmission Detonation Through an Orifice," *Combustion Flame*, **56**, 215–225, 1984.

14. Bartlma, F., and Schroder, K., "The Diffraction of a Plane Detonation Wave at a Convex Corner," *Combustion Flame*, **66**, 237–248, 1986.

15. Desbordes, D., "Transmission of Overdriven Plane Detonations: Critical Diameter as a Function of Cell Regularity and Size," In: *Dynamics of Explosions.* (Eds. A. Kuhl *et al.*), Progress in Astronautics and Aeronautics Ser., AIAA Inc., N.Y., **114**, 170–185, 1988.

16. Edwards, D. H., Thomas, G. O., and Nettleton, M. A., "The Diffraction of a Planar Detonation Wave at an Abrupt Area Change," *J. Fluid Mechanics*, **95**, Part 1, 79–96, 1979.

17. Gvozdeva, L. G., Baklanov, D. I., Sherbak, N. B., "Propagation of Gas Detonation in Channels with a Sudden Expansion," *Proc. 15th ICDERS*, Boulder, 1995.

18. Moen, J. O., Sulmistras, A., Thomas, G. O., Bjerketvedt, D., and Thiebault, P. A., "Influence of Cellular Regularity on the Behavior of Gaseous Detonations," In: *Dynamics of Explosion. Progress in Astronautics and Aeronautics* Ser. (Eds. J. R. Bowen, J.-C. Leyer, and R. I. Soloukhin), N.Y., **106**, 1986.

19. Oran, E., Kailasanath, K., and Guiguis, R. H., "The Structure of Detonation Waves," *J. de Physique*, **C4**, 105–116, 1987.

20. Lefebvre, M. H., Oran, E., Kailasanath. K., Van Tiggelen, P. J., "The Influence of Heat Capacity and Diluent on Detonation Structure," *Combustion Flame*, **95**, 206, 1993.

21. Mac Cormack, R. W., "The Effect of Viscosity on Hypervelocity Impact Cratering," Technical Report 69-354, AIAA Paper, 1969.

22. Boris, J. P., and Book, D. L., "Flux Corrected Transport. III. Minimal-Error FCT-Algorithms," *J. Comp. Physics*, 397–431, 1976.

23. Book, D. L., Boris, J. P., Frey, M. A., Guirguis, R. H. and Kuhl, A. L., "Adaption of Flux-Corrected Transport Algorithms for Modelling Blast Waves," *Proc. 8th Conference (International) on Numerical Methods in Fluid Mechanics*, Aachen, 1982.

24. Korobeinikov, V. P., Levin, V. A., Markow, V. V., and Chernyi, G. G., "Propagation of Blast Waves in a Combustible Gas," *Acta Astronautica*, **17**, 529–537, 1972.

25. Oran, E., Boris, J. P., Young, T. R., Flanigan, M., Jr., Picone, M., and Burks, T., "Simulations of Gas Phase Detonations: Introduction of an Induction Parameter Model," NLR Memo Report 4255, Naval Research Lab., 1980.

26. Maas, U., and Warnatz, J., "Ignition Processes in Hydrogen–Oxygen Mixtures," *Combustion Flame*, **74**, 53–69, 1988.

27. Stull, D. R., and Prophet, P., "JANAF Thermochemical Tables. National Standard Reference Data Series," **37**, Technical Report, U.S. National Bureau of Standards, Gaithersburg, MD, 1971.

28. Pantow, E., *Visualisierung von zweidimensionalen Stromungsfeldern*. Diplomarbeit, Universitat Stuttgart, 1993.

INVESTIGATION OF H_2 + AIR FAST FLAME PROPAGATION AND DDT IN A TUBE WITH MULTI-DIMENSIONAL ENDPLATES

B. E. Gel'fand, S. V. Khomik, S. P. Medvedev,
A. N. Polenov, A. M. Bartenev, W. Breitung, and A. Veser

A set of experiments in a tube filled with H_2–air mixtures with partially obstructed area and multi-dimensional endplate has been carried out. Three main regimes of loading by explosive combustion of H_2–air mixtures near an obstructed area were distinguished on the basis of the performed tests. The interaction of a decaying complex "shock wave – decelerating flame front," emitted from the obstructed section, with concave reflector gave rise to secondary explosion waves. Those waves came from hot exothermic centers located near a non-flat reflector at H_2 concentrations in the range of 15%–20% (vol.)

INTRODUCTION

Investigations of explosion processes and detonations performed in hydrogen–air mixtures (including the additives of water steam or carbon dioxide) indicate that the sources of hazardous loads are conditioned by fast combustion regimes [1–22]. The fast combustion regimes take place mainly in the obstructed area. Different types of obstructions, wherein the flame can propagate, are described in [1–15]. The effects of pressure waves or shock waves driven by propagating flames are also of interest from the point of view of limiting loading levels, in particular, in case those waves undergo focusing at non-flat surfaces, angles, curved channels and objects [23]. Interaction of pressure or shock waves with such construction elements enhances the probability of self-ignition of combustible mixture in the vicinity of curved surfaces.

It is worth comparing the level of over-pressures produced by fast combustion regimes with some characteristic values. The first value corresponds to the considerable damage limit for structural materials, $\Delta P_1^* \approx 0.01$ MPa. The second, $\Delta P_2^* \approx (0.5$–$0.8)$ MPa, corresponds to a possibility of self-ignition due to focusing at the concave surfaces [23].

Shock waves are usually generated if the velocities of flame propagation in hydrogen–air mixtures exceed 100 m/s. However, it is known that in any mixture of gaseous fuel with air, the normal flame velocity u_n and visible flame velocity $u_\nu = \sigma u_n$ are well below 100 m/s (here $\sigma = \rho_u/\rho_b$ is the expansion ratio, ρ_u the density of unburned mixture, ρ_b the density of combustion products). The investigations in [17–22] showed that the velocities $S > 100$ m/s in hydrogen–air mixtures can be achieved under forced turbulization of the gaseous flow in an obstructed channel. The high flame propagation speed is caused by the increase in the burning surface due to flow turbulization by the obstacles.

To study the effect of obstacles on combustion, various systems were used: perforated screens [1], a set of rods [3], spirals [4], and a system of screens with orifices [4]. The obstacles were mounted in channels of diameter up to 2.5 m [4, 5, 7] and in volumes with cylindrical symmetry [11, 12]. A set of tests were run in a series of concentric perforated spheres [2]. The simplest types of obstructed channels are the tubes with repeated steps of obstacles, or tubes with rough walls [1, 2]. These constructions were used for the investigations of accelerating or quasi-stationary combustion regimes with velocities $S > a$ in tubes of diameters $d = 50$–300 mm and lengths $L = 3$–12 m (a is the sound speed in the unburned mixture). The combustion regimes with pressure waves $\Delta P > \Delta P_1^*$ and $\Delta P > \Delta P_2^*$ were obtained in experiments [17–22].

The existence of pressure waves, able to cause self-ignition at non-flat reflectors, expands the range of dangerous situations and requires a special investigation. So far, the processes of flame propagation in obstructed channels and specific features of ignition under reflection conditions have been studied independently. Such an approach of splitting the problem is too simplified. Thus, joint investigations of the following factors and their effect on the expected loads are necessary:

(1) pressure wave generation due to fast burning of a gaseous mixture in obstructed channels;

(2) self-ignition and secondary explosion as a result of pressure wave focusing by non-flat surfaces.

To select the method of investigation and determine the range of initial conditions, it is necessary to analyze the main outcomes of the previous studies on combustion regimes of hydrogen–air mixtures in (fully or partially) obstructed volumes. The main result of observations in [17–22] is proof that fast combustion regimes in obstructed channels exist. These regimes were accompanied by the generation of pressure waves overtaking a combustion front. So, the problem is concerned with the interaction within a non-steady complex "pressure wave – fast deflagration front."

214
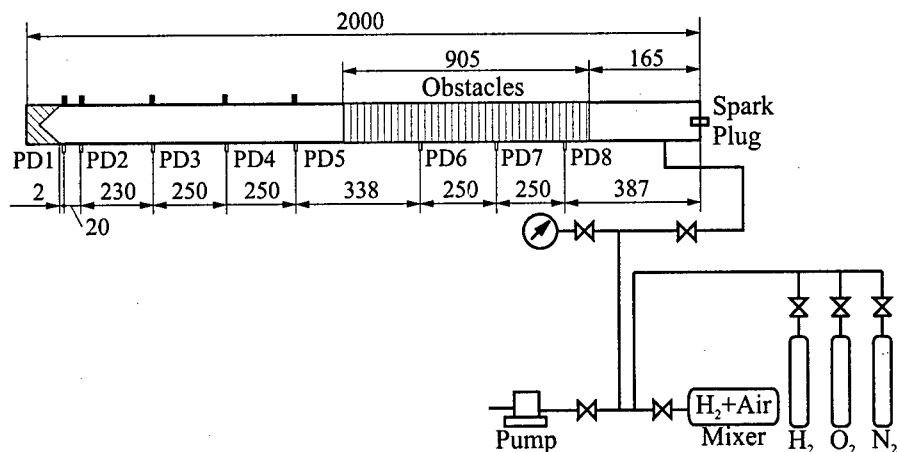
Figure 1 Schematic of the laboratory experimental setup. PG — pressure gauges, PD — photodiodes

EXPERIMENTAL PROCEDURE, EXPERIMENTAL SETUP AND INTERPRETATION METHOD

To perform experimental studies on the interaction of pressure waves generated by a propagating hydrogen–air flame with a non-flat reflector, a shock tube technique was used.

Small Scale Setup

The inner diameter of the tube was 0.054 m and the length was 2 m. The scheme of the experimental setup is presented in Fig. 1. The tube was first evacuated and then filled with a hydrogen–air mixture, prepared separately in a mixing chamber. To ignite the mixture, an electric spark plug was placed in the center of the tube end wall. The opposite end of the tube was closed by a flat endplate or a curved reflector under investigation. Replacing the reflectors allowed investigation of the effect of the focusing process on the self-ignition. A system of periodic metal rings inserted into the tube played the role of a flame accelerator. The width of each ring was 5 mm, outer diameter was 51 mm and the inner diameter was variable.

The distance from the spark location to the first ring was 165 mm in all the tests. The inner diameter of the rings was 34 mm and 23 mm, which corresponds

215
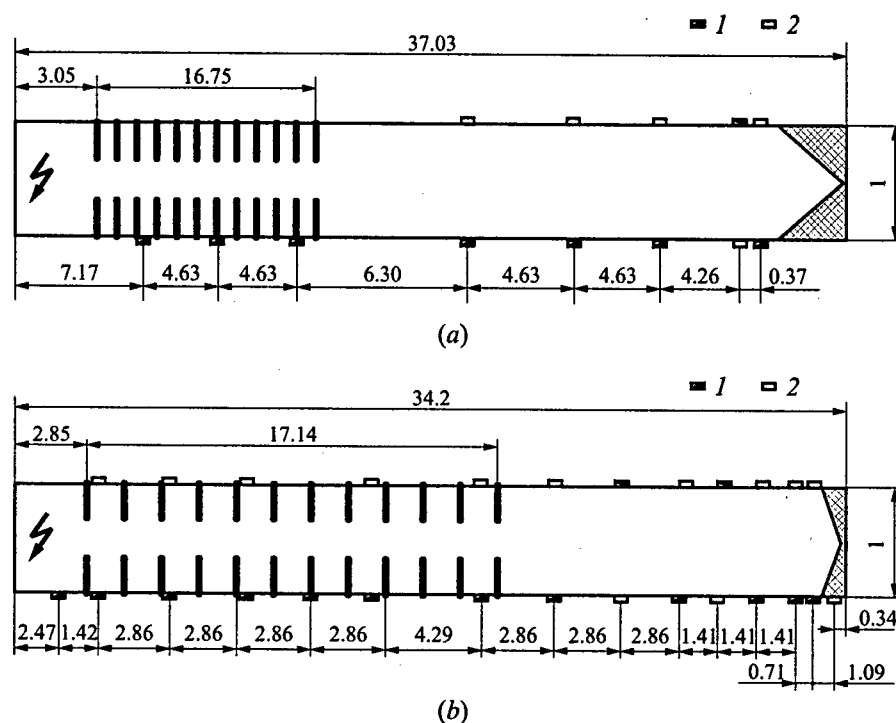
Figure 2 Schematic of small (a) and large (b) experimental facilities. 1 — photo gauges, 2 — pressure gauges

to blockage ratios $BR = 0.5$ and 0.71, respectively. Ring spacing to tube diameter ratio, s/d was varied within the range $0.93 < s/d < 8.9$. The total length of the obstructed tube was from 905 mm to 1350 mm, so that the flame could propagate along a smooth part of the tube between the reflector and the end of the obstruction for at least 700 mm.

The flame front propagation velocity and parameters of emitted shock waves were measured. To record the track of the flame front, 8 photo-diode gauges PD1 to PD8 were used. The diodes were positioned on the side wall of the tube. The pressure was recorded by 5 piezoelectric gauges PG1 to PG5, placed in the same cross-sections as photo gauges PD1 to PD5 (see schematic of Fig. 1). From now on, the references to cross-section numbers (1 to 8) will be consistent with the position of corresponding photo gauges.

The experimental studies were performed for the mixtures containing 10 to 25% (vol.) H_2 in air, at initial pressures 0.05 to 0.3 MPa. A non-flat reflector was a cone with base diameter $D = 54$ mm and height $H = 81$ mm, i.e. with $H/D = 1.5$.

216

Large Scale Simulations

The set of laboratory explosion tubes in the N. N. Semenov Institute of Chemical Physics (IChPh) and the large-scale facility in the the INR FZK allows direct comparison of dynamic characteristics of deflagration to detonation transition, taking into account the scaling factor. For this purpose, the laboratory experiment was reproduced on the large-scale equipment in the INR FZK. In the experiments in the INR FZK facility, the basic geometrical sizes of the labware were reproduced (whenever possible) taking into account the geometrical factor

$$\varphi = \frac{d_{\mathrm{INR}}}{d_{\mathrm{IChPh}}} = \frac{0.35}{0.054} \approx 6.48$$

where $d_{\mathrm{INR}} = 0.35$ m is the diameter of the INR FZK facility, and $d_{\mathrm{IChPh}} = 0.054$ m is the diameter of explosion set-up in the IChPh. In order to simplify further comparison, all linear sizes were presented in the terms of their ratio to a tube diameter. In Fig. 2a, the basic details of the IChPh laboratory setup are shown in a dimensionless form, and in Fig. 2b the basic details of explosion installation in the INR FZK are given in a similar way. The corresponding values in experiments on the full-size installation at the INR FZK are: $(s/d)_{\mathrm{INR}} = 1.43$, $BR = 0.6$ at $s = 500$ mm. According to data given in [17–22], the specified difference in magnitudes of parameters s/d and BR is insignificant for dynamics of flame acceleration in the obstructed part of the channel.

All large scale experiments on flame acceleration were carried out at the initial pressure of 0.1 MPa.

MAIN EXPERIMENTAL RESULTS

Figures 3 and 4 present the pressure profiles (thin lines) and photo-diode records (thick lines) at cross-sections 1 to 8 for the experiments on flame propagation in the mixture 15% H_2 + 85% air at $s/d = 1.85$, $BR = 0.71$, $P_0 = 0.1$ MPa. Figure 3 corresponds to the case with the flat end wall, and Fig. 4 shows the data for the cone reflector with $H/D = 1.5$. Here (and further in similar graphs), the ordinate of the beginning of each line corresponds to the distance from the igniter. The scales for determining time and pressure magnitudes are shown in the figures. To distinguish the signals from closely located gauges, the records of PD1 and PG1 are drawn by dashed lines.

The measured maximal flame velocity (670 m/s) and flame acceleration dynamics are in good agreement (within the accuracy of 10%) with previous experiments [17–22] performed for quite similar values of parameters: concentrations,

217
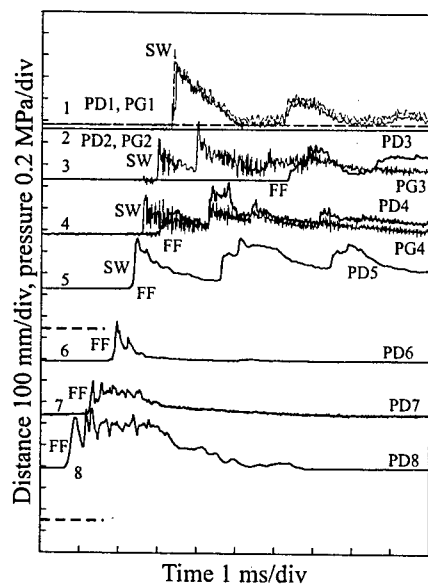
Figure 3 Pressure profiles and photo gauge outputs for propagating flames in 15% H_2 + 85% air mixture at p_0 = 0.1 MPa, $BR = 0.71$, $s/d = 1.85$, $L = 905$ mm. Reflection at the flat end wall. 1, 2, ... , 8 are the cross section numbers, PG_i and PD_i are the pressure and photo gauges shown in Fig. 1. SW is the shock wave front, FF is the flame front
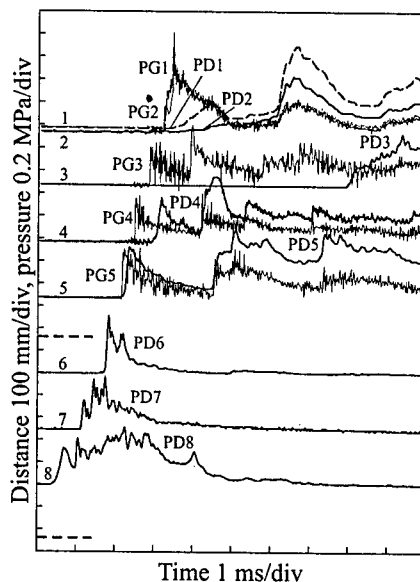
Figure 4 Pressure profiles and photo gauges outputs for propagating flames in the 15% H_2 + 85% air mixture at p_0 = 0.1 MPa, $BR = 0.71$, $s/d = 1.85$, $L = 905$ mm. Reflection at the conical end wall with $H/D = 1.5$ (H is the cone height, D is the cone diameter). 1, 2, ... , 8 are the cross section numbers, PG_i and PD_i are the pressure and photo gauges shown in Fig. 1. SW is the shock wave front, FF is the flame front

BR, and s/d. The event of self-ignition, resulting from shock wave (SW) focusing at a non-flat reflector, can be unambiguously proved if the flame front signal from PD1 and PD2 is detected earlier than the flame signal from PD3. It should be noted that the identification of the flame in the cross-section 3 as the initial flame front, rather than the flame from self-ignition, is not straightforward in the general case. The records of the gauges in cross-sections 1 and 2 are presented separately in Figs. 5 and 6.

The comparison of pressure records in cross-sections 1 and 2 for the flat and concave reflection surfaces shows differences in: a) maximal pressure value prior to self-ignition, that is caused by different geometries; b) slower pressure decrease after the self-ignition in the case of cone reflector.

218
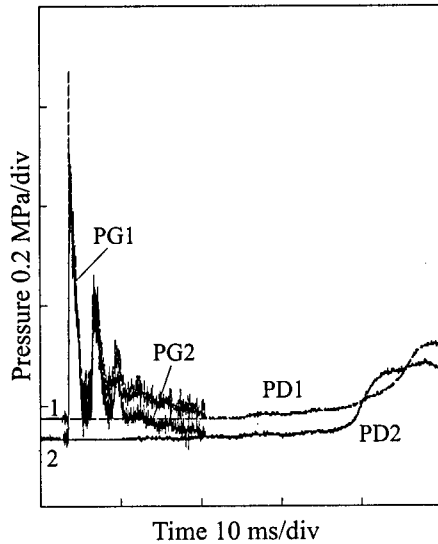
Figure 5 Pressure profiles and photo gauge outputs in cross sections 1 and 2 in 15% H_2 + 85% air mixture at p_0 = 0.1 MPa, BR = 0.71, s/d = 1.85, L = 905 mm. Reflection at the flat end wall
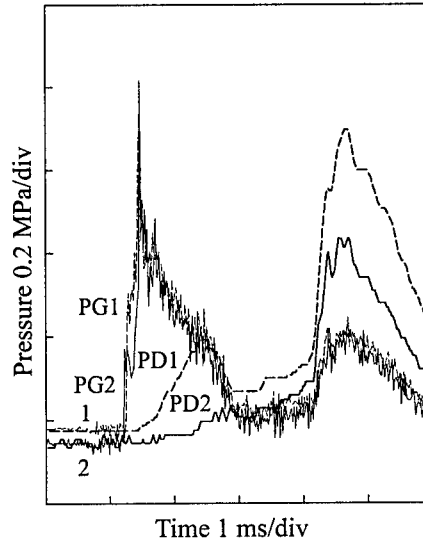
Figure 6 Records of pressure and photo gauge in cross sections 1 and 2 in 15% H_2 + 85% air mixture at p_0 = 0.1 MPa, BR = 0.71, s/d = 1.85, L = 905 mm. Reflection at conical end wall with H/D = 1.5 (H is the cone height, D is the cone diameter)

Photo-gauge records are more different and confirm the fact of self-ignition due to focusing, which took place in a mild regime [19] under current initial conditions.

Comparison of the results leads to a conclusion that the flame velocity increases with hydrogen concentration. The flame behavior after leaving the section with obstacles is also different. In the case of 15% H_2 + 85% air mixture, the flame front lags behind the generated shock wave. In the case of 25% H_2 + 75% air mixture, the flame and the shock propagate close to each other. In the case of 10% H_2 + 90% air mixture, no shock waves were observed at the current initial conditions and uniform pressure rise along the tube was recorded.

Along with the data for s/d = 1.85 presented above, the experiments with more compact (s/d = 0.93) and more rare (s/d = 8.9) obstacle spacing have been conducted. No significant qualitative changes in comparison with the data for s/d = 1.85 were observed, except for some drop in the maximum flame speed (down to ~ 550 m/s). Thus, when using a system of obstacles with s/d > 8 for

219
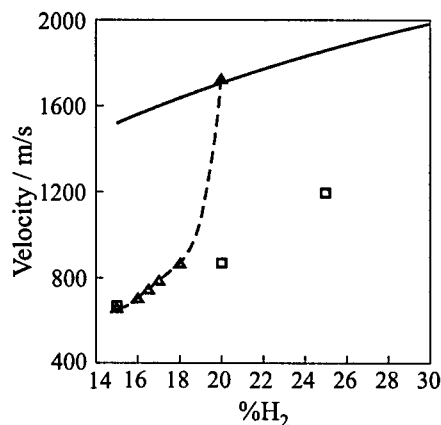
Figure 7 The measured velocity of shock waves in the experimental facilities of different scale. Symbol □ corresponds to the shock wave velocity in the tube of $d = 54$ mm, symbol △ corresponds to the shock wave velocity in the tube of $d = 350$ mm, solid line corresponds to the calculated detonation velocity

the generation of fast combustion regimes, one has to take into account that the interaction of several pressure waves can occur in the vicinity of obstructed area. The decrease in blockage ratio BR, from 0.71 to 0.5, influences the overall process insignificantly. The variation of initial pressure within the range from 0.05 to 0.3 MPa, results in the proportional change in the total pressure level. No systematic effect on the flame and shock wave velocities was revealed. This is demonstrated for the of 15% H_2 + 85% air mixture, at $BR = 0.5$, $s/d = 1.85$ and at different pressures.

The experimentally obtained dependence of the average wave speed vs. mixture composition is shown in Fig. 7. The calculated dependence of the detonation speed on the hydrogen concentration at the initial conditions $P = 0.1$ MPa and $T = 300$ K is also plotted. Clearly, the system of obstacles used ($s/d = 1.43$, $BR = 0.6$) causes the formation of a detonation wave in the INR FZK facility at hydrogen concentration 18–20%. It is worth mentioning that, according to [23], detonation parameters in a tube of $d = 50$ mm are observed for mixtures with hydrogen contents greater than 25%.

As shown in small scale tests, a shock wave generated by the accelerating flame and reflected from a concave conic end can cause self-ignition of hydrogen–air mixture. To investigate the influence of scale factor on this phenomenon, the experiments in the INR FZK facility were carried out. The end wall in these experiments was a cone with the apex angle 70° and height to diameter ratio $L/D = 0.71$. Because of the size of the reflector, it was possible to mount a pressure gauge on its lateral surface, 120 mm from the cone. It was also possible to investigate a flow field in the vicinity of the cone apex by means of the ionization gauge. Figure 8 demonstrates the focusing effect in the case of 16% H_2 + 84% air mixture. The notations in Fig. 8 are completely similar to those used in Fig. 2b. The thick dashed lines represent signals of the ionization gauges. One of the ionization gauges was mounted on the tube axis at a distance of 35 mm inside the cone. The existence of ignition after shock wave reflection at a surface of the cone (focusing process) is testified by the direction of flame propagation from the cone apex (time sequence of the signals provided by the
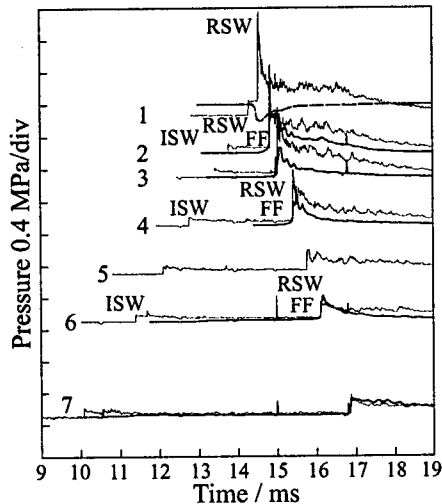
Figure 8 Example of focusing phenomena in 16% H_2 + 84% air mixture in a large scale setup. Thin lines correspond to pressure records, thick to photo gauges, dashed to ionization probes. ISW is the incident shock wave, RSW is the reflected shock wave, FF is the flame front

ionization gauge at the cone apex and the photo gauges in sections 2, 3, and 4) and proves to be true in terms of the magnitude of the reflected shock speed. This value is less than the incident shock speed in the case of ignition, but exceeds the incident shock speed approximately by 1.5–2 times in the case of the strong ignition mode.

The value of the maximum pressure during the interaction of the pressure waves, generated by the accelerating flame, with a reflector is not always a growing function of hydrogen concentration in hydrogen–air mixture [24]. In Figs. 9 and 10, pressure records in sections 1 (inside reflector) and 2 (the nearest to reflector) are reproduced for three characteristic cases: wave reflection (for a 15% H_2+85% air mixture) in the absence of ignition, reflection of a detonation wave (20% H_2 + 80% air), and the reflection of the complex "shock wave – flame front." Clearly, the most dangerous for the given configuration (from the point of view of pressure loading) are the mixtures with composition close to 18% H_2 + 82% air. To provide the full description of the system, one should specify the parameters of the obstacles, the type of reflector and the distance between obstacles and the reflector.

CONCLUDING REMARKS

The main trends in the development of the flow field, when changing mixture composition, initial pressure and the level of obstruction, were experimentally determined. Three main regimes (Fig. 11) of pressure loading produced by explosive combustion of hydrogen–air mixtures in obstructed volumes can be distinguished on the basis of the experiments performed.

Regime I: At a hydrogen concentration in air larger than 20% (vol.), a non-decaying quasi-steady complex QC is emitted from the section with obstacles. This complex consists of the pressure wave SW_1, followed by the combustion
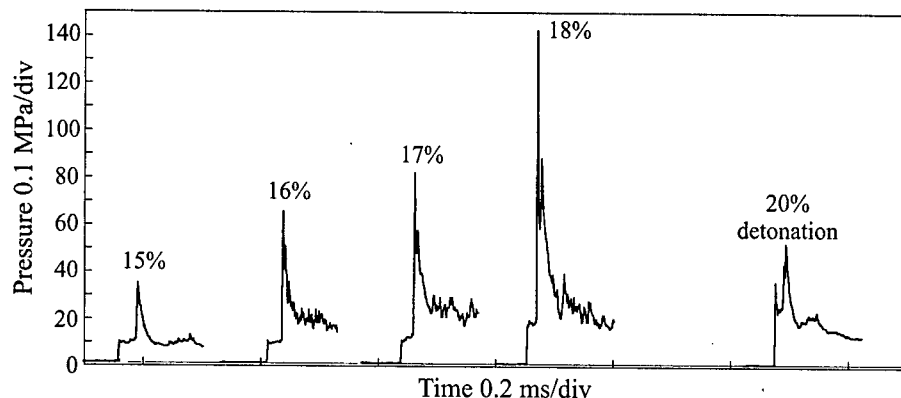
Figure 9 The dependence of pressure loads inside the reflector (cross section 1) on the composition of H_2–air mixtures
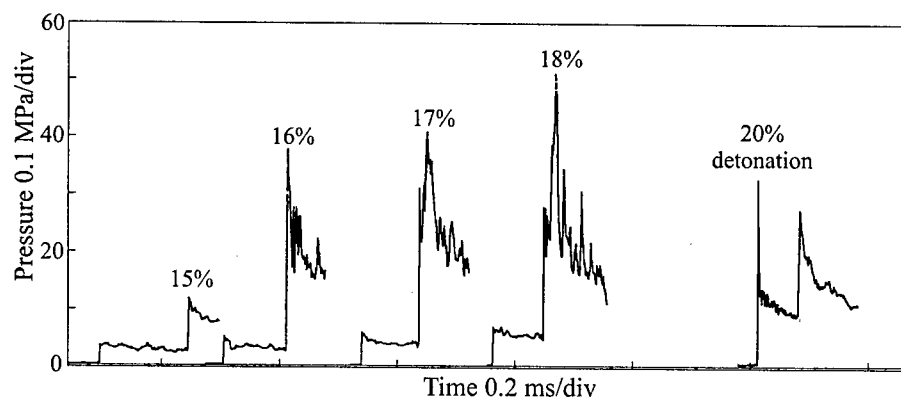
Figure 10 The dependence of pressure loads near the reflector (cross section 2) on the composition of H_2–air mixtures

zone FF_1. The speeds of SW_1 and FF_1 are close to each other. The reflection of the QC at the end wall gives birth to a reflected wave RW in combustion products, and the process does not depend on the reflector type.

Regime II: At a hydrogen concentration in air of 15–20% (vol.), a decaying complex "shock wave SW_2 – decelerating flame front FF_2" is emitted from the section with obstacles. The reflection of SW_2 results in a reflected shock wave RSW moving in the unburnt mixture ahead of the flame front FF_2. The reflection
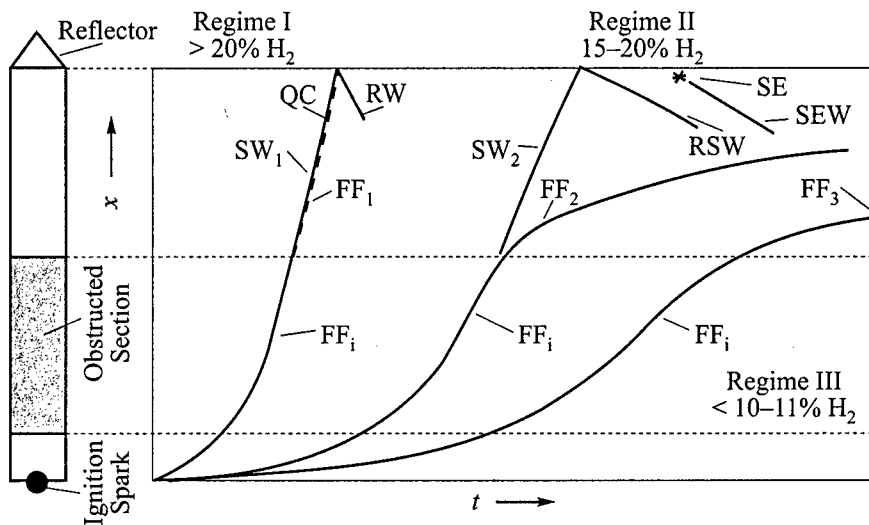
Figure 11 Main explosion regimes in the channel with a non-flat endplate

at the flat end wall is not accompanied by self-ignition. A concave reflector gives rise to the onset of secondary explosion waves SEW from hot exothermic centers.

Regime III: At a hydrogen concentration in air below 10–11% (vol.), the speed of the propagating flame FF_i inside the obstructed zone is sufficient to generate only a set of acoustic waves ahead of the decelerating flame front FF_3. The reflection of these waves from the reflector of any type results in insignificant effect on the overall pressure rise during combustion in the tube.

REFERENCES

1. Chapman, W. R., and Wheeler, J., *J. Chemical Society*, **214**, 1, 1927.
2. Dorge, K., and Wagner, H.-Gg., *Acta Astronautica*, **3**, 1053–1076, 1976.
3. Moen, I., Donato, M., and Lee, J. H. S., *Combustion Flame*, **39**, 1–2, 21–32, 1980.
4. Eckhoff, R., Fuhre, K., and Lee, J. H. S., Rep. CMI, No.790750-1, 1980.
5. Moen, I., Lee, J. H. S., and Fuhre, K., *Combustion Flame*, **42**, 1–2, 31–52, 1987.
6. Hjertager, B., *Combustion Science Technology*, **27**, 2–3, 159–170, 1982.

7. Hjertager, B., and Fuhre, K., Report CMI, No.843403-5, 1984.

8. Chan, C., Lee, J. H. S., and Moen, I., *Proc. 1st Meeting (International) of the Combustion Institute*, 1981, 479–484.

9. Chan, C., Lee, J. H. S., and Moen, I., *Combustion Flame*, **49**, 1, 27–38, 1983.

10. Urtiew, P., Brandles, J., and Hogan, W., *Combustion Science Technology*, **39**, 1–6, 105–119, 1983.

11. Wingarden, C., and Zeeuwen, J.-P., *J. Hazardous Materials*, **8**, 2, 139–156, 1983.

12. Wingarden, C., and Zeeuwen, J. P., *Progress in Astronautics and Aeronautics Ser.*, AIAA Inc., N.Y., **106**, 53–65, 1986.

13. Stock, M., Geiger, W., and Giesbrecht, H., *Progress in Astronautics and Aeronautics Ser.*, AIAA Inc., N.Y., **134**, 3–20, 1991.

14. Schildknecht, M., Geiger, W., and Stock, M., *Progress in Astronautics and Aeronautics Ser.*, AIAA Inc., N.Y., **94**, 474–490, 1984.

15. Benedick, W. B., In: *Fuel–Air Explosions*. University of Waterloo, Waterloo, 597–551, 1982.

16. Eichert, H., *Int. J. Hydrogen Energy*, **12**, 3, 171–176, 1987.

17. Mayinger, F., Strube, G., and Beauvais, R., Abschlussbericht, BMU-SR-403, Techn. Universität München, 1988.

18. Mayinger, F., and Brehm, N., Abschlussbericht, BMFT 150 0712 4, Techn. Universität München, 1988.

19. Lee, J. H. S., Knystautas, R., and Freiman, A., *Combustion Flame*, **56**, 2, 227–239, 1984.

20. Becker, T. P., *Ger. Chem. Eng.*, **8**, 313–320, 1985.

21. Mayinger, F., and Strube, G., Abschlussbericht, BMTF-GRS-150 0769, Techn. Universität München, 1990.

22. Mayinger, F., and Brehm, N., Abschlussbericht, BMTF-GRS-150 06150, Techn. Universität München, 1987.

23. Gelfand, B. E., Medvedev, S. P., Breitung, W., and Khomik, S. V., Report of the IChPh RAS and the INR FZK, 1995, .

24. Chan, K., and Dewit, W. A., *Proc. 26th Symposium (International) on Combustion*, Combustion Institute, Pittsburgh, PA, 1996, 2679–2684.

INITIATION OF DETONATION IN A SUPERSONIC FLOW BEHIND A SHOCK WAVE UNDER NON-EQUILIBRIUM EXCITATION OF VIBRATIONAL DEGREES OF FREEDOM OF MOLECULES

A. M. Starik and N. S. Titova

The effect of delayed excitation of molecular vibrations on the dynamics of detonative combustion in supersonic and subsonic reactive flows behind shock waves was analyzed. Non-equilibrium excitation of molecular vibrations is shown to decrease the combustion rate in a supersonic flow behind a shock wave and promote combustion processes in a subsonic flow, as compared with calculations based on conventional models which ignore this effect. The mechanisms of combustion initiation by pre-excitation of vibrations of H_2 and N_2 molecules in front of a shock wave have been considered. Preliminary excitation of H_2 and N_2 molecules was shown to result in a significant intensification of combustion and reduction in induction and combustion zone lengths by an order of magnitude.

INTRODUCTION

The dynamics of detonative combustion of various mixtures behind shock waves was studied elsewhere [1–4]. In these studies, the delayed excitation of molecular vibrations behind a shock wave and vibrational excitation of molecules forming as a result of chemical reactions were assumed to have no effect on the principal characteristics of the process. It was only recently demonstrated, that the delayed excitation of molecular vibrations of H_2 and O_2 during detonative combustion of H_2–O_2 mixtures may noticeably influence the induction and combustion zone lengths in a number of practically important cases [5]. Moreover, the preliminary (in front of a shock wave) excitation of vibrational degrees of freedom in H_2 or O_2 molecules has a significant effect on the rates of all chemical processes behind the shock front and results in a reduction of the combustion zone length.

The main difficulties arising during numerical modeling of combustion processes involving vibrationally excited molecules are due to the need for a sufficiently complete and reliable model of chemical reactions with vibrational energy exchange and the interrelation between vibrational kinetics and chemical transformation.

The distinctive feature of detonative combustion, in comparison with combustion in a closed reactor, is that the energy transition into translational degrees of freedom due to vibrational relaxation or chemical transformations takes place in a moving gas. As a result, the effect of heat release on temperature and density of the flow is more pronounced. This fact, together with the variation of reaction rate constants caused by non-equilibrium excitation of molecular vibrations, leads to an essential change in the rate of detonative combustion.

Presented in this paper are the results of a detailed analysis of these effects for detonative combustion of a H_2–air mixture behind a stationary shock wave.

FORMULATION

The analysis is based on the flow scheme discussed in [2, 3]. A premixed reactive gas moves at the velocity u_0 (subscript "0" denotes parameters in the nonperturbed flow; subscript "1" denotes parameters behind a shock front) and interacts with a shock front declined at angle $\beta \leq 90°$ relative to the direction of u_0.

When crossing the shock front, only the normal velocity component, u_n varies, and the tangential component, u_τ remains unchanged, i.e.,

$$u_{\tau 1} = u_{\tau 0}, \qquad u_{\tau 0} = u_0 \cos \beta$$

Assume that the rotational and translational degrees of freedom are in thermodynamic equilibrium at all characteristic spatial dimensions inherent to the problem, and the populations of vibrational levels and molar concentrations of components remain unchanged in the "viscous" shock. In this case, the parameters prior to and behind the shock front are related by the following formulas:

$$\frac{P_1}{P_0} = \frac{2\kappa}{\kappa + 1} M_{0n}^2 - \frac{\kappa - 1}{\kappa + 1}$$

$$\frac{\rho_1}{\rho_0} = \frac{(\kappa + 1)M_{0n}^2}{(\kappa - 1)M_{0n}^2 + 2}$$

$$\frac{T_1}{T_0} = \frac{P_1 \rho_0}{P_0 \rho_1}$$

$$u_{1n} = \sqrt{\frac{(P_1 - P_0)\rho_0}{(\rho_1 - \rho_0)\rho_1}}$$

$$u_1 = (u_{1n}^2 + u_{1\tau}^2)^{1/2}$$

$$M_{0n} = u_{0n} \bigg/ \sqrt{\kappa \frac{R}{\mu_0} T_0} \tag{1}$$

$$\kappa = 1 + \left(\frac{3}{2} + \sum_{i=1}^{L} \gamma_{i0} + \frac{3}{2} \sum_{i=L+1}^{S} \gamma_{i0}\right)^{-1}$$

$$\mu = \sum_{i=1}^{m_1} \mu_i \gamma_i$$

$$\gamma_i = \frac{N_i}{N}$$

$$N = \sum_{i=1}^{m_1} N_i$$

where P, ρ, and T are the gas pressure, density, and temperature, respectively; R is the universal gas constant, N_i is the density of molecules of the ith sort, μ_i is their molecular mass, m_1 is the number of atomic and molecular components in the mixture, L is the number of molecular components formed of linear molecules; and S is the total number of molecular components. Following [5], it is further assumed that each vibrational mode is in the local thermodynamic equilibrium with its own vibrational temperature T_ξ ($\xi = 1, \ldots, n$).

Consider the variation of parameters in the relaxation zone of a shock wave along the stream line, whose direction coincides with that of vector u_1. The equations governing the flow of reacting gas with vibrational non-equilibrium can be written in the form

$$\frac{d(\rho u)}{dx} = 0$$

$$u \frac{du}{dx} + \frac{1}{\rho} \frac{dP}{dx} = 0$$

$$\frac{dH}{dx} + \sum_{i=1}^{S} \frac{de_V^i}{dx} + u \frac{du}{dx} = 0$$

$$P = \rho \frac{RT}{\mu}$$

$$u\frac{d\gamma_i}{dx} = G_i - \gamma_i \sum_{j=1}^{m_1} G_j$$

$$u\frac{d\varepsilon_\xi}{dx} = Q_V^\xi + Q_{Ch}^\xi$$

$$G_i = \sum_{q=1}^{m_2} S_{iq}$$

$$S_{iq} = \frac{\alpha_{iq}^- - \alpha_{iq}^+}{N}\{R_q^+ - R_q^-\}$$

$$R_q^{+(-)} = k_{+(-)q} \left/ N_A^{n_q^{+(-)}-1} \prod_{j=1}^{n_q^{+(-)}} N_j^{\alpha_q^{+(-)}}\right.$$

$$\varepsilon_\xi = \frac{g_\xi y_\xi}{1 - y_\xi}$$

$$y_\xi = \exp\left(-\frac{\theta_\xi}{T_\xi}\right)$$

$$Q_V^\xi = N\left[\sum_{p=1}^{L_1} \frac{l_\xi}{g_\xi^{l_\xi} g_p^{l_p}} L_{\xi,p} W_{\xi,p} - (\varepsilon_\xi - \varepsilon_{\xi 0})(1 - y_{\xi 0}) \sum_{i=1}^{m_1} W_{\xi,0}^i \gamma_i\right]$$

$$Q_{Ch}^\xi = \sum_{r=1}^{L_2} \frac{\alpha_{kr}^- - \alpha_{kr}^+}{N_k}\left[(\chi_{r\xi}^+ - \varepsilon_\xi)R_r^+ - (\chi_{r\xi}^- - \varepsilon_\xi)R_r^-\right]$$

$$L_{\xi,p} = \varepsilon_\xi^{l_\xi}(g_p + \varepsilon_p)^{l_p} - \varepsilon_p^{l_p}(g_\xi + \varepsilon_\xi)^{l_\xi} \exp\left(\frac{l_\xi\theta_\xi - l_p\theta_p}{T}\right)$$

$$C_{RT} = \left(\frac{5}{2} + \sum_{i=1}^{L} \gamma_i + \frac{3}{2}\sum_{i=L+1}^{S} \gamma_i\right)\frac{R}{\mu}$$

$$y_\xi = \exp\left(-\frac{\theta_\xi}{T_\xi}\right)$$

$$\varepsilon_{0\xi} = \varepsilon_\xi(y_\xi = y_{\xi 0})$$

$$y_{\xi 0} = y_\xi(T_\xi = T)$$

$$H = \sum_{i=1}^{m_1} h_{0i}\gamma_i + C_{RT}T$$

$$e_V^i = \gamma_i \frac{R}{\mu} \sum_{\xi=1}^{n_i} \theta_{\xi i}\varepsilon_{\xi i}$$

(2)

where h_{0i} is the enthalpy of formation of the ith component at $T = 298$ K, N_A is the Avogadro number, m_2 is the number of reactions resulting in the formation (destruction) of the ith component; θ_ξ is the characteristic temperature of the ξth mode; g_ξ is the degeneration multiplicity of the latter; l_ξ is the number of vibrational quanta lost or acquired by the ξ-mode in the vibrational–vibrational (V–V′) exchange (the total number of these processes is L_1); $W_{\xi,p} = \sum_{i=1}^{m_1} W_{\xi,p}^i \gamma_i$ and $W_{\xi,p} = W_{\xi,p}\gamma_i$ $(\xi \leftrightarrow i,\ p \leftrightarrow j)$, in the case of the intra-molecular and inter-molecular V–V′ exchange, respectively, $W_{\xi,p}^i$ and $W_{\xi,p}$ are the rate constants of intra- and inter-molecular V–V′ exchange, $W_{\xi,0}^i$ is the rate constant of vibrational–translational (V–T) relaxation in a collision against the ith partner; α_{iq}^+ and α_{iq}^- are the stoichiometric coefficients of the qth reaction; $n_q^{+(-)}$ is the number of components involved in the direct $(+)$ and reverse $(-)$ reactions; $k_{+(-)q}$ are the rate constants of these reactions, and $\chi_{r\xi}^{+(-)}$ is the average number of quanta acquired (lost) by the ξ-mode in a single event of formation (destruction) of a molecule containing the ξ-mode $(i \leftrightarrow \xi)$ in the rth reaction.

The values of $k_{+(-)q}$ and $\chi_{r\xi}^{+(-)}$ are defined by the formulas [6]:

$$k(T,T_j) = k_q^0(T) \frac{\prod_{j=1}^{b_q}(1-y_{j0})^{-g_j}}{\prod_{j=1}^{b_q}(1-y_j)^{-g_j}} \exp\left[\frac{E_q^*}{K}\left(\frac{1}{T} - \frac{\sum_{j=1}^{b_q}\beta_{qj}^2}{\sum_{j=1}^{b_q}\beta_{qj}^2 T_j}\right)\right]$$

$$\chi_{r\xi}^{+(-)} = \frac{E_r}{K\theta_\xi}\eta_{r\xi}^{+(-)}$$

$$\eta_{r\xi}^+ = \frac{\beta_{r\xi}^2}{\sum_{i=1}^{b_r}\beta_{ri}^2}$$

$$\eta_{r\xi}^- = \frac{\beta_{r\xi}^2 T_\xi^2 \sum_{i=1}^{b_r}\beta_{ri}^2}{\left(\sum_{j=1}^{b_r}\beta_{rj}^2 T_j\right)^2}$$

(3)

where $k_q^0(T)$ is the equilibrium rate constant of the qth chemical reaction at $T_j = T$ (for the sake of simplicity, the plus and minus subscripts are omitted for all quantities with subscript q in Eq. (3)); β_{qj} denotes the coefficients of expansion of the qth reaction in coordinates of normal vibrations, b_q is the number of modes included into the qth reaction, K is the Boltzmann constant, E_q^* is the energy

corresponding to a certain vibrational level that plays the role of a bottleneck during the transition of vibrationally excited molecules to the quasi-continuous continuum, E_r is the fraction of the activation energy per vibrational degrees of freedom of molecules for the rth reaction; and $E_{ar}^{+(-)}$ is the activation energy of the rth chemical reaction directed to destruction (production) of a vibrationally excited molecule.

For bimolecular exchange and dissociation reactions, it is assumed that $\eta_{r1}^{-} = \eta_{r2}^{-} = \ldots = 1/b_r$, where b_r is the number of modes involved in the rth reaction.

The value of E_q^* is not a constant and depends on the gas temperature, vibrational temperature, and some other parameters which are reactant-dependent [6]. For the sake of simplicity, these parameters are assumed to be constant within the temperature range $T = 600\text{--}3000$ K and $T_j < 5000$ K. In accordance with [7], the dissociation reactions of diatomic and triatomic molecules were supposed to have the values of $E_q^* = (0.5\text{--}0.6)E_{ar}$, and the chemical exchange reactions — $E_q^* = (0.7\text{--}1)E_{ar}$.

The value of E_r is defined by the formulas [5]

$$E_r = \alpha_r E_{ar}^{+}, \qquad \alpha_r = \frac{E_{ar}^{+}}{E_{ar}^{+} + E_{ar}^{-}}$$

KINETIC SCHEME OF NON-EQUILIBRIUM PROCESSES BEHIND A SHOCK FRONT

One of the most complex problems encountered is constructing a kinetic scheme of elementary processes which, on the one hand, adequately describes principal characteristics of combustion behind a shock wave (induction zone length, L_{in}, combustion zone length, L_c, the final temperature, and other gasdynamic parameters) and, on the other hand, is relatively simple. The point is that it appears impossible to completely account for the mutual influence of non-equilibrium vibrational excitation and chemical transformation, even for a simple system, such as H_2–O_2. The reason for this is that the chemical reactions involve both diatomic molecules H_2, O_2, OH, and polyatomic molecules H_2O, O_3, HO_2, H_2O_2. For most of them, no models of vibrational energy transfer have been developed so far. For H_2–O_2–N_2 or (H_2–air) system, the situation is much more complicated.

A fairly complete description of the H_2–air system is provided by the 152-step chemical kinetic scheme, which includes the following species: O_2, H_2, O, H, H_2O, OH, HO_2, H_2O_2, O_3, N, N_2, NO, NO_2, N_2O, HNO, HNO_3, NO_3, NH, NH_2, NH_3, N_2H, N_2H_2, N_2H_3, N_2H_4 [8]. Clearly, such a scheme cannot be used to analyze the combustion processes behind a shock front under taking into account the non-equilibrium excitation of vibrational degrees of freedom of the

230

molecules. For constructing a kinetic scheme which would provide correct values of L_{in}, L_c, T_e, and M_e and concentration profiles of key species behind a shock wave, and would include a minimal number of chemical reactions and molecular species, a possibility of reducing the complete set of reactions was considered. It was assumed that $\tau_V \ll \tau_{ch}$, where $\tau_V = \min(\tau_{VV'}, \tau_{VT})$, $\tau_{VV'}$ and τ_{VT} are the characteristic times of V–V′-exchange and V–T-relaxation respectively, and τ_{ch} is the minimal characteristic time of chemical reactions behind a shock front. In other words, the equilibrium between translational, rotational and vibrational degrees of freedom of molecules was assumed to be established with the chemical reactions proceeding on the background of this established equilibrium ($T_\xi = T$). In this case, the gasdynamic parameters behind a shock front are determined by solving the following equations [3]:

$$\lambda_{n1} = \lambda_{n0}^{-1}$$

$$h_1 - h_0 = \frac{1}{2}\frac{P_0}{\rho_0}\left(\frac{P_1}{P_0} - 1\right)\left(\frac{\rho_0}{\rho_1} + 1\right)$$

$$-\chi_{0e}M_{n0}^2 = \left(\frac{P_1}{P_0} - 1\right)\left(\frac{\rho_0}{\rho_1} - 1\right)$$

$$\gamma_{i0} = \gamma_{i1}$$

$$h = C_{RT}^0 T + \frac{R}{\mu_0}\sum_{i=1}^{S}\gamma_i\sum_{j=1}^{z}g_{ij}\theta_{ij}\left[\exp\left(\frac{\theta_{ij}}{T}\right) - 1\right]^{-1}$$

$$M_{n0} = u_{n0}\Big/\sqrt{\chi_{e0}\frac{R}{\mu_0}}, \qquad \lambda_n = u_n\Big/\sqrt{\frac{2\chi_e RT}{(\chi_e + 1)\mu}}$$

$$\chi_e = 1 + \left\{\frac{\mu}{R}C_{RT} - 1 + \sum_{i=1}^{S}\gamma_i\sum_{j=1}^{z}\left(\frac{\theta_{ij}}{T}\right)^2 g_{ij}\exp\left(\frac{\theta_{ij}}{T}\right)\left[\exp\left(\frac{\theta_{ij}}{T}\right) - 1\right]^{-2}\right\}^{-1}$$

For calculating the change in T, P, u, and γ_i along the OX-axis, the set of Eqs. (1) with the equation for ε_ξ excluded is used.

Several kinetic schemes were considered:

(1) a complete scheme composed of reactions (1)–(152) involving 27 species [8];

(2) a scheme composed of 35 reactions involving 12 species (H_2O, O_2, H_2, OH, H, O, N, N_2, NO, NO_2, HO_2, H_2O_2);

(3) a scheme composed of 19 reactions involving 10 species (i.e., HO_2 and H_2O_2 excluded, as compared to (2)).

231

Table 1 The calculated values of principal parameters for combustion of $2H_2 + O_2 + 3.76N_2$ mixture ($T_0 = 300$ K, $P_0 = 133$ Pa) behind a shock front for different kinetic schemes

Parameter	$M_0 = 6$			$M_0 = 8$			$M_0 = 10$		
	Kinetic scheme			Kinetic scheme			Kinetic scheme		
	1	2	3	1	2	3	1	2	3
T_1, K	791	791	791.1	1167	1167	1167	1626.1	1626.1	1626.1
L_{in}, cm	1.23(4)	1.18(4)	1.21(4)	4.35(2)	4.33(2)	4.55(2)	77.1	78.6	78.6
L_c, cm	2.35(4)	2.32(4)	3.15(4)	9.34(3)	9.83(3)	1.64(4)	6.35(3)	6.11(3)	9.98(3)
T_e, K	2312.5	2306.5	2433.74	2360.7	2354.3	2475.76	2420.68	2413.64	2527.26
γ_{NO}^e	4.67(-3)	4.69(-3)	5.69(-3)	5.29(-3)	5.31(-3)	6.36(-3)	6.09(-3)	6.1(-3)	7.2(-3)
$\gamma_{NO_2}^e$	2.39(-7)	2.31(-7)	3.23(-7)	2.78(-7)	2.69(-7)	3.47(-7)	3.25(-7)	3.13(-7)	3.87(-7)

$A(n)$ corresponds to $A \cdot 10^{-n}$

Table 1 shows the results of the numerical calculations of the temperature behind a shock front T_1, induction zone length L_{in}, combustion zone length L_c, equilibrium temperature T_e, and equilibrium values of NO and NO_2 concentration γ_{NO}^e, $\gamma_{NO_2}^e$ at the end of the combustion zone for different Mach numbers M_0. These calculations were performed with the kinetic schemes described above for the stoichiometric hydrogen–air mixture at $T_0 = 300$ K, $P_0 = 133$ Pa (thermodynamic and molecular parameters required for the calculations were taken from [9]). The value of L_{in} was determined as the length to reach the maximum in the profile of $\gamma_H(x)$ and the value of L_c was determined as the length to reach $T = 0.99T_e$. The results show that scheme (3) provides rather accurate values of L_{in}, but this scheme results in significant errors in L_c, T_e, γ_{NO}^e, and $\gamma_{NO_2}^e$ values. A good accuracy in L_{in}, L_c, and T_e values, and in the profiles of species concentrations under detonative combustion behind a shock wave, may be achieved using scheme (2). The list of reactions relevant to scheme (2) with the corresponding rate coefficients ($k_{+q}^0(T)$ and $k_{-q}^0(T)$, $k_q^0(T) = A_q T^{n_q} \exp(-E_{aq}/T)$) is given in Table 2. For this set of chemical processes, the scheme of vibrational exchange includes the channels of V–V′ exchanges between symmetric, stretch-deformed and asymmetric (ν_1, ν_2, ν_3) vibrational modes of H_2O molecule, the modes of $H_2(\nu_4)$, $O_2(\nu_5)$, $OH(\nu_6)$, $N_2(\nu_7)$, and $NO(\nu_8)$ molecules, symmetric, stretch-deformed, and asymmetric (ν_9, ν_{10}, ν_{11}) modes of NO_2 molecule, and V–T relaxation processes of the modes ν_2, ν_4, ν_5, ν_7, ν_8 and ν_{10} [8]. The temperature dependencies of $W_{\xi,p}^i$, $W_{\xi,p}$ and $W_{\xi,0}^i$ for these processes were taken in the same form as in [8]. Additionally, the V–T relaxation processes for HO_2 and H_2O_2 molecules were included into this vibrational kinetic scheme. Unfortunately, there is no information about V–V′ and V–T relaxation rate constants for HO_2 and H_2O_2 molecules. The HO_2 molecule has three modes ν_{12}, ν_{13},

Table 2 The list of chemical reactions and reaction rate constants in the mathematical model of combustion of H_2–air mixture behind a shock wave

No	Reaction	k^0_{+q}, (cm^{-3}/mol)$^{n-1}$s^{-1}			k^0_{-q}, (cm^{-3}/mol)$^{n-1}$s^{-1}		
		A_q	n_q	E_{aq}	A_q	n_q	E_{aq}
Reactions with H_2O, OH, O, H, H_2, O_2							
1.	$H_2 + M = OH + H + M$	1(24)	−2.2	−59000	2.2(22)	−2	0
2.	$H_2 + M = 2H + M$	2.2(14)	0	−48300	9(17)	−1	0
3.	$O_2 + M = 2O + M$	2.6(18)	0	−59580	1.1(14)	−1	900
4.	$OH + M = H + O + M$	8.5(18)	−1	−50830	7.1(18)	−1	0
5.	$H_2 + O = OH + H$	1.8(10)	1	−4480	8.3(9)	1	−3500
6.	$O_2 + H = OH + O$	2.2(14)	0	−8455	1.3(13)	0	−350
7.	$H_2O + O = 2OH$	5.8(13)	0	−9059	5.3(12)	0	−503
8.	$H_2O + H = OH + H_2$	8.4(13)	0	−10116	2(13)	0	−2600
9.	$H_2 + O_2 = 2OH$	1.7(15)	0	−24200	1.7(13)	0	−24100
Reactions with N, N_2, NO							
10.	$N_2 + M = 2N + M$	3.72(21)	−1.6	−113272	7.94(19)	−1.6	0
11.	$NO + M = N + O + M$	5.25(17)	−0.5	−75600	1(17)	−0.5	0
12.	$O + N_2 = N + NO$	1.74(14)	0	−38455	4(13)	0	−504
13.	$O + NO = N + O_2$	1.51(9)	1	−19439	6.46(9)	1	−3147
14.	$H + NO = N + OH$	1.7(14)	0	−24500	4.5(13)	0	0
15.	$NO_2 + M = NO + O + M$	1.1(16)	0	−32712	1.1(15)	0	941
Reactions with NO_2							
16.	$OH + NO = H + NO_2$	2(11)	0.5	−15500	3.5(14)	0	−740
17.	$O_2 + NO = O + NO_2$	1(12)	0	−23568	1(13)	0	−302
18.	$NO_2 + N = 2NO$	3.6(12)	0	0	1.1(11)	0	−39200
19.	$2NO_2 = 2NO + O_2$	2(12)	0	−13500	1.2(9)	0	530
Reactions with HO_2							
20.	$HO_2 + M = H + O_2 + M$	2.1(15)	0	−23000	1.5(15)	0	500
21.	$H_2 + O_2 = H + HO_2$	1.9(13)	0	−24100	1.3(13)	0	0
22.	$H_2O + O = H + HO_2$	4.76(11)	0.372	−28743	1(13)	0	−540
23.	$H_2O + O_2 = OH + HO_2$	1.5(15)	0.5	−36600	3(14)	0	0
24.	$H_2O + OH = H_2 + HO_2$	7.2(9)	0.43	−36100	6.5(11)	0	−9400
25.	$2OH = H + HO_2$	1.2(13)	0	−20200	2.5(14)	0	−950
26.	$OH + O_2 = O + HO_2$	1.3(13)	0	−28200	5(13)	0	−500
27.	$N + HO_2 = NO + OH$	1(13)	0	−1000	2.69(12)	0	−41630
28.	$OH + NO_2 = NO + HO_2$	1(11)	0.5	−6000	3(12)	0.5	−1200
Reactions with H_2O_2							
29.	$H_2O_2 + M = OH + OH + M$	1.2(17)	0	−22900	9.1(14)	0	2650
30.	$H + H_2O_2 = HO_2 + H_2$	1.7(12)	0	−1900	6(11)	0	−9300
31.	$H + H_2O_2 = H_2O + OH$	5(14)	0	−5000	2.4(14)	0	−40500
32.	$2HO_2 = H_2O_2 + O_2$	1.8(13)	0	−500	3(13)	0	−21600
33.	$HO_2 + H_2O = H_2O_2 + OH$	1.8(13)	0	−15100	1(13)	0	−910
34.	$OH + HO_2 = H_2O_2 + O$	5.2(10)	0.5	−10600	2(13)	0	−2950
35.	$H_2O + O_2 = H_2O_2 + O$	3.4(15)	0.5	−44800	8.4(11)	0	−2130

$A(n)$ corresponds to $A \cdot 10^{-n}$

233

ν_{14} ($\theta_{12} = 4910$ K, $\theta_{13} = 2002$ K, $\theta_{14} = 1577$ K) and H_2O_2 molecule has five modes ν_{15}, ν_{16}, ν_{17}, ν_{18}, and ν_{19} ($\theta_{15} = 5182$ K, $\theta_{16} = 1998$ K, $\theta_{17} = 1260$ K, $\theta_{18} = 5199$ K, and $\theta_{19} = 1823$ K). To describe the vibrational relaxation in HO_2 and H_2O_2 molecules, it was supposed that populations of all vibrational states in HO_2 molecule depend on the unified vibrational temperature T_{14}, and populations of all vibrational states in H_2O_2 molecule depend on the unified vibrational temperature T_{17}. For these molecules, only one channel of vibrational exchange — V–T relaxation — was taken into account. The rate constants for V–T relaxation processes for ν_{14} and ν_{17} modes were calculated using the Millikan–White equation [10]. In accordance with the recommendations of [11], the modes ν_9 and ν_{10} were assumed to be in a quasi-equilibrium state. Therefore, equations of vibrational kinetics were solved only for $\varepsilon_1, \ldots, \varepsilon_8, \varepsilon_{10}, \varepsilon_{11}, \varepsilon_{14}$, and ε_{17}.

SOLUTION METHOD AND MAIN RESULTS

The set of Eqs. (2) (consisting of twelve chemical and twelve vibrational kinetic equations, and three gasdynamic equations) was solved numerically using the implicit second-order difference scheme.

First, consider the effect of delayed excitation of molecular vibrations behind a shock front on the variation of gasdynamic parameters, and on the chemical reactions in the reacting gas H_2–O_2–N_2. Figure 1a shows the variation of T_j (curves of similar numbers, $j = 1$–11), T (curve 12), M (13), and P (14); and Fig. 1b shows the variation of γ_i along the OX-axis obtained in calculations of a flow behind a shock wave (the profiles of $T_{14}(x)$, $T_{17}(x)$ and concentration of HO_2, H_2O_2 are not presented). Solid curves correspond to the calculations performed with the allowance for the delayed excitation and its effect on the rate of chemical reactions; dashed lines correspond to the calculations assuming the instantaneous establishment of equilibrium between vibrational and translational degrees of freedom. This case relates to the flow of a chemically reacting gas under vibrational equilibrium [2–4]. It is seen from these distributions that T_4, T_5, and T_7 are less than T over the entire length of the induction zone behind a shock front, and the equality of T_4, T_5, T_7 and T is attained only at the end of the induction zone due to V–T exchange. Thus, the flow behind a shock front exhibits heat removal from the translational degrees of freedom. In the linear approximation, the variation of gasdynamic parameters in the relaxation zone behind a shock front in the interval $[0, L_{in}]$ is defined by the following relations [12]:

$$P = P_1 - \frac{\rho_1 M_1^2 (\kappa - 1)}{1 - M_1^2} I$$
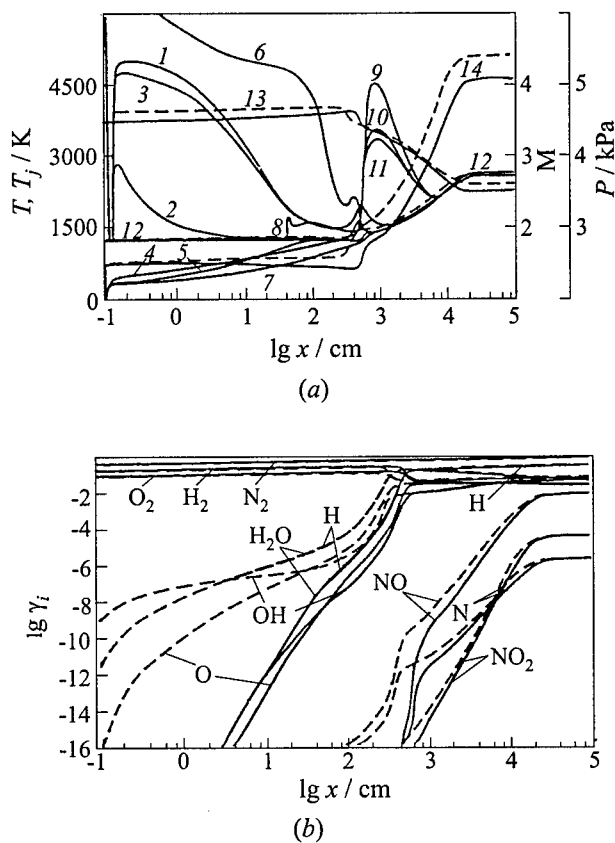
Figure 1 Variation of (a) T_j (curves *1–11*), T (*12*), M (*13*), and P (*14*), and (b) γ_j along the OX-axis under detonation of $2H_2 + O_2 + 3.76N_2$ mixture at $M_0 = 8$

$$\rho = \rho_1 - \frac{\rho_1(\kappa - 1)}{a_1^2(1 - M_1^2)}I$$

$$T = T_1 + \frac{1 - M_1^2\kappa}{C_{RT}(1 - M_1^2)}$$

$$u = u_1 + \frac{M_1^2(\kappa - 1)}{u_1(1 - M_1^2)}I$$

$$a_1 = \sqrt{\kappa\frac{R}{\mu_1}T_1}$$

$$(4)$$

$$I = (E_{V1} - E_{V\infty}) \exp\left(-\frac{ux}{\tau_V}\right)$$

$$E_V = \sum_{i=1}^{s} e_V^i$$

$$E_{V\infty} = E_V(x = L_{in})$$

In the considered case, $E_{V1} < E_{V\infty}$ (vibrations are excited behind a shock front), i.e., $I < 0$. Since in this case $M_1 > 1$, T and P decrease, and u increases. The decrease in P results in a decrease in the number of collisions and the rates of all chemical reactions. Another reason for the deceleration of chemical transformations is the fact that T_4, T_5, and T_7 are less than T, because the rate constants of reactions (2), (3), (5), (8), and (9) (which are the sources of O, H, and OH, whose rate of formation has a straightforward effect on the intensity of combustion processes) decrease (as compared to the equilibrium case). The rates of NO and NO_2 production in processes (12) and (17) also decrease.

Obviously, the length of the induction and combustion zones (L_{in} and L_c) are greater than the corresponding values obtained in the calculation disregarding the delayed excitation of molecular vibration of N_2, O_2, and H_2. With this approximation, the values of P, T and M at the end of the combustion zone appear to be somewhat overestimated.

The increase in the Mach number of the incident flow, and therefore in the translational temperature behind a shock, leads to an increase in the error of determining gasdynamic parameters at the end of the combustion zone, P_c, T_c, M_c (P_c having the highest and T_c the lowest error), as well as in L_{in} and L_c, when ignoring the delayed excitation of molecular vibrations of reacting species behind a shock. In this case, some error arises in determining equilibrium concentrations of different gases at the end of the combustion zone. This fact is illustrated by Table 3, giving the dimensionless values of P_c, T_c, M_c, L_{in}, L_c, and species concentrations γ_i ($i = H_2O$, H_2, O_2, OH, O, H, N_2, N, NO, NO_2) at the end of combustion zone, calculated with due regard for the delayed excitation of molecular vibrations and its effect on the rates of chemical reactions (our model). All values are related to the values obtained using the approximation of vibrationally equilibrium flow of a chemically reacting gas, $y = y/y_e$ (the equilibrium parameters are labeled by the subscript e). It is seen that at high M_0 ($M_0 = 14$) the error in determining P_c may be as high as 16%; L_c — 30%; and L_{in} — even 80%. Note that at $M \geq 14$ the process behind a shock front exhibits energy absorption, i.e. the gas temperature and pressure decrease as a result of chemical reactions, but the Mach number, in contrast, increases. For a subsonic flow behind a shock wave, the values of L_c obtained in the calculations, with the delayed excitation of molecular vibration taken into account, are less than the corresponding values obtained in the calculations with only chemical kinetics taken into account.

236

Table 3 The effect of delayed excitation of molecular vibrations on various parameters at the end of the combustion zone

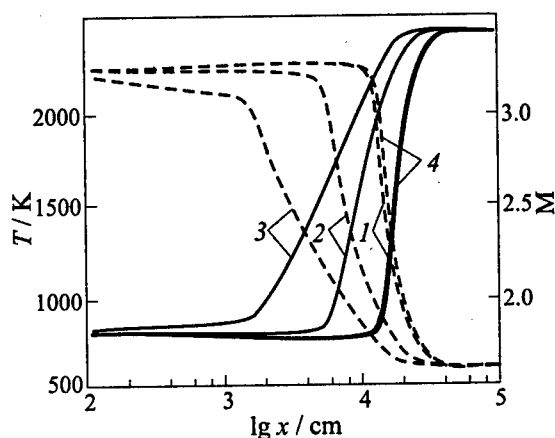| M_0	6	10	14
$\overline{T}_c$	0.99	0.99	0.99
$\overline{M}_c$	0.97	0.97	0.97
$\overline{P}_c$	0.97	0.91	0.84
$\overline{L}_{in}$	1.26	1.67	1.8
$\overline{L}_c$	1.14	1.28	1.3
$\overline{\gamma}_{H_2O}$	1	1	1.05
$\overline{\gamma}_{H_2}$	1	0.99	0.99
$\overline{\gamma}_{O_2}$	1	1	1
$\overline{\gamma}_{OH}$	1	0.99	0.98
$\overline{\gamma}_{H}$	1	0.98	0.99
$\overline{\gamma}_{O}$	1	0.99	0.95
$\overline{\gamma}_{N_2}$	1	1	1.01
$\overline{\gamma}_{N}$	0.99	0.92	0.86
$\overline{\gamma}_{NO}$	1	0.98	0.96
$\overline{\gamma}_{NO_2}$	1	0.96	0.93
$\overline{\gamma}_{HO_2}$	1	0.98	0.95
$\overline{\gamma}_{H_2O_2}$	1	0.96	0.92

Figure 2 Variation of T (solid curves), and M (dashed curves) behind the shock wave at $M_0 = 6$, $\beta = 30°$ for different degrees of excitation of H_2 molecular vibrations ($T_{40} = T_1$ (1), $2T_1$ (2), $3T_1$ (3), T_0 (4))

Consider now the effect of pre-excitation of N_2 and H_2 molecules in front of the shock wave on the detonative combustion of a H_2–air ($2H_2 + O_2 + 3.76N_2$) mixture at $T_0 = 300$ K and $P_0 = 133$ Pa. The vibrational excitation of N_2 and H_2 molecules may be realized by using the electric discharge of high efficiency ~ 70–90%. Table 4 shows the predicted results of the effect of pre-excitation of molecular vibrations on L_{in}, L_c, T_c, and M_c values under combustion behind a shock wave with $M_0 = 6$, $\beta = 20°$, 30°, and 80° for various degrees of excitation of N_2 and H_2 molecules. The profiles of $T(x)$ and $M(x)$ behind the shock at $M_0 = 6$ and $\beta = 20°$ under different degrees of pre-excitation of H_2 molecule ($T_{40} = T_1$, $2T_1$, $3T_1$) are shown in Fig. 2. It is seen that pre-excitation of H_2 and N_2 molecules leads to a significant decrease in L_{in} and L_c. This fact is due to the increased intensity of the chain mechanism of combustion for a H_2–air mixture, both under supersonic ($\beta = 20°$; 30°) and subsonic flow conditions ($\beta = 80°$) behind the shock wave. Moreover, under low temperature behind the shock ($\beta = 20°$), pre-excitation of N_2 and H_2 molecular vibrations leads to self-ignition of the H_2–air mixture.

Intensification of the chain mechanism under pre-excitation of H_2 molecules is due to enhanced accumulation of OH radicals and O and H atoms. The main channel of OH radical formation under pre-excitation of H_2 vibrations is reaction 9 (Table 2). The major source of H atoms in this case is dissociation of

Table 4 Variation of L_{in}, L_c, T_c, and M_c values under different degrees of pre-excitation of H_2 and N_2 molecular vibrations (T_{40} and T_{70}) at $M_0 = 6$, $T_0 = 300$ K, $P_0 = 133$ Pa

β, deg.	T_1, K	T_{j0}	L_{in}, cm	L_c, cm	T_c, K	M_c
20	518.8	$T_{j0} = T_0$	—	—	—	—
		$T_{70} = 2T_1$	—	—	546.18	4.23
		$T_{70} = 3T_1$	4.79(5)	5.3(5)	2381.3	1.806
		$T_{70} = 4T_1$	6.54(4)	1.1(5)	2390.6	1.795
		$T_{70} = 6T_1$	7.78(3)	4.46(4)	2410.8	1.77
30	803.2	$T_{j0} = T_0$	1.495(4)	3.55(4)	2431.6	1.63
		$T_{70} = 2T_1$	4.75(3)	2.3(4)	2442.6	1.61
		$T_{70} = 3T_1$	1.9(3)	1.74(4)	2456.5	1.596
		$T_{40} = 2T_1$	6.67(3)	2.67(4)	2433.5	1.624
		$T_{40} = 3T_1$	2.38(3)	2.14(4)	2438.3	1.62
80	2318.3	$T_{j0} = T_0$	76.5	1440	2539.6	0.596
		$T_{70} = T_1$	5.67	1200	2550	0.608
		$T_{70} = 2T_1$	4.82	550	2570	0.633
		$T_{70} = 3T_1$	4.59	490	2588	0.664
		$T_{40} = T_1$	7.82	1400	2542	0.6
		$T_{40} = 2T_1$	7.87	1240	2552	0.61
		$T_{40} = 3T_1$	7.93	1130	2563	0.623

$A(n)$ corresponds to $A \cdot 10^{-n}$

H_2 molecules (reaction 2). The rate of reaction 2 significantly increases under the excitation of H_2 molecular vibrations. The O atoms are produced in reaction 6.

Under pre-excitation of N_2 molecules, the mechanism of formation of O and H atoms and OH radicals is considerably different. The main factor that causes the acceleration of self-ignition is an increased production of N and O atoms. This is clearly seen from the comparison of the profiles of production (depletion) rates $S_i(x)$ for O, OH and N shown in Fig. 3 for $T_{70} = 3000$ K, $T_{j0}(j \neq 7) = T_0$, and $T_{j0} = T_0$ at $M_0 = 6$ and $\beta = 30°$. It is seen that the excitation of N_2 results in a drastic increase in the rate of dissociation reaction (10), and thus, an enhanced production of N atoms. An increase in the production of O atoms occurs via the reverse reaction (13). Both of these processes are responsible for the increase in NO production. An enhanced production of O atoms stimulates the chain process (reactions (5) and (6)) and the formation of H atoms and OH radicals, although not so pronounced as in the case of the excitation of H_2 molecules. Another mechanism of combustion intensification behind a shock front is the significant variation of T, ρ, P, and u in the induction zone, caused by the transfer of the vibrational energy of N_2 molecules to the translational degrees of freedom (in this case, L_{in} is less than $L_{VT} = u\tau_{VT}$, where τ_{VT} is the characteristic time of V–T relaxation for N_2 molecular vibrations). This fact
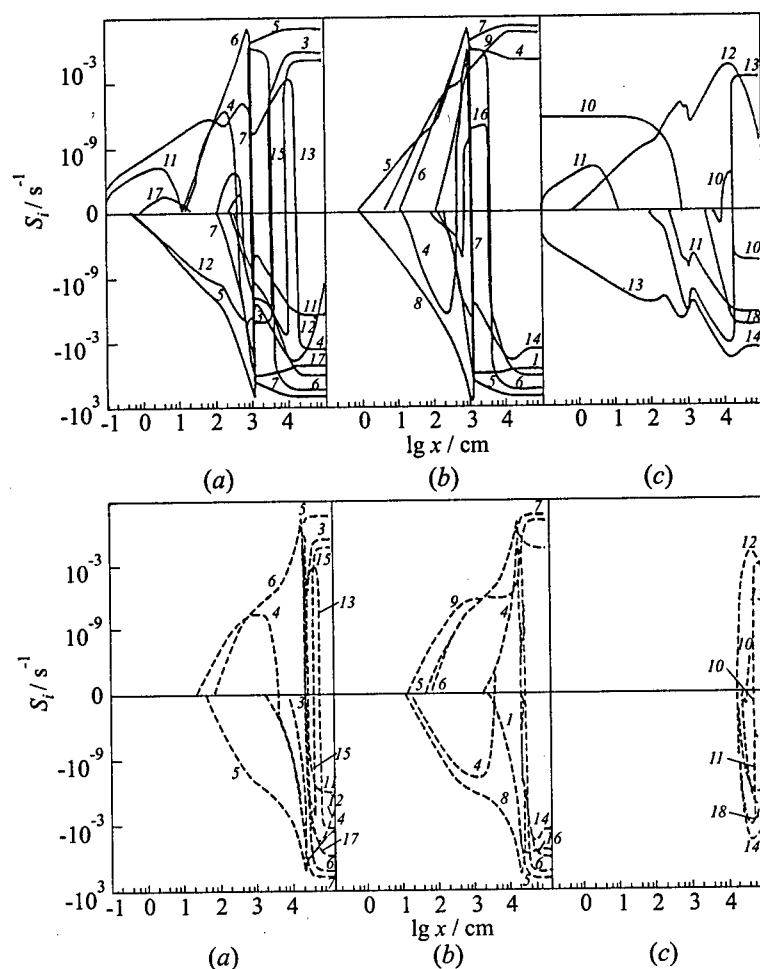
Figure 3 Variations of production ($+$) and depletion ($-$) rates S_i behind a shock front for O (a), OH (b), and N (c) under $T_{70} = 3000$ K, $T_{j0}(j \neq 7) = T_0$ (solid curves) and $T_{j0} = T_0$ (dashed curves), $M_0 = 6$, $\beta = 30°$, $P_0 = 133$ Pa

leads to a significant increase in T at the end of the induction zone and to the enhancement of the rate of all chemical reactions.

CONCLUDING REMARKS

General remarks concerning the obtained results can be made. Delayed excitation of molecular vibrations of initial reactants under detonation of a H_2–air

mixture behind the front of a stationary shock wave considerably influences the kinetics of chemical processes and combustion dynamics. Neglecting this effect may result in significant errors (up to 60%) in determining L_{in} and L_c. Preliminary excitation of molecular vibrations of H_2, O_2, and N_2 leads to a considerably increased intensity of combustion and reduction of the combustion zone length (up to 10 times). The mechanisms of intensification are different when exciting H_2 and N_2. In the former case, the intensification of the chain mechanism of combustion prevails through a more intense production of active centers O, H, or OH. In the latter case, the local increase in the translational temperature behind the induction zone is caused by the energy release stored in vibrational degrees of freedom of N_2 in the V–T relaxation process.

ACKNOWLEDGMENTS

REFERENCES

1. Takeno, T., Uno, T., and Kotani, Y., *Acta Astronautica*, **6**, 891, 1979.
2. Yip, T., Ignition Delay and Characteristic Reaction Length in Shock Induced Supersonic Combustion, AIAA Paper No.89-2567, 1989.
3. Dautov, N. G., and Starik, A. M., *Rus. J. Physics Combustion Explosion*, **32**, 1, 94, 1996.
4. Li, C., Kailasanath, K., and Oran E. S., *Combustion Flame*, **108**, 1, 173, 1997.
5. Dautov, N. G., and Starik, A. M., *Rus. J. Applied Mechanics Technical Physics*, **36**, 6, 25, 1995.
6. Kuznetsov, N. M., *The Kinetics of Monomolecular Reactions*. Nauka, Moscow, 1982.
7. Losev, S., Sergievskaya, A., Starik, A., and Titova, N., Modeling of Thermal Non-Equilibrium Multicomponent Kinetics in Gas Dynamics and Combustion, AIAA Paper No.97-2532, 1997.
8. Starik, A. M., and Dautov, N. G., *Rus. J. Kinetics Catalysis*, **37**, 3, 322, 1996.
9. Gurvich, L. V., Khachkuruzov, G. A., Medvedev, V. A., *et al.*, *Thermodynamic Properties of Individual Substances: A Reference Book*. USSR Academy Sci. Publ., Moscow, **1**, 1978.
10. Millikan, R. C., and White, D. R., *J. Chemical Physics*, **59**, 6, 2787, 1963.
11. Zuev, A. P., and Starikovskii, A. Yu., *Sov. J. Chemical Physics*, **9**, 7, 877, 1990.
12. Kirmusov, I. P., and Starik, A. M., *Izvestiya USSR Academy Sci., Ser. Fluid Mechanics*, **6**, 137, 1991.

CONTROL OF PREDETONATION EXPLOSION PROCESSES IN PROPELLANTS

A. A. Sulimov and B. S. Ermolaev

Deflagration-to-detonation transition in porous propellants includes two predetonation intermediate stages: convective burning (CB) and low-velocity detonation. This paper summarizes the results of experimental and theoretical studies of CB stabilization and control. Quasisteady modes of CB in propellants with low porosity (2–10%) are analyzed. The spatial structure of a CB-wave, stabilization mechanisms, characteristics of quasisteady CB, and the factors effecting the rate of chemical transformation in the burning zone (within the range of CB velocity 1–200 m/s) are discussed. The experimental data illustrating the specific features of the processes are discussed and the effects of the initial properties of charges are considered. The experimental data are compared with the results of calculation. Also discussed are applications of CB in low-porosity propellants for increasing the efficiency of propulsion and barrel systems.

INTRODUCTION

Deflagration-to-detonation transition (DDT) is a complex multistage process which, in general, comprises four stages: initial layer-by-layer burning governed by heat conduction, two intermediate processes — CB and low-velocity detonation (LVD), and the final stage of explosion development, that is normal detonation. The stages differ by the mechanisms of reaction initiation and energy transfer and by the ranges of propagation velocities and pressures.

The term "convective burning" normally applies to flame propagation in gas permeable energetic materials (EM). The mechanism of CB is associated with the filtration of the gaseous combustion products through pores and also with convective ignition of the porous EM. Convective burning, which provides penetration of combustion inward the EM and creates the conditions for the detonation-like mode of spreading the chemical reaction, is one of the most important stages in DDT. The traditional treatment of CB, as a nonsteady accelerating process, stems from the investigations of both explosion development in fine grained

explosives in a closed vessel and flame permeation into cracks in solid rocket propellants [1]. Therefore, determining the conditions under which CB can be stabilized, as well as studying the properties of stabilized CB, is attractive not only as an interesting theoretical problem, but will enable one to solve a number of practical explosion safety and applied problems. Before the works of the present authors, there were quite meagre data on the stabilized CB, which were obtained in experiments with short charges of high explosives of loose-packed density (or close to it) [2–4].

In our investigations [5–8], EM of low porosity (5 to 12%) and specially designed combustion chambers, equipped with an afterburning section and a nozzle, were used. These combustion chambers permitted simultaneous monitoring of flame propagation (by photography) and pressure variations at several sites distributed along the charge length and in the afterburning section (by means of piezoquartz pressure gauges). These studies revealed a burning mode with the average velocity of the CB-wave and the maximum pressure remaining nearly constant along fairly long charges, at the pressure in the afterburning section being constant. This process was referred to as the quasisteady CB. The performed studies furnished the data that shed light on the mechanism and spatial structure of CB-waves and on the mechanism and conditions of CB stabilization that preclude spontaneous flame acceleration and pressure build-up. Experimental data were supplemented by theoretical simulations.

LIMITS OF CONVECTIVE BURNING

When the pressure at the flame front exceeds the critical runaway pressure P_{CB}, convective burning arises. Low-velocity detonation arises when the pressure in the combustion wave exceeds the threshold value P_{LVD}, providing generation of hot spots due to visco-plastic deformation of pores. Convective burning is possible whenever the pressure in the combustion wave, P_x lies within the range $P_{CB} < P_x < P_{LVD}$.

METHODOLOGY OF THE STUDY OF STABILIZED CONVECTIVE BURNING

The essence of the approach systematically employed in our DDT studies is the separate exploration of the intermediate stages, CB and LVD. Through this, the limits of their existence are determined and the conditions governing stabilization of these propagation modes at controlled levels of propagation velocities and pressures are found. The use of the stabilized modes provided the benefit of

investigating long charges and significantly simplified obtaining and interpreting the experimental data.

The initial charge properties, including the EM type and reactivity, grain size, porosity, gas permeability, and the presence of various inhibiting additives, were varied within a wide range. The measurements provided a great body of data on the behavior of the process and enabled us to single out the key parameters controlling both its development and the characteristics to be compared with theoretical models. Of most importance is the fact that, in addition to individual parameters of the process, their dependencies on the initial properties were compared with those provided by theoretical models.

The following EM were studied:

- composite propellant (from now on propellant A) containing 78% ammonium perchlorate and 22% polyvinyl butyral binder with grains of various shape and size of effective diameter $d_{ef} = 1.9$, 0.96 and 0.66 mm,

- double-base propellant NB containing 40% nitroglycerine with $d_{ef} = 0.81$ mm,

- fine-grained single-channel pyroxylin propellant C with $d_{ef} = 0.5$ mm,

- PETN with $d_{ef} = 0.5$ mm.

The propellants studied had strong grains which were not destroyed under pressing the charges.

The following inert materials were used as inhibiting additives: paraffin (P), polyvinylbutyral (PVB), and ethylcellulose (EC). The additives were applied on the surface of an EM particle in the form of thin coatings by depositing them from solutions with subsequent drying. Charges with a preset porosity ranging between 2 and 15% were prepared by pressing (normally with no preheating).

EXPERIMENTAL FACILITIES AND TECHNIQUES, MEASURED PARAMETERS

To study the characteristics of stabilized CB, we used the set-up shown schematically in Fig. 1. The device comprises two sections: a cylindrical transparent high-pressure chamber with a tested charge and the afterburn section. The combustion chamber consists of a PMMA tube 15 or 18 mm in diameter. The tube is inserted tightly into a polished channel of a steel casing, in which a narrow slit is cut along the axis in order to photograph the process. Several orifices are drilled in the chamber along its axis in which high-frequency Kistler-type piezoquartz gauges are mounted. The afterburning section, 750 cm^3 in volume, is equipped
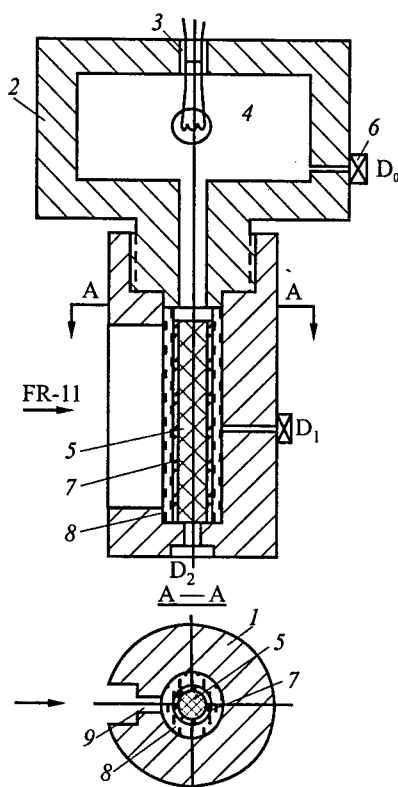
243

Figure 1 Schematic of the set-up designed to study stabilized convective burning: *1* — casing, *2* — afterburn section, *3* — nozzle, *4* — igniter, *5* — tested EM, *6* — piezoelectric pressure gauges (D_0, D_1, D_2), *7* — glycerine, *8* — PMMA tube, *9* — longitudinal slot

with the replaceable nozzle, which controls the outflow of the combustion products, and a piezoelectric pressure gauge. The process was initiated with an electric igniter cap, igniting a fast burning combustible mixture for producing a desired initial pressure in the chamber.

The set-up permitted the measurements to be conducted within a pressure range of up to 300 MPa. At the highest pressure, the inner PMMA tube was destroyed, but the steel casing with pressure gauges remained intact and was used repeatedly. The EM studied was pressed to produce pellets of a diameter which is slightly less than the inner diameter of the channel in the casing. The pellets were stacked to form a cylindrical charge of a length ranging from 70 to 200 mm. The side walls of the charge were coated with epoxy resin. After curing the resin, the charge was inserted into the channel of the casing and a small gap between the charge and casing walls was filled with glycerin. Electric signals from the pressure gauges were recorded on Data Lab digital recorder. Luminosity of the process was photographed with FR-11 and ZhFR-2 streak cameras differing in their sweep velocity.

Figure 2 shows the streak camera photographs of the pulsating quasisteady CB of propellant A. The corresponding pressure records and the procedure of joint processing of the piezometric and photographic data are exemplified in Fig. 3. From the measurements, the average flame velocity (W) (based on the slope of the luminous front track), average pressure in the afterburning section during flame propagation (P_b^*), pressure profiles at several sites along the charge length, the pressure at the flame front (P_f) (by matching the streak camera photographs and pressure signals), maximum pressure in the wave (P_x), the filtration zone thickness L_{fil} (based on the pressure profiles and velocity W), period T and amplitude (A_p) of the pressure pulses in the combustion chamber, and the mean step (h) of the jump-wise flame front displacement in camera
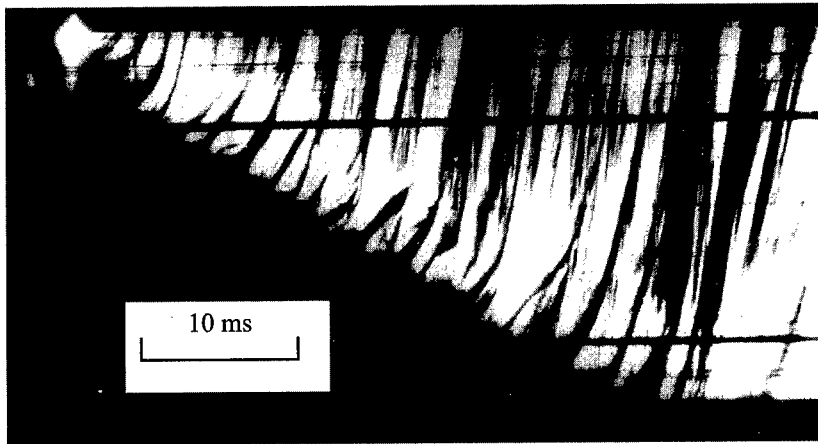
Figure 2 Streak photograph of pulsating quasisteady CB of propellant A+5% paraffin
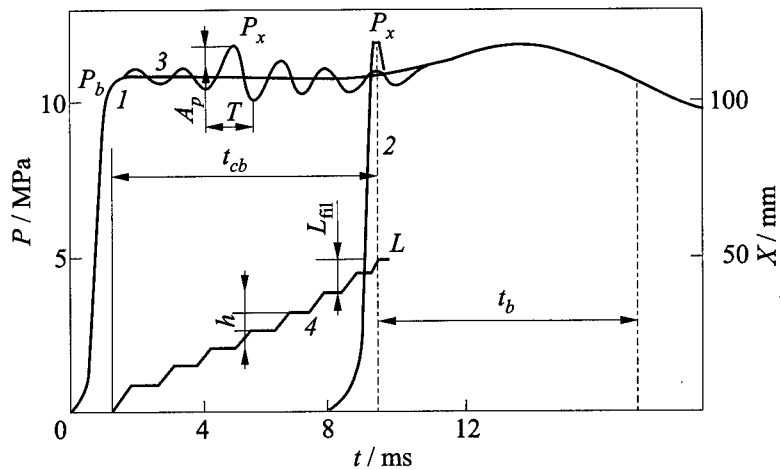
Figure 3 Schematic diagram illustrating the joint processing of streak photographs and pressure records for quasisteady convective burning: 1–3 — pressure–time histories recorded by gauges D_0, D_2, and D_1, respectively, 4 — trajectory of the flame front, A_p is the amplitude of pressure oscillations, T is the period of oscillations, h is the depth of flame front oscillations, t_{cb} is the time of convective burning propagation through the charge, t_b is the burning time of EM particles, and L_{fil} is the width of the filtration zone

Figure 4 Schematic of the convective combustion wave structure in a low-porosity EM charge burning in a combustion chamber from which the combustion products are discharged: *1* — filtration zone, *2* — preheat zone, *3* 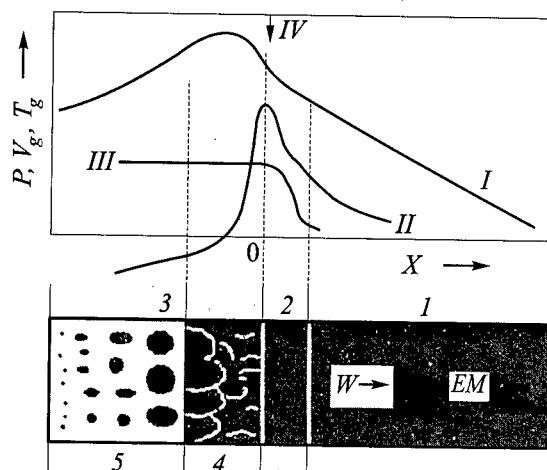— ignition and combustion zone, *4* — frontal part of the combustion zone, *5* — burn-down zone, *I* — pressure profiles, *II* — gas velocity, *III* — gas temperature, *IV* — flame front

photographs, were extracted. In addition, the pressure records in the afterburning section were used for estimating the burning time of EM particles (t_b), the burn-down zone length (L_b) and gas formation intensity in the CB-wave. The burning time (t_b) was measured as the difference between the start of the exponential pressure decay in the afterburning section and the instant when the flame spreads throughout the charge length, as determined from the joint processing of the pressure records and streak photographs. The gas formation intensity and the mean specific burning surface A_b were estimated from curve $P_b(t)$.

MECHANISMS AND CONDITIONS OF EXISTENCE OF QUASISTEADY CONVECTIVE BURNING IN LOW-POROSITY ENERGETIC MATERIALS

The spatial structure of a CB-wave and information on the profiles of the basic variables in burning low-porosity energetic materials, deduced from experimental and theoretical studies, are presented schematically in Fig. 4. The following spatial zones are distinguished: the filtration zone, where the cooled combustion products transfer their heat to the pore walls into which they have permeated and decelerated; the preheat zone, where the pore surface is heated to the ignition temperature due to convective heat transfer from the combustion products; and

Table 1 Basic characteristics of quasisteady convective burning of propellant A

EM	d_{ef} mm	P'_b MPa	W m/s	A_p MPa	T ms	L_{fil} mm	h mm	L_b mm	t_b ms
Propellant A	0.66	4.8	1.2	1.2	—	17	—	—	31
		10	4.7	2.0	2	6	9	—	23
	0.96	6	4.1	4	3.1	—	13	700	38
		11	9.3	5.2	1.4	24	12	800	30
	1.9	4.9	5.2	1.8	—	18	—	900	—
		9.2	11.3	2.0	1.9	16	22	1400	75
Propellant A + 5% P	0.96	14.6	23.5	2.8	—	21	—	1900	60
		11	1.4	1	11	30	16	—	52
		17	2.2	2.2	4.4	24	10	—	48
		17.6	2.2	2.2	4	—	8	—	—

Note: P is paraffin.

the ignition and combustion zone, where chemical conversion of EM begins in the ignition mode with subsequent regression (burning) of the pore surface. The interface between this latter zone and the preheat zone will be referred to as the ignition front, or the flame front. Here, the velocity of the gas flowing into the pores attains its maximum. Behind the flame front, the gas velocity decreases, and at the point, where the pressure peaks, passes through zero and changes its sign. This point can be referred to as the flow separation point.

An idea about the burn-down zone length can be found from estimates of parameter L_b listed in Table 1. Although the EM in this zone undergoes chemical transformation in the regime of layer-by-layer burning over the surface of ignited pores, the flame rapidly covers a vast area due to the difference between the rates of layer-by-layer and convective burning, which may be as large as 1000-fold. It is the extended burn-down zone with a well developed surface area, which is responsible for the high propensity of CB to acceleration due to the feedback through the pressure build-up.

The major result of this study is the proof of the fact that by affecting the burning zone one can slow down the evolution of an explosion process and, under certain conditions, even stabilize it at the CB stage. The burning process is affected via two ways: (i) dynamic unloading of the burning zone due to outflow of the reaction products to an afterburning chamber equipped with a nozzle, and (ii) decrease in the intensity of chemical conversion by diminishing the burning surface area due to a decrease in the specific surface area of EM particles and due to coating the particle surface with films of inert materials.

The data on the filtration zone thickness L_{fil} are listed in Table 1. The representative L_{fil} values range between 15 and 30 mm. The attempts to find a correlation between L_{fil} and any other parameters were failed. On the contrary,

the fluctuating characteristics of the burning process are closely related, as seen from the data presented in the same table, to the pressure and CB velocity. Generally speaking, the higher the pressure and the CB velocity, the greater are the amplitude (A_p) and frequency ($1/T$) of the pressure fluctuations and shorter is the length of flame hops (h).

The conditions needed for stabilizing CB in the experimental device with an afterburning section can be formulated as follows:

1. The initial porosity and gas permeability of a charge should not exceed the threshold values equal to about 15% and 10^{-7} cm^2, respectively. When the porosity and gas permeability of charges were higher, we failed to stabilize the pressure in the afterburning section and the burning velocity by varying the nozzle throat. The process proceeded with an appreciable increase in the flame velocity with time, throughout the major portion of the charge, and a decrease in the velocity, as the flame approached the closed rear charge end.

2. The pressure range, within which CB was stabilized, is bounded by the upper and lower boundaries. These boundaries can be compared with the threshold pressures P_{CB} and P_{LVD}.

An analysis of the mechanism of quasisteady CB has shown that the important factor, which allows the process to be stabilized by constraining the pressure rise in the burning zone, is the periodic dispersion of burning EM under tensile stresses arising from the outflow of the combustion products. Because of dispersion, the flame speed and pressure fluctuate, but their average values remain nearly constant.

CONTROL OF PROPAGATION OF QUASISTEADY CONVECTIVE BURNING IN LOW-POROSITY ENERGETIC MATERIALS

Further studies were aimed at understanding the effect exerted on the basic characteristics of quasisteady combustion waves by such parameters as the pressure in the afterburning section P_b' (the mean pressure at the "shelf" portion), initial particle size, charge porosity, and inhibitor content. The results of measurements for propellant A, at a 5% charge porosity, are summarized in Table 1.

Consider the pressure dependence of the quasisteady convective burning velocity. Figure 5 shows the CB velocity as a function of the maximum pressure for three different EM: PETN, double-base propellant NB, and composite propellant A. Propellant A has the highest burning velocities, whereas PETN exhibits the strongest pressure dependence of the burning velocity. From the above data,
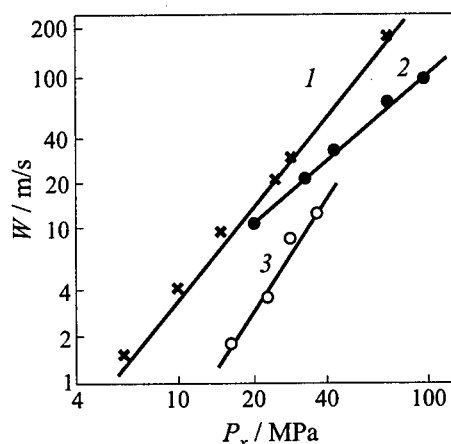
Figure 5 Pressure dependence of the quasisteady burning velocity for three EM: *1* — propellant A (d_{ef} = 0.96 mm; *2* — double base propellant NB (d_{ef} = 0.9 mm); *3* — PETN (d_{ef} = 0.5 mm)

treated in the form of a power dependence $W = B_c P_x^{\nu_c}$, we infer that in the row: PETN, propellant A, and propellant NB — ν_c equals to 2.7, 2.0, and 1.45, respectively. There is no correlation between the convective and layer-by-layer burning modes in the velocity values and pressure exponent.

Table 2 lists more comprehensive data on coefficients B_c and ν_c, which control the pressure dependence of the CB velocity. The table also presents the burning velocities at a pressure of 20 MPa and in the pressure range relevant to current measurements.

The effect of the initial porosity on the pressure dependence of the CB velocity is illustrated in Fig. 6 for propellant A. As is seen, an increase in φ_0 raises W and does not affect ν_c. With rising d_{ef}, W increases, whereas ν_c decreases.

Figure 7 shows the velocity of CB as a function of pore diameter for propellant A at two pressure levels. By and large, although the data are scattered, a trend to larger velocities with increasing the pore diameter is clearly seen.

Table 2 Velocity of quasisteady convective burning and its pressure dependence

EM	$\dfrac{d_{ef}}{mm}$	B_c	ν_c	W, m/s, at $P_c' = 20$ MPa	Pressure range MPa
PETN	0.5	8.8×10^{-4}	2.7	2.9	10–15
Propellant A	1.9	0.23	1.6	20.6	4–60
	0.96	0.040	2.0	16	5–70
	0.66	0.0214	2.2	15.6	6–90
A + 3% P	0.96	0.132	1.1	3.6	8–20
A + 5% P	0.85	0.19	0.8	2.1	4–20
A + 5% EC	0.85	1.0	0.45	3.9	5–50
Propellant NB	0.82	0.15	1.45	11.5	20–90
NB + 3% PVB	0.82	0.95	0.8	10.4	20–100
Propellant C + 7.5% PVB	0.5	1.05	0.53	5.1	30–160

Note: PETN charges have porosity of 10%, other charges have porosity of 5%; P is paraffin, EC is ethyl cellulose, and PVB is polyvinyl butyral.
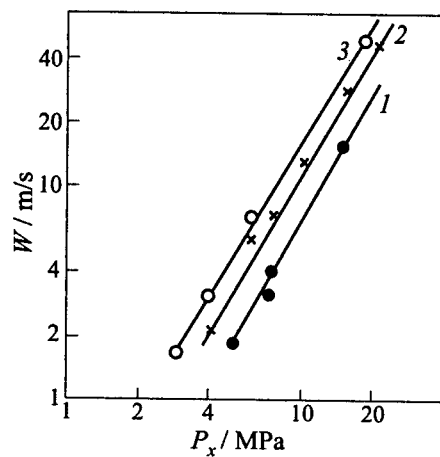
Figure 6 The effect of the initial porosity φ_0 on the pressure dependence of the convective burning velocity for propellant A $(d_{ef} = 1.9$ mm): 1 — $\varphi_0 = 2\%$, 2 — 5%, 3 — 12%
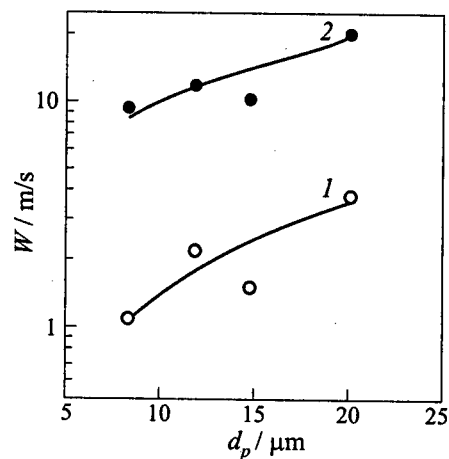

Figure 7 The correlation between the convective burning velocity and pore diameter for propellant A at 1 — $P_x = 6$ MPa and 2 — 16 MPa
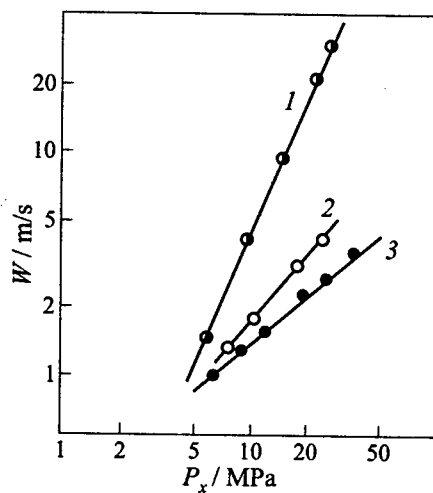

Figure 8 The effect of paraffin additives on the velocity of convective burning of propellant A $(d_{ef} = 0.96$ mm$)$ at a 5% porosity: 1 — A, 2 — A + 3% paraffin, 3 — A + 5% paraffin
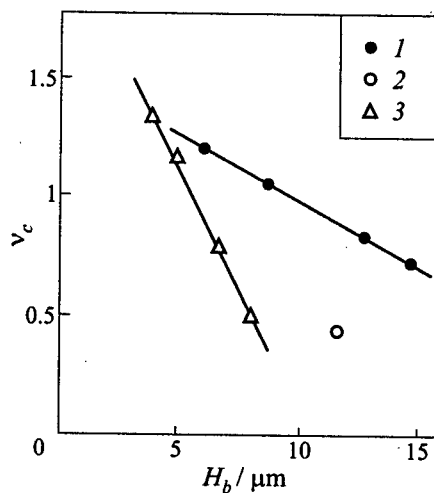

Figure 9 Correlation between the adiabatic exponent ν_c and the binder film thickness: 1 — paraffin, 2 — ethyl cellulose, 3 — polyvinyl butyral

The effect of inhibitor additives was also analyzed. As is seen from Fig. 8, introduction of paraffin significantly reduces the CB velocity and exponent ν_c, with the latter quantity dropping below unity. The inhibitor effect increases with the amount of additive introduced. Similar data were obtained for the other EM, which exhibits no break of granules during charge preparation.

Comparison of various inhibitors has demonstrated that the inhibiting effect tends to rise for additives with higher thermal stability.

The analysis of the above data indicates that the thicker the inhibitor film on the particle surface, the more pronounced is the inhibiting effect. The graph demonstrating this result is shown in Fig. 9. Thus, to obtain the same inhibiting effect with smaller particles, one should increase the additive content.

THEORETICAL MODELING OF QUASISTEADY CONVECTIVE BURNING

A Model of Pulsating Quasisteady Convective Burning

The model is based on the above-discussed experimental observations of periodic pressure fluctuations, jump-wise flame front propagation, and dispersion of EM charges in the course of their quasisteady CB. The basic factors that contribute to CB stabilization in low-porosity EM are the periodical dispersion of the burning charge fraction and removal of burning fragments, both limiting the pressure rise. The calculation results from this model [5, 9] are compared with the available experimental data.

The dependencies predicted by this model for the characteristics of pulsating burning mode are compared with experimental findings in Table 3. The agreement can be considered to be satisfactory. Thus, the results of modeling support the hypothesized pulsating mechanism of quasisteady CB.

APPLICATIONS OF THE HIGH-SPEED CONTROLLED CONVECTIVE BURNING OF THE COMPACTED LOW-POROSITY PROPELLANTS

Convective burning of low-porosity charges makes it possible to achieve well-controlled high rates of chemical energy release in the charge and to increase 1.5- or 2-fold the energy concentration per unit volume of the chamber, as compared to the traditional burning modes in pulsed rocket motors and guns. Our investigations laid scientific and practical grounds for solving this problem.

Table 3 Experimental and theoretical relations for quasisteady pulsating CB

Characteristics of pulsating quasisteady burning	Experiment	Theoretical modeling
Convective burning velocity W	$W \propto P_x^{\nu_c}$, $\nu_c = 1.6\text{--}2.8$ $W \uparrow$, if $d_p \uparrow$ and $\sigma_R \uparrow$	$W_0 \propto d_p A_p^{3/2} P_f^{(\nu_c + 1/2)}$
Period of fluctuations T	$T \propto P_x^{-1.5}$ and $\neq f(d_p)$ $T \downarrow$ if $\sigma_R \uparrow$	$T \propto A_p^{-1} P_f^{-2\nu_c}$ and $\neq f(d_p)$
Amplitude of fluctuations A_p	$A_p \uparrow$ if $\sigma_R \uparrow$ and $P_x \uparrow$	$A_p \uparrow$ if $\sigma_R \uparrow$ and $\neq f(P_f)$
Pitch at the acceleration stage h	$h \propto d_{ef}$, $h \downarrow$ if $P_x \uparrow$	$h \propto d_p A_p^{1.2} P_f^{(1/2 - \nu_c)}$

Note: P_x is the maximum pressure in the convective burning wave, P_f is the pressure at the flame front.
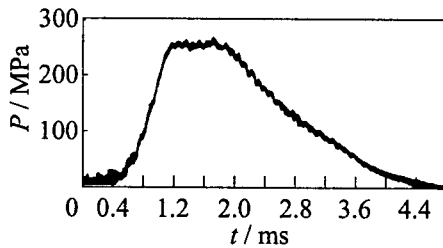

Figure 10 The pressure–time diagram with a plateau in 23 mm barrel system

To study ignition, convective burning, and internal ballistics of low-porosity energetic materials, the experimental measuring facilities were designed and manufactured to perform complex studies under conditions simulating intrachamber processes at pressure of up to 400 MPa. The studies performed have demonstrated fundamental feasibility of a significant increase (up to 1.4 g/cm³) of the loading density in pulse rocket motors and guns, and of obtaining reproducible pressure–time histories of a controlled flat-top shape (Fig. 10). The use of compacted high-progressive low-porosity charges in cartridges increases the projectile velocity up to 20% (as compared to the traditional charges), when maximum pressure of shot is invariable.

CONCLUDING REMARKS

In this paper,

- comprehensive data on the stabilization conditions and characteristics of stabilized convective burning are obtained,

- stabilization mechanisms are studied,

Table 4 Effect of control factors on the basic characteristics of quasisteady CB

Parameters	Initial porosity	Particle size	Inhibitor additives	Thermal stability of additive	Layer-by-layer burning velocity	Charge strength
P_{CB}	↓↓	↓	↑	?	↓↓	~
P_{LVD}	~	?	↑	?	?	
W	↑	↑↓	↓↓	↓	~	?
ν_c	~	↓	↓↓	↓	~	?
t_b	↓	↑	↑↑	↑	↓↓	↑
A_b	↑↑	↓	↓↓	↓		↑

Note: ↑ signifies that an increase in the factor indicated in the column entails an increase in the parameter indicated in the row, ↓ means the reverse effect. Double arrow indicates that the effect is strong; ~ points to the lack of influence; ? indicates that the dependence is not firmly established.

— factors controlling the CB stability and characteristics are ascertained, and

— theoretical models for explaining experimental observations and checking the underlying hypotheses are developed.

Table 4 summarizes the effects of various factors on the limits and basic characteristics of quasisteady CB. The strongest remedy is the use of inhibiting films coating EM grains. The effect of inhibitors manifests itself both at the stage of flame propagation and during burning of dispersed EM particles. Inhibiting additives efficiently reduce the convective burning velocity, its pressure dependence, and intensity of the reaction within the burning zone. Of particular interest is a possibility of reducing the pressure exponent ν_c to values below unity. The mechanism of the effect exerted by the inhibitors consists in ignition delaying by the inert coating. The effect is enhanced as the film thickness and thermal resistance increase.

Among other factors, one can single out the initial charge porosity (its variation allows controlling such parameters as the low limit of quasisteady convective burning, burning intensity, and flame speed) and the size of EM particles (its variation affects all the characteristics of convective burning, except, may be, for the upper limit of convective burning).

ACKNOWLEDGMENTS

253

REFERENCES

1. Belyaev, A. F., Bobolev, V. K., Korotkov, A. I., Sulimov, A. A., and Chuiko, S. V., *Deflagration-to-Explosion Transition in Condensed Systems*. Nauka, Moscow, 1973.

2. Taylor, T. W., *Combustion Flame*, **6**, 103, 1962.

3. Andreev, K. K., and Chuiko, S. V., *Sov. J. Physical Chemistry*, **37**, 6, 1034, 1963.

4. Cole, R. A., and Fifer, J. E., *Proc. 7th Symposium (International) on Detonation*, CPIA Publications, Annapolis, MD, **1**, 1981, 164.

5. Ermolaev, B. S., Sulimov, A. A., Foteenkov, V. A., *et al.*, *Sov. J. Physics Combustion Explosion*, **16**, 3, 24, 1980.

6. Khrapovskii, V. E., and Sulimov, A. A., *Sov. J. Physics Combustion Explosion*, **24**, 2, 39, 1988.

7. Roman'kov, A. V., Sulimov, A. A., Sukoyan, M. K., and Biryukov, M. S., *Sov. J. Chemical Physics*, **11**, 7, 983, 1992.

8. Sulimov, A. A., Ermolaev, B. S., Borisov, A. A., *et al.*, *Proc. 6th Symposium (International) on Detonation*, Arlington, VA, 1976, 250.

9. Sulimov, A. A., and Ermolaev, B. S., *Rus. J. Chemical Physics*, **16**, 10, 1997. -

254

ON ONE REGIME OF LOW-VELOCITY
DETONATION IN POROUS MEDIA

A. A. Korzhavin, V. A. Bunev, V. S. Babkin, M. Lawes, and D. Bradley

The physical model of the combustion wave, propagating at the sonic velocities 100 to 800 m/s in a premixed gas filling the inert porous medium, is proposed. It is assumed that the ignition is induced by convection. The pulsations of combustible gas control the propagation velocity of the wave. The level of velocity fluctuations is governed by the conditions of hydrodynamic quenching of the flame. Combustion supports the compression wave, which is the intrinsic component of the combustion wave structure. Adiabatic compression in the compression wave results in pressure and temperature growth in the fresh gas. Therefore, high propagation velocity of the combustion wave is observed. At the leading front, the compression wave has a small value of pressure gradient. It is determined by the square of velocity and other parameters describing the inertial resistance of the medium. The experimental data on combustion of hydrogen–air mixtures in various porous media confirm the physical model of the phenomenon. These data also demonstrate the effect of the Lewis number in the sonic velocity regime.

INTRODUCTION

Combustion of gas in inert porous media (PM) is of scientific and special interest in different applications, namely, the power industry, chemical and building technologies, ecology, and fire and explosion safety. Presently, there are five distinctive steady-state propagation regimes of gas combustion in inert PM known: the low-velocity regime (LVR) with the characteristic wave propagation velocities $u \cong 10^{-4}$ m/s, high velocity regime (HVR) with $u = S \cong 0.1$–10 m/s, sonic velocity regime (SVR) with $u = S \cong 10^2$ m/s, low-velocity detonation (LVD) with $u = D \cong 800$–1500 m/s, and normal detonation with heat and momentum losses (ND) with $u = D \cong 1500$–2500 m/s [1]. These regimes differ from each other in the ranges of characteristic velocities of the combustion waves, and in the mechanisms of ignition transport in a combustion wave.

Since it has been poorly investigated thus far, the SVR is a regime of particular interest. This regime exhibits a wide range of velocities, which are intermediate between those for deflagration and detonation, and exhibits, in some sense, both detonation and deflagration properties. On the one hand, the structure of the SVR-wave includes a compression wave with a characteristic gradual pressure rise. Therefore, it is appropriate to refer to it as "supersonic" burning, i.e. detonation. On the other hand, the propagation velocity of the wave is rather low, and its intensity (the degree of gas compression) is not sufficient for the self-ignition of a combustible mixture with a short ignition delay. Hence, the most likely mechanism of ignition transport in the combustion wave is convection. Theoretical aspects of detonation waves of the LVD-regime were considered in [2–5].

In the present work, on the basis of authors' own data and experimental data from the literature, the mechanism of combustion wave propagation in the SVR, as well as the reason for wave velocity stabilization and the effects of compressibility and Lewis number are discussed. Ideas for generalizing the experimental data are also presented.

EXPERIMENTAL DATA ON THE PROPAGATION VELOCITIES OF COMBUSTION WAVES IN THE SONIC VELOCITY REGIME

During combustion of a gas in an inert PM, there exists a filtration zone in front of the combustion wave, where the motion of the gas, caused by expansion of combustion products, is damped by friction and blockage of flow by the PM. Because of the low level of flame velocities, the filtration zone thickness in the HVR is large, compared to the combustion zone length, therefore, the combustion process may be treated as isobaric. Experiments confirm this conclusion [6].

Another situation arises in SVR. The filtration and combustion zone lengths are comparable and the chemical reaction proceeds in a compression wave at elevated pressure and temperature. Therefore, the velocities in SVR are much higher than in HVR [1]. Shown in Table 1 are the experimental data on flame propagation velocities for the hydrogen–air mixture in SVR. As PM, the open-cell polyurethane foam (PF) with porosity $\varepsilon = 0.98$ and the characteristic size of pores $d = 2.8$ mm was used. The borders of the domain of existence of SVR are poorly investigated. It is known that either flame quenching [7] or transition to any of the other known steady-state regimes (HVR, LVD, ND) occurs at these borders. Transition to HVR or to flame quenching is observed usually under reducing mixture reactivity, burning velocity S_u, or initial pressure p_i [8]. The

Table 1 Experimental data on hydrogen–air flame velocities in polyurhetane foams. The values of burning velocities are taken from [11]

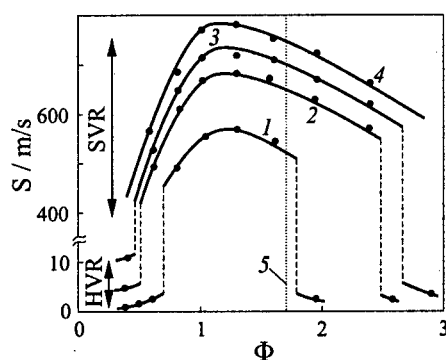| Hydrogen content %	Burning velocity S_u cm/s	Initial pressure p_i MPa	Flame velocity S m/s	Reynolds number Re
15	35	0.093	2.9	272
20	85	0.080	6.2	438
25	160	0.080	744	$5.5 \cdot 10^4$
30	220	0.050	274	$1.1 \cdot 10^4$
30	220	0.070	809	$4.7 \cdot 10^4$
30	220	0.120	977	$9.8 \cdot 10^4$
35	260	0.054	510	$2.1 \cdot 10^4$
40	280	0.080	829	$4.7 \cdot 10^4$
46	265	0.080	527	$2.7 \cdot 10^4$
46	265	0.100	835	$5.4 \cdot 10^4$
50	250	0.122	833	$6.2 \cdot 10^4$

Figure 1 Dependencies of the flame velocity on the equivalence ratio for hydrogen–air mixtures in granular polyethylene under various pressures. 1 — 0.1; 2 — 0.2; 3 — 0.3; 4 — 0.5 MPa; 5 — position of maximum in the laminar burning velocity. SVR — sonic velocity regime, HVR — high velocity regime

transition to high-velocity LVD or ND regimes occurs, on the contrary, under increasing p_i, S_u, or the diameter of porous channel d (Fig. 1). Usually, the transition shows the jumpwise behavior, but sometimes it occurs smoothly, without jumps in the propagation velocity. Apparently, the smooth behavior is caused by the polydispersity of the PM. Available information on the structure of the SVR combustion wave is scarce. It is known that the pressure in the wave does not usually exceed the value of the maximum pressure of gas explosion in a closed vessel. A smooth pressure rise at the front of a compression wave and a smooth decay of pressure in the combustion products are characteristic for SVR.

In HVR, the wave velocity depends strongly on such parameters as S_u, p_i, and d. It is possible to analyze the dependence of the wave velocity on these parameters in terms of Re(Pe), where Re $= (S - S_u)d/\nu$ is the Reynolds number, and Pe $= S_u d/\kappa$ is the Peclet number. It was shown that for wide ranges of
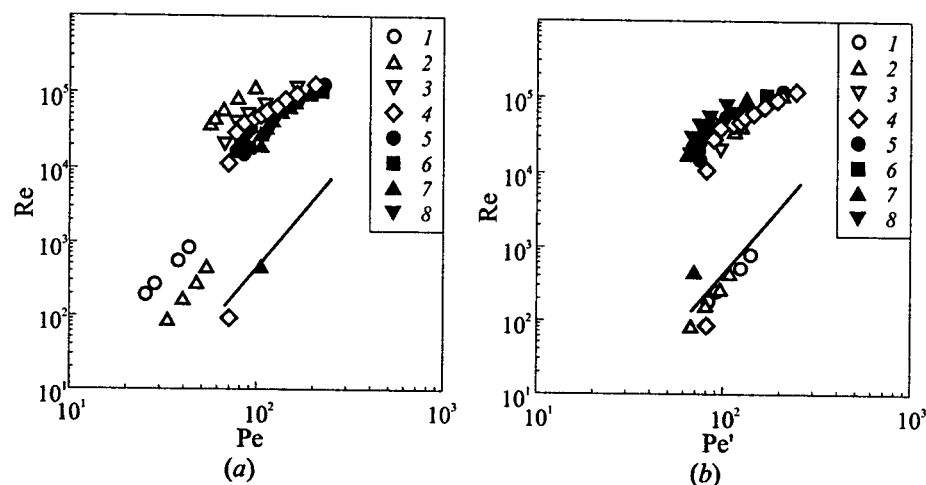
Figure 2 Dependencies Re(Pe) and Re(Pe') for combustion of hydrogen–air mixtures in polyurethane foam at various initial pressures and mixture compositions. Hydrogen content: *1* — 15%, *2* — 20, *3* — 25, *4* — 30, *5* — 35, *6* — 40, *7* — 46, *8* — 50. The line corresponds to burning CH_4–air mixtures in the high velocity regime [9]

the governing parameters, the data on propagation velocities are generalized by the universal dependence Re $\sim$ Pe^3. This dependence is in agrement with a theoretical estimation based on the assumption of local flame quenching due to convective cooling in the fastest velocity pulsation [9].

The parametric dependencies in the SVR are qualitatively similar to those in HVR; combustion wave velocity increases with S_u, p_i, and d. Therefore, SVR can be analyzed in terms of the same dimensionless parameters (Re and Pe) as in HVR. Another argument in support of this approach is the convective nature of ignition transfer in the combustion wave. Indeed, experiments [10] show that even in oxygen-enriched (with up to 28.7% O_2) hydrogen–air mixtures, the interaction of shock waves with rough walls does not result in mixture ignition if the wave velocity is less than 900–1300 m/s.

The Re–Pe dependencies of combustion wave velocities in hydrogen–air mixtures in PF, relevant to HVR and SVR, are shown in Fig. 2a. The values of burning velocities are taken from [11]; it is assumed that they are independent of p_i. It is seen that the data are grouped in two separate areas: Re = 10^2–10^3 for the HVR and Re = 10^4–10^5 for the SVR. For the sake of comparison, the generalized dependence for the flame propagation velocities in methane–air
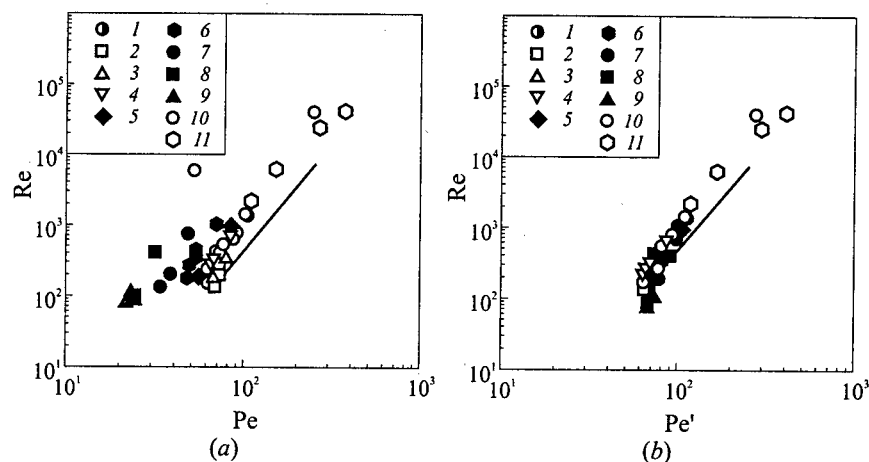
Figure 3 Dependencies Re(Pe) and Re(Pe′) for combustion of various propane–air mixtures in porous substrate made of aluminum foil (*1–8*), polyurethane foam (*9–11*), and aluminum honeycomb (*12*) [9]. Propane content: *1* — 3.25%; *2* — 3.50; *3* — 3.75; *4, 10, 12* — 4.00; *5* — 4.50; *6, 11* — 5.00; *7* — 5.50; *8* — 6.00; *9* — 6.50. The lines correspond to burning of C_3H_8–air mixtures in high velocity regime

mixtures in HVR is also shown in Fig. 2. The dependence obeys the equation $Re \sim Pe^3$ [9]. Taking into account that the border between viscous and inertial flow regimes in porous media lies at $Re \cong 10^2$ [12], it appears that the flow of interest is turbulent, inertial and small-scale.

Figure 2a also demonstrates a remarkable separation of the HVR data depending on the fuel content in the mixture. Lean mixtures correspond to lower values of the Peclet number. Earlier [9], similar segregation of the Re(Pe) dependencies for different compositions was observed in the HVR for propane–air flames (Fig. 3a); it was explained by the Lewis number effect. It is interesting to note, the segregation by composition is also observed in Fig. 2a in the area of SVR, but it is less pronounced than for HVR. Figure 4a shows the results of processing the data on combustion of hydrogen–air mixtures in polyethylene grains (PG) with characteristic pore size $d = 1$ mm. Clearly, the specific features are similar to those for PF (Fig. 2a). There are two remarks worth mentioning: the abnormally low values of Pe numbers are obtained for the 15% H_2–air mixture in which the flame is able to propagate in a porous medium (Pe = 12, Fig. 4a), and the Re(Pe) dependence for the 20%-mixture exhibits a smooth HVR → SVR transition. Figure 5a shows the results of processing the com-
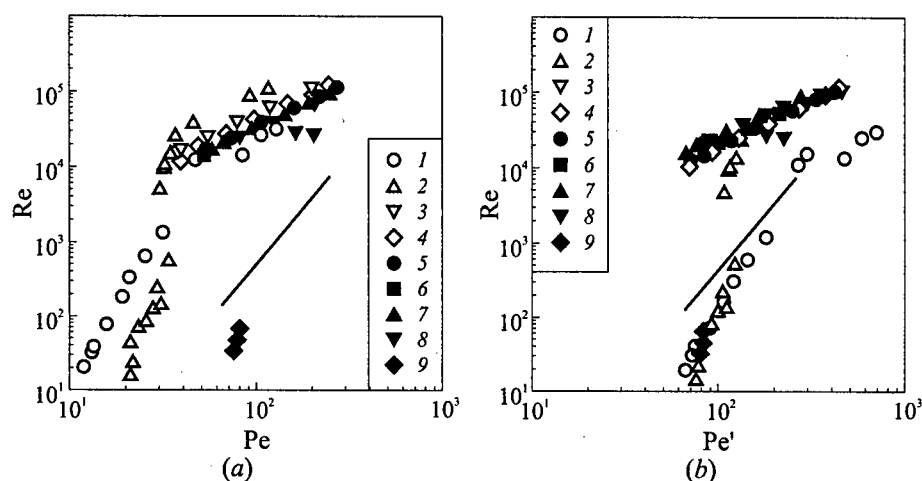
259

Figure 4 Dependencies Re(Pe) and Re(Pe′) for combustion of hydrogen–air mixtures in polyethylene grains at various initial pressures and mixture compositions. Hydrogen content: *1* — 15%; *2* — 20; *3* — 25; *4* — 30; *5* — 35; *6* — 40; *7* — 45; *8* — 50; *9* — 52.5. The line corresponds to burning of CH_4–air mixtures in the high velocity regime [9]

bustion velocity data for hydrogen–air mixtures in PM in a form of steel balls (SB) [8].

LEWIS NUMBER EFFECTS

It is shown in [9], the Lewis number effects are very pronounced in HVR. They are displayed in the shift of the maximum flame velocity, S_{max} relative to the stoichiometric line, $\Phi = 1$, toward rich propane–air and lean methane–air mixtures, where $Le = \kappa/D < 1$. Here D is the diffusion coefficient of a component that is deficit in the mixture. The abnormal effect is also displayed in the segregation of the Re(Pe) curves by composition (Fig. 3a).

Lewis number effects are usually connected with the thermo-diffusion process and the hydrodynamic stretching of the flame. Based on the hypothesis of preferential diffusion [13], it is assumed that in the flames which are convex towards the fresh mixture, the most mobile light reagent enriches the chemical reaction zone in the vicinity of the leading point because of a difference in diffusion co-
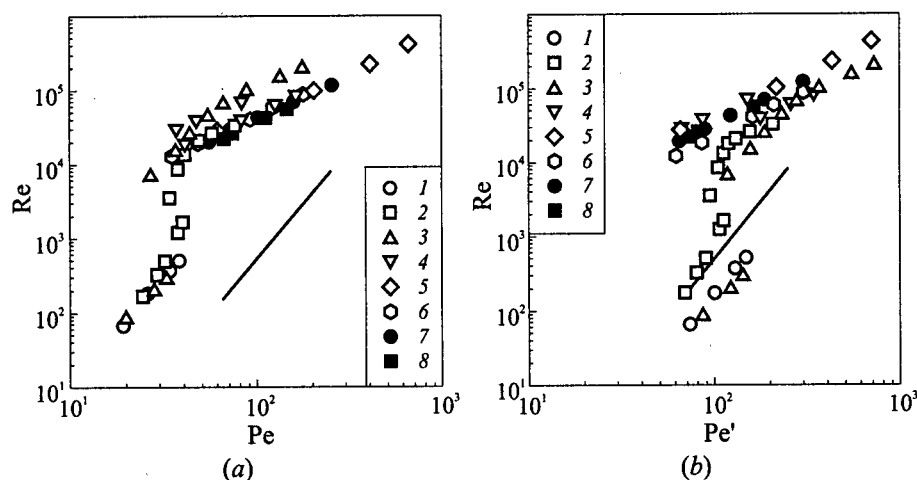
Figure 5 Dependencies Re(Pe) and Re(Pe′) during combustion of hydrogen–air mixtures in packed steel balls of various diameters at different initial pressures and mixture compositions [8]. Ball diameter: *1, 6, 8* — 2.5 mm; *2, 4, 7* — 5; *3, 5* — 11.5. Hydrogen content: *1, 2, 3* — 15%; *4* — 20; *5, 6* — 29.6; *7, 8* — 50

efficients of fuel and oxidizer. The result is a localized increase in the burning velocity in the case when the light reagent is the limiting species. A decrease in the burning velocity is observed when the light reagent is in excess in the initial mixture.

At near-limit flame propagation in PM, heat losses cause non-uniform temperature distribution along the flame front. It results in local variations in the burning velocity and the flame front curvature. The front curvature, in turn, causes preferential diffusion, stretching of the front, and increase in the overall area of the flame.

Consequently, the increased burning velocity in curved flames and low values of the critical Pe numbers (based on S_u of the flat flame) may be expected near the limits of both lean hydrogen and methane flames, and rich heavy hydrocarbon flames. This hypothesis was validated in [7]. In inert PM, HVR was shown to have a variable critical Peclet number Pe = Pe* at the flamability limits under variation of mixture composition, as it follows from the critical diameter theory [14]
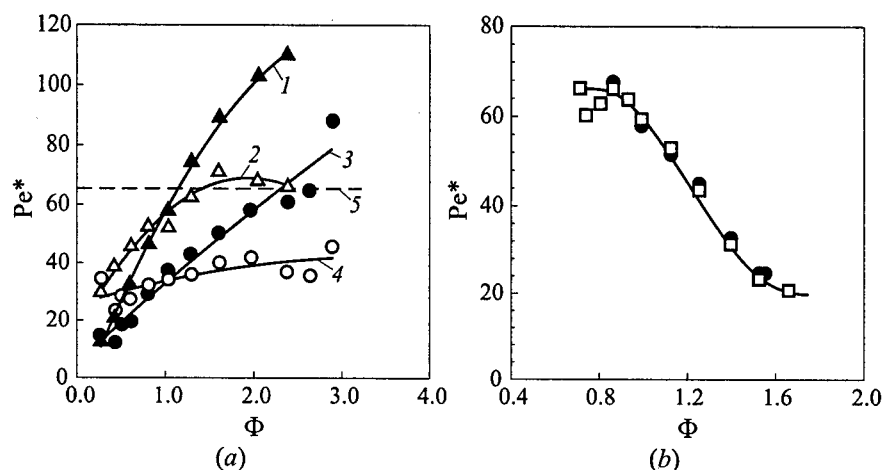
$$\text{Pe}^* = \frac{S_u d}{\kappa} = const \qquad (1)$$

261

Figure 6 Dependencies of Pe*(Φ) for combustion of hydrogen–air (a) and propane–air (b) mixtures of various compositions. (a) Porous media: $1, 2$ — granular polyethylene; $3, 4$ — polyurethane foam; $1, 3$ — Pe* is based on S_u of the flat flame; $2, 4$ — Pe* is based on Eq. (3); 5 — Pe* = 65. (b) Pe* is based on S_u of the flat flame; open symbols — aluminium foil substrate, p_i = 0.056–0.20 MPa; closed symbols – polyurethane foam, p_i = 0.097–0.20 MPa

The value of Pe* increases with enriching the mixture with fuel in hydrogen and methane flames and decreases in flames of heavy hydrocarbons (Fig. 6).

The correction of Eq. (1) on the Le number effects may be obtained by using the equation

$$S_u - S_{uc} = L\alpha \qquad (2)$$

suggested in [15] for considering curvature, stretch of the flame front, and the effects of preferential diffusion. In Eq. (2), S_u and S_{uc} are the burning velocities of flat and curved flames, respectively, L is the Markstein length, α is the rate of flame stretch. It is assumed that α takes into account the effects of stretch and curvature of the flame. Rearranging Eq. (2) to the dimensionless form gives

$$Pe_c = Pe(1 - Ma \cdot Ka) \qquad (3)$$

where Pe and Pe_c are the Peclet numbers based on S_u and S_{uc}, respectively, Ma = L/δ_0 is the Markstein number, Ka = $\alpha\delta/S_u$ is the Karlovitz number, and $\delta = \kappa/S_u$ is the flame front thickness.

262

Using the experimental data on limiting pressures for the hydrogen–air flames in PG and PF (Fig. 6a), taking Markstein length L and burning velocities S_u from [11], and assuming $\alpha = 4S_u/d$, the limiting values of Ma, δ, and Pe can be calculated. The results of the Pe_c^* calculations using Eq. (3) are shown in Fig. 6 by the open symbols. It is seen that Eq. (3) is indeed better than Eq. (1), and it agrees with the condition of constancy of Pe^* at the limit. The range of Pe^* values was reduced from 15–110 to 25–70.

The Lewis number effects are strongly marked in hydrogen–air mixtures. An attempt to use Eq. (3) for theoretically correcting the data in Figs. 2 to 4 results in essential reduction of segregation of the Re(Pe) curves by mixture composition. However, an approach combining theoretical and experimental data proved to be more efficient.

Assuming (in the considered range of Pe) that the function $(1 - \text{Ma} \cdot \text{Ka})$ remains constant for a given combustible mixture and for a specific PM, it is possible to write: $Pe_c = Pe(Pe_c^*/Pe^*) = Pe(1 - \text{Ma} \cdot \text{Ka})^*$, where superscript $*$ denotes the values at the flammability limit. When calculating Pe_c, it is possible to treat Pe^* as an experimentally determined value (Fig. 6 for a given PM and Φ), and $Pe_c^* = 60.5$ (theoretical value at the flammability limit [16]) or $Pe_c^* = 65$ (the universal average value for a large array of experimental data [17]). Taking $Pe_c^* = 65$, one finally obtains:

$$Pe' = Pe\frac{65}{Pe^*} \tag{4}$$

The results of the corrections based on Eq. (4) are shown in Figs. 2(b) to 5(b). It is seen that the suggested procedure significantly reduces the segregation of the Re(Pe) curves by composition in all cases encountered. The efficiency of the procedure can be explained as follows. Function $(1 - \text{Ma} \cdot \text{Ka})$ is sensitive to fuel type, mixture composition, and the pore size. This is taken into account in the correction procedure; all of these parameters are kept constant. Further, the values of Pe usually differ from the critical values by less than an order of magnitude. Therefore, function $(1 - \text{Ma} \cdot \text{Ka})$ slightly differs from its value at the limit within the considered range of Pe. Lastly, according to the physical model of flame stabilization in HVR, it is important that the local burning velocities are corrected under the limiting conditions.

THE MECHANISM OF FLAME PROPAGATION IN HIGH AND SONIC VELOCITY REGIMES

The corrected Re(Pe') dependencies in HVR are shown in Fig. 7 for hydrogen–air and propane–air flames. Also shown are the data for methane–air flames [9].
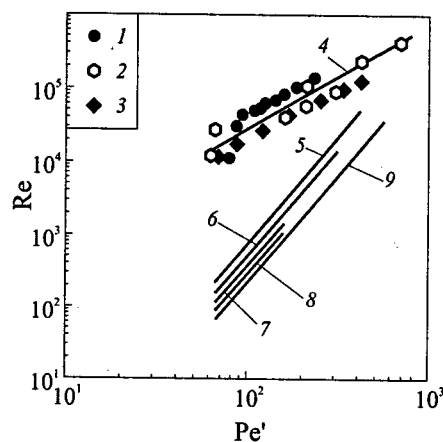
Figure 7 Dependencies Re(Pe′) for combustion of hydrogen–, methane–, and propane–air mixtures in porous media. Sonic velocity regime: *1* — polyurethane foam, $\Phi = 1$, Fig. 2*b*; *2* — steel balls, $\Phi = 1$, Fig. 5*b*; *3* — granular polyethylene, $\Phi = 1$, Fig. 4*b*; *4* is the line corresponding to Eq. (5). High velocity regime: *5* — C_3H_8–air, $\Phi = 1$, Fig. 3*b*; *6* — CH_4– air, [9]; *7* — polyurethane foam, $\Phi = 1$, Fig. 2*b*; *8* — steel balls, Fig. 5*b*; *9* — granular polyethylene, Fig. 4*b*
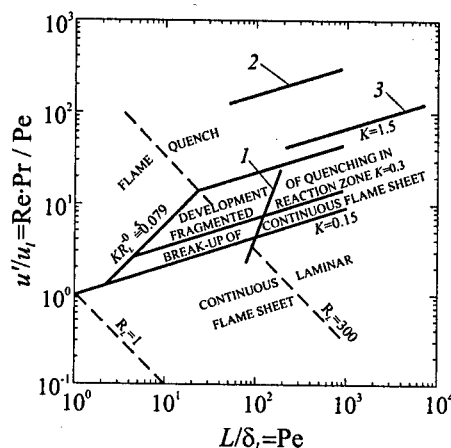
Figure 8 The position of main dependencies for high velocity regime and sonic velocity regime on the turbulent flame regimes diagram [18]. *1* — high velocity regime, the curve corresponds to the dependence *6*, Fig. 7; *2* — sonic velocity regime, the curve corresponds to Eq. (6), computation on cool gas parameters; *3* — sonic velocity regime, the curve corresponds to Eq. (5) with computation based on hot gas parameters

It is seen that all the data are well generalized by the uniform dependence $Re \sim (Pe')^3$, which qualitatively agrees with the theoretical equation obtained earlier. This may be considered as a confirmation for the physical model [9] of isobaric flame propagation in HVR. According to this model, the flame propagation velocity in HVR is stabilized due to local flame quenching in the fastest pulsation present in a wide spectrum of turbulent flame pulsations. Flame quenching is caused by heat loss from the flame zone into the solid PM. The intensity of heat loss is determined by physical and chemical properties of the mixture burned, and also by the relative velocity of the mixture with respect to PM. On the diagram of turbulent flame regimes [18], the generalized curve for methane–air mixtures representing the whole family of the HVR curves (Fig. 7) lies in the area corresponding to partial flame quenching (Fig. 8).

For analyzing SVR, we chose stoichiometric compositions as the most representative for the whole range of composition of hydrogen–air mixtures. Indeed,

on the one hand, the stoichiometric compositions are the most conservative in terms of the Le number effects. On the other hand, as seen from Figs. 2(a), 4(a), and 5(a), they correctly express the general features of the Re(Pe$'$) dependence in all groups of experimental data (for PF, PG, and SB). The corresponding dependencies for the three porous media, corrected on the Le number effects, are presented in Fig. 7. All the data are well generalized by the curve

$$\text{Re} = 65(\text{Pe}')^{4/3} \tag{5}$$

The fact, that induction ignition of the mixture is impossible, appears to be a sufficient argument to consider the mechanism of ignition transfer in a SVR-wave to be conductive–convective. Hence, for the SVR, it is possible to assume that the mechanism of flame velocity stabilization (limitation from above) is identical to the mechanism in the HVR but occuring under conditions of elevated pressure and temperature. It should seem that high sensitivity of the wave velocity to mixture temperature ($S \sim S_u^3 \sim T^6$) lifts the limitation on the propagation velocity up to 10^2 m/s. However, in this case it becomes difficult to explain a low exponent of Pe in the dependence Re(Pe$'$): (Pe$'$)$^{4/3}$ in SVR vs. Pe^3 in HVR. Taking high turbulence intensity in SVR into account, it may be assumed that flame quenching in maximal pulsations, that control the propagation velocity, occurs by hydrodynamic flame quenching rather than by the conductive–convective mechanism of heat loss in porous channel walls. According to [18], for $\text{R}_L > 300$ hydrodynamic quenching begins at $K > 1.5$, where $K = 0.157(u'/S_u)^2 \text{R}_L^{-0.5}$, $\text{R}_L = u'L/\nu$, u' is the r.m.s. turbulent velocity, and L is the turbulent length scale. Assuming $u' = S$ and $L = d$, the condition of flame quenching may be rearranged as:

$$\text{Re} = 12.4(\text{Pe}')^{4/3} \tag{6}$$

Comparing the exponents of Pe$'$ in Eqs. (5) and (6), one observes a good agreement between these dependencies.

Shown in Fig. 8 are the curves provided by Eq. (5) for cool mixtures (curve 2) and mixtures heated in the compression wave (curve 3). For the compression wave, it was assumed that $p/p_i = 7.3$, $c_p/c_v = 1.3$, and the exponent of temperature dependence of the burning velocity is $m = 2$. It is seen that the data on flame velocities are indeed in the field of hydrodynamic flame quenching in Re–Pe coordinates. The line corresponding to Eq. (5) is parallel to the line representing the onset of hydrodynamic quenching $K > 1.5$.

DISCUSSION AND CONCLUDING REMARKS

In inert porous media, two steady-state turbulent combustion regimes, corresponding to combustion at constant pressure (HVR) and combustion in a com-

pression wave, may be realized. In both regimes, the flame velocity is controlled by the leading pulsations, the level of which is determined by the conditions of flame quenching due to heat loss in porous medium (HVR) and as a result of hydrodynamic quenching (SVR). The experimental data confirm this physical model. Unlike HVR, in SVR combustion proceeds at elevated values of pressure and temperature due to adiabatic compression of the fresh mixture. The increase in pressure and temperature in the chemical reaction zone provides high flame velocities. The compression wave exhibits a small value of pressure gradients at the front leading edge. This gradient is determined by the square of the flame velocity and by the parameters describing inertial resistance of PM.

Imagine that ignition propagates by micro-choking, i.e. by the passage of the reacting gas through contractions and expansions in a porous medium. Then, it is obvious that the critical (sonic) flow of the fresh mixture and combustion products may also become a reason for velocity stabilization. The case when only combustion products pass the channels of a porous medium corresponds to the greatest possible velocity in the SVR.

In the regimes under discussion, the Lewis number effects are primarily pronounced in HVR. Considering the discretization of steady-state regimes in PM, it is worth noting that the smooth and continuous regime transitions are not rare (see Figs. 2, 4, and 5). This fact is apparently caused by the spectral character of the pore sizes and fluctuations of the parameters of a fresh mixture. As a matter of fact, the term "the velocity of a steady-state wave" is usually treated as the average velocity at apparently non-one-dimensional and non-steady-state flow in PM. The velocity of the wave in all the regimes is highly sensitive to the variations in d and p_i. Therefore, it is worth assuming, that various velocity regimes can be realized in separate pores, especially in boundary zones. It should result in a variable sharpness of regime transitions. Note that at Pe $\geq 10^3$ the HVR does not exist because hydrodynamic quenching dominates. Therefore, the probability of a sporadic realization of various regimes in individual pores is rather significant. At Pe $= 10^3$ this phenomenon may take place, for example, in some experiments depicted in Figs. 3 and 4.

Finally, because of the presence of a compression wave in the chemical reaction zone, adiabatic compression of the reactive mixture in this wave, and sustenance of the wave due to combustion, the SVR looks rather similar to usual detonation. This is the motivation of using the term "detonation" in the title of this paper.

ACKNOWLEDGMENTS

REFERENCES

1. Babkin, V.S., "Filtrational Combustion of Gases. Present State of Affairs and Prospects," *Pure and Applied Chemistry*, **65**, 2, 335–344, 1993.

2. Tunik, Yu. V., "Self-Sustained Regime of High-Velocity Gas Combustion in Inert Porous Media of Bulk Density," *Sov. J. Physics Combustion Explosion*, **26**, 6, 98–104, 1990.

3. Chue, R. S., Clarke, J. F., and Lee, J. H., "Chapman–Jouguet Deflagrations," *Proc. Royal Society London*, **A 441**, 607, 1993.

4. Ershov, A. P., "Isotermal Detonation," *Combustion Flame*, **101**, 339–346, 1995.

5. Brailovsky, I., and Sivashinsky, G. I., "Momentum Loss as a Mechanism for Deflagration-to-Detonation Transition," submitted to *Combustion Theory and Modeling*, 1998.

6. Babkin, V.S., Bunev, V.A., Korzhavin, A.A., Klimenko A.S. *et al.*, "Gas Combustion in a Vessel with a Highly Porous Inert Medium," *Sov. J. Physics Combustion Explosion*, **21**, 5, 519–523, 1985.

7. Korzhavin, A.A., Bunev, V.A., Potytnyakov, S.I., Babkin, V.S., Bradley, D., and Lawes, M., Submitted to *Combustion Flame*.

8. Pinaev, A.V., "Combustion Modes and Flame Propagation Criteria for an Encumbered Space," *Rus. J. Physics Combustion Explosion*, **30**, 4, 448–461, 1994.

9. Babkin, V.S., Korzhavin, A.A., and Bunev, V.A., "Propagation of Premixed Gaseous Explosions in Porous Media," *Combustion Flame*, **87**, 2, 182–190, 1991.

10. Babkin, V.S., and Kozachenko, L.S., "Genesis of Detonation in Gases in Rough Tubes," *Sov. J. Applied Mechanics Technical Physics*, **3**, 165–174, 1960.

11. Dowdy, D. R., Smith, D. B., Taylor, S. C., and Williams, A., "The Use of Expanding Flames to Determine Burning Velocities and Stretch Effects in Hydrogen/Air Mixtures," *Proc. 23rd Symposium (International) on Combustion*, The Combustion Institute, Pittsburgh, PA, 1990, 325–332.

12. Aerov, M. E., Todes, O. M., and Narinskii, D. A., *Apparatus with Stationary Grain Layer. Hydraulic and Thermal Basic Principles of Work.* Khimiya, Leningrad, 1979.

13. Lewis, B., and Elbe, G., *Combustion, Flames and Explosion of Gases.* Academic Press Inc., N.Y.–London, 1961.

14. Zel'dovich, Ya. B., "Theory of the Limit of Quiet Flame Propagation," *Sov. J. Applied Mechanics Technical Physics*, **11**, 1, 159–169, 1941.

15. Clavin, P., "Dynamic Behavior of Premixed Flame Fronts in Laminar and Turbulent Flows," *Prog. Energy Combustion Sci.*, **11**, 1, 1–59, 1985.

16. Spalding, D. B., "A Theory of Flammability Limits and Flame Quenching," *Proc. Royal Society London*, **A240**, 1220, 83–100, 1957.

17. Rozlovskii, A. I., *Basic Principles of Explosion Safety under Operation with Combustible Gases and Vapors*. Khimiya, Moscow, 1980.

18. Bradley, D., and Lau, A. K. C., "The Mathematical Modeling of Premixed Turbulent Combustion," *Pure and Applied Chemistry*, **62**, 5, 803–814, 1990.

PART FOUR

APPLICATIONS OF DETONATION PHENOMENA

RAM ACCELERATORS IN THE DETONATIVE MODE

K. Kailasanath and C. Li

In this paper, an overview of the research on ram accelerators in the detonative mode of operation is presented. After a brief review of the early concepts, the focus is shifted to the essentially transient nature of the detonation process in ram accelerators. These transient processes are shown to impose gas dynamic limits for the successful operation of the system. Then, the structure of detonations in ram accelerators and its similarity to the structure of oblique detonations on wedges is explored. The role of unsteady numerical simulations in designing the shape of the projectiles for successful operation is established. Some practical problems, such as the effects of material heating and burning on system performance are also discussed. Finally, the implications of the research experiences with the ram accelerator for other propulsion applications of detonations is conjectured.

INTRODUCTION

In a ram accelerator, a projectile that resembles the center body of a ramjet, travels at a supersonic speed through a premixed fuel–oxidizer–diluent mixture enclosed in a tube [1, 2]. Since the projectile travels at supersonic speeds, oblique shocks are formed at the nose of the projectile and they subsequently reflect from the side walls of the tube and the projectile body. Depending on the strength of these oblique shocks, ignition may occur behind the initial shock or subsequent reflections. Depending on the velocity of the projectile, different modes of combustion and correspondingly different modes of operation of the system are possible. When the velocity of the projectile is greater than the Chapman–Jouguet (CJ) velocity, an oblique detonation wave can be stabilized on the projectile, resulting in the detonative mode of operation. A schematic of the ram accelerator operating in the detonative mode is shown in Fig. 1. In order to maximize performance, the oblique detonation must be generated and stabilized at appropriate locations in the system. Therefore, successful development of such systems depends on the knowledge of the structure and stability of these
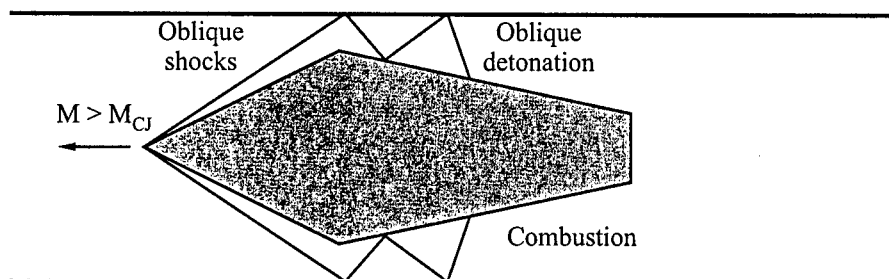
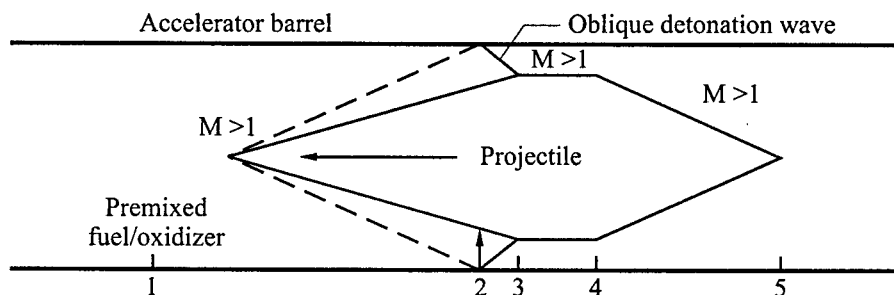**Figure 1** A schematic of a ram accelerator in the detonative mode

Figure 2 Early concept of a detonative mode

detonation waves and understanding the related transient physical and chemical processes. The rest of this paper deals with these issues after a brief discussion of the background work.

Since the early days, detonation has been discussed as a means to attain very high velocities, including escape velocities [1]. In that paper and several subsequent works, the structure of the detonative mode was described by the schematic shown in Fig. 2. The projectile nose cone angle and the sound speed in the mixture selected were tailored to avoid combustion behind the initial shock, but initiation behind the first shock reflected from the tube wall. It was emphasized that the first reflected shock should strike the projectile body just aft of the shoulder [1]. If the system needed to be designed so precisely, successful operation would indeed be difficult in practical situations. Further research has shown that the system is far more stable and the particular scenario sketched in Fig. 2 actually occurs just prior to system failure. There were early reports of successful attainment of super-detonative velocities [3] but the experimen-

tal emphasis shifted to the successful development of sub-detonative modes of operation except at the Institute of Saint-Louis (ISL), where research on the detonative mode has continued [4–6].

Numerical simulations [7, 8] and theoretical studies [9, 10] based on simplified analytical models of super-detonative ram accelerators were started in the early days and have made a significant impact over the past decade. These early studies confirmed the potential of ram accelerators to efficiently accelerate large masses to escape velocities and low Earth orbit. The steady-state simulations of Yungster [11] highlighted the role of the projectile velocity (or Mach number) and showed that detonation could occur at different locations along the projectile body, depending on the projectile Mach number (defined as the ratio of the velocity of the projectile to the speed of sound in the premixed mixture). This work also raised the issue of combustion in the boundary layers along the projectile. Both of these issues will be elaborated on later, using results from our time-dependent numerical simulations.

A related issue, that was being studied in the early 90's, was the detailed structure and stability of oblique detonations on wedges [12, 13]. The implications of these results on the structure of detonations in the ram accelerator will be explored in this paper and more recent results on the detonation structure [14] will also be presented.

Since the projectile velocity changes continuously in the ram accelerator, steady-state simulations can, at best, be thought of as trying to characterize an instantaneous snapshot of the system. The importance of the transient processes was first highlighted in the work of Li *et al.* [15]. This, as well as subsequent work [16] that will be discussed later, has shown the importance of taking into account the time-dependent nature of the flow in the ram accelerator in describing phenomena such as unstarts and other system failures. The use of time-dependent numerical simulations as an effective tool to explore system design changes is also discussed in this paper. Finally, some recent experimental results and the difficulties encountered [6] in the practical development of ram accelerators in the detonative mode are discussed.

NUMERICAL MODELS

The basic equations, solved for the numerical simulations presented in the next section, are the time-dependent conservation equations for mass, momentum, and energy in conjunction with a two-step parametric model for chemical reactions. In the reaction model, the first step represents radical formation and accumulation and the second step represents energy release [17, 18]. The individual processes in the conservation equations are solved separately and the results are coupled using time-step splitting techniques [19]. The convection part of the

273

conservation equations is solved using the Flux-Corrected Transport algorithm (FCT) [20]. This algorithm is conservative, accurate, stable, and monotonic (positivity-preserving). Monotonicity is achieved by introducing a diffusive flux and later correcting the calculated results with an antidiffusive flux modified by a flux limiter.

The Virtual Cell Embedding (VCE) [21, 22] technique is used to accurately represent the complex shape of the projectile on an orthogonal mesh. With this technique, one can calculate the flow fields around complicated geometric shapes. These calculations can be done without incurring the computational penalty associated with either unstructured grids, which are difficult to vector-ize or parallelize, or body-fitted meshes, which require small time-steps or long iteration times. In this approach, non-orthogonal virtual cells are embedded in the orthogonal mesh at curved boundaries or boundaries which are not aligned with the computational grid. The projected areas of the boundary surface of these virtual cells in each coordinate direction are precomputed. These areas are then used to calculate the mass, momentum, energy, and species fluxes in a manner very similar to calculations of the fluxes for the interior cells. There-fore, the computation for these virtual cells can be packaged into the original FCT algorithm and only requires a small amount of additional computational effort. Also, different virtual cells at boundaries can be easily embedded in the original, orthogonal mesh based on geometry changes. Therefore, this method is particularly suitable to study the impact of projectile shape changes on the performance of the ram accelerator.

Since the flow field in ram accelerators is highly transient due to the rapid acceleration of the projectile, it is necessary to conduct fully time-dependent simulations of the reactive flow around the projectile. The acceleration of the projectile is coupled into the flow calculations by using a noninertial frame of reference. In this frame, the grid system is attached to the projectile and the velocity at the inlet of the computational domain changes, according to the speed of the projectile. The pressure distribution on the projectile surface is computed. This pressure distribution is integrated to obtain the thrust exerted on the projectile by the reacting flow and, thus, the acceleration of the projectile. Then, the acceleration is used to calculate the noninertial force term for every cell in the non-inertial frame attached to the projectile. These force terms are treated as source terms in the momentum conservation equations. This approach yields smooth changes in the flow field over a range of accelerations up to a million g.

COMPUTATIONAL RESULTS AND DISCUSSION

Several simulations are discussed to highlight various issues concerning the ram accelerator in the detonative mode. The first issue highlighted is tailoring the

shape of the projectile for successful operation in the detonative mode. Then, the role of transient processes and dynamics of detonations during acceleration is discussed. Finally, the structure and stability of detonations in ram accelerators and how they are related to the structure of oblique detonations on wedges is explored.

SHAPE TAILORING FOR SUCCESSFUL OPERATION

For the three cases discussed below, the inlet pressure and temperature are 25 atm and 300 K, respectively. In all cases, the initial Mach number of the projectile is 8 and the mixture considered is a 2:1:3.76/hydrogen–oxygen–nitrogen mixture. The inner diameter of the ram-accelerator tube is 38 mm and the mass of the projectile is 70 gm. The system is axisymmetric and the size of the computational domain is 19 mm in the Y-direction. The length of the domain in the X-direction is 250 mm and the tip of the projectile is located at 5.0 mm from the inlet of the computational domain. The computational cells are 0.5 mm and 0.25 mm in the X- and Y-directions, respectively. Other grid resolutions have also been used to show that the numerical solutions are grid-independent.

Deceleration

In the first case, the size and shape of the projectile was chosen to be the same as that used in the experiments conducted at the University of Washington [1, 2]. The flow properties from one instant in the simulation, shown in Fig. 3, indicate that the shock system in the front part of the projectile is not strong enough to generate sufficiently high temperatures to produce a detonation on any part of the projectile body. The only place where combustion and energy release are observed is in the recirculation region behind the projectile. The pressure generated on the rear part of the projectile is too low to produce a positive thrust and the projectile decelerates. Therefore, the projectile shape needs to be modified for successful operation in this mixture at Mach 8.

Low Acceleration

The second projectile shape studied has a similar aft body (contracting part) as that above, but the cone angle of the fore body is steepened from the original 10°
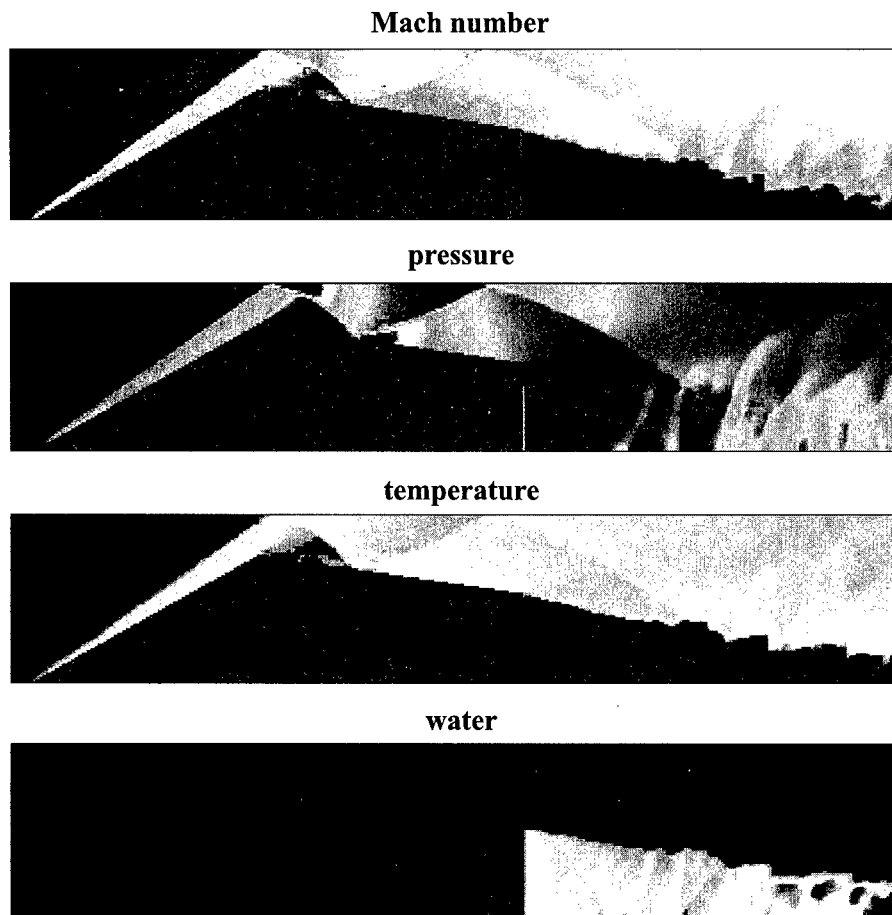
275

Mach number

pressure

temperature

water

Figure 3 Visualization of the flowfield in a ram accelerators with no positive acceleration

to 20°. Also, the diameter of the widest part of the projectile body is increased from 28.8 mm to 30.2 mm, reducing the gap between this part of the body and the launch tube from 4.6 mm to 3.9 mm. Due to these changes, the reflected shocks are strengthened and a detonation is generated on the contracting part of the projectile body (Fig. 4). Although the detonation generates high pressures on the rear part of the projectile, the high-pressure region is still quite far from the widest part of the body and the positive force on the body is not large. In addition, the pressure behind the oblique shock on the front part of body is
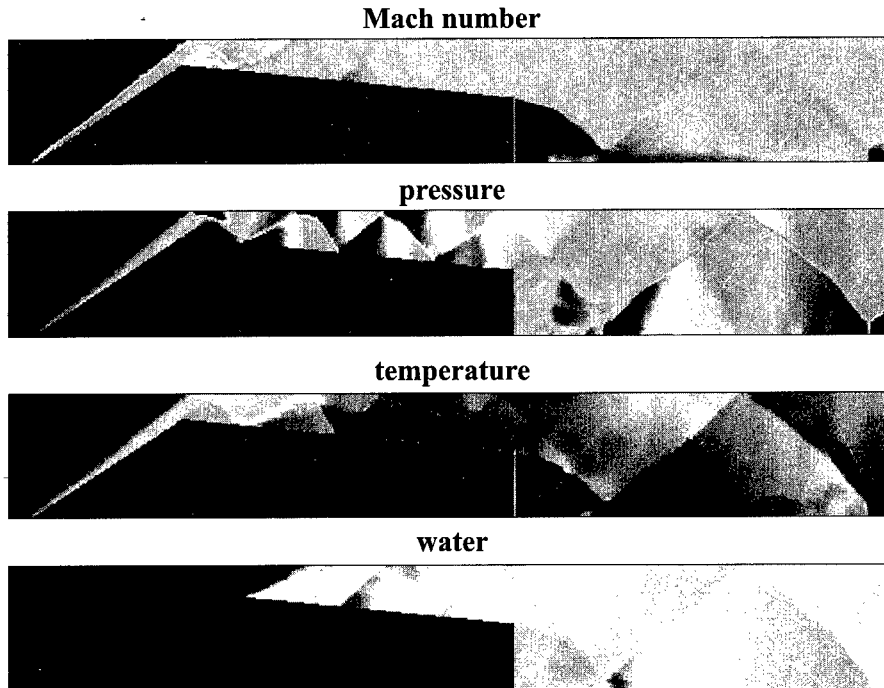
Mach number

pressure

temperature

water

Figure 4 Visualization of the flowfield in a ram accelerator with a low positive acceleration

also very high due to the steep cone angle, resulting in a strong negative force. Therefore, the total thrust is just slightly positive and the acceleration (around $103g$) is too weak for the projectile to gain significant velocity increase in a reasonable distance.

High Acceleration

In order to generate a detonation immediately behind the widest part of the projectile and keep the pressure relatively low on the front part of body, the projectile shape was further modified. The cone-angle is 15° and the gap between the widest part of the projectile and the launch tube is further reduced from 4.6 mm to 2 mm. The simulations (Fig. 5) show that the detonation is located near the widest part of the projectile and the high-pressure region covers the front half of the contracting part of the projectile. This pressure distribution
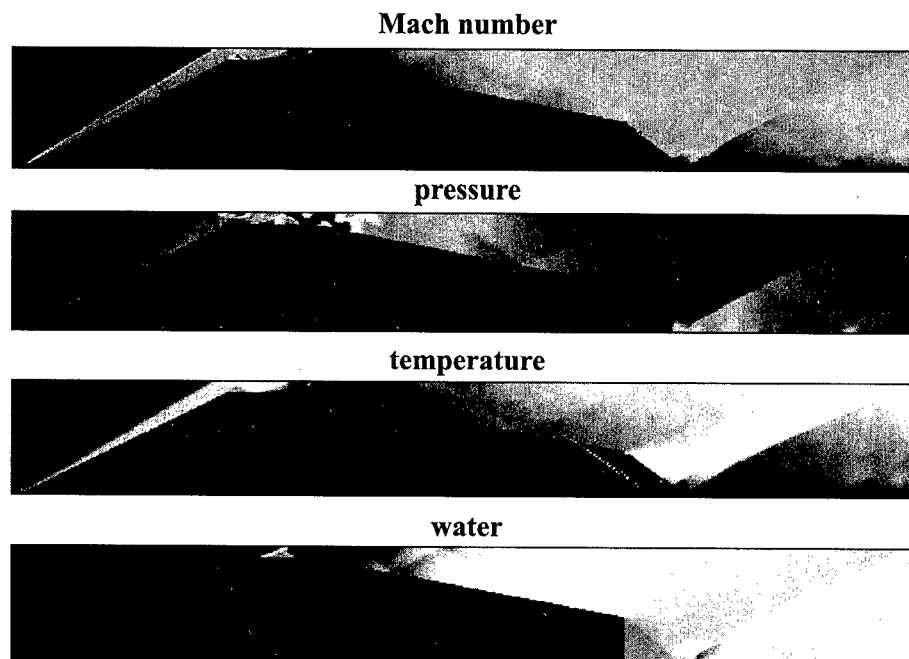
277

Mach number

pressure

temperature

water

Figure 5 Visualization of the flowfield in a ram accelerator with a large positive acceleration

yields a significant positive thrust which results in an acceleration, ranging from $2 \times 10^5 g$ to $3 \times 10^5 g$. This results in the projectile being continuously accelerated from Mach 8 (3200 m/s) to Mach 10 (4000 m/s) over a distance of 12 m. These simulations indicate that the detonation structure can be maintained on the projectile body over a wide range of flow conditions. However, during the acceleration, the location of ignition moves upstream from one reflected shock to another. Further details of the dynamics of this transition and its effect on the operation of the system are discussed next.

DYNAMICS OF DETONATIONS IN RAM ACCELERATORS

To illustrate the dynamics of detonations in the ram accelerator, two snapshots of the flow field, from the third case discussed above (where the projectile accel-
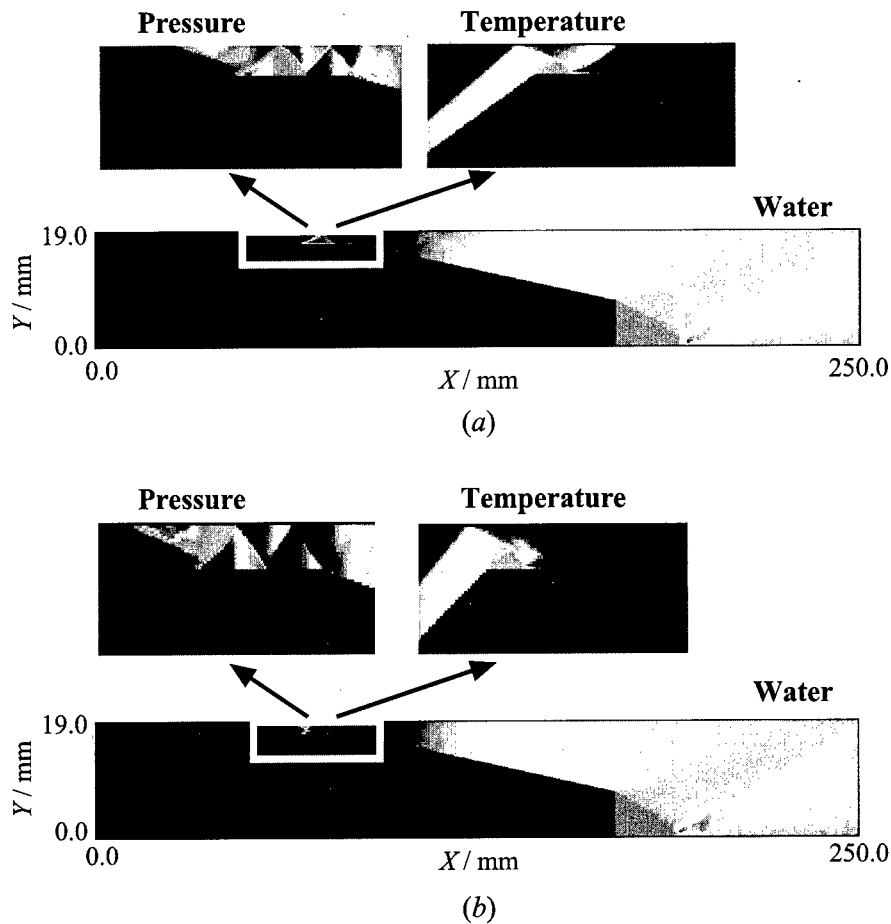
Figure 6 Visualization of the flowfield at two instants (a) Mach number 9.05 and (b) Mach number 9.15 during the acceleration of the projectile shown in Fig. 5 from Mach number 8 to 10

erated from Mach 8 to 10), are shown in Fig. 6. Case (a) is when the projectile Mach number is 9.05 and Case (b) is when it is 9.15. For both cases, the main illustrations show the concentration of water and the two inserts show the pressure and temperature in a selected region of the flow field. At the instant shown in Fig. 6 a, the pressure and temperature behind the first reflected shock are not very high and combustion and energy release (as indicated by the water concentration) are taking place only behind the second reflected shock. That is, the

279

detonation can be said to occur behind the second reflected shock. By the time the projectile has accelerated to Mach 9.15, the leading shock has strengthened, raising the pressure and temperature behind the first reflected shock and causing detonation to occur there.

The behavior discussed above is seen throughout the operation of the ram accelerator in the detonative mode. That is, detonations in ram accelerators are dynamic and move from shock to shock as the projectile accelerates. Eventually, the detonation would occur just after the first shock and the whole system would cease to operate, since there would not be any positive thrust. Hence, the shape of the projectile has to be chosen carefully so that the detonation can move over the projectile body and still produce positive thrust over the regime of interest.
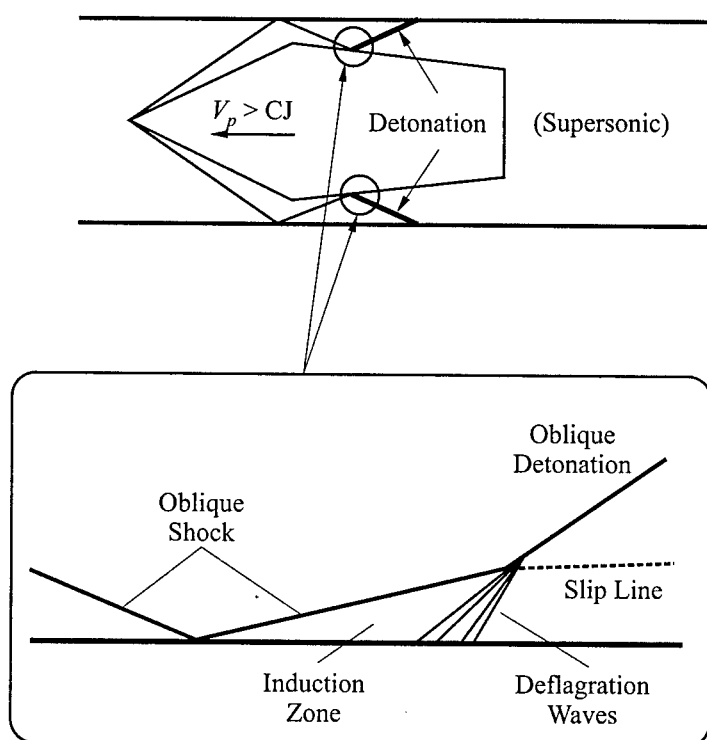

Figure 7 Schematic showing the detailed structure of an oblique detonation and its relation to the detonation structures in ram accelerators

STRUCTURE AND STABILITY OF OBLIQUE DETONATIONS

As seen in the simulations discussed above, detonations in ram accelerators are oblique. A crucial issue is the structure and stability of these detonations. Extensive studies have been carried out in the past on oblique detonations. In our earlier studies [12–13], we showed that the basic structure of an oblique detonation generated by a wedge consists of a nonreactive shock, an induction region, deflagration waves and a detonation wave, in which the pressure increase due to the energy release is closely coupled to the shock front. This basic structure and a schematic of how it might relate to the detonations in ram accelerator is shown in Fig. 7. Our earlier studies also showed that over a wide range of flow and mixture conditions, the basic detonation structure is stable and very resilient to disturbances in the flow.

Although the schematic shows how to relate the basic oblique detonation structure to that in ram accelerators, the actual detonation structure in ram-accelerators is likely to be more complex, because of the expansion waves and multiple shocks that are generated due to the geometric complexity of the system. Therefore, a systematic study was undertaken to investigate the detailed structure of detonations in ram accelerators under a variety of flow conditions [14]. The results of that work have been summarized in Fig. 8, where the detailed detonation structure is shown for three flow Mach numbers. Again, the essential similarity of these more complex structures to the basic structure of oblique detonations is evident.

CONCLUDING REMARKS

In this paper, an overview of the ram accelerator in the detonative mode of operation has been presented. The applicability of results on basic oblique detonation structures for the more complex geometry of the ram accelerator has been shown. The three different projectile shapes simulated highlight the importance of tailoring the shape of the projectile for successful operation over a range of conditions. Even a small change in the projectile shape appears sufficient to make a significant change in the overall detonation structure and acceleration. During the acceleration, ignition and, consequently, detonation are observed to move from one reflected shock to an earlier reflection. The essential unsteadiness of the detonation process has also been highlighted by these simulations.

There are still other problems to be solved before the practical attainment of the high velocities, that are possible in the detonation mode. A major prob-
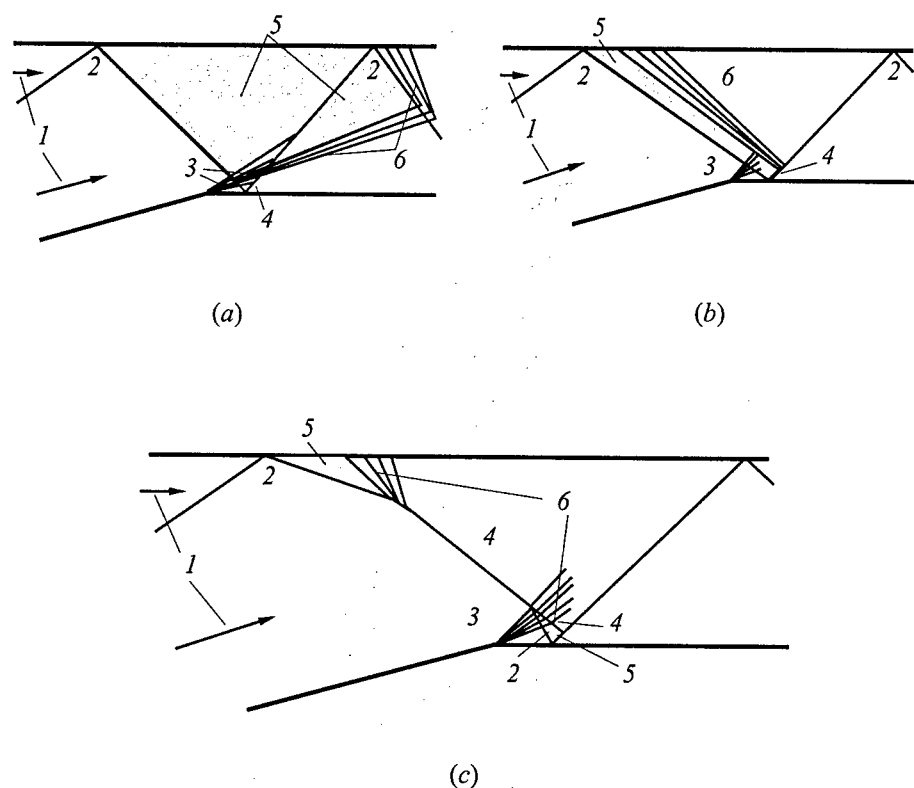
Figure 8 The detailed structure of detonations in ram accelerators operating at (a) Mach number 7.6, (b) 8.0, and (c) 8.4. 1 — flow direction, 2 — shock waves, 3 — expansion waves, 4 — detonation wave, 5 — induction region, 6 — deflagration waves

lem has been the inability of the materials used to withstand the high temperatures and stresses induced during the detonative mode [6]. This is an issue that also needs to be considered in discussing the potential of detonations for other propulsion applications. On the positive side, the results reported here highlight the valuable role that numerical simulations can play in the design and development of advanced propulsion systems and in the development of a detailed understanding of the underlying physics of detonations.

ACKNOWLEDGMENTS

REFERENCES

1. Bruckner, A. P., and Hertzberg, A., IAF 87-211, AIAA Inc., Washington, DC, 1987.

2. Hertzberg, A., Bruckner, A. P., and Bogdanoff, D. W., *AIAA J.*, **26**, 195–203, 1988.

3. Kull, A., Burnham, E., Knowlen, C., Bruckner, A. P., and Hertzberg, A., AIAA Paper No.89-2632, AIAA Inc., Washington, DC, 1989.

4. Patz, G., Seiler, F., Smeets, G., and Srulijes, J., *Proc. Second International Workshop on Ram Accelerators*, University of Washington, Seattle, WA, 1995.

5. Seiler, F., Patz, G., Smeets, G., and Srulijes, J., *Proc. Second International Workshop on Ram Accelerators*, University of Washington, Seattle, WA, 1995.

6. Seiler, F., Patz, G., Smeets, G., and Srulijes, J., AIAA Paper No.98-3445, AIAA Inc., Reston, VA, 1998.

7. Brackett, D.C., and Bogdanoff, D.W., *J. Prop. Power.*, **5**, 3, 276–281, 1989.

8. Yungster, S., Eberhardt, S., and Bruckner, A.P., AIAA Paper No.89-0673, AIAA Inc., Washington, DC, 1989.

9. Rom, J., and Kivity, Y., AIAA Paper No.88-2969, AIAA Inc., Washington, DC, 1988.

10. Humphret, J.W., AIAA Paper No.90-2470, AIAA Inc., Washington, DC, 1990.

11. Yungster, S., AIAA Paper No.91-1916, AIAA Inc., Washington, DC, 1991.

12. Li, C., Kailasanath, K., and Oran, E. S., *Proc. 13th ICDERS (1991), published in Progress in Astronautics and Aeronautics Ser.*, **153**, 231–240, 1993.

13. Li, C., Kailasanath, K., and Oran, E. S., *Physics Fluids*, **6**, 1600–1611, 1994.

14. Li, C., Kailasanath, K., and Oran, E. S., *Combustion Flame*, **108**, 173–186, 1997.

15. Li, C., Kailasanath, K., Oran, E. S., Boris, J. P., and Landsberg, A. M., AIAA Paper No.93-1916, AIAA Inc., Washington, DC, 1993.

16. Li, C., Kailasanath, K., Oran, E. S., Landsberg, A. M., and Boris, J. P., *Proc. 14th ICDERS (1993), published in Int. J. Shock Waves*, **5**, 97–101, 1995.

17. Oran, E. S., Boris, J. P., Young, T., Flanigan, M., Burk, T., and Picone, M., *Proc. 18th Symposium (International) on Combustion*, The Combustion Institute, Pittsburgh, PA, 1981, 167–175.

283

18. Kailasanath, K., Oran, E. S., Boris, J. P., and Young, T. R., *Combustion Flame*, **61**, 199–211, 1985.

19. Oran, E. S., and Boris, J. P., *Numerical Simulation of Reactive Flow*. Elsevier Science, NY, 1987.

20. Boris, J. P., and Book, D. L., *Methods in Computational Physics*, **16**, 85–102, 1976.

21. Landsberg, A. M., Young, Jr. T. R., and Boris, J. P., AIAA Paper No.94-0413, AIAA Inc., Washington, DC, 1994.

22. Landsberg, A. M., and Boris, J. P., AIAA Paper No.97-1982, AIAA Inc., Reston, VA, 1997.

SOME ESTIMATIONS OF A POSSIBILITY TO UTILIZE SHOCK-INDUCED COMBUSTION IN PROPULSION SYSTEMS

L. Bezgin, A. Ganzhelo, O. Gouskov, V. Kopchenov, and Yu. Yarunov

Problems concerning the flow field in shock-induced combustion are considered. Attention is focused on the wave pattern–chemical reactions interaction and detonation wave formation. The set of computer codes, developed in the Central Institute of Aviation Motors (CIAM), was used for calculating supersonic reacting flows in a scramjet duct with detailed kinetic schemes for hydrogen–air mixtures. The codes are based on solving Euler, and parabolized, and full Navier–Stokes equations. An adaptive grid is implemented for the high resolution of the flow field. Results are presented for a ramp flame holder in a duct, and a model Shock-Induced Combustion Ramjet (shcramjet). Flow simulation in the duct of a ram accelerator is also performed as an example of the application of the code.

INTRODUCTION

Shock-induced combustion is the focus of attention due to possible applications in hypersonic propulsion. Three applications have been studied intensively: a Shock-Induced Combustion Ramjet (shcramjet) [1–4], ram accelerators [5–7], and pulse detonation engines [8].

The first application considered is the shock-induced combustion in a supersonic ramjet. Air-breathing hydrogen-fueled engines with combustion in a supersonic flow (scramjets) are considered as promising propulsion systems for hypersonic flight. One promising concept for flame ignition and stabilization is the positioning of an oblique shock wave in the flow [1–4]. The oblique shock wave is considered an essential detail in the concept of the oblique detonation wave engine [1–3]. This concept is based on the fuel and air being premixed

prior to a combustor, e.g., in the engine inlet. Premixing is expected to reduce the combustor length. The main problems in this concept deal with the efficiency of premixing, a possibility of premature ignition of the mixture prior to the combustor, and the influence of non-ideal mixing on the engine efficiency. Recently, the interest on shock-induced combustion with fuel–air premixing has been renewed [4, 9, 10]. Therefore, it is worth considering the interaction between gasdynamic and chemical processes, taking into account a wide range of conditions in the free stream. The main goals of the research performed by the authors are: (1) a feasibility of fuel–air premixing when fuel is injected upstream of the engine entry, and (2) mixture ignition and flame stabilization by the shock in the engine duct taking into account a realistic fuel–air mixture composition. Moreover, an attempt at estimating the influence of the boundary layer at the vehicle wall and in the engine duct on the shock-induced combustion and, in particular, on the premature ignition before the engine entry [11], was made.

The second problem deals with the ram accelerator [5–7, 12]. A projectile is inserted into a launch tube, which is filled with a premixed fuel–oxidizer–diluent mixture. Thrust is generated due to combustion in the region between the tube wall and the projectile. Combustion is initiated and stabilized by the interaction of shock waves attached to the projectile tip with barrel walls. Of importance is a possibility of initiating and stabilizing the combustion front in such a position so that positive thrust. Therefore, the flow through the duct must be simulated taking into account the gasdynamics–chemistry interaction over the whole range of projectile velocities.

The flow structure in these problems is complicated due to interaction of multiple shocks and expansion waves with chemical processes. The model problem [13, 14] on the flow of a hydrogen–air mixture in a duct with a shock induced by a ramp, that is located on the wall, is considered here. Relevant results for detonation formation on the wedge have been published earlier [15–17]. The main objective here is the study of the flow structure in the duct under transition from a shock-induced combustion with an appreciable ignition delay to the ideal oblique detonation. In view of it, one of the most interesting questions is the formation of detonation and flow evolution under the variation of free stream conditions. It is worth noting that the conditions of detonation initiation have also been studied, e.g. in [18, 19].

Numerical simulation of such flows requires high spatial resolution of the flow elements, in particular, shocks, expansion waves, mixing layers, induction and heat release zones. The computer codes [20], developed in CIAM on the basis of high-order finite difference schemes, are used in this study. A detailed kinetic scheme was used in these calculations. Most of the calculations were performed on adaptive grids. Important features of the flow caused by the wave–chemistry interactions, were able to be resolved.

COMPUTATIONAL MODELS AND CODES

For the numerical solution of these problems, the SUPNEF code [20] developed in CIAM was used. The averaged, parabolized Navier–Stokes equations (PNS) for a multi-species mixture with real-gas effects at high temperature are solved. The single-equation differential model of turbulence [21] is employed. At the preliminary stage of investigations, wall boundary layers were not taken into account. A set of 11 detailed and simplified kinetic schemes (including those for gaseous hydrocarbons [22]) is implemented into the SUPNEF code for reacting flow simulations. The detailed kinetic scheme [23] is used in this work for simulating hydrogen combustion. The numerical solution of the governing equations is obtained using the method, which is based on the explicit high-order monotone Godunov finite volume predictor–corrector scheme [24] for steady supersonic flows with the implicit approximation of chemical source terms. The calculations were performed on adaptive grids. The adaptation procedure [25] is based on the "spring analogy," and it provides grid compression in the regions of shocks, mixing layers and reaction zones.

Another code, FNAS2D [20], is used for the numerical simulation of viscous non-equilibrium flows with boundary layers, subsonic regions and/or transient effects. The averaged Navier–Stokes equations are solved numerically by using the finite-volume, fully implicit technique based on the modification of the well known Godunov scheme [24]. Steady state solutions are obtained with the aid of the time relaxation method. The modified scheme provides the second order accuracy for steady solutions on spatially uniform grids, but only first order accuracy in time for the transient flow. Second-order accuracy in time can be realized using the predictor–corrector scheme, which is similar to that employed in the SUPNEF code for steady supersonic flows.

FLOW STRUCTURE IN A DUCT OF FIXED LENGTH AND THE CONVERGENCE RATIO AT VARIABLE WALL ANGLE

The following model problem is considered [13]. A compression ramp flame holder is installed in the duct (see Fig. 1). The homogeneous premixed hydrogen–air mixture enters the duct. The flow structure, i.e. shock pattern and the positions of chemical reaction zones, is of primary concern in this section. In addition, the sensitivity of flow structure to inlet conditions and duct geometry is of interest. In all of the calculations, the inlet pressure and Mach number were fixed. The influence of the inlet temperature and ramp angle on the flow structure was investigated. The value of α, the air-to-fuel ratio divided by the

287

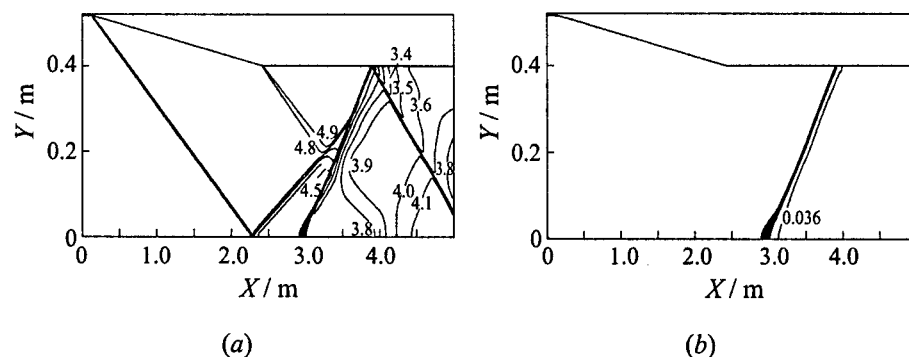(a)   (b)

Figure 1 Predicted Mach number (a) and H_2O mass fraction (b) fields at $\theta = 3°$ (enlarged duct). (a) Step of isolines is 0.100 with minimum 2.981 and maximum 5.000. (b) Step of isolines is 0.002 with minimum 0.000 and maximum 0.037

stoichiometric air-to-fuel ratio (the air-to-fuel equivalence ratio), was varied for a specific wedge angle only.

Conditions governing the formation of detonation were numerically determined. The detailed analysis of computational results was performed to compare the obtained flow patterns with existing theoretical models [27–29] for waves and reactive shocks. The relations for reactive discontinuities, with certain values taken from the numerical solution, were the basis of this analysis. The value of heat release and the angle of flow deflection were estimated using the computational results. All other parameters behind the presumed discontinuity were obtained from the aforementioned relations. Some results of this procedure were presented previously [11, 26].

The angle of the wedge, which is designated to support ignition and combustion stabilization of the fuel–air mixture, may be either greater or less than the Chapman–Jouguet (CJ) angle. Calculations for the variable wedge angle were made using SUPNEF code for the Euler equations. Hydrogen–air flow in a 2D duct of fixed length (3.5 m) and fixed heights of entry (0.52 m) and exit (0.4 m) cross-sections was considered. The duct was shaped in such a way that the entry and exit sections were of constant height. The length of the entry section was fixed. The entry section is followed by the convergent section with the constant inclination angle of the upper wall. The inclination angle was varied within a wide range in such a way that the duct convergence ratio is fixed. The parameters of hydrogen–air mixture at the entry were chosen as follows: Mach number $M = 5$, temperature $T = 875$ K, pressure $P = 10^5$ Pa, the air–to–fuel equivalence ratio $\alpha = 7$. The inclination angle of the convergent section was varied from 3° to 15°. The CJ angle for these conditions is $\theta_{CJ} \approx 6.74°$. The maximum

288
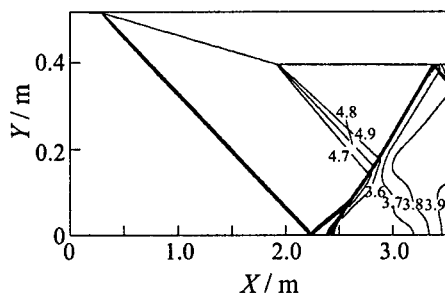
Figure 2 Predicted Mach number field, $\theta = 4°$. Step of isolines is 0.100 with minimum 3.048 and maximum 5.000
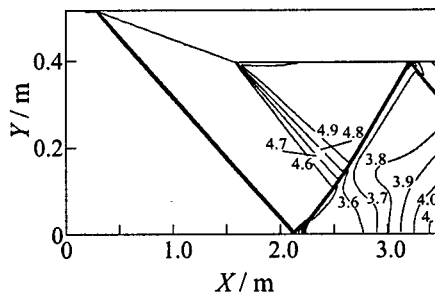
Figure 3 Predicted Mach number field, $\theta = 5°$. Step of isolines is 0.100 with minimum 3.058 and maximum 5.000

flow deflection angle in the oblique detonation shock under these conditions is $\theta_{max} \approx 43.7°$.

The analysis of computational results indicates that in the duct under consideration, ignition occurs behind the reflected shock at the wedge angle of $3°$. Detonation formation behind the reflected shock is observed if the length of the duct is taken to be somewhat greater than 3.5 m. The Mach number and water mass fraction fields are shown in Fig. 1. Clearly, a considerable ignition delay exists near the lower wall, where a supersonic combustion wave forms [30]. At some distance from the wall, behind the reflected adiabatic shock, the primary detonation shock forms. This primary detonation shock interacts with the adiabatic reflected shock, resulting in generation of a stronger detonation shock. The primary detonation shock is induced by the heat released from combustion in the supersonic flow. The reflected shock, supersonic combustion wave, primary detonation shock and the resulting detonation shock form the characteristic λ-structure. A similar flow structure was observed at $\theta = 4°$ and $\theta = 5°$. The flow patterns are shown in Figs. 2 and 3, respectively. The difference between the flow patterns of Figs. 2 and 3 from that shown in Fig. 1 is seen in the decrease of the λ-stem size due to change in the ignition delay near the lower wall as θ increases. At $\theta = 4°$ and $\theta = 5°$, it is necessary to note two things: the major part of the reflected shock is the detonation shock and the combustion occurs primarily in this detonation shock.

A dramatic change in the flow structure is observed at further, comparatively small, increases in θ. The flow field at $\theta = 5.05°$ is illustrated by Fig. 4. The combustion zone arises in the supersonic flow near the upper wall downstream of the break point. The combustion process in the upper part of the duct is almost completed upstream of the reflected shock. In the lower part of the
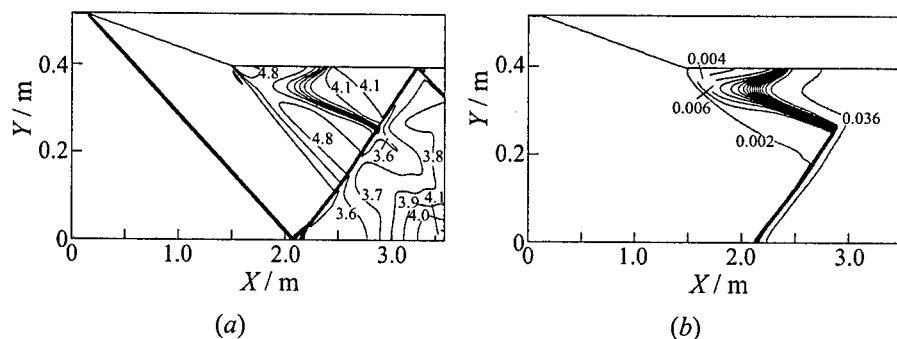
289

Figure 4 Predicted Mach number (a) and H_2O mass fraction (b) fields at $\theta = 5.05°$. (a) Step of isolines is 0.100 with minimum 3.285 and maximum 5.000. (b) Step of isolines is 0.002 with minimum 0.000 and maximum 0.037
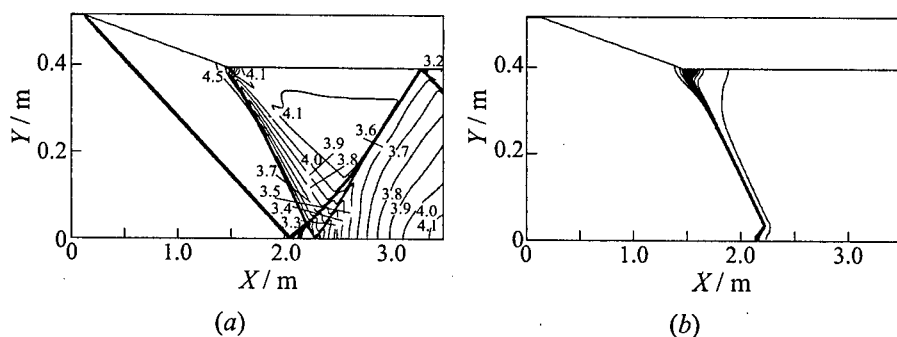

Figure 5 Predicted Mach number (a) and H_2O mass fraction (b) fields at $\theta = 5.1°$. (a) Step of isolines is 0.100 with minimum 2.933 and maximum 5.000. (b) Step of isolines is 0.002 with minimum 0.000 and maximum 0.037

duct, combustion takes place in the detonation shock that forms after reflection of the adiabatic bow shock. If the angle is increased to 5.1°, combustion in the supersonic flow near the upper wall is so intense that a primary detonation shock is generated. The flow fields for this case are shown in Fig. 5. In the upper part of the duct, combustion takes place in the supersonic combustion wave in the detonation shock followed by the deflagration wave. Behind the reflected shock, combustion is observed only in the small region near the lower wall. A similar flow structure is established at $\theta = 5.15°$ (see Fig. 6). A slight difference between
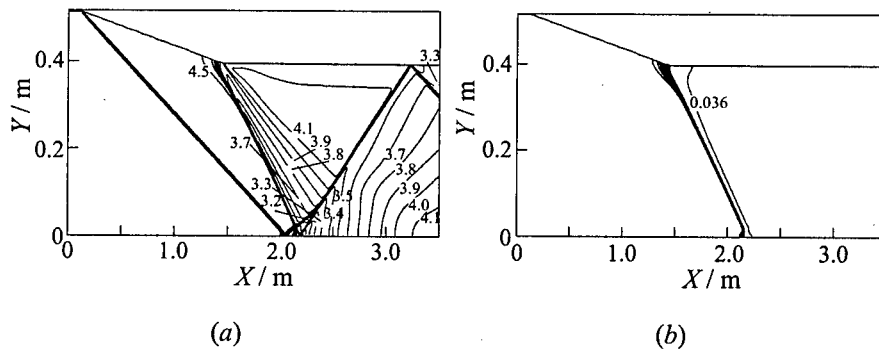
(a)   (b)

Figure 6 Predicted Mach number (a) and H_2O mass fraction (b) fields at $\theta = 5.15°$. (a) Step of isolines is 0.100 with minimum 2.871 and maximum 5.000. (b) Step of isolines is 0.002 with minimum 0.000 and maximum 0.037

(a)   (b)

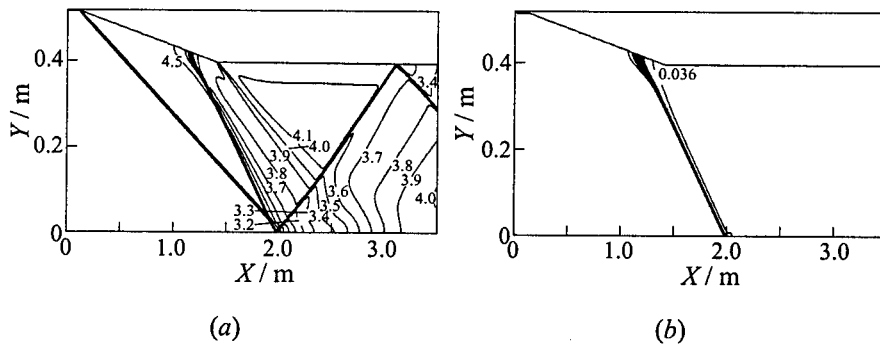**Figure 7** Predicted Mach number (a) and H_2O mass fraction (b) field at $\theta = 5.3°$. (a) Step of isolines is 0.100 with minimum 2.706 and maximum 5.000. (b) Step of isolines is 0.002 with minimum 0.000 and maximum 0.037

Figs. 5 and 6 can be detected in the region located immediately near the lower wall. The combustion zone behind the reflected shock ceases to interact with the reflected shock; instead, it interacts with the primary detonation shock. As indicated by Figs. 5 and 6, the expansion wave, generated by the second break point on the upper wall, is immediately adjacent to the reaction zone that is located downstream of the combustion-induced primary detonation shock.

The combustion region and the combustion-induced primary detonation shock move upstream as θ increases. The flow field at $\theta = 5.3°$ is shown in Fig. 7.
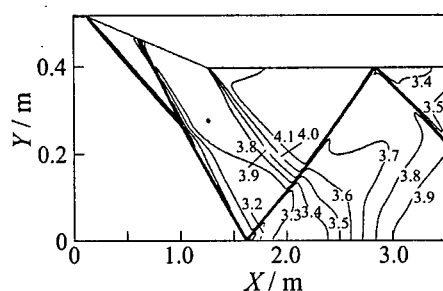
Figure 8 Predicted Mach number field at $\theta = 6°$. Step of isolines is 0.100 with minimum 2.961 and maximum 5.000
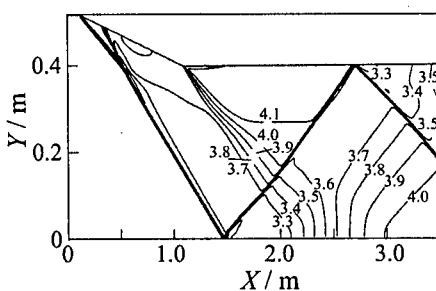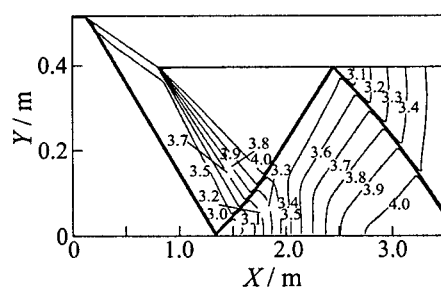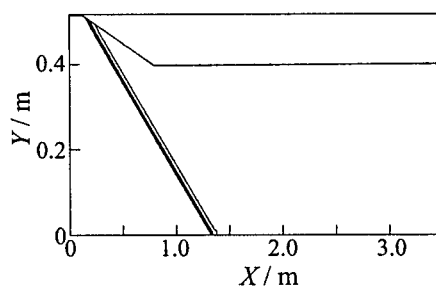
Figure 9 Predicted Mach number field at $\theta = 7°$. Step of isolines is 0.100 with minimum 3.017 and maximum 5.000

(a)

(b)

Figure 10 Predicted Mach number (a) and H_2O mass fraction (b) fields at $\theta = 10°$. (a) Step of isolines is 0.100 with minimum 2.909 and maximum 5.000. (b) Step of isolines is 0.002 with minimum 0.000 and maximum 0.037

The primary detonation shock interacts with the adiabatic bow shock. Formation of a secondary detonation shock below the interaction point is a result of the interaction. As a result, the λ-structure near the upper wall forms. It is obvious that the combustion region begins to separate from the expansion wave. The growth of θ is followed by the decrease in the λ-stem dimensions. This is clear from Figs. 8 and 9 plotted for $\theta = 6°$ and $\theta = 7°$, respectively. It is interesting to note, there is little change in the flow structure for these two cases, in spite of the transition through the CJ regime for the whole shock–reaction zone system. Finally, the bow shock becomes the classical overdriven detona-

tion shock attached to the wedge apex at $\theta = 10°$ (see Fig. 10). A similar flow structure is observed at angle $\theta = 15°$. However, at $\theta \geq 15°$ the bow detonation shock begins to interact with the expansion wave.

Thus, the considered examples testify that there exists the essential influence of the duct convergence angle on the resultant flow field. High sensitivity of the flow pattern to the convergence angle is detected in a very small range of wedge angles, $5° \leq \theta \leq 6°$. When the angle of wall inclination varies within this range, the combustion zone moves from the reflected shock to the bow shock. The most dramatic transformations in the flow structure occur at the angle variation from $5°$ to $5.3°$. In this case, it is difficult to postulate in advance the resultant flow structure.

PRELIMINARY ESTIMATION OF A POSSIBILITY TO UTILIZE SHOCK-INDUCED COMBUSTION IN A HYPERSONIC PROPULSION SYSTEM

Some results of preliminary studies aimed at gaining a better understanding of the possibility to realize the scramjet engine are presented in this section. It was assumed that the hydrogen jet is injected upstream of the engine entry to prepare the fuel–air mixture at the duct entry. The following issues were addressed: a possibility to mix hydrogen with air and the evaluation of the mixing efficiency at the engine duct entry, influence of the boundary layer generated on the forebody and on the inlet walls on the mixing process, feasibility of premature ignition upstream of the duct entry, a possibility to ignite the non-uniform hydrogen–air mixture in the engine duct by the shock generated on the leading edge of the engine cowl, the peculiarities of the combustion process in the engine duct and estimating the combustion efficiency. The investigations were performed for a small-scale vehicle with a ramjet hypersonic propulsion system.

The first-stage computations were performed using SUPNEF code for a 2D case on the basis of the PNS equations. In this case, the wall boundary layer was not taken into account. The configuration of the lower surface of the vehicle and the engine duct are presented in Fig. 11a (the total vehicle length is approximately 8.1 m). The computational domain includes: the forebody, inlet, engine duct, nozzle, and afterbody. The free stream conditions correspond to the flight Mach number 12, flight altitude 36.2 km, and the angle of attack 10°. Hydrogen is injected downstream of the shock, generated by the second wedge, at some distance from the wall. The hydrogen jet parameters used are as follows: $M_j = 2.45$, $P_j = 0.5$ atm, $T_j = 450$ K.

The main results for this case are presented in Figs. 11a–c by the Mach number and water and hydrogen mass fraction fields. It is evident that combustion
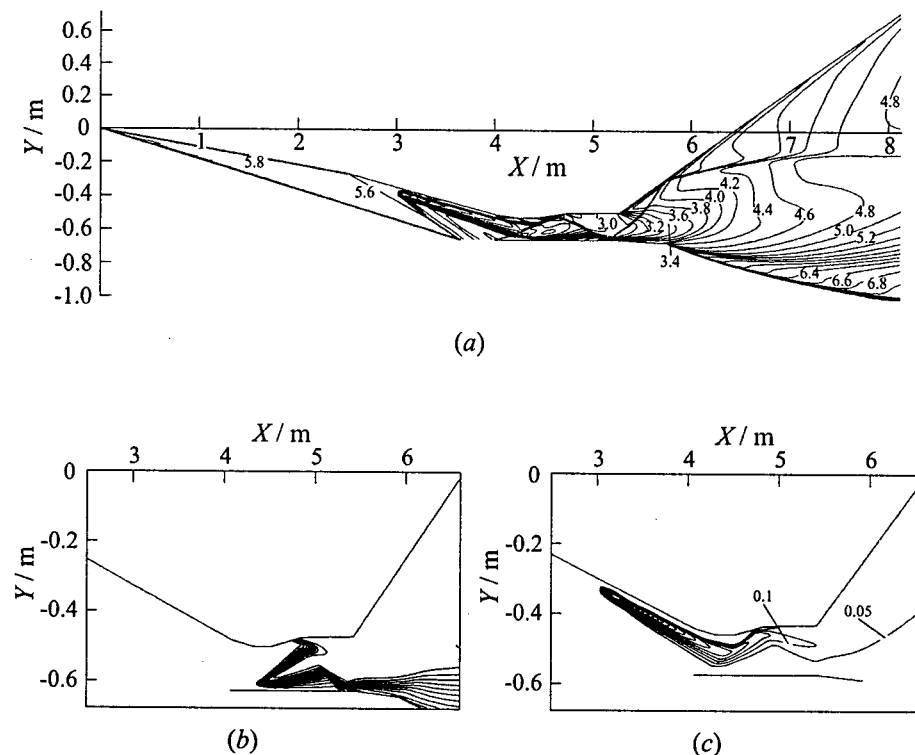
Figure 11 Predicted Mach number (a), H_2O mass fraction (fragment) (b), and H_2 mass fraction (fragment) (c) fields. (a) Step of isolines is 0.200 with minimum 2.450 and maximum 12.000. (b) Step of isolines is 0.020 with minimum 0.000 and maximum 0.249. (c) Step of isolines is 0.050 with minimum 0.000 and maximum 1.000

is initiated at some distance downstream of the shock generated by the engine cowl. The ignition delay is most pronounced near the cowl wall in the duct. The intense combustion process, with water formation in a narrow region downstream of the shock, is observed in the central part of the duct. In the upper part of the duct, intense combustion takes place downstream of the shock that is generated after the reflection of the shock arising at the leading edge of the cowl. It is necessary to note, the hydrogen jet is deflected to the upper wall after interaction with the cowl shock.

The performance analysis shows that the mixing efficiency at the duct entry is approximately 0.41. The mixing efficiency is defined as the possibility of a realistic mixture to release energy in the flow in accordance with local fuel and
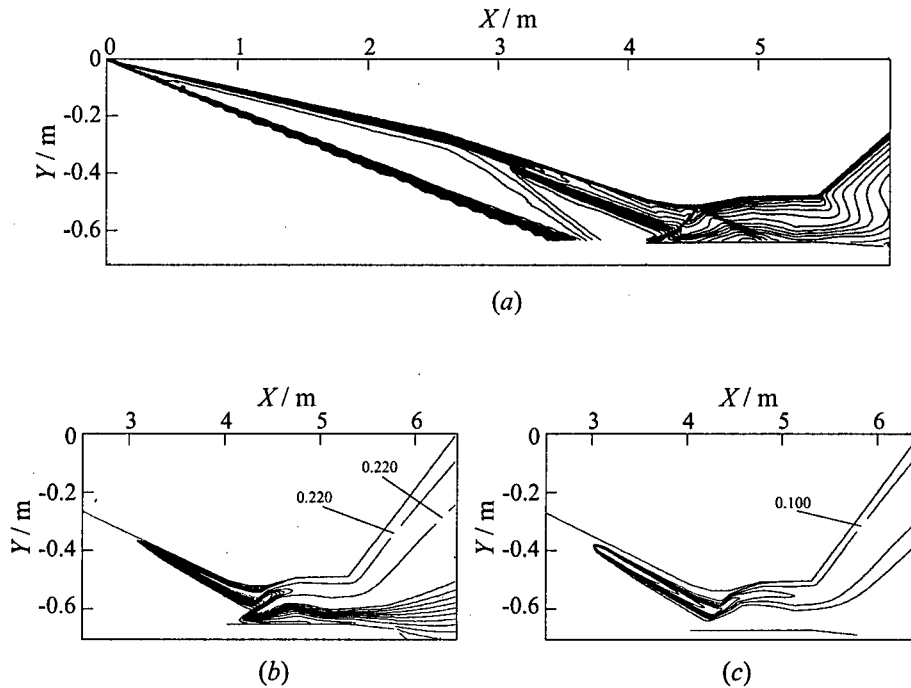
Figure 12 Predicted Mach number (a), H_2O mass fraction (fragment) (b), and H_2 mass fraction (fragment) (c) fields

oxidizer concentrations, provided a single global reaction is considered [20]. The combustion efficiency at the engine exit (estimated from the energy release) is approximately 0.52 at the mixing efficiency of 0.85.

The results presented (for example, the configuration of a hydrogen jet) lead to the assumption that the boundary layer on the forebody–inlet–engine walls can become a crucial factor for achieving shock-induced combustion with the chosen injection method. Additional calculations, for estimating the effect of the wall boundary layer, were performed using FNAS2D code (full Navier–Stokes equations). The results are shown in Figs. 12a–c. The Mach number field shows that the hydrogen jet is injected near the external edge of the boundary layer on the vehicle surface. As a result of interaction between the hydrogen jet and the wall boundary layer, the hydrogen jet is ignited at a small distance from the injection site and diffusive combustion occurs upstream of the engine duct entry. Intense combustion (with fast water formation and energy release) induced by the shock is observed only in the central part of the duct. Diffusive combustion

takes place in the duct in the region adjacent to the cowl. The mixing and combustion efficiencies at the engine entry, with the boundary layer effects taken into account, are approximately 0.55 and 0.05, respectively. The mixing and combustion efficiencies at the engine exit cross-section are approximately 0.77 and 0.5, respectively.

Thus, in order to succeed with the concept under consideration, it is necessary to find a correct position and to choose a rational injector for fuel supply, as well as to properly design the lower surface of the vehicle and engine duct.

SHOCK-INDUCED COMBUSTION IN RAM ACCELERATOR

The following example is considered [7]. The tube of 19 mm radius is filled with a homogeneous stoichiometric hydrogen–air mixture at a temperature of 300 K
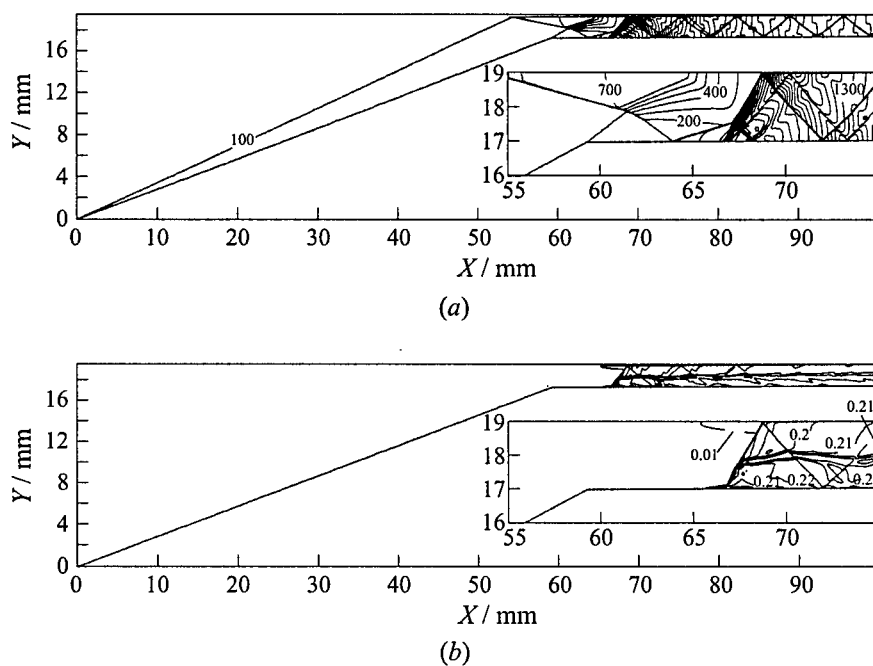

Figure 13 Static pressure (atm) (*a*) and H_2O mass fraction (*b*) fields at M = 7. (*a*) Step of isolines is 100.001 with minimum 16.383 and maximum 6785.982. (*b*) Step of isolines is 0.010 with minimum 0.000 and maximum 0.273

and a pressure of 25 atm. Calculations of the whole region, including a conic part of the projectile and the gap between the cylindrical segment of a projectile and the duct surface, are made with the code SUPNEF. The influence of the entry Mach number on the flow structure is the main focus.

The minimal value of the free stream Mach number, at which ignition occurs, is higher than 6. At $M = 7$, ignition occurs in the annular gap. The bow shock reflects from the duct wall, passes through the expansion wave and reflects from the cylindrical segment of the projectile. Ignition of the mixture occurs downstream of this reflected shock with a considerable delay near the surface of the projectile. The predicted Mach number and water mass fraction fields are shown in Figs. 13a and 13b. At $M = 9$, ignition occurs downstream of the bow shock reflection from the duct wall. The combustion zone near the duct wall is formed with a small delay downstream of the reflected shock. The flow fields at $M = 11$ (see Fig. 14) are similar to those for $M = 9$. However, the ignition delay is almost absent near the duct wall downstream of the reflection of the bow shock. At $M = 13$, ignition occurs near the cone surface at a certain distance
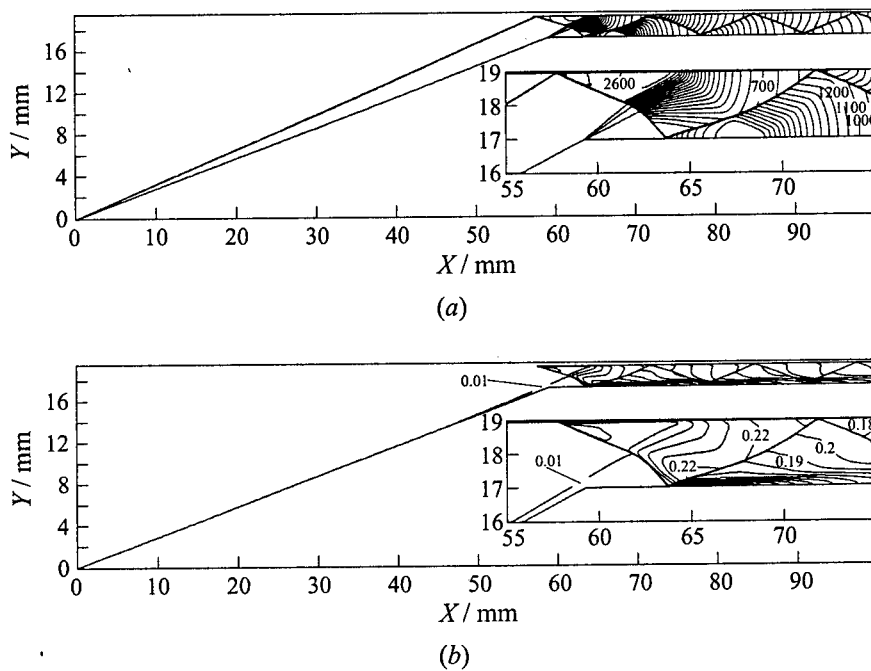

(a)

(b)

Figure 14 Static pressure (atm) (a) and H_2O mass fraction (b) fields at $M = 11$. (a) Step of isolines is 100.001 with minimum 21.537 and maximum 3716.633. (b) Step of isolines is 0.010 with minimum 0.000 and maximum 0.235

297

from the cone vertex. In this case, a detonation wave that propagates towards the duct wall forms.

CONCLUDING REMARKS

The results presented above show that the flow structure in the region of shock-induced combustion strongly depends upon the interaction of gas dynamics and chemical factors in accordance with free-stream conditions and duct geometry. High sensitivity of the flow structure to small variations in duct geometry and free-stream conditions can take place. Real effects, such as the wall boundary layer and non-uniformities in mixture composition can play an important role in the transformation of the flow structure.

REFERENCES

1. Sislian, J. P., and Atamanchuk, T. M., "Aerodynamic and Propulsive Performance of Hypersonic Detonation Wave Ramjets," ISABE Paper No.89-7109, 1989.

2. Atamanchuk, T., and Sislian, J., "On- and Off-Design Performance Analysis of Hypersonic Detonation Wave Ramjets," AIAA Paper No.90-2473, 1990.

3. Kuznetsov, M. M., Neyland, V. Ja., and Sayapin, G. N., "Efficiency Investigation of Scramjet with Detonation and Shockless Supersonic Combustion," *Utchenye Zapisky TsAGI*, **23**, 2, 30–37, 1992.

4. Sislian, J. P., Dudebout, R., Schumacher, J., and Oppitz, R., Inviscid Propulsive Characterstics of Hypersonic Shcramjets, AIAA Paper No.96-4535, 1996.

5. Humphrey, J. W., Parametric Study of an ODW Scramaccelerator for Hypersonic Test Facilities, AIAA Paper No.90-2470, 1990.

6. Yungster, S., Eberhardt, S., and Bruckner, A. P., "Numerical Simulation of Hypervelocity Projectiles in Detonable Gases," *AIAA J.*, **29**, 2, 187–199, 1991.

7. Li, C., Kailasanath, K., and Oran E. S., "Detonation Structures Generated by Multiple Shocks on Ram-Accelerator Projectiles," *Combustion Flame*, **108**, 173–186, 1997.

8. Eidelman, S., and Grossman, W., Pulsed Detonation Engine. Experimental and Theoretical Review, AIAA Paper No.92-3168, 1992.

9. Gonzalez, D.E., Computational Study of Inlet Injection for Premixed Shock-Induced Combustion, AIAA Paper No.96-4560, 1996.

10. Chinitz, W., On the Use of Shock-Induced Combustion in Hypersonic Engines, AIAA Paper No.96-4536, 1996.

11. Bezgin, L, Ganzhelo, A., Gouskov, O., and Kopchenov V., Some Numerical Investigation Results of Shock-Induced Combustion, AIAA Paper No.98-1513, 1998.

12. Jeong-Yoel, Choi, In-Seuck, Jeung, and Youngbin, Yoon, "Numerical Study of Scram Accelerator Starting Characteristics," *AIAA J.*, **36**, 6, 1029–1038, 1998.

13. Bussing, T. R. A., and Murman, E. M., "Numerical Investigation of Two-Dimensional H_2–Air Flameholding over Ramps and Rearward-Facing Steps," *J. Propulsion Power*, **3**, 5, 448–454, 1987.

14. Cambier, J. L., Adelman, H. G., and Menees, G. P., "Numerical Simulation of Oblique Detonations in Supersonic Combustion Chambers," *J. Propulsion Power*, **5**, 4, 482–491, 1989.

15. Cambier, J. L., Adelman, H., and Menees, G. P., "Numerical Simulation of an Oblique Detonation Wave Engine," *J. Propulsion Power*, **6**, 3, 315–323, 1990.

16. Vlasenko, V., and Sabelnikov, V., Numerical Simulation of Inviscid Flows with Hydrogen Combustion After Shock Waves and in Detonation Waves, AIAA Paper No.94-3177, 1994.

17. Nekhamkina, O. A., and Strelets, M. Kh., "Numerical Simulation of Detonation Waves with the Use of Efficient TVD Scheme," *J. Comp. Mathematics Mathematical Physics*, **32**, 9, 1992.

18. Levin, V. A., and Markov, V. V., "Detonation Initiation at the Concentrated Energy Supply," *Sov J. Physics Combustion Explosion*, **11**, 4, 623–633, 1975.

19. Vasiliev, A. A., "The Main Results of Investigation of Detonative Combustion of Gaseous Mixtures Excited by a Fast Flying Body," *Rus. J. Physics Combustion Explosion*, **33**, 5, 85–102, 1997.

20. Bezgin, L., Ganzhelo, A., Gouskov, O., Kopchenov, V., Laskin, I., and Lomkov, K., "Numerical Simulation of Supersonic Flows Applied to Scramjet Duct," ISABE Paper No.95-7082, 1995.

21. Gulyaev, A. N., Kozlov, V. Ye., and Secundov, A. N., "A Universal One-Equation Model for Turbulent Viscosity," *J. Fluid Dynamics*, **28**, 4, 485–494, 1993.

22. Miller, J. A., and Bowman, C. I., "Mechanism and Modeling of Nitrogen Chemistry in Combustion," *Progress Energy Combustion Sci.*, **15**, 287, 1989.

23. Dimitrow, V. I., "The Maximum Kinetic Mechanism and Rate Constants in the H_2–O_2 System," *React. Kinetic Catal. Lett.*, **7**, 1, 81–86, 1977.

24. Godunov, S. K., Zabrodin, A. V., Ivanov, M. Ya., Kraiko, A. N., and Prokopov, G. P., *Numerical Solution of Multi-Dimensional Gas Dynamics Problems*. Nauka, Moscow, 1976.

25. Baruzzi, G., "Structured Mesh Grid Adapting Based on Spring Analogy," *Proc. Conference CFD Society of Canada*, Montreal, 1993.

26. Bezgin, L., Ganzhelo, A., Gouskov, O., and Kopchenov, V., "Numerical Simulation of Viscous Non-Equilibrium Flows in Scramjet Elements," ISABE Paper No.97-7131, 1997.

299

27. Courant, R., and Friedrichs, K. O., *Supersonic Flow and Shock Waves.* Interscience, N.Y., 1948.

28. Chernyi, G. G., "Supersonic Flow Around Bodies with Detonation and Deflagration Fronts," *Acta Astronautica,* **13**, 5 & 6, 467–480, 1968.

29. Zel'dovich, Ya. B., "Theory of Combustion and Detonation," In: *Chemical Physics and Hydrodynamics.* Nauka, Moscow, 1984.

30. Chernyi, G. G., *Gas Dynamics.* Nauka, Moscow, 1988.

USE OF ELECTRO-PHYSICAL PROPERTIES OF DETONATION PRODUCTS IN EXPLOSIVE FAST OPENING SWITCHES

V. K. Chernyshev, V. V. Vakhrushev, G. I. Volkov, and V. A. Ivanov

Realization of Academician A. D. Sakharov's concept of magnetic cumulation has made it possible to create an explosive magnetic generator (EMG) with a stored energy up to 10^8 J. Although, if some special measures fail to be undertaken, the EMGs cannot form a current pulse of microsecond duration. Utilization of the effect of current contour rupture by means of explosive fast opening switches helps to perform fast energy supply from the EMG to the load. The rate of energy supply from the EMG to the load depends on the electro-physical properties of detonation products of the explosive charge. The use of electro-physical properties of detonation products in explosive fast opening switches is considered in this paper.

INTRODUCTION

The implementation of the magnetic cumulation concept proposed by Academician A. D. Sakharov [1] made it possible to create explosive magnetic generators (EMG) with a stored energy up to 10^8 J [2]. However, EMG cannot produce the current pulses of microsecond duration in the load without special conditions, as the high power is achieved in EMG only at the end of operation during several microseconds. When the load is placed sequentially in EMG compression contour, a low current will pass through the load over a long time. The amount of time that current passes through the load, is the amount of time the generator will be powered with the initial energy and the time of EMG operation (several tens of microseconds). The fast energy delivery from EMG into the load can be achieved only by the rupturing a section of EMG contour and by connecting the ruptured section ends to the load circuit. The devices providing the rupture of electric circuit and formation of current pulse in the load were called "opening switches." In 1961, the first EMG, 80 mm in diameter, with the opening switch

allowing the production of a current pulse with the amplitude of several thousands kiloampers per 0.5 μs was created by the group of researchers from the All-Union Research Institute for Experimental Physics (VNIIEF) [3, 4].

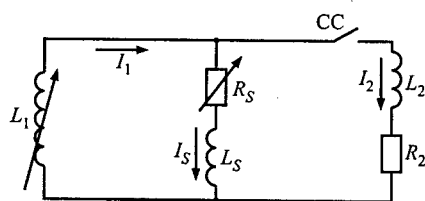# STATEMENT OF THE PROBLEM AND EXPERIMENTAL RESULTS

Figure 1 Equivalent electric commutation-circuit

Because of the development of the works at VNIIEF on plasma heating in gas-discharge chambers with plasma focus, in chambers with ultra-sonic magnetic gas-dynamic nozzle and devices providing the compression of thermonuclear targets using the liner accelerated by the EMG magnetic field [5, 6], advanced high-power pulse current sources, significantly different from those developed earlier in terms of the output energy level and in the time of its transfer into the load, were created. The electrical schematic of commutation is shown in Fig. 1. The following designations are used: L_1, L_2, and L_s are the inductance of the ruptured contour, load and ruptured circuit, respectively; I_1, I_2, and I_s are the currents in the ruptured contour, load and ruptured circuit, respectively; R_2 and R_s are the resistance in the load and ruptured circuit, respectively.

The following system of equations describes the operation of the commutation circuit:

$$(I_1 L_1)' + (I_2 L_2)' + I_2 R_2 = 0$$

$$(I_2 L_2)' + I_2 R_2 - I_s R_s - I_s' L_s = 0$$

$$I_1 = I_2 + I_s$$

In a realistic commutation circuit $L_s \ll L_1$, so that the influence of the ruptured circuit inductance on the process of current commutation into the load may be neglected. Thus, if the inductances of the ruptured contour and load circuit are changed slightly ($\Delta L_1 < 0.1 L_1$ and $\Delta L_2 < 0.1 L_2$) during commutation, it may be assumed that $L_1 = const$ and $L_2 = const$ at the time of commutation. For zero initial conditions ($t = 0$, $I_1 = I_1^0$, $I_1 = I_s$, $I_2 = 0$), the solution of the equations is [4]:

302

$$I_s(t) = I_1^0 e^{-\int R_s(t)/L_s \, dt}$$

$$I_2(t) = I_1^0 \frac{L_s}{L_2} \left(1 - e^{-\int R_s(t)/L_s \, dt}\right)$$

where

$$L_s = \frac{L_1 L_2}{L_1 + L_2}$$

The maximum value of current in the load is $I_{max} = I_1^0 L_s / L_2$. The current in the load reaches the level of $0.1 I_{max}$ at $t_{0.1}$, defined as $\int_0^{t_{0.1}} (R_s(t)/L_2) \, dt = 0.1$. It can also be seen that the current in the load will be $0.9 I_{max}$ at $t_{0.9}$, defined as

$$\int_0^{t_{0.9}} \frac{R_s(t) dt}{L_s} = 2.3$$

These relations also show that the amount of time the current increases in the load is specified not only by the value of the introduced resistance, but also, by the integral $\int R_s(t) \, dt$ and the value of L_s. The voltage on the opening switch is defined by the following relation:

$$U_s(t) = I_1^0 R_s(t) e^{-\int_0^t R_s(t)/L_s \, dt}$$

The electrical contour can be ruptured in various ways: by using electronic techniques, by exploding the conductor electrically, or by using high explosives (HE). The opening switches based on the electrical explosion of conductor [7] and application of HE [4] gained the greatest acceptance in the production of multi-megaamper-current pulses.

The opening switches based on HE have a more complicated design; but, they make it possible to utilize the energy stored in the EMG more efficiently, because the conductor is ruptured due to the energy of the HE charge. In the electrical explosive opening switches, some energy accumulated in EMG earlier is consumed for evaporating the conductor material. Rupturing of the electrical contour with the HE charge is performed due to the gaps made by HE in the current-carrying conductor, which is the integral part of the electrical contour [4], due to quenching the plasma electric arc by the detonation products (DP) [8], or due to the application of the conductive zone behind the front of a detonation wave [9]. The gaps in the conductor can be made either by cutting the conductor with gas or dielectric cumulative jets [5], or by projecting the conductor at the ribbed dielectric barrier [4].

Let us consider an opening switch with the ribbed barrier. The diagram of an opening switch with the conductor placed at the ribbed barrier is shown in Fig. 2. The aluminum or copper foil is used as the ruptured conductor in the
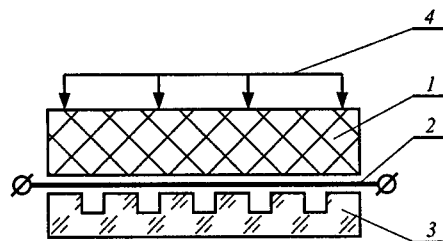
Figure 2 Explosive current peaker. *1* — explosive charge, *2* — aluminum foil, *3* — ribbed barrier, *4* — initiation system

opening switch. Consider the mechanism of foil rupturing at the barrier ribs. When the detonation wave arrives at the foil surface, the foil regions, located opposite to the grooves, move at considerably higher velocity than the foil regions located opposite to the barrier shoulders. The foil is ruptured inside the barrier grooves. The transversel gaps formed in the foil are filled with the DP, which have the resistance several orders of magnitude higher than the resistance of metals [10]. The high velocity of resistance introduction is provided from this method of rupture due to the following: the formation of multiple gaps in the conductor, high velocity of conductor inside the ribbed barrier grooves, and relatively high value of DP specific resistance. The value of resistance that is introduced into the contour due to the HE-assisted rupture of the conductor can be represented by the following relation:

$$R_s(t) = \sum_{i=1}^{n} \frac{\delta(t)}{\lambda_{\mathrm{DP}}(t) S_i(t)}$$

where $\delta(t)$ is the length of the transversel gap in the conductor, $\lambda_{\mathrm{DP}}(t)$ is the DP conductivity, $S_i(t)$ is the cross-section area of DP conductive layer, n is the number of grooves at the barrier. If the conductor is ruptured in the same way inside each groove, the above relation will reduce to:

$$R_s(t) = n \frac{\delta(t)}{\lambda_{\mathrm{DP}}(t) S(t)}$$

Assuming that the electric field strength, $E(t)$ is constant along the opening switch when the conductor with the passing current is ruptured, the voltage at the opening switch may be found from

$$U_s(t) = nE(t)\delta(t)$$

To estimate the value of the introduced resistance and the voltage at the opening switch it is necessary to know the size of a gap in the conductor, specific resistance of DP conductive area, and the electric strength of DP. The knowledge of these characteristics is important in order to properly choose the HE composition to achieve maximum possible values of resistance and voltage at the opening switch, as well as to calculate the main components of the opening switch.

304

Two radiographic experiments were carried out to estimate the size of gaps when the foil is ruptured at the ribbed barrier. In the first experiment, the dummy opening switch with the aluminum foil 1 mm thick was used. The width of a groove at the ribbed barrier made of acrylic plastic was 10 mm and the depth of this groove was 40 mm. The bursting charge, 24 mm thick, was made of TG 30/70 high explosive. Photographs of a dummy opening switch before the shot and at the time corresponding to the beginning of commutation, that is 3.5 μs after arrival of the detonation wave at the surface of the ruptured foil, are presented in Fig. 3. A preliminary shot with the current in the opening switch was perfomed for estimating the time of commutation beginning.

As the radiograms in Fig. 3 show, the rupture of foil at the ribs has a jet nature and the ribs of dielectric barrier are squeezed under the DP pressure and shaped like a mushroom. The average velocity of rib surface displacement is 2.5 km/s and the average velocity of jet central part is 5 km/s, relative to the rib surface (the average velocity relative to the initial position of rib surface is 7.5 km/s). The radiogram also shows the gaps appearing inside the grooves due to the tension the foil. The narrowest width of these gaps is 0.2 of the initial width of the groove.

The character of foil rupture in the opening switch with the supports 5 mm high on the ribs of dielectric barrier was studied in the second experiment. The photographs of an initial state and that corresponding to the beginning of commutation (3–4 μs after detonation arrived at the foil surface) are presented in Fig. 4. As it follows from the radiogram, the supports apparently did not change their position. The gaps formed in the foil are greater than those in the first experiment. Their sizes achieve 1/3 of the width of the groove in the ribbed barrier.

To experimentally estimate the conductivity of DP of the composition TG 30/40, the shots were carried out using the electric contact measuring technique [10]. The experimental setup is presented in Fig. 5. Several pairs of electrodes from 1 to 18 mm long were mounted at the opposite sides of the rectangular bar, $10 \times 15 \times 150$ mm in size, made of HE. The detonation wave propagated from the end along the HE charge. The change of voltage at the resistance R_m was recorded at the time when the detonation wave was passing between the electrodes. In this case, the inter-electrode resistance, R_x, is: $R_x = R_m U_m(t)/(U_m^0 - U_m(t))$, where U_m is the initial voltage at R_m before the passage of the detonation wave between the electrodes, $U_m(t)$ is the voltage after the passage of the detonation wave between the electrodes.

The voltage oscillogram, U_m, obtained in one of the shots is presented in Fig. 6. The history of DP resistance, $R(t)$, is presented in Fig. 7 for composition TG 30/70. The curve shows that the effective time of resistance decreases from $10 R_{DP\,min}$ down to $1.1 R_{DP\,min}$ in the space between the electrodes is comparable with the time resolution of the recording system ($L/R = 0.05$–0.1 μs), and in all cases it is about 0.1 μs. Then it decreases negligibly. So, the effective detonation
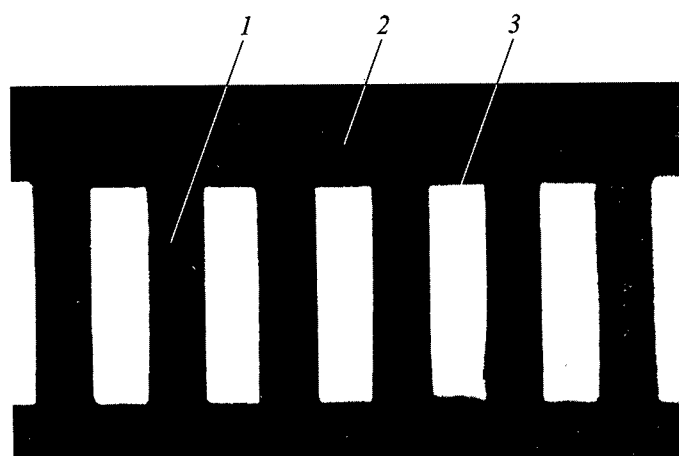
(a)
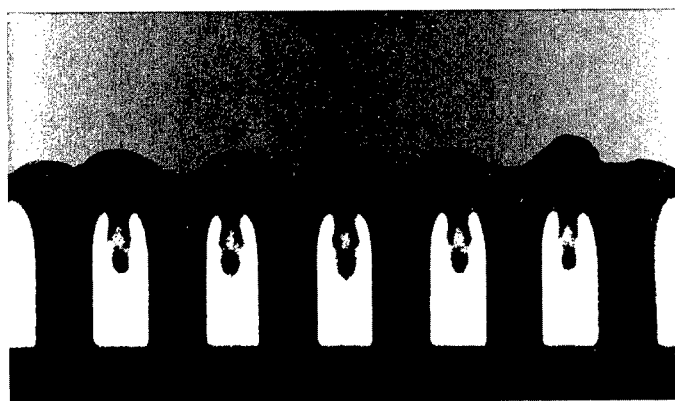
(b)

Figure 3 Radiograms of a dummy opening switch with a ribbed barrier before the shot (a) and 3.5 μs after the arrival of the detonation wave at the surface of the foil (b). 1 — ribbed barrier, 2 — high-explosive charge, 3 — aluminum foil

zone falls only within the narrow region behind the front of detonation wave. Considering that the time of attaining the minimum value of DP resistance between the electrodes is $l_{\min} = (l + 2\Delta)/D$, where l is the electrode length, Δ is the width of the conductive zone, and D is the detonation velocity, the width of the conductive zone can be expressed as: $\Delta = (Dt_{\min} - l)/2$. The conductivity of DP can be determined from the relation $\lambda = b/R_{\rm DP}h$, where b is the size of the inter-electrode space, and h is the electrode width.

306
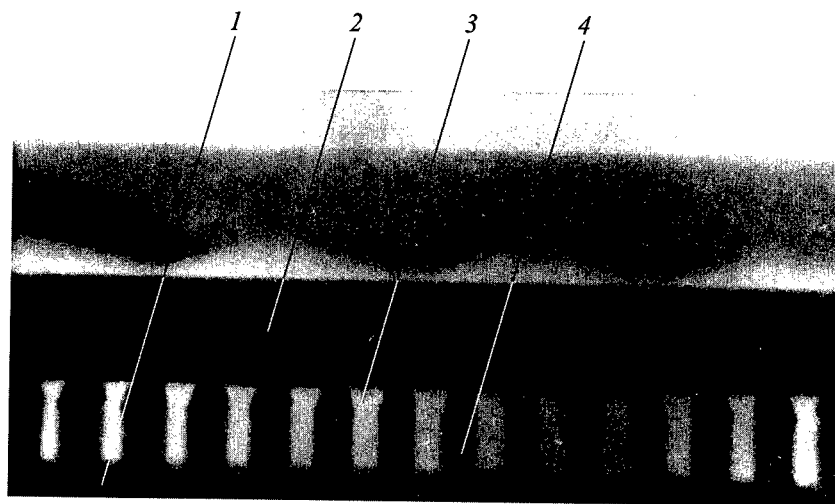
(a)
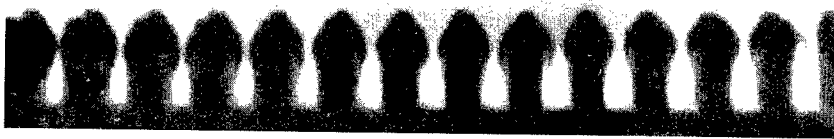
(b)

Figure 4 Radiograms of dummy opening switch with a ribbed barrier and copper supports before the shot (a) and 3–4 μs after the arrival of the detonation wave at the surface of the foil (b). 1 — ribbed barrier, 2 — high-explosive charge, 3 — aluminum foil, 4 — copper support

It follows from the relation for λ, that the conductivity of DP for the composition TG 30/70 with density 1.71 g/cm^3 is 4 Ohm^{-1}cm^{-1}, and the thickness of the conductive zone is 1 mm.

The setup for measuring the electric strength of DP is shown in Fig. 8. The disk-shaped HE charge, 100 mm in diameter and from 3 to 5 mm thick, was placed between the electrodes 6 mm in diameter. The charge was initiated in a
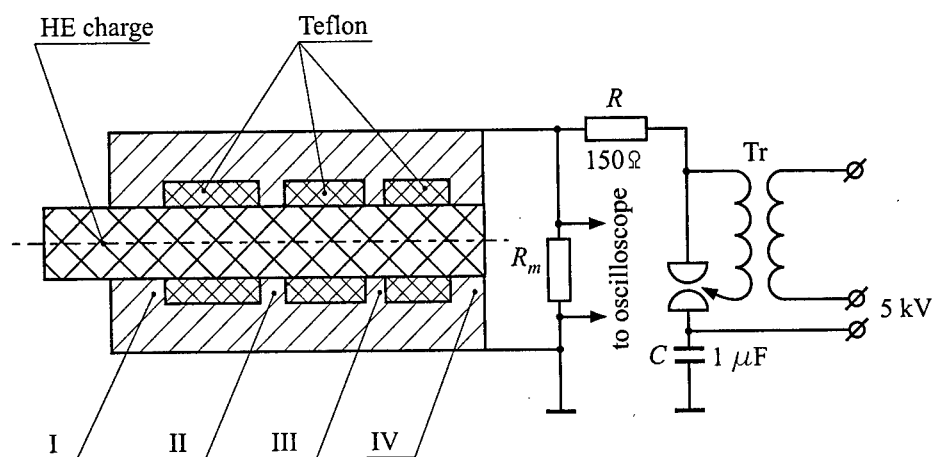
Figure 5 Experimental setup for studying the electric conductivity of detonation products with electrodes of plane geometry. Numbers I to IV denote electrodes
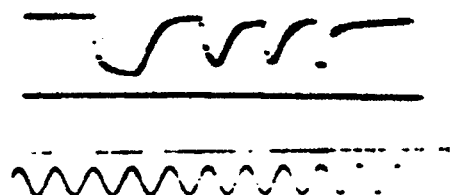
Figure 6 Typical oscillogram of voltage at R_m in the shot according to the schematic in Fig. 5. Frequency $f = 500$ kH
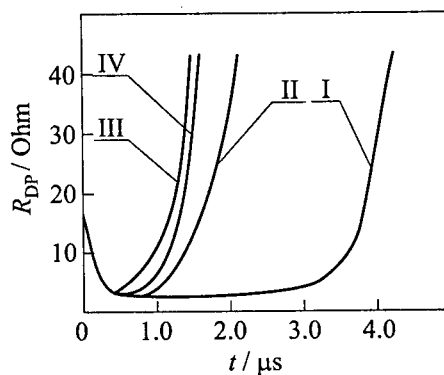
Figure 7 The measured history of the resistance of detonation products. Numbers I to IV denote electrodes in Fig. 5

single point at the cylindrical surface of the disk. The electrodes were placed at the center of the disk. They were connected to the capacitor bank of capacity 108 μF with the operating voltage up to 20 kV. When the detonation wave reached the electrodes, the current in the discharge circuit was produced either due to DP conductivity (about 10 kA), or due to the inter-electrode breakdown (about 50 kA). So, the presence or absence of the breakdown was determined from the value of current in the discharge circuit. The breakdown in the inter-
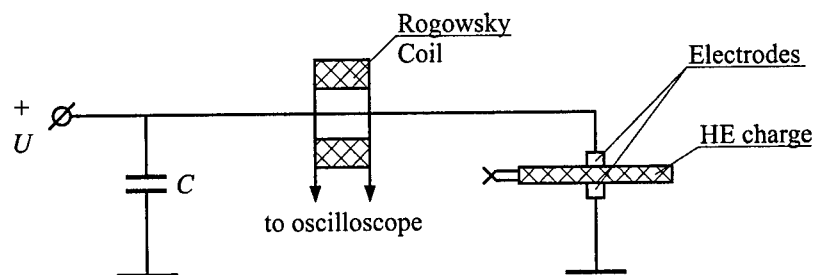
Figure 8 Experimental setup for measuring the electric strength of detonation products

electrode space was observed for DP of composition TG 30/70 at the electric field strength of 5 kV/mm. At the field strength of 4.5 kV/mm, the breakdown in the space took place within about 10 μs after the detonation wave had passed between the electrodes. At the electric field strength of 4 kV/mm, there was no breakdown. Thus, one arrives at the following conclusion: for composition TG 30/70, the electric strength of DP in the vicinity of the detonation front is about 4.5 kV/mm.

The authors have developed the pulse current source for studying the operation of a gas-discharge plasma chamber with a supersonic nozzle. This source is made up of a helical explosive-magnetic generator 160 mm in diameter and an explosive opening switch 200 mm in diameter based on the foil rupturing at the ribbed barrier by means of the HE charge made of composition TG 30/70 [11]. The aluminum foil, 0.4 mm thick and 200 mm long, was used in the opening switch as the rupturing foil. The width of grooves in the ribbed barrier was 2 mm, the number of grooves was 50. Using this generator, the current pulse, with the amplitude of 5.5 MA, was produced in the inductive load of 15 nH per 1.3 μs. At the instant of foil rupturing, the voltage at the opening switch was 93 kV. The value of resistance at the instant of maximum voltage was recorded to be equal to about 48 mOhm. As it was noted earlier, after the rupture, the gaps of 0.2 of the groove width were produced in each groove in the foil. This means that the total width of gaps in the foil, when there were 50 grooves, was 20 mm. The foil width in the opening switch was 630 mm. According to the data presented above, the conductivity of DP for composition TG 30/40 was 4 Ohm^{-1}cm^{-1} and the width of the conductive zone was about 1 mm. At these DP parameters, the resistance of the opening switch had to be 79 mOhm by 1.0–1.5 μs after the detonation wave arrived at the foil surface. This value was 1.6 times higher than the resistance recorded in the shot. The discrepancy might be due to the heating of the detonation plasma by the passing current. When esti-

309

mating the value of the opening switch resistance, the heating of plasma by the current was not taken into account. It is known that the resistance introduced into the contour after foil rupturing depends on the value of the current passing through the opening switch. When the total size of gaps produced in the foil is 20 mm, the value of voltage at the opening switch must achieve 90 kV at the electrical conductivity of DP equal to 4.5 kV/mm. The experimental value of voltage is 93 kV. It is in a good agreement with the calculations.

The parallel connection of several explosive opening switches makes it possible to increase the amplitude of current pulse produced in the load. When testing the ten-module EMG [11], the current pulse with the amplitude of 50 MA was produced in about 1.5 μs in the inductive load of 1.5 nH.

CONCLUDING REMARKS

Thus, the experiments showed that the use of the opening switches based on rupturing the electric contour by detonation products of HE charge, leads to production of the current pulses with the amplitude of about 10^8 A and microsecond rising time in the load.

REFERENCES

1. Sakharov, A. D., "Explosive-Magnetic Generators," *Uspekhi Phys. Nauk*, **88**, 4, 725–734, 1966.
2. Chernyshev, V. K., and Mokhov, V. N., "On the Progress in the Development of High-Power Explosive-Magnetic Sources of Energy for Compressing Thermonuclear Target)," *Sov. J. Voprosy of Atomic Science and Technology*, **4**, 23–24, 1992.
3. Chernyshev, V. K., Protasov, M. S., Shvetsov, B. A., *et al.*, "Explosive-Magnetic Generators of "Potok" Family," *Sov. J. Voprosy of Atomic Science and Technology*, **4**, 33–41, 192.
4. Pavlovskii, A. I. *et al.*, "Study on Accumulating the Commutation of High Energy Densities. Ultra-High Magnetic Fields," In: *Physics. Technology. Application.* Nauka, Moscow, 410–415, 1984.
5. Yershov, A. P., Zubkob, P. I., and Lukianchikov, L. A., "Application of Electric Conductivity Zone in the Detonation Wave of Condensed HE and of Electrical Strength of Detonation Products for Generating High-Current Pulses and Cutting High Currents," In: *Dynamics of Continuous Media.* Institute of Hydrodynamics Publ., Novosibirsk, **16**, 1974.
6. Brish, A. A., Tarasov, M. S., and Tsukerman, V. A., "Electrical Conductivity of Explosion Products from the Condensed Explosives," *Sov. J. Experimental Theoretical Physics*, **37**, 6(12), 1542–1530, 1950.

PART FIVE

DETONABILITY OF ADVANCED FUELS

APPLICATION OF FUEL BLENDS FOR CONTROLLING DETONABILITY IN PULSED DETONATION ENGINES

S. M. Frolov, V. Ya. Basevich, A. A. Belyaev,
and M. G. Neuhaus

The operational ability of Pulsed Detonation Engines (PDE) is considerably dependent on the fuel used. The fuel detonability within a wide range of operation conditions is of particular importance. A set of measures, aimed at meeting the requirements of PDE performance, is suggested. Reliable detonation initiation can be attained by adopting a stratified charge concept through controlled fuel/additive distribution about the initiator and along the detonation chamber. The sensitivity of detonation dynamics to variable ambient conditions and to deviations in injector/initiator timing can be reduced by applying the controlled distributed injection of several fuels that exhibit essentially different detonability. Fuel detonability within the Octane Number (ON) concept is considered. Within this concept, blends of prospective fuels are modeled in terms of standard n-heptane–iso-octane blends. The characteristics of detonability for the standard blends — auto-ignition delay — is studied theoretically. The study is based on the semi-empirical oxidation mechanism accounting for both low- and high-temperature fuel oxidation. Characteristic reaction times were calculated for a wide range of conditions: ON (0–100), temperature (650–1200 K), pressure (1–100 bar), and equivalence ratio (0.5–2.0). The change in blend composition is shown to provide efficient control of detonability and, if required, sustenance of a desired detonability under a variation of conditions in the detonation chamber.

1 INTRODUCTION

A Pulsed Detonation Engine (PDE) is currently considered a possible alternative to other propulsion devices (gas turbine engines, ramjets) for flight Mach numbers M < 2–2.5. The basic advantage of PDE is associated with the high thermodynamic efficiency of detonative combustion. However, there are a number of problems facing attainment: the requirement of fast evaporation of liquid

313

hydrocarbon fuel and mixing with air, reliable detonation initiation in the fuel–air mixture (FAM) at relatively short distances (1–2 m), preventing premature ignition of FAM at hot surfaces, etc. In addition, special measures should be undertaken to better adapt the PDE performance to variations in the flight Mach number and altitude, and to ensure performance stability.

A set of measures, aimed at meeting the requirements of PDE performance and stability, is suggested in [1]. Reliable detonation initiation can be attained by adopting a stratified charge concept through controlled fuel/additive distribution about the initiator and along the detonation chamber. The sensitivity of detonation dynamics to variable ambient conditions and to deviations in injector/initiator timing can be reduced by applying the controlled distributed injection of several (e.g. two) fuels that exhibit essentially different detonability. In view of the insufficient information on detonability of fuel blends, there is a need for PDE applications in fundamental studies of ignition characteristics, detonation initiation and propagation in blended fuels, as well as in searching the advanced fuel compositions.

In this paper, detonability requirements for advanced fuels are considered in terms of standard n-heptane–iso-octane blends. Thus, fuel detonability within the Octane Number (ON) concept is considered. The characteristics of detonability — auto-ignition delay — is studied theoretically. The study is based on the semi-empirical oxidation mechanism containing two blocks of reactions: (1) a semi-empirical block including reduction reactions of high hydrocarbons to C_1–C_2-hydrocarbons and the reactions of high peroxides responsible for low-temperature oxidation, and (2) a non-empirical block of oxidation reactions of C_1–C_2-hydrocarbons. Characteristic reaction times were calculated for the range of operation conditions of a PDE. Based on the calculated dependencies of the ignition delay on the fuel blend ON, temperature, pressure and FAM composition, the controlling strategies of PDE performance are discussed.

2   OPERATION CONDITIONS OF A PULSED DETONATION ENGINE

It is instructive to indicate the range of operation conditions for the PDE assuming that it is designed for producing thrust for a flying vehicle. A schematic of a PDE is shown in Fig. 1.

The operation cycle of a PDE includes four phases: (1) detonation initiation, (2) mixture burnout in a propagating detonation wave, (3) expansion of detonation products through a nozzle, and (4) injection of fuel into the detonation chamber and mixing of fuel with incoming air.

Subsequent detonation initiation in the new charge of fuel starts the new operation cycle. In principle, a provision should be made for a mechanical (e.g.
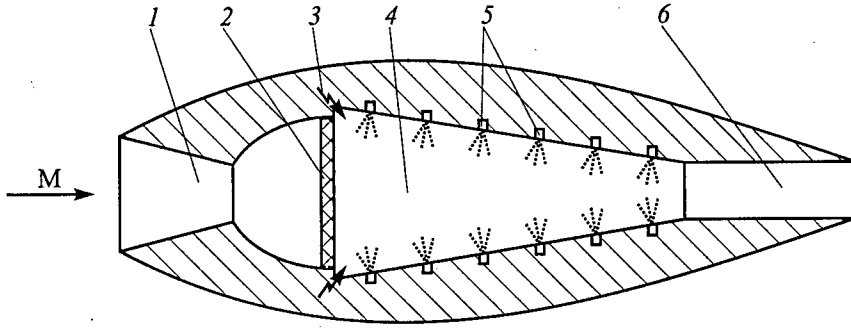
314

Figure 1 Schematic of the Pulsed Detonation Engine. *1* — intake (supersonic diffuser), *2* — mechanical valve, *3* — initiator, *4* — detonation chamber, *5* — fuel injectors, *6* — nozzle

rotary or flapper) valve to prevent detonations or shocks from moving outward through the intake, to provide a sufficient time for mixing of fuel with air, and to ensure a controlled inward flow rate of fresh air. The performance of a PDE is determined, among other things, by the frequency of generating the detonation waves in the chamber. For competing with other propulsion devices in terms of performance, the estimated frequency of 100–200 Hz is required. For increasing the PDE performance, preliminary pressurization of air can also be used.

Table 1 shows the estimated variations of the initial (stagnation) pressure (p_{20}) and temperature (T_{20}) of the incoming air in the detonation chamber, as well as the detonation shock pressure (p_s) and temperature (T_s) in a PDE-based supersonic vehicle over the flight Mach number (M) range from 1.0 to 2.0, and an altitude (H) range from 0 (sea level) to 10 km. Also shown in the table are the values of static ambient pressure (p_a) and temperature (T_a), the isentropic stagnation pressure (p_{10}), the coefficient of pressure loss in the shock (κ), the coefficient of pressure recovery in the supersonic diffuser (η) [2], the speed of sound in a fresh FAM (a_m), and the Mach number of the detonation wave (M_s). For the estimations, the following relationships were used:

$$p_{10} = p_a \left(1 + \frac{\gamma - 1}{2} M^2\right)^{\frac{\gamma}{\gamma - 1}}$$

$$p_{20} = \eta(M)\kappa(M)p_{10}$$

$$\kappa = \left(\frac{\gamma + 1}{2}\right)^{\frac{\gamma + 1}{\gamma - 1}} \frac{M^{\frac{2\gamma}{\gamma - 1}}}{\left(1 + \frac{\gamma - 1}{2} M^2\right)^{\frac{\gamma}{\gamma - 1}} \left(\gamma M^2 - \frac{\gamma - 1}{2}\right)^{\frac{1}{\gamma - 1}}}$$

Table 1 Estimated variations of pressure and temperature in the detonation chamber of a PDE-based supersonic vehicle

M	1.0			1.5			2.0		
H, km	0.0	3.0	10.0	0.0	3.0	10.0	0.0	3.0	10.0
p_a, bar	1.0	0.692	0.261	1.0	0.692	0.261	1.0	0.692	0.261
T_a, K	288	269	223	288	269	223	288	269	223
p_{10}, bar	1.89	1.31	0.49	3.67	2.54	0.96	7.82	5.41	2.04
κ	1.0	1.0	1.0	0.93	0.93	0.93	0.721	0.721	0.721
η	1.0	1.0	1.0	1.049	1.049	1.049	1.157	1.157	1.157
p_{20}, bar	1.89	1.31	0.49	3.58	2.48	0.94	6.52	4.51	1.7
T_{20}, K	346	323	268	418	390	323	518	484	401

$$\Phi = 1.0, \quad D_{st} = 1800 \text{ m/s}$$

	1.0			1.5			2.0		
a_m, m/s	372	360	328	410	396	360	456	441	401
M_s	4.84	5.00	5.49	4.39	4.55	5.00	3.95	4.08	4.49
p_s, bar	51.6	38.2	17.2	80.5	59.9	27.4	118.7	87.6	40.0
T_s, K	1570	1570	1570	1570	1570	1570	1570	1570	1570

$$\Phi \approx 0.6, \quad D_{lean} = 1600 \text{ m/s}$$

	1.0			1.5			2.0		
a_m, m/s	372	360	328	410	396	360	456	441	401
M_s	4.30	4.44	4.88	3.90	4.04	4.44	3.51	3.63	3.99
p_s, bar	40.8	30.1	13.6	63.5	47.2	21.6	93.7	69.3	31.6
T_s, K	1240	1240	1240	1240	1240	1240	1240	1240	1240

$$T_{20} = T_a \left(1 + \frac{\gamma - 1}{2} M^2 \right)$$

$$a_m = \sqrt{\gamma R T_{20}}$$

$$M_s = \frac{D}{a_m}$$

$$p_s \approx \frac{2\gamma_m}{\gamma_m + 1} p_{20} M_s^2$$

$$T_s \approx \frac{2\gamma_m(\gamma_m - 1)}{(\gamma_m + 1)^2} T_{20} M^2$$

where γ is the specific heat ratio of air taken equal to 1.4, and D and γ_m are the detonation velocity and specific heat ratio of FAM, respectively. Two sets of estimated data for a_m, M_s, p_s and T_s are presented in Table 1: (1) for $D = D_{st} = 1800$ m/s and $\gamma_m = 1.4$ characteristic for stoichiometric hydrocarbon–air mixtures, and (2) for $D = D_{lean} = 1600$ m/s and $\gamma_m = 1.4$ characteristic for the

fuel-lean mixtures of fuel–air ratio $\Phi \approx 0.6$. Examination of Table 1 shows that at Mach number 2.0 the inlet conditions in the detonation chamber may range from 520 K and 6.5 bar at sea level to 400 K and 1.7 bar at 10 km. The effect of changing the flight Mach number on the inlet air temperature and pressure may be seen in the range of operation conditions at 10 km, where the inlet conditions in the detonation chamber vary from 270 K and 0.5 bar at Mach number 1.0 to 400 K and 1.7 bar at Mach number 2.0. Clearly, according to the data of Table 1, the fuel should detonate within the range of initial temperatures from 270 K to 520 K and initial pressures from 0.5 bar to 6.5 bar.

Other observations come from examining the data for p_s and T_s in Table 1. Depending on the Mach number and flight altitude, the pressure in the leading shock wave is expected to range from 14 to 94 bar for fuel-lean mixtures and from 17 to 120 bar for the stoichiometric composition, while the shock temperature changes from approximately 1240 K for the fuel-lean mixture to 1570 K for the stoichiometric composition. At fixed flight Mach number and altitude, the shock pressure and temperature in fuel-lean and stoichiometric mixtures differ by a factor $(D_{st}/D_{lean})^2$, i.e. by about 27%.

Taking into account the dependence of both physical and chemical processes constituting the operation phases of PDE on temperature and pressure, one realizes that special measures should be taken in order to ensure proper timing between repeated detonation initiation and fuel injection. Note that the critical initiation energy depends on the initial temperature and pressure, and on mixture composition. For detonating lean hydrocarbon–air mixtures detonation tubes of large diameter are required. The humidity of air is also known to effect the fuel detonability [4]. Thus, one concludes that the basic requirement to the PDE fuel is that it should readily detonate with low sensitivity to initial conditions in terms of temperature and pressure. In addition, since the PDE should operate at the lowest possible overall fuel–air ratio and high combustion efficiency, the PDE fuel should exhibit wide detonability limits in terms of mixture composition.

Another requirement to the PDE fuel, which contradicts the above requirements, is avoiding surface ignition of FAM before or after triggering the initiator, or uncontrolled auto-ignition of FAM due to mixing with residual combustion products. Premature ignition is expected to arise near the hot walls of the detonation chamber (at temperatures exceeding 600–800 K), providing that the cycle duration is longer than the auto-ignition delay of the FAM. In view of it, the PDE fuel should exhibit high resistance to ignition by a hot surface. A particular issue is avoiding premature ignition in the vicinity of the initiator. It is expected that the surfaces located near the initiator and the initiator itself can get very hot during operation, and the abnormal combustion can produce thermal damage in a very short time.

For propulsion applications, the PDE fuel is preferably a liquid hydrocarbon (or other liquid compound) due to high energy density. The requirement of fast mixing of fuel with incoming air implies that the PDE fuel should exhibit high

vapor pressure at operation conditions. One of possible solutions is recuperative fuel preheating. The presence in the PDE fuel of non-volatile hydrocarbons and additives containing metals and polymeric compounds can promote premature ignition due to their deposit-forming tendency. The deposits are known to produce the thermal isolation effect increasing the wall temperature.

In addition to the fuel detonability requirements mentioned above, a set of vehicle design requirements (low pressure loss, low weight, size constraints, etc.) should be met. Clearly, some of the requirements appear to be quite contradictory, and a sort of compromise must usually be achieved.

It is hardly possible that a single fuel could meet the requirement of high detonability, on the one hand, and low reactivity at temperatures less than or about 800 K relevant to the premature ignition phenomenon, on the other hand. A possible solution is to apply two fuels with essentially different detonability rather than a single fuel. In this case, a readily detonable compound should be distributed closer to an initiator, and the less sensitive compound — in the rest of the detonation chamber. This implies that distributed injection of both fuels along the detonation chamber could be applied. In view of it, a number of problems arise dealing with detonability of fuel blends within the wide range of pressure, temperature and mixture composition. The most intricate problems are:

- controlling a local fuel–air ratio in the vicinity of the initiator to ensure robust initiation of detonation at variable conditions;

- controlling fuel distribution along the detonation chamber to ensure a desired detonability and sensitivity to premature ignition;

- maintaining a desired overall fuel–air ratio in the course of repeated detonation initiation.

Clearly, for assessing the detonability of fuel blends, a proper criterion should be introduced. There exist several available approaches based on the concepts of (1) Octane Number, coming back to late 20-s [4, 5, 3], (2) detonation run-up distance [6], (3) critical initiation energy [7, 8], and (4) limiting tube diameter [9, 10].

The ON concept is usually applied to a test fuel in a piston engine to assess the detonability in terms of the percentage of *iso*-octane (by volume) in the *n*-heptane–*iso*-octane blend that matches the test fuel in allowable compression ratio. Since there are definite reasons of considering engine 'knock' to be identical to the detonation phenomenon [11], the ON concept seems attractive for at least qualitative analyses. In spite of certain limitations of the concept, we will use it to illustrate how one can control detonability by applying fuel blends in PDE. For this purpose, we have undertaken a kinetic study of the auto-ignition behavior of *n*-heptane–*iso*-octane blends under the conditions specified above.

318

3 OXIDATION MECHANISMS FOR HEAVY HYDROCARBONS

Kinetic submodels for studying auto-ignition, combustion, and detonation processes in PDE must simulate phenomenological features typical for hydrocarbon fuel oxidation within the wide ranges of pressure and temperature outlined above. This implies that both low- and high-temperature oxidation mechanisms should be incorporated into a kinetic submodel [11]. Simultaneous action of both mechanisms can result in two-stage auto-ignition. Hydrocarbons exhibiting two-stage auto-ignition are known to have substantially wider auto-ignition limits.

The kinetic mechanism in the two-stage regime is very complicated. At the first stage of induction period, typical features of cool flames manifest themselves. These include significant amounts of peroxides and specific variation of the reaction rate with temperature and pressure. At the second stage, typical features of high-temperature ignition (hot explosion) are observed.

At low temperatures and elevated pressures, auto-ignition reactions proceed mainly through the low-temperature mechanism, sometimes until hot explosion. At high temperatures and low pressures, the high-temperature mechanism dominates. Paraffin hydrocarbons, and certain other hydrocarbons and their derivatives exhibit two-stage auto-ignition. However, there is a number of fuels which do not ehxibit cool flames in the course of their auto-ignition. The primary reference hydrocarbons exemplifying the conventional fuels (gasoline, kerosene, etc.) applied in transportation and propulsion devices are n-heptane and iso-octane. Therefore, our attention here is restricted to considering the oxidation of n-heptane–iso-octane blends.

In general, the kinetics of n-heptane and iso-octane oxidation must contain the oxidation mechanisms of methane (involving H_2, CO, H_2CO), C_2-hydrocarbons (C_2H_2, C_2H_4, C_2H_6), heavy hydrocarbons of various structures and their oxygen compounds (alcohols, aldehydes, ethers, etc.). The kinetic mechanisms of methane and methanol oxidation developed so far appear to be quite satisfactory. Oxidation mechanisms of C_2- and heavier hydrocarbons have been developed to a far lesser extent. Nevertheless, some versions of a detailed reaction mechanism of n-heptane and iso-octane oxidation are available in literature.

Mechanisms of n-heptane oxidation for studying n-heptane flames are reported in [12, 13]. No reactions responsible for n-heptane auto-ignition are included in the mechanisms. A detailed kinetic mechanism for n- and iso-octane oxidation was proposed in [14, 15]. The mechanism contains about 500 reactions with 70 reactants; however, it is applicable at relatively high initial temperatures, $T > 850$–900 K. An automatic procedure of generating a reaction mechanism for n-heptane was used in [16]. As a result, a detailed kinetic scheme was developed containing 2300 elementary stages with 620 reactants. This scheme is claimed

319

to represent a non-empirical reaction mechanism. Recently, a detailed reaction mechanism for n-heptane oxidation was developed [17]. Discussed in [17] are the classes of elementary reactions and reaction pathways relevant to the oxidation process. It is shown that the mechanism provides generally a good agreement between computed and measured results in flow reactors, shock tubes, and rapid compression machines at initial pressure $p_0 = 1$–42 bar, temperature $T_0 = 550$–1700 K, equivalence ratio $\Phi = 0.3$–1.5 and nitrogen–argon dilution 70-99%. Unfortunately, the mechanism itself is not reported.

General features of an empirical scheme for n-heptane oxidation containing 4 reactions with 5 reactants were reported in [18]. A relatively concise reaction scheme of n-heptane oxidation was used in [19]; however, the scheme itself was not presented. A semi-empirical four-step description of n-heptane auto-ignition is proposed in [20]. Nowadays, such mechanisms are most suitable in terms of the number of reacting species, since they exhibit two-stage auto-ignition followed by combustion and, at the same time, they are sufficiently concise to be efficiently used in multidimensional calculations.

Presented below is a reaction mechanism developed for studying auto-ignition of iso-octane, n-heptane and their blends under conditions relevant to PDE.

4 OXIDATION MECHANISM FOR n-HEPTANE–iso-OCTANE BLENDS

Modeling of two-stage auto-ignition of hydrocarbon fuels is based on well-known principles discussed elsewhere [11, 16–22]. At low temperatures (roughly below 800 K), reaction branching is assumed to proceed through alkyl peroxide decomposition, whereas at higher temperatures (roughly above 1100 K) it is due to decomposition of hydrogen peroxide, also involving reactions of formaldehyde (with a further temperature increase, the branching process tends to go on mainly through the reaction of H atom with oxygen). Transition between the branching mechanisms is, most probably, a result of the temperature increase and change in the relative rates of formation, isomerization and decomposition of alkyl peroxide radical RO_2, as well as subsequent reactions of emerging products with each other, and with oxygen and radicals.

The initial kinetic mechanism of n-heptane and iso-octane oxidation contains two groups of reactions. The first group is the auto-ignition block (see Table 2).
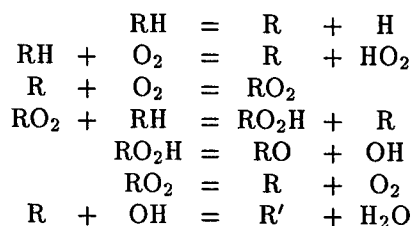
It contains 29 reactions with 26 reactants, including a few empirical reactions written in a conventional form of elementary stages (reactions 3, 11, 12, 25, and 29). They are included to reduce C_7- and C_8- to C_1- and C_2-hydrocarbons. Note that in some relevant papers, less severe, but less compact, reductions are used, e.g., in [12, 13] from C_7–C_8- to C_3–C_4- hydrocarbons. No chemical or physical law is violated when considering all these reactions together. Formally,

Table 2 The block of reactions describing auto-ignition chemistry of n-heptane–iso-octane–air mixture

No.	Reaction	$A/(l,mol,s)$	n	$(E/R)/K$	$H/(cal/mol)$
1	$C_7H_{16} \Rightarrow C_7H_{15} + H$	4.300e+14	0.000	3.500e+04	-9.630e+04
2	$C_7H_{15} \Rightarrow C_6H_{12} + CH_3$	4.300e+14	0.000	2.500e+04	-4.000e+04
3	$C_6H_{12} + O_2 \Rightarrow C_2H_4O_2 + C_2H_3 + C_2H_5$	2.000e+10	0.000	0.000e+00	4.170e+04
4	$C_7H_{16} + OH \Rightarrow C_7H_{15} + H_2O$	4.800e+07	0.000	5.000e+02	2.170e+04
5	$C_7H_{15} + O_2 \Rightarrow C_7H_{15}O_2$	2.770e+07	0.000	-5.000e+02	2.200e+04
6	$C_7H_{15}O_2 \Rightarrow C_7H_{15} + O_2$	2.000e+14	-1.000	1.250e+04	-2.200e+04
7	$C_7H_{15}O_2 + C_7H_{16} \Rightarrow C_7H_{15}O_2H + C_7H_{15}$	1.000e+06	0.000	1.000e+02	-7.000e+03
8	$C_7H_{16} + O_2 \Rightarrow HO_2 + C_7H_{15}$	1.500e+06	0.000	2.000e+04	-5.330e+04
9	$CH_3O_2 + C_7H_{16} \Rightarrow CH_3O_2H + C_7H_{15}$	1.200e+06	0.000	5.000e+02	-2.300e+03
10	$C_7H_{15}O_2H \Rightarrow C_7H_{15}O + OH$	4.300e+13	0.000	1.500e+04	-4.300e+04
11	$C_7H_{15}O \Rightarrow C_6H_{11} + CH_3 + OH$	1.330e+13	0.000	1.300e+04	-1.150e+05
12	$C_6H_{11} + O_2 \Rightarrow C_2H_4O_2 + C_2H_3$	2.000e+10	0.000	0.000e+00	1.994e+05
13	$C_7H_{15}O_2 + C_7H_{15} \Rightarrow C_7H_{15}O + C_7H_{15}O$	3.600e+08	0.000	0.000e+00	3.060e+04
14	$C_7H_{15}O_2 + HO_2 \Rightarrow C_7H_{15}O_2H + O_2$	2.230e+06	0.000	-1.300e+03	4.630e+04
15	$C_7H_{15} + HO_2 \Rightarrow OH + C_7H_{15}O$	9.000e+06	0.000	0.000e+00	2.530e+04
16	$C_8H_{18} \Rightarrow C_8H_{17} + H$	4.000e+14	0.000	3.500e+04	-9.600e+04
17	$C_8H_{17} \Rightarrow C_6H_{12} + C_2H_5$	4.000e+14	0.000	2.500e+04	-3.870e+04
18	$C_8H_{18} + OH \Rightarrow C_8H_{17} + H_2O$	2.400e+08	0.000	2.000e+03	2.200e+04
19	$C_8H_{17} + O_2 \Rightarrow C_8H_{17}O_2$	2.400e+07	0.000	0.000e+00	2.170e+04
20	$C_8H_{17}O_2 \Rightarrow C_8H_{17} + O_2$	1.920e+14	-1.000	1.150e+04	-2.170e+04
21	$C_8H_{17}O_2 + C_8H_{18} \Rightarrow C_8H_{17}O_2H + C_8H_{17}$	2.400e+06	0.000	1.250e+03	-7.100e+03
22	$C_8H_{18} + O_2 \Rightarrow HO_2 + C_8H_{17}$	2.400e+09	0.000	2.500e+04	-5.300e+04
23	$CH_3O_2 + C_8H_{18} \Rightarrow CH_3O_2H + C_8H_{17}$	2.400e+06	0.000	1.000e+03	-2.000e+03
24	$C_8H_{17}O_2H \Rightarrow C_8H_{17}O + OH$	4.000e+13	0.000	1.500e+04	-4.300e+04
25	$C_8H_{17}O \Rightarrow C_6H_{11} + CH_3 + CH_3O$	1.200e+13	0.000	1.300e+04	-8.700e+04
26	$C_8H_{17}O_2 + C_8H_{17} \Rightarrow C_8H_{17}O + C_8H_{17}O$	3.200e+08	0.000	0.000e+00	2.950e+04
27	$C_8H_{17}O_2 + HO_2 \Rightarrow C_8H_{17}O_2H + O_2$	2.000e+06	0.000	-1.300e+03	4.590e+04
28	$C_8H_{17} + HO_2 \Rightarrow OH + C_8H_{17}O$	8.000e+06	0.000	0.000e+00	2.460e+04
29	$C_2H_4O_2 \Rightarrow CO_2 + CH_4$	4.000e+15	0.000	0.000e+00	0.000e+00

the endothermic reaction 29 is represented as thermally neutral; however, when considering reactions 3, 12, and 29 together, the heat balance is not violated. The remaining 24 auto-ignition reactions are realistic. They have been selected from hundreds of reactions for C_7–C_8-hydrocarbons (the breaking of C–C and C–H bonds, the reactions of addition, isomerization, decomposition, disproportionation, etc., see for example [17]) and are designed to represent a realistic oxidation process. Therefore, the Arrhenius parameters adopted for these reactions, as derived from the ignition delay time calculations, differ from the actual values published in available literature.

The reactions of the auto-ignition block describe cool flames and two-stage auto-ignition under certain critical conditions. They include competing reactions (separately for n-heptane and iso-octane) which ensure transition from low-temperature to high-temperature oxidation mechanism and differ from already existing kinetic mechanisms, although the basic steps in this kinetic mechanism are represented by the well-known processes:

$$
\begin{aligned}
RH &= R + H \\
RH + O_2 &= R + HO_2 \\
R + O_2 &= RO_2 \\
RO_2 + RH &= RO_2H + R \\
RO_2H &= RO + OH \\
RO_2 &= R + O_2 \\
R + OH &= R' + H_2O
\end{aligned}
$$

where $R = C_7H_{15}$ or C_8H_{17}.

The second group of reactions is a non-empirical detailed oxidation mechanism of C_1–C_2-hydrocarbons containing 255 elementary reactions with 30 reactants (some of them similar to those in the first block), described in detail in [23]. In the present study, it is modified for application to a wider range of initial pressures, from sub-atmospheric to 100 bar. The position of the transition zone between low and high pressures for decomposition and recombination reactions is known [24] to depend on both the number of atoms in a molecule and the molecule structure. It is taken into account that the decomposition (recombination) reactions of multi-atomic molecules exhibit bi-molecular (tri-molecular) behavior at low pressure and mono-molecular (bi-molecular) behavior at high pressure. In the intermediate pressure range, the approach [25] was applied. For extending the mechanism to sub-atmospheric pressures (0.5–1 bar), the versions of the kinetic scheme incorporating some important heterogeneous processes and the molecular heat transfer to the reactor wall were used.

Verification of the kinetic mechanism for pressures exceeding 15 bar was made earlier in [26–28] by comparing predicted auto-ignition delay times with available measurement data [29–40]. The ignition delay time was calculated by assuming a homogeneous, isochoric, adiabatic ignition process, and was obtained from temperature histories, as well as the histories of alkyl peroxide radical

concentration. The ignition delay time was defined as the time interval required for the rate of temperature rise to reach the value of 10^7 K/s [41]. Also checked were some alternative definitions of ignition delay time [34, 42]. The induction time of a cool flame was defined as the time interval required for the concentration of alkyl peroxide to reach a maximum value.

It is shown in [26–28] that the kinetic mechanism provides a good agreement with measured ignition delays and the concentration histories of basic species within wide ranges of initial pressure (15–40 bar), temperature (800–1200 K), and fuel–air ratio (0.5–2). Three reduced reaction mechanisms containing (1) 27 reactions and 18 species, (2) 23 reactions and 16 species, and (3) 21 reactions and 13 species were developed in [28].

5   CONTROL OF DETONABILITY

Figure 2, taken from [43], shows the measured dependence of ignition delay τ_i of various stoichiometric n-heptane–iso-octane–air mixtures at temperature $T_0 = 900$ K and pressure $p_0 \approx 10$ bar. The measurements in [43] were made in a rapid compression machine. Clearly, depending on the mixture ON, the ignition delay varies from $\tau_i \approx 3$ ms for ON $= 0$ to $\tau_i \approx 20$ ms for ON $= 100$. The sensitivity of τ_i to the ON varies non-linearly, being most sensitive in the region of ON $= 60$. There is no evident change of τ_i in the ranges $90 <$ ON < 100 and $0 <$ ON < 30.

A more detailed diagram showing the predicted dependence of τ_i on the ON of the stoichiometric n-heptane–iso-octane–air mixture at a pressure $p_0 = 15$ bar and temperatures $670 < T_0 < 1200$ K is presented in Fig. 3. Three important observations follow from analizing the figure:

1. At a fixed ON and low temperatures (670–900 K), the ignition delay for the fuel blend is almost insensitive to temperature. With temperature increase, the range of Octane Numbers where τ_i remains insensitive to temperature narrows (e.g., at $T_0 = 900$ K, it is $0 <$ ON < 30).

2. At low temperatures (670–900 K), the ignition delay for the blends of different ON may differ by an order of magnitude, being the lowest for ON $= 0$, and the highest for ON $= 100$. The highest sensitivity of τ_i to ON is attained at the lower temperature (670 K).

3. At high temperatures ($T_0 > 1000$ K), the ignition delay for the blends with ON < 80–90 is almost insensitive to ON.

Shown in Fig. 4 are the temperature histories of auto-ignition for fuel blends of ON $= 0$ (curves 1), 60 (2), 90 (3), and 100 (4) at $T_0 = 670$ K (a), 750 K (b),
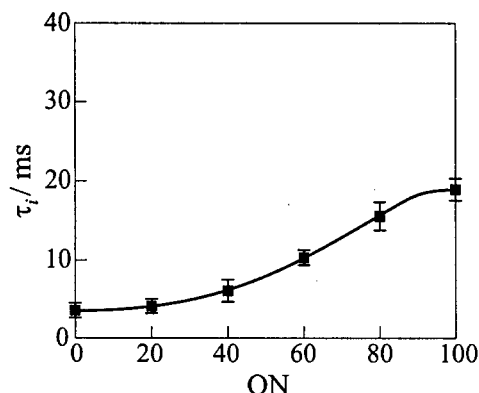
323

Figure 2 Measured dependence of the ignition delay of various stoichiometric n-heptane–iso-octane–air mixtures at temperature $T = 900$ K and pressure $p_0 \approx 10$ bar. The measurements were made in a rapid compression machine [43]
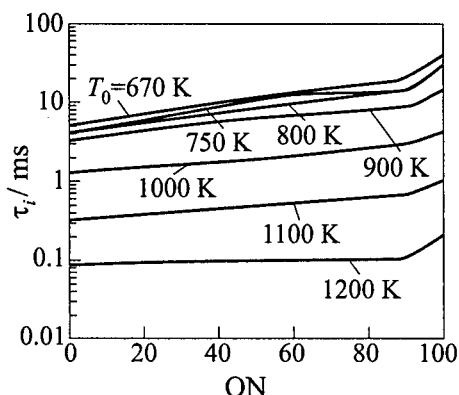
Figure 3 Predicted effect of the Octane Number on the ignition delay of the stoichiometric n-heptane–iso-octane mixture at initial pressure $p_0 = 15$ bar and different initial temperatures T_0

800 K (c), and 1150 K (d). The curves in Fig. 4 are terminated in points where the rate of temperature rise attains the value of 10^7 K/s (ignition criterion). It follows from the figure that with temperature increase the two-stage temperature history transforms into a single-stage process. The iso-octane–air mixture (ON = 100) exhibits the longest duration of the cool-flame stage.

Figure 5 shows the predicted effect of pressure on the ignition delay of fuel-lean ($\Phi = 0.5$) iso-octane–air mixture (ON = 100) at $T_0 = 800$ K. Plotted for comparison are the experimental data of [40] for $\Phi = 0.5$ (points 1), [35] for $\Phi = 1.0$ (2) and [11] for $\Phi = 1.0$ (3). At initial pressures $1 < p_0 < 30$–40 bar, the sensitivity of τ_i to p_0 is significantly higher than at $p_0 > 30$–40 bar.

Figure 6 shows the predicted temperature histories for the auto-ignition of lean ($\Phi = 0.5$) iso-octane–air mixture at $T_0 = 800$ K and pressure $p_0 = 20$ bar (curve 1), 28 bar (2), 37 bar (3), 40 bar (4), and 50 bar (5). The duration of the cool-flame stage decreases non-linearly with pressure, being almost insensitive to pressure at $p_0 = 50$ and 40 bar, and increasing significantly at $p_0 < 40$ bar.

The predicted effect of fuel–air ratio and temperature on the ignition delay of the fuel blend with ON = 90 at $p_0 = 40$ bar is shown in Fig. 7. The ignition delay of the fuel-rich mixture ($\Phi = 2.0$) appeared to be shorter than that of the stoichiometric mixture within a wide range of temperatures. This result agrees with experimental findings (see [18]). Such a behavior of fuel-rich mixtures is reasonable, since these mixtures are known to exhibit higher sensitivity to cool-
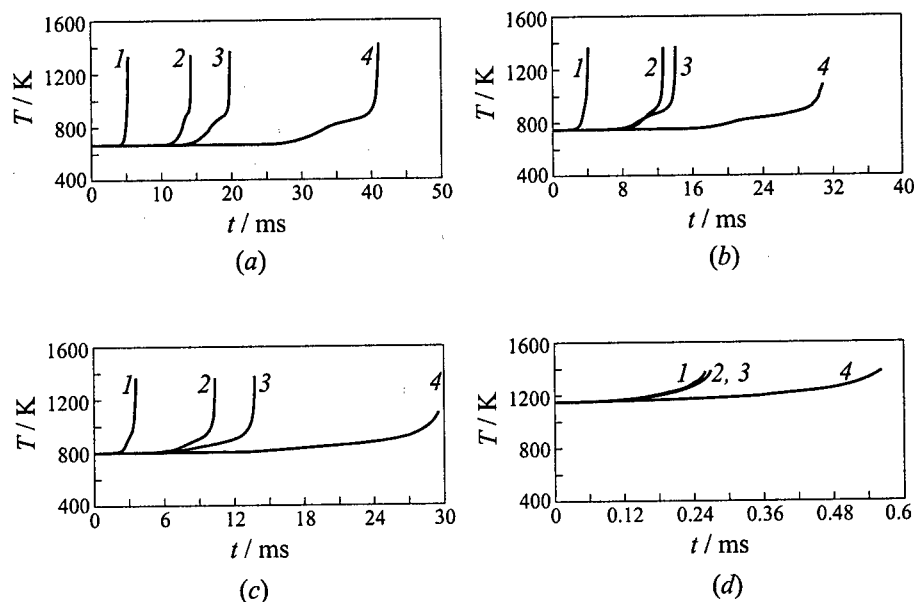
324

Figure 4 Predicted temperature histories of auto-ignition for n-heptane–iso-octane blends of Octane Number ON $= 0$ (curves 1), 60 (2), 90 (3), and 100 (4) at $T_0 = 670$ K (a), 750 K (b), 800 K (c), and 1150 K (d) and $p_0 = 15$ bar. The curves are terminated in points where the rate of temperature rise attains the value of 10^7 K/s (theoretical ignition criterion)

flame chemistry and ignition staging than stoichiometric and fuel-lean mixtures. The latter is illustrated by Fig. 8 showing the temperature histories of auto-ignition of fuel-lean (curve 1), stoichiometric (2), and fuel-rich mixture of ON $= 90$ at $p_0 = 40$ bar and $T_0 = 670$ K.

Thus, within the framework of the fuel blend detonability concept based on the Octane Number, it is possible to elaborate detonability control strategies aimed at meeting the requirements for the PDE operation. Depending on the designed operation frequency of PDE, vehicle size, flight Mach number and altitude, one can readily estimate the timing of PDE operation phases. To avoid uncontrolled auto-ignition and premature ignition, the FAM of high ON should be arranged in the flow regions that are most distant from the initiator. At the operation frequency greater than 100 Hz, the ignition delay exceeding 10 ms seems satisfactory. According to Fig. 3, such ignition delays are attained for stoichiometric and fuel-lean compositions with ON > 60 at $p < 15$ bar and $T < 800$ K. Fuel-rich mixtures should be avoided in these regions (see Fig. 8).
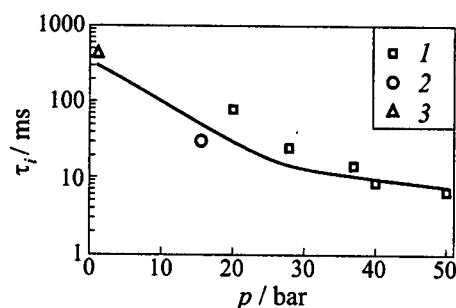
325

Figure 5 Predicted effect of pressure on the ignition delay of fuel-lean ($\Phi = 0.5$) iso-octane–air mixture (ON = 100) at $T_0 = 800$ K. Symbols correspond to experimental data of [40] for $\Phi = 0.5$ (points 1), [35] for $\Phi = 1.0$ (2) and [11] for $\Phi = 1.0$ (3)
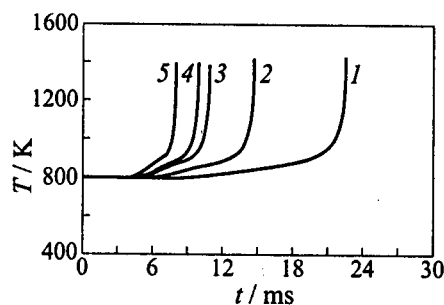
Figure 6 Predicted temperature histories for the auto-ignition of lean ($\Phi = 0.5$) iso-octane–air mixture at $T_0 = 800$ K and pressure 20 bar (curve 1), 28 bar (2), 37 bar (3), 40 bar (4), and 50 bar (5)

An increase in the operation pressure and temperature requires transition to the fuel-lean mixtures with higher ON in the regions at risk of premature ignition (Figs. 5 to 7).

Detonation initiation is a special issue. Intuitively, mixture composition near the initiator should have the lowest possible ON and/or special promoting additives should be locally injected. The initiation energy, the type and a number of initiators and their locations are the issues of primary importance for further research. Available data for the initiation energies of gaseous [44] and heterogeneous [45] detonations are obtained basically at the normal ambient temperature, sub-atmospheric and ambient pressures, and for spatially uniform fuel distribution. In most relevant studies, primary reference fuels were detonated rather than the fuel blends. The problem is also compounded by the fact that there is little information on detonation transition through the stratified FAM [46–48].

It is important to find out, whether a fully-developed detonation is necessarily needed for attaining a high performance of PDE or an accelerating shock-flame complex could also be a good solution. In the latter case, the requirements to the initiation sources and their energy would be much less severe. Anyway, the concept of fuel charge stratification near the initiator and along the detonation tube seems to have a number of advantages in that it may be effective in solving the problem of premature ignition and reducing the overall fuel–air ratio of PDE operation.

The reaction mechanism used in this study, and in particular, the reduced reaction mechanisms [28] allows, in principle, 1D and 2D numerical simula-
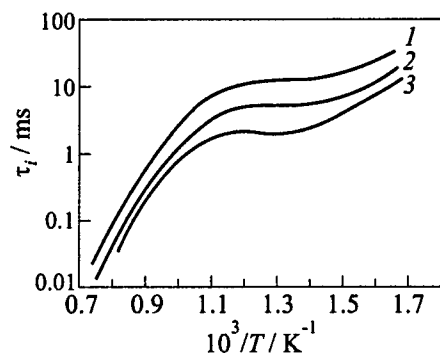
326

Figure 7 Predicted effect of fuel–air ratio and temperature on the ignition delay of the fuel blend with Octane Number ON = 90 at p_0 = 40 bar. 1 — Φ = 0.5, 2 — 1.0, 3 — 2.0
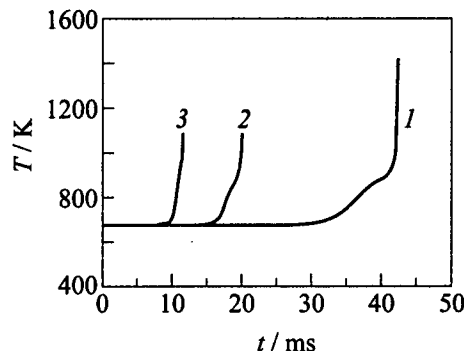
Figure 8 Predicted temperature histories of auto-ignition of fuel-lean mixture with Φ = 0.5 (curve 1), stoichiometric (2), and fuel-rich mixture with Φ = 2.0 (3) of ON = 90 at p_0 = 40 bar and T_0 = 670 K

tions of processes in PDE to be performed. The proposed kinetic models cover the whole range of PDE operation parameters, including ignition, auto-ignition, flame propagation and detonative combustion. However, when applying 1D numerical simulation, a caution is necessary in using the reaction mechanisms to modeling detonation initiation and propagation [49]: the reaction times in 1D detonation structure can be significantly underestimated if the non-uniformity of ignition in realistic detonation fronts is not taken into account.

6 CONCLUDING REMARKS

The characteristics of detonability — auto-ignition delay — are studied theoretically for the n-heptane–iso-octane blends. The study is based on the semi-empirical oxidation mechanism containing two blocks of reactions: (1) a semi-empirical block including reduction reactions of high hydrocarbons to C_1–C_2-hydrocarbons and the reactions of high peroxides responsible for low-temperature oxidation, and (2) a non-empirical block of oxidation reactions of C_1–C_2-hydrocarbons. Characteristic reaction times were calculated for a wide range of conditions meeting the PDE operation: ON (0–100), temperature (650–1200 K), pressure (1–100 bar), fuel–air ratio (0.5–2.0). It is shown that the change in the FAM Octane Number and composition along the detonation chamber allows efficient control of detonability in PDE and, if required, sustenance of a desired detonability under variation of conditions in the PDE.

327

ACKNOWLEDGMENTS

REFERENCES

1. Frolov, S. M., Basevich, V. Ya., Belyev, A. A., and Neuhaus, M. G., In: G. D. Roy, S. M. Frolov, K. Kailasanath, and N. N. Smirnov Eds. *Advances in Experimentation and Computation of Detonations. Book of Abstracts.* ENAS Publ., Moscow, 106, 1998.

2. Loitsianskii, L. G., *Fluid Mechanics.* 5th Edition, Nauka, Moscow, 736, 1978.

3. Owen, K., and Coley, T., *Automotive Fuels Handbook.* Warrendale, PA, SAE Inc., 108, 1990.

4. Campbell, C., Lovell, P., and Boyd, T. A., *Ind. and Eng. Chem.*, **20**, 1045, 1928.

5. Campbell, C., Lovell, P., and Boyd, T. A., *Ind. and Eng. Chem.*, **23**, 26, 555, 1931.

6. Sokolik, A. S., *Combustion and Detonation in Gases.* Gostekhteorizdat, Moscow–Leningrad, 1934.

7. Zel'dovich, Ya. B., Kogarko, S. M., and Simonov, N. N., *Sov. J. Technical Physics,* 1744, 1956. Translation: *Sov. J. Phys. Techn.*, **1**, 1689, 1957.

8. Bach, G. G., Knystautas, R., and Lee, J. H., *Proc. 12th Symposium (International) on Combustion*, The Combustion Institute, Pittsburgh, PA, 1967, 665.

9. Frolov, S. M., In: A. G. Merzhanov and S. M. Frolov Eds. *Combustion, Detonation, Shock Waves. Proc. Zel'dovich Memorial.* **1**, ENAS Publ., Moscow, 266, 1995.

10. Agafonov, G. L., and Frolov, S. M., *Rus. J. Physics Combustion Explosion*, **28**, 2, 189, 1994.

11. Sokolik, A. S., *Selfignition, Flame and Detonation in Gases.* Israel Program for Scientific Translation, Jerusalem, 1963.

12. Warnatz, J., *Proc. 20th Symposium (International) on Combustion*, The Combustion Institute, Pittsburgh, PA, 1984, 845.

13. Bui-Pham, M., and Seshadri, K., *Combustion Science Technology*, **79**, 293, 1991.

14. Axelsson, E. I., Brezinsky, K., Dryer, F. L., Pitz, W. J., and Westbrook, C. K., *Proc. 21st Symposium (International) on Combustion*, The Combustion Institute, Pittsburgh, PA, 1987, 783.

15. Axelsson, E. I., Brezinsky, K., Dryer, F. L., Pitz, W. J., and Westbrook, C. K., Lawrence Livermore National Laboratory Report UCRL–94449, 1986.

16. Chevalier, C., Goyal, G., Louessard, P., and Warnatz, J., *Proc. Joint Meeting of the Soviet and Italian Sections of the Combustion Institute*, Pisa, 1990, 5.10.

17. Curran, H. J., Gaffuri, P., Pitz, W. J., and Westbrook, C. K., *Combustion Flame*, **114**, 149, 1998.

18. Müller, U. S., Peters, N., and Linan, A., *Proc. 24th Symposium (International) on Combustion*, The Combustion Institute, Pittsburgh, PA, 1992, 777.

19. Poppe, Ch., Schreber, M., and Griffiths, J. F., *Proc. Joint Meeting of the British and German Sections of the Combustion Institute*, Cambridge, 1993, 360.

20. Williams, F. A., In: G. D. Roy Ed. *Propulsion Combustion: Fuels to Emissions.* Washington, Talor & Francis, 93, 1998.

21. Benson, S. W., *J. American Chem. Society*, **87**, 972, 1965.

22. Kondrat'ev, V. N., *Comprehensive Chemical Kinetics.* Elsevier Publ., New York, 1969.

23. Basevich, V. Ya., In: N. P. Cheremisinoff Ed. *Handbook of Heat and Mass Transfer.* Gulf Publ. Co., Houston, 769, 1990.

24. Robinson, P. J., and Holbrook, K. A., *Unimolecular Reactions.* London, 1972.

25. Luther, K., Troe, J., *Proc. 17th Symposium (International) on Combustion*, The Combustion Institute, Pittsburgh, PA, 1978, 535.

26. Basevich, V. Ya., Belyaev, A. A., Brandstätter, W., Frolov, S. M., Neuhaus, M. G., and Tatschl, R., In: S. M. Frolov Ed. *Combustion, Detonation, Shock Waves. Proc. Zel'dovich Memorial.* **2**, ENAS Publ., Moscow, 5, 1994.

27. Basevich, V. Ya., Belyaev, A. A., Brandstätter, W., Neuhaus, M. G., Tatschl, R., and Frolov, S. M., *Rus. J. Physics Combustion Explosion*, **30**, 6, 15, 1994.

28. Basevich, V. Ya., and Frolov, S. M., *Rus. J. Chemical Physics*, **13**, 8-9, 146, 1994.

29. Teichmann, H., *Zeitschrift fur Elektrochemie und Angewandte Physikalische Chemie*, **47**, 297, 1941.

30. Scheuermeyer, M., and Steigerwald, H., *Motortechn. Z.*, **5**, 229, 1943.

31. Roegener, H., *Zeitschrift fur Elektrochemie und Angewandte Physikalische Chemie*, **53**, 389, 1949.

32. Taylor, C. F., Taylor, E. S., Livengood, J. C., Russell, W. A., and Leary, W. A., *SAE Quart. Trans.*, **4**, 232, 1950.

33. Voinov, A. N., Skorodelov, D. I., Borisov, A. A., and Lyubimov, A. V., *Sov. J. Physical Chemistry*, **41**, 1150, 1967.

34. Halstead, M. P., Kirsch, L. J., Prothero, A., and Quinn, C. P., *Proc. Royal Society London*, **A346**, 1647, 1975.

35. Halstead, M. P., Kirsch, L. J., and Quinn, C. P., *Combustion Flame*, **30**, 45, 1977.

36. Cox, R. A., and Cole, J. A., *Combustion Flame*, **60**, 109, 1985.

37. Fieweger, K., Ciezki, H., and Adomeit, G., *Proc. 19th Symposium (International) on Shock Waves. Book of Abstracts*, Universite de Provence Publ., Marseille, 1, 1993, 253.

38. Ciezki, H., and Adomeit, G., *Proc. 16th Symposium (International) on Shock Tubes and Waves*, Niagara Falls, 1987, 481.

39. Downs, D., Walsh, A. D., and Wheeler, R. W., *Phil. Trans. Roy. Soc.*, **A243**, 463, 1951.

329

40. Fish, A., Read, L. A., Affleck, W. S., and Haskell, W. W., *Combustion Flame*, **13**, 39, 1969.

41. Schapertons, H., and Lee, W., SAE Paper No.850502, 1985.

42. Natarajian, B., and Bracco, F. V., *Combustion Flame*, **57**, 179, 1984.

43. Griffiths, J. F, Halford-Maw, P. A., and Mohamed, C., *Combustion Flame*, **111**, 327, 1997.

44. Vasil'ev, A. A., Mitrofanov, V. V., and Topchian, M. E., *Sov. J. Physics Combustion Explosion*, **23**, 5, 109, 1987.

45. Vasil'ev A. A., Zhdan, S. A., and Mitrofanov, V. V., In: G. D. Roy, S. M. Frolov, K. Kailasanath, and N. N. Smirnov Eds. *Gaseous and Heterogeneous Detonations: Science to Applications*. Moscow, ENAS Publ., 25, 1999.

46. Donato, M., Donato, L., and Lee, J. H. S, *Proc. 1st Specialist Meeting (International) of The Combustion Institute*, Bordeaux, 1982, 467.

47. Thomas, G. O., Sutton, P., and Edwards, P. N., *Combustion Flame*, **84**, 312, 1984.

48. Benoan, F., and Teodorczyk, A., *Archivum Combustionis*, **13**, 1–2, 21, 1993.

49. Borisov, A. A., In: G. D. Roy, S. M. Frolov, K. Kailasanath, and N. N. Smirnov Eds. *Gaseous and Heterogeneous Detonations: Science to Applications*. Moscow, ENAS Publ., 3, 1999.

SUPPRESSION OF DETONATIONS BY EFFICIENT INHIBITORS

V. V. Azatyan, H.-Gg. Wagner, G. K. Vedeshkin, and R. G. Aivazyan

New experimental results on suppression of detonation of hydrogen–air mixtures at atmospheric and elevated pressures by means of gas-phase inhibitors, which are significantly more efficient than halons, are described. The important role of the chain mechanism in different modes of gas-phase combustion of hydrogen-containing compounds and a number of other combustible gases is considered.

INTRODUCTION

The influence of inhibitors on combustion processes provides perspective methods for combustion control. As is known, inhibition of combustion is caused by the intensification of chain termination via reactions involving the inhibitor. The peculiarities and mechanisms of branching-chain reactions and, in particular, their inhibition, are usually investigated at very low pressures. As the present paper is devoted to inhibition of detonations at atmospheric pressure, at first we briefly consider the role of competition between the reactions of chain branching and termination in various combustion modes under atmospheric and elevated pressures.

It has been commonly accepted for a long time that ignition and combustion of gases at pressures exceeding a few dozen Torrs resulted by progressively accelerating self-heating of a reactive mixture. For the model branching-chain process, that is, combustion of hydrogen in oxygen atmosphere, these pressures were considered to be bounded by the second self-ignition limit at moderate temperatures. As to the third ignition limit, so far it was commonly considered as having a "purely" self-heating origin and exhibiting self-heating behavior (e.g. [1–8]). In exclusively rare cases, it was recognized in principle, that the gas-phase combustion occurs by a chain mechanism. However, even in these cases, the occurrence of the process at pressures exceeding dozens of Torrs was regarded only in terms of the conventional thermal theory of combustion, using the equations of simple

reactions with the first or second order kinetics [9]. In a number of papers, dealing with the numerical simulation of combustion at atmospheric pressure, certain elementary steps were included into the reaction scheme among a great number of all possible and particularly quite unimportant reactions, some of which could in principle form a reaction chain. However, the relative rates of chain and self-heating factors were not considered and/or only thermal character of ignition and combustion at these pressures was emphasized [1–8]. The conclusion on the important role of the chain mechanism in the combustion of various gases both at low and high pressures was made in [10–13] on the basis of experimental data and the analysis of kinetic equations. However, as it was noted in [14, 15], when considering the features of combustion at near-atmospheric pressures, the process is represented most frequently as a single-step reaction, and self-heating is considered as the only factor responsible for ignition and combustion.

Recently, new experimental data were obtained showing that the branching-chain mechanism is predominant in the ignition and combustion of hydrogen and a number of other gases not only at low pressures, but at atmospheric and elevated pressures as well [13, 16, 17]. Particularly, the data, on the effect of very small amounts of efficient inhibitors on the concentration limits of ignition, combustion intensity, and the rate of deflagration at pressure of 1 and 5 atm, were obtained.

It should be noted, that the effect of inhibitors on the concentration limits was known earlier. However, in almost all earlier investigations, halons (halogen derivatives of hydrocarbons) were used as inhibitors. The amount of these inhibitors required for attaining a considerable effect is rather large, and so far their effect at atmospheric pressure is often treated as a result of increasing the specific heat of the reactive mixture due to the presence of the inhibitor, and even as a consequence of dilution of the combustible mixture. Efficiency of the inhibitors used in this study is significantly greater than that of halons (see Fig. 1). A significant suppression effect of rather small amounts of these inhibitors on different combustion modes at atmospheric and elevated pressures, as well as the different activity of the inhibitors having about the same molecular-kinetic characteristics, show unequivocally that their influence on combustion is only due to active participation of the additives in chain termination. This was one of the
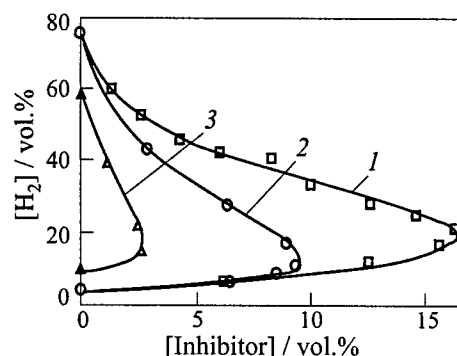

Figure 1 Concentration limits of chain ignition (*1, 2*) and chain-thermal explosion (*3*) of hydrogen in air in the presence of various amounts of inhibitors: *1* — halon ($C_2F_4Br_2$), *2, 3* — AKAM-3 (propenol)

332

evidences of the branching-chain character of ignition and combustion at high pressures. It was shown as well, that self-heating becomes important in the development of chain combustion and intensifies the chain avalanche (positive feed-back). These data indicated, that the suggested inhibitors might also be successfully employed for suppression of detonation in a number of combustible gases at atmospheric and elevated pressures.

It is known [18, 19], that at 50 Torr the additions of CF_3Br slightly decrease the propagation velocity of a detonation wave in the stoichiometric mixture of H_2 and O_2 diluted with 50% Ar and, when taken more than 5–6%, prevent detonation at all. The observed suppression of detonation was reasonably interpreted in [18, 19] as a result of chain termination by the added inhibitor. Though initial concentration of the combustible mixture in the mentioned investigations is very low and corresponds to the domain of the self-ignition peninsula, the temperatures in the course of detonation were obviously higher in these experiments than those relevant to the peninsula. There also exist the experimental data on chemical initiation of detonations.

The comparison of the rates of O_2 consumption by the branching-chain mechanism and by the molecular (non-chain, "purely" thermal) mechanism in a model process of hydrogen combustion shows that the competition of reaction chain branching and termination is the dominant factor at these pressures and temperatures even exceeding 2000 °C [13]. These temperatures correspond to those relevant to hydrogen-air detonation at atmospheric pressure [20] and, together with the data mentioned above [18–20], point to the realistic possibility of essential detonation inhibition by small additives of the suggested inhibitors at atmospheric and elevated pressures.

EXPERIMENTAL RESULTS

Two kinds of experiments were performed in this investigation. In the first set of experiments, hydrogen–oxygen mixtures were detonated in perspex tubes (2.6 cm in diameter and 625 cm long). Detonation was initiated by a spark plug. Shchelkin spiral was used to enhance the transition process. Small amounts (0.5%, 1.0%, and 2.0% vol.) of the suggested inhibitor AKAM-3 (propenol) were added to the combustible mixture. The components were perfectly premixed before initiating the detonation. High-speed filming of flame propagation was performed by a camera with the aperture allowing observation of the whole length of the reaction tube. The appearance of detonation was registered in the film as a black spot in the negative image (corresponding to high luminescence region). Detonation was accompanied by the characteristic sound and, in some runs, also by destruction of the reaction tube. The induction length of detonation

333

onset was determined as the distance between the location of the blackening on the film and the ignition point.

In these experiments, efficient inhibition was attained: addition of 2.0% or more of the inhibitor prevented detonation of the stoichiometric mixture. Addition of less than 2.0% of the inhibitor increases the induction period, the latter rising progressively with the amount of the inhibitor. Similar suppression effect was observed in the experiments with mixtures, containing 23%, 25%, and 31% H_2.

The second set of the experiments was also performed at atmospheric pressure. However, the process was carried out under conditions of flow of the combustible gas in a stainless-steel cylindrical chamber (9.8 cm in diameter and 400 cm long). The flow velocity of the gas was between 7 and 37 m/s. The apparatus consisted of a special system of injecting and mixing the components, pressure measurement at the reactor inlet and outlet, dynamic pressure measurements (4 transducers along the reaction chamber) with signal registration at the oscilloscope, as well as temperature measurements. Measurements and their processing were computerized. Compositions of gas mixtures were choosen near the detonability limits for each amount of AKAM-3 inhibitor. The detonation onset was registered by means of oscilloscope records from 4 transducers. Detonation was accompanied by the characteristic noise.

The obtained concentration limits of detonation in the absence of inhibitor are 17% and 58% H_2. These values are close to those known for detonation in static conditions (e.g. [20]), equal to 18.2 and 58.9% H_2. Thus, at flow velocities up to 37 m/s, the limits of un-inhibited detonation do not actually change for hydrogen detonation under flow conditions.
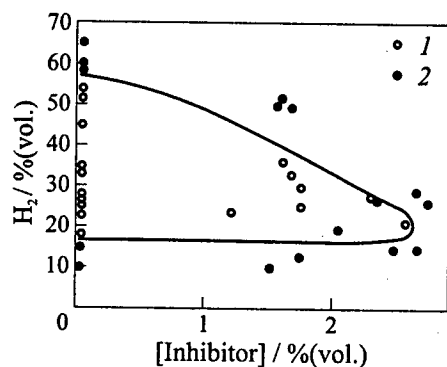

Figure 2 Domains of combustion and detonation of hydrogen–air mixtures in presence of various amounts of AKAM-3 inhibitor. *1* — deflagration, *2* — detonation

It was established, that the addition of inhibitor increases the delay in detonation onset, as in the first set of the experiments described above. Because in the second set of experiments the reaction occurred under flow conditions, special precautions were required to prevent distortion: long induction periods might exceed the time taken for the combustible gas to pass the reaction chamber. Taking this into account, smaller gas flow velocities, 7 to 14 m/s, were used. This provided the correct measurements of concentration limits and other characteristics of inhibition.

The results show, that addition of the inhibitor effectively narrows the

concentration limits of detonation (Fig. 2). It is also seen, that the apex of the concentration peninsula corresponds to 2.5% (vol.) of the inhibitor, i.e. such amount of the inhibitor is sufficient to supress detonation of hydrogen–air mixtures of any composition. The data in Fig. 2 also indicate, that even if the additions are smaller, they considerably affect the detonability limits. For instance, addition of 1.5% of inhibitor reduced the upper detonability limit to about 40% H_2, i.e. by 18%.

DISCUSSION AND CONCLUDING REMARKS

Thus, in both sets of experiments, the efficient influence of inhibitor on the concentration limits of detonation and its induction period at atmospheric pressure were observed. The amounts of gas-phase inhibitors used in these experiments were too small to cause considerable changes in the specific heat or other thermal characteristics of the gas mixture, in particular if one takes into account, that the molecular mass of the inhibitor does not exceed 70. The possibility of detonation supression by such small additives unequivocally shows that the observed effect is caused primarily by the inhibitor induced intensification of reaction chain termination, rather than by changes in thermal characteristics of the reactive gas or by its dilution.

In the second set of the experiments, the effect of the inhibitor on the propagation velocity of a detonation wave and on the detonation pressure was not investigated. However, as inhibition is caused by chain termination, it affects the kinetics of all combustion modes as well. Indeed, the rate W of chain combustion is expressed by the following formula, confirmed experimentally [10, 21]:

$$\frac{W}{B_0} = k_b n_0 \exp \int_{t_0}^{t} (f - g) \, dt$$

where B_0 is the starting concentration of the initial molecular reagent participating in chain branching, k_b is the rate constant of branching, n_0 is the concentration of an active intermediate realizing chain branching, f and g are the rates of chain branching and termination per unit concentration of the active intermediate, and t_0 is the time interval after which the chain origination by molecular reaction may be neglected.

The inhibitor increases the value of g and results in decreasing the rate of combustion reaction and consequently the rate of heat release. This is in good agreement with experimental data. The suppressing effect of inhibitors AKAM-3 and $C_2F_4Br_2$ on the rate of reaction in the modes of chain combustion and chain-thermal explosion at atmospheric pressure was demonstrated experimentally [17].

ACKNOWLEDGMENTS

REFERENCES

1. Kondratiev, V. N., and Nikitin, E. E., *Chemical Processes in Gases*. Nauka, Moscow, 1981.
2. Frank-Kamenetskii, D. A., *Diffusion and Heat Transfer in Chemical Kinetics*. Nauka, Moscow, 1987.
3. Semenov, N. N., *On Certain Problems of Chemical Kinetics and Reactivity*. USSR Academy Sci. Publ., Moscow, 1958.
4. Maas, U., and Warnatz, J., *Combustion Flame*, **74**, 53, 1988.
5. Gontkovskaya, V. T., Gordopolova, I. S., and Ozerkovskaya, N. I., *Sov. J. Physics Combustion Explosion*, **24**, 1, 53, 1987.
6. Hernandes, Z., Grespo, A., and Dujm, N., *Combustion Flame*, **101**, 113, 1995.
7. *Chemical Encyclopedia. Combustion*. Soviet Encyclopedia Publ., Moscow, 1984.
8. Buckmaster, J., and Giovangly, V., *Combustion Flame*, **94**, 113, 1993.
9. Zel'dovich, Ya. B., Barenblatt, G. I., Librovich, V. N., and Machviladze, G. M., *Mathematical Theory of Combustion*. Nauka, Moscow, 1981.
10. Azatyan V. V., *Sov. J. Kinetics Catalysis*, **18**, 2, 282, 1977.
11. Azatyan, V. V., *Sov. J. Physics Combustion Explosion*, **15**, 1, 62, 1979.
12. Azatyan, V. V., Andreeva, N. V., and Elnatanov, A. I., *Sov. J. Chemical Physics*, **7**, 6, 821, 1988.
13. Azatyan, V. V., *Sov. J. Kinetics Catalysis*, **37**, 4, 512, 1996.
14. Warnatz, J., *Proc. 18th Symposium (International) on Combustion*, The Combustion Institute, Pittsburgh, PA, 1981, 369.
15. Peters, N., and Rogg, B., *Reduced Kinetic Mechanisms for Applications in Combustion Systems*. Springer-Verlag, Berlin, N.Y., 1993.
16. Azatyan, V. V., *Rus. J. Fire and Explosion Safety*, **3**, 4, 13, 1994.
17. Azatyan, V. V., Aivazyan, R. G., Kalachev, B. I. *et al.*, *Rus. J. Chemical Physics*, **17**, 2, 117, 1998.
18. Lubouton, J. C., Dormal, M., and Van-Tiggelen, P. J., *Proc. 15th Symposium (International) on Combustion*, The Combustion Institute, Pittsburgh, PA, 79, 1975.
19. Nzeyimana, E., and Van-Tiggelen, P. J., *Dynamics of Detonations and Explosions*, Progress in Astronautics and Aeronautics Ser., AIAA Inc., Washington, DC, **133**, 77, 1991.
20. Lewis, B., and Von-Elbe, G., *Combustion, Explosion and Flame in Gases*. Academic Press, N.Y.–London, 1987.
21. Azatyan, V. V., and Shavard, A. A., *Sov. J. Doklady USSR Academy Sci., Ser. Chemistry*, **11**, 2460, 1977.

STUDY OF DETONATION INITIATION IN UNCONFINED ALUMINUM DUST CLOUDS

W. Ingignoli, B. Veyssiere, and B. A. Khasainov

It is now commonly accepted that suspensions of solid reactive particles in air, and even in oxygen, are difficult to detonate. Evidence of detonation propagation has been reported only in a limited number of experimental studies performed in tubes, where it was shown that, tube lengths greater than 10 m were necessary for the detonation regime to be reached. Until now, it has not been proven possible to initiate self-sustained detonations in unconfined clouds of solid particles. Nevertheless, many two-phase systems of this kind have a specific energetic content comparable (or even greater) to that of "classical" detonable gaseous mixtures. Thus, it is necessary to find out what conditions are required to generate a sufficiently fast heat release able to support a detonation. We have performed experiments in aluminum–oxygen suspensions contained in polyethylene balloons of about 0.4 m^3. A spherical blast wave was generated inside the clouds by exploding a TNT charge of variable mass (up to 150 g). Experiments have been performed with either atomized powder (mean diameter 3.5 μm) or with flakes, at different nominal mass particle concentrations. Until now, no detonation has been observed to form in the cloud. The terminal shock front velocity was usually far lower than the CJ value. In a few experiments where the velocity of the leading wave approached the CJ value at the end of propagation in the cloud, the propagation regime was still nonstationary. Initiation of two-phase clouds of suspended aluminum particles was studied numerically in configurations corresponding to the above experimental conditions. Preliminary results show that for particles having a diameter less than 5 μm, the blast wave generated by the initiator decreases rapidly, whereas solid particles are ignited in the flow downstream. After about 0.45 m the reaction rate increases, thus increasing the velocity of the leading front. However, after 1 m of propagation, the leading front velocity is not constant and yet smaller than the CJ velocity. This indicates that smaller size particles (< 2 μm) and clouds of larger dimension (> 2 m diameter) are required (even with pure oxygen based mixtures) to form self-sustained detonations in suspensions of aluminum particles. This indicates the necessity of performing experiments at larger scale than that of our laboratory-scale experimental setup.

INTRODUCTION

It is well known that dust explosions often generate severe damages. However, the actual combustion regime reached during these explosions is rarely well identified. Particularly, it is important to find out in which conditions a self-sustained detonation may be formed.

The case of aluminum particles is of great interest as it is a material with high specific energy, which enters in the composition of numerous propellant and explosive compositions. Only a few works have been devoted to the study of detonability of aluminum dust suspensions in air or oxygen.

The early ones are the Strauss experiments [1] in tubes. He studied aluminum suspensions in oxygen contained in shock tubes of 2.7 m length with an inner diameter of 26.4 or 44 mm. Initiation was performed by detonators or explosive wires. Strauss observed detonations with 40 μm flakes and 5 μm atomized particles. The detonation velocity and pressure peak were found to be significantly below the thermodynamic values and seemed weakly sensitive to the particle diameter and concentration. On account of the reduced dimensions of the experimental set up, it is not certain that a self-sustained propagation regime had been reached (in length and diameter). In addition, Strauss reported observation of spinning detonations, which is characteristic of a strong influence of the confinement on the detonation propagation.

Tulis [2] performed experiments in tubes of larger dimensions (5.5 m long and 152 mm internal diameter), but with air suspensions. Ignition was performed by a solid explosive charge (3 g). Typical values of the leading wave velocity of 1300–1500 m/s have been observed at the end of the tube, even 1650 m/s in some experiments. These values are far below the thermodynamic ones, and reported experimental data do not indicate that detonation of aluminum–air mixtures is possible.

The most convincing experimental results have been reported by Borisov *et al.* [3]. Experiments were performed in several tubes (4.2 m long and 122 mm diameter, or 2 m long and 55 mm or 145 mm diameter) with 1 μm-thick flakes and 1 μm-, 11 μm-, and 33 μm-diameter atomized particles suspended in air. It was shown that aluminum particles larger than 10 μm were impossible to detonate, either in oxygen or in air. On the contrary, flakes as well as 1 μm spherical particles were able to detonate in air. Quasi-steady propagation was observed, and typical detonation velocities of 1800 m/s were obtained for concentrations equal or greater than stoichiometry, which is close to the thermodynamic value at stoichiometry. However, streak photographs show that in most cases a spinning detonation wave was observed.

More recently, Pu *et al.* [4] have performed experiments in a 14 m-long tube with a 0.14 m inner diameter. They have ignited mixtures of 6 μm aluminum particles suspended in air at concentrations of 350 and 500 g/m^3 with black powder ignitors providing an energy of 2770 J. In these conditions, they have

recorded typical velocities of 2000 m/s for the leading front after 10 m of propagation. This allows one to assume that deflagration to detonation transition has occurred in the terminal part of the tube.

However in all these experiments, the walls of the confinement obviously play an important role in the propagation of these so-called detonations. A decisive proof of detonability could be given by the observation of unsupported detonations in unconfined conditions. Large scale experiments have been performed by Tulis [5] in order to detonate unconfined aluminum–air suspensions. He initiated 10 m and 15 m long clouds with a 2.27 kg solid explosive charge. Even if typical values of 1550 m/s for the velocity of the leading front have been reached in some parts of the cloud (which is comparable with the thermodynamic value at this nominal particle concentration), it is hazardous to conclude that a true detonation regime has been obtained. Large fluctuations of the velocity have been recorded, the extreme ones being far below the thermodynamic CJ value. In addition, unexpected values of the pressure at the front have been observed which, according to the author [5] are susceptible to be attributed to shock coalescence. As for us, we have already reported the results of a first series of experiments performed in unconfined clouds of aluminum particles suspended in oxygen [3]. In these experiments, the aluminum dust was dispersed in a balloon of 0.385 m^3 filled beforehand with oxygen, and ignited in the center by a charge of solid explosive (125 g). Ignition of aluminum particles and acceleration of the reaction zone behind the blast wave was observed, but a detonation was not formed at the end of the propagation.

Further work is still needed to unambiguously prove that a suspension of aluminum dust can support or not a self-sustained detonation. Here, the unconfined configuration was chosen so that influence of the confinement on detonation propagation could be discarded. We have tried to relate our experimental measurements to the dynamic parameters of detonations (such as detonation cell size).

EXPERIMENTAL SETUP

The principle of the experimental setup is the same as in our preceding studies [6], but with substantial modifications. The two-phase medium is prepared in a cylindrical polyethylene bag (diameter 0.70 m, height 1 m, volume 0.385 m^3) placed on a steel platform (see Fig. 1). First, the bag is filled with pure oxygen. The dust is contained in five hemispherical cups mounted on the platform, and dispersed by simultaneously discharging the pressurized tanks containing oxygen. The initiation is achieved with a charge of solid explosive ignited by a blasting cap, located at the top of the bag on its central axis (see Fig. 1). Thus, the blast wave generated by the detonation of the solid explosive can propagate over a
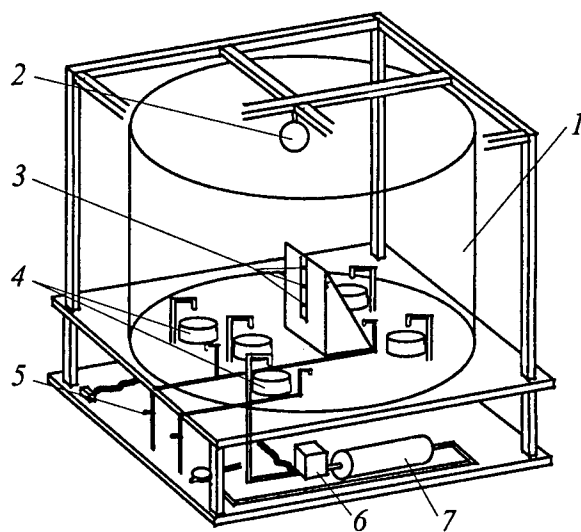
339

Figure 1 Experimental setup. *1* — polyethylene bag, *2* — TNT charge, *3* — pressure gauges K_1, K_2, and K_3, *4* — cups containing particles, *5* — oxygen supply for the bag, *6* — electric valve, *7* — pressurized oxygen tank

distance of about 1 m downward in the two-phase mixture. To record the time of arrival of the front wave and the pressure in the flowfield behind it at different positions, a special steel support is mounted on the platform inside the bag. It is designed to place three pressure gauges (Kistler 603B) along the vertical axis of propagation of the blast wave at 0.50 m, 0.60 m, and 0.70 m from the initiation point. Vertical rectangular (0.50 m × 0.45 m) steel plates covered with a thin layer of soot are also installed on the still support, to record the cellular structure of detonation waves.

EXPERIMENTS

In spite of its potential detonation properties due to high energy content, as predicted by thermodynamic calculations, the aluminum–oxygen mixture is difficult to detonate. It is likely that one possible cause is related to the elevated ignition temperature of aluminum particles, which is responsible for a long ignition delay of chemical heat release behind the front shock wave. Hence, a high amount of energy is required to initiate the detonation. We have used different masses of solid explosive, up to 150 g TNT equivalent charge. These charges were blasted without the reactive mixture to test the effect induced in the surrounding field.
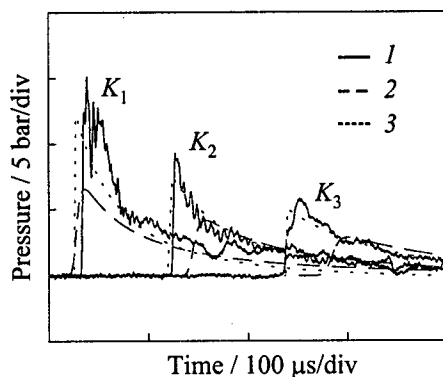
Figure 2 Blast wave generated by a 125 g TNT charge: comparison of pressure profiles recorded at positions K_1, K_2, and K_3 (1) with calculations: 2 — point source explosion 3 — finite dimension charge

An example is shown in Fig. 2, where the pressure profiles, recorded by the pressure gauges after the explosion of a 125 g TNT equivalent charge, are displayed. These pressure profiles have the classical shape of a decaying wave generated by the explosion of a TNT charge. We have compared the characteristic parameters dimensioned in the usual manner with the classical TNT parameter curves built by Baker *et al.* [7]. As can be seen in Fig. 3, where the dependence of the overpressure Δp_s at the front of the wave and the time of arrival t_a on the propagation distance are displayed, our experimental results fit quite well with the Baker parametric curve. The agreement is acceptable even for the smallest distances, that is for pressures measured at the nearest gauge from the initiating charge. Anyway, it is clear that the amount of energy used in our experiments is very high, and if we consider, for example, the characteristic influence radius of the explosive ($[E/p_0]^{1/3}$), it
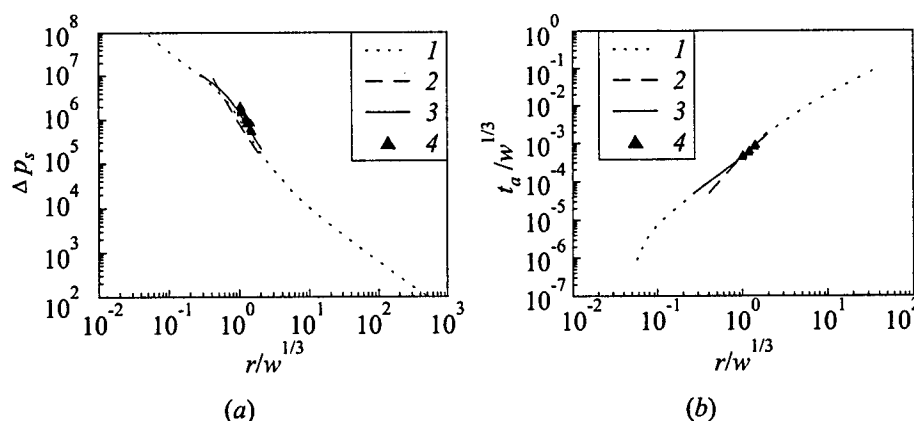

(a)

(b)

Figure 3 Comparison of the overpressure Δp_s and arrival time t_a measured at positions K_1, K_2, and K_3 for different TNT charges with the correlated values of Baker *et al.* [7] and calculations. 1 — Baker [7], 2 — point explosion (calculated), 3 — finite dimension charge (calculated), 4 — experiments

341

can be verified that it exceeds the dimensions of our balloon. Therefore, it is unlikely to observe self-sustained detonations in our conditions, since at the end of propagation the leading blast wave will not have sufficiently decayed, even if the shock front strength is clearly smaller than the theoretical value of the thermodynamic detonation pressure. But our purpose is to display experimental evidence of the possibility for the detonation regime to be generated in the two-phase mixture. By analogy with gaseous mixtures, we believe that this can be done by displaying the cellular structure which is characteristic of the detonation wave. As shown in gaseous mixtures [8], the detonation cell size decreases when the rate of overdrive of the detonation increases. Should the existence of the cellular structure be shown, it would be an important clue of the possibility to generate a detonation and would predict, by extrapolation, the cell size of the self-sustained detonation.

Attempts to detonate aluminum–oxygen mixtures have been done with different kinds of aluminum particles: atomized particles having a mean diameter of 3.5 m (Alcan), and flakes with a thickness less than 1 μm and a longitudinal size up to 25 μm (Metaux et Chimie). Flakes have a larger surface-to-volume ratio which *a priori* gives them a greater reactivity. In our experiments, the initial mass of aluminum powder poured in the cups was determined so that the theoretical nominal equivalence ratio inside the cloud should be equal or greater than stoichiometry. Most of the experiments have been performed in the range of richness 1.6 to 2.7. Due to the probable important inhomogeneity of the dust distribution inside the balloon, this was supposed to ensure that a sufficient particle concentration (at least larger than the lean flammability limit) was achieved elsewhere in the cloud. Synchronization of the instant of initiation with the dispersion of particles was determined by preliminary experiments during which the dispersion process was recorded with a high frame rate video camera: the average duration of dust dispersion was about 200 ms. In our experiments, we have assigned three different delays: 160, 220, and 260 ms.

With atomized particles, we have observed ignition of aluminum particles behind the leading blast wave (see Fig. 4). This resulted in the formation of a secondary discontinuity wave in the flowfield. However, this secondary wave did not catch up to the front wave at the end of propagation in the cloud. In the example of Fig. 4, the mean velocity of the leading front measured between the two gauges is only 1220 m/s and the pressure jump recorded at the last gauge is 30 bar (the thermodynamic CJ velocity and pressure for the corresponding aluminum concentration are 1320 m/s and 45 bar, respectively).

With flakes, ignition of aluminum seems to occur more rapidly. As can be seen in Fig. 5, the effect of aluminum burning is detectable from the first pressure gauge. The beginning of the reaction zone takes place closer to the leading front, but the effect is contradictory. In the case reported in Fig. 5, the shock front velocity recorded between the pressure gauges is 1168 m/s and 1134 m/s, which is far smaller than the thermodynamic CJ value of 1493 m/s for the given
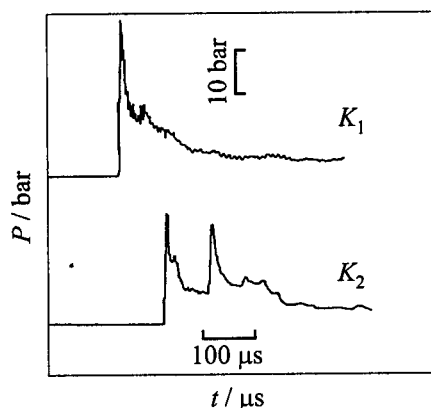
342

Figure 4 Pressure profiles recorded with atomized (3.5 μm) particles (initiator: 125 g TNT) at positions K_1 and K_2
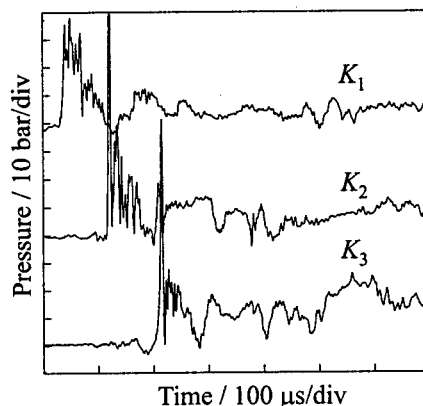
Figure 5 Pressure profiles recorded with flakes particles (initiator 150 g TNT) at positions K_1, K_2, and K_3

aluminum concentration. In contrast, very important overpressures of the order of 80 bar are recorded (the predicted CJ pressure is 42 bar). Such high levels are rather surprising and might be attributed to the interaction of the leading blast wave with the steel support, used to maintain the pressure gauges. Indeed, noticeable precursor effects are observed, especially on the last pressure gauge. Apart from that, the remaining pressure signals indicate that the reaction zone is not yet sufficiently close to the leading front to permit coupling between the reaction zone and the shock front. The burning of aluminum is manifested because of a high level of pressure over a long duration (several hundreds of microseconds) behind the leading wave, which allows one to assume that the reaction rate of aluminum is not yet sufficiently fast to support the propagation of a detonation.

In all these experiments, no cellular structure has been recorded on the steel plates placed inside the cloud, which corroborates the conclusion that the detonation regime was not reached. However, there exists an unique experiment with flakes which provides additional information. In this experiment, a leading front velocity of 1650 m/s has been recorded between the last two pressure gauges, and the pressure peak values recorded at the last two gauges are 36 and 52 bar, respectively (corresponding CJ velocity and pressure are 1493 m/s and 42 bar). In addition, the steel plate reveals the existence of some structures (see Fig. 6), which is not easy to discern because of the disturbance caused by condensation of aluminum oxide on the plate. It is also difficult to determine
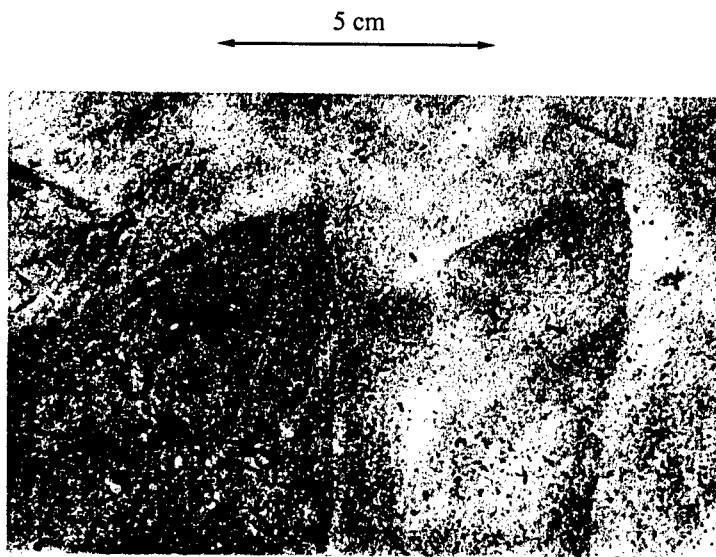
5 cm

Figure 6 Photograph of structures recorded on a soot plate

the exact nature of these structures, should it be detonation cells. Only part of the cells can be observed here, but the limited dimension of the setup does not allow farther observation. The characteristic "cell" width would be about 5–10 cm. Still, there is a suspicion that it could be really detonation cells, since observation of these structures coincides with the registration of front velocity and pressure peak values slightly higher than the CJ ones. Unfortunately, it was not possible to repeat this experiment.

From the experiments reported above, the difficulty to detonate aluminum suspensions is confirmed, even in the case of aluminum particles suspended in pure oxygen. Many reasons may be invoked to explain this situation. First, the dispersion system does not guarantee that proper concentration is achieved throughout the balloon, to permit the propagation of a detonation. If too large concentration gradients exist, especially with existence of lean concentration zones, a detonation might be formed temporarily, but be quenched after a limited distance of propagation. Detonation failure may also be due to the kinetics of aluminum oxidation. Aluminum particles, when subjected to ambient air, are naturally oxidized and covered with a thin layer of aluminum oxide, which prohibits oxygen diffusion and, as a result, prevents ignition of particles. In static conditions, aluminum particles should be heated at the melting temperature of aluminum oxide (2310 K) to be ignited, which is a prohibitive condition to ini-

344

tiate a detonation in a suspension of aluminum particles. It is likely that such severe conditions are not required here to ignite the particles (see [9]). But, the initial state of the particle surface is not known. No indication has been given by the powder manufacturers about the state of the surface or about a possible surface treatment in order to prevent superficial oxidation. By the way, the change with time of the properties of a given dust, after opening of its container, is not known as well. A reason facilitating their natural surface oxidation, and therefore decreasing their detonability may be that the flakes have a greater reactivity than atomized particles on account of their larger surface-to-volume ratio.

Because it determines the velocity and temperature relaxation behind the shock, the flowfield structure behind the leading blast wave propagating in a dusty gas may also play an important role in the detonation formation. We examine this aspect hereafter with the help of numerical modeling.

NUMERICAL STUDY

For this study, we used the numerical model designed by Khasainov and Veyssiere [9, 10]. It is a standard two-phase model considering different velocity, density and temperature of phases. Mass, momentum and heat exchanges between phases were taken into account in the balance equations for each phase. Chemical reactions are described by empirical global kinetic laws. Detonation is described by the ZND model. A time-dependent set of equations is integrated by the LCPFCT numerical scheme [11]. All the details concerning this model can be found in preceding works [9, 10]. Thus, we have investigated, in 1D configuration, the problem of detonation initiation in a spherical cloud ignited at its center.

First, we calculated the propagation of the blast wave that was generated in the surrounding field by the detonation of the solid explosive, used to ignite the cloud. Initially, we assumed that the initiating charge could be considered as an ideal explosion source point. Results of the calculations are compared in Fig. 2 with experimental results. The agreement is reasonable. Then, we numerically simulated the conditions which could lead to detonation initiation.

Figure 7 shows the pressure profiles calculated at different distances of the ignition point with an ignition energy of 150 g of TNT, for a particle concentration $\sigma=1500$ g/m^3 (which corresponds approximately to stoichiometry) and for 13 μm and 3.5 μm particles. The 13 μm particles are ignited, but due to their large relaxation time, they release their heat too far behind the leading front. Therefore, losses caused by particle relaxation play a dominant role, and the blast wave produced by the initiating charge is weakened and decelerated down to 350 m/s.
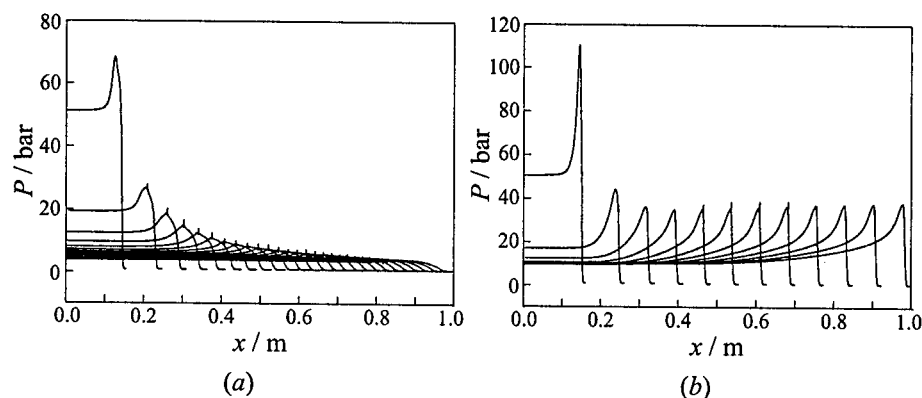
345

Figure 7 Calculated pressure profiles for a suspension of aluminum particles in pure oxygen at a concentration of 1500 g/m^3 for 13 μm (a) and 3.5 μm (b) particles (point source explosion initiation — 150 g TNT)

On the contrary, for finer 3.5 μm particles, the leading front stops decelerating after 0.45 m and then shock progressively accelerates due to the burning of particles. After 1 m of propagation, the front is still accelerating and its velocity is 1490 m/s, clearly smaller than the thermodynamic value (1595 m/s), indicating that the steady detonation regime has not yet been reached. For 5 μm and 2 μm particles, the behavior is globally the same, but the velocity after 1 m of propagation is only 1420 m/s for 5 μm particles, whereas for 2 μm particles, the shock front reaches a velocity of 1548 m/s, which is closer to the CJ value.

The evolution of the leading shock velocity as function of the distance from initiation point is shown in Fig. 8 for 13, 5, 3.5, and 2 μm particles. It is clear that the steady self-sustained detonation regime is not reached after 1 m of propagation, whatever the particle size. In the latter case, one can estimate that the steady detonation regime would be reached at a distance of about 1.2–1.5 m from the initiation point.

The case of flakes is more difficult to model, because their complicated shape may increase the reactivity of the particles. However, the shape also modifies the drag coefficient of particles and, as a result, their relaxation characteristic time. More precise information is needed on the modifications induced on these two factors before simulating the behavior of flake-type particles.

Pressure, gas and particle velocity and temperature profiles behind the shock front in the case of 2 μm particles are displayed in Fig. 9. They show that the particular structure of the combustion wave is due to relaxation of particles, but the velocity relaxation time is longer than the temperature relaxation time. This contradicts the approximation of a one-velocity model for the suspension chosen by Fedorov *et al.* [12] for their calculations.
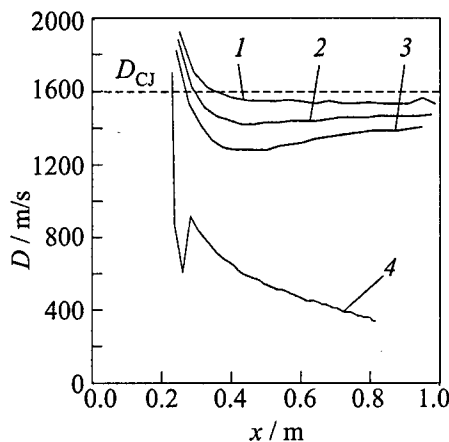
346

Figure 8 Variation of shock front velocity D versus distance from the initiation point, as function of particle diameter. 1 — 2 μm, 2 — 3.5 μm, 3 — 5 μm, 4 — 4 μm
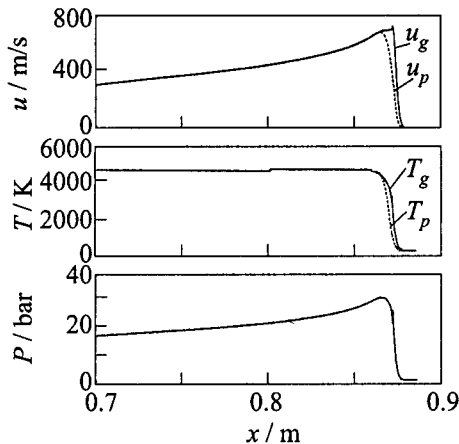
Figure 9 Predicted evolution of pressure P, gas u_g and particle u_p velocities, gas T_g and particle T_p temperatures behind the shock front. Particle diameter 2 μm, distance from the initiator 0.875 m

Another uncertainty comes from the assumption of the ideal (point) explosion source, because this approximation does not allow one to correctly calculate the characteristic of the flowfield in the vicinity of the initiator. Indeed, the dimension of the solid explosive charge is not negligible and could explain the deviation of measured overpressures (especially at the first pressure gauge) with those predicted by Baker *et al.* [7], as mentioned above. Therefore, we have calculated the propagation of the blast wave, taking into account an initiating charge having a finite dimension, under the assumption of its instantaneous detonation.

The calculated results at K_1, K_2, and K_3 positions are compared in Fig. 2 with the solution obtained under the assumption of an ideal (point) source. It can be seen that a better agreement with experiments is obtained on the magnitude of the overpressures and on the time of arrival on the pressure gauges. If one examines the reduced overpressures Δp_s, calculated under the two assumptions, it can be seen in Fig. 3 that the agreement is rather good with the experimental values and the predictions of Baker *et al.* [7] (that is, the characteristic parameters at the shock front). However, it appears (see Fig. 10) that the flow structure in the far field behind the leading wave is very different and much more complicated. Particularly, one can observe the existence of a discontinuity which has been formed at the boundary of the initiating charge after its detonation. This had already been shown by Brode [13] in an analogous configuration. Figure 10
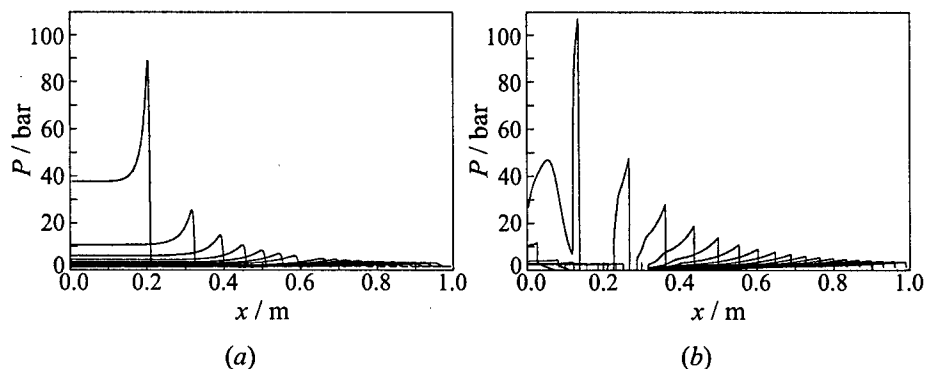
347

Figure 10 Comparison of the calculated pressure profiles of the blast wave generated by the initiating charge: (a) point explosion, (b) finite dimension charge

shows that during the first stage of propagation after the initiation, very steep gradients of flow parameters exist in the rear zone adjacent to the shock front.

At later instants of propagation, the differences between the parameters profiles, calculated under the two assumptions, progressively vanish. The effect on particle relaxation may be considered as unimportant when the leading shock reaches the position where the pressure gauges are located. On the contrary, this flow structure may play a predominant role on the velocity relaxation of particles in the first stage of propagation. Therefore, additional calculations of detonation initiation in aluminum–oxygen suspensions are needed, but under the assumption of an initiating charge of finite dimension.

DISCUSSION

In the present state of our studies, it appears that the self-sustained detonation regime has not been reached in our experiments. It is possible to speculate about the critical conditions which would permit initiation of a detonation in an aluminum–oxygen suspension. Numerical modeling indicates that over the distance chosen for our calculations (1 m), a detonation cannot be formed. Particles of smaller size ($< 2\ \mu m$) than those considered here are needed to expect detonation formation within this distance. This corroborates our experimental observations with 3.5 μm particles. Regarding the special case for which the beginning of detonation formation is suspected to have been observed (see Fig. 6), it is not easy to relate it to numerical simulations, since it has been obtained with flakes. What is the exact nature of the recorded structures? Obviously, they

manifest the existence of triple points, which could be connected with the multi-headed structure of a detonation wave. They arise at a distance of about 0.70 m from the initiating point, but unfortunately, due to the size of these structures (several cm) and the limited dimensions of the plates, further evolution of the phenomenon has not been recorded. Assuming that they are parts of real detonation cells, their estimated width would be about 5–10 cm. In the case of gases, it corresponds to mixtures very difficult to detonate. These experimental results, as well as numerical predictions, display the necessity to perform experiments on a larger scale than that of our laboratory-scale experimental setup.

ACKNOWLEDGMENTS

REFERENCES

1. Strauss, W. A., "Investigation of the Detonation of Aluminum Powder–Oxygen Mixtures," *AIAA J.*, **6**, 9, 1753–1756, 1968.
2. Tulis, A. J., and Selman, J. R., "Detonation Tube Studies of Aluminum Particles Dispersed in Air," *Proc. 19th Symposium (International) on Combustion*, The Combustion Institute, Pittsburgh, PA, 1982, 655.
3. Borisov, A. A., Khasainov, B. A., Veyssiere, B., Saneev, E. L., Fomin, I. B., and Khomik, S. V., "On Detonation of Aliminium Dusts in Air and Oxygen," *Sov. J. Chemical Physics*, **102**, 369–402, 1992.
4. Pu, Y. K., Ke, Y. L., and Jarosinski J., "Transition to Detonation in Alumnium Dust–Air Mixtures Under Weak Ignition Conditions," *Proc. 16th ICDERS*, Cracow, Poland, 1997, 259–262.
5. Tulis, A. J., "On the Unconfined Detonation of Aluminum Powder–Air Clouds," *Proc. 1st Colloquium (International) on Explosibility of Industrial Dusts*, Baranow, Poland, 1985.
6. Veyssiere, B., Desbordes, D., and Lee, J. H. S., "Preliminary Experiments for Direct Initiation of Spherical Detonations in Two-Phase Mixtures (Oxygen – Solid Particles)," *Archivum Combustionis*, **7**, 1–2, 185–196, 1987.
7. Baker, W. E., Cox, P. A., Westine, P. S., Kulesz, J. J., and Strehlow, R. A., *Explosions Hazards and Evaluation*. Elsevier, N.Y., 1983.
8. Desbordes, D., "Transmission of Overdriven Plane Detonations: Critical Diameter as a Function of Cell Regularity and Size," *Progress in Astronautics and Aeronautics Ser.*, AIAA Inc., N.Y., **114**, 170–185, 1988.

349

9. Veyssiere, B., and Khasainov, B. A., "Structure and Multiplicity of Detonation Regimes in Heterogeneous Hybrid Mixtures," *Int. J. Shock Waves*, **4**, 3, 171–186, 1994.

10. Khasainov, B. A, and Veyssiere, B., "Initiation of Detonation Regimes in Hybrid Two-Phase Mixtures," *Int. J. Shock Waves*, **6**, 9–15, 1996.

11. Oran, E. S., and Boris, J. P., *Numerical Simulations of Reactive Flows*. Elsevier, N.Y., 1987.

12. Fedorov, A. V., and Tetenov, E. V., "Initiation of the Heterogeneous Detonation of Aluminum Particles Dispersed in Oxygen," *Sov. J. Physics Combustion Explosion*, **28**, 3, 83–89, 1992.

13. Brode, H. L., "Blast Wave From a Spherical Charge," *Physics Fluids*, **2**, 217, 1959.

STRUCTURE OF A DETONATION WAVE IN A CHANNEL PARTIALLY FILLED WITH A RDX PARTICLE SUSPENSION

S. A. Zhdan and E. S. Prokhorov

The computational study of a layered detonation of volatile secondary high explosive suspensions is presented. The suspension is arranged in the form of an annular layer adjacent to a cylindrical channel wall. A mathematical model of a double-phase double-velocity medium is used. The formation dynamics and some structural features of the two-dimensional reaction zone of the detonation wave in the RDX-particle suspension in gas are considered. The detonation mode with the reaction zone exhibiting a vortex structure is obtained for the first time.

INTRODUCTION

A theoretical analysis of one-dimensional stationary and non-stationary detonation waves (DW) in gas suspensions of a monofuel [1–2] has shown that the wave structure is qualitatively similar to the Zel'dovich–Neumann–Döring model. The dynamics of the two-dimensional DW propagating through the RDX particle suspension in air was discussed in [3]. The detonation of a free cylindrical charge of the monofuel-particle suspension in vacuum, exhibiting the shockless reaction zone, was investigated in [4]. This paper deals with studying the structures of the two-dimensional reaction zone of a self-sustaining heterogeneous DW propagating through the circular layer of the RDX-particle suspension in a cylindrical channel.

FORMULATION

Consider the case when high explosive (HE) particles of diameter d_0 and true density ρ_2^0 are suspended uniformly with a volume concentration α_{20} in a cylindrical channel of radius r_c. In this case, the suspension in the left side of the

channel ($x < 0$) occupies the channel cross-section entirely, and that in the right side ($x > 0$) occupies only the annular layer of thickness $\Delta r = r_c - r_0$, where r_0 is the radius of the internal particle-free cavity. A stationary DW in the gas suspension propagates through the channel. The leading front of the wave reaches location $x = 0$ at $t = 0$, and the Chapman–Jouguet (CJ) plane at this moment is at the point $x = -l_{\text{CJ}}$. It is required to determine the detonation dynamics at $t > 0$ as a function of r_c, r_0, d_0, and initial densities of phases, ρ_{10} and ρ_{20}.

Consider the two-dimensional unsteady motion of monodisperse particles of the secondary HE (RDX, PETN, HMX, etc.) in a gas phase, taking into account combustion of particles. Assume that:

(1) gasification of volatile HE particles starts when they are heated to the evaporation temperature T_s;

(2) the rate of particle combustion is limited by the rate of their gasification;

(3) reaction products obey the ideal gas law, particles are incompressible and spherical;

(4) initial parameters of the gas are as follows: pressure p_0, temperature T_0, and density ρ_{10}.

Equations of the mechanics of the two-phase reactive medium [1] for the two-dimensional unsteady detonation in the axisymmetric formulation have the form:

$$\rho_{i,t} + (\rho_i u_i)_x + r^{-1}(\rho_i v_i r)_r = (-1)^{i+1} j$$

$$n_t + (n u_2)_x + r^{-1}(n v_2 r)_r = 0$$

$$(\rho_i u_i)_t + (\rho_i u_i^2)_x + r^{-1}(\rho_i u_i v_i r)_r + \alpha_i p_x = (-1)^i (f_x - j u_2)$$

$$(\rho_i v_i)_t + (\rho_i u_i v_i)_x + r^{-1}(\rho_i v_i^2 r)_r + \alpha_i p_r = (-1)^i (f_r - j v_2)$$

$$(\rho_i H_i)_t + \left[\rho_i u_i \left(H_i + \frac{p}{\rho_i^0}\right)\right]_x + r^{-1}\left[\rho_i v_i r \left(H_i + \frac{p}{\rho_i^0}\right)\right]_r$$

$$= (-1)^i (q + f_x u_2 + f_r v_2 - j H_2)$$

$$H_i = e_i + \frac{u_i^2 + v_i^2}{2}$$

$$\rho_i = \alpha_i \rho_i^0 \tag{1}$$

$$\alpha_1 + \alpha_2 = 1$$

$$\vec{f} = \frac{1}{8} n \pi d^2 \rho_1^0 C_D(\text{Re}, \text{M}_{12}) \mid \vec{u}_1 - \vec{u}_2 \mid (\vec{u}_1 - \vec{u}_2)$$

$$q = n\pi d\lambda_1 \text{Nu} \left[T_1 - T_2 + \frac{\text{Pr}^{1/3}(\vec{u}_1 - \vec{u}_2)^2}{2c_1} \right]$$

$$j = \frac{n\pi d\lambda_1 \text{Nu}}{c_1} \ln[1 + c_1(T_1 - T_s)/l_2]$$

$$\text{Nu} = 2 + 0.459 \text{Pr}^{1/3} \text{Re}^{0.55}$$

$$\text{Re} = \frac{\rho_1^0 d \mid \vec{u}_1 - \vec{u}_2 \mid}{\mu_1}$$

$$\text{Pr} = \frac{\mu_1 c_1}{\lambda_1}$$

where α_i, ρ_i, and ρ_i^0 are the volume fraction, the mean and true densities, respectively; u_i and v_i are the components of the velocity vector $\vec{u}_i$; e_i, T_i, and c_i are the internal energy, temperature, and specific heat of the ith phase ($i = 1$, 2), respectively; p is the gas pressure; n is the number of particles in a unit volume; $\vec{f}$, q, and j are the intensities of force, heat and mass interactions between phases, respectively (by assumption (1), the mass exchange intensities are $j = 0$ at $T_2 < T_s$ and $q = 0$ at $T_2 \geq T_s$); d is the particle diameter; l_2 is the latent heat of vaporization; μ_1, λ_1 are the coefficients of viscosity and thermal conductivity of gas, respectively, which are temperature dependent according to the exponential law: $\mu_1 = \mu_{10}(T_1/300)^{0.7}$, $\lambda_1 = \lambda_{10}(T_1/300)^{0.7}$; $C_D(\text{Re}, \text{M}_{12})$ is the drag coefficient of spherical particles determined by Henderson's data [5]. The coefficient C_D is a function of Reynolds and Mach numbers with $\text{M}_{12} = |\vec{u}_1 - \vec{u}_2|/a$, where $a = (\gamma p/\rho_1)^{0.5}$ is the sound velocity.

The system (1) is supplemented by the equations of state for phases:

$$p = \rho_1^0 \tilde{R} T_1, \quad e_1 = (c_1 - \tilde{R})T_1, \quad \rho_2^0 = const, \quad e_2 = c_2 T_2 + q_0 \qquad (2)$$

where $\tilde{R}$ is the gas constant and q_0 is the thermal effect of chemical reactions per unit mass of HE. The system of Eqs. (1)–(2) is closed.

INITIAL AND BOUNDARY CONDITIONS

As the initial conditions in the domain ($-l_{\text{CJ}} \leq x \leq 0$), we define the one-dimensional solution for the reaction zone of the ideal CJ detonation propagating through the gas suspension at the velocity [6]

$$D_{\text{CJ}} = 0.5 D_{\text{CJ}}^0 \sqrt{Y_{20}} \left(1 + \sqrt{1 + 4Y_{10}Y_{20}^{-1} \left(\frac{a_{10}}{D_{\text{CJ}}^0} \right)^2} \right) \qquad (3)$$

353

where $Y_{10} = \rho_{10}/(\rho_{10} + \rho_{20})$ is the initial mass fraction of the gas phase in a mixture, $Y_{20} = 1 - Y_{10}$, a_{10} is the sound velocity in the initial gas, $D^0_{CJ} = (2(\gamma^2 - 1)(q_0 + c_2 T_0))^{0.5}$ is the ideal detonation velocity in a vacuum-suspension, $\gamma = c_1/(c_1 - \tilde{R})$ is the ratio of specific heats.

At $x > 0$, the initial data take the form:

$$(0 < r < r_c): \quad \rho_1 = \rho_{10}, \quad p = p_0, \quad T_1 = T_0, \quad u_1 = v_1 = 0$$

$$(r > r_0): \quad \rho_2 = \rho_{20}, \quad T_2 = T_0, \quad u_2 = v_2 = 0 \tag{4}$$

The boundary conditions in the computational domain are specified as follows: the slip conditions for gas $(u_{1n} = 0)$ at the lower (a symmetry axis $r = 0$), left $(x = -l_{CJ})$, and upper $(r = r_c)$ boundaries; the strong discontinuity conditions [7] at the right moving boundary (at the leading shock front)

$$[\rho_1]D_n - [\rho_1 u_{1n}] = 0$$

$$[\rho_1 u_{1n}]D_n - [p + \rho_1 u_{1n}^2] = 0$$

$$[\rho_1 H_1]D_n - \left[\rho_1 \left(H_1 + \frac{p}{\rho_1^0}\right) u_{1n}\right] = 0 \tag{5}$$

$$[\vec{u}_{1t}] = 0$$

Here $u_{1n} = (\vec{u}_1, \vec{n})$ is the normal velocity component, $\vec{u}_{1t} = \vec{u}_1 - u_{1n}\vec{n}$ is the tangent velocity component of $\vec{u}_1$ with respect to the boundary; D_n is the propagation velocity of the wave front directed along the normal $\vec{n}$. The condition at the left boundary signifies the instant shutdown of the channel by a shutter at $t = 0$ with the aim to stop a piston action of detonation products behind the CJ plane $(x = -l_{CJ})$.

Given the thermodynamical properties of the phases, the solution of Eqs. (1) and (2) with initial and boundary conditions (3), (4) depends on five governing parameters: three scale factors (channel radius r_c, internal cavity radius r_0, particle diameter d_0) and two initial mean phase densities (ρ_{10}, $\rho_{20} = \alpha_{20}$ and ρ_2^0).

Introduce the following dimensionless functions: $R_i = \rho_i/\rho_{20}$, $U_i = u_i/\sqrt{q_0}$, $V_i = v_i/\sqrt{q_0}$, $E_i = e_i/q_0$, $\Theta_i = T_i/T_s$, $C_i = c_i T_s/q_0$, $(i = 1, 2)$, $P = p/(\rho_{20}q_0)$, $J = jx_0/(\rho_{20}\sqrt{q_0})$, $F_x = f_x x_0/(\rho_{20}q_0)$, $F_r = f_r x_0/(\rho_{20}q_0)$, $Q = qx_0/(\rho_{20}q_0^{3/2})$, $N = n/n_0$, and coordinates $\tau = t\sqrt{q_0}/x_0$, $\xi = x/x_0$, $\eta = r/x_0$, where x_0 is the characteristic dimension of the problem which will be defined below.

For rarefied suspensions in gas (these will be precisely investigated later on) the number of the governing parameters in the problem (1)–(4) is reduced to four. Actually, at low volume fractions ($\alpha_{20} \ll 1$) but for a finite concentration of particle (ρ_{20}), by choosing (similar to [4]) the characteristic dimension of the problem (1)–(4) as $x_0 = d_0^2 \rho_2^0 \sqrt{q_0}/18\mu_{10}$, one can demonstrate that the

dimensionless solution is governed (with the accuracy $O(\alpha_{20})$) only by four dimensionless combinations:

$$K = \frac{\rho_{20} d_0 \sqrt{q_0}}{18 \mu_{10}}$$

$$Y_{10} = \frac{\rho_{10}}{\rho_{10} + \rho_{20}}$$

$$\eta_c = \frac{r_c}{x_0}$$

$$L = \frac{\Delta r}{r_c}$$

(6)

where L is the relative thickness of the suspension layer in the channel. At $L = 1$, one obtains the one-dimensional problem on the reaction zone structure of the ideal CJ detonation in the gas suspension. At $L = 0$ one obtains the one-dimensional problem on the planar shock attenuation with the solution depending solely on two parameters: K and Y_{10}. Notice that at $Y_{10} \rightarrow 0$ the limiting transition to vacuum-suspensions is achieved.

The problem (1)–(4) was solved numerically. The velocity and gas-dynamic structure of the self-sustaining non-ideal DW in the channel partially filled with the HE-particle suspension was found by the method of transition to a steady state. To integrate the system of equations governing the gas flow, the second order Godunov–Kolgan scheme with moving grids [7, 8], capable of capturing the leading shock front, was used. The equations governing the HE-particle motion are solved by the method of large particles [9]. The accuracy of solution of Eqs. (1) is controlled by the value of imbalance in the integral laws of mass and energy conservation. In all calculations, this value does not exceed one percent.

CALCULATION RESULTS

The numerical investigations were performed for the volatile secondary HE particles, RDX, having the following thermodynamic phase parameters [10–12]: $\rho_2^0 = 1820$ kg/m^3, $T_0 = 300$ K, $c_2 = 1600$ J/(kg·K), $T_s = 613$ K, $l_2 = 0.49$ MJ/kg, $q_0 = 4.4$ MJ/kg, $c_1 = 1800$ J/(kg·K), $\mu_{10} = 1.6 \cdot 10^{-5}$ kg/(m·s), $\lambda_{10} = 4.5 \cdot 10^{-2}$ W/(m·K), $\gamma = 1.25$, $D_{CJ}^0 = 2340$ m/s. When solving the two-dimensional non-stationary problem (1)–(4) at a fixed value of $K = 316$, all the dimensionless governing parameters (Y_{10}, η_c, and L) were variable.

First, consider the effect of the channel radius η_c and the thickness of the layer of the two-phase medium L on the detonation dynamics at a fixed value of $Y_{10} = 1/2$. The x-dependence of the DW front velocity near the wall ($\eta = \eta_c$) is
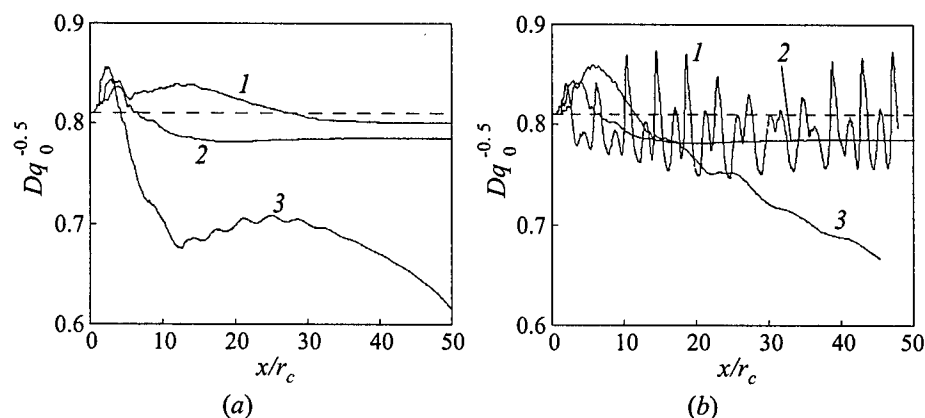
Figure 1 The x-dependence of the DW velocity front near the channel wall. (a) $\eta_c = 0.02$; L: $1 - 3/4$; $2 - 1/2$; $3 - 1/4$; (b) $L = 1/2$; η_c: $1 - 0.04$; $2 - 0.02$; $3 - 0.01$. The dashed line corresponds to the CJ detonation velocity in RDX–particle suspention

shown in Fig. 1. At the initial stage of the test (until the acoustic disturbance from the boundary of the two-phase medium reaches the channel wall), the front velocity is constant and equal to that of the ideal CJ detonation, D_{CJ}, in a gas suspension. At $Y_{10} = 1/2$ for RDX particles, $D_{CJ} = 1730$ m/s (a dashed line in Fig. 1). From this figure, one notices that the non-stationary DW (at a distance of a few channel radii) propagates in the overdriven mode until its velocity becomes less than D_{CJ}. Further behavior of D depends on the governing parameters η_c and L. At certain values of η_c and L, the non-stationary DW (at distances of 20–40 channel radii) reaches the self-sustaining detonation mode with either constant velocity $D_{st} = D(\eta_c, L) < D_{CJ}$ (curves 1 and 2 in Fig. 1a) or periodical pulsating velocity (curve 1 in Fig. 1b). The calculations showed that there exist geometric limits of detonation, i.e. such critical values of the layer thickness L^* and the channel radius η_c^*, that at $L < L^*$ or $\eta_c < \eta_c^*$ a "break-down" is observed and the DW decays (curves 3 in Fig. 1a and b).

Table 1 Calculated detonation velocities D_{st}/D_{CJ} depending on η_c and L

$\dfrac{\eta_c}{L}$	1	$\dfrac{3}{4}$	$\dfrac{1}{2}$	$\dfrac{1}{4}$
0.01	1	×	×	×
0.02	1	0.988	0.968	×
0.04	1	0.995*	0.973*	0.85*

*The detonation mode of type II.

Thus, at given values of governing parameters, two types of self-sustaining detonation modes were found in the cylindrical channel partially filled with the RDX particles: type I involving the stable wave structure, and type II involving the unstable (pulsating) structure. The calculated detonation velocities D_{st}/D_{CJ} for a number of values of η_c and L are given in Table 1. At $Y_{10} = 1/2$, the
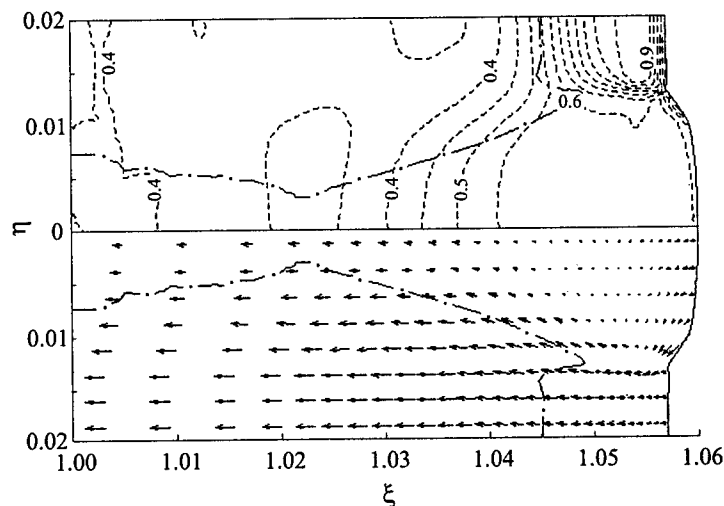
Figure 2 The pressure distribution (upper part) and the velocity field (lower part) in the reaction zone of DW having a stable flow structure

DW velocity in the channel is lower than the D_{CJ} velocity regardless of the type of wave structure. In this case, the DW velocity decreases with decreasing particle layer thickness. Unfilled positions in Table 1 correspond to the "break-down" of detonation at the given values of η_c and L.

Let us analyze the structure of the two-dimensional DW reaction zone for the type I modes. Isobars P (the upper part of Fig. 2) and the velocity vector field in a gas phase in the coordinate system that is attached to the wave front (the lower part of Fig. 2) in the reaction zone of DW propagating at the constant velocity $D_{st}/D_{CJ} = 0.968$ at $\eta_c = 0.02$, $L = 1/2$, are shown in Fig. 2. The dot-and-dash line marks the acoustic line (the isoline of Mach number $M = 1$) separating the subsonic and supersonic solution regions. It is seen from the figure that the gasdynamic flow pattern in the cylindrical channel is essentially two-dimensional. The shock front passing through the two-phase medium is rectilinear over the length of one third of the channel radius and then it arches in the direction of wave propagation. Combustion of HE particles in the reaction zone of gas suspension results in a pressure rise (a maximum pressure $P_{max} = 0.95$ is attained near the channel wall at a distance of $\sim 0.1 r_c$ from the front), and then gaseous products expand laterally from the combustion zone towards the channel axis. The straight acoustic line near the channel wall is normal to the incident gas flow and is located at $\sim 0.6 r_c$ from the shock front. It follows from the calculations that a small portion of the RDX particles ($\sim 6\%$) burns out in the supersonic
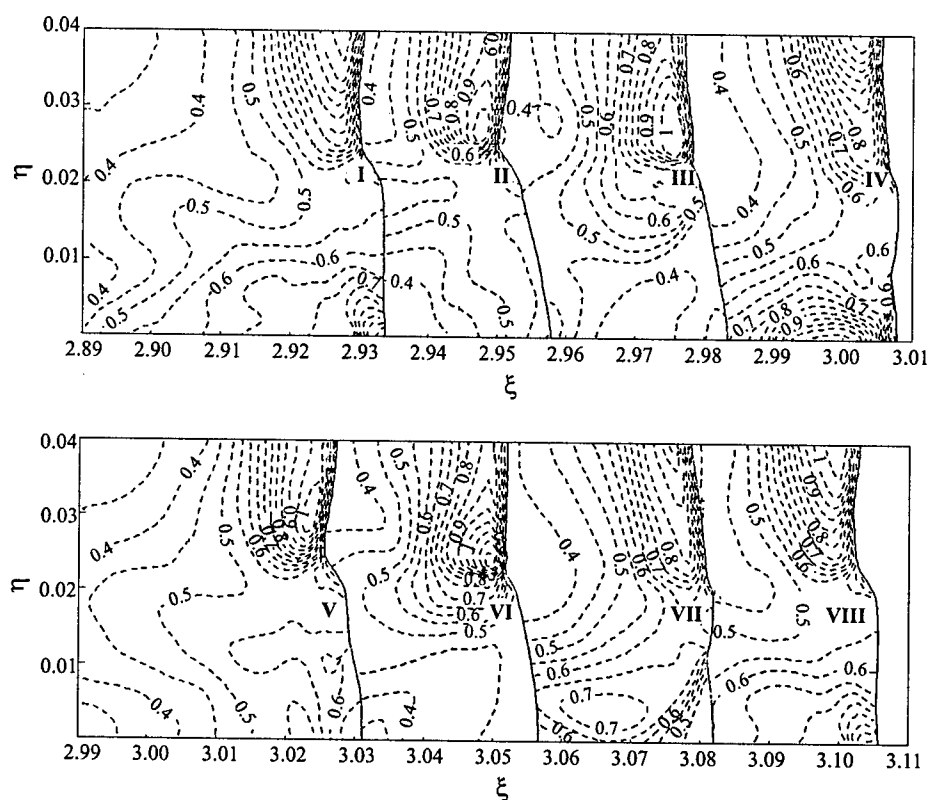
Figure 3 The evolution of pressure distribution in the reaction zone of the pulsating DW during one-seventh of the pulsation period. The wave propagates from left to right from position I to VIII

zone. At $\eta < 0.013$, the acoustic line recedes from the leading front and merges with the symmetry axis at a distance of $\sim 30r_c$. Note that the Mach number of the axial gas flow M $= 0.985$ is attained at a distance of $\sim 2.5r_c$ from the shock front at the point where the acoustic line approaches the symmetry axis. The velocity field in the gas phase indicates that stationary heterogeneous DW of type I is the channel wave exibiting a classic "flow-type" structure. That is to say, the gas coming through the shock front into the axial channel region at a subsonic velocity is first compressed by the products of HE-particle combustion, and then accelerates and flows out through the center at a supersonic velocity. As it will be seen later, it is not always the case that the gas phase flows through the axial channel region.

Let us analyze the two-dimensional DW structure of type II. The velocity behavior near the channel wall for a pulsating DW at $\eta_c = 0.04$ and $L = 1/2$

is shown in Fig. 1b (curve 1). Longitudinal pulsations in the velocity of the wave leading front during the period $\sim 4.3r_c$ are caused by lateral pressure pulsations in the channel. The last statement follows from the analysis of the evolution of pressure distribution in the DW reaction zone for one seventh of the pulsation period (Fig. 3). It is evident from the figure that lateral pulsations of gas-dynamic parameters are due to reflection of the compression wave not only from the axis and channel walls but also from the boundary with the two-phase medium. When superimposing the two vibrations, the pulse amplitude beats of the front velocity are clearly observed. In this case the beats are more pronounced on the centerline of the channel rather than on the wall. It appears from the calculations that if the channel radius is larger than two lengths of the reaction zone for the one-dimensional CJ wave ($r_c > 2l_{CJ}$), unstable (pulsating) detonation modes of type II are generated in the channel.
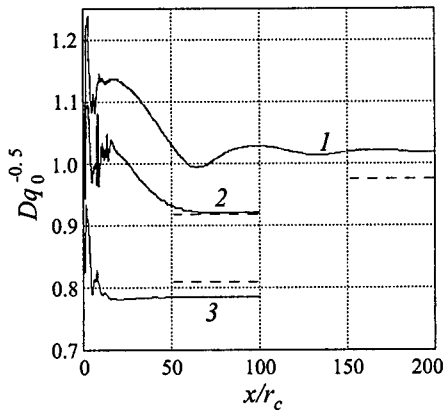
Let us consider the effect of the initial mass fraction of the gas phase Y_{10} on the detonation dynamics at constant values of $\eta_c = 0.02$ and $L = 1/2$. The dependence of the DW front propagation velocity along the centerline of the channel ($\eta = 0$) on the passed distance is shown in Fig. 4. For the sake of comparison, the ideal detonation velocities D_{CJ} are presented by the dashed lines. With a decrease in the initial gas pressure (a decrease in Y_{10}) the non-stationary DW velocity increases at the early stage, and attains the stationary value D_{st} at a later stage. The calculated velocities of the ideal detonation, D_{CJ} (Eq. (6)) and the non-ideal detonation, D_{st}, as well as the distance of attaining the stationary mode, x_{st}, depending on the initial mass fraction of the gas phase, are given in Table 2. It is worth noting that at $Y_{10} \leq 1/3$ the heterogeneous DW may propagate in the cylindrical channel in the undercompressed mode.

Figure 4 The x-dependence of the DW front velocity along the centerline of the channel for a number of Y_{10} values: 1 — $1/4$; 2 — $1/3$; 3 — $1/2$

Figure 5a shows the velocity vector field and isobars of the gas phase in the reaction zone of the stationary DW ($Y_{10} = 1/3$) using the same notations as in Fig. 2. Here, the shock front is considerably curved and stretched ($\sim 0.7r_c$) along the direction of detonation propagation. At the center of the channel, a stationary subsonic zone occurs (the acoustic line is closed and goes into the shock front) of longitudinal size $\sim 2.6r_c$. Observed in the subsonic zone are the maximum pressure domain in the two-phase medium and two maximum pressure

Table 2 Calculated parameters of ideal and non-ideal detonations depending on the gas phase mass fraction

Y_{10}	D_{CJ}, m/s	$\dfrac{D_{st}}{D_{CJ}}$	$\dfrac{x_{st}}{r_c}$	$\dfrac{l_z}{r_c}$	$\dfrac{l_w}{r_c}$	$\dfrac{r_w}{r_c}$
$\dfrac{1}{2}$	1730	0.968	50	—	—	—
$\dfrac{1}{3}$	1962	1.003	70	2.60	1.56	0.53
$\dfrac{1}{4}$	2085	1.045	160	3.05	1.78	0.53

domains in the gas at the channel centerline. The velocity field of the gas phase allows one to argue that the stationary vortex of combustion products of RDX particles is generated in the wave structure. In this case, the gas coming through the shock front into the center of the channel is forced to flow around a gas vortex moving away from the symmetry axis to a near-wall region. A similar stationary vortex structure of the reaction zone is observed at $Y_{10} = 1/4$ (Fig. 5b). The detonation modes involving the vortex wave structure will be referred to as the modes of type III. The corresponding values of lengths of the subsonic zone (l_z) and the vortex (l_w) along the channel centerline, as well as the normal coordinate of the vortex center (r_w) are also given in Table 2. The values of l_z and l_w increase with decreasing initial mass fraction of gas. The values of r_w are virtually unchanged and equal approximately to one-half of the channel radius.

Thus, the numerical simulation of non-ideal heterogeneous detonation in the cylindrical channel partially filled with the HE-particle suspension demonstrated, for the first time, that the self-sustaining stationary DW with a vortex structure is generated in the channel over a certain range of governing parameters ($Y_{10} \leq 1/3$). A vortex of hot gaseous products, flowing around HE particles incoming into the zone, promotes particles to warm up and ignite. In other words, by decreasing the initial gas pressure p_0 (decreasing Y_{10}) the transition occurs from shock-induced to convective mechanism of HE particles ignition. The latter is realized as a vortex of hot products in the structure of the DW reaction zone.

CONCLUDING REMARKS

This paper is concerned with the numerical study of heterogeneous detonation in an annular layer of the HE-particle suspension adjacent to the cylindrical channel wall. The study was performed using the model of a two-phase, double-velocity, double-temperature medium. The following results were obtained:
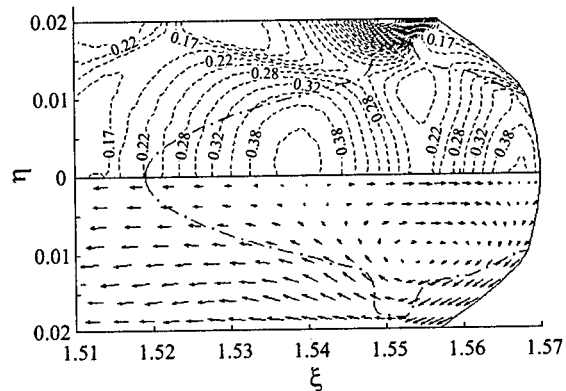
(a)
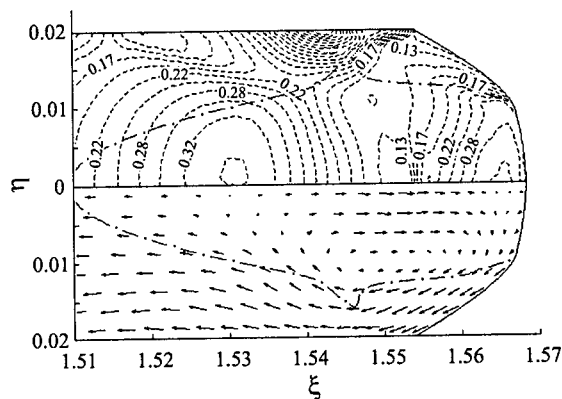
(b)

Figure 5 The pressure distribution (upper part) and the velocity vector field (lower part) in the reaction zone of DW exhibiting a stable vortex structure. (a) $Y_{10} = 1.3$; (b) $Y_{10} = 1.4$

(1) three types of spatial structures of the two-dimensional reaction zone were revealed for DW in RDX-particle suspension in gas, namely, the stable "flow-type," unstable (pulsating), and stable vortex structures;

(2) it was found that with decreasing the initial gas pressure, the transition occurs from shock-induced to convective mechanism of HE-particle ignition. The latter was achieved in a stationary vortex of hot combustion products in the DW reaction zone.

361

ACKNOWLEDGMENTS

REFERENCES

1. Nigmatulin, R. I., *Dynamics of Multiphase Media*. Part 1, Hemisphere Publ., New York, 1991.

2. Medvedev, A. E., Fedorov, A. V., and Fomin, V. M., Structure of a Heterogeneous Detonation Wave in Gas Suspensions, Preprint No. 36-86, Institute for Theoretical and Applied Mechanics, Siberian Branch of the USSR Academy Sci., Novosibirsk, 1986.

3. Eidelman, Sh., and Yang, X., "Detonation Wave Propagation in Combustible Mixtures with Variable Particle Density Distributions," In: *Dynamic Aspects of Explosion Phenomena*. (Eds. A. L. Kuhl *et al.*), Progress in Astronautics and Aeronautics Ser., **154**, 1993, 228–251.

4. Zhdan, S. A., and Prokhorov, E. S., "Free Charge Detonation of an Unitary-Fuel Dust Suspension in Vacuum," *Rus. J. Physics Combustion Explosion*, **32**, 3, 86–94, 1996.

5. Henderson, C. B., "Drag Coefficient of Spheres in Continuum and Rarefied Flows," *AIAA J.*, **14**, 707–708, 1976.

6. Mitrofanov, V. V., *Detonation Waves in Heterogeneous Media*. Novosibirsk State University Publ., Novosibirsk, 1988.

7. S. K. Godunov Ed. *Numerical Solution of Multidimensional Gas-Dynamics Problems*. Nauka, Moscow, 1976.

8. Kolgan, V. P., "The Application of a Minimum Principle for Derivative Values in Constructing Finite Difference Schemes for Calculations of Discontinuous Solutions in the Gas Dynamics," *Sci. Proc. CASI*, **3**, 6, 68–77, 1972.

9. Korobeinikov, V. P., Markov, V. V., and Men'shov, I. S., "Numerical Modeling of Shock Wave Propagation in Non-Uniform Dust–Gas Mixture," *Sov. J. Doklady USSR Academy Sci.*, **290**, 4, 816–819, 1986.

10. Andreev, K. K., *Thermal Decomposition and Combustion of Explosives*. Nauka, Moscow, 1966.

11. Belyaev, A. F., *Combustion, Detonation, and Work of an Explosion of Condensed Systems*. Nauka, Moscow, 1968.

12. Sichel, M., Baek, S. M., Kauffman, C. W., *et al.*, "The Shock Wave Ignition of Dusts," *AIAA J.*, **23**, 1375–1380, 1985.

CONCLUDING REMARKS: NEW FRONTIERS IN DETONATION RESEARCH

G. D. Roy

Of the three fundamental combustion phenomena — deflagration, explosion and detonation — both deflagration and explosion have been widely exploited in commercial, civilian and military applications. Extensive research has been undertaken over several decades on the fundamental theory and the mechanisms involved in detonation, and one can find extensive information in literature. However, practical applications have not emerged to the extent detonation phenomena warrant. This is partly due the fact that the science and technology is very complex, due to the intense and fast energy release rates, and their interaction with the confinement prescribed by the application. However, another factor that prevented the transition of detonation science to technology has been the lack of decisive demand for devices based on detonation phenomena. The climate has changed in both of these areas. In order to understand and control detonation wave propagation in confined geometry, measurements have to be taken with very high spatial and temporal resolution, which are possible now. Recent advances in computational combustion dynamics and the capability of modern computers, make it possible to perform meaningful computations, parametric studies, and scale-up. Further, the evolution of micro-electromechanical systems enable advanced control strategies. With the increasing emphasis in cost and economic fuel usage, simple and thermodynamically more efficient engines are receiving added attention.

Pulse Detonation Engine (PDE) concept has been successfully demonstrated for drilling application [1]. Utilization of PDE for propulsion and stationary engines has not received a focussed attention from the research community until the last couple of years. PDE in principle can provide higher efficiency and performance over a wide operating range, with fewer moving parts. In a PDE, detonation is initiated in a tube that serves as the combustor. The detonation wave rapidly traverses the chamber resulting in a nearly constant volume heat addition process that produces a high pressure in the combustor and provides the thrust. This near-constant volume cycle provides the edge in the thermodynamic cycle efficiency as compared to conventional Brayton (constant pressure) cycle [2]. The operation of multi-tube configurations at high frequencies (> 100 Hz) can produce a near-constant thrust.

The positive attributes to PDE for propulsion engines are simplicity and easy scaling, which will result in lower development time and cost, subsonic to supersonic operation with a single engine without booster to bring up to ram speed, and reduced fuel consumption resulting in increased range for the same fuel tank volume. From the size considerations, the fuels of choice should be liquids. The most striking advantage for stationary power plant engines is the fuel efficiency that will result in reduced operational cost and consequently the cost of electricity.

Conventional hydrocarbon fuels such as JP-10 are difficult to detonate by direct injection in air. Oxygen enrichment, premixing or predetonation chamber are penalties since they increase the total weight and volume of the PDE. Various methodologies are proposed, which include multi-fuel blends and distributed injection [3], a tailored configuration rather than a circular tube [4], electrical enhancement of detonation [5], etc. An alternate approach would be to seek fuels that could be detonated easily by direct injection into the oxidant. Strained liquid hydrocarbon fuels offer potential due to strained molecular structure, where the molecular bond can be broken with less initiation energy, while offering enhanced microexplosion characteristics [6]. As the PDE system becomes complex, ingenious packaging is necessary, particularly for air-borne application. In a multi-tube configuration, one tube can be the predetonator, and the number of tubes can be varied as dictated by thrust requirements. However total system studies are essential to assess the effect of geometric configuration and other parameters on operational performance, such as thrust and maneuverability. The ultimate choice will depend upon the particular application and priorities (For example, a variable cross-section detonation tube may improve performance, but will be more complex and difficult to package). There is more flexibility for stationary application.

Several fundamental issues still remain to be addressed. The complex physical, chemical and thermodynamic phenomena associated with gaseous and liquid phase injection, mixing and ignition, those which influence rapid development of planar detonation waves, and the role of transverse waves in the detonation process, are to be revisited in the context of PDE. Understanding of the dynamic coupling between multi-tube detonation chambers, and the efficient integration of PDE with mixed compression supersonic inlets and high performance exhaust nozzles are required. Knowledge of adaptive, active control to ensure optimal performance while maintaining margin of stability is needed.

A number of research and development programs world wide are addressing the various issues, and focussed research initiatives are also underway [2]. In order to stay competitive and promote a new technology, the old paradigm of conducting research, transferring research findings to development, further to prototype demonstration, and then to a product should change. Though the various phases in the development of a new product require different time scales, in the new paradigm, these should be integrated and occur simultaneously with

continuous feedback and dialogue. More than ever, team work and international cooperative efforts are required to bring the concept of PDE to a practical reality.

The International Colloquium on Advances in Experimentation and Computation of Detonations has been a first active step to promote this awareness, and to provide an opportunity for researchers to have a dialogue established. In Russia, a number of goal-oriented research projects are sponsored by the Russian Foundation for Basic Research. In the U.S. the Office of Naval Research has initiated a Multidisciplinary University Research Initiative focussing on detonation phenomena for propulsion. Industries in the U.S. and Europe are investing in the development of PDEs. International cooperation has been stressed in the panel discussion at the Colloquium. With a well-planned, integrated research and development effort, it would be possible to utilize detonation phenomena for propulsion and stationary engines of the future.

REFERENCES

1. Smirnov, N. N., Nikitin, V. F., Boichenko, A. P., Tyurnikov, M. V., and Baskakov, V. V., "Deflagration to Detonation Transition in Gases and its Application to Pulsed Detonation Devices," In: *Gaseous and Heterogeneous Detonations: Science to Applications.* (Eds. G. D. Roy, S. M. Frolov, K. Kailasanath, and N. N. Smirnov), ENAS Publ., Moscow, 1999, 65–94.

2. Roy, G. D., "Pulsed Detonation Engines for Propulsion," *Proc. 2nd Asia-Pacific Conference on Combustion*, Tainan, Taiwan, 1999.

3. Frolov, S. M., Basevich, V. Ya, Belyaev, A. A., and Neuhaus, M. G., "Application of Fuel Blends for Controlling Detonability in Pulsed Detonation Engines," In: *Gaseous and Heterogeneous Detonations: Science to Applications.* (Eds. G. D. Roy, S. M. Frolov, K. Kailasanath, and N. N. Smirnov), ENAS Publ., Moscow, 1999, 313–330.

4. Baklanov, D. I., Gvozdeva, L. G., and Scherbak, N. B., "Formation of High-Speed Gas Flow at Combustion in the Regime of Multi-Step Detonation," In: *Gaseous and Heterogeneous Detonations: Science to Applications.* (Eds. G. D. Roy, S. M. Frolov, K. Kailasanath, and N. N. Smirnov), ENAS Publ., Moscow, 1999, 141–152.

5. Afanas'ev, V. V., Ilyin, S. V., Tarasov, N. A., Kuzmin, A. K., and Kidin, N. I., "On Detonation Control in Ducts by Electric Discharges," In: *Advances in Experimentation & Computation of Detonations. Book of Abstracts.* (Eds. G. D. Roy, S. M. Frolov, K. Kailasanath, and N. N. Smirnov), Moscow, ENAS Publ., 1998, 84.

6. Roy, G. D., "High Density Strained Hydrocarbon Fuels for Propulsion: Opportunities and Challenges," *Proc. 2nd Symposium (International) on Advanced Energy Conversion Systems and Related Technologies*, Nagoya, Japan, 1998.